MARTIN MARIETTA ENERGY SYSTEMS LIBRARIES
3 4456 0350969 2

ornl

ORNL/TM-11984

OAK RIDGE NATIONAL LABORATORY

MARTIN MARIETTA

Ceramic Technology Project Semiannual Progress Report for April 1991 Through September 1991

Prepared for
U.S. Department of Energy
Assistant Secretary for
Conservation and Renewable Energy
Office of Transportation Technologies
Materials Development Program

CERAMIC TECHNOLOGY FOR ADVANCED HEAT ENGINES

OAK RIDGE NATIONAL LABORATORY
CENTRAL RESEARCH LIBRARY
CIRCULATION SECTION
4500N ROOM 175
LIBRARY LOAN COPY
DO NOT TRANSFER TO ANOTHER PERSON
If you wish someone else to see this report, send in name with report and the library will arrange a loan.
UCN-7969 (3 9-77)

MANAGED BY
MARTIN MARIETTA ENERGY SYSTEMS, INC.
FOR THE UNITED STATES
DEPARTMENT OF ENERGY

This report has been reproduced directly from the best available copy.

Available to DOE and DOE contractors from the Office of Scientific and Technical Information, P.O. Box 62, Oak Ridge, TN 37831; prices available from (615) 576-8401, FTS 626-8401.

Available to the public from the National Technical Information Service, U.S. Department of Commerce, 5285 Port Royal Rd., Springfield, VA 22161.

This report was prepared as an account of work sponsored by an agency of the United States Government. Neither the United States Government nor any agency thereof, nor any of their employees, makes any warranty, express or implied, or assumes any legal liability or responsibility for the accuracy, completeness, or usefulness of any information, apparatus, product, or process disclosed, or represents that its use would not infringe privately owned rights. Reference herein to any specific commercial product, process, or service by trade name, trademark, manufacturer, or otherwise, does not necessarily constitute or imply its endorsement, recommendation, or favoring by the United States Government or any agency thereof. The views and opinions of authors expressed herein do not necessarily state or reflect those of the United States Government or any agency thereof.

ORNL/TM-11984

Metals and Ceramics Division

CERAMIC TECHNOLOGY PROJECT SEMIANNUAL PROGRESS REPORT FOR APRIL 1991 THROUGH SEPTEMBER 1991

D. R. Johnson
Project Manager

Date Published: March 1992

NOTICE: This document contains information of a preliminary nature. It is subject to revision or correction and therefore does not represent a final report.

Prepared for
U.S. Department of Energy
Assistant Secretary for Conservation and Renewable Energy
Office of Transportation Technologies
Materials Development Program
EE 51 01 00 0

Prepared by the
OAK RIDGE NATIONAL LABORATORY
Oak Ridge, Tennessee 37831-6285
managed by
MARTIN MARIETTA ENERGY SYSTEMS, INC.
for the
U.S. DEPARTMENT OF ENERGY
under Contract DE-AC05-840R21400

MARTIN MARIETTA ENERGY SYSTEMS LIBRARIES
3 4456 0350969 2

REPORTS PREVIOUSLY ISSUED

ORNL/TM-9325	Period March 1983-September 1983
ORNL/TM-9466	Period October 1983-March 1984
ORNL/TM-9497	Period April 1984-September 1984
ORNL/TM-9673	Period October 1984-March 1985
ORNL/lM-9947	Period April 1985-September 1985
ORNL/TM-10079	Period October 1985-March 1986
ORNL/TM-10308	Period April 1986-September 1986
ORNL/TM-10469	Period October 1986-March 1987
ORNL/TM-10705	Period April 1987-September 1987
ORNL/TM-10838	Period October 1987-March 1988
ORNL/TM-11116	Period April 1988-September 1988
ORNL/TM-11239	Period October 1988-March 1989
ORNL/TM-11489	Period April 1989-September 1989
ORNL/TM-11586	Period October 1989-March 1990
ORNL/TM-11719	Period April 1990-September 1990
ORNL/TM-11859	Period October 1990-March 1991

Research sponsored by the U.S. Department of Energy, Assistant Secretary for Conservation and Renewable Energy, Office of Transportation Technologies, as part of the Ceramic Technology Project of the Materials Development Program, under contract DE-AC05-84OR21400 with Martin Marietta Energy Systems, Inc.

CONTENTS

SUMMARY 1

0.0 PROJECT MANAGEMENT AND COORDINATION 3

1.0 MATERIALS AND PROCESSING 5

INTRODUCTION 5

1.1 MONOLITHICS 7

1.1.1 Silicon Carbide 7

High Temperature Hexoloy SX Silicon Carbide (Carborundum) 7

Improved Processing of Ceramic Composites (Southern Illinois University) 13

1.1.2 Silicon Nitride 22

Sintered Silicon Nitride (AMTL) 22

Microwave Sintering of Silicon Nitride (ORNL) . . . 27

Characterization of Attrition Milled Silicon Nitride Powder (NIST) 34

Scalability Demonstration Program for Silicon Nitride by the Sullivan Process (Sullivan) 39

1.1.4 Processing of Monolithics 44

Improved Processing (Norton) 44

Improved Processing (ORNL) 79

Processing Science for Si_3N_4 Ceramics (University of California) 81

1.2 CERAMIC COMPOSITES 89

1.2.2 Silicon Nitride Matrix 89

In-Situ Toughened Silicon Nitride (GCCD) 89

Optimization of High-Temperature Properties of Silicon Nitride Ceramics (University of Michigan) 102

Characterization of Grain Boundary Phase in Silicon Nitride Ceramics (University of Michigan) 105

Fabrication of SiC-AlN Composites (University of Michigan) 109

Optimization of Silicon Nitride Ceramics (University of Michigan) 112

1.2.3 Oxide Matrix 115

Dispersion-Toughened Ceramic Composite (ORNL) . . . 115

1.2.4 Silicate Matrix 139

Low Expansion Ceramics for Diesel Engine Applications (VPI) 139

1.3 THERMAL AND WEAR COATINGS 153

Fabrication and Testing of Corrosion-Resistant Coatings (ORNL) 153

Development of Adherent Ceramic Coatings to Reduce Contact Stress Damage of Ceramics (GTE) 156

Wear-Resistant Coatings (Caterpillar) 183

1.4 JOINING 193

1.4.1 Ceramic-Metal Joints 193

Joining of Ceramics for Heat Engine Applications (ORNL) 193

Analytical and Experimental Evaluation of Joining Silicon Nitride to Metal and Silicon Carbide to Metal for Advanced Heat Engine Applications (GTE) 198

2.0 MATERIALS DESIGN METHODOLOGY 215

INTRODUCTION 215

2.1 MODELING 217

2.1.1 Modeling 217

Microstructural Modeling of Cracks (University of Tennessee) 217

2.2 CONTACT INTERFACES 220

2.2.1 Static Interfaces 220

Elastic Properties and Adherence of Thin Films and Coatings (University of Tennessee) 220

2.2.2 Dynamic Interfaces 222

Studies of Dynamic Contact of Ceramics and Alloys for Advanced Heat Engines (Battelle) 222

Development of Standard Test Methods for Evaluating the Wear Performance of Ceramics (ORNL) 230

2.3 NEW CONCEPTS 233

Advanced Statistical Concepts of Fracture in Brittle Materials (GE) 233

3.0 DATA BASE AND LIFE PREDICTION 239

INTRODUCTION 239

3.1 STRUCTURAL QUALIFICATION 241

Microstructural Analysis of Structural Ceramics (NIST) 241

Mechanical Properties and Microstructural Characterization of Si_3N_4 Ceramics (ORNL) 247

Project Data Base (ORNL) 257

3.2 TIME-DEPENDENT BEHAVIOR 261

Characterization of Toughened Ceramics (AMTL) . . . 261

Fracture Behavior of Toughened Ceramics (ORNL) . . 265

Cyclic Fatigue of Toughened Ceramics (ORNL) 271

Rotor Data Base Generation (ORNL) 297

Toughened Ceramics Life Prediction (NASA Lewis Research Center) 305

Life Prediction Methodology (Allison) 320

Life Prediction Methodology (GAPD) 330

3.3 ENVIRONMENTAL EFFECTS 345

Environmental Effects in Toughened Ceramics (University of Dayton) 345

3.4 FRACTURE MECHANICS 362

Testing and Evaluation of Advanced Ceramics at High Temperature in Uniaxial Tension (North Carolina A&T State University) 362

Standard Tensile Test Development (NIST) 369

Development of a Fracture Toughness Microprobe (Rice University) 379

3.5 NONDESTRUCTIVE EVALUATION DEVELOPMENT 387

Nondestructive Characterization (ORNL) 387

NDE Standards for Advanced Ceramics (ORNL) 398

X-ray Computed Tomographic Imaging (ANL) 399

Nuclear Magnetic Resonance Imaging (ANL) 408

Physicochemical Characterization and Surface Modification of Silicon Nitride Ceramic Powders (University of Wisconsin-Madison) 413

Surface Adsorption (University of Florida) 416

Physicochemical Characterization and Surface Modification of Silicon Nitride Ceramic Powders (Rutgers University) 421

4.0 TECHNOLOGY TRANSFER 439

4.1 TECHNOLOGY TRANSFER 439

4.1.1 Technology Transfer 439

Technology Transfer (ORNL) 439

IEA Annex II Management (ORNL) 440

Characterization of Ceramic Powders (NIST) 446

Ceramic Mechanical Property Test Method Development (NIST) 450

CERAMIC TECHNOLOGY PROJECT SEMIANNUAL PROGRESS REPORT FOR APRIL 1991 THROUGH SEPTEMBER 1991

SUMMARY

The Ceramic Technology Project was developed by the Department of Energy's Office of Transportation Systems (OTS) in Conservation and Renewable Energy. This project, part of the OTS's Materials Development Program, was developed to meet the ceramic technology requirements of the OTS's automotive technology programs.

Significant accomplishments in fabricating ceramic components for the Department of Energy (DOE), National Aeronautics and Space Administration (NASA), and Department of Defense (DoD) advanced heat engine programs have provided evidence that the operation of ceramic parts in high-temperature engine environments is feasible. However, these programs have also demonstrated that additional research is needed in materials and processing development, design methodology, and data base and life prediction before industry will have a sufficient technology base from which to produce reliable cost-effective ceramic engine components commercially.

An assessment of needs was completed, and a five-year project plan was developed with extensive input from private industry. In July 1990 the original plan was updated through the estimated completion of development in 1993. The objective of the project is to develop the industrial technology base required for reliable ceramics for application in advanced automotive heat engines. The project approach includes determining the mechanisms controlling reliability, improving processes for fabricating existing ceramics, developing new materials with increased reliability, and testing these materials in simulated engine environments to confirm reliability. Although this is a generic materials project, the focus is on the structural ceramics for advanced gas turbine and diesel engines, ceramic bearings and attachments, and ceramic coatings for thermal barrier and wear applications in these engines. This advanced materials technology is being developed in parallel and close coordination with the ongoing DOE and industry proof-of-concept engine development programs. To facilitate the rapid transfer of this technology to U.S. industry, the major portion of the work is being done in the ceramic industry, with technological support from government laboratories, other industrial laboratories, and universities.

This project is managed by ORNL for the Office of Transportation Technologies, Office of Transportation Materials, and is closely coordinated with complementary ceramics tasks funded by other DOE offices, NASA, DoD, and industry. A joint DOE and NASA technical plan has been established, with DOE focus on automotive applications and NASA focus on aerospace applications. A common work breakdown structure (WBS) was developed to facilitate coordination. The work described in this report is organized according to the following WBS project elements:

0.0 Management and Coordination

1.0 Materials and Processing

- 1.1 Monolithics
- 1.2 Ceramic Composites
- 1.3 Thermal and Wear Coatings
- 1.4 Joining

2.0 Materials Design Methodology

- 2.1 Modeling
- 2.2 Contact Interfaces
- 2.3 New Concepts

3.0 Data Base and Life Prediction

- 3.1 Structural Qualification
- 3.2 Time-Dependent Behavior
- 3.3 Environmental Effects
- 3.4 Fracture Mechanics
- 3.5 Nondestructive Evaluation Development

4.0 Technology Transfer

- 4.1 Technology Transfer

This report includes contributions from all currently active project participants. The contributions are arranged according to the work breakdown structure outline.

0.0 PROJECT MANAGEMENT AND COORDINATION

D. R. Johnson
Oak Ridge National Laboratory

Objective/scope

This task includes the technical management of the project in accordance with the project plans and management plan approved by the Department of Energy (DOE) Oak Ridge Field Office, and the Office of Transportation Technologies. This task includes preparation of annual field work proposals, initiation and management of subcontracts and interagency agreements, and management of ORNL technical tasks. Monthly management reports and bimonthly reports are provided to DOE; highlights and semiannual technical reports are provided to DOE and program participants. In addition, the program is coordinated with interfacing programs sponsored by other DOE offices and federal agencies, including the National Aeronautics and Space Administration (NASA) and the Department of Defense (DoD). This coordination is accomplished by participation in bimonthly DOE and NASA joint management meetings, annual interagency heat engine ceramics coordination meetings, DOE contractor coordination meetings, and DOE Energy Materials Coordinating Committee (EMaCC) meetings, as well as special coordination meetings.

1.0 MATERIALS AND PROCESSING

INTRODUCTION

This portion of the project is identified as project element 1.0 within the work breakdown structure (WBS). It contains four subelements: (1) Monolithics, (2) Ceramic Composites, (3) Thermal and Wear Coatings, and (4) Joining. Ceramic research conducted within the Monolithics subelement currently includes work activities on green state ceramic fabrication, characterization, and densification and on structural, mechanical, and physical properties of these ceramics. Research conducted within the Ceramic Composites subelement currently includes silicon carbide, silicon nitride, and oxide-based composites. Research conducted in the Thermal and Wear Coatings subelement is currently limited to oxide-base coatings and involves coating synthesis, characterization, and determination of the mechanical and physical properties of the coatings. Research conducted in the Joining subelement currently includes studies of processes to produce strong, stable joints between zirconia ceramics and iron-base alloys.

A major objective of the research in the Materials and Processing project element is to systematically advance the understanding of the relationships between ceramic raw materials such as powders and reactant gases, the processing variables involved in producing the ceramic materials, and the resultant microstructures and physical and mechanical properties of the ceramic materials. Success in meeting this objective will provide U.S. companies with new or improved ways for producing economical, highly reliable ceramic components for advanced heat engines.

1.1 MONOLITHICS

1.1.1 Silicon Carbide

High Temperature Hexoloy SX Silicon Carbide

K. Chia and G. V. Srinivasan (The Carborundum Company)

Introduction

Hexoloy® SA (a registered trademark of The Carborundum Company) silicon carbide, a pressureless sintered α-SiC, has shown excellent oxidation, corrosion, erosion and wear resistance. Its toughness and strength retention at elevated temperatures up to 1500°C in air also has been demonstrated. Powder availability, price competitiveness, and net shape forming capability make this SiC an attractive candidate for many structural applications. However, relatively low strength, primarily due to its low toughness, still represent limitations for some applications involving higher stresses, such as gasifier rotors in advanced gas turbine engines.

Approaches to enhance the fracture toughness and strength through the modification of microstructure and fracture characteristics of the material by the incorporation of appropriate sintering additives and variation of processing conditions have been considered. It is based on these philosophies that Carborundum had recently developed an improved SiC material, namely Hexoloy SX.

Hexoloy SX has been demonstrated to posses higher toughness and strength than Hexoloy SA. Its toughness is about 50% to 100% higher than that of SA and its typical room temperature MOR value ranges between 620-915 MPa (90-133 ksi). However, from the preliminary data available, it is found that Hexoloy SX retains only about 50%-70% of its room temperature strength at 1232°C. Although the reasons for this decrease are not fully established, it is believed that the high temperature mechanical properties can be improved via proper optimization of composition, powder selection and processing conditions.

Objective/scope

The approach taken for this work is to first establish a complete mechanical property database and conduct detailed microstructural characterization on the first generation SX material currently available. After that, the emphasis will then be focused on the selection of a best SiC powder source and the optimization of processing conditions for this first generation material via a systematic designed experimental method. In the meantime, a Carborundum in-house sponsored program with the objective of identifying a second generation additive composition with improved high temperature properties will also be conducted in parallel. Once this second generation composition is identified, the information will be fed into the current program. Then a second set of designed experiments will be conducted to optimize the properties of this second generation SX material. Finally, the complete property database will then be established for the second generation composition.

The three major objectives for the current program are as follows: (1) to establish property database and conduct detailed characterization for the current best SX material, (2) to improve the processing conditions of that material via a designed experimental method, and (3) to develop a second generation SX material with superior high temperature properties. To achieve these objectives, the work is split into six tasks:

Task	Objective	Duration
1	Complete Characterization of First Generation SX	April '91-Dec. '91
2	Selection of Powder Source	Aug. '91-Oct. '91
3	Property Optimization of First Generation SX	Nov. '91-April '92
4a	Property Optimization of Second Generation SX	May '92-Aug. '92
4b	Complete Characterization of Second Generation SX	Sep. '92-Nov. '92
5	Develop Improved Dispersion Technique	April '91-Oct. '91

From previous internal work at Carborundum, a particular composition of Hexoloy SX, SX-G1, with 2 wt% total additive, has shown excellent MOR strengths. Preliminary evaluation of its creep and dynamic fatigue resistance has also been encouraging. SX-G1 has therefore been chosen as the composition for the work to be conducted in Tasks 1, 2, 3, and 5 of this contract.

Technical highlights

- Three of the six SiC powder sources yielded densities in excess of 99% T.D. after over-pressure treatment.
- Powder with very high surface area was obtained by Turbomilling and the compacted green bodies yielded excellent green densities (66%).
- An unexpectedly low MOR strength problem was encountered in Task 1. This problem was corrected using in-house resources. Higher strength was obtained after modification of the sintering cycle.
- A revised schedule has been submitted.
- All tasks are on schedule per the revised plan.

Task 1 Objective: Complete Characterization of Generation I SX-SiC Material.

In this task, a complete mechanical and microstructural characterization is being conducted. Mechanical characterization includes MOR, tensile strength, and K_{1C} determinations at room and elevated temperatures; stress rupture, dynamic fatigue, and creep measurements at elevated temperatures. Microstructural characterization includes x-ray diffraction, quantitative image analysis, optical, scanning electron and Auger microscopies.

To prepare samples for such characterizations, two twenty pound batches of SiC powder from source A were mixed with sintering additives and spray

dried into soft flowable powder agglomerates. The powder was compacted into 63.5 mm square plates and subsequently isostatically pressed. The plates were pressureless sintered to a density of 3.09 gm/cc and then over-pressure treated to a density of 3.21 gm/cc, a value very close to the theoretical density of 3.217 gm/cc calculated by the rule of mixtures method.

These plates were cut into Mil Std 'B' MOR bars and tested at room temperature. A mean MOR of only 586 MPa (85 ksi) was obtained. This MOR value was substantially lower than mean MOR values of 758-917 MPa (110-133 ksi) obtained on samples with the same composition fabricated before program startup (Table 1). At this point work on Task 1 was temporarily put on hold until this problem could be corrected.

Fractography revealed that larger than usual volumetric flaws associated with pools of second phase were the predominant fracture origins. Work carried out under an internally funded program traced this problem to process variables. The original sintering temperature was determined to be slightly beyond the acceptable process window. This was further compounded by a scale-up effect related to sintering atmosphere. When these variables were adjusted, MOR testing of 75 test bars from three mixes gave average MORs in the 793-896 MPa range (113-130 ksi), consistent with the original data obtained before program startup (Table 2). As a result, work on Task 1 was resumed in August. A revised program schedule was submitted and has been approved.

Additional mixes were then prepared. New plates were sintered using the modified sintering conditions. About 200 Mil Std 'B' size bars were fabricated. Fifty rods of 23 mm in diameter and 210 mm in length were also sintered for tensile bar specimens. It was found that a slightly different sintering cycle had to be used to accommodate for the increased volume. The rods were then over-pressure treated to a density of >3.21 gm/cc. These rods have been sent to an outside vendor for machining into "ORNL Buttonhead" Tensile samples.

The machined MOR bars are being tested for MOR, K_{1C}, stress rupture, and dynamic fatigue. Tension tests are expected to commence in the beginning of November at HTML/ORNL.

Task 2 Objective: SiC Powder Selection.

SX-G1 mixes were made with SiC powders from 5 additional sources (B, C, D, E and F) with various particle size distributions and oxygen contents. The sintering and over-pressure treatment conditions were the same as those used in Task 1. Before the sintering experiments, particle size distribution (HORIBA) and surface area analysis (BET) were determined for all these SiC powders. The density values obtained along with the particle size and surface area data are summarized in Table 3. The plates made with SiC powders A, C, and F densified to >94% T.D. after pressureless sintering and >99% T.D. after over-pressure treatment. The plates made with SiC powder from source D did not densify adequately even after over-pressure treatment. The plates from other two powder sources yielded only moderate densities. Although all of these powders have a mean particle size of about 0.45 μm, their surface areas vary from 8.2 to 32.0 m^2/gm. It appears from these data that the densification is greatly influenced by surface area. However, powder chemistry may also play a role. The densified

Table 1. Room temperature MOR for SX-G1 SiC

	Task 1 Results 6/91	1/1990 Results	9/1990 Results
Density, gm/cc	3.21	3.21	3.21
Mean MOR, ksi	85 (586 MPa)	120 (827 MPa)	133 (917 MPa)
No Samples	20	12	10
MOR Range, ksi	50-107 (345-738 MPa)	85-143 (586-986 MPa)	101-155 (696-1069 MPa)

Table 2. Room temperature strength for new Task 1 SX-G1 samples sintered at modified schedule

Mix	1	2	3
Density, gm/cc	3.21	3.21	3.21
Mean MOR, ksi	120 (827 MPa)	130 (896 MPa)	113 (779 MPa)
No Samples	10	20	15
MOR Range, ksi	86-156 (593-1076 MPa)	101-146 (696-1007 MPa)	63-140 (434-965 MPa)

Table 3. Sinterability results for various SiC powders

				Density*	
SiC Powder Source	Surface Area	Median Particle Size μm	% Particles ≤ 1 μm	Pressureless Sintered gm/cc	Overpressure Treated gm/cc
A	17.1	0.45	99.3	3.088	3.210
B	9.3	0.45	78.1	2.937	3.063
C	16.3	0.44	92.2	3.024	3.185
D	11.7	0.43	82.0	2.937	3.082
E	8.2	0.48	70.9	2.525	2.779
F	32.0	0.44	99.9	3.120	3.210

*T.D. from rule of mixtures = 3.217 gm/cc.

plates have been sent for machining into Mil Std bars for MOR and K_{1c} evaluations. A best powder will then be selected based on densification and mechanical property results as well as powder availability and manufacturing considerations.

Task 5 Objective: Development of an Improved Dispersion Process.

There are three approaches being studied in parallel to improve mixing and dispersion. The first one is the use of nitrate and alkoxide chemical precursors as sintering aids. Three batches of mixes (mix 1a, 1b and 1c) were prepared with total additive levels of 2.0 w/o, 2.5 w/o and 3.0 w/o, respectively.

The second approach is to use preground fine powders as sintering additives. All the sintering aids are preground with a laboratory attrition mill to a size around 0.5 μm. Three batches of SX mixes were prepared with total additive levels of 2.0 w/o, 2.5 w/o, and 3.0 w/o (mix 2a, 2b and 2c), respectively.

Unexpectedly low levels of sintering aid retention were found in the mixes formed from both of these routes. The amount of second phase present in the final microstructures was only about one-half the amount expected. As a result, the two mixes with 2.0 w/o starting sintering aids were difficult to sinter (Table 4). Nevertheless, mixes with 3.0 w/o starting sintering aids reached full density after post-treatment.

Table 4. Densities for SX-G1 mixes with chemical precursors and preground additions

Mix #	Additive Level	Sintered Density gm/cc	Post-Treated Density gm/cc	Theoretical Density (rule of mixture)
1a	2.0 w/o	2.287	2.332	3.225
1b	2.5 w/o	2.924	3.039	3.231
1c	3.0 w/o	3.081	3.226	3.234
2a	2.0 w/o	2.370	2.449	3.217
2b	2.5 w/o	3.073	3.213	3.222
2c	3.0 w/o	3.154	3.223	3.223

The microstructures and second phases distribution of these samples are being examined. Mechanical properties will then be evaluated.

The third approach is the use of a powerful Turbomilling technique to grind both SiC and additive powders down to the submicron size range. Four grinding trials with SiC grinding media were conducted at Southern Illinois University by Prof. Wittmer with the SX-G1 composition mix. The BET

surface area of these four Turbomilled mixes after 2 to 4 hours of milling ranged from 18.6 m^2/g to 22.8 m^2/g compared to 15.0 m^2/g for the standard G1 mixes.

The densities of pressure filtered green pucks from these mixes were much higher than those from standard SX-G1 mixes, ranging from 2.04 to 2.24 gm/cc compared to 1.61 gm/cc. Densification studies are in progress.

Improved Processing of Ceramic Composites

D. E. Wittmer (Associate Professor, Southern Illinois University at Carbondale, Carbondale, IL 62901)

Objective/Scope

The purpose of this work is to continue the investigation of the turbomilling process as a means of improved processing for SiC whisker-ceramic matrix composites and dispersion of matrix powders prior to composite processing.

Technical Progress

Phase II is divided into 4 major tasks:

Task 1. Beneficiation of SiC whiskers.
Task 2. Development of aspect ratio reduction parameters.
Task 3. Dispersion Trials and ß-Si_3N_4 Seed Development
Task 4. Final Report

Task 1. Beneficiation of SiC whiskers

Task 1 was completed ahead of schedule as reported previously.

Task 2. Development of aspect ratio reduction parameters.

Task 2 was completed as reported in the previous semi-annual report.

Task 3. Dispersion Trials and ß-Si_3N_4 Seed Development

Dispersion Trials

This part of Task 3 was completed during this reporting period. The effect of pH on the relative floc size and the effect of temperature on the viscosity of Si_3N_4 slurries, prepared from three commercial Si_3N_4 powders were investigated.

Figure 1 shows the effect of solids loading on the relative floc size as a function of pH for Stark LC-12SX Si_3N_4 slurries. Relative floc size was determined by calibration of the Lasentec Scanning Laser Microscope using 10 μm latex spheres. These results show that increasing the solids

loading reduces the relative floc size and increases the flocculation range to somewhat slightly higher pH.

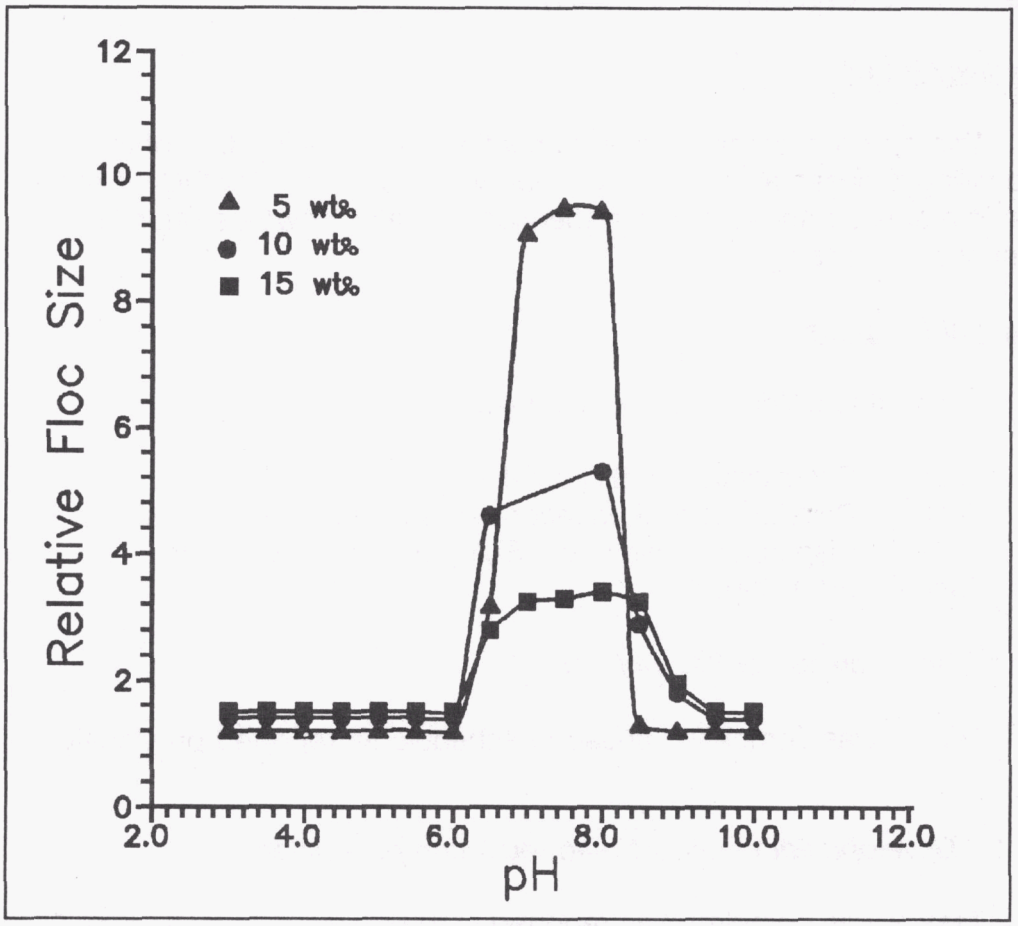

Figure 1. Effect of solids loading on the relative floc size as a function of pH for Starck LC-12SX Si_3N_4

At the 5 wt.% solids loading, the slurry is well dispersed up to a pH of slightly greater than 6; illustrated by the relative floc size of about 1 μm. Between the pH's of 6 and 8 the slurry becomes flocculated, with a relative floc size of about 10 μ. Above a pH of slightly greater than 8, the slurry is once again well dispersed.

Increasing the solids loading is seen to reduce the relative floc size in the pH range of 6 to 8 to about 5 μm for the 10 wt.% solids loading and about 3 μm for the 15 wt.% solids loading. Also, the flocculated range for both higher solids loading is extended to slightly higher pH.

As mentioned in previous bimonthly and semiannual progress reports, the temperature of the cooling water used for the turbomill was

noticed to have a significant effect on the viscosity of Si_3N_4 slurries, during turbomilling and subsequent processing. Since the turbomill is cooled with the available building cold water, the temperature of the cooling water will vary with the season. In the winter months it has been recorded to be as low as 13°C and in the summer as high as 39°C.

To determine the effect of temperature on the viscosity of three commercial Si_3N_4 powders (Starck LC-10N and LC-12SX, and Ube E-10), well-dispersed slurries containing 45 vol.% Si_3N_4 of each powder were prepared with a light-duty homogenizer, using water at 25°C and ammonium hydroxide for pH control (≈10). The viscosity of each slurry was measured with a rotary viscometer equipped with a circulating cup attached to a refrigerated cooling supply. At each temperature, the slurry was allowed to equilibrate for 15 min. prior to the viscosity measurement. The viscosity of each slurry was initially determined at 25°C and then cooled to 5°C. The temperature was then increased in ≈20° intervals up to 55°C, after which it was then decreased back to 5°C, in order to observe any hysteresis behavior.

As seen in Fig. 2, the slurry containing the Starck LC-10N Si_3N_4 exhibits a strong viscosity vs. temperature hysteresis behavior. It is believed that the powder surface charge is affected by the solubility of surface ions. It is suspected that as the temperature is increase the floc size also increases and results in the higher viscosity. As the temperature is lowered, the flocs do not spontaneously disperse and the viscosity remains higher than that initially measured.

The hysteresis behavior is not as pronounced for the Starck LC-12SX, with only very small changes in viscosity as a function of temperature. This is most likely do to a difference in the surface charge on the LC-12SX compared with the LC-10N; the floc size and viscosity for the same solids loading are initially quite different. It might be that slurries made from LC-12SX with higher solids loadings would behave similar to the LC-10N.

The Ube E-10 Si_3N_4 slurry showed no hysteresis behavior for viscosity as a function of temperature. The observed behavior is similar to that of water in that the viscosity decreased with increased temperature. This behavior may be the result of the higher surface purity for the Ube powder, compared with the Starck powders, giving a much lower viscosity for this solids loading. It may be that as higher solids loading, slurries made from Ube E-10 may also show some hysteresis behavior. This should be a goal of further research.

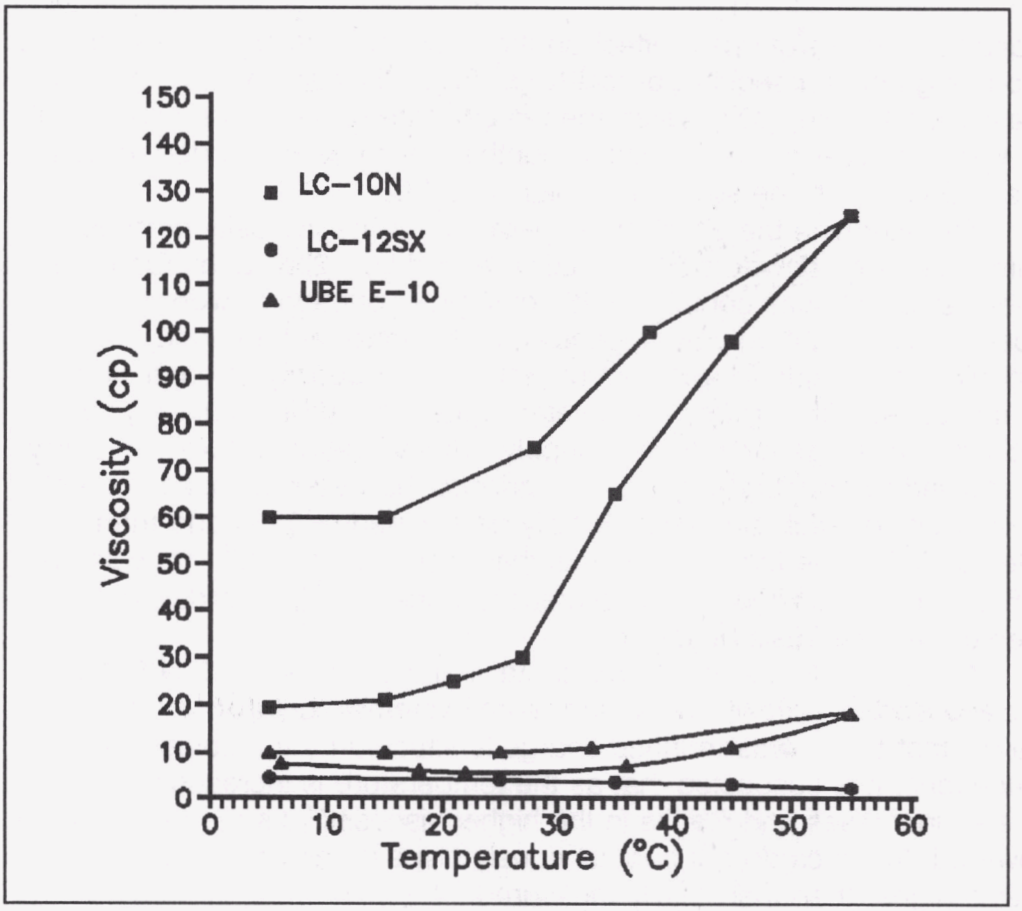

Figure 2. Effect of temperature on viscosity of 45 vol.% slurries made from 3 commercially available Si_3N_4 powders.

ß-Si_3N_4 Seed Development

During this reporting period, additional ß-Si_3N_4 seed was produced by the addition of 2% Y_2O_3 to Ube E-10 Si_3N_4 with subsequent processing, as described in the previous semiannual report. The ß-Si_3N_4 produced by thermal treatment is shown in Fig. 3 and the seed produced by turbomilling is shown in Fig. 4. It can be seen from these figures that the initial elongated ß-Si_3N_4 is reduced to a fine particulate "seed" by turbomilling.

Figure 3. SEM photomicrograph of ß-Si_3N_4 prior to turbomilling.

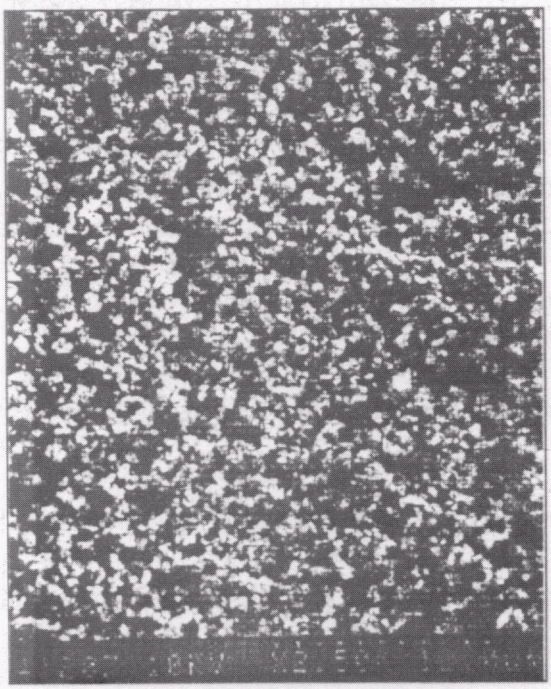

Figure 4. SEM photomicrograph of ß-Si_3N_4 seed prepared by turbomilling the thermal conversion product shown in Fig. 3.

Development of Self-Reinforced Si_3N_4 with Reduced Sintering Aids

A2Y6-Si_3N_4 was produced, with and without the addition of 5 and 10 wt.% ß-Si_3N_4 seed, by turbomilling and pressure casting.

A2Y6-Si_3N_4 Matrix

For the A2Y6-Si_3N_4 matrix (no ß-Si_3N_4 seeds), the raw materials were batched in the appropriate amounts for a 0.5 kg lot and processed in the turbomill, containing 2 kg of the YTZ milling media and 500 cc distilled water. After the turbomill was loaded, the pH was adjusted to about 10 by the addition of ammonium hydroxide. Following turbomilling for 1 h at 1200 r.p.m., the resulting slurry was discharged through a 60/200 mesh screen stack. The slurry was then pressure cast (using N_2 gas gradually increased from 700 Pa (5 psig) up to 14.5 KPa (40 psig)) into green discs 7.6 cm in diameter by ≈ 2.2 cm thick, using a commercial filter press. The discs from filter pressing were then dried under vacuum at 100°C for 24 h. Following drying, the discs were isopressed at 310 MPa to obtain a green density of about 60-65% of theoretical. The pressure cast discs were then sintered at 1880°C for 4 h at 300 psig N_2. Following sintering the discs were cut into standard test bars and flexural strength and fracture toughness (controlled flaw) were measured. Standard XRD was also used to determine the phases present following sintering.

The baseline A2Y6-Si_3N_4 matrix sintered to >99% of theoretical density at 1880°C for 4 h under 300 psig N_2 overpressure. Based on 4 test bars each, the 4-pt flexural strength was 925-1025 MPa and the fracture toughness was 8-10 MPa-$m^{½}$. XRD results indicated complete conversion to ß-Si_3N_4. The microstructure of the etched A2Y6 matrix showed a small amount of uniformly distributed porosity about 6 μm in diameter, some fine grained material, and some elongated ß-Si_3N_4 approximately 1-2 μm in diameter by 4-6 μm long. The microstructure given in Fig. 5 is characteristic of the sintered A2Y6 matrix after polishing and thermal etching.

A2Y6-Si_3N_4 with 5 wt.% ß-Si_3N_4 Seed

A similar procedure was used for the addition of the ß-Si_3N_4 seed to the baseline A2Y6-Si_3N_4 matrix. After turbomilling the baseline composition for 2 h, the appropriate amount of ß-Si_3N_4 was added to obtain a 5 or 10 wt.% addition. Turbomilling was then continued for an additional 30 min. to disperse the seed. The resulting slurry was then pressure cast, dried and isopressed for the same conditions as the baseline composition without ß seed.

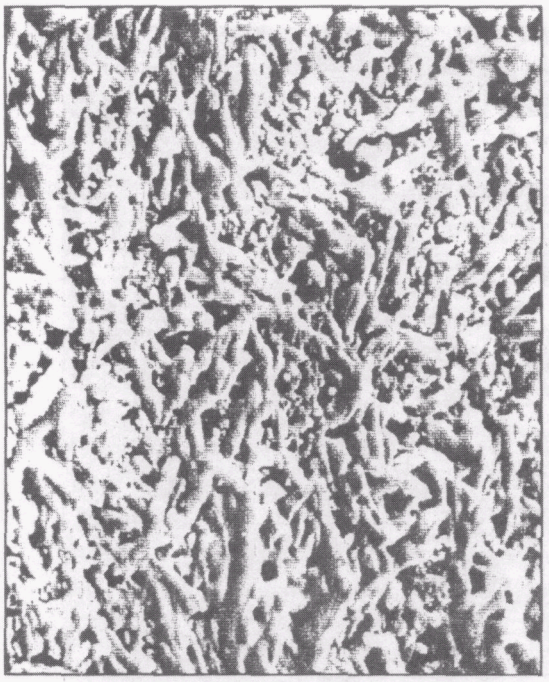

Figure 5. SEM photomicrograph of etched A2Y6-Si_3N_4 after sintering, showing elongated ß-Si_3N_4 grains.

The seeded A2Y6 also sintered to >99% of theoretical density at 1880°C for 4 h under 300 psig N_2 overpressure. Based on 4 test bars each, the 4-pt flexural strength was 750-950 MPa and the fracture toughness was 10-13 MPa-$m^{1/2}$. As with the matrix, XRD results indicated that the seeded composition completely converted to ß-Si_3N_4. The microstructure of the seeded Si_3N_4 (Fig. 6) showed a small amount of uniformly distributed porosity about 6 μm in diameter, however there was much less fine grained material, and a greater amount of elongated ß-Si_3N_4 than observed in the baseline A2Y6-Si_3N_4 matrix. Also, the ß-Si_3N_4 appears to be larger in diameter (2-3 μm) and slightly longer (6-8 μm) for the seeded A2Y6-Si_3N_4. The reduction in the fine grained material would be expected to lower the flexural strength, while the increased volume of the elongated ß phase would likely increase the toughness, as was observed. Based on these limited results, it appears that ß seeding of Si_3N_4 compositions is a means of altering the sintered microstructure to increase the fracture toughness.

Work is continuing on this task to increase the database and produce more statistically valid data. Additional materials have been prepared and are presently being machined into test bars.

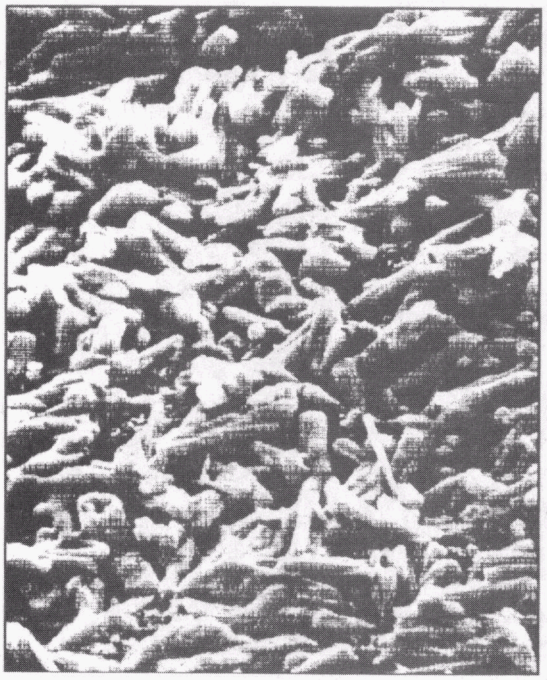

Figure 6. **SEM photomicrograph of thermally etched sintered A2Y6-Si_3N_4 containing 5 wt. ß-Si_3N_4 seed, showing enhanced growth of ß-phase.**

Status of Milestones

1.	Run Beneficiation Trials and Report in Bimonthly	Completed
2.	Run Aspect Ratio Reduction Trials and Report in Bimonthly	Completed
3.	Run Matrix Dispersion Trials and Report in Bimonthly	Completed
4.	Develop ß-Si_3N_4 Seed and Report in Bimonthly	Completed
5.	Develop Self-Reinforced Si_3N_4 with Reduced Sintering Aids and Report in Bimonthly	On Schedule New Target
6.	Rough Draft of Final Report to Contract Monitor	On Schedule New Target

Publications

D. E. Wittmer and T. E. Paulson, "Evaluation of SiCw-Si_3N_4 Composites Containing Beneficiated/Heat-Treated SiCw," Ceramic Engineering and Science Proceedings, Vol. 12, No. 9-10, pp. 1318-1326 (1991).

D. E. Wittmer, D. Doshi and T. E. Paulson, "Development of ß-Si_3N_4 for self-reinforced composites," 4th International Symposium on Ceramic Materials & Components for Engines, June 10-12, 1991, Goteborg, Sweden, Elsevier, Amsterdam (in press).

T. E. Paulson, "Effects of Aspect Ratio and Thermal Treatment of SiC Whiskers on SiCw-Si_3N_4 Composites," Thesis for Master of Science in Mechanical Engineering, Dept. of Mechanical Engineering and Energy Processes, Southern Illinois University, Carbondale, IL, August, 1991.

Presentations

D. E. Wittmer*, D. Doshi and T. E. Paulson, "Development of ß-Si_3N_4 for Self-Reinforced Composites," 4th International Symposium on Ceramic Materials & Components for Engines, June 10-12, 1991, Goteborg, Sweden.

1.1.2 Silicon Nitride

Sintered Silicon Nitride

J. Mangels (Ceradyne Inc.)
G.E.Gazza (Army Materials Technology Laboratory)

Objective/Scope

The program is currently conducted on contract to Ceradyne Inc. with support from AMTL. The contract has the overall objective of developing scale-up processing conditions for a silicon nitride material having the general composition 85.8m/o Si_3N_4-4.73m/o Y_2O_3-9.47m/o SiO_2-1.0m/o Mo_2C and characterizing the properties of this composition with the goal of producing complex components for testing in related heat engine programs. The first task of the program will concentrate on processing studies and data base generation while the second task will focus on producing and characterizing engine components.

Technical Progress

Matrix 4 billets 4" x 4" x 1/2" in size were isopressed from the Matrix 4 powders (with 0 and 1 mol% Mo_2C) to be used for mechanical testing of the material after sintering. A processing temperature of 1850C for 5 hours was chosen for both compositions based on results from previous runs. A total of four sintering runs were conducted, MTL 23-26. MTL run 23 was performed on half billets in two different packing powders (with 0 and 2% SiO_2 additions) in order to establish which of the packing powders should be used as well as to verify the sinterability of larger samples. Since samples of both compositions sintered to density only in 0% SiO_2 packing powder (Table I), it was chosen for all the remaining runs.

Densities: Full size billets sintered in MTL runs 24-26 all reached density irrespective of composition. Billet densities for mix 6 were 3.258 ▪ 0.003 g/cu.cm and for mix 7, 3.278 ▪ 0.006 g/cu.cm. About 50% of the billets experienced shrinkage induced cracking that originated from the billet edges and extended radially into the billet for up to approximately 1/2 in. Cracks were observed on samples of both compositions. It is believed that this problem could be overcome by slowing down the heating rate in the last 100C temperature range and by changing the way the parts are loaded in the sintering furnace.

Weight losses of billets with no Mo_2C ranged from 1-2%. Billets with Mo2C had losses of 1.5-3.6%. These values are typically lower than for smaller samples which were used in previous Matrix 4 sintering runs.

Samples were found to contain $Y_2Si_2O_7$ (card #22-1103) as a second phase irrespective of which composition was used. Molybdenum carbide or silicides were not detectable on XRD.

Surfaces of polished samples were examined and were similar to surfaces observed in Matrix 4 on smaller samples. In general, mix 7 samples (containing 1 mol% Mo_2C) appeared to contain more pores and have a larger average pore size than samples from mix 6.

Hardness and Toughness: Material from runs MTL 23-26 had hardnesses in the 1380 kg/sq.mm range (Table I). These values are lower than in previous Matrix 4 sintering runs. Toughness values remained in the range of 5.5-8.0 $MPam^{1/2}$.

Characterization of Matrix 4 Test Bars

Billets with dimensions 3.3" x 3.3" x 0.52" were processed using the Matrix 4 conditions and then were machined into MOR bars at Bomas Maching Spec. Inc., Somerville, MA. Billet compositions with and without Mo_2C were processed and identified as Mix 7 and Mix 6, respectively. The characterization results are summarized in Table II. The density, hardness, fracture toughness, and phase composition are all consistent with the values obtained in the Matrix 4 processing experiments.

Mix 6 (without Mo_2C) contained a uniform distribution of 18-25 micron size pores, while Mix 7 had porosity ranging up to 30-40 microns. The pores in Mix 7 composition appeared to have a metallic phase associated with them. SEM analysis indicated that this phase was $MoSi_2$.

The modulus of rupture was determined for these materials using the MIL-STD-1942B design. The results are summarized in Table III for Mix 6 and Table IV for Mix 7 along with an analysis of the fracture origins. The mean strength of both compositions, 468 MPa for Mix 6 and 437 MPa for Mix 7, was lower than the program goal. In addition, the Weibull Modulus, 3.2 for Mix 6 and 6.3 for Mix 7, was also low.

An analysis of the fracture origins indicated that the problems could be attributed to three causes:

(1) Incomplete mixing of the additives into the Si_3N_4 powder resulted in large pores which were shown to be deficient in sintering aditives.

(2) Contamination of the Si_3N_4 mix with silicon during the spray drying process resulting in inclusions of silicon.

(3) Large pores associated with the Mo_2C conversion to $MoSi_2$ in Mix 7 during sintering.

It was concluded that the remaining material characterization, scheduled for these materials, be deferred pending the results of an additional set of processing experiments.

Matrix 5 Processing Experiments

The starting material for Matrix 5 will be silicon powder rather than Si_3N_4 powder. The specimens will be processed according to the sintered-reaction bonded Si_3N_4 process. This processing change will:

(1) Eliminate the potential for cross contamination.

(2) Result in a more uniform distribution of sintering additives.

Matrix 5-Sintering: Matrix 5 samples were sintered at 1850C, 1875C, and 1950C. The densities and weight losses from these are summarized in Table V. Near theoretical densities were obtained at 1875C using new packing powder. In general, higher densities were obtained in samples that did not contain Mo_2C additions. Additionally, greater density variations were observed between runs performed under the same conditions than with prior materials.

Samples containing 1 mol% Mo_2C were found to have porosity larger than 10 um in all areas of the sample. The Mo_2C-free samples had a 3/16" thick surface region which was virtually pore free. The center of these samples had some isolated 10-30 um sized pores.

All samples contained $Y_{4.67}(SiO_4)_3O$ as a second phase. Mo_2C or $MoSi_2$ were detected in samples with Mo_2 additions.

Established Milestones

(A) Establish powder processing approach for preparing selected composition. Determine preferred sintering conditions. Generate data base for room temperature and high temperature properties.
July 1991

(B) Fabricate, inspect, and make components available for engine testing in a gas turbine ceramic component development/evaluation program.
July 1992

Program Status

The need to perform another processing matrix has put the program approximately six months behind schedule. Use of the sintered-reaction bonded approach or a modified slip-casting process being developed at MTL may improve the quality of the sintered product.

TABLE I. Characterization of sintered samples of mix 6 (0% Mo_2C) and mix 7 (1m/o Mo_2C) for run MTL 23

Temperature-1850C time-5 hrs.
Packing powders: (1) 0% SiO_2 (2) 2% SiO_2
parts: rods and half billets crucible: graphite

Parts	mix 6		mix 7	
packing powd.	(1)	(2)	(1)	(2)
wt. loss (%)				
half-billet	1.600	0.400	2.100	1.300
rod	1.000	0.700	2.600	2.200
density				
half billet	3.257	3.119	3.286	3.068
rod	3.259	3.230	3.294	3.271
% Theor.	0.999	0.957	0.999	0.933
	1.000	0.991	1.001	0.994
Phase compos.				
half billet	a-$Y_2Si_2O_7$		a-$Y_2Si_2O_7$	
Hardness (kg/sq.mm)	1388		1373	
Toughness ($MPam^{1/2}$)	5.5		7.6	

Table II. Characterization of Mix 6 and Mix 7 MOR Bars.

	Mix 6 (0% Mo_2C)	Mix 7 (1% Mo_2C)
Density		
Bars	3.262 g/cc	3.274 g/cc
Billets	3.258 g/cc	3.276 g/cc
Hardness		
HVS	1480 kg/mm^2	1400-1500 kg/mm^2
Fracture Toughness	5.3-5.8 MPam$^\circ$	5.3-6.8 MPam$^\circ$
Phase Composition	beta-Si_3N_4 no second phase	beta-Si_3N_4 $Y_2Si_2O_7$ Mo_2C $MoSi_2$
Optical Microstructure	18-25 um pores	30-40 um pores

Table III. Room Temperature Strength of Mix 6 Composition

Bar #	M.O.R.(ksi)	Failure Origin
1	58.1	inclusion (Si)
2	44.5	pore
3	37.8	pore
4	54.2	pore
5	39.2	
6	33.1	pore
7	72.7	
8	84.8	
9	26.8	
10	69.9	
11	77.4	
12	66.2	
13	73.4	pore
14	89.2	
15	86.3	pore
Summary Statistics		
Mean Strength	60.9 ksi	
Std. Dev.	19.9 ksi	
Char. Strength	67.9 ksi	
M	3.2	

Table IV. Room Temperature Strength of Mix 7 Composition.

Bar #	M.O.R. (ksi)	Failure Origin
1	61.2	pore
2	53.5	pore
3	61.2	
4	62.4	pore
5	57.0	inclusion (Si)
6	56.6	pore
7	70.8	pore
8	44.0	pore
9	32.4	
10	69.9	
11	76.8	
12	59.1	pore
13	66.6	
14	54.9	
15	62.3	

Summary Statistics

Mean Strength	59.2 ksi
Std. Dev.	10.5 ksi
Char. Strength	63.4 ksi
M	6.3

Table V. Results from Matrix 5 Sintering Experiments.

Temperature (C)	Mo_2C(m/o)	Density (g/cc)	Density (% theor.)	Wt.Loss(%)
1850	0	2.98	91.3	3.7
1850	1	2.92	88.7	5.3
1875	0	2.98-3.27	91-100	5.8
1875	1	2.99-3.24	90-99.2	7.4
1950	0	3.11	95.4	7.0
1950	1	3.05	92.5	10.0

Microwave Sintering of Silicon Nitride

T. N. Tiegs, J. O. Kiggans, and P. A. Menchhofer
(Oak Ridge National Laboratory)

Objective/scope

The objective of this research element is to identify those aspects of microwave processing of silicon nitride that might (1) accelerate densification, (2) permit sintering to high density with much lower levels of sintering aids, (3) lower the sintering temperature, or (4) produce unique microstructures. The investigation of microstructure development is being done on dense silicon nitride materials annealed in the microwave furnace. The sintering of silicon nitride involves two approaches. The first approach comprises heating of silicon nitride and sialon powder compositions in the 2.45- or 28-GHz units. The second approach deals with using reaction-bonded silicon nitride as the starting material and is done entirely in the 2.45-GHz microwave furnace.

Technical highlights

Microstructure development

Microstructural changes occurring during the annealing of silicon nitride materials have been previously reported. Significant grain growth depending on the intergranular phase composition and the annealing conditions has been observed.

To determine the effects of the initial microstructure on the changes that occur during microwave annealing, a series of samples have been fabricated by hot-pressing, machining into modulus of rupture (MOR) bars, and microwave annealing at 1400°C for 20 h. The series represents a wide range of intergranular phase chemistry, crystallinity, starting β-phase content and grain size as shown in Table 1. The MOR bars have been polished, and fracture toughness measurements are in progress.

Table 1. Samples fabricated for determining influence of initial microstructure on effect of microwave thermal annealing

Additive composition	Hot-press conditions (°C/h)	Density (% T. D.)	β-Si_3N_4 content (%)
6% Y_2O_3-2% Al_2O_3	1725/1	99.8	75
	1800/1.5	100	100
	1800/3	100	100
8% La_2O_3-2% Al_2O_3	1725/1	98.2	100
	1800/1.5	100	100
	1800/3	100	100
6% Y_2O_3-2% SrO	1725/1	98.0	75
	1800/1.5	100	97
	1800/3	100	100
4% Y_2O_3	1800/1.5	98.6	92
	1800/3	99.5	98

In addition to these annealing tests, rods of two commercial silicon nitrides have been annealed and will be fabricated into tensile specimens for creep testing. Rods of SNW-1000 (GTE-Wesgo, Belmont, California) were annealed at 1400 and 1500°C for 20 h. These samples will be tested at North Carolina A&T University and the results compared to previous data on as-fabricated materials. Rods of PY6 (GTE Laboratories, Waltham, Massachusetts) were annealed at 1500°C for 20 h and will be tested at ORNL. Again, the results will be compared to previous data on as-fabricated materials.

Sintering

Microwave heating of silicon nitride-based materials occurs predominantly via power absorption by the sintering additives and/or the intergranular phases. In the case of dense materials, the heat is readily transferred to the surrounding matrix because of the high thermal conductivity.[1] With powder compacts, however, the heat transfer is dominated by convection and radiant transfer mechanisms within the compact and, consequently, is very slow. Problems with non-uniform heating can occur due to imperfect sintering aid distribution, inhomogeneities in the powder compact (such as green density or agglomerates), and also variations in the microwave power field. At low additive contents, these effects are the most critical. They can lead to a sequence of localized thermal runaways or "hot spots," which cause differential sintering and shrinkage and, finally, sample cracking. To minimize or prevent this series of events, one can (1) increase the additive content or (2) increase the microwave frequency. In previous studies, we observed improved heating of powder compacts with additions of Si, SiC, and SiAlON particulates. The silicon additions were nitrided to silicon nitride in processing and prior to sintering. Increasing the sintering additive contents (using Y_2O_3 and Al_2O_3) also exhibited improved heating and densification. By increasing the microwave frequency from 2.45 to 28 GHz, increases in heating uniformity and sintering behavior, as compared to samples heated by conventional techniques, were observed. However, since the 2.45-GHz microwave furnaces are readily available on a commercial basis and represent better potential for near-term application, it is of greater interest to emphasize this frequency.

In the last reporting period, numerous attempts were made to sinter Si_3N_4-6% Y_2O_3-1.5% Al_2O_3 compositions at 1750 to 1850°C in the 2.45-GHz furnace with very little success. Poor coupling behavior, because of the low additive content, led to severe cracking problems and decreased densification. Presintering of the samples in a conventional furnace to about 70% density to increase the thermal conductivity decreased the cracking problem, but densification was still in the range of 80 to 90% T. D. This is only slightly higher than densities achieved in a conventional furnace and not sufficient to obtain good mechanical property measurements. Higher temperatures are required to densify a composition of this type, and it is evident that without a gas overpressure of nitrogen in the microwave, we will be limited to compositions with relatively high additive contents.

Consequently, to obtain specimens for the milestone involving comparison of mechanical properties between microwave- and conventional-sintered

silicon nitride, samples of Si_3N_4-12% Y_2O_3-4% Al_2O_3 were fabricated and densified. Those results, shown in Table 2, indicated good densification was obtained with uniform densities > 95% T. D. Also shown are results on the Si_3N_4-6% Y_2O_3-1.5% Al_2O_3 composition microwave sintered at 1800°C. Those samples had high weight losses (> 5%) and did not show significant improvement over the samples sintered at the lower temperatures. Replacing the Y_2O_3 with La_2O_3, which is less refractory of a composition, produced materials that could be microwave sintered to high densities at 1800°C. All of the specimens that achieved high densities were machined into MOR bars for mechanical testing. We also attempted to study the effects of microwave sintering at high ramp rates with the Si_3N_4-12% Y_2O_3-4% Al_2O_3 composition samples. While the densities achieved were comparable to the samples heated at the slower rates, these samples were badly cracked and were not suitable for mechanical property testing.

Table 2. Summary of results on sintering of silicon nitride compositions by conventional and microwave heating

Sintering conditions (°C/min)	Conventional densities (g/cm^3, % T. D.) 1750/60	Microwave densities (g/cm^3, % T. D.)			
		1700/30	1700/60	1750/60	1800/60
6% Y_2O_3-1.5% Al_2O_3	2.46, 75.5	--	--	2.57, 78.8	2.68, 82.2
12% Y_2O_3-4% Al_2O_3	3.25, 97.0	3.27, 97.6	3.33, 99.4	--	--
12% Y_2O_3-4% Al_2O_3[a]	--	3.21, 95.8	3.29, 98.2	--	--
6% Y_2O_3-2% Al_2O_3-10% Si	--	--	3.26, 97.3	--	--
8% La_2O_3-2% Al_2O_3	2.56, 76.9	--	--	2.81, 84.4	3.22, 96.7

[a]Heating rate from 1400°C to sintering temperature was 20°C/min; heating rate for all other runs was 5°C/min in same temperature range.

Comparisons of conventional and microwave sintering also showed increased weight losses for the latter case (Fig. 1). This behavior is believed due to the manner in which heat is absorbed by the silicon nitride materials. Conventionally, weight losses are associated with SiO volatilization from the intergranular phases and decomposition of the silicon nitride.[2,3] It has long been recognized that packing of silicon nitride was necessary during sintering to reduce weight losses and achieve good densification.[4] These powder beds decompose to "create" a protective

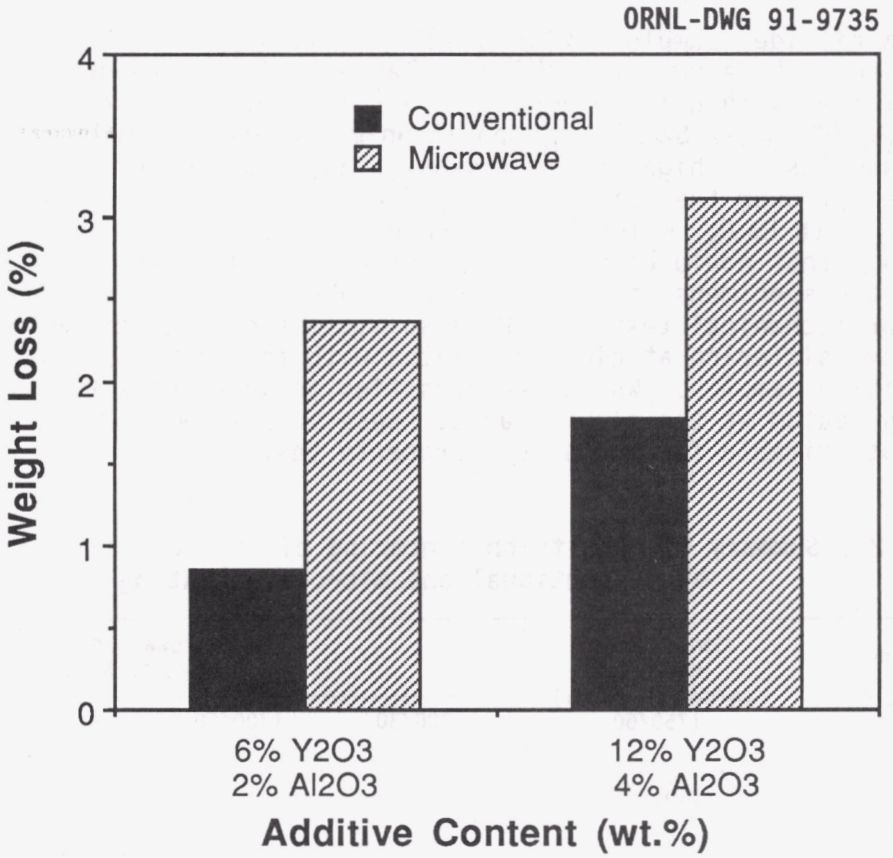

Fig. 1. Comparison of weight losses during sintering of silicon nitrides with different additives. Samples sintered at 1750°C for 1 h; microwave heating at 2.45 GHz.

environment. In the microwave, the samples are the hottest part of the system, and typically there is a steep thermal gradient existing from the samples outward through the insulation. In this arrangement, the packing powder bed does not decompose sufficiently to form a protective atmosphere around the samples to prevent material volatilization. Thus, packing arrangements and powder bed compositions appear to be of critical importance in the case of microwave sintering and will be an area of continued study. Accelerated weight losses may also be driven by any enhanced diffusion that may occur in the microwave field. Greater than conventional weight losses have been observed in microwave annealing of dense silicon nitrides where it was highly dependent on the SiO_2 content of the packing powder.[5] This behavior was attributable to enhanced diffusion of Si-O species within the intergranular phases.

The specimens that achieved densities > 90% T. D. were tested for fracture toughness and flexural strength (Table 3). Of particular interest was the fracture toughness because of previous results showing increased grain growth by microwave sintering and the interest in in-situ toughening of silicon nitrides.

Table 3. Summary of results on mechanical properties of microwave sintered silicon nitride materials

Additive composition	Sintering method	Sintering temperature/ time (°C/min)	Sintered density (g/cm^3, % T. D.)	Flexural strength (MPa)	Fracture toughness (MPa$\sqrt{m}$)
6% Y_2O_3-2% Al_2O_3-2% SiC[a]	Microwave 28 GHz	1750/60	3.13, 93.3	588 ± 53	6.4
6% Y_2O_3-2% Al_2O_3-2% TiN[a]	Microwave 28 GHz	1750/60	2.97, 91.0	743 ± 60	6.7
12% Y_2O_3-4% Al_2O_3[a]	Microwave 28 GHz	1750/60	3.13, 91.0	651 ± 102	6.5
12% Y_2O_3-4% Al_2O_3-2% SiC[a]	Microwave 28 GHz	1750/60	3.20, 95.6	657 ± 114	6.7
12% Y_2O_3-4% Al_2O_3-2% TiC[a]	Microwave 28 GHz	1750/60	3.15, 93.1	544 ± 64	7.1
12% Y_2O_3-4% Al_2O_3-2% TiN[a]	Microwave 28 GHz	1750/60	3.27, 96.6	639 ± 129	--
12% Y_2O_3-4% Al_2O_3-2% SiC[a]	Microwave 2.45 GHz	1750/60	3.22, 95.7	664 ± 91	6.6
12% Y_2O_3-4% Al_2O_3-2% TiC[a]	Microwave 2.45 GHz	1750/60	3.15, 93.1	708 ± 13	6.7
12% Y_2O_3-4% Al_2O_3-2% TiN[a]	Microwave 2.45 GHz	1750/60	3.25, 96.1	823 ± 66	--
12% Y_2O_3-4% Al_2O_3[b]	Microwave 2.45 GHz	1700/60	3.27, 97.6	--	6.6
12% Y_2O_3-4% Al_2O_3[b]	Microwave 2.45 GHz	1700/60	3.30, 98.5	--	6.5
12% Y_2O_3-4% Al_2O_3[b]	Microwave 2.45 GHz	1700/60	3.30, 98.4	--	6.9
12% Y_2O_3-4% Al_2O_3[b]	Conventional	1700/60	3.29, 98.1	--	6.3
12% Y_2O_3-4% Al_2O_3-2% Si[b]	Microwave 2.45 GHz	1700/60	3.24, 96.8	--	7.1
12% Y_2O_3-4% Al_2O_3-2% Si[b]	Conventional	1700/60	3.24, 96.7	--	6.5
9% Y_2O_3-3% Al_2O_3[b]	Microwave 2.45 GHz	1700/60	3.27, 98.5	--	6.8
9% Y_2O_3-3% Al_2O_3[b]	Conventional	1700/60	3.21, 96.7	--	6.4
11% La_2O_3-3% Al_2O_3[b]	Microwave 2.45 GHz	1700/60	3.32, 98.3	--	6.9

[a]Samples were fabricated by vibromilling, drying, and isopressing.

[b]Samples were fabricated by turbomilling, pressure-casting, and drying.

As shown in Table 3, the strength is mainly dependent on the density of the samples achieved during sintering. Only marginal differences in mechanical properties were observed between the conventionally and microwave-sintered materials. Comparisons of the fracture toughness revealed that the microwave-sintered materials consistently exhibited slightly increased toughness over the conventionally heated materials. This is believed to be a direct result of the increase in grain size in the microwave-sintered samples.

Sintering in silicon nitride materials occurs by a number of distinct steps. Initially, liquid phase formation occurs by the reaction between the sintering additives and the silica on the surface of the silicon nitride particles. This typically takes place in the temperature range from 1200 to 1600°C. Initial densification begins via particle rearrangement aided by the liquid phase and capillary action. Further densification takes place by a solution-diffusion-reprecipitation process whereby α-Si_3N_4 is transformed into β-Si_3N_4. The formation of the liquid phase and particle rearrangement are processes that should not be affected whether the thermal energy is supplied through microwave or conventional heating. Consequently, densification should proceed in the same manner and at the same rate for both heating methods. But the solution-diffusion-reprecipitation process should be very dependent. It has been previously reported that microwave heating increases diffusional processes. Thus, the improvement in densification and increased grain size during microwave heating are a result of increased diffusion through the liquid phase during the α-to-β-Si_3N_4 transformation. In the compositions with high additive contents, shrinkage by particle rearrangement is the major densification process. Therefore, the sintered densities are not significantly different between the microwave and conventionally heated samples. However, increased grain growth during microwave heating results in the slightly improved fracture toughness. An optimization of the microwave sintering method may involve sintering to high density followed by a grain growth cycle and then an intergranular phase crystallization step. Samples to explore this possibility have been fabricated and fired. Evaluation of these materials is in progress.

References

1. D. L. Johnson, "Microwave Heating of Grain Boundaries in Ceramics," *J. Am. Ceram. Soc.* 74[4], 849-50 (1991).

2. F. F. Lange, "Volatilization Associated with the Sintering of Polyphase Si_3N_4 Materials," *J. Am. Ceram. Soc.* 65[8], C-120-21 (1982).

3. N. Hirosaki and A. Okada, "Change in Oxygen Content of Y_2O_3-Nd_2O_3-Doped Silicon Nitride During Firing," *J. Am. Ceram. Soc.* 72[12], 2359-60 (1989).

4. R. Pompe and R. Carlsson, "Sintering of Si_3N_4-Based Materials Using the Powder Bed Method," pp. 219-24 in *Progress in Nitrogen Ceramics*, ed. F. L. Riley, Martinus Nijhoff Pub., The Netherlands (1983).

5. T. N. Tiegs, M. K. Ferber, J. O. Kiggans, K. L. More, C. M. Hubbard, and D. W. Coffey, "Microstructure Development During Microwave Annealing of Dense Silicon Nitride," to be published in *Ceramic Transactions, Microwaves: Theory and Application in Materials Processing*, ed. D. E. Clark, F. D. Gac, and W. H. Sutton, American Ceramic Society, Westerville, Ohio (1988).

Status of milestones

Milestone 112404 - Draft report on "Mechanical Properties of Microwave-Sintered Silicon Nitride" was completed.

Publications

"Fabrication of Silicon Nitride Ceramics by Microwave Heating" by T. N. Tiegs and J. O. Kiggans, to be published in *Proceedings of the 4th International Symposium on Ceramic Materials and Components For Engines*, Swedish Ceramic Society.

"Sintered Silicon Nitride Ceramics Using Microwave Heating" by T. N. Tiegs, J. O. Kiggans, and P. A. Menchhofer, to be published in *Proceedings of the European Ceramic Society Second Conference*.

Characterization of Attrition Milled Silicon Nitride Powder

S. G. Malghan and D. B. Minor (National Institute of Standards and Technology)

Objective/Scope

Currently, the starting materials in the manufacture of silicon nitride ceramic components are fine powders. These fine sized powders tend to form agglomerates due to van der Waals attractive forces. For improved reliability in the manufacture of ceramic components, the agglomerates in the powders should be eliminated since they form defects. In addition, the powders should have an appropriate range of size distribution and specific surface area for achieving a near-theoretical density of the ceramic after densification. These factors necessitate the use of powder milling as one of the major powder processing unit operations. Therefore, milling of powders is an integral unit operation in the manufacture of silicon nitride components for advanced energy applications. The production and use of these powders require the use of efficient milling techniques and understanding of characteristics of the milled powders in a given environment. High energy attrition milling appears to offer significant advantages over conventional tumbling and attrition mills.

The objectives of this project are to: (1) develop fundamental understanding of surface chemical changes taking place when silicon nitride powder is attrition milled in aqueous environment, and (2) demonstrate the use of high energy attrition milling for silicon nitride powder processing, by developing measurement techniques and data on the effect of milling variables on the resulting powder. This study will provide data and models for effective application of high energy attrition milling to industrial processing of silicon nitride powder. It also will provide recommended procedures for physical and surface chemical characterization of powders and slurries involved in the milling process.

Technical Progress

During this period three major tasks were addressed: 1) testing of the milling kinetics model, ESTIMILL, 2) completion of milling tests with 3.0 mm media, 3) comparison of milling results 2.0 and 3.0 mm diameter media.

Testing of Milling Kinetics Model. The linear, size discretized, model for breakage kinetics is obtained by dividing the particulate assembly being milled into "n" narrow size intervals (x_i , x_{i+1}), where i = 1, 2, ----, n. Then a mass balance for the material in the i-th size interval at time t yields, for i = 1, 2, ---, n:

$$\frac{d[Hm_i(t)}{dt} = - s_i \, Hm_i(t) + \sum_{j=1}^{i=1} b_{ij} s_j \, m_j(t)$$

In this equation, $m_i(t)$ is the mass fraction of material in the i-th size interval and H is the total mass of material being milled. S_i, the size-discretized breakage rate function for the i-th size interval, denotes the fractional rate at which the material is milled out of the i-th size interval and b_{ij}, the size-discretized breakage function, represents the fraction of the primary breakage product of material in the j-th size interval which appears in the i-th size interval. The set of n simultaneous differential equations in eq. 1 are represented by a matrix equation and an analytical solution is obtained. A detailed discussion of the model and a computer program is published by the University of Utah Comminution Center (UCC). Presently, we are collaborating with Prof. Rajamani at the UCC in the development and usage of this program for silicon nitride powder milling.

This model was developed in early 60's. However, since 1980's the University of Utah has taken this model and developed a computer program that has been utilized for numerous applications. Our current task is to modify and test the program for simulation of silicon nitride powder milling in a high energy agitation ball mill.

The model testing was primarily directed towards estimation of the model parameters -- breakage rate function (S_i) and breakage distribution function (B_{ij}). After certain modifications, the model has been successfully estimating the parameters. The input data are the feed and product size distributions at various milling times. The model utilizes these data to provide functional forms of breakage rate and breakage distribution functions. Subsequently, these functions are expected to fully describe the size distribution of milled products at various milling conditions. The best estimates of S_i and B_{ij} for the milling of this silicon nitride powder with 2.0 mm media area:

$$S_i = 0.0144 \left(\frac{\bar{d}_i}{\bar{d}_1} \right)^{7.1867} \qquad \text{and}$$

$$b_{ij} = \phi_1 \left(\frac{d_i}{d_{j+1}} \right)^{\phi_2} + (1-\phi_1) \left(\frac{d_i}{d_{j+1}} \right)^{\phi_3}$$

where

$$\phi_1 = 0.5096,\ \phi_2 = 0.4111, \text{ and } \phi_3 = 0.6430$$

Using these parameters, we have attempted to simulate size distribution of milled powders under a variety of conditions. These trials have been very successful.

Milling with 3.0 mm Media. Milling tests with 3.0 mm media were completed and samples have been analyzed for specific surface area, and particle size distribution. As expected, the milling rate decreased

significantly with the 3.0 mm media, compared to that with the 2.0 mm media. The primary counteracting factors that come into play in changing the media size from 2.0 mm to 3.0 mm are:

1. Larger size media exert higher impact force during compression of the particles by the media.

2. Larger size media decrease the total number of spherical balls available per unit volume. The number of balls per ml decreases from 125 to 37 (under dynamic loading) when the media diameter decreases from 3.0 mm to 2.0 mm.

The higher impact force of larger media is more suitable for breakage of larger size particles. From the data of tests conducted in this series, it is evident that the particle size of SNE-03 powder is not large enough to require the impact force of 3.0 mm media.

Some examples of the milling rate comparison are shown in Figures 1 and 2. The rate of increase of specific surface area as a function of milling time is much slower with the 3.0 mm media. In fact, even after milling for 160 min. with the 3.0 mm media, the surface area has increased only to 6.2 m^2/g. Similarly, the d_{50} of these powders shows very little decrease with the 3.0 mm media. Some interesting features of these data are: 1) product size continues to decrease though slowly, with the 3.0 mm media; 2) product size appears to reach a plateau after milling for an hour with the 2.00 mm media. These factors indicate the need for utilizing an optimum size media for obtaining enhanced milling kinetics.

Further analysis of the milling kinetics data of 2.0 and 3.0 mm diameter media shows that similar forces are active at a given combination of milling parameters. As shown in Table 1, at high slurry density, high rotor speed and low feed rate, both media produce a powder of the highest specific surface area. On the other hand, at low slurry density, low rotor speed and high feed rate, the specific surface area of powder is one of the lowest for both media sizes. Particle size distributions as measured by d_{50} are consistent with the specific surface area measurements. This type of behavior of this milling system is an indication that no significant changes in the size reduction mechanisms were prevalent under these milling conditions when using 2.0 vs 3.0 mm diameter media.

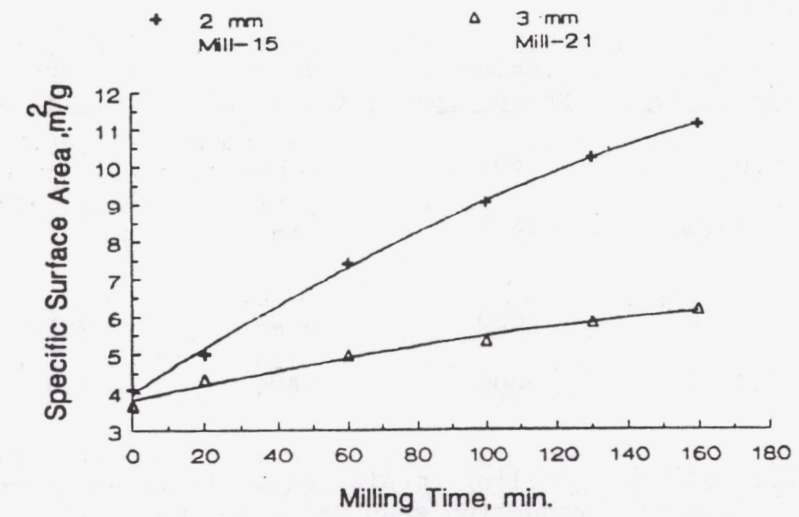

Figure 1. Comparison of milling kinetics of 2.0 and 3.00 mm diameter media. The d_{50}, mean diameter of particles, is compared at 44% volume of solids, 2800 rpm rotor speed, and 480 cc/min. feed rate.

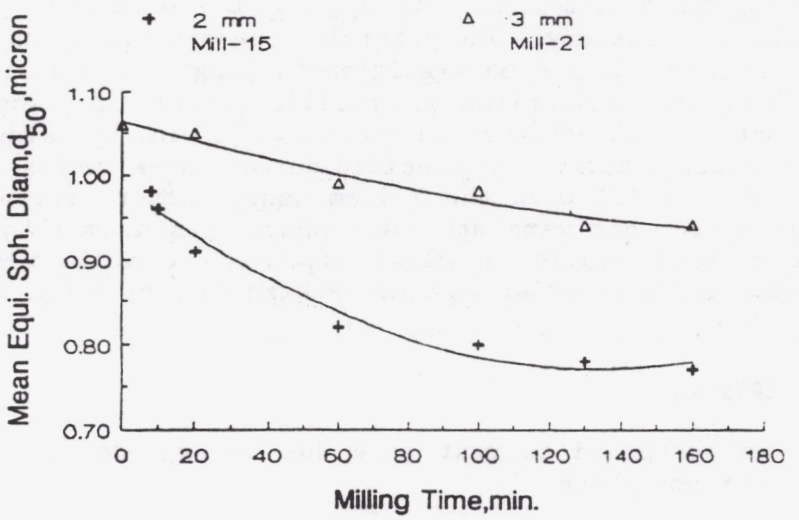

Figure 2. Comparison of milling kinetics of 2.0 and 3.00 mm diameter media. The d_{50}, mean diameter of particles, is compared at 34% volume of solids, 2000 rpm rotor speed, and 480 cc/min. feed rate.

Table 1. Comparison of Specific Surface Area and of SNE-3 Silicon Nitride Powder Milled for 160 min. Using Specified Milling Parameters

Media Diam., mm	Slurry Density, %v/v	Rotor Speed, rpm	Feed Rate, mL/min	Surface Area, m^2/g	d_{50}, μm
2.0	44.0	2800	240	11.1	0.77
3.0	44.0	2800	240	6.2	0.94
2.0	34.0	2000	480	4.9	0.85
3.0	34.0	2000	480	4.4	1.07

Another aspect of the milling media size is slow kinetics of deagglomeration and size reduction when using 3.0 mm media. Since one of the major advantages of this milling system is its ability to perform both deagglomeration and size reduction, it is necessary to evaluate the impact of media size on the resulting size distribution. The results of tests carried out with 3.0 mm diameter media showed that the rate of deagglomeration decreased significantly. As shown in Figure 2, the use of 2.0 mm media resulted in a significant decrease in d_{50}, in the first 20 min. or 60 min. milling period. This shift in the d_{50} during the initial milling period is considered to be due to deagglomeration, rather than size reduction by intraparticle fracture. This conclusion is supported by the determination of d_{10} and micrographs obtained by scanning electron microscopy. The particle size distributions obtained by using 3.0 mm media showed no significant changes in the initial 20 min. In addition, the comparison of specific surface area show that a significant increase was achieved in the first 20 min. by using the 2.0 mm media. In relative terms, the specific surface area increased by 43% with 2.0 mm media vs 19% with the 3.0 mm media, after milling for 20 min. Similar increments were achieved after 60 min. milling. Once again, these results provide a clear direction towards the use of smaller diameter media in order to achieve high rate of deagglomeration or size reduction.

Status of Milestones

Milestone 5 was postponed to next page due to expanded experimental design in the current phase.

Publication

None

Scalability Demonstration Program for Silicon Nitride by the Sullivan Process

Thomas Milton Sullivan (Sullivan Mining Corporation)

Objective/Scope

This work involves scale-up of the Sullivan™ Process for silicon nitride with the delivery of over 864 net shape flexural bars and other test samples for evaluation by the High Temperature Materials Laboratory at Oak Ridge National Laboratory. Both a low temperature and a high temperature silicon nitride shall be produced and characterized. Data on process optimization and system economics are establishing the operating parameters for a larger Sullivan™ Process system.

Technical Progress

Task 1 - Demonstrate Preliminary Scalability

1.1 **Assemble Four-Inch System** - Complete.

1.2 **Polymerization** - Clorosilanes are polymerized prior to supercritical fluid processing to remove reaction byproducts using less expensive equipment than relatively expensive supercritical fluid processing equipment. Glass lined reactors such as those manufactured by DeDetrich and others are commonly used to polymerize chlorosilanes. Reactor manufacturers rent the use of reactors and related equipment for test purposes. Rental of equipment needed to complete this task has been repeatedly delayed due to scheduling conflicts. This activity will proceed as soon as laboratory time can be contracted.

1.3 **Net Shaping** - Mass production ceramic components like ceramic roller cam followers, are sold at very low prices requiring centerless finishing methods. Methods capable of finishing several parts per second are required.

Ceramic blanks must be made in the tens of millions per year with precise dimensions. Roller internal dimensions must be made so that ID is parallel to the OD within 0.025 mm. Roller ends must be perpendicular within 0.025 mm. Unless this level of precision can be achieved, parts must be chucked, a process too slow and expensive for mass production.

Rollers were produced with parallelism and perpendicularity measuring within the ± 0.025 mm specified tolerance using a Talyrond 150 made by Rank Taylor Hobson Inc. Larger unit volumes will prove mass production capability the Sullivan™ process with respect to precision.

1.4 **MOR Bar Casting -** MOR bars have been cast in multiple cavity molds. Casting in multiple cavity molds involves several aspects of the process technology that are difficult to accurately predict. Material flow in molds becomes difficult to control as part density increases. Iteration was needed to develop multiple cavity molds with channels and gates in the correct locations to simultaneously cast several parts with consistent density and dimensions. Bar to bar uniformity is deemed more important for this task than material properties.

Bars now accurately replicate mold dimensions and features. As expected, post supercritical fluid processed part density is increasing as the process is iterated using a statistical design of experiments matrix and greater control of the entire process is exerted.

Multiple cavity casting activity is essentially complete with respect to flexural bar shapes. Material properties and microstructure will be improved in Task 3.

1.5 **Estimate Economics -** Process economics were estimated based on operating experience with the 4" Process System.

Built at a cost of $269,518, the 4" supercritical fluid processing system is capable of producing 1,556.8kg in a 252 day year. The cost of supercritical fluid

processing (not including overhead) can be obtained by dividing the depreciation (five years) by the amount of material produced, since maintenance cost is negligible. Energy and raw materials are included in overhead and materials respectively.

Ceramic components are heat treated in a furnace at high temperature by an outside vendor. Furnace work costs $750 per run on a toll basis. This is considerably higher than the pro rata cost of owning and operating a furnace of similar size. Dividing the cost of a furnace run by the material fired gives the furnace cost per kilogram of material produced.

Only one person is needed to operate the system. Amortizing the cost of direct labor over the total amount of material produced gives the cost of labor.

Materials are selected from a group of inexpensive silicon containing liquid chemicals and ammonia. Though prices fluctuate, available silicon in silanes generally costs $2.20 to $3.31 per kilogram. Yield factors raise the cost of raw materials per kilogram of product to $8.82/kg.

The cost of material produced in the 4" Process System, not including finishing, therefore is:

4" Process System $269,518 cost ÷ 5 yr depreciation period ÷ 1,556.8kg/yr	$34.62/kg
Heat Treatment $750/run x 63 runs ÷ 1,556.8kg/yr	30.35
Direct labor $50,000/man-yr ÷ 1,556.8kg/yr	32.12
Materials	8.82
Overhead @ 120%	43.34
TOTAL COST	$149.25

Task 2 Composition for High Temperature Properties

2.1 **Modify Composition** - Low additive levels and acicular shaped grains will improve performance of the material at high temperature.

Complete elimination of additives was attempted. Silicon nitride bonded weakly. Iterations did not show promise, so this approach was abandoned in favor of low additive levels.

Acicular grain shapes can be formed at high temperatures or by changing process chemistry at low temperature. Test specimens of silicon nitride were reacted and extracted in the supercritical fluid process system prior to firing at temperatures up to 1820°C. Acicular grains measuring less than one micron in diameter and more than twenty microns in length were formed in a part with an amorphous exterior. Grain orientation is apparently influenced by material porosity. Grains tend to grow into pores.

Forming acicular grains at low temperature by chemical reaction has the advantage of reducing porosity while orienting grain axes.

2.2 **MOR Bar Casting** - Work continues on casting technique to achieve a preferred axial orientation for grains, however, MOR bar casting for high temperature properties is essentially complete.

Task 3 Process Optimization

3.1 **Low-Temp Microstructure Refinement** - Work continues on improving material properties prior to high temperature firing. Recent improvements in understanding the function of catalysts has steadily increased post-supercritical fluid processing density. More work is nevertheless required.

3.2 **Heat Cycle Acicular Microstructure** - Progress to date indicates that an all liquid approach is more conducive to acicular grain shaping than heat cycle grain shaping.

Work is currently directed at unidirectional acicular grain orientation.

Milestones

Critical milestones are on schedule.

Publications

A paper, titled Ceramic Metal Forming Tools, was presented to the Society of Manufacturing Engineers on June 5, 1991.

Thomas Sullivan addressed the Motor Vehicle Manufacturer's Association of the United States on June 27 and the annual Contractor's Coordination Meeting on October 29, 1991.

1.1.4 Processing of Monolithics

Improved Processing

V. K. Pujari, D. M. Tracey, N. D. Corbin, M. R. Foley, A. K. Garg,
N. I. Paille, P. J. Pelletier, L.C. Sales, R. H. van de Merwe,
C. A. Willkens, R. L. Yeckley (Norton Company)

OBJECTIVE/SCOPE

The goals of the program are to develop and demonstrate significant improvements in processing methods, process controls, and nondestructive evaluation (NDE) which can be commercially implemented to produce high-reliability silicon nitride components for advanced heat engine applications at temperatures to 1370°C. Achievement of this goal shall be sought by:

- The use of silicon nitride - 4% yttria composition which is consolidated by glass encapsulated HIP'ing.
- The generation of baseline data from an initial process route involving injection molding.
- Fabrication of tensile test bars by colloidal techniques - injection molding and colloidal consolidation.
- Identification of (critical) flaw populations through NDE and fractographic analysis.
- Correlation of measured tensile strength with flaw populations and process parameters.
- Minimization of these flaws through innovative improvements in process methods and controls.

The quantitative program goals are: 1) mean RT tensile strength of 900 MPa and Weibull modulus of 20, 2) mean 1370°C fast fracture tensile strength of 500 MPa, and 3) mean 1230°C tensile stress rupture life of 100 hours at 350 MPa.

TECHNICAL PROGRESS

The technical progress against the major tasks described in the statement of work is summarized in the following. The major tasks are: 1) Material Selection and Characterization; 2) Material Processing and Process Control; 3) Development and Application of NDE; 4) Property Testing and Microstructural Evaluation; 5) Reporting; 6) Quality Assurance.

Efforts were focused towards process optimization utilizing factorial designed experiments, testing of NSF bars derived from these experiments and application of NDE in process control and monitoring:

NSF bars were fabricated in a set of experiments (iterations) utilizing key process variables in a planned and systematic manner. HIP'ed tensile bars from each experiment were tested to establish mean tensile strengths and Weibull moduli. Data from each iteration serve to establish a response surface. Several experimental conditions were identified which show potential for meeting or exceeding ultimate program target properties of 900 MPa (tensile strength) and Weibull modulus of 20.

Fracture toughness (K_{IC}) of the material was identified to be a key process control parameter. HIP process conditions were found to significantly influence the fracture toughness. Based upon these experiments, control limits for K_{IC} were established (6.0 - 6.4 MPa$\sqrt{m}$).

An instrumented multistation casting apparatus was designed, built and successfully tested for reproducibly fabricating NSF bars. Special features of this apparatus include i) closed loop operation, ii) in-line ultrasonication and filtration and iii) continuous monitoring of pressure tank slurry level.

The potential for in-situ monitoring and control of the casting process utilizing ultrasonics (UT) was successfully demonstrated. UT signal amplitude and time of flight in a through transmission mode were recorded. Highest value of the amplitude and the lowest value of the time of flight were found to coincide with completion of the casting process.

TASK 1 MATERIAL SELECTION AND CHARACTERIZATION

Materials at each stage of processing are being analyzed according to established standard operating procedures (SOP). Statistical Process Control (SPC) charts are being developed for all key process parameters during Stage II for overall process monitoring purposes.

TASK 2 MATERIALS PROCESSING AND PROCESS CONTROL

i) Process Control

Table 1 provides a summary of the effort to date, and lists the control variables being examined together with a subset of the performance measures. For each batch a sufficient number of NSF bars were cast and HIP'ed to measure the effect of a particular variable on process yield and mechanical properties. Shaded areas

in the body of the table indicate either work-in-progress or work planned for the immediate future. Each of the performance measures provides a goodness criterion relative to the specific unit operation, and is not a cumulative measure of yield from the initial unit operation of the process.

Based upon total process yield, the following variables and their levels have been fixed to define SOP:

Surfactant	S1	Casting Pressure Profile	P2
Solids Loading %	HI	Pre-HIP preparation	PH1
Binder System	BO		

HIP and machining conditions having potential for yielding final program property objectives have been identified:

HIP Fixturing	None
HIP Settings	Non Standard
Machining Procedure	C

Experiments are currently underway to examine Post-HIP and Post-Machining treatment conditions.

Table 1: Stage II Control Variables/ Performance Measures

Batch #	Surfactant	Solids Load, %	Binder	Cast Press.	*Cast Yield*	Pre-HIP Prep	*Green Yield*	HIP		*Dense Yield*	Post HIP	Machine Proce.	Post Machine	*Test Yield*
								Fixture	Profile					
C13-N	S1	HI	B0	P1	*HI*	PH1	*AVG*	Y	S	*LO*	CH1	A	OH1	*LO*
												B	OH1	*LO*
								N	S	*AVG*	CH1	A	OH1	*LO*
												B	OH1	*LO*
C14-O	S1	HI	B0	P2	*HI*	PH2	*LO*	N	S	*HI*	CH1	A	OH1	*LO*
												B	OH1	*LO*
												C	OH1	*HI*
C15-P	S1	HI	B1	P1	*HI*	PH2	*LO*	N	S	*AVG*	CH1	A	OH1	*LO*
													OH2	*AVG*
												C	OH1	*HI*
													OH2	*HI*
C16-Q	S2	LO	B0	P2	*LO*	PH2	*LO*	N	S	*HI*	CH1	A	OH2	*AVG*
												C	OH2	*HI*
												D	OH1	*LO*
													OH2	*HI*
C17-R	S2	HI	B0	P2	*HI*	PH2	*LO*	N	S	*HI*	CH1	A	OH2	*HI*
												C	OH2	*HI*
												D	OH1	*LO*
													OH2	*HI*
C19-S	S1	HI	B0	P2	*HI*	PH2	*LO*	N	S	*HI*	CH1	C	OH2	*HI*
C20-T	S1	HI	B0	P2	*HI*	PH1	*HI*	N	NS	*HI*	CH1	C	OH1	*HI*
													OH2	*HI*
C21-U	S1	HI	B0	P2	*HI*	PH1	*HI*	N	S	*HI*	CH1	C	OH2	*HI*
C23-V	S1	HI	B0	P2	*HI*	PH1	*HI*	N	S	*HI*	CH1	C	OH2	*HI*
											CH1	C	OH1	*HI*
											CH2	C	OH1	*HI*
											CH2	C	OH2	*HI*
C24-W *	S1	HI	B0	P2	*HI*	PH1	*LO*	N	S					
C25-XXX	S1	HI	B0	P2	*HI*	PH1	*HI*	N	S	*HI*	CH1	C	OH2	
									NS	*HI*	CH1	C	OH2	
C26-X **	S1	HI	B0	P2	*HI*	PH1	*HI*	N	NS		CH1	C	OH2	
									S	*HI*	CH1	C	OH2	
C27-Y	S1	HI	B0	P2										

* MLP ITERATION.
** ITERATIONPROCESSED ON NEW CASTING UNIT.

ii) Powder Processing

Eight ~29kg batches (C015-C025) were prepared for colloidal consolidation studies. X-ray diffraction of the starting powder shows very little variation in alpha phase from lot-to-lot. The in-coming Ube E03 and E05 are almost 100% alpha and the E10 is ~97% alpha silicon nitride. There has been significant variation in particle size, surface area and oxygen content from lot-to-lot. In most cases milling conditions have been adjusted to bring properties within specifications, Figure 1.

A statistical quality control software package has been implemented with the ability of providing programmed indication of Out-of Control (OOC) conditions (SQCpack/Plus, PQ Systems, Inc., Dayton, Ohio). Control charts for oxygen, surface area, average particle size and yttria level have been transferred to the new system. Control limits ($\pm 3\sigma$) and specifications have been established for the milled powder properties.

Microfocus X-ray examination has proven several instances of metallic inclusions in the in-coming silicon nitride powder (20-30 μm). Inclusions are not found after the milling process, which includes both magnetic separation and filtration. From Batch O tensile rod testing, several metallic failure origins were observed, which is atypical of past performance where inclusion failure were almost nonexistent. The origins were up to 100 μm in size and in several cases undetected in the dense rod by microfocus X-ray. SEM showed the 100 μm regions to be composed of scattered fine (<5μm) grains of an iron alloy, probably iron silicide. These were individually below the limits of microfocus X-ray. A likely source of the contamination was identified downstream of milling, and has been removed from the system.

Surfactant system S2 resulted in similar milling efficiency (by particle size distribution) and oxygen content as the baseline surfactant system, S1, but yielded a significantly higher (25%) surface area. This may be due to insensitivity of the Sedigraph 5100 in the less than 0.2 micron range. Other particle size distribution analysis techniques are being studied.

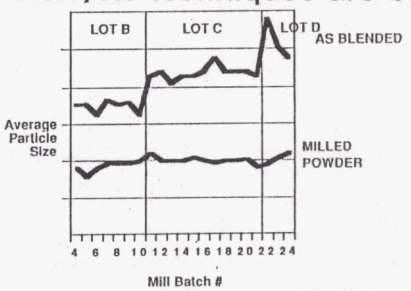

Figure 1: Particle Size (D50) Before and After Milling

iii) Colloidal Consolidation

a) Slip Formulation

The milled and concentrated batches described in the previous section were conditioned following the established SOP. This includes sonication with an ultrasonic horn for five minutes, followed by deairing in vacuum (60 mm of Hg). In addition, the slip was characterized for agglomerate population using an agglomerator gage. Approximately ten samples per casting batch were examined to ascertain the agglomerate population in the slip. Typically, agglomerates in the size range 20-25 μm have been observed in milled batches (CO17 through CO22) prepared for casting.

A study to determine the effects of type of surfactants on suspension stability (aging), rheology, agglomerate formation and casting behavior was also completed. The control surfactant being utilized currently for the aqueous milling (S1) and an alternate (S2) shown to have potential for minimizing agglomerate formation were evaluated.

Specimens cast from milled batches CO16 and CO17 (surfactant S2) showed higher green density and superior green microstructure when compared to specimens from S1 slurries. The green state fracture surfaces were found to be uniform and smooth (flat) as compared to that derived from S1 slip. This may suggest that the agglomerate size may be further reduced using surfactant S2.

However, as described in the next section, the casting behavior of this slip was found to be less reproducible. The cast NSF bars from this slip were found to be less flexible (higher elastic modulus) and hence showed cracking due to shrinkage in the mold. Various binders and pH modifications were evaluated with minimal success to improve the deformation (viscoelastic) behavior of the cast bodies. Based upon the study no further work on surfactant S2 will be pursued.

b) Tensile Bar Casting

Large scale NSF bar casting iterations N through R were performed to evaluate the effects of the key slip variables (i.e. surfactant type and solids loading) and the applied casting pressure profiles. For these iterations, the aqueous milled suspensions prepared from the established standard process utilizing surfactants S1 and S2 were used.

In each iteration, greater than 70 NSF tensile bars were cast, dried, degassed and HIP'ed, machined, radiographed and tensile tested.

During the casting of NSF bars, some difficulty was encountered in establishing the necessary time for completion of the casting process. In some cases, overcasting resulted in shrinkage related cracking at the buttonhead radius. These forming defects are possible failure origins during tensile testing, so that an improved casting regulator is being implemented to alleviate this problem.

Three casting batches designated T, U and V were also prepared this period using milled batches CO19, CO21 and CO22, respectively. NSF bars in all three iterations were cast using identical mold design which involves two gates at each end of the bar with a portion of the filtration surface sealed to prevent casting from that region. However, for iterations U and V the sealed portion of the plaster mold was replaced by a non-porous plastic. This modification resulted in considerable improvement in the casting process reproducibility.

For each of the above iterations, a specific pressure profile was used during casting. The profile was defined through a separate set of experiments which established the relationship between pressure level and casting rate as a function of time.

For Q.C. purposes, a set of discs (pucks) were also cast from each milled batch using the prescribed pressure/time profile, SOP.

c) Instrumented Casting Equipment

A new casting machine has been designed and built and is currently being brought on line. This unit has the capability of casting two, four, or six tensile rods simultaneously. Provisions have been made to control the pressure in either a manual or fully automated mode. In addition, it is now possible to load the system directly from a holding tank and to deair and deagglomerate the slurry directly on the casting machine.

iv) Hot Isostatic Pressing

Using an alternative loading procedure, the HIP capacity has effectively been doubled. This alternative loading procedure does

not use fixtures. The HIP procedures (with and without fixtures) were compared with tensile rods from the same batch (batch N). Green density gradients were minimal in these rods, eliminating this as a factor during the HIP process. Improved TIR (less bending) and density uniformity without fixtures was found, as can be seen in the data of Table 2 for batch N.

A total of six HIP runs have been completed with the new procedure. Table 2 summarizes the results and it is apparent that in all cases excellent TIR and density values were achieved.

Table 2: HIP Data for Iterations N-R

Mill Batch	Cast Batch	HIP			
		Condition	Fixture	TIR	Density
C013	N	Standard	Yes	.0320	3.1786
		Standard	No	.0200	3.2111
C014	O	Standard	No	.0216	3.2192
		Standard	No	.0222	3.2203
C015	P	Standard	No	.0315	3.2200
C016	Q	Standard	No	.0230	3.2228
C017	R	Standard	No	.0380	3.2236

Improved tensile rod yields from a HIP loading procedure without fixtures has been consistently demonstrated (Figure 2). Typically less than 10% of the bars in a HIP run are rejected. Rejection is based upon density (<99.5% TD) and axial warpage (>0.060"). Low density bars are thought to result from non-uniform conditions in the HIP. Warpage has been found to result from density variations in the green state. Casting controls are being incorporated to address this issue. As mentioned in section iii, by incorporating programmed pressure profile during casting, density gradients have been minimized to acceptable levels.

HIP experiments were conducted to establish how microstructure, toughness and strength depend on HIP temperature, time and pressure. Toughness data for 2 temperature levels and 3 cycle times are given in Figure 3. Corresponding flexure strength data are plotted in Figure 4.

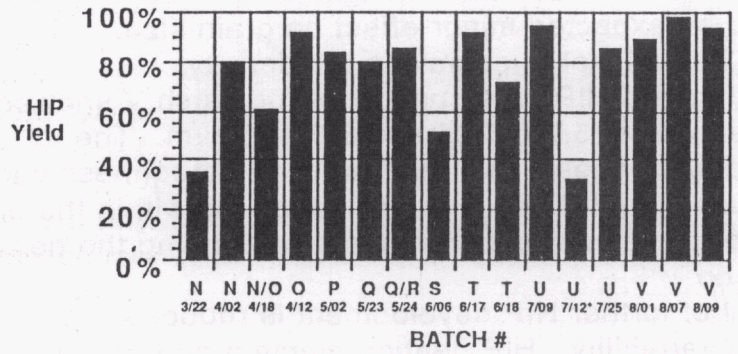

Figure 2: HIP Yield Control Chart

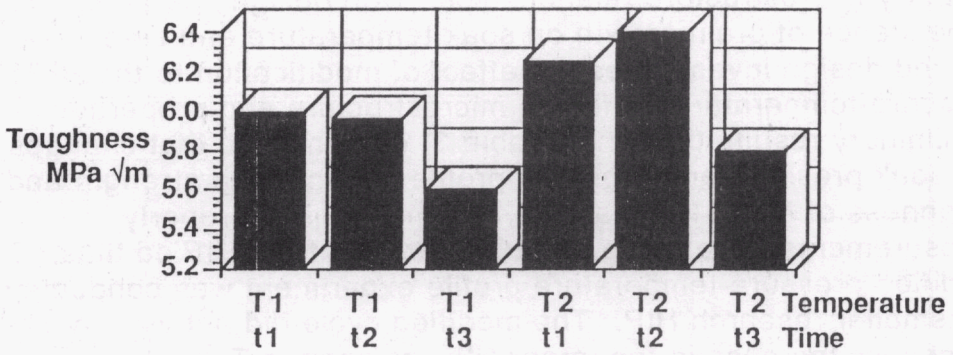

Figure 3: Toughness Dependence on HIP Temperature and Time

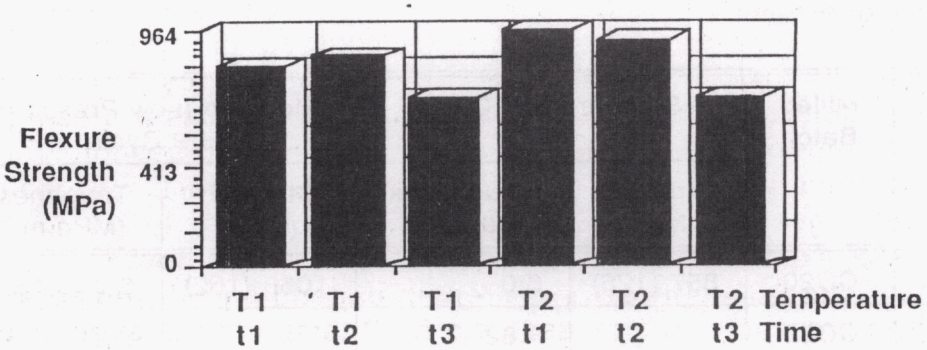

Figure 4: Strength Dependence on HIP Temperature and Time

Pressure was found to have insignificant effect on fracture toughness and an expected minor effect on grain size. Nevertheless, it is critical to achieving full density.

Three standard HIP runs conducted for Batch V showed toughness averages of 5.73, 5.85 and 6.51 MPa$\sqrt{m}$. The experimental data suggests that this run-to-run toughness variation is caused by unscheduled temperature variations within the unit. Control thermocouples are apparently not performing the necessary power regulation.

The goal of further HIP development is reduced run-to-run HIP toughness variability. HIP heating element and power consumption monitoring will be evaluated as methods to meet this goal. In addition, various temperature soaks will be evaluated to establish the potential of toughness increase to the 6.5-7.0 MPa$\sqrt{m}$ range.

Two experimental designs are underway to investigate property-microstructure relationships. One design characterizes the dependence of grain growth on soak temperature and time. The second design investigates the effect of modification to the HIP pressure-temperature profile on microstructure and properties. Preliminary results (shown in Table 3) demonstrate that changes in the soak pressure and pressure profile can improve strength and toughness of NCX5102 material. All mechanical property measurements were made on MOR bars cut from HIP'ed tiles. The modified pressure-temperature profile experiment was conducted in the smaller research HIP. The modified cycle did not yield a similar toughness increase in the larger HIP, as seen in Table 3. However, the toughness of the modified cycle was higher than the standard cycle. Additional work is planned to reproduce the toughness increases observed in the smaller research HIP.

Table 3: Effect of Modified Temperature-Pressure HIP Cycle on Properties.

Process Condition / HIP Type	Milled Batch	Standard HIP Cycle		Modified (Low Pressure) HIP Cycle	
		Strength (MPa)	Toughness (MPa $m^{1/2}$)	Strength (MPa)	Toughness (MPa $m^{1/2}$)
Small Hip	CO20	857 (126)	6.0	1050 (162)	6.7 (0.15)
Large Hip	CO20	-	5.82	-	6.21

TASK 3: DEVELOPMENT AND APPLICATION OF NDE

i) Microfocus Radiography Technique Developments

a) Density Gradients

A sintered Si_3N_4 step wedge was made with steps that vary in thickness by 1% to simulate density gradients. The thickness of the wedge is approximately that of the gage section of a HIP'ed tensile rod. The wedge has 7 steps and its thickness varies from .2345 to .2500 inches. The step wedge was examined using film radiography and all steps were clearly seen as shown in Figure 5. This step wedge will be used in the future as a tool to quantify density gradients.

b) Agglomerate Detection Study

An investigation into the detection sensitivity of agglomerates in green and HIP'ed NSF bars was conducted during the reporting period. It has been previously established that agglomerates in powder or slip have the radiographic appearance of high density regions. Agglomerates of Si_3N_4 powder were produced in sizes from 50 to 400 μm and samples were taped to the surface of an 11 mm diameter green NSF bar. Agglomerates 100 μm and larger were easily detected through the 11 mm diameter. Smaller samples could not be taped without crumbling so that agglomerates from a new batch calcined at higher temperature will be tested.

Simulated dense agglomerates were produced by crushing a HIP'ed NCX-5102 billet sample. The pieces were sized from 50 - 400 μm and as in the green testing, samples were taped to a dense NSF bar. In this case, the gage diameter is 6 mm and agglomerates as small as 65 μm were readily detected. X-ray conditions for improved detectability are being evaluated.

c) Characterizing X-ray Beam

Several experiments were conducted in order to study variations in the intensity of the x-ray beam. In order to quantify density gradients in cast specimens, there is a need to know when density variation indications are intrinsic to the sample and not due to scatter or non-uniformity of the x-ray beam. Indirectly, the intensity of the x-ray was measured

over the width of beam and variations up to 15% were discovered.

Two approaches have been pursued to dampen the variations in the beam intensity. Pb diaphragms were tested and found to reduce the beam intensity difference to 7%. Presently, we are in the process of manufacturing tungsten targets with different angles in order to improve the gray level uniformity.

d) Shadow Formations in Microfocus Radiography

Shadow formations have been observed on magnified x-ray film images. The shadows occur on the edge of test objects and are seen as an increase in film density. It has been determined that these shadows are due to secondary radiation produced internally in the tube head. At this point, several types of filter material have been evaluated for beam hardening and the reduction of internal scatter. One filter was found which absorbed the internal scatter and nearly eliminated the edge burnout on cylindrical samples which vastly improves the detection capabilities. We are now in the process of making modifications to our tubehead to prevent the formation of secondary radiation.

ii) Microfocus X-ray of Iterations

MFX examination of various type specimens from powder to final machined NSF bars is being utilized to monitor/control the quality of the various processing steps. MFX is also being used for identification of strength impairing flaws in test-ready bars for correlation with fractographic data and development of a failure prediction capability.

a) MFX of Colloidal Suspensions

New batches of recently made slip have been radiographed for the presence of inclusions and agglomerates. No agglomerates over 100 μm were detected. An alternate technique utilizing a "Hegman Gage" is also being utilized to evaluate the size of the agglomerates in the suspension. For batch S, agglomerates less than 25μm were measured using this technique. In order to monitor the aging effect on the slip, agglomerate frequency and size are monitored several times a day.

b) MFX Examination for Process Control

The improvement in processing over the course of the program can be plotted in terms of flaw population data versus iteration. Figure 6 provides plots of average flaw size and number of flaws per sample for iteration #1 through #5. The flaws include pores, inclusions and agglomerates detected in the gage length volume. The plots indicate dramatic improvement in both size and frequency, corresponding to strength improvements discussed under Task 4. Another illustration of process improvement is provided in Figure 7 which plots the percentage of bars which have defects detectable by MFX. Iteration #5 is seen to have only 39% of its samples with flaws above detectability limits, down from a high of 88% for iteration #2.

c) Detection of Strength Impairing Flaws

NSF bars from iterations #'s 3, 4, and 5 (batches N, O, P) were examined both in the green and HIP'ed conditions during the reporting period. The green examination was performed at 4X magnitude, while the HIP'ed bars were examined at 5X. In total, 13 iteration #3, 38 iteration #4 and 23 iteration #5 bars were examined. A variety of flaws were found in the gage section of the bars, including pores, agglomerates and inclusions. Approximately 50% of the bars showed no flaw indications and, as Figure 6 suggests, there was roughly one flaw averaging 75 μm in each of the samples which had indications.

MFX and liquid dye penetrant flaw indications have been interpreted relative to fractographic flaw data from iteration #3 and #4 samples. A total of 29 specimens which fractured in the gage section were among the 51 specimens examined prior to mechanical testing. Sixteen (16) of these 29 NDE evaluations resulted with no flaw detected. Fractographic analysis suggests that the majority of these specimens failed from machining damage. However, there were two volume inclusion failures among this group (100 μm and 165 μm). Refinements in digitized image enhancement are being pursued to increase the probability of detection of such flaws.

The balance of the 29 specimens (i.e. 13 bars) did have NDE indications and these can be compared to the failure origins suggested by SEM fractography. The comparison shows cases of notable agreement, cases where the NDE

indications did not correspond to the failure origin and, cases where the NDE data favorably supplements incomplete fractographic conclusions. The analysis of the data is being pursued with the goal of validating the interpretations for an eventual strength prediction capability.

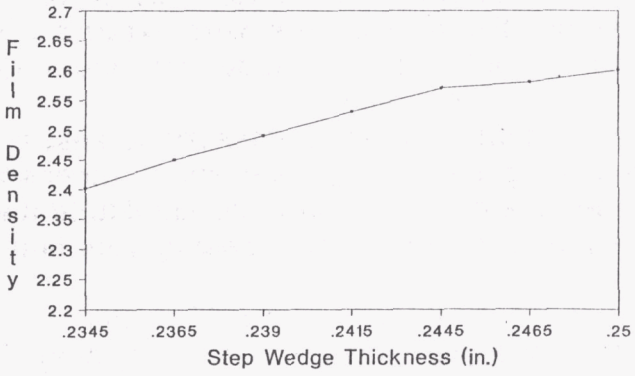

Figure 5: Density Gradient Si_3N_4 Step Wedge

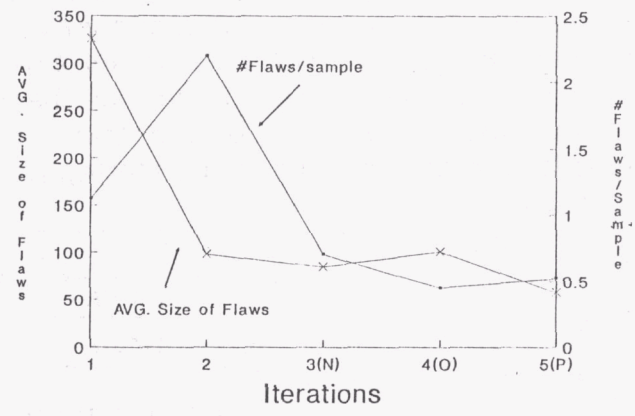

Figure 6: Microfocus X-ray Flaw Detection

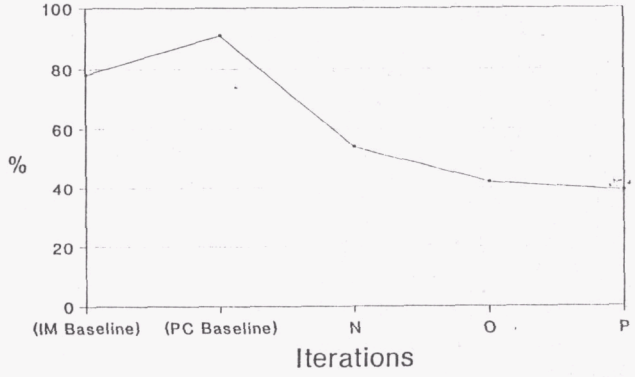

Figure 7: % Of Rods With Flaws Detected by MFX

iii) Ultrasonics (PAD) - In-Situ Monitoring of Casting

The potential for in-situ monitoring and control of the casting process was evaluated at Precision Acoustic Devices, Inc. Near net shape buttonhead tensile bar molds were equipped with 1.5 MHz transducers at each end of the mold cavity, positioned to be flush with the eventual end surfaces of the tensile bars. Plaster of Paris molds were used in the work. The transducers were fixtured in the mold to assure positive contact with the cast body throughout the casting process.

The ultrasonics experiment involved a pressurized suspension to simulate the iteration casting operation. The casting process was monitored by recording the time history of both the amplitude and velocity (time of flight) of the ultrasonic signal passing from one end of the mold to the other.

As shown in Figure 8, the amplitude of the UT signal increases, whereas the time of flight decreases as the casting proceeds. This is expected because as the cast layers build up on the mold surface, the conductance of the cast body increases. At the completion of the casting process, as marked in Figure 8, the amplitude and time flight reach their maximum and minimum values, respectively. Beyond this point the cast body begins to dry and hence the UT signal drops sharply. This point thus defines the completion of the casting process. It is anticipated that this procedure will be utilized to advantage for on-line monitoring and control of the casting process.

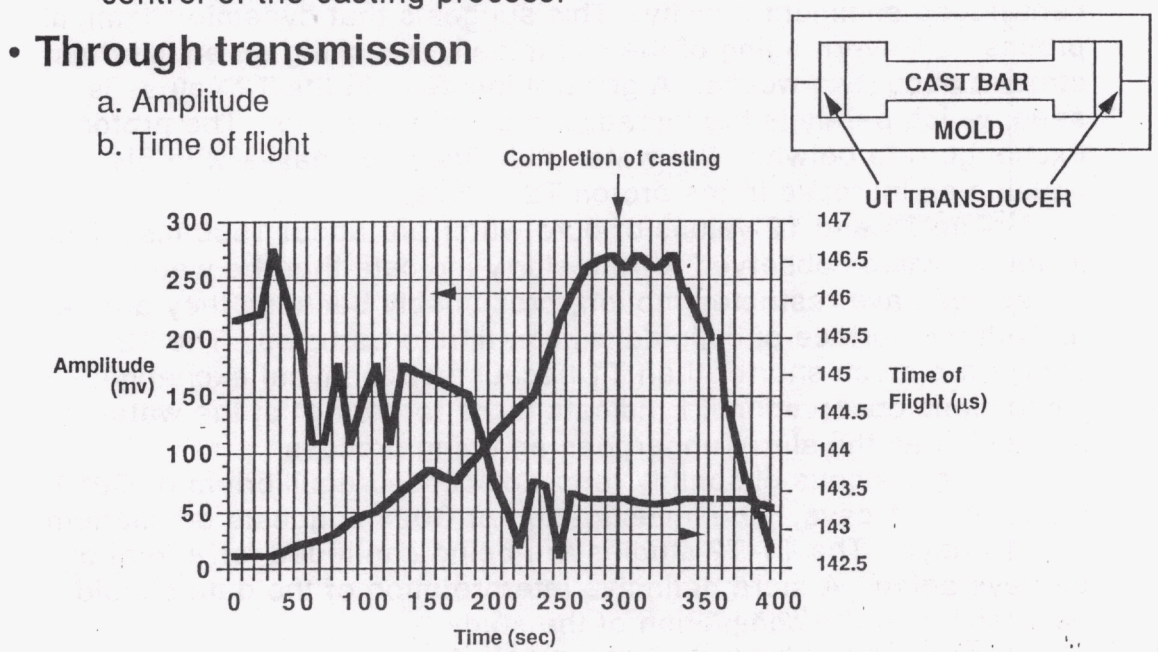

Figure 8: In-Situ Monitoring of Tensile Bar Casting by Ultrasonic Imaging

iv) NMR Spectroscopy (ANL) - Slurry Characterization

A comprehensive study was conducted for Batch C024 water milled silicon nitride slurry for a period of 24 days following the concentration of the milled batch. The investigation was focused at establishing the cause-effect relationship involving slurry behavior and certain basic slurry parameters. Measurements of viscosity, pH, centrifuged sediment packing density, and hard agglomerate size were made (at Norton Company) daily for the first 5 days, and then at one week intervals. Simultaneously, NMR spin-lattice or longitudinal relaxation time (T1) and spin-spin or transverse relaxation time (T2) measurements were conducted at Argonne National Laboratory.

The viscosity (Brookfield, @30 RPM) of the slurry remained at 22 cp during the aging. Largest agglomerate size as measured by a Hegman gage was relatively constant at 25μm. The slurry pH was found to increase from an initial value of 9.8 to final value of 10.4, and the packing density of the sediment (obtained by centrifuging the slurry for 30 min at ~ 1000 g) was found to increase from ~ 57 vol% to 60.5 vol% during the 24-day aging period, Figure 9.

The changes in the proton NMR longitudinal and transverse relaxation times are given as a function of aging time in Figure 10. In general, a reduction in the T1 value is observed with increasing aging time. During the initial stages, the T1 demonstrates oscillatory behavior. It subsequently stabilizes at ~ 680 ms after 13 days of aging. The decrease in T1 parallels the increase in the centrifuged sediment density. This suggests that dynamic chemical processes govern aging of the slip initially, reaching an equilibrium state in about two weeks. A general increase in the T2 values is seen, which parallels the increase in pH of the slurry. The proton exchange rate between the water molecules decreases with pH, causing an increase in the proton T2 values.

The T1 and T2 values of pure water are about 1500 ms. The lower T1 values observed for the slurry indicate that the water molecules have restricted motion, presumably because they are tied up with the surface of colloidal silicon nitride particles. The T2 values are much shorter than T1 because of chemical exchange. Reductions observed in T1 indicate more "ordering" of the water molecules as the slurry undergoes an aging process.

The previous bimonthly report discussed equilibrium of C019 slurry at ~ 11 days. The investigation of C024 suggests equilibrium at ~ 14 days. The T1-T2 studies are being continued for a total of 52 days aging. A more definitive interpretation of the data should be possible at the completion of the study.

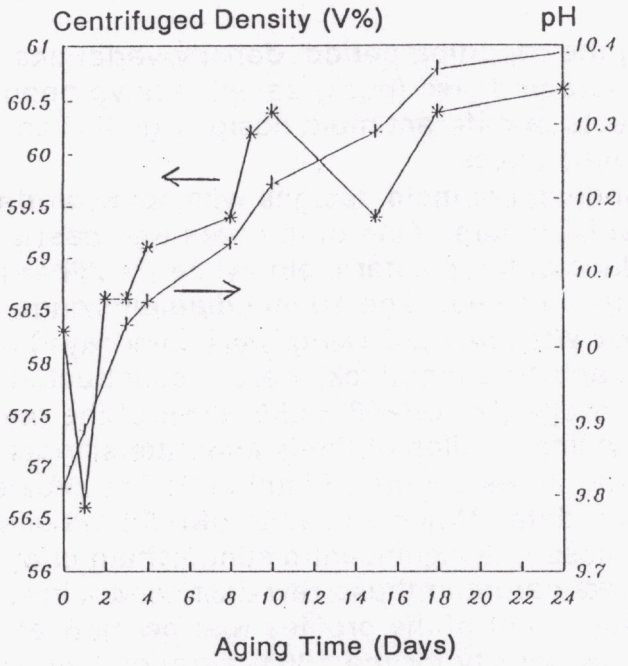

Figure 9: **Aging Behavior of Aqueous Ceramic Slurry pH and Sediment Density**

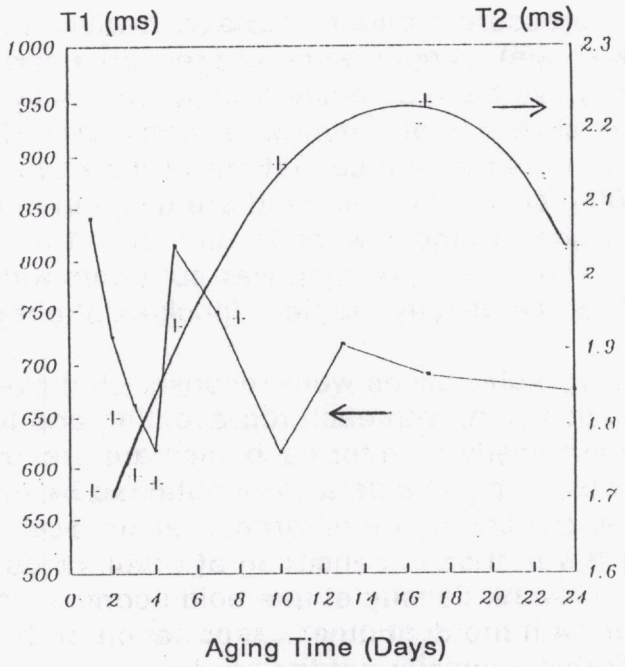

Figure 10: **Aging Behavior of Aqueous Ceramic Slurry T1 and T2 by NMRS**

iv) Computed Tomography (Argonne National Laboratory)

During the reporting period, density variations within green NSF tensile bars and disc (puck) samples have been evaluated to establish effects of different mold designs (NSF bars) and casting pressure profiles (discs).

A comparison of mold designs was completed on a pair of pressure cast NSF bars. One of the bars was cast using 100% filtration surface of the plaster mold, while the other had a portion of the mold surface sealed. The 10 mm diameter gage sections of the two specimens were imaged using identical x-ray CT parameters. Four slices (each 1.06 mm thick) were reconstructed with a tomographic image size of 256 x 256 pixels. The results are represented in line profiles of the image intensity across two diameters at 90° to each other, Figure 11. The profiles display raw pixel grey level data. While smoothing would aid interpretation, there nonetheless is a significant distinguishing characteristic of the two CT scans apparent in these raw data, and it involves the intensity at the center of the profiles (bar centerline). This location is a point of low density for the 100% filtration case, while it is a point of high density for the partial filtration case. These results suggest the possibility that the mechanism of cracking during drying of as-cast bars in the 100% filtration case involves the low density core indicated by the data.

Casting pressure profile trials have involved disc samples (hockey puck shape) using a range of pressures and mold materials. CT specimens have been obtained from the discs by diametrically sectioning thin slivers (5 or 8 mm wide) from them. Results from a CT evaluation of a specimen cast at ambient pressure to a bulk density of 2.00 g/cc in a plaster mold are given in Figure 12. The puck diameter and thickness were 76 mm and 11 mm respectively for this case. The sliver specimen was cut 5 mm wide and was mounted so that the density gradient (puck axial direction) was vertical.

Ten tomographic slices were reconstructed over the 11 mm height of the specimen, with each representing one-tenth of the height. Image intensity data for each slice are presented in Figure 12 from top to bottom. The data were obtained by averaging pixel intensities over the center 1 mm^2 area of each slice. The results indicate a 15% variation in density (gray level) through the puck thickness, with lowest density at the mold surface (bottom). These data combined with those of other cases form a basis for defining pressure profiles for density gradient control.

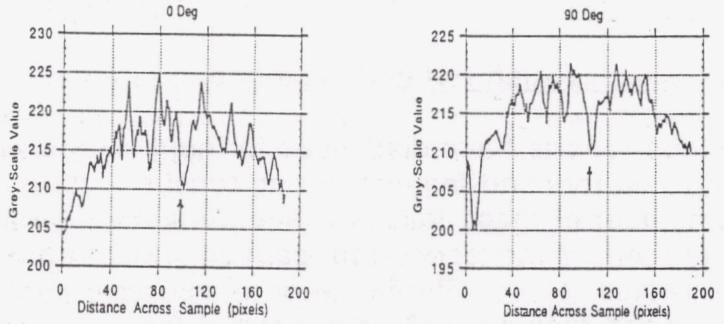

Figure 11: Diametrical Density Profiles for Two Mold Designs

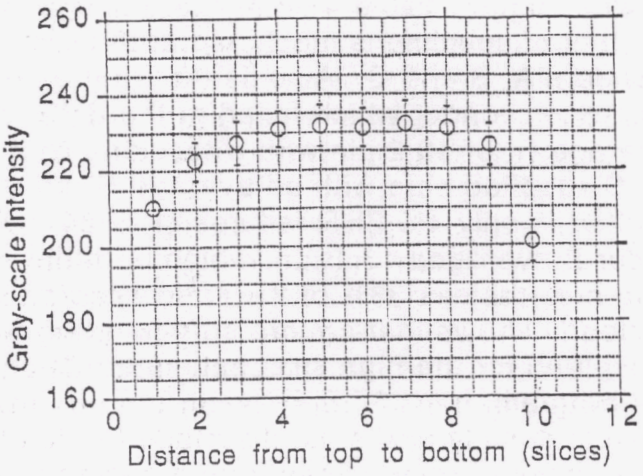

Figure 12: CT Green Density Data for Disc Cast Under Ambient Pressure

TASK 4: PROPERTY TESTING AND MICROSTRUCTURAL EVALUATION

i) Machining Surface Finish Related Buttonhead Failure

Previous reports have discussed forming issues which have contributed to buttonhead failures during tensile testing. A significant number of these failures have persisted, even after resolution of the forming issues that caused critical flaws in the buttonhead radius region. Profilometer measurements were taken at the buttonhead radius (BHR) of a large number of specimens of iteration #3 and #4 to establish whether poor surface finish was the source of the problem. The results clearly show that surface finish was the major cause of the problem.

The finding which implicates BHR surface finish was a serendipitous outcome of the machining requalification study which concluded during the reporting period. This study was initiated independent of the buttonhead failure problem and was pursued to obtain an update concerning cost, quality and delivery of NSF bars from different machine shops.

The average finish specification (R_a) at the gage and BHR is 16 μin (0.41μm). The three shops involved in the study routinely met and exceeded this requirement in the gage length, with R_a values of 5-7μin. The finish of the BHR varied significantly both above and below the spec and this provided the basis for correlating buttonhead failure to finish.

The overall average BHR surface finish of NSF specimens which failed at the BHR was found to be 20 μin. The average for non-BHR failure was 15 μin. Table 4 gives the average R_a measured at the BHR of specimens machined at three shops, designated as vendors A, B and C. Also listed are the percentages of specimens from each vendor which failed at the BHR. Vendor A finished to an average R_a of 19.2 μin with a resulting 51% BHR failures. Vendor C supplied bars with an average R_a equal to 9.7 μin. and this resulted in only 4% BHR failures (1 of 24). The R_a results from vendor B averaged 13.1 μin. which is within specifications, but nonetheless 33% of the specimens failed at the BHR. The data clearly shows that a more stringent surface finish specification is required for the high strength materials being processed in this program.

Table 4: Buttonhead Radius Surface Finish - Failure Data

VENDOR	AVERAGE R_a microinches	BUTTONHEAD FAILURES %	n
A	19.2 +/- 2.2	51	38
B	13.1 +/- 3.0	33	18
C	9.7 +/- 2.4	4	24

ii) Iteration N Tensile Data and Fractography

A set of 18 NSF tensile bars were tested for room temperature fast fracture strength. These were machined prior to the resolution of the surface finish problem, using procedures A and B, so that there was a high incidence of buttonhead failures (11 of 18). The 7 successful gage length fractures demonstrated exceptionally high strength levels. The data ranged from 818-1056 MPa with a mean strength of 920 MPa and Weibull modulus of 13.

The individual test and fractography data for these RT specimens and four high temperature specimens are given in Table 5. The fractography data show that machining damage is a major factor in the failure events. Three of the specimens failed from the effects of machining damage in combination with a surface pore or agglomerate, Figures 13a, b. A surface scratch normal to the tensile direction was the failure origin of specimen N-G, Figure 14. This damage may have been inflicted during the rough grinding operation.

There was one volume failure in the set of seven room temperature fast fracture tests. Specimen N-B failed due to a 30 um agglomerate in the gage section, Figure 15. Two elevated temperature (1370°C) fast fracture tests were conducted in this iteration. In one case, specimen N-M, failure originated from one of the numerous (2-20 μm surface length) machining pullouts that marred the surface of this specimen, Figure 16. The second 1370°C test was conducted on a specimen without noticeable machining defects. Its failure origin was not evident from fractographic evaluation. The 1370°C strength levels were 395 and 397 MPa, which are approximately 80% of the end of program target value of 500 MPa.

Two 1230°C stress rupture tests were conducted. The first test was run at an applied stress level of 250 MPa. Specimen N-J failed after 2 hours and the origin was traced to a surface machining

groove and subsequent slow crack growth, Figure 17. The second test was run at a reduced stress of 200 MPa but survived only 0.8 hours due to failure from a 165 um Fe/Y rich volume inclusion, Figure 18.

Table 5: Iteration 3 Tensile Test Data

Specimen	Temp. Test	Fast Fracture Strength (MPa)	Applied Stress (MPa)	Stress Rupture Life (hrs)	Flaw Origin		
					Location	Type	Size (um)
N-65	RT	898	-	-	S	M/A	45
N-B	RT	939	-	-	V	A	30
N-G	RT	879	-	-	S	Scratch	100
N-K	RT	946	-	-	S	M/A/P	50
N-22	RT	818	-	-	S	M/A/P	30
N-P	RT	1056	-	-	S	M	20
N-F	RT	902	-	-	S	unknown	-
N-M	1370°C	395	-	-	S	pullout	20
N-R	1370°C	397	-	-	S	unknown	-
N-J	1230°C	-	250	2	S	M/SCG	-
N-O	1230°C	-	200	0.8	V	I(Fe/Y)	165

M = machining groove A = agglomerate P = pore/porosity
SCG = slow crack growth I = inclusion S = surface
V = volume

iii) Iteration 4 (Batch O) Tensile Data and Fractography

The machining requalification study described above was conducted in part with specimens from iteration #4 and, as has been discussed, a large number of BHR failures were encountered. Nineteen (19) of 32 room temperature NSF fast fracture tests were successful gage length failures. In spite of excellent surface finish (R_a = 5-7 μin), SEM fractography suggests that the majority of these gage failures initiated from machining defects, ranging from 5 μm wide axial grinding marks to >750 μm transverse scratches, Figures 19a, b, c. A small percentage of the failure origins involved inclusions ranging in size from 20 to 135 μm, Figures 20a, b, c. In many instances, the SEM images provide incomplete detail on the character of the failure precursors, because of shattering of the

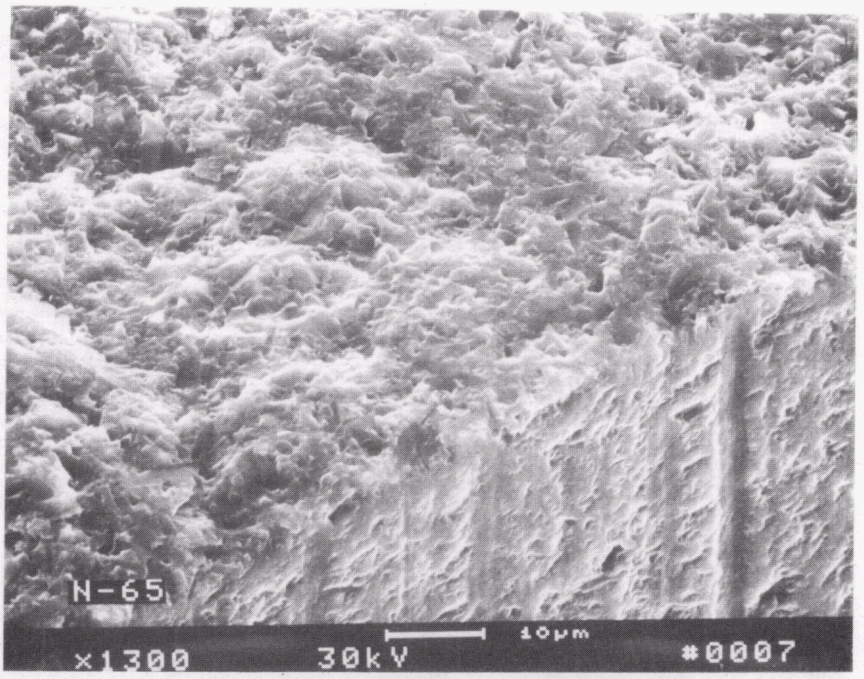

Figure 13a: Secondary Electron Image (SEI) of the failure origin of specimen N-65 (σ_f=898MPa) fractured at RT showing machining marks and agglomerate at the surface.

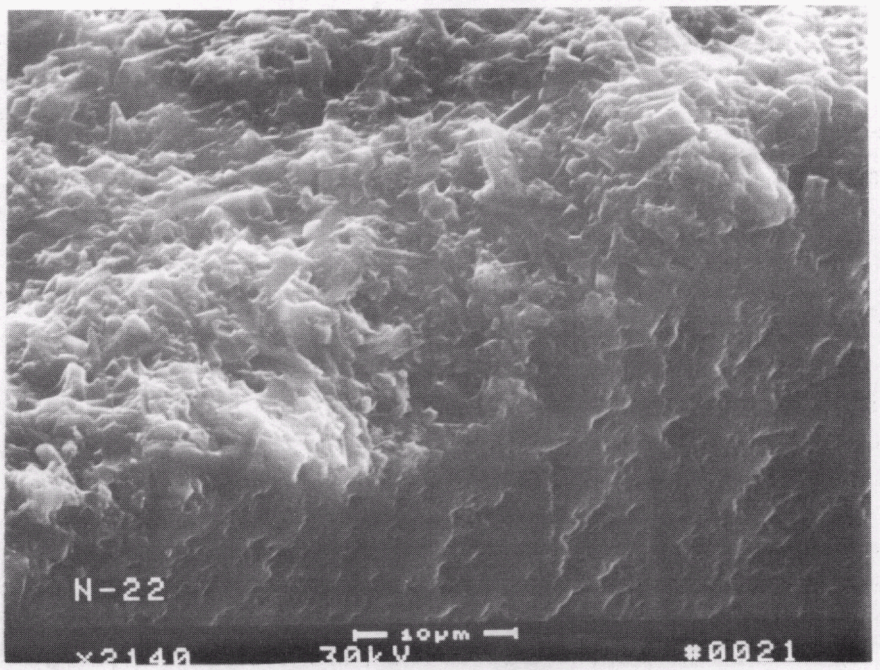

Figure 13b: SEI of the failure origin of specimen N-22 fractured at RT (σ_f=818 MPa) showing a machining mark associated with an agglomerate/or a pore.

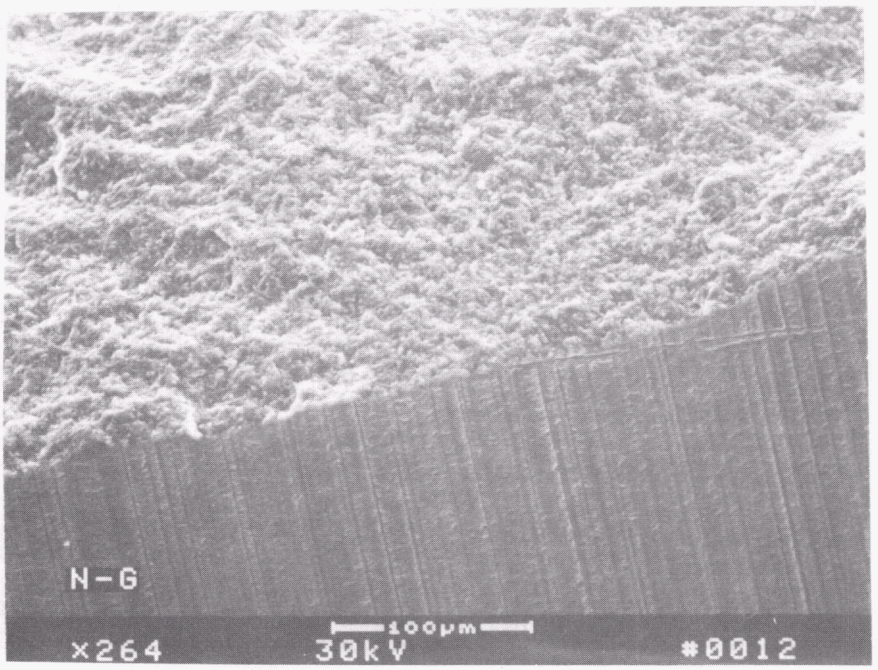

Figure 14: SEI of the failure origin of specimen N-G fractured at RT (σ_f=879MPa) showing a severe scratch normal to the longitudinal axis of the specimen

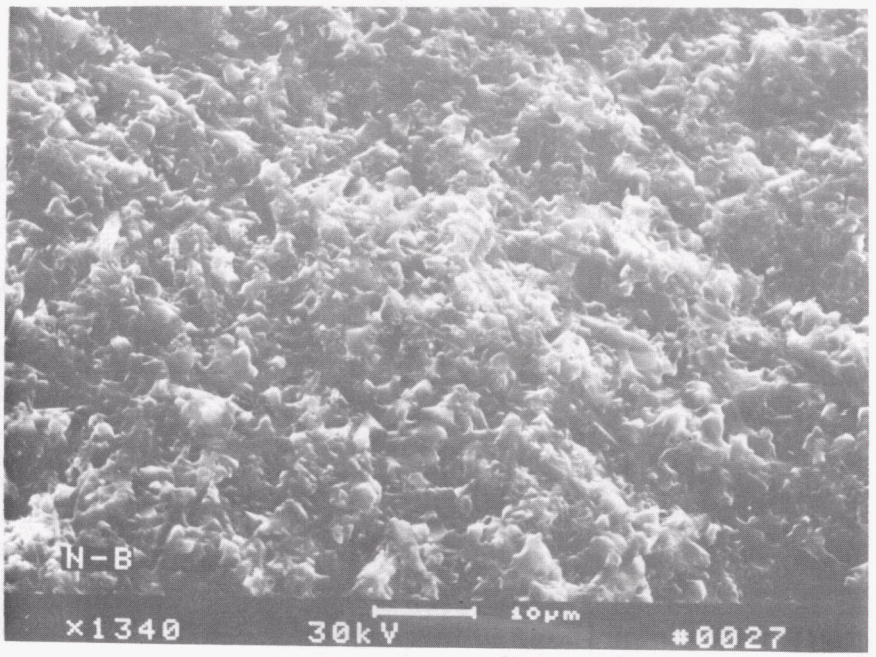

Figure 15: SEI of the failure origin of specimen N-B fractured at RT (σ_f=939 MPa) showing a ~30 µm diameter agglomerate.

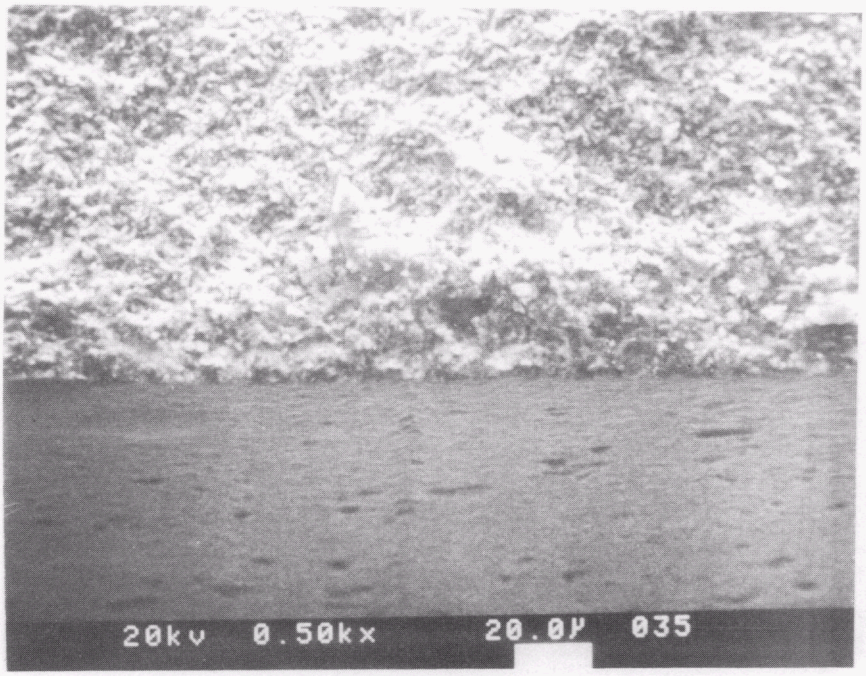

Figure 16: SEI of the machined surface and failure origin of specimen N-M fractured at 1370°C (σ_f=395MPa) showing pullouts from machining of sizes 2-20 µm.

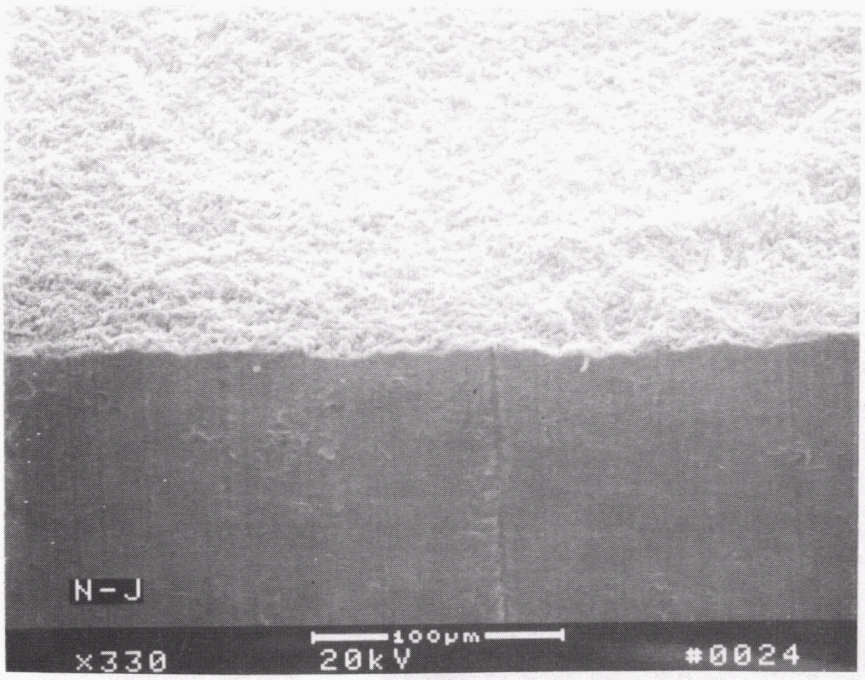

Figure 17: SEI of the failure origin of specimen N-J fractured at 1230°C during stress rupture showing a machining mark and slow crack growth.

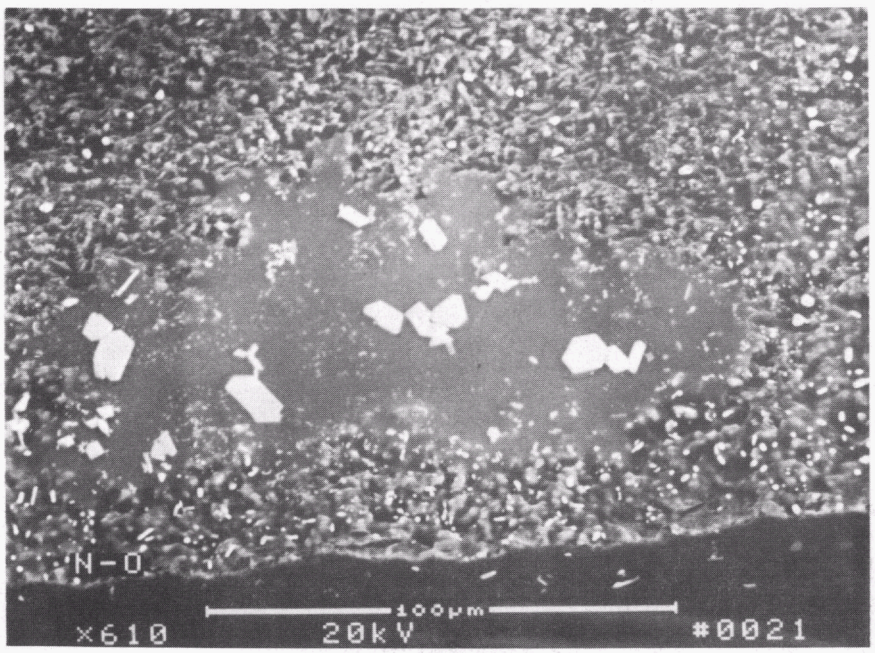

Figure 18: Back scattered Electron Image (BEI) of the failure origin of specimen N-O fractured at 1230°C during stress rupture showing an iron/yttrium rich inclusion.

failure origin or one of a variety of other reasons. Axial grinding marks, for example, are dominant features in a number of fractographs, even though they would seem to be unlikely precursors due to their benign orientation. Synergistic effects involving other subsurface flaws are probable causes of failure. Fracture mechanics is being employed to provide critical flaw size predictions which serve to guide the fractograph interpretations.

The tensile test and fractography data are summarized in Table 6. The room temperature fast fracture strength ranged from 586 to 950 MPa and averaged 789 MPa, with a characteristic strength of 839 MPa and Weibull modulus of 8.5. The fact that the specimens were machined at three sites suggests that a more definitive statistical analysis should separate the data into subsets. Considering the fact that two HIP runs were used in the iteration, four distinct subsets can be identified.

One of the iteration subsets (designated IV) involves the 8 specimens listed in Table 6 which were machined by vendor C. Statistical analysis indicates that the strength data of this subset are unprecedented in terms of the Weibull modulus measure of reliability: the analysis indicates a Weibull modulus of 28.1 with a characteristic strength of 904 MPa (mean strength of 889 MPa).

The surface finish comparisons conducted in the machining study indicated no statistically significant surface finish difference in the gage length region of specimens machined by vendors A, B and C. Nonetheless, the strength data for subset IV is so outstanding that the machining method employed by vendor C (roughing as well as finish grinding) will be incorporated as SOP in further iterations. Vendor C provided the best quality BHR surface finish in addition to the superior gage length grinding and as a result it will be recommended as primary program vendor, contingent upon contractual agreement.

Elevated temperature tests in this iteration involved four 1370°C fast fracture tests and one 1230°C stress rupture test, Table 6. The fast fracture strengths ranged from 140 MPa (slow crack growth from a machining defect) to 457 MPa (failure from a 100 μm volume Fe inclusion).

One stress rupture test was conducted on specimen O-58 using an initial applied stress to 200 MPa, holding at temperature for 24 hours, increasing the stress to 250 MPa, holding for 24 hours and then increasing to 300 MPa, with the intention of maintaining this stress level to failure. The specimen failed during the increase to 300 MPa. SEM fractography suggests that the failure origin was a surface defect/inclusion with a Fe, yttria, glass composition.

Table 6: Iteration 4 Tensile Test Data

Specimen	Test Temp.	Fast Fracture Strength (MPa)	Applied Stress (MPa)	Stress Rupture Life (hrs)	Failure Origin			Machine Shop
					Location	Type	Size (um)	
0-5	RT	787	-	-	V	I (Fe,Cr,Ni)	135	A
0-19	RT	685	-	-	S	M/I (Fe)	20	A
0-21	RT	666	-	-	S	M	25	A
0-23	RT	904	-	-	S	Unknown	-	A
0-25	RT	873	-	-	S	M	10	A
0-60	RT	726	-	-	V	I/A (Fe)	85	A
0-66	RT	796	-	-	S	M	10	A
0-12	RT	596	-	-	S	M	>750	B
0-22	RT	586	-	-	S	M	80	B
0-51	RT	618	-	-	S	M (Scratch)	>150	B
0-59	RT	650	-	-	S	Unknown	-	B
0-9	RT	827	-	-	S	M/P	40	C
0-11	RT	908	-	-	S	P	20	C
0-13	RT	950	-	-	S	P/A	20	C
0-15	RT	899	-	-	S	M	5	C
0-16	RT	884	-	-	S	M	5	C
0-37	RT	894	-	-	S	M	10	C
0-39	RT	870	-	-	S	Unknown	-	C
0-49	RT	879	-	-	S	M	10	C
0-27	1370°C	140	-	-	S	SCG	-	B
0-41	1370°C	457	-	-	V	I (Fe)	100	A
0-43	1370°C	306	-	-	S	P	25	B
0-45	1370°C	394	-	-	S	Unknown	-	A
0-58	1230°C	-	200-300	48	S	I (Fe/Y)	-	A

M = machining groove
P = pore/porosity
I = inclusion
V = volume

A = agglomerate
SCG = slow crack growth
S = surface

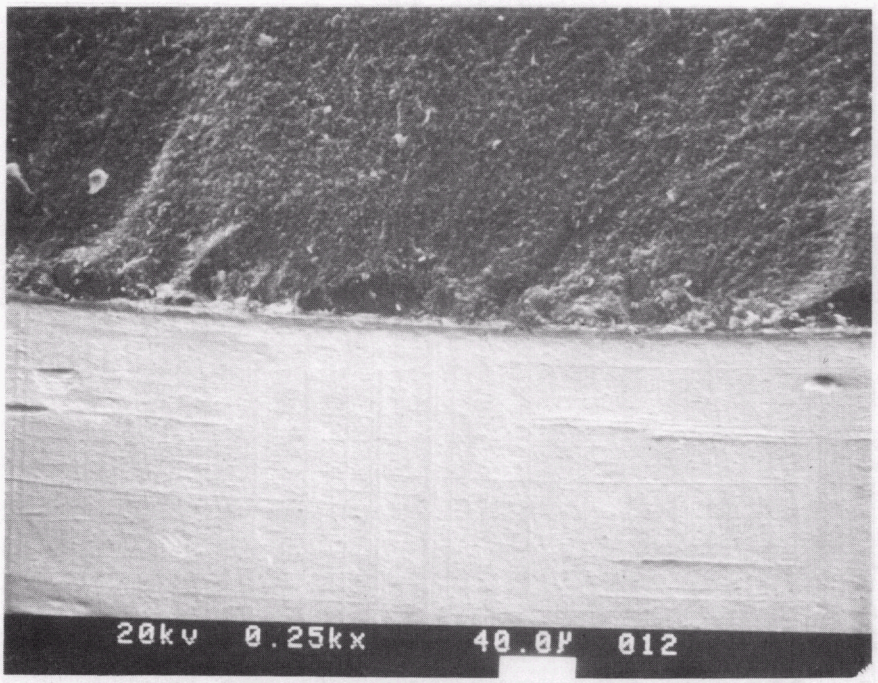

Figure 19a: SEI of the failure origin of specimen O-12 fractured at RT (σ_f=596MPa) showing a severe radial grinding mark.

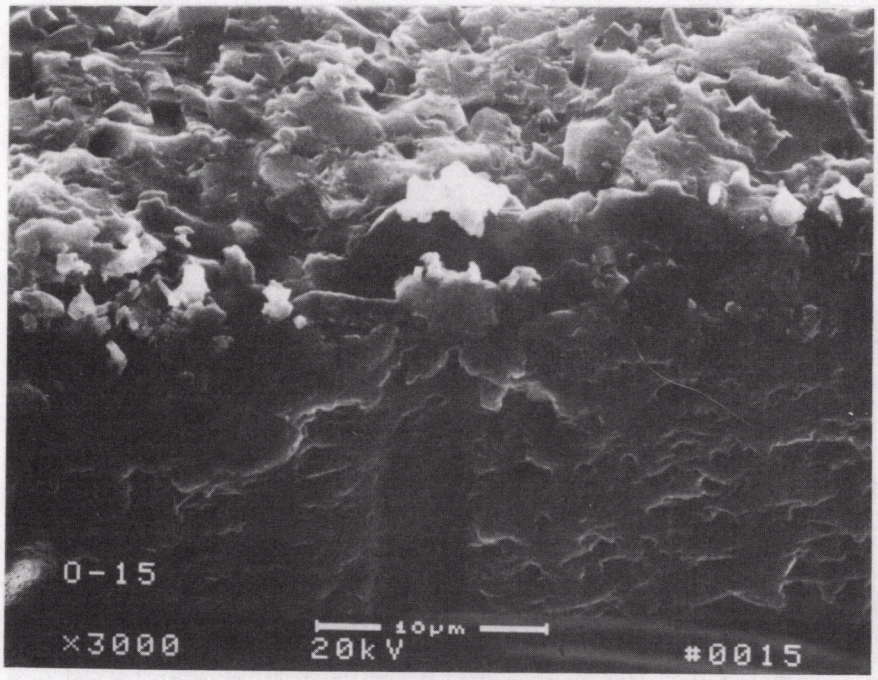

Figure 19b: SEI of the failure origin of specimen O-15 fractured at RT (σ_f=899 MPa) showing a 5 µm wide machining mark.

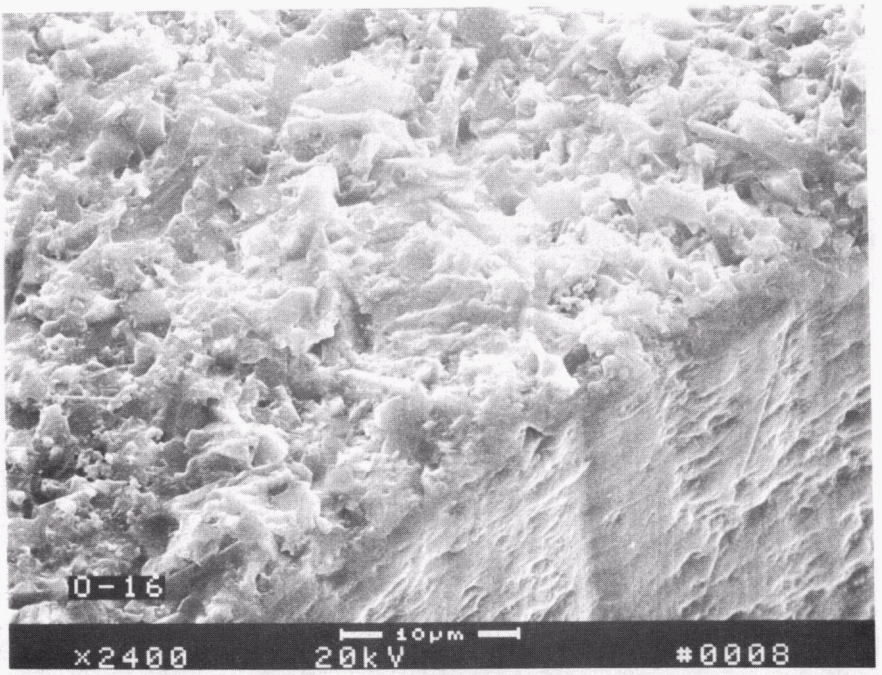

Figure 19c: SEI of the failure origin of specimen O-16 fractured at RT (σ_f=889MPa) showing a 5 μm wide machining groove.

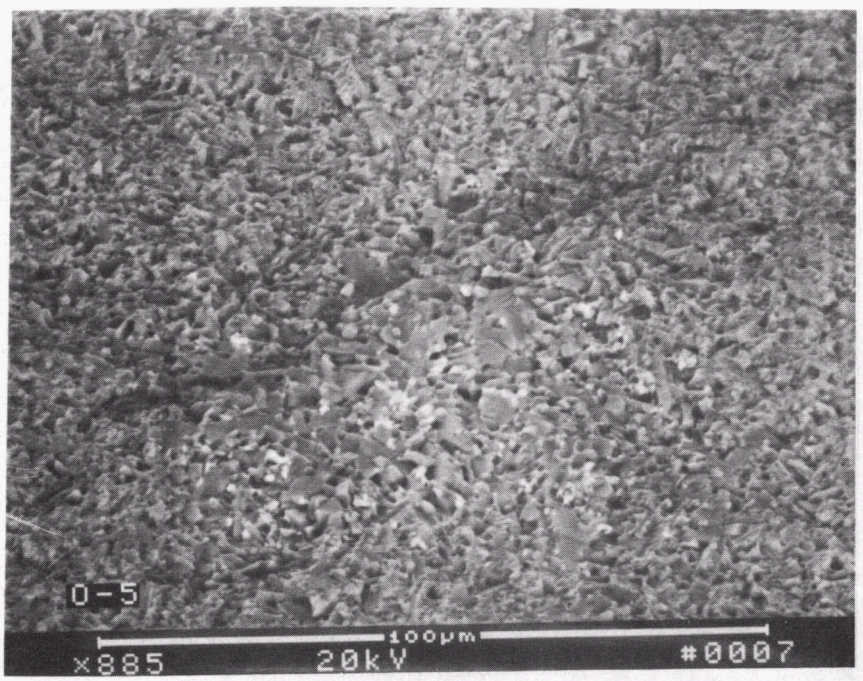

Figure 20a: BEI of the failure origin of specimen O-5 fractured at RT (σ_f=787MPa) showing an inclusion containing Fe, Cr, Ni.

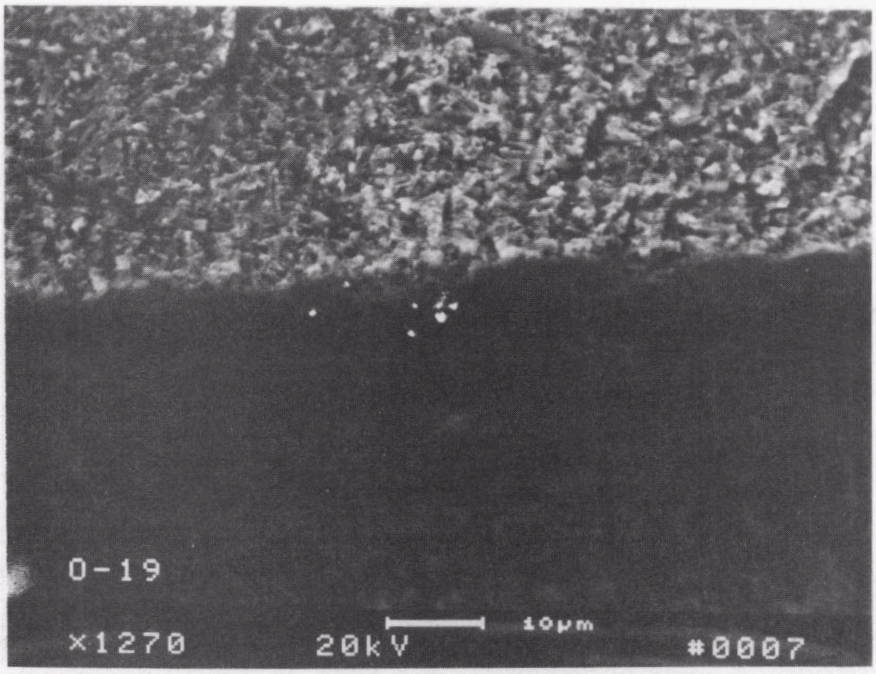

Figure 20b: BEI of the failure origin of specimen O-19 fractured at RT (σ_f=685MPa) showing an iron rich inclusion at the surface.

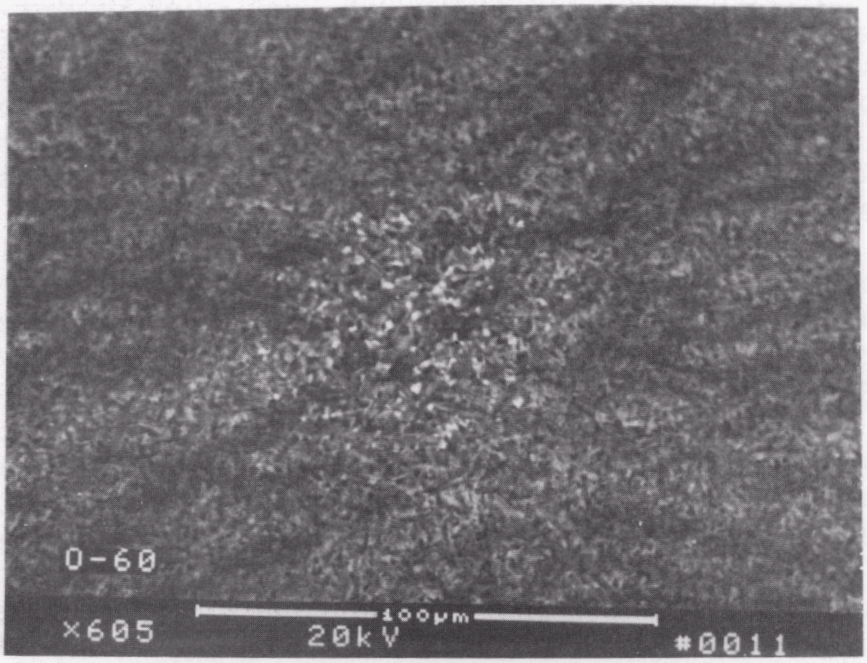

Figure 20c: BEI of the failure origin of specimen O-60 (σ_f=726MPa) showing an inclusion/agglomerate containing iron.

iv) Fractography - Strength Correlation

Utilizing fracture mechanics, the strength σ_f of a tensile specimen determined in a fast fracture test can be used in conjunction with the material's fracture toughness K_{IC} to estimate the size of the critical, fracture-initiating flaw. The approach has been used in conjunction with fractographic evaluation of surface failures to establish the character of fracture precursors. The simplest model neglects residual stress and considers the critical surface flaw as a semi-circular sharp crack oriented normal to the applied stress. In this case, the surface length (twice the depth) of the critical flaw is given by, Ref.(1):

$$\text{critical flaw surface length} = 2/\pi\ (K_{IC}/0.8\ \sigma_f)^2$$

Iteration #4 surface failures were analyzed by this approach using a K_{IC} value of 6.2 MPa $m^{1/2}$, which is representative of this batch of material. The fracture mechanics (FM) prediction for the surface length of the flaw is given in Table 7 along with the corresponding SEM observation, for each of the 10 surface failures attributed solely to machining damage. Also given in the table are R_v values from profilometric analyses of the gage section surface finishes.

R_v is a measure of the maximum depth of the surface profile below the mean. The profile was measured in the circumferential direction corresponding to the axial finish grinding. The values of R_v are on the order of 1μm and it is clear that there is no correlation with strength. This is not surprising in view of the axial orientation of the grinding profile. SEM/FM suggests that the size of the critical flaws exceed R_v values by 1-2 orders of magnitude.

The SEM/FM data fall into two sets, corresponding to low strength/large flaw size and high strength/small flaw size. In the low strength cases, there is reasonable agreement between SEM and FM, suggesting that the dominant precursor has been derived from the SEM image.

The semi-circular flaw model is clearly inappropriate for the >750 μm machining scratch of specimen O-12. A high aspect ratio semi-elliptical model would seem to be more realistic for this case. For such a flaw the relevant dimension is the flaw depth (minor semi-axis) and analysis using this model, Ref (2), suggests that the scratch penetrated to a depth of 38 μm causing fracture at 596 MPa.

There is significant variance between the SEM observations and FM predictions for the higher strength cases (796-899 MPa). FM estimates of surface length fall in the range 47-60 μm, while SEM precursor feature dimensions are in the 5-10 μm range. This

variance suggests that the dominant failure origin character has not been captured in the SEM images. Additional evaluation is being conducted to resolve the discrepancies on a case by case basis.

Table 7: SEM Fractography & Fracture Mechanics Predictions

#	σ_f (MPa)	Flaw Surface Length (μm)		R_v (μm)
		SEM*	FM Prediction**	
0-22	586	80	111	.39
0-12	596	>750	107	.71
0-51	618	>150	100	.40
0-21	666	25	86	-
0-66	796	10	60	1.29
0-25	873	10	50	-
0-49	879	10	50	.82
0-16	884	5	49	.51
0-37	894	10	47	.95
0-15	899	5	47	.68

** Semi-circular surface crack model
* Largest evident surface feature near mirror

v) Residual Stress in NSF Bars

An assessment of near surface, machining induced residual stress states in NSF tensile bars was completed during the reporting period, meeting the June 30, 1991 milestone on this subject.

The work was conducted at the Army Materials Technology Laboratory. The x-ray diffraction approach with Cu K_α radiation was used. The $\sin^2$ psi stress measurement technique was employed to provide quantitative data on a total of 13 NSF bars. A number of MOR bars and a Si_3N_4 powder sample were evaluated in the course of the developmental work. This technique provides a stress measurement which represents a bulk volume average, as opposed to point values. In this study, 50% of the diffracted volume is within 22.8 μm of the specimen surface.

The stresses in the gage section were the primary focus of this work. Longitudinal stresses measured at the center of the gage length were found to be invariably compressive, with magnitude ranging from 200 to 400 MPa. Hoop stresses when detectable were found to be tensile with magnitude ranging to 70 MPa.

The technique was utilized to establish the dependence of residual stress on post-machining heat treatments, grinding methods of different machine shops and forming (injection molding vs. pressure casting) methods. No effect was found on the as-machined stress state after a series of trial heat treatments. Likewise, no significant differences in residual stress were found in the assessment of specimens machined at three machine shops. A difference was found when comparing injection molded and pressure cast final machined specimens. The cast specimens were found to have a higher level of compressive stress, 350 MPa vs. 245 MPa for injection molded specimens. This could be a result of the green density gradients inherent to the casting process, which cause HIP related residual stresses.

In an attempt to measure HIP related residual stresses, one specimen (R-16) was partially machined in the gage section. Residual stress analysis was performed at 8 orientations corresponding to four different depths of machining as well as the as-HIP'ed surface (0° orientation). No significant difference in residual stress was found after grinding to depths of 0.012, 0.048, 0.104 and 0.114 inches.

An unexpected result in this study involved the x-ray diffraction integrated intensity which was found to increase with depth of machining, Figure 21. This integrated intensity is proportional to the % ß-phase Si_3N_4. As such, the data forms a trace of the diminishing α-phase of the HIP reaction layer. This result suggests a potentially useful Q.C. method for assessment of reaction layer removal in machining.

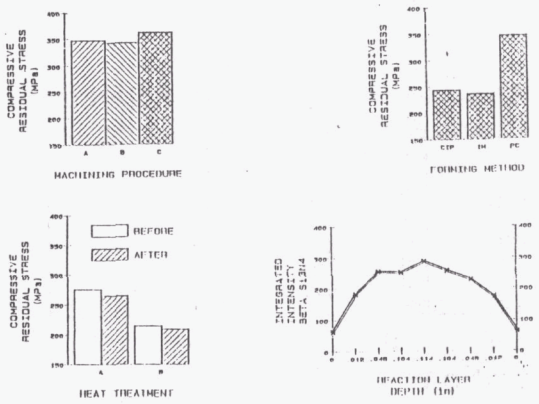

Figure 21: X-ray Diffraction Residual Stress Results

vi) Stage II Tensile Strength Data Summary

The Stage II experimental plan (Table 1) involves 14 NSF bar iterations with 10 control variables and one MLP iteration. The iteration schedule spans the 15 month period 2/1/91 to 4/30/92. Eleven NSF bar iterations have been started and are at various stages of completion. Tensile data have been obtained for specimens from iterations N through V. These data are summarized in Figure 22.

The data suggest that there are numerous process conditions (control variable combinations) which have the potential of producing 900 MPa strength levels. Systematic fractography and NDE studies are being used to isolate reliability impairing conditions/defects. An example is the machining procedure which was identified in iteration O. Another reliability impairment source that has been found to have increased in significance through Stage II is iron contamination. Actions have been initiated to control this source of variability.

An important in-process performance measure has been found to be the K_{IC} of qualification tile that are HIP'ed with NSF specimens. Since K_{IC} is an intrinsic measure of the material microstructural fracture resistance, a densification acceptance criterion (accept/reject) based upon K_{IC} has been established.

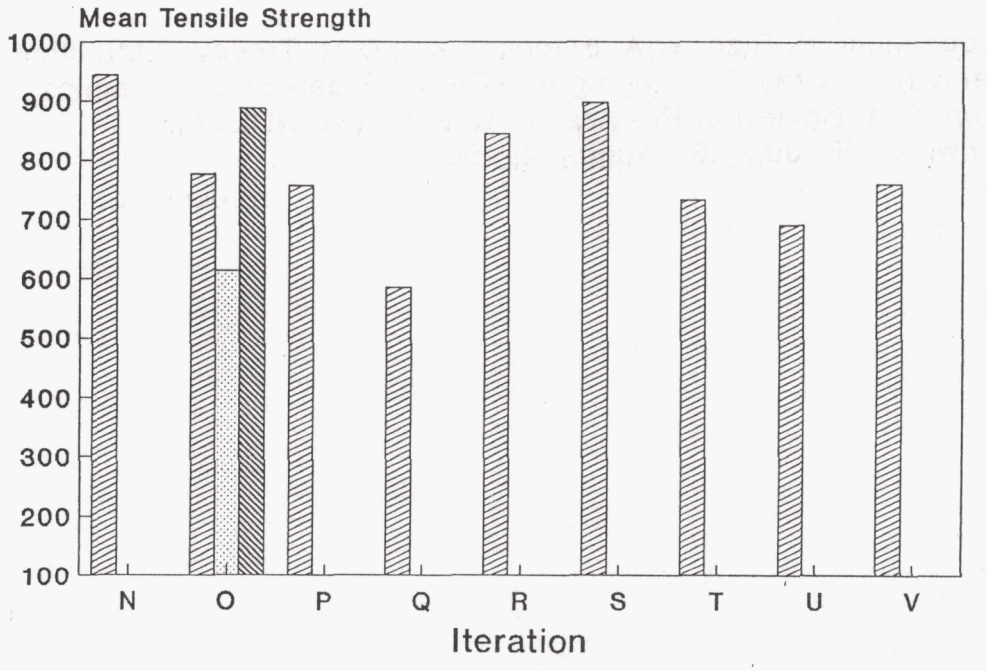

Figure 22: Mean Tensile Strengths from Stage II Iterations

References

1. D.M. Tracey, "3D Elastic Singularity Element for Evaluation of K Along an Arbitrary Crack Front," Int'l J. Fracture, 9, 1973, pp. 340-343.

2. H.L. Ewalds and R.J.H.Wanhill, Fracture Mechanics, 1984, Edward Arnold Publishers, Ltd, Baltimore, pp.42-43.

Status of Milestones

All Milestones are on schedule. Milestone #114115, (Determine residual stresses in machined NSF bars and relationships to grinding/finishing methodology) completed as scheduled on 6/30/91.

Publications

1. V.K. Pujari, K.E. Amin and P.H. Tewari, "Development of Improved Processing and Evaluation of Silicon Nitride", ASME paper 91-GT-317, presented at Int'l Gas Turbine and Aeroengine Congress and Exposition, Orlando, FL, June 3-6, 1991.

2. V.K. Pujari, "Process Control in Injection Molding of Non-Oxide Ceramics", presented at Powder Injection Molding Int'l Symposium, Albany, NY, July 15-17, 1991.

3. N. Gopalsami, P. Rizo, W.A. Ellingson and D.M. Tracey, "Detection Sensitivity of X-ray CT Imaging for NDE of Green-State Ceramics", presented at Review of Progress in Quantitative NDE Conf., Brunswick, ME, July 28 - August 2, 1991.

Improved Processing

S. D. Nunn, O. O. Omatete, A. E. Pasto, and
R. A. Strehlow (Oak Ridge National Laboratory)

Objective/scope

To determine and develop the reliability of selected advanced ceramic processing methods. This program is to be conducted on a scale that will permit the potential for manufacturing use of candidate processes to be evaluated. The emphasis of this program is on silicon nitride. Issues of practicality; safety, hygiene, and environmental issues; and in-process testing methods are to be addressed in addition to technical feasibility. The methodology includes selection of candidate processes and evaluation of their range of applicability to various kinds of commercially available ceramic powders.

Technical highlights

I. Silicon nitride gelcasting and sintering

Work continued on preparing test plate specimens. A specification for a series of varied compositions has been prepared for silicon nitride plates using yttrium and aluminum oxides as sintering aids. The following specimens were processed during the period:

1. gelcast three 6% yttria-2% alumina plates;
2. sintered three half plates of 8% yttria-4% alumina at 1900°C, 300 psig (2×10^6 Pa); and
3. sintered at 1750°C and 15 psig (2×10^5 Pa) the matching half plates for comparative studies of sintering conditions.

In addition, several other parts were gelcast for drying studies, and specimens of varying thickness were prepared in the range of 1 to 2 cm. This is part of a series on maintenance of shape integrity of gelcast parts.

Work was interrupted on the preparation of test plate specimens by repair operations on the high-pressure furnace used for sintering.

II. Drying studies

We found earlier that:

1. Humidity is the dominant variable, and room-temperature drying may be adequate for thin parts.
2. There is no constant-rate drying period.
3. The length of drying can be significantly reduced by varying the humidity and/or the temperature.

Drying studies continued using gelcast silicon nitride specimens. A drying study on a silicon nitride part was conducted using a full-plate specimen of 6% yttria-2% alumina at constant conditions of 75% RH and 35°C. The results are being analyzed.

III. Alternate systems development

Experiments in alternate systems not based on acrylamide have continued. Two effective alternate systems have been found and are being evaluated.

IV. Cooperative research agreement with Garrett Ceramic Components

The objective of this work is for Garrett Ceramic Components (GCC) and the Oak Ridge National Laboratory (ORNL) to perform a collaborative research program to examine the gelcasting process for fabrication of ceramic components using GCC's GN-10 silicon nitride material. This program will investigate whether the process exhibits advantages over slipcasting, pressure slip casting, or injection molding in terms of the resultant material properties, part quality, and shape-forming ability. The applicability of the process to GN-10 complex-shaped parts, such as turbocharger rotors and advanced gas turbine rotors, will be examined.

All parts originally scheduled to be gelcast were completed and shipped to GCC. After they were glass-encapsulation hot isostatically pressed (HIP'ed) by GCC, they were returned to ORNL for tensile testing. The parts included: 11 flat plates for subsequent tensile testing, 11 T-25 turbocharger rotors, four 3-cm-diam rods, and two "doughnut" specimens – to test for flaw introduction due to shrinkage on gelation.

Machining of test specimens was begun. Two plates were selected and returned to GCC for test and evaluation. The plates were from runs that produced three plates and two rotors. The GCC test procedure will be for modulus of rupture (MOR) specimens to be prepared from these plates, and the results are to be compared with those from ORNL tensile specimens.

Twenty-two square cross-section bars cut from one of the silicon nitride plates have been tested for uniaxial tensile strength. The test bars had a nominal 6 by 6-mm cross section and were chamfered before being mounted in the grips. The material had an average fracture strength of 334.3 MPa (48.5 ksi) with a standard deviation of 31.3 MPa (4.5 ksi). The calculated Weibull modulus was 11.03 for this group of samples.

Optical examination of the fracture surfaces indicated that the fracture origins were at internal process-related flaws. These appear to be primary pores that were filled by the sintering aid glass during densification. This resulted in inclusion particles, which acted as critical flaws. Five of the 22 specimens were selected for scanning electron microscopy/energy-dispersive microscopy (SEM/EDS) analysis of the fracture surfaces. In addition, one of the rods prepared in this work has been prepared for SEM analysis.

Eleven rotors made in the effort have been tomographically analyzed. The resulting images are being analyzed.

It has been agreed that, based on the results of this work, additional efforts would be undertaken to develop the process of gelcasting silicon nitride. Further casting trials are being planned using added materials that have been received from GCC.

Processing Science for Si_3N_4 Ceramics F.F. Lange, D.S. Pearson (University of California, Santa Barbara)

Objective/scope.

We are trying to increase the understanding of the role of interparticle forces in the processing of ceramics. The effects of electrolyte addition and pH changes on the rheological properties of dispersions, the kinetics of pressure filtration, and the mechanical properties and microstructure of the resulting bodies will be compared to each other and to existing models of interparticle forces (*i.e.* DLVO theory).

Technical progress.

We are formulating a new processing paradigm. The current paradigm is based on producing slurries with long-range repulsive forces. We propose that strong, short-range repulsive forces produce better slurries and green bodies. Unlike long-range repulsive forces which permit particle segregation, short-range repulsive forces prevent particle segregation by permitting particles to weakly agglomerate without surface/surface contact.

In addition, we have seen evidence that this short-range repulsive force can be tailored to create a shear-thinning slurry where particles can be separated and mixed at high shear rates and the mixing frozen in place when no shear is applied. The green bodies formed from these weakly agglomerated slurries are plastic when saturated and dry without cracking.

We examined two silicon nitride systems with short-range repulsive forces: one aqueous and the other non-aqueous.

Aqueous systems.

Alumina slurries have shown improved processing when salt is added[1] and we have attempted to determine if this effect occurs in silicon nitride. In alumina, the viscosity of the slurry is increased by the addition of salt while the green body remains plastic with little effect on the green-density.

Silicon nitride powder.

Continuing our study of the fundamental properties of powders and how these properties are related to their dispersion

behavior, we had the electrophoretic mobility of UBE SN-E3 silicon nitride powder examined at Rutgers University.

Figure 1 shows the results tested by the ultrasonic technique. The mobility at low pH is significantly less than the mobility at high pH. This agrees with our observations on the stability of silicon nitride slurries: Dispersed suspensions made at pH 10 are more stable and produce consolidated bodies with a higher green density than slurries made at pH 2. The isoelectric point is seen to be at approximately pH 5.5, close to the isoelectic point (pH 6) we observed in our electrophoretic mobility apparatus.

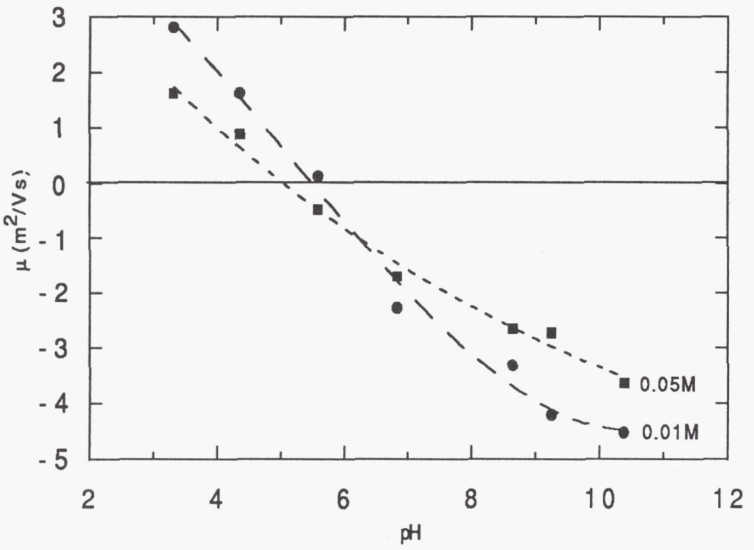

Figure 1. Acoustophoretic mobility measurements on UBE E-3 powder.

Consolidated bodies.

The density of consolidated bodies formed from coagulated slurries was investigated over the pressure range from .1 to 10 MPa. Pressure was applied by either centrifugation or pressure filtration. While the density of these bodies remained relatively constant regardless of the consolidating pressure, it was found that the rheology of these bodies varied considerably. All of the consolidated bodies appeared elastic, although bodies consolidated below 2 MPa were disrupted by ultrasound or vigorous shaking and the body becomes fluid.

Removing agglomerates from the powder prior to consolidation improved the rheology of the body formed. A body prepared from as-received powder was dispersed in water by ultrasound. This slurry was then consolidated by pressure filtration (2 MPa) and the newly formed body was disrupted by ultrasound such that a viscous slurry was recovered. Another body was formed by identical procedures, but the starting powder was cleaned of larger agglomerates by centrifuging. The rheology of these bodies are shown in figure 2 and it is clear that the de-agglomerated powder forms a body which is much less viscous.

Presently, we are subjecting consolidated bodies to uniaxial loads superimposed over hydrostatic pressures. This is commonly termed a triaxial test. The hydrostatic pressure generates a purely compressive stress in the sample, while the uniaxial load generates a shear stress.

If no hydrostatic load is applied (and we can observe the sample during the test), the bodies fracture vertically (*ie.* split). Under hydrostatic load, the body yields, but this may be due to either micro- or macroscopic cracking. In some cases the samples appear to have cracked during the test. Since no sample has come out of the apparatus flowing, we have concluded that we have not yet achieved fluidization. Some samples flow when touched after testing. Again, it is impossible to quantify this type of yielding.

Figure 3 shows the yielding behavior of silicon nitride bodies made from dispersed slurries under several hydrostatic loads. The yield stress increases with increasing hydrostatic pressure. This is consistent with results found in soil mechanics. Unfortunately, these samples appeared to have cracked rather than fluidized.

Bodies made from salt-added slurries also exhibited a yield (figure 4). After testing, these samples would then flow when touched; however, they also appeared cracked so it can not be concluded that fluidization has occured during the test. The yield stress for these samples is much lower than for the dispersed samples; this is an indication that the added salt is reducing the interparticle forces.

Since these types of materials are usually dilatant at these high volume fractions (~50%), we plan on performing our tests at extremely slow rates to avoid excessive stresses as the particles move past each other necessitating a volume expansion. We also plan on running our test with much larger hydrostatic pressures.

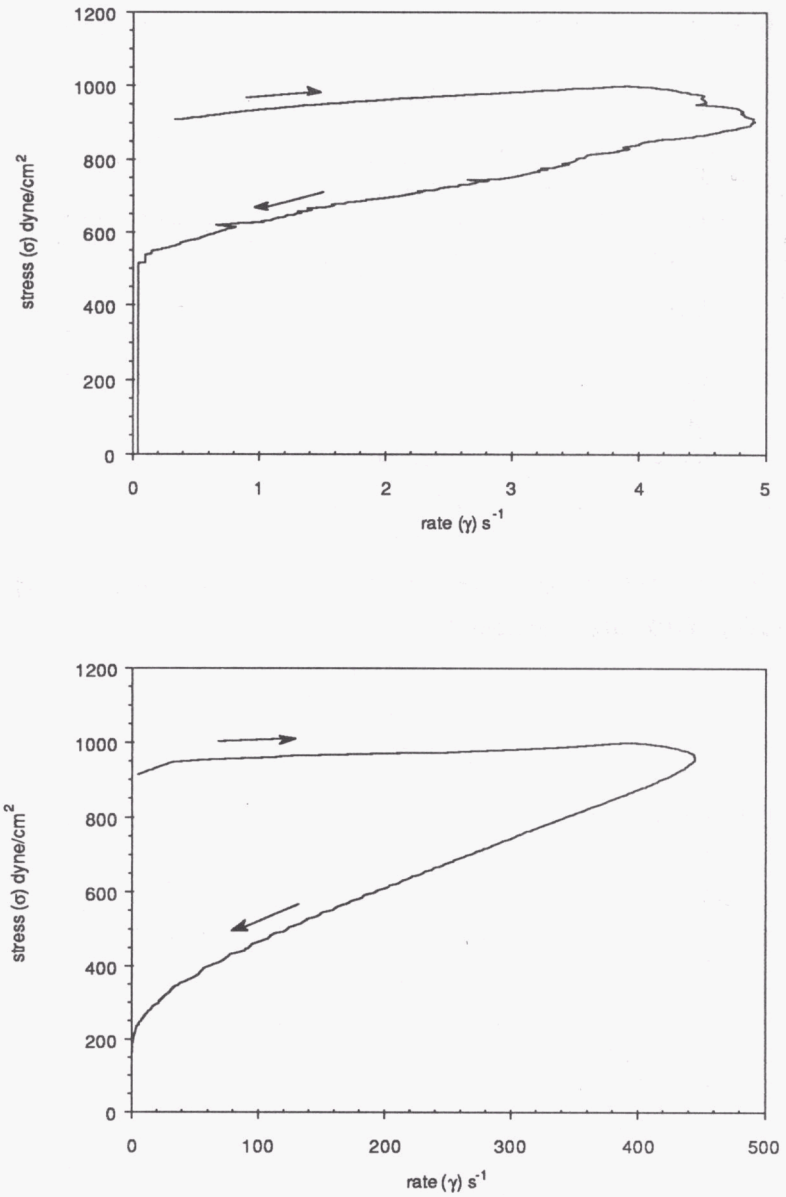

Figure 2. Stress *vs.* rate for sample A (upper), the as-received powder, and sample B (lower), the cleaned powder. Arrows indicate direction of stress ramp. Note the scale change on the x-axis.

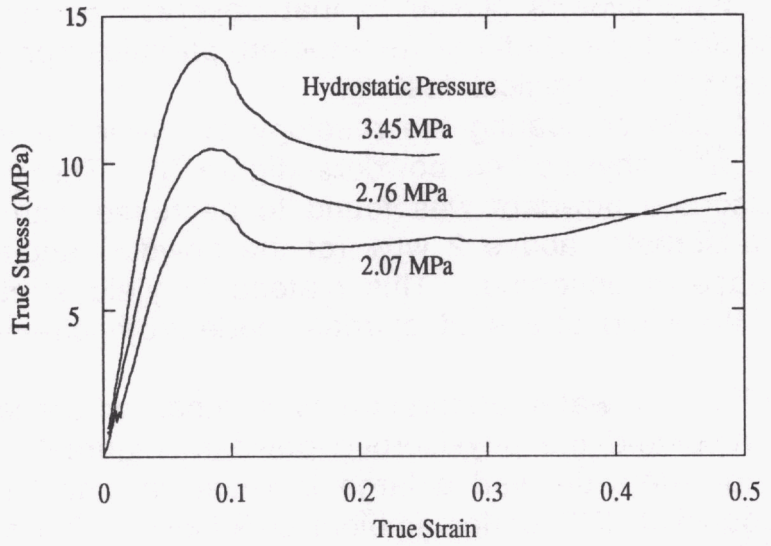

Figure 3. Triaxial compression of pellets from dispersed slurry (no salt added).

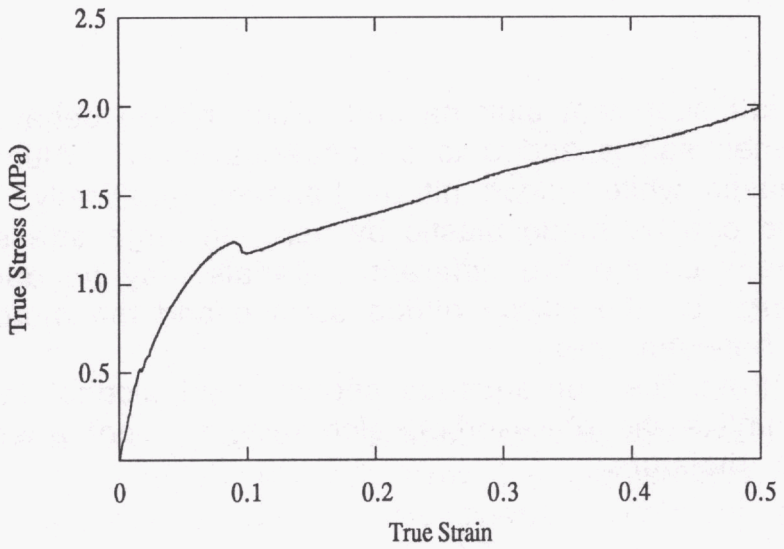

Figure 4. Pellet from salt-added slurry with 2.76 MPa hydrostatic pressure. Note the change in scale.

Nonaqueous systems

We are expanding the range of molecular weights of the molecules which we are reacting with the surface. The rheology of these reacted particles is similar to that observed earlier. We are currently making large batches of reacted particles for producing green bodies for mechanical testing.

We are also comparing the rheology of slurries made from chemisorbed and physisorbed powders (figure 5). The yield stress of the physisorbed powders was found to decrease with increasing addition of adsorbate; above 2 wt% (of the powder) addition, no further increase is observed. This plateau in yield stress is still higher than the yield stress of slurries made from chemisorbed powder.

The effect of water adsorption is another difference between the chemisorbed and the physisorbed powders (figure 6). The physisorbed powders showed a large increase in viscosity when they were cooled to 5°C under ambient conditions. The tool had water droplets which had formed from moisture in the air. If the sample (and the tool) were kept under dry nitrogen, no water condensation occured and the viscosity was similar to that at room temperature and to that of the chemisorbed material at room temperature and at 5°C; the chemisorbed material was not affected by condensation of moisture.

Summary.

We have seen that alumina and silicon nitride behave differently when salt is added to an aqueous slurry. Alumina becomes plastic while silicon nitride behaves elastically. The silicon nitride can be made plastic by applying large stresses. The difference between the two different materials may be due to the reduced charge on the silicon nitride surface and the morphology differences between them.

In contrast, the non-aqueous chemisorbed alcohol system is plastic and unlike the physisorbed alchohols it is not affected by atmospheric moisture.

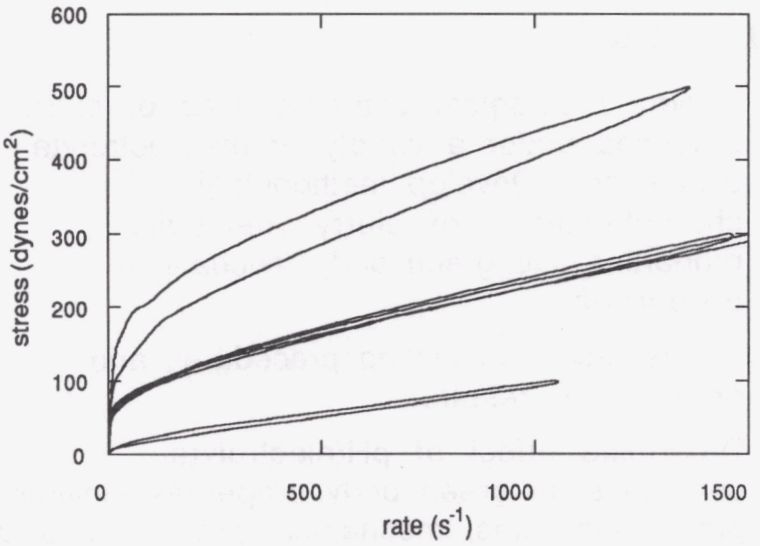

Figure 5. The effect of adsorbate concentration. The bottom curve is a chemisorbed sample, the top curve is 1% physisorbed, and the middle two curves are 2 and 5% physisorbed.

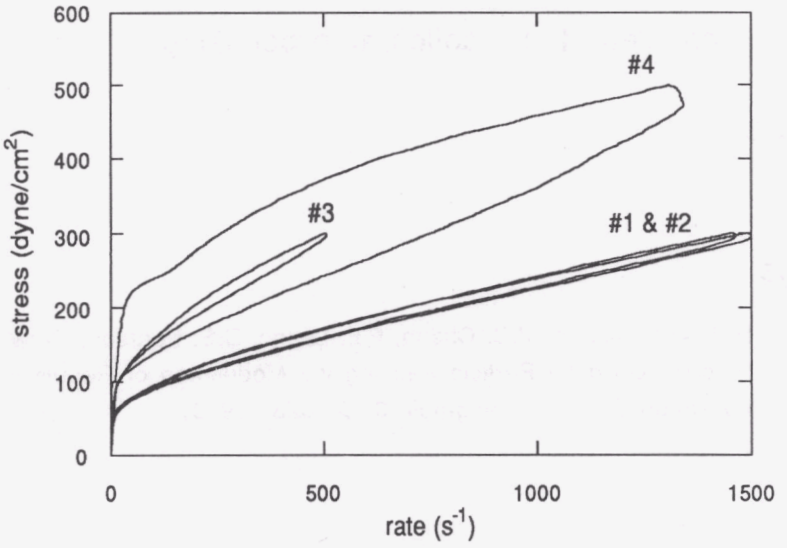

Figure 6. The effect of water on 5% physisorbed powder. Curves #1 and #2 are before low temperature excursion, #3 is after the first excursion, and #4 is after a second excursion.

Status of milestones.

114401	Survey rheological characteristics of slurries produced under a variety of pH/electrolyte conditions. Develop methodologies for characterization of slurry rheological properties and green body mechanical properties.	ok
114402	Status report on testing procedures and preliminary results.	ok
114403	Determine effect of pH/electrolyte conditions on green body properties including processing rates, mechanical properties, and density.	ok
114404	Status report on green body properties and processing relationships.	1 Nov 91
114405	Explore other means to modify interparticle interactions (polymers such as PVA).	1 Apr 92
114406	Status report on polymer effects.	1 May 92
114407	Examine flaw populations in sintered bodies.	1 Oct 92
114408	Final report on colloidal processing.	1 Nov 92

Publications

None.

References

(1) B.V. Velamakanni, J.C. Chang, F.F. Lange, D.S. Pearson, "New Method for Efficient Colloidal Particle Packing via Modulation of Repulsive Lubricating Hydration Forces", Langmuir **6**, p.1323 (1990).

1.2 CERAMIC COMPOSITES

1.2.2 Silicon Nitride Matrix

In-Situ Toughened Silicon Nitride (Phase IIA)

H. Yeh, J. Pollinger, D. Newson, E. Solidum (Garrett Ceramic Components)
J. Yamanis, M. Behi, C-W. Li, P. Whalen (Allied-Signal Research and Technology)

OBJECTIVE/SCOPE

The objective of this program is to improve the properties of a newly developed *in-situ* reinforced high temperature Si_3N_4 material (AS-700), and to develop net-shape component fabrication processes. This effort is targeted for heat engine applications, and the goals for the key properties are listed below:

Flexural Strength at 1370°C	490 MPa
Stress Rupture 490 MPa @1200°C	>100 hr
Fracture Toughness	> 10 MPa·$m^{1/2}$
Weibull Modulus	> 18

This effort consists of five (5) technical tasks: Task 1 - Slip Casting Development; Task 2 - Improvements of Densification and Grain Growth Processes; Task 3 - Alternate Raw Materials; Task 4 - Fabrication of Test Specimens and Task 5 - Material Characterization.

The technical efforts were initiated January 2, 1991; Tasks 1, 2, and 3 were conducted in this reporting period.

TECHNICAL HIGHLIGHTS

TASK 1 - SLIP CASTING DEVELOPMENT

The objective of this task is to develop a process to pressure slip cast the baseline AS-700 Si_3N_4 material in thin cross-section test plates and thick parts with varying cross-sections. Material shall be densified and heat-treated using established baseline procedures. Mechanical properties and microstructures will be characterized and compared with current baseline cold isostatic pressed AS-700.

Research sponsored by the U.S. Department of Energy, Assistant Secretary for Conservation and Renewable Energy, Office of Transportation Technologies, as part of the Ceramic Technology for Advanced Heat Engines Project of the Advanced Materials Development Program under contract DE-AC05-840R2140 with Martin Marietta Energy Systems, Inc., Work Breakdown Structure Subelement 1.2.2.1.

1.1 Slip Development

The goal of this subtask is to develop an AS-700 Si_3N_4 slip with desirable properties for slip casting both thin and thick cross-section components. To achieve the desired green part properties of homogeneous microstructure, high green density, and ability to be cast into complex-shape and large cross-section parts, the desirable slip properties are high solids content, low viscosity, long-time stability, agglomerate-free, and sintering aid powder particles of the same size or smaller than the silicon nitride powder particles. AS-700 slip development was divided into two tasks - generate desirable slip properties that result in acceptable rheology, forming, and green densities; and generate a homogeneous green microstructure.

Homogeneous green microstructures were achieved by slip milling procedure modification. The original AS-700 green microstructure formed by cold isostatic pressing of alcohol milled powders is shown in Figure 1. The SEM backscatter image shows that the sintering aids (light color) are somewhat agglomerated and the agglomerates are greater in size than the silicon nitride powder (dark color). The baseline slip casting process (milling time T) has reduced the size and number of sintering aid powder agglomerates (Figure 1), but further homogenization was desired. The milling time was increased to time 4T and the result was a further reduction of sintering aid agglomerate size and number (Figure 1), but not to the desired level. A sintering aid powder premilling step was added and the sintering aid powder agglomerates were effectively eliminated (Figure 1). The premilling step was also designed to prevent any contamination during the milling. The sintering aid premilling slip fabrication process was implemented as the optimized slip milling preparation procedure.

Slip property development utilized designed experiments to improve AS-700 slip properties - achievable solids content, viscosity, and green density, by evaluation of the following variables: dispersant composition, dispersant concentration, milling time/procedure as described above, and pH adjustment additive concentration. The investigative process used was to optimize slip properties at the baseline slip solids content of 70 wt% solids, then increase the slip solids content and investigate further slip process improvements. Figure 2 shows that the improvements made in slip processing resulted in greatly improved properties (lower viscosities and high solids contents) and higher green densities.

The properties of the baseline slip solids content of 70 wt% was improved by dispersant concentration and milling time optimization and the slip viscosity was lowered and green density increased from 61% to 63.5%. But the viscosity was so low that further slip improvements were barely detectable, and the low solids content results in long casting times. The solids content was increased to 73 wt%, where the majority of slip processing improvements were conducted. As Figure 2 shows, the slip viscosity was extensively decreased and the cast green

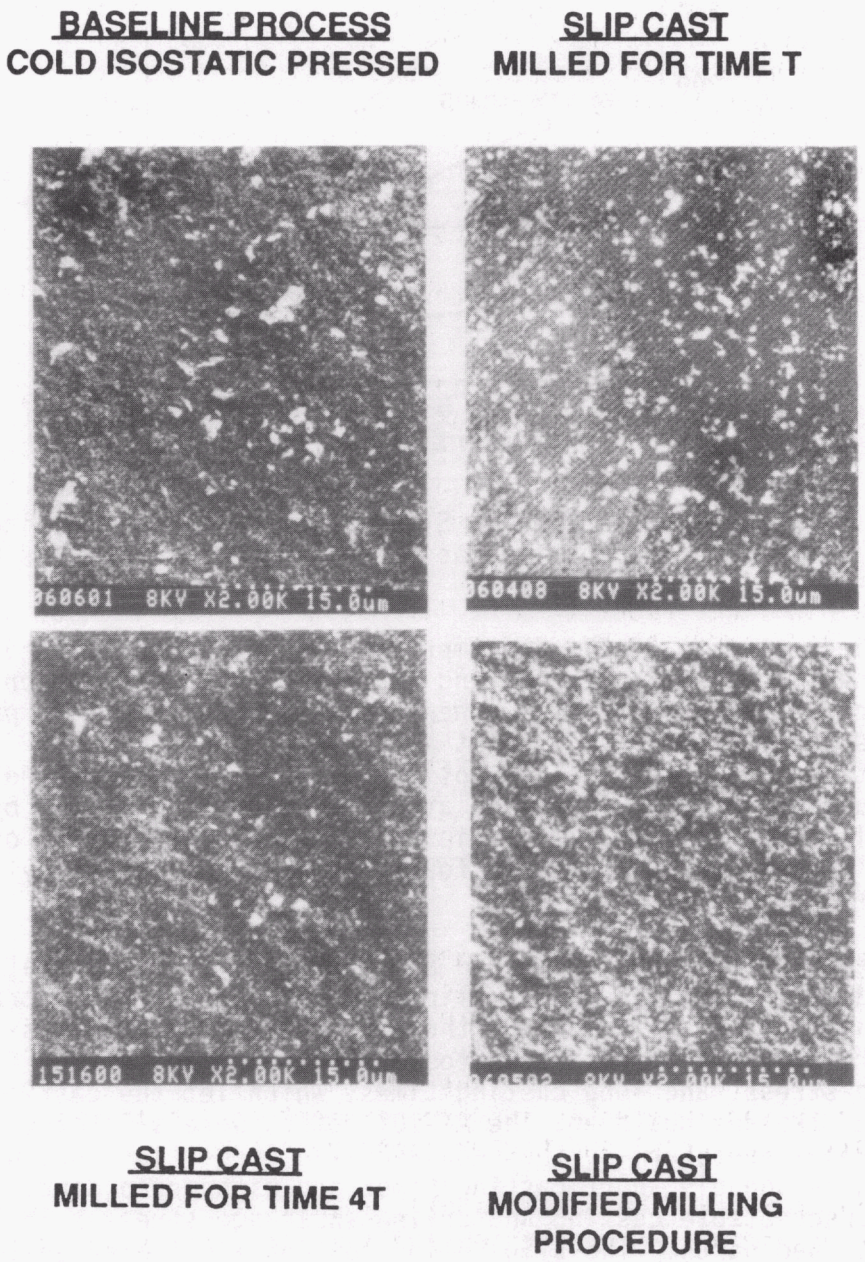

Figure 1. Green Microstructure Homogeneity Development in AS-700 Silicon Nitride.

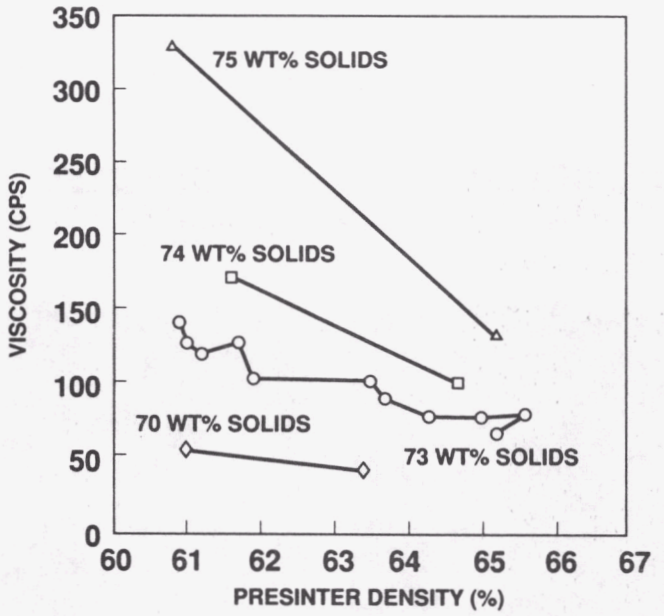

Figure 2. Improvements in AS-700 Slip Properties and Resulting Presintered Densities as a Function of Slip Solids Content.

density increased to 65.6%. The improvements were accomplished through a dispersant composition change and concentration optimization, milling procedure optimization (the sintering aid premilling procedure described above) and pH adjustment additive concentration optimization. The 73 wt% solids optimized AS-700 slip was used to successfully slip cast 2" by 3" plates and large 3" diameter by 2.5" tall cylindrical billets. The slip proved to be very stable over the relatively long casting required for forming the cylinders by unidirectional casting.

Casting of the complex-shaped AGT101 rotors revealed that the optimized 73 wt% solids content slip resulted in some rotor cracking during casting and drying due to the green density, which was low enough (relatively) to result in too much casting and drying shrinkage/stress, and long casting times, which let the casting shrinkage stresses build up. The AGT101 rotors were slip cast for just this reason - to determine the required slip properties that would result in reasonably short casting times and high green densities to prevent unacceptable casting and drying shrinkage stresses in large complex shaped parts. The slip solids content was increased to 74 wt%, and then 75 wt% solids. The 75 wt% solids slip properties were further optimized by slight changes in dispersant concentration, required by the changing colloidal dispersion environment (relative water volume-to-powder surface area ratio and amount of double layer crowding). The optimized 75 wt% solids slip was used to successfully slip cast the AGT101 rotors.

1.2 Forming Development

The goal of this subtask is to take the AS-700 slip developed in Subtask 1.1 and develop pressure slip casting process parameters for generation of uniform high green density, warpage and crack-free green parts, both thin and thick varying-cross-section.

Three AS-700 slip cast specimen geometries were selected to evaluate the forming capability of the AS-700 slip being developed. The geometries (shown in Figure 3) were the 2" by 3" by .5" plate, the 3" diameter by 2.5" tall cylindrical billet, and the AGT101 radial rotor. The plate was used to evaluate basic slip casting capability such as achievable cast green density. The large cylindrical billet was used to evaluate slip stability and green density needed to cast thick cross-section components without cracking due to casting or drying shrinkage. The AGT101 rotor was selected to be the ultimate test of the AS-700 slip, as Garrett Ceramic Component's previous experience showed that the rotor required a very stable slip because of its long casting time, and high green densities to prevent casting and drying shrinkage stresses.

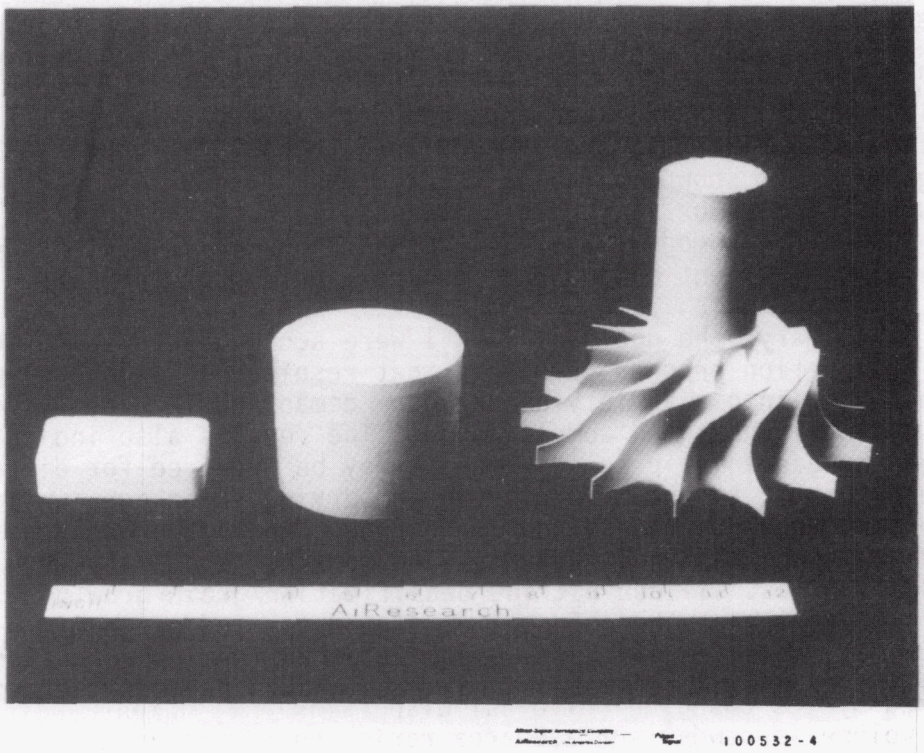

Figure 3. Slip Casting Component Geometries Selected for Development.

Slip casting, drying, and presintering of the 2" by 3" plates revealed no problems with any of the slips developed, from 70 wt% solids through 75 wt% solids. The thin cross-section (0.5") and simple geometry present minimal drying problems or shrinkage stress concerns and low cast green densities do not result in unacceptable stresses. The plate geometry has proven to be very insensitive to slip instability because of its short casting time.

Pressure slip casting of the large cylinders was investigated using two casting front geometries - unidirectional, and side and bottom dewatering. The bottom and side dewatering approach resulted in rapid casting times but the billets typically cracked radially during drying due to the green density and moisture gradients generated by the multiple casting fronts. Billets cast using the unidirectional approach were successfully cast, dried, and presintered without defects. Increasing the slip solids content to 74 wt% resulted in high enough green densities that the removal of moisture from the billet was more difficult and cracking during drying sometimes occurred. A slip solids content of 73 wt% was selected as the optimum for the large diameter billets.

Pressure slip casting of the AGT101 radial rotors was first evaluated using 73 wt% solids optimized AS-700 slip. The rotors exhibited some blade and hub cracking during casting and drying due to the lower than required green density generated by the 73 wt% solids content. Increasing the solids content to 74 wt% did not eliminate cracking. The solids content was increased to 75 wt% solids and the green density achieved was enough to prevent cracking by reducing the casting and drying shrinkage and stress to suitable levels. Presintered AGT101 rotors were sectioned to evaluate green density homogeneity. As shown in Table 1, the green density distribution throughout the rotor is very homogeneous, with the highest difference only 0.6%. This homogeneity in powder packing will result in densified parts with excellent dimensional control and reproducibility.

In summary, the goals of Task 1 were accomplished, with an AS-700 slip preparation process developed that resulted in stable slips able to be formed into a variety of shapes - demanding in terms of cross-sectional thickness and complex shape. The results also indicate that slight changes in slip solids content may be required for different geometry parts, to optimize casting and drying shrinkage, while not inhibiting moisture removal during drying. The high green densities, homogeneous green microstructures, and forming capability should allow AS-700 slip cast silicon nitride densification/grain growth development without the obfuscation of unoptimized green microstructure or requirement for subsequent green forming refinement which might modify the densification and grain growth process mechanisms.

Table 1. Achievement of homogeneous presintered density in AS-700 slip cast AGT101 rotors.

VERTICAL EVALUATION	
SAMPLE NO.	DENSITY
10	63.2%
20	63.1%
30	63.1%
40	63.3%
50	63.5%
VARIATION =	0.6%

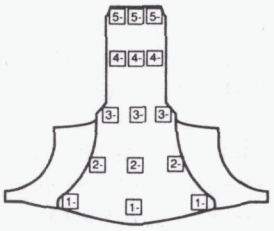

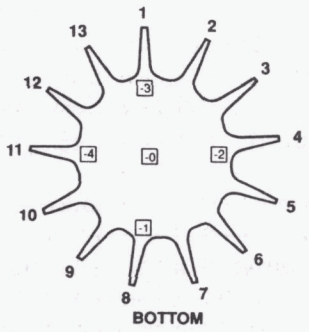

RADIAL EVALUATION									
HUB AT BOTTOM		HUB AT MIDDLE		HUB AT TOP		SHAFT AT MIDDLE		SHAFT AT TOP	
SAMPLE NO.	DENSITY	SAMPLE NO.	DENSITY	SAMPLE NO.	DENSITY	SAMPLE NO.	DENSITY	SAMPLE NO.	DENSITY
10	63.2%	20	63.1%	30	63.1%	40	63.3%	50	63.5%
11	63.3%	21	63.0%	31	63.2%	41	63.4%	51	63.4%
12	63.3%	22	62.9%	32	63.2%	42	63.5%	52	63.5%
13	63.2%	23	63.2%	33	63.3%	43	63.4%	53	63.4%
14	63.3%	24	63.2%	34	63.2%	44	63.3%	54	63.4%
VARIATION =	0.2%	VARIATION =	0.4%	VARIATION =	0.3%	VARIATION =	0.3%	VARIATION =	0.2%

NOTE: SAMPLE NO. INDICATES SAMPLE LOCATION WITHIN PART

TASK 2 - Improvement of Densification and Grain Growth Processes

The objective of this task is to establish improved densification and heat treatment process conditions for AS-700 Si_3N_4. The evaluation criteria shall be density, microstructure, mechanical properties, as-processed surface quality, and shape retention. Density and mechanical properties shall be the primary screening criteria. Large AS-700 samples (approximately 3" diameter by 2" high) will be used as the primary samples for densification and grain growth process development.

A number of slip cast AS-700 small plates (2" by 3" by .63") were processed through the baseline densification/heat treatment cycle. The plates were formed using the optimized AS-700 dispersion process and baseline (milling time M_1) and improved milling procedures M_2 (longer milling time) and M_3 (sintering aid powder premilling). The results are presented in Table 2. The results of milling time M_1 show basically equivalent properties to CIPed AS-700 baseline material. The material formed from milling time M_2 slip shows slightly lower strengths. The material formed from the optimized M_3 milling procedure shows significantly lower toughness and room temperature strength compared to the baseline CIP material. This is inspite of the fact that these specimens have achieved the highest sintered densities of any AS-700 yet processed. Microscopy also indicates large exaggerated grains (much larger than those in the typical AS-700 CIPed *in-situ* reinforced microstructure). It is theorized that the improved homogeneity green microstructure of the

TABLE 2. AS-700 Si_3N_4 Small Plate Properties as a Function of Milling Procedure.

SAMPLE	SLIP MILLING TIME	SINTER DENSITY (g/cc)	FRACTURE TOUGHNESS CN (MPa m)	25°C STRENGTH (ksi)	1000°C STRENGTH (ksi)	1375°C STRENGTH (ksi)
CIPED	------	3.29-3.33	9.0	108.5	92.0	71.0
S910014B	M_1 (T)	3.30	----	103.5 (3)	92.5 (2)	59.2 (3)
S910014D	M_1 (T)	3.29	----	108.1 (2)	94.2 (2)	71.5 (3)
S910014E	M_1 (T)	3.29	----	107.9 (3)	98.0 (3)	71.3 (3)
S910066D	M_1 (T)	3.26	8.20	96.6 (2)	82.8 (2)	67.2 (2)
S910067B	M_2 (6T)	3.26	----	94.5 (3)	84.9 (3)	64.7 (3)
S910091A	M_3 (5T AFTER PREMILL)	3.30	6.97	85.8 (5)	---	---
S910091B		3.30	7.54	84.2 (5)	---	---

T - RELATIVE MILLING TIME
() - NUMBER OF SAMPLES TESTED

M_3 slip milling procedure results in a more reactive compact during densification, allowing sintering to higher densities and that the baseline grain growth thermal processing temperatues may now be too high and need to be reduced to control the development of the *in-situ* reinforced microstructure. The grain morphology obviously affects the balancing act between high strength due to fine grain size and high toughness due to high aspect ratio interlocked grains. There are also indications that the increased green compact homogeneity and reactivity during densification and grain growth are effecting slight changes in the grain boundary phases, which also affects mechanical properties, especially at high temperature.

Thus the potential benefit of the improved green microstructure homogeneity and resulting reactivity to generate improved mechanical properties requires refinement of the densification/grain growth process to be taken advantage of. Designed experiments were then developed to explore such parameters as lowered densification and grain growth temperatures, heating and cooling rates, and thermal processing hold times using slip cast plates with the optimized M_3 milling procedure.

Preliminary results fron the designed densification experiments on the small slip cast plates with optimized green microstructure

explored the effect of hold time at densification/grain growth temperature. Four hold time combinations were explored - the baseline hold time t_1, t_2 ($.8t_1$), t_3 ($.6t_1$), and t_4 ($.4t_1$). The plates were all processed at the baseline densification/heat treatment temperatures. The plates processed for times t_1, t_2, and t_3 all achieved full density. The plate densified at time t_4 only reached 97.3% density and was not further evaluated. All the plates contained amorphous grain boundary phase, measured by XRD. The mechanical properties, shown in Table 3, were independent of densification hold time. The room temperature flexural strengths are now close to but slightly below the baseline cold isostatic pressed strengths. The program goal of 490 MPa fast fracture strength at 1370°C is also slightly greater than the current 1370°C of 452 MPa. The desired fracture toughness of 8.5 - 9 MPa$\sqrt{m}$ is also above the current fracture toughness of 7.65 MPa$\sqrt{m}$.

Table 3. Small Slip Cast Plate Mechanical Properties.

SAMPLE PLATE	DENSIFICATION HOLD TIME	DENSITY	4-PT FLEXURE STRENGTH (MPa) RT	1100°C	1375°C	RETAINED STRENGTH 20 Kg INDENT (MPa)	FRACTURE TOUGHNESS CHEVRON NOTCH (MPa$\sqrt{m}$)
S910177E	t_1	100%	669 (4)	576 (3)	454 (3)	317 (3)	---
S910177F	t_1	100%	649 (6)	645 (3)	440 (3)	319 (3)	---
S910177A	t_2	100%	666 (5)	560 (3)	460 (3)	326 (3)	7.54 (2)
S910177C	t_3	100%	717 (5)	---	---	315 (4)	7.74 (2)
S910177D	t_3	100%	676 (4)	---	---	310 (3)	7.66 (2)
S910167F	t_4	97.6%	---	---	---	---	---
CIP STANDARD	t_1	100%	748	634	490	357	9.0
PROGRAM GOALS	----	100%	---	---	490	---	10.0

NOTES:

1) () - Denotes No. of Samples Tested

2) [$t_2 = .8t_1$, $t_3 = .6t_1$, $t_4 = .4t_1$]

To further optimize the small slip cast plate densification and heat treatment process to meet program property goals, the designed experiments are being continued. They are two level designs that will examine densification/heat treatment hold temperature, heating rates and cool down rate. The experiment matrix is expected to be completed in early November 1991.

The investigation of densification of the large diameter AS-700 Si_3N_4 billets was also initiated. Two slip cast large billets (S910104A and S910104B) were densified using the intermediate heating rate firing schedule F_2 (50% of the baseline cycle heating rate) to prevent thermal upshocking of the large cross-section parts. The billets reached densities of 96.7 and 97.6% and no cracking occurred. Billet S910104B was machined into 3 x 4 x 50 mm flexure bars for density and material strength distribution evaluation. From the density data shown in Figure 4, it is clear that the interior of the billet did not sinter as well as the exterior. In addition, the bottom of the cylinder (placed in contact with the crucible) did not reach high density, even in the exterior region. Test bars taken from this bottom region tended to have lower strengths, as shown in Figure 5. Uneven sintering due to uneven heat distribution was the cause of the vertical density gradient and the furnace and part fixturing were modified to generate a homogeneous hot zone. Overall, the strengths were lower than similarly fabricated small plates and CIPed baseline AS-700.

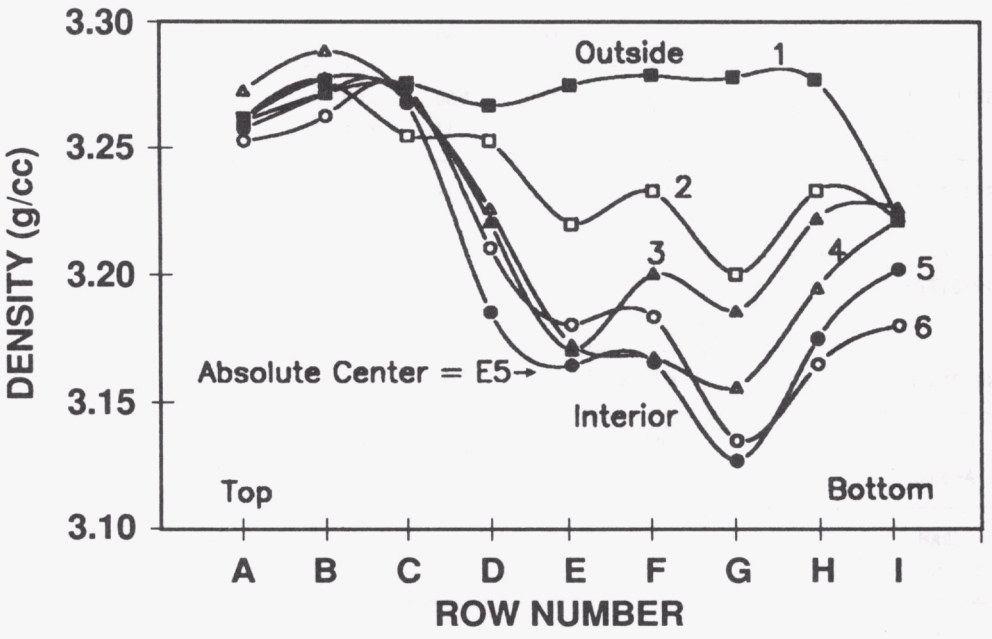

Figure 4. Measured Densities of Bars Cut From Large Slip Cast Billet S910104B.

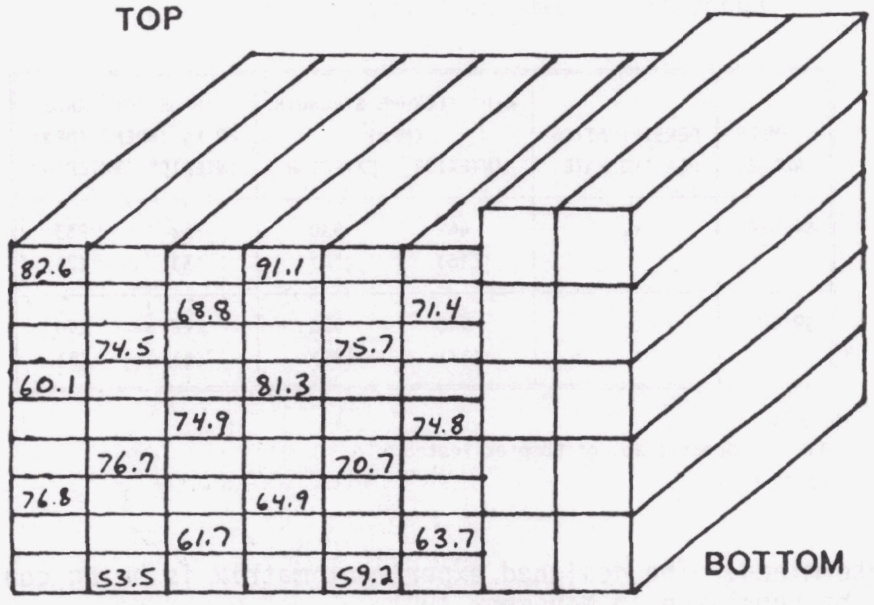

Figure 5. Room Temperature 4-pt Bend Fracture Strengths of Test Bars Cut From Large Slip Cast Block S910104B.

Initial indications are that densification occurs at and near the surface before the core of the cylinders, with the resulting accicular microstructure inhibiting subsequent consolidation in the interior, resulting in lower density centers.

A set of designed experiments was developed and is being implemented to achieve full density throughout the large cross-section parts, with desired microstructure development and corresponding mechanical properties. Experimental parameters being examined include heat-up rates, hold times, densification/grain growth temperatures, and cool down rates.

Preliminary experimental results examining the effect of heating rates (cycle F_2 heating rate versus the baseline cycle heating rate which is twice the cycle F_2 rate) resulted in improved flexure strengths and indented test bar strengths. Compared to a 3" dia. by 2.5" billet densified using the standard AS-700 process, the same size billet heated at twice the heated rate exhibited greater interior and exterior region room temperature flexure strengths and higher indented test bar retained strengths, as shown in Table 4. Both of the large billets were completely converted to beta-Si_3N_4 and exhibited amorphous grain boundary phase in the interior and approximately 70-80% crystalline grain boundary phase in the exterior regions. The change in microstructure that results in this increase in properties and the reason why heating rate affects these properties is still

Table 4. Mechanical Properties of Large Cylindrical Billets as a Function of Heating Rate.

SAMPLE NUMBER	DENSIFICATION HEATING RATE	4-PT FLEXURE STRENGTH (MPa) INTERIOR	EXTERIOR	DAMAGE TOLERANCE 20 Kg INDENT (MPa) INTERIOR	EXTERIOR
S910247	t_1	442 (16)	530 (14)	252 (3)	233 (2)
S910211	t_2	548 (17)	578 (24)	297 (6)	290 (5)

NOTES:
1) () - Denotes No. of Samples Tested
2) $t_2 \equiv 2t_1$

being determined. The designed experiment matrix is being continued and will be completed in November 1991.

The final experiments of Task 2 will be to evaluate densification of the slip cast AS-700 AGT101 rotors using the optimized densification process developed for large billets. These experiments are planned for November 1991.

The optimized densification/heat treatment process to be used to fabricate samples in Task 4 will be selected from the processes developed for either the small slip cast plates, or more desiredly, from the large cylinders.

TASK 3 - ALTERNATE RAW MATERIALS

The objective of this task is to evaluate the influence of the chemistry and physical characteristics of the starting Si_3N_4 powders on *in-situ reinforcement* processing and resultant properties. After an extensive search of silicon nitride powders with a variety of characterisitics, three critical silicon nitride powder characteristics were selected for evaluation:

1) Surface area/particle size distribution.
2) Oxygen content.
3) Trace element impurity levels.

Alternate Si_3N_4 powders were then selected. Selection criterion was to keep all other powder characterisitics similar to the baseline powder, while having a lower or higher value of one of the three critical Si_3N_4 powder characteristics to be evaluated. Six commercially

available powders meeting these requirements were selected and efforts are now underway to evaluate them in the AS-700 system.

The goal for each alternate silicon nitride powder was to fabricate 2" by 3" slip cast AS-700 plates with a minimum green density of 60.7% and with a homogeneous green microstructure. This will eliminate any convolution of results due to different packing densities or green microstructure. The sintering aid premilling procedure developed in Task 1 was used to fabricate the various slips. The plates will then all be densified using the optimized densification/grain growth process being developed in Task 2.

Plates of all six alternate silicon nitride powders have been successfully cast meeting the green denity and homogeneity requirments. The plates are awaiting the optimized densification/grain growth process being developed in task 2. The mechanical properties and microstructure of the densified plates will be characterized and effects of the various powder characteristics analyzed.

STATUS OF MILESTONES

Milestones are on schedule.

PUBLICATIONS/PRESENTATIONS

J. Pollinger and J. Yamanis presented a program status at the Automotive Technology Development Contractors Coordination Meeting in Dearborn, MI on October 28, 1991.

Optimization of High-Temperature Properties of Silicon Nitride Ceramics

T. S. Sheu and T. Y. Tien (The University of Michigan)

Objective/scope

Silicon nitride ceramics with a fibre-like structure of the β-Si_3N_4 grains exhibit the highest fracture toughness and flexure strength. Ceramics with long β-Si_3N_4 grains can be obtained by sintering the silicon nitride ceramics at higher temperatures under a higher nitrogen pressure. The composition of the sintering additives will also affect the microstructural development and their mechanical properties. The mechanical properties can further be improved by characteristics of the grain boundary phase. However, the additives usually become a glassy grain boundary phases after sintering which cause an inferior high temperature property. The major goal of this project is to develop monolithic silicon nitride ceramics with optimum mechanical properties at room temperature as well as at high temperatures. α'-SiAlON has an equiaxied grain morphology and its composition can be expressed as $Y_xSi_{12-(m+n)}Al_{m+n}N_{16-n}O_n$ which has a stuffed derivative structure of α-Si_3N_4. By proper batch formulation, the starting materials form liquid which aid densification of the silicon nitride ceramics at the beginning of the sintering process. At the later stage of sintering, the liquid enters the silicon nitride lattice forming α'-SiAlON. The final product contains only the fiber like β-Si_3N_4 grains and equiaxied α'-SiAlON grains without any liquid phase at the grain boundaries. It is expected that silicon nitride contains no glass grain boundary would which have better mechanical properties at high temperatures.

Technical progress

Ceramics containing β-Si3N4 and α'-SiAlON were synthesized in the system Si,Al,Y/N,O. Compositions of these ceramics can be fund on the join Si_3N_4-Y_2O_3:9AlN as shown in Fig. 1. These compositions were hot-pressed at 1780°C under a unidirectional pressure of 300 Kg/cm2. During hot pressing, samples with various compositions showed different sintering behavior. The results are given in Fig. 2. Samples with a lower α' phase content require a longer time to achieve full densification.

Flexure strength and fracture toughness at room temperature, as well as at 1400°C, as a function of phase contents were given in Fig. 3. Samples with 20 - 40 wt% α'-SiAlON show both flexure strength and fracture toughness. Temperature-dependence of strength curves for samples containing 20 - 40 wt% α'-SiAlON phase hot pressed at different conditions are shown in Fig. 4. The highest strength observed was ~1300 MPa at 25°C, and ~800 MPa at 1400°C. A SEM micrograph in Fig. 5 shows one of these

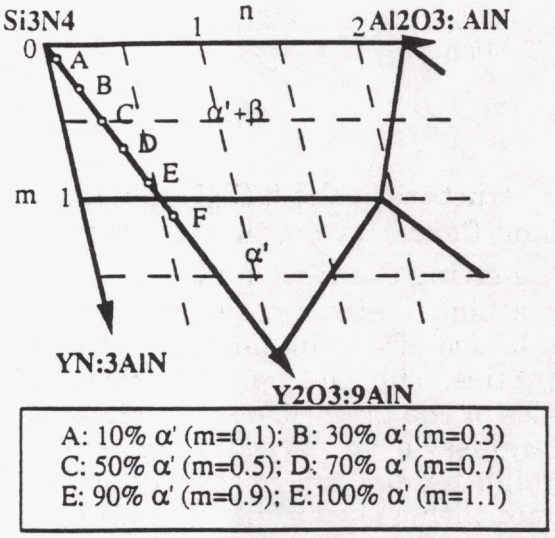

Fig. 1. Y-Si-Al-O-N phase diagram.

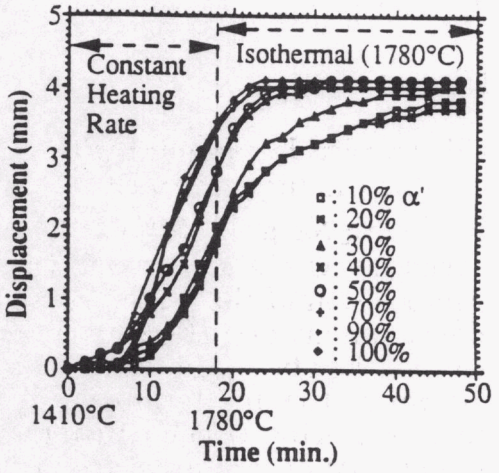

Fig. 2. Sintering behaviour during hot pressing.

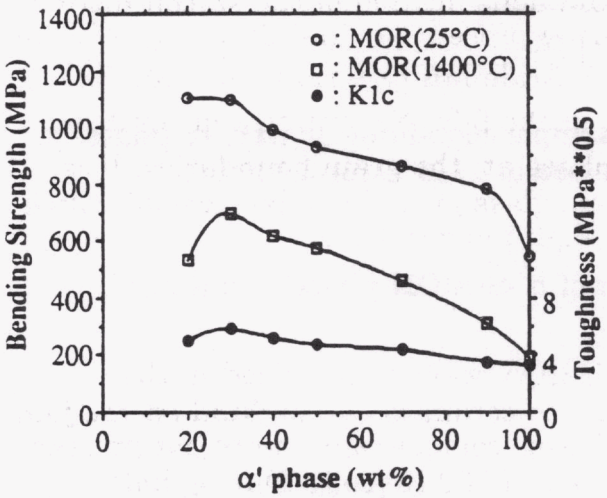

Fig. 3. The relationships among fracture strength, fracture toughness, phase portion, and temperature.

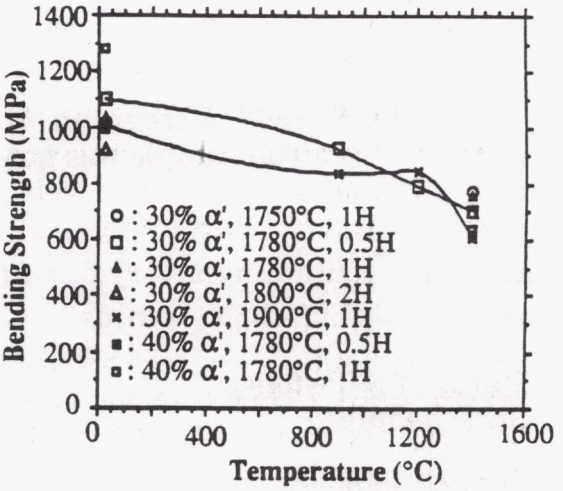

Fig. 4 Bending Strength versus temperature.

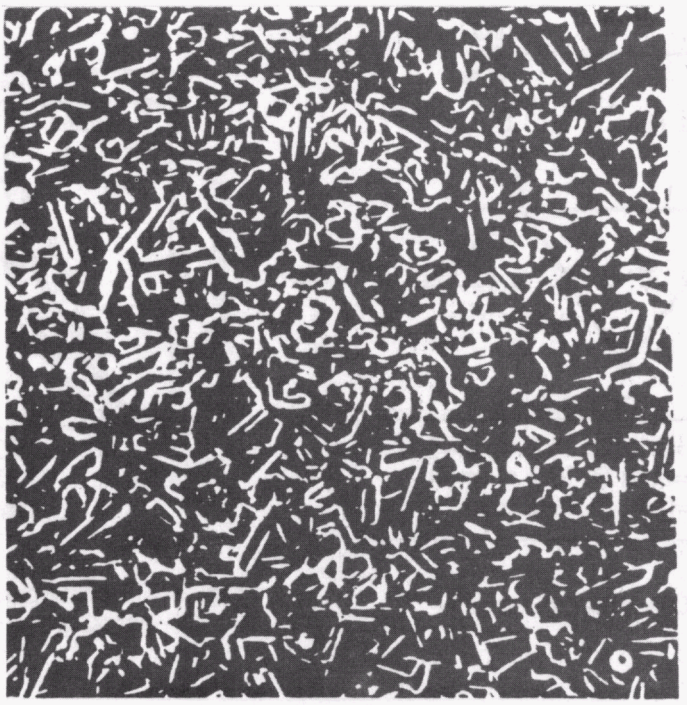

Fig. 5. SEM micrograph of a sample containing 30 wt% α' phase. This sample was hot-pressed at 1780°C for 0.5 hour.

materials containing a very fine grain of α'-SiAlON phase and a high aspect ratio of β-Si_3N_4 grains.

Status of Milestones
On schedule.

Publications
None.

Characterization of Grain Boundary Phase in Silicon Nitride Ceramics

Wen-Cho Teng and T. Y. Tien
(The University of Michigan)

Objective/scope

The objective of this investigation is to develop silicon nitride ceramics with high flexural strength, high fracture toughness and superior creep resistance. The fibre-like structure of the β-Si_3N_4 grains can be obtained by sintering the silicon nitride ceramics at higher temperatures under higher nitrogen pressure. The composition of the sintering additives will affect the microstructural development, grain boundary characteristics, and hence, the mechanical properties. However, the grain boundary phase has never been synthesized and their properties have never been studied. The goal of this project is to synthesize and characterize the grain boundary phase and to understand the relationships between the nature of the grain boundary phase and the properties of silicon nitride ceramics. It is believed that with a thorough understanding of these relationships, ceramics with optimum mechanical properties can be obtained.

Technical progress

Compositions studied were: 10 wt% SiAlON - 90 wt% $Y_2Si_2O_7$, 20 wt% SiAlON - 80 wt% $Y_2Si_2O_7$ and 30 wt% SiAlON - 70 wt% $Y_2Si_2O_7$. These compositions were designated as 9010, 8020 and 7030, respectively. Starting powders were weighed and mixed using isopropanol and an ultrasonic mixer. Mixtures were dried and melted in a covered BN crucible at 1700°C under a nitrogen pressure up to 40 bars and then furnace cooled. The melts were analyzed by XRD and EDX. Nitrogen contents of the samples were analyzed by an inert gas fusion technique. Thermal expansion of these samples was measured using a dilatometer. The results are discussed in the following sections.

Compositions 9010 and 8020 were amorphous to XRD and 7030 was found to contain a small amount of β-Si_3N_4 crystals. The nitrogen contents after melting are given in Fig. 1. Nitrogen loss was observed for all compositions when melted under one atmosphere of nitrogen, and very little change in the nitrogen content was observed for compositions melted at higher pressures.

Typical thermal expansion curves are given in Fig. 2. From these curves, the thermal expansion coefficients and glass transformation temperatures were computed. The composition dependence of the thermal expansion coefficients are given in Fig. 3, and the glass transformation temperatures are given in Fig. 4. These curves show that the thermal expansion coefficients increased with increasing nitrogen content, and no clear trend can be observed for the glass transformation temperature.

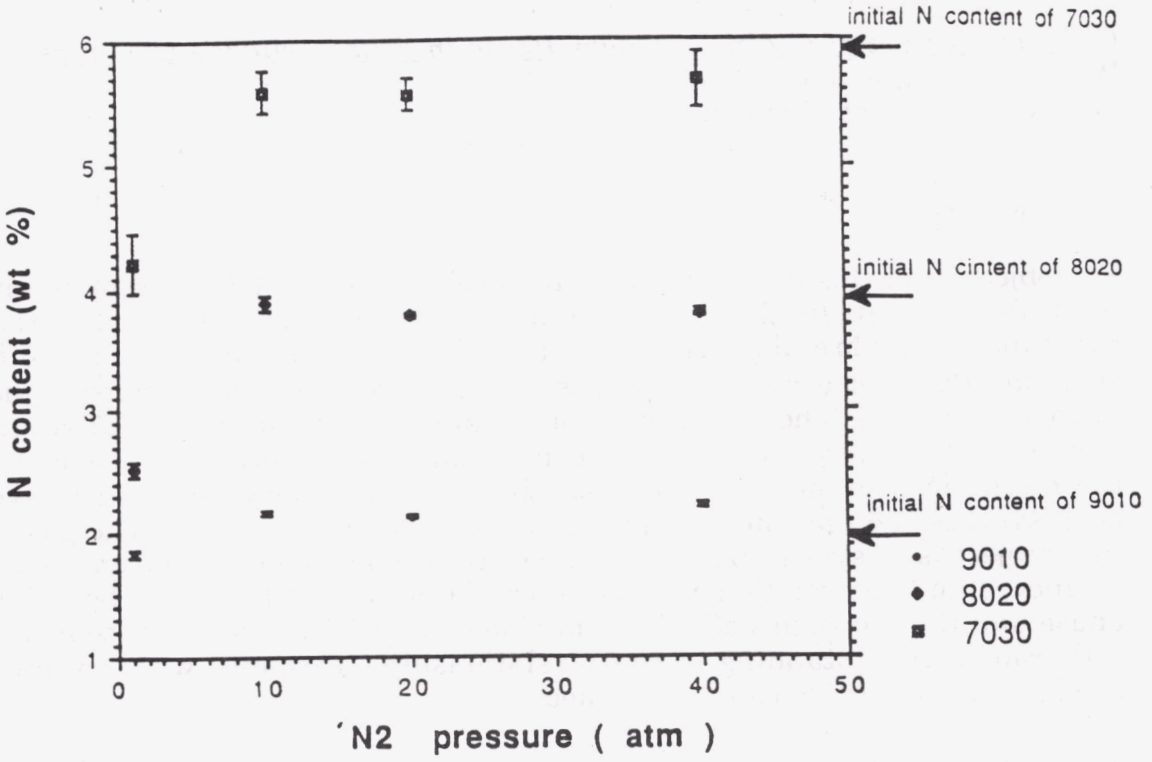

Fig. 1. Nitrogen content of glasses analyzed by the inert gas fusion technique.

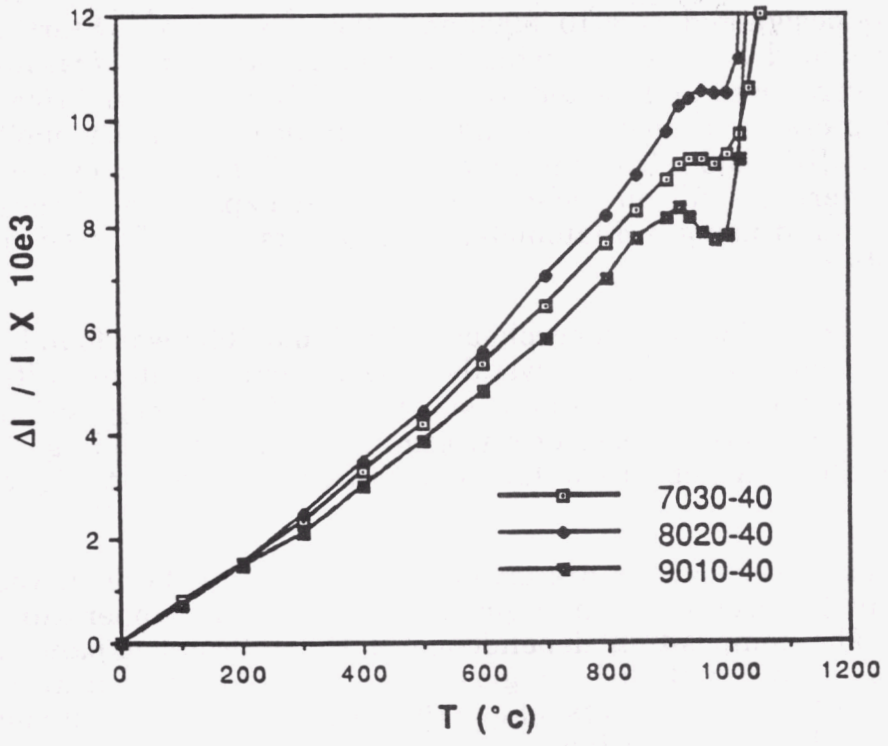

Fig. 2. Thermal Expansion curves for Specimens melted at 1700°C under 40 atmospheres of Nitrogen.

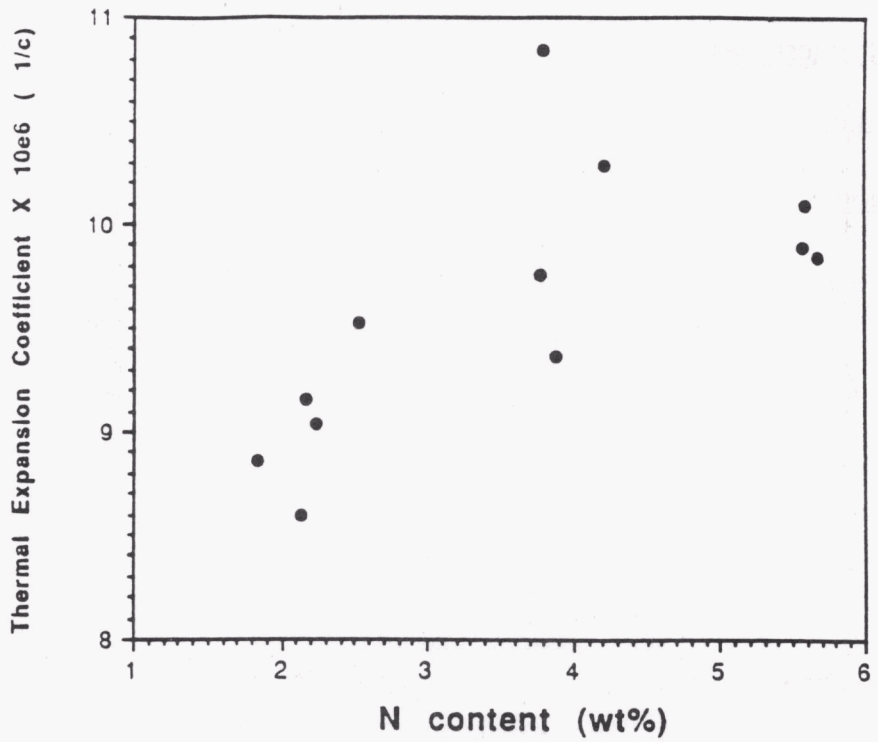

Fig. 3. Thermal Expansion Coefficients of Glasses melted a 1700°C under Different Nitrogen Atmospheres.

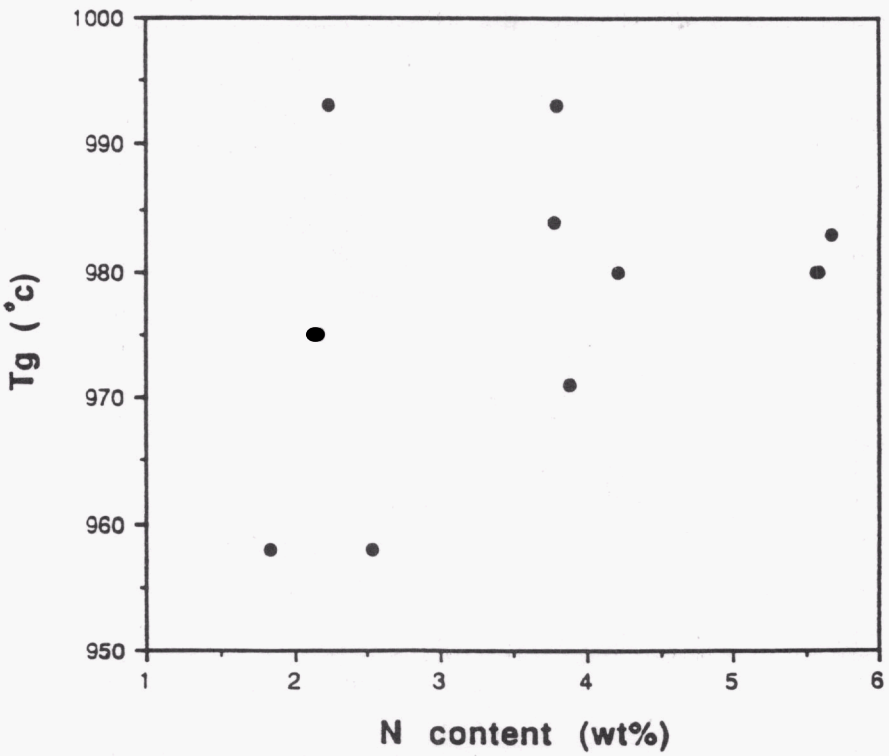

Fig. 4. Transformation Temperatures of Glasses melted a 1700°C under Different Nitrogen Atmospheres.

Status of milestones

On schedule.

Publications

None.

FABRICATION OF SiC-AlN COMPOSITES

G. E. Hilmas and T. Y. Tien
(The University of Michigan)

Objective/scope

The goal of this project is to obtain dense SiC-AlN composites containing AlN-polytypoid phases(s) as a dispersed second phase. AlN-polytypoids (8H, 15R, 12H, 21R and 27R) form as elongated rod-like or platelet-like grains and are stable at high temperatures potentially producing an in-situ reinforcement phase in advanced composites. Hot-pressing was selected for this study to optimize densification at high temperatures.

Technical progress

1.0 INTRODUCTION

The formation of AlN-polytypoids and subsequent SiC matrix:AlN-polytypoid composites have been described in the last two semi-annual reports [1,2], including microstructural and mechanical property data. To this point, samples prepared with 90 vol.% β-SiC and 10 vol.% 12H (AlN-polytypoid) have resulted in the desired microstructure containing a SiC matrix phase with a well dispersed AlN-polytypoid second phase. This AlN-polytypoid second phase has formed in a platelet-like morphology and has strongly enhanced the fracture toughness of the SiC composite while maintaining a good room temperature strength (8.5 MPa-$\sqrt{m}$ and ~550 MPa, respectively). Samples designed to contain 20 vol.% and greater of the 12H-polytypoid second phase have resulted in phases and microstructures that are competing between forming the desired two-phase microstructure and one that contains α-SiC(2H) and AlN(2H) in coexistence or possibly in solid-solution. The resulting microstructures for these samples are generally fine-grained with lower fracture toughness values comparable to dense SiC monoliths.

It is believed that several of the above compositions may not have reached their equilibrium phases and/or microstructures. Since lower temperature annealing is not likely to alter the present phase content, it is necessary to perform longer hot-press cycles at 2100 °C to determine if equilibrium has been or can be obtained. In order to perform the above analysis, hot-pressed billets of all five compositions [BS90:12H(II), BS80:12H(II), BS70:12H(II), BS60:12H(II) and BS50:12H(II)] must be prepared for longer hold times at 2100 °C. It is the intent of this report to discuss preliminary results on samples prepared for hold times of 2 and 5 hours at 2100 °C.

2.0 EXPERIMENTAL

The compositions [BS90:12H(II), BS80:12H(II), BS70:12H(II), BS60:12H(II) and BS50:12H(II)] have been prepared by hot-pressing at 2100 °C for hold times of 2 and 5 hours. In order to try and improve the high temperature mechanical properties of these materials, 1 wt.% of C was added during powder processing. Since elemental C is already present, the excess C will not affect the phase equilibria. It will act to increase the effective surface energy by reducing the SiO_2 and free Si contents at the grain boundaries. This should both promote sintering and limit grain growth of the SiC matrix phase.

Sections of the hot-pressed samples were machined and then ground and polished down to a 1 μm diamond finish for preliminary mechanical properties measurements. Fracture toughness values were determined from direct crack measurements from Vickers diamond indents and calculated from the equation of Anstis et al. [3].

3.0 RESULTS AND DISCUSSION

The results of the fracture toughness measurements are summarized in figure 1 along with earlier data from samples hot-pressed for 1 hour at 2100 °C. The values for samples hot-pressed for 2 and 5 hours are generally quite consistent with previous results obtained on samples hot-pressed for 1 hour. Although the compositions BS90:12H(II) and BS80:12H(II) exhibit fracture toughness values somewhat lower than the high of 8.5 MPa-√m, the values are still quite good and these specimens are expected to have higher flexural strength values.

The samples are currently being evaluated by XRD and SEM to determine their phase content and microstructural morphology. Bend test bars are also being machined from the hot-pressed billets to evaluate their room temperature and elevated temperature flexural strength.

Status of milestones

On Schedule.

Publications

None.

References

[1] G. E. Hilmas and T. Y. Tien, "Fabrication of SiC-AlN Composites," Semi-annual report submitted to ORNL under Contract No. SC-19X-SA125C, April, 1991.

[2] G. E. Hilmas and T. Y. Tien, "Fabrication of SiC-AlN Composites," Semi-annual report submitted to ORNL under Contract No. SC-19X-SA125C, October, 1990.

[3] G. R. Anstis, P. Chantikul, B. R. Lawn and D. B. Marshall, "A Critical Evaluation of Indentation Techniques for Measuring Fracture Toughness: I. Direct Crack Measurements," *J. Am. Ceram. Soc.*, **64** [9] 533-543 (1981).

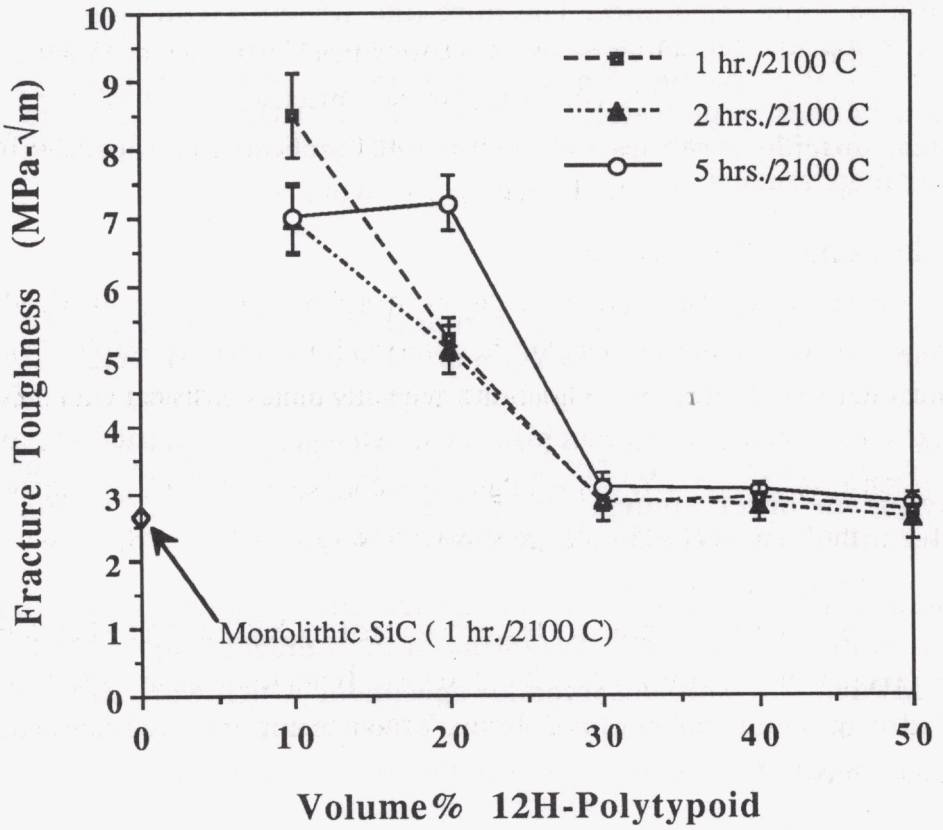

Figure 1. Plot of fracture toughness vs. volume% 12H-polytypoid for samples hot-pressed for times of 1, 2 and 5 hours at 2100 °C.

Optimization of Silicon Nitride Ceramics

K. R. Lai and T. Y. Tien
(The University of Michigan)

Objective/scope

To develop processing methods to optimize fracture strength, fracture toughness and creep resistance of monolithic silicon nitride ceramics. Silicon nitride ceramics with fibre-like grains will have higher fracture strength and toughness and also creep resistance. The fibre-like structure can be obtained by sintering the silicon nitride ceramics at high temperature under a nitrogen over-pressure. The mechanical properties can further be improved by controlling the composition and grain boundary phase(s). The major goal of this project is to develop monolithic silicon nitride ceramics with optimum mechanical properties and to understand their mechanisms.

Technical progress

Fracture toughness, flexural strength and microstructural features of β-Si_3N_4 ceramics containing 6 wt.% Y_2O_3 and 2 wt.% Al_2O_3 (B6Y2A) as sintering aids were studied. The fracture toughness was measured using the Vicker's indentation method[1] and the precracking strength testing method.[2]. Four-point flexural strength was measured following the standard of MIL-STD-1942A with the fixture having an outer span of 20 mm and inter span of 10 mm. Grain sizes were determined using the disintegration method.

The grain size dependences of the fracture toughness and flexural strength are plotted in Fig. 1 and Fig. 2. Optimum mechanical properties (σ = 1,000 MPa, K_{IC} = 9.0 MPa.$m^{1/2}$) were observed for specimens which were sintered at 1900°C under a 10 atm. pressure of N_2 for 1 hour. These samples have an aspect ratio of 8.7 and grain length and width of 7.25 μm and 0.833 μm, respectively.

Similiar mechanical behaviors were observed for β-Si_3N_4 ceramics containing 10 wt.% $Y_3Al_5O_{12}$. It appears that the crack propagates intergranularly when the grain size of β-Si_3N_4 is small. Transgranular propagation becomes dominant in specimens containing larger β-Si_3N_4 grains.

(1) G. R. Anstis, P. Chantikul, B. R. Lawn and D. B. Marshall, " A Critical Evaluation of Indentation Techniques for Measuring Fracture Toughness: I. Direct Crack Measurements," *J. Am. Ceram. Soc.,* **64** [9] 533-539(1981).

(2) P. Chantikul, G. R. Anstis, B. R. Lawn, and D. B. Marshall, " A Critical Evaluation of Indentation Techniques for Measuring Fracture Toughness: II, Strength Method, " *ibid,* **64** [9] 539-543 (1981).

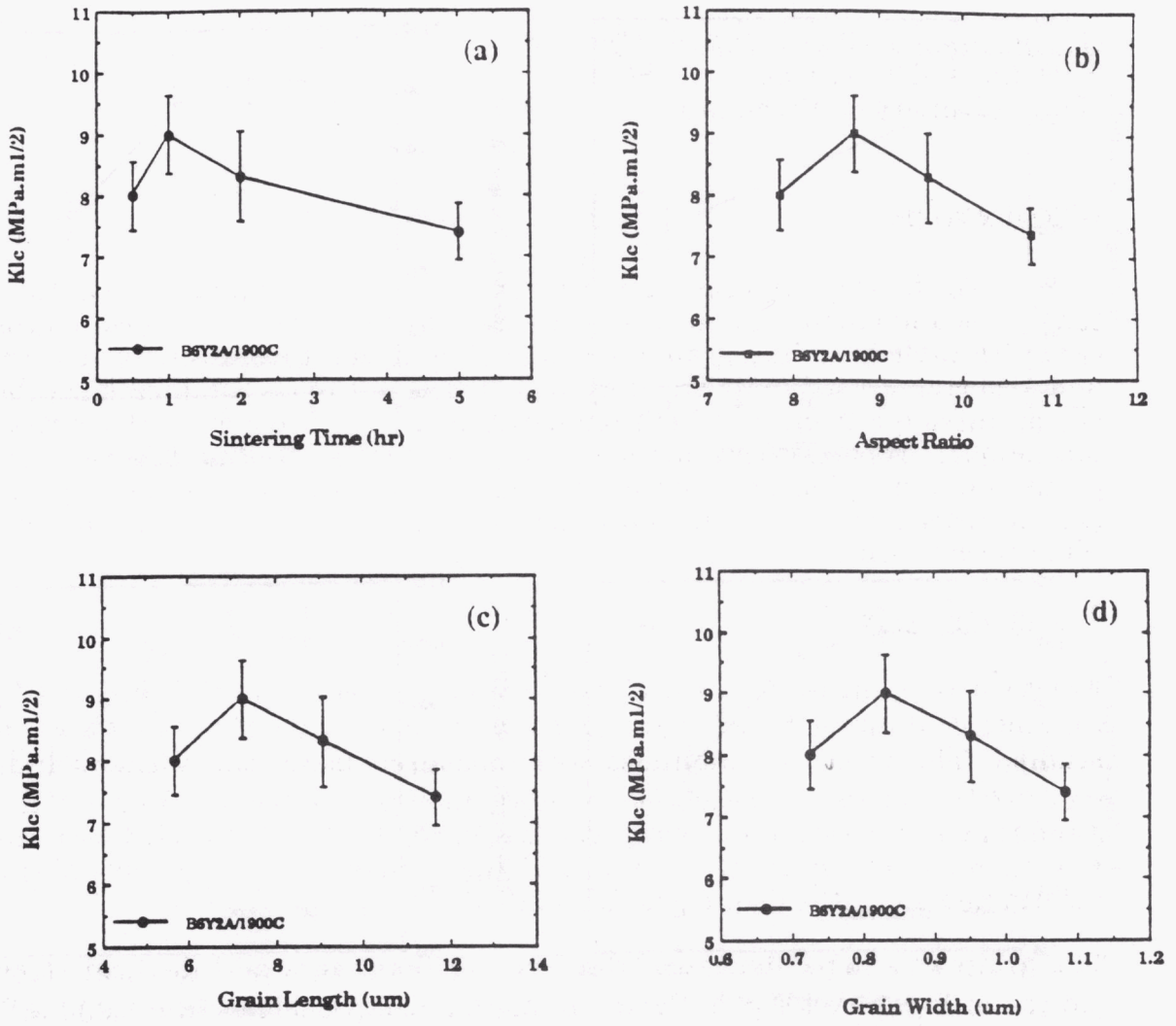

Fig. 1 Fracture toughness of B6Y2A-Si_3N_4 ceramics as a function of (a) sintering time, (b) aspect ratio, (c) grain length, (d) grain width. Samples were sintered at 1900°C under 10 atm. N_2 pressure.

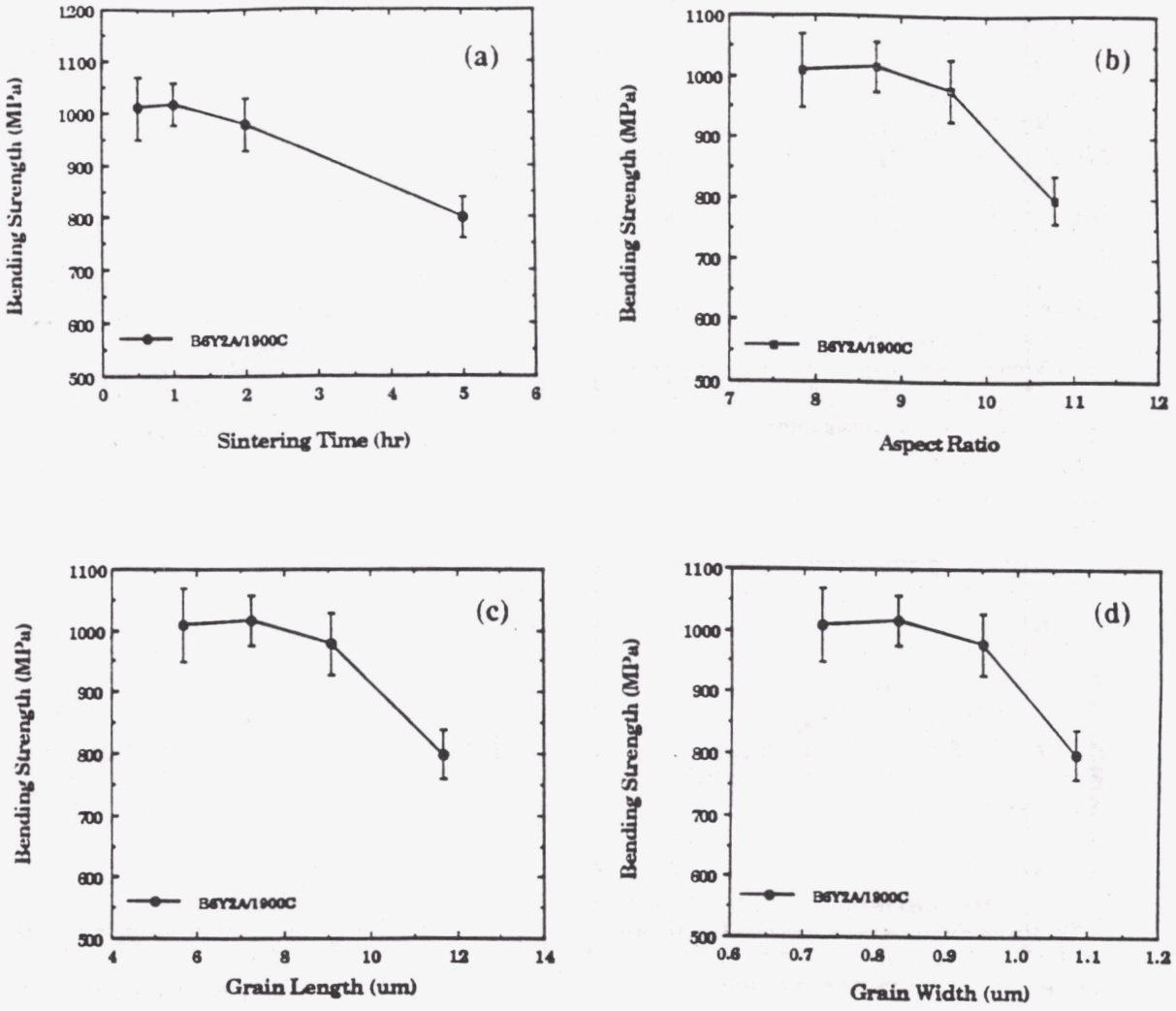

Fig. 2 Bending strength of B6Y2A-Si_3N_4 ceramics as a function of (a) sintering time, (b) aspect ratio, (c) grain length, (d) grain width. Samples were sintered at 1900°C under 10 atm. N_2 pressure.

Status of milestones

On schedule.

Publications

None.

1.2.3 Oxide Matrix

Dispersion-Toughened Ceramic Composite

T. N. Tiegs, P. A. Menchhofer, W. H. Elliott, and D. W. Coffey
(Oak Ridge National Laboratory)

Objective/scope

Initially, this work involved development and characterization of SiC whisker-reinforced ceramic composites for improved mechanical performance. To date, most of the efforts involving SiC whisker-reinforced alumina, mullite, silicon nitride, and sialon have been completed. In addition, studies of whisker-growth processes were initiated to improve the mechanical properties of SiC whiskers by reducing their flaw sizes and, thereby, improving the mechanical properties of the composites. Currently, in-situ acicular grain growth is being investigated to improve fracture toughness of silicon nitride materials.

Technical highlights

SiC whisker growth

Previous work identified optimized SiC whiskers that were calculated to give high toughness to silicon nitride matrix composites.[1] Numerous flaws were identified in commercial SiC whiskers that reduced whisker strength and, therefore, reduced their toughening effect. The flaws identified were artifacts from the whisker growth process and included (1) central axial core regions or holes and (2) crystallographic changes (that act as stress concentrators) along the axial length. In addition, it was determined that larger diameters in the 1 to 3 μm range would also be effective in increasing the toughness of silicon nitride. Thus, studies were initiated to determine the process parameters that would reduce flaw generation in SiC whiskers and increase their diameters. During the same time frame, however, concerns about the cost of the whiskers, the processing difficulties encountered during fabrication of whisker composites, and the health and safety issues associated with the acicular nature of the whiskers caused the emphases of the work to shift from whisker-reinforced composites to in-situ grain growth to achieve high-toughness silicon nitride materials. This report summarizes the work that was done to determine the process parameters affecting SiC whisker growth, but the work has been discontinued and the effort redirected.

It has long been recognized that vapor-liquid-solid whisker growth could produce a very high-strength and large-diameter whisker.[2,3] However, because the yields from this type of process are low, the process was not considered a viable one for production of economical whiskers for heat engine applications. Therefore, we chose a process that would be amenable to production of large quantities of SiC whiskers. The patent literature showed that processes using carbothermic reduction of silica and carbon were commercially successful; therefore, the initial work investigated this area.[4-8]

A few requirements are necessary for whisker growth to occur in the carbothermic reduction of silica-carbon system. The most obvious is that

whiskers need space to grow. Rice hulls that are used in many of the commercial processes are a very fortuitous structure in that they not only provide silica and carbon but also pore space for whisker growth. A catalyst of some kind is also necessary and is most commonly supplied by adding iron to the reactants. A final requirement is gas phase transport of the reactants. If these requirements are met then whisker growth can occur, and, in fact, it is almost impossible to prevent whisker growth. This may help explain why the open and patent literature reports have such a wide variety of conditions where whisker growth has been observed.

Numerous silica sources have been used in various investigations including rice hulls, colloidal silica, silica gel, sea sand, and silica plates. In our study, we examined colloidal silica (particle size ~ 70Å) and various sizes of particulate silica (1 to 38 μm). Carbon sources in the literature are also varied and include carbon black, charcoal, sucrose, and gaseous carbon. Our investigations looked at several grades of carbon black and graphite powders with surface areas ranging from 1 to 120 m^2/g. Both the silica and carbon sources were relatively high purity. Our earlier studies have identified the impurities in whiskers made from rice hulls as a source of the inclusions which act as one of the major flaws in this type of whiskers. Silica-to-carbon weight ratios of 0.6 to 3 have been used in the patent and open literature reports, and our work standardized on a ratio of 1. Bulk densities for the powder mixtures were generally in the range of 0.1 to 0.5 g/cm^3.

Effect of raw materials – the particle size of the silica greatly affected the ability to grow whiskers. With the small particle sizes, whisker growth was evident, but with silica particle sizes > 5 μm whisker growth was essentially nonexistent. The particle size (and surface area) affect the generation of SiO gas, which needs to be sufficiently high enough for axial whisker growth at reasonable rates. Thus, all further work used silica sources with small particle size and high surface areas for most of the work done with colloidal silica (Cab-O-Sil M-5, 70Å particle size and 120 m^2/g surface area).

Effect of catalysts – reported catalysts include just about every metal and its compounds (Fe, Al, B, Co, Ni, Nb, Ta, Y, La, Mn, etc.). In the present study, the following materials were tested: Fe, Co, Ni, CaO, B_2O_3, and FeSi.

A wide variation in the whisker-growth characteristics was observed due to the catalyst addition to the silica-carbon mixture. General observations indicated additions of Co or Ni (added as < 44 μm particles) that resulted in a great deal of very thin whisker growth, as shown in Fig. 1. The use of Fe as a catalyst resulted in whiskers with a wide range of diameters but larger than the Co- or Ni-catalyzed whiskers (Fig. 2). Obviously, the catalyst dictates the wetting angle and stability during axial whisker growth. Use of B_2O_3 as a catalyst resulted in considerable growth of small-diameter whiskers having apparent crystallographic variations along the length (Fig. 3). Similar growth was observed previously with CaO-catalyzed whiskers.[9] FeSi was used as a catalyst to provide a growth nucleus with considerable presence of Si, thereby requiring no further absorption from the SiO gas prior to whisker growth. These whiskers generally had larger diameters and an unusual growth habit as shown in Fig. 4. It is believed that the small-diameter whiskers at the end of the larger ones developed during furnace cooldown.

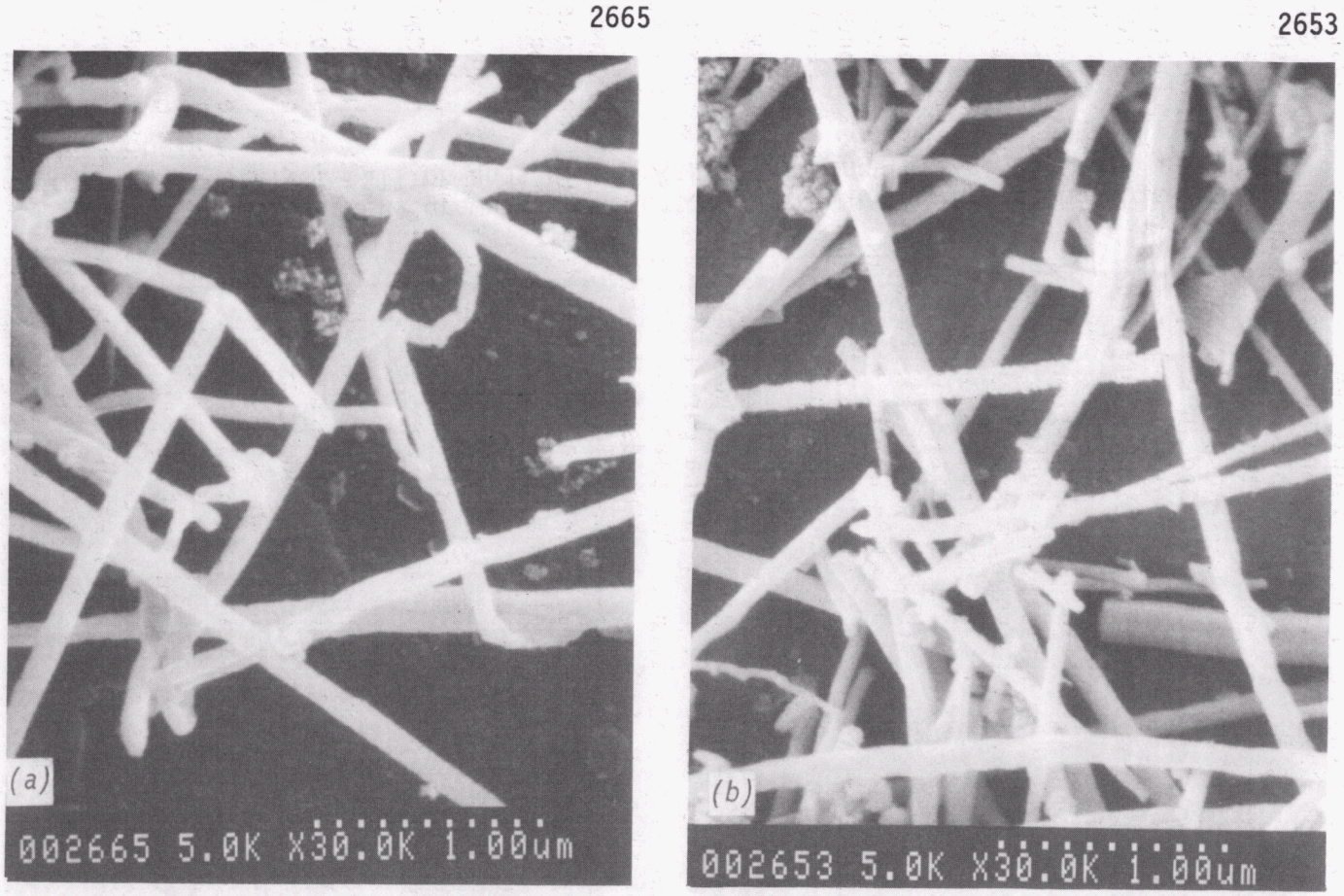

Fig. 1. SiC whiskers grown with (*a*) Co catalyst and (*b*) Ni catalyst. Heating rate of 20°C/min to 1600°C in Ar-4% H_2.

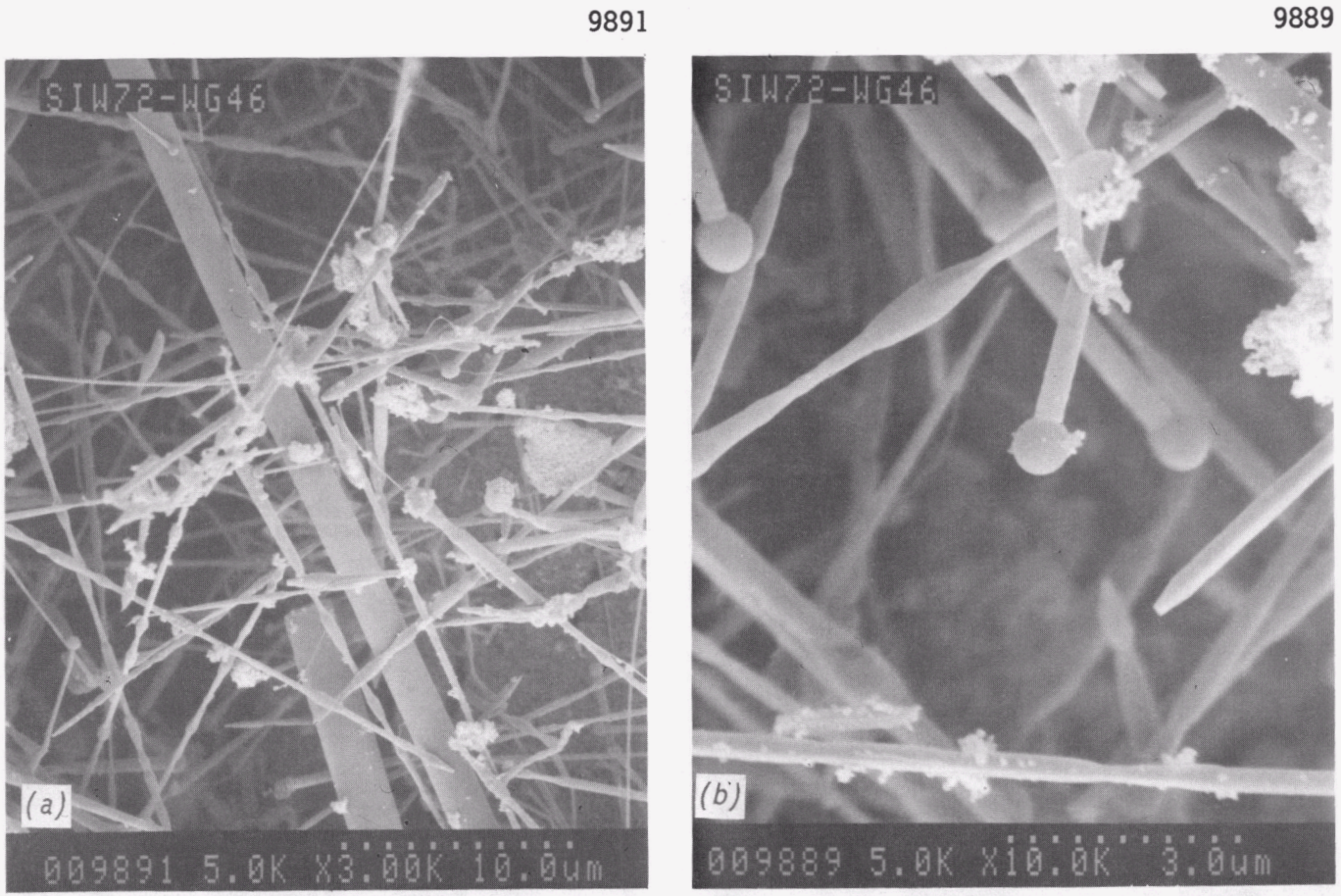

Fig. 2. SiC whiskers grown with Fe catalyst showing (*a*) range of whisker diameters and (*b*) catalyst ball on ends of whiskers. Heating rate of 20°C/min to 1600°C in Ar-4% H_2.

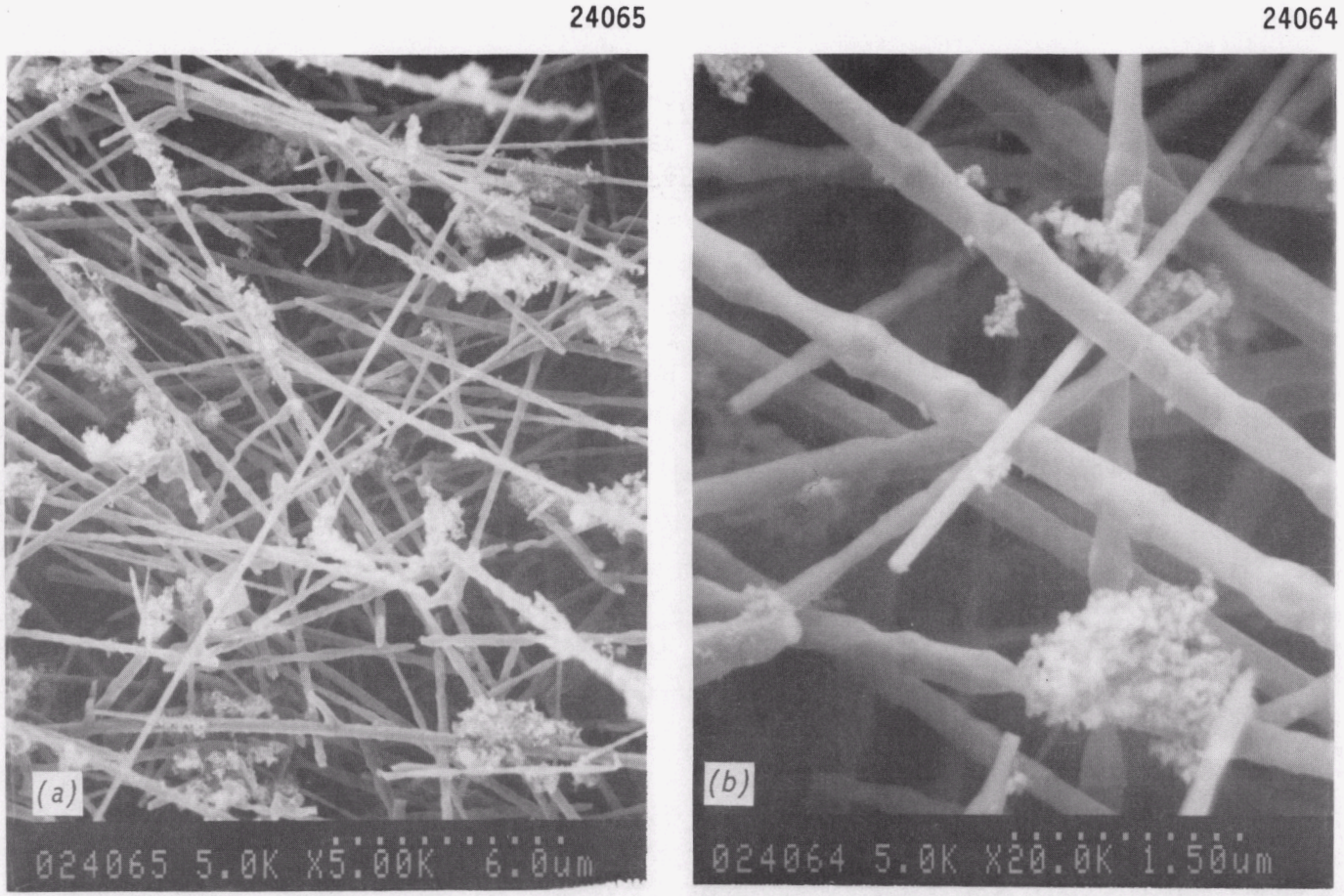

Fig. 3. SiC whiskers grown with B_2O_3 catalyst showing (*a*) fine whisker diameters and (*b*) crystallographic changes along length of whiskers. Heating rate of 20°C/min to 1600°C in Ar-4% H_2.

8143

8141

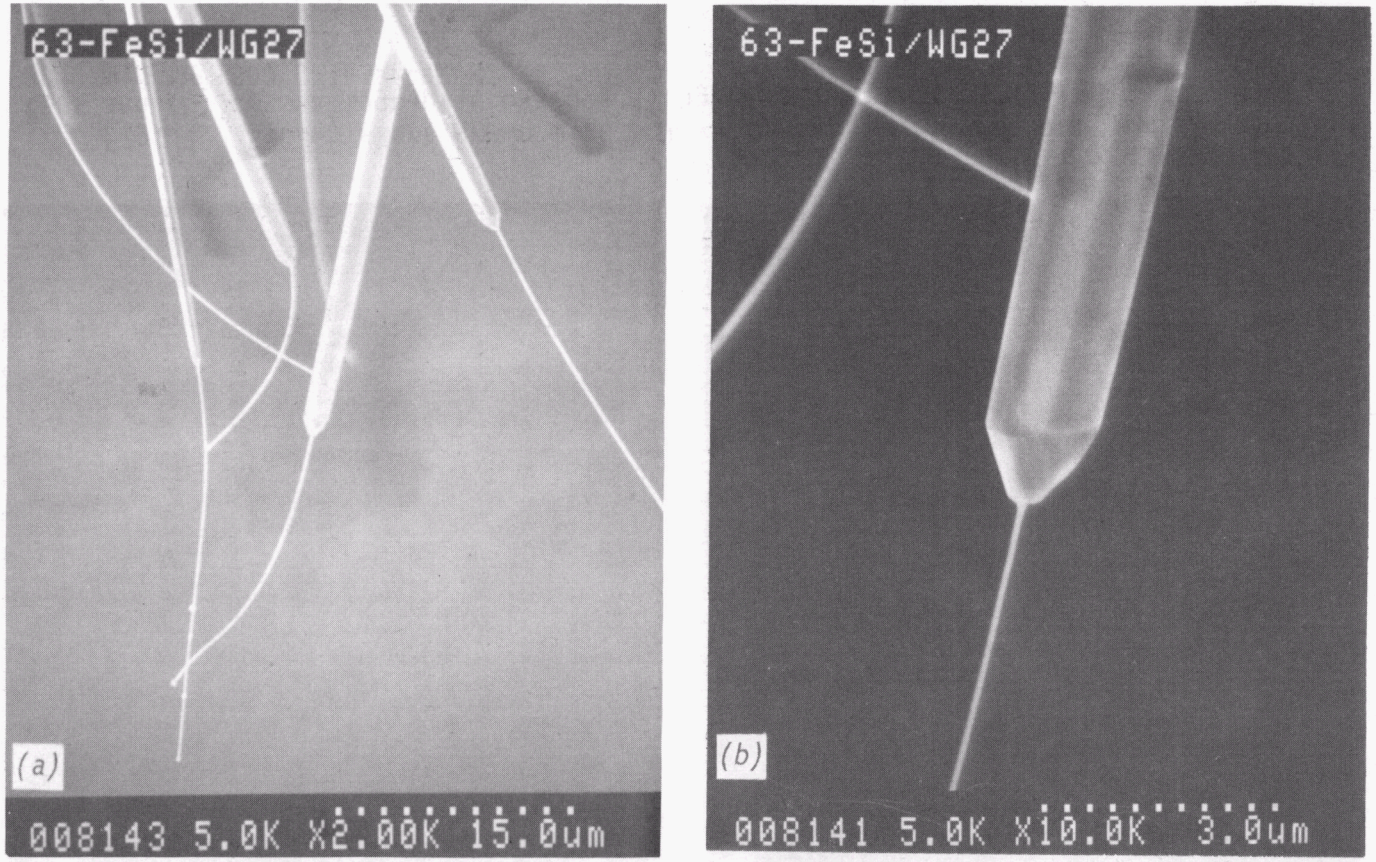

Fig. 4. SiC whiskers grown with FeSi catalyst showing (*a*) end of whisker and unusual growth habit and (*b*) whisker diameters with relatively smooth surfaces. Heating rate of 20°C/min to 1700°C in Ar-4% H_2.

Effect of heating rate – mixtures of SiO_2-50% C-1% Fe were heated at rates of 2, 20, and 200°C/min to 1700°C and held for 1 h to examine the effect of heating rate and SiO generation on whisker growth. The morphology of the whiskers changed as shown in Figs. 5 through 7. At the fast heating rate and high SiO generation rate, the whisker growth was very rapid and uncontrolled. There was a wide range of diameters and many misshapen whiskers. As the rate was decreased, the uniformity and straightness of the whiskers improved. Whisker growth during the slowest heating rate (2°C/min) apparently took place over an extended period of time as indicated by the changing diameter along the length. This is most likely a result of a change in catalyst wetting with increasing temperature. Because of the relatively smooth surfaces, the whiskers grown at the slower rates are preferred to minimize stress concentrators due to rough surfaces.

One feature of SiC whisker growth by carbothermal reduction of SiO_2-C mixtures was observed in every reaction experiment. Severely distorted whiskers were at the bottom of every powder-whisker bed as shown in Fig. 8. These types of morphologies are associated with whiskers high in silicon.[10] With our reactor geometry, SiO gas preferentially segregated to the bottom of the reaction bed because it is heavier than the atmospheres in the furnace. Consequently, the gas available for whisker growth was concentrated in SiO at the lower levels during the growth process. Reactor geometry and methods to eliminate these types of problems would be needed as the reactors were scaled up for commercial quantities of materials.

In-situ toughening of silicon nitride by microstructure development

Microstructure development during hot pressing – a series of silicon nitride materials to assess the role of additive chemistry on elongated-grain growth, fracture toughness, and high-temperature properties has been fabricated and machined into test specimens. The compositions, hot-pressing conditions, mechanical properties, and phase compositions have previously been reported. The mechanical properties are reported under work breakdown structure (WBS) 3.2.1.3 of the present progress report. Oxidation tests of the materials are currently being performed at 800 and 1000°C, and those results are summarized in Figs. 9 and 10. The oxidation tests are continuing.

To investigate if β-Si_3N_4 nucleation could be enhanced by seeding of the matrix, several samples were fabricated with 5 and 20 wt % β-Si_3N_4 or β-sialon powders. Previous results showed some improvement in fracture toughness of a 6% Y_2O_3-2% Al_2O_3 composition with 40 wt % β-Si_3N_4 addition but that the densification was diminished. Microstructure examination of the samples containing 5% β-sialon additive showed extensive elongated grain growth (Fig. 11). Testing of the mechanical properties is in progress and will confirm if the fracture toughness has been improved by the elongated grains.

Mechanical property reductions associated with the crystallization of the glass phase in silicon nitride systems have long been observed in numerous silicon nitride systems.[11-13] Samples have been fabricated in the hot press where crystallization (with and without applied pressure) has been done to determine if the volume decreases associated with the crystallization processes affect the property changes. The effect on the strength and toughness will be determined.

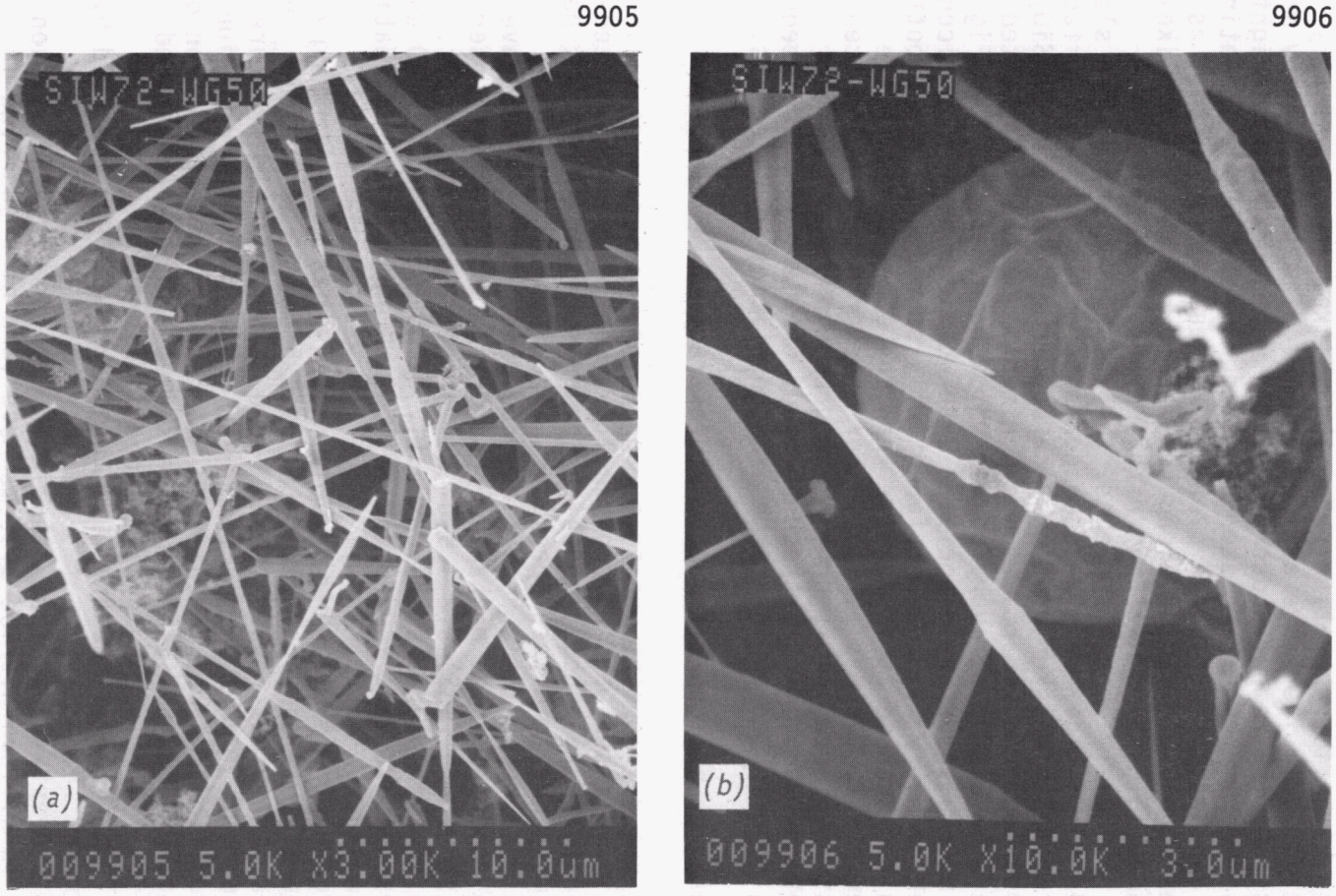

Fig. 5. SiC whiskers grown with Fe catalyst showing (*a*) range of whisker diameters and (*b*) variation of diameters along length of whiskers. Heating rate of 2°C/min to 1600°C in Ar-4% H_2.

9890

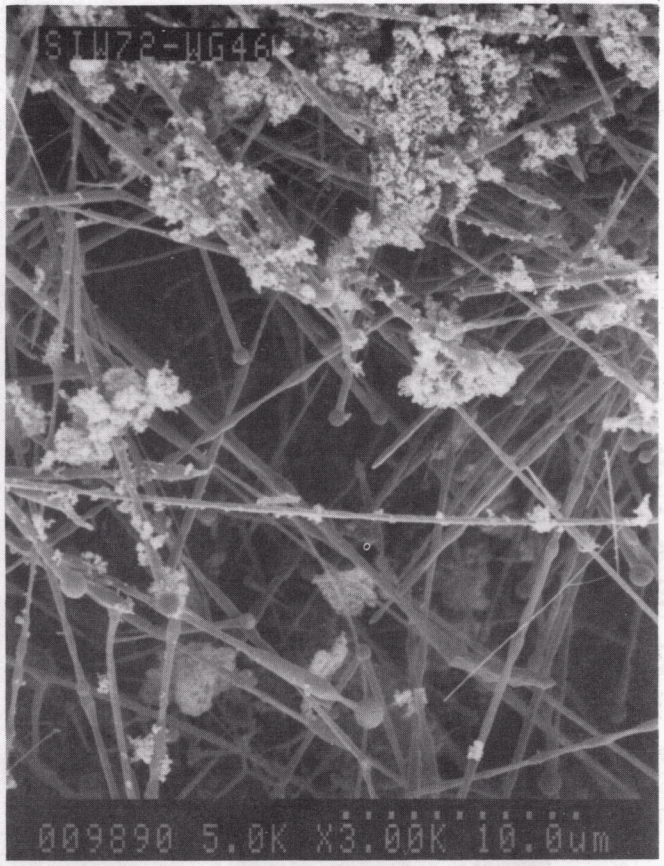

Fig. 6. SiC whiskers grown with Fe catalyst showing a range of whisker diameters. Heating rate of 20°C/min to 1600°C in Ar-4% H_2.

9803

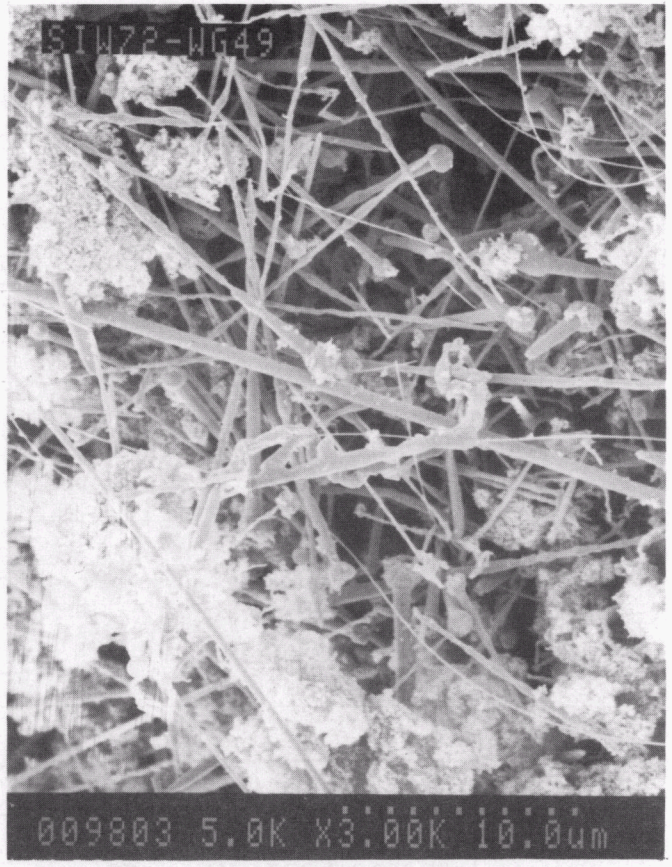

Fig. 7. SiC whiskers grown with Fe catalyst showing a range of whisker diameters. Heating rate of 200°C/min to 1600°C in Ar-4% H_2.

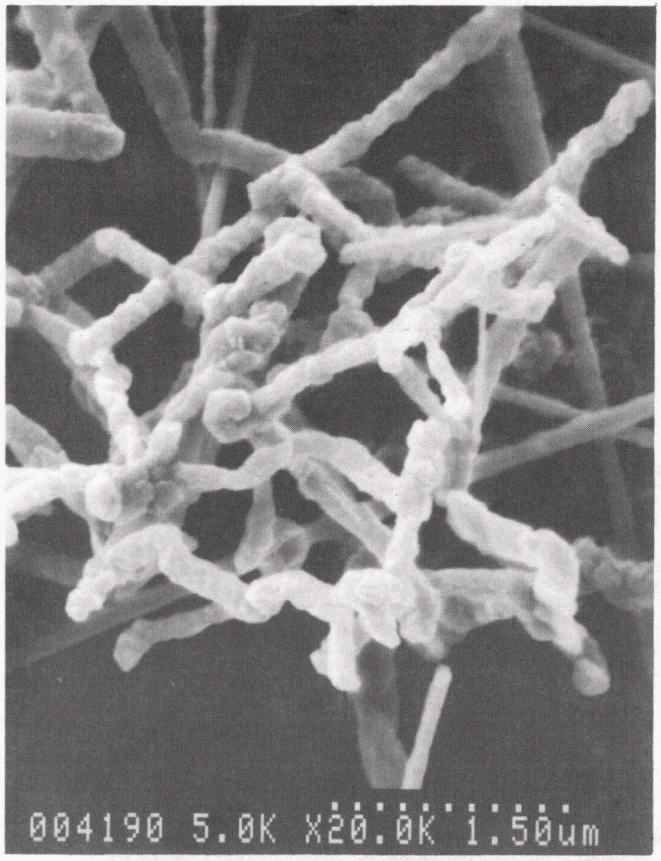

Fig. 8. SiC whiskers grown with Fe catalyst showing distorted whisker growth at bottom of powder bed due to high SiO concentrations. Heating rate of 20°C/min to 1700°C in N_2.

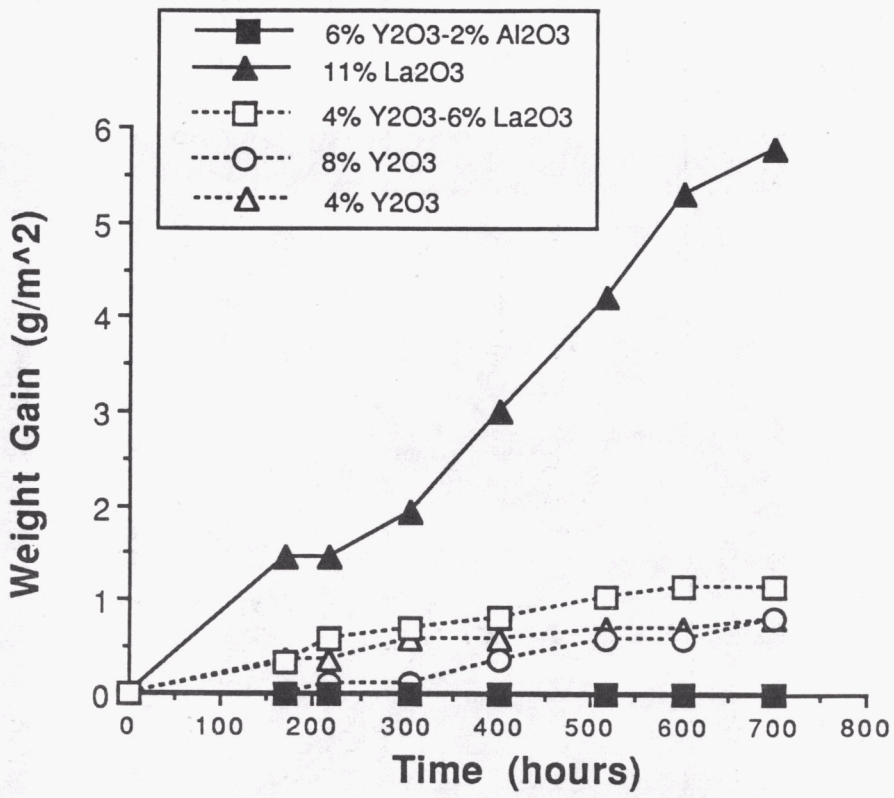

Fig. 9. Summary of weight changes during oxidation of silicon nitride compositions at 800°C.

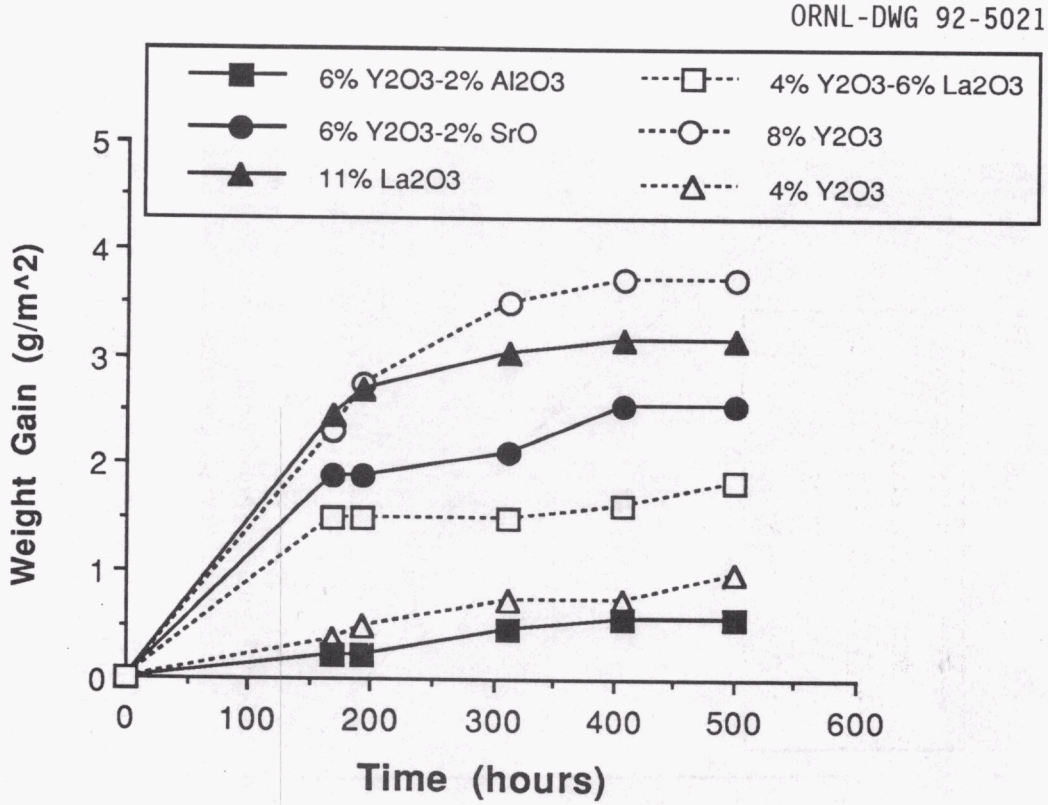

Fig. 10. Summary of weight changes during oxidation of silicon nitride compositions at 1000°C.

Microstructure development during gas-pressure-sintering – gas-pressure-sintering (GPS) is one technique used to grow elongated grain structures and obtain high-toughness silicon nitrides with refractory grain-boundary phases.[14-17] Initial samples at ORNL were fabricated and sintered at both normal atmosphere (0.2 MPa at 1850°C) and with a nitrogen overpressure (2 MPa at 1850 and 1900°C). The results of weight loss and densification behavior showed significant improvement in densification with GPS (Tables 1 and 2). With the relatively low refractory compositions (Y_2O_3-Al_2O_3 and La_2O_3-Al_2O_3), high densities were obtained at 1850°C. At higher sintering temperatures, grain growth was observed, and increases in density to near 100% T. D. were obtained. Because the rare-earth SiO_2 compositions are highly refractory, they are more difficult to sinter to high densities and did not achieve full densities even at 1900°C. Recent literature[18,19] has shown that combinations of rare-earth oxides can be used to aid in promoting densification, and it is anticipated that the Y_2O_3-La_2O_3 currently being tested will densify by GPS. Further sintering runs were attempted at 1950°C for increased grain growth in the low-refractory compositions and increased density in the highly refractory compositions, but a malfunction of the controlling thermocouple resulted in temperatures of

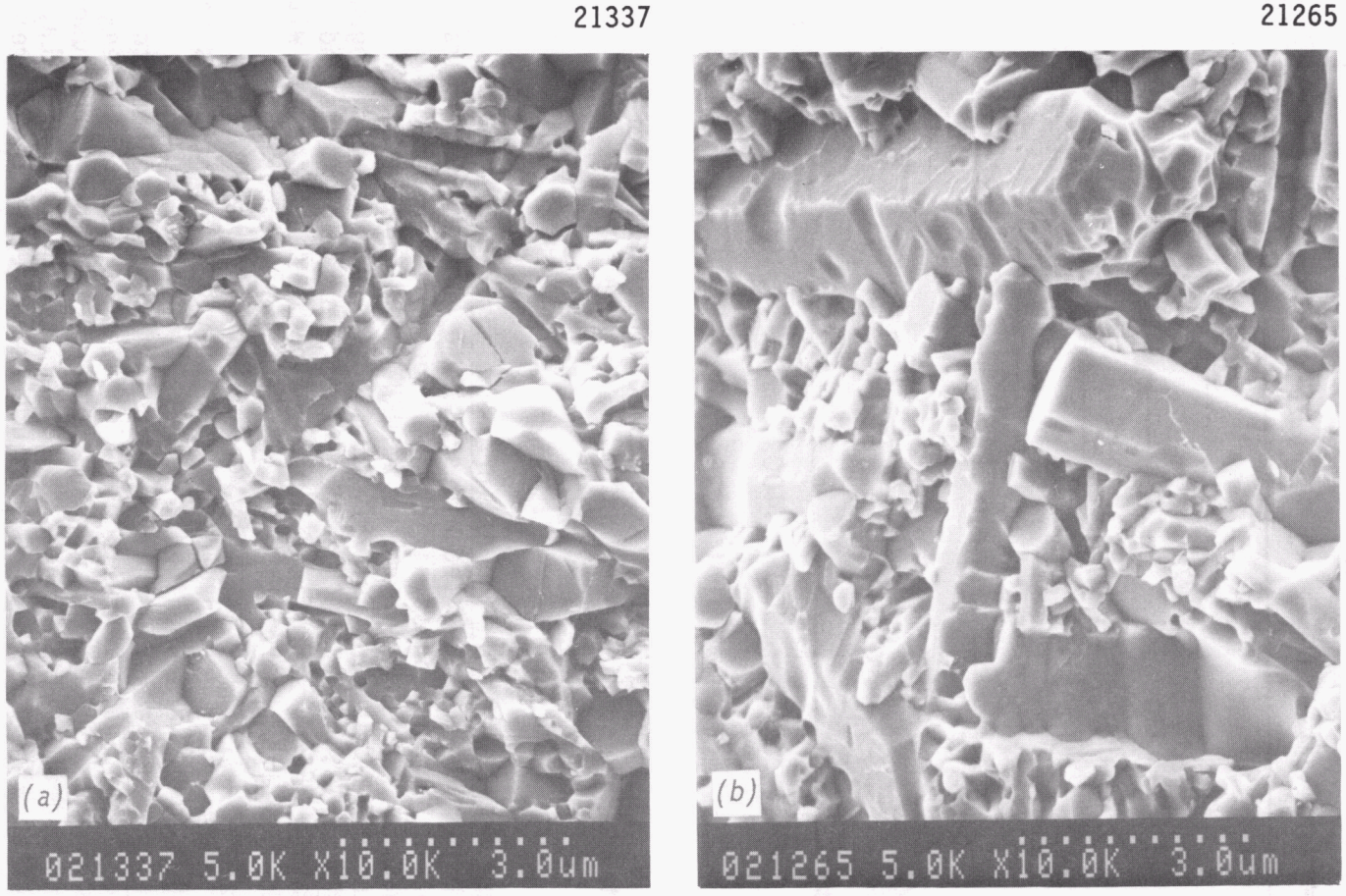

Fig. 11. Fracture surfaces of (*a*) Si_3N_4-6% Y_2O_3-2% Al_2O_3 and (*b*) Si_3N_4-6% Y_2O_3-2% Al_2O_3 (with 5% β-sialon addition) samples hot pressed to > 99% T. D. showing enhanced grain growth with the sialon addition.

Table 1. Comparison of sintering with and without an overpressure of nitrogen (conditions at 1850°C for 4 h)

Additive composition	1 atm nitrogen (0.1 MPa)			20 atm nitrogen (2 MPa)		
	Weight loss (%)	Density (g/cm^3)	Density (% T. D.)	Weight (%)	Density (g/cm^3)	Density (% T. D.)
6% Y_2O_3-2% Al_2O_3[a]	4.67	2.85	87.4	1.70	3.24	99.4
6% Y_2O_3-2% Al_2O_3[b]	4.37	3.14	96.2	3.44	3.26	99.9
6% Y_2O_3-2% Al_2O_3[c]	4.35	2.29	68.9	2.68	2.42	72.6
8% La_2O_3-2% Al_2O_3[a]	4.42	3.07	92.3	3.43	3.30	99.09
8% La_2O_3-2% Al_2O_3[b]	5.96	3.32	99.6	4.76	3.32	99.6
6% La_2O_3-4% Y_2O_3[a]	4.12	2.62	80.4	2.34	2.63	80.6
8% La_2O_3-1% Y_2O_3[b]	4.23	2.77	82.7	3.58	2.91	86.9
8% La_2O_3-1% Y_2O_3[a]	8.53	2.56	76.5	6.41	2.78	83.1

[a] Si_3N_4: Ube E-10.

[b] Si_3N_4: Starck LC-12SX.

[c] Si_3N_4: Denka 9FW.

Table 2. Summary of results on gas-pressure sintering of selected silicon nitride compositions at 1850 and 1900°C

Composition	1850°C			1900°C		
	Weight loss (%)	Density (g/cm^3)	(% T. D.)	Weight loss (%)	Density (g/cm^3)	% T. D.
6% Y_2O_3-2% Al_2O_3	1.70	3.24	99.4	2.08	3.22	98.8
8% La_2O_3-2% Al_2O_3	3.43	3.30	99.1	3.99	3.31	99.4
6% La_2O_3-4% Y_2O_3	2.34	2.63	80.6	2.42	3.12	95.6

over 2050°C and severe degradation of the samples. Failure of the temperature control system required replacement of all the thermocouples and shutdown of the furnace for an extended period of time. Consequently, furnace runs at 1900 and 1950°C and other runs using two-stage gas pressure were not completed during the present reporting period.

All of the samples sintered at 1850 and 1900°C to ≥ 95% T. D. were machined into modulus of rupture (MOR) bars for mechanical property testing. The flexural strength and fracture toughness values are given in Table 3. As indicated, the toughness values are comparable to those obtained from hot-pressed materials reported previously. However, the values are low in comparison to other published work on high-toughness silicon nitrides fabricated by GPS.[14,15] Further examination of the available literature on high-toughness materials fabricated by GPS showed that all of those materials were processed at temperatures ≥ 1950°C to grow the large grains.[20,21] These levels of temperature were not attained in the present samples and, thus, high-fracture toughness should not be expected. Other studies have shown that significant grain growth does not occur until temperatures of 1950 to 2000°C are reached.[22-25] Some increase was noted in the Si_3N_4-6% Y_2O_3-2% Al_2O_3 samples as the sintering temperature was increased from 1850 to 1900°C. Examination of the microstructures showed significant grain growth during GPS (Fig. 12).

Examination of the GPS samples showed that a density gradient was present over the cross section of the sintered samples. SEM evaluation of fracture surfaces showed no obvious differences in the microstructures. Gradients of this type have been reported in the literature and are minimized by the use of two-stage gas-sintering techniques.[26] Due to the maintenance difficulties with our furnace, this work has been delayed.

Microstructure development of refractory grain-boundary phase compositions – as reported previously,[27,28] samples have been fabricated by hot pressing with 1 to 12% rare earth oxide (Y_2O_3, La_2O_3, or Yb_2O_3) and 1 to 8% SiO_2 additives to take advantage of some of the good high-temperature properties exhibited by these materials (Table 4). With a sufficient volume of liquid phase present during fabrication, elongated β-Si_3N_4 growth will occur for increased fracture toughness, but the intergranular phases will be refractory enough for good high-temperature properties. The SiO_2 additions were used to control the intergranular phases and maintain the composition in an appropriate phase compatibility area so oxidation problems are not encountered. Testing of the mechanical properties is in progress and will confirm if the fracture toughness has been improved by the elongated grains. The mechanical properties will be correlated with the observed microstructures.

Examination of the microstructures showed that with highly refractory compositions and low volumes of intergranular glass, elongated grain growth is inhibited and a fine grain structure is produced (Fig. 13). With higher volumes of refractory intergranular glass, increased acicular growth is observed (Fig. 14), but the grain diameter is very similar to the lower glass volume compositions. This indicates that the β-Si_3N_4 grain nucleation mechanism is probably similar for both compositions, but the acicular grain growth is not. The mechanical properties will be correlated with the observed microstructures.

Table 3. Summary of mechanical properties on gas-pressure-sintered silicon nitride at 1850 and 1900°C for 4 h at 2 MPa nitrogen pressure

Composition	Density (g/cm^3) 1850°C, 1900°C	Sintering temperature			
		1850°C		1900°C	
		Flexural strength (MPa)	Fracture toughness (KIC, MPa√m)	Flexural strength (MPa)	Fracture toughness (KIC, MPa√m)
Si_3N_4-6% Y_2O_3-2% Al_2O_3[a]	3.24, 3.22	703 ± 218	5.7 ± 0.1	--	5.9 ± 0.1
Si_3N_4-8% La_2O_3-2% Al_2O_3[a]	3.30, 3.31	827 ± 51	6.8 ± 0.1	--	--
Si_3N_4-6% Y_2O_3-2% Al_2O_3[b]	3.26, --	720 ± 92	6.1 ± 0.1	--	--
Si_3N_4-8% La_2O_3-2% Al_2O_3[b]	3.32, --	650 ± 53	6.7 ± 0.1	--	--
Si_3N_4-6% La_2O_3-4% Y_2O_3[a]	2.91, 3.12	--	--	649 ± 124	7.0 ± 0.1

[a] Si_3N_4 E-10 from Ube, Japan.

[b] Si_3N_4 LC-12SX from Starck, Germany.

One problem observed in random samples was an apparent degradation of grains (Fig. 15). It is believed to have been caused by poor dispersion of the SiO_2 additive during powder processing. Cabosil was used as the SiO_2 source in these samples and because of its very fine particle size (< 0.1 μm), it is very difficult to disperse. The affected samples are being remade with increased milling and mixing times to improve the dispersion.

Microstructure development of alternate grain-boundary phase compositions – another series of samples have been fabricated by hot pressing with alternate grain-boundary phases. The grain-boundary phases will aid in densification but be of a transient nature and crystallize into a refractory grain-boundary phase. Such grain-boundary phases include the rare earth-oxide and nitride apatites as discussed by Thompson.[29] The grain-boundary phases include a wide range of stable apatites of composition $A_2B_8(SiO_4)_6O_2$, where A is a divalent cation (typically Mg, Mn, Pb, Ca, Sr, Ba) and B is a trivalent cation (typically Y, La, Ce, Nd). An advantage of the nitrogen apatite is that it can oxidize without a large volume expansion. Compositions currently being fabricated are shown in Table 5. As shown in Figs. 16 and 17, significant grain growth can occur in these systems.

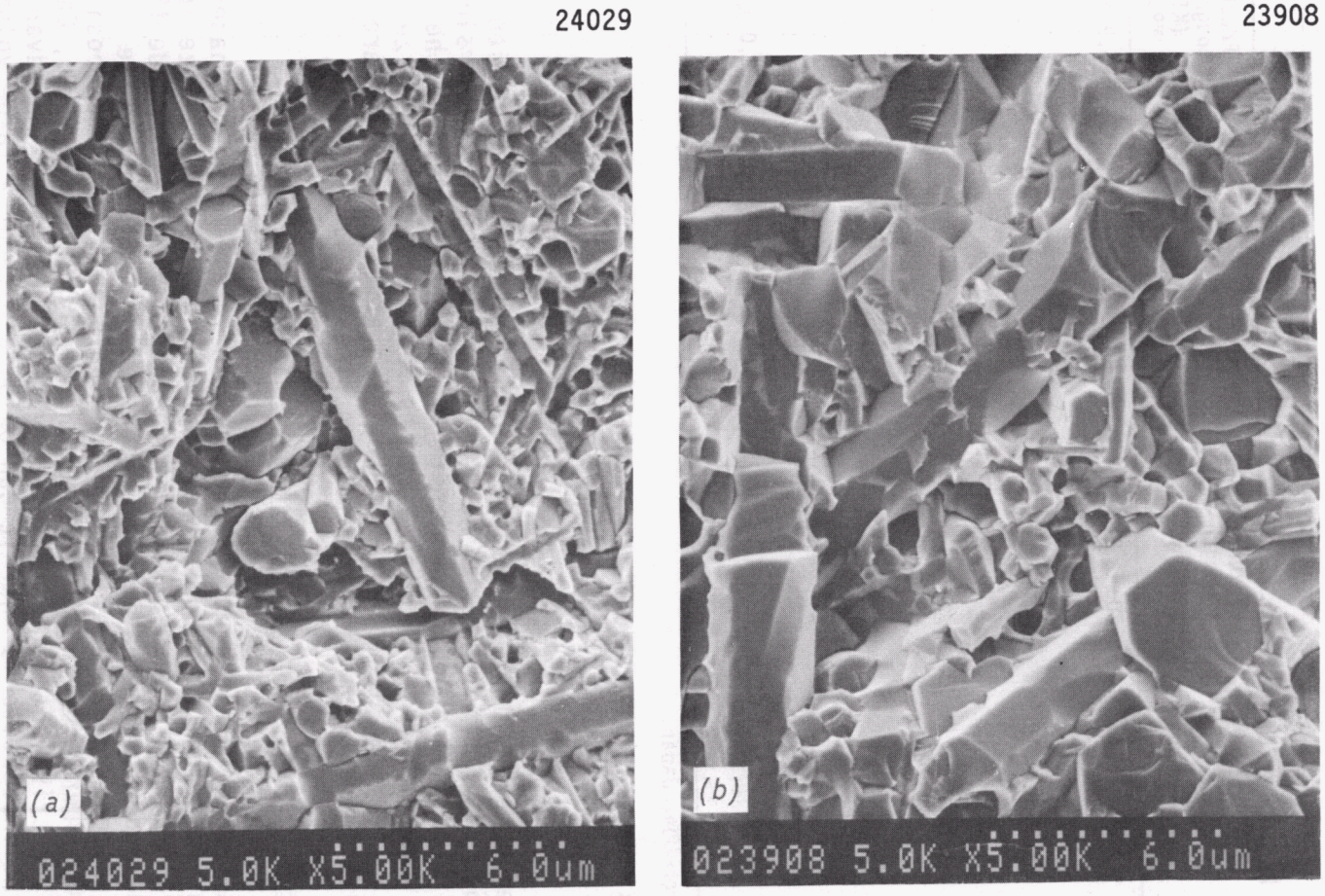

Fig. 12. Fracture surfaces of gas-pressure-sintered Si_3N_4-6% Y_2O_3-2% Al_2O_3 (*a*) 1850°C and (*b*) 1900°C showing enhanced grain growth at the higher sintering temperature. Gas-pressure sintered at 20 MPa nitrogen for 4 h.

Table 4. Silicon nitride compositions (wt %) fabricated for testing of combination of toughness and high-temperature properties

Sample	Y_2O_3 contents	La_2O_3 contents	SiO_2 contents
SC-247[a]	1	--	8
SC-256	4	--	4
SC-257	--	11	4
SC-258	4	6	4
SC-259	4	--	8
SC-260	8	--	4
SC-268	7[b]	6	4

[a]Sample did not densify.

[b]Yb_2O_3.

21281

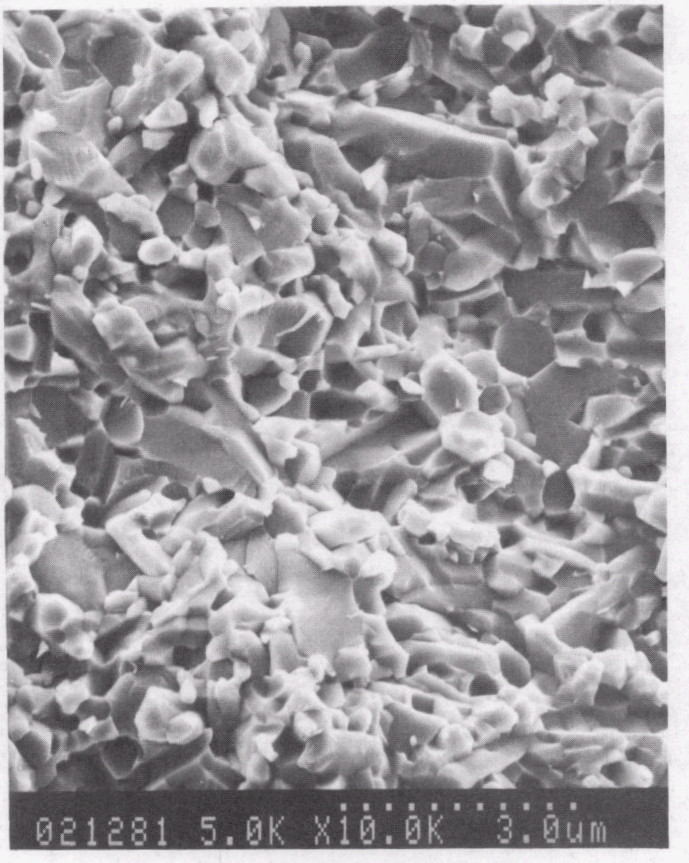

Fig. 13. Fracture surface of a Si_3N_4-7% SiO_2-1% Y_2O_3 sample hot pressed to > 96% T. D. showing fine-grain microstructure produced by refractory grain-boundary phases.

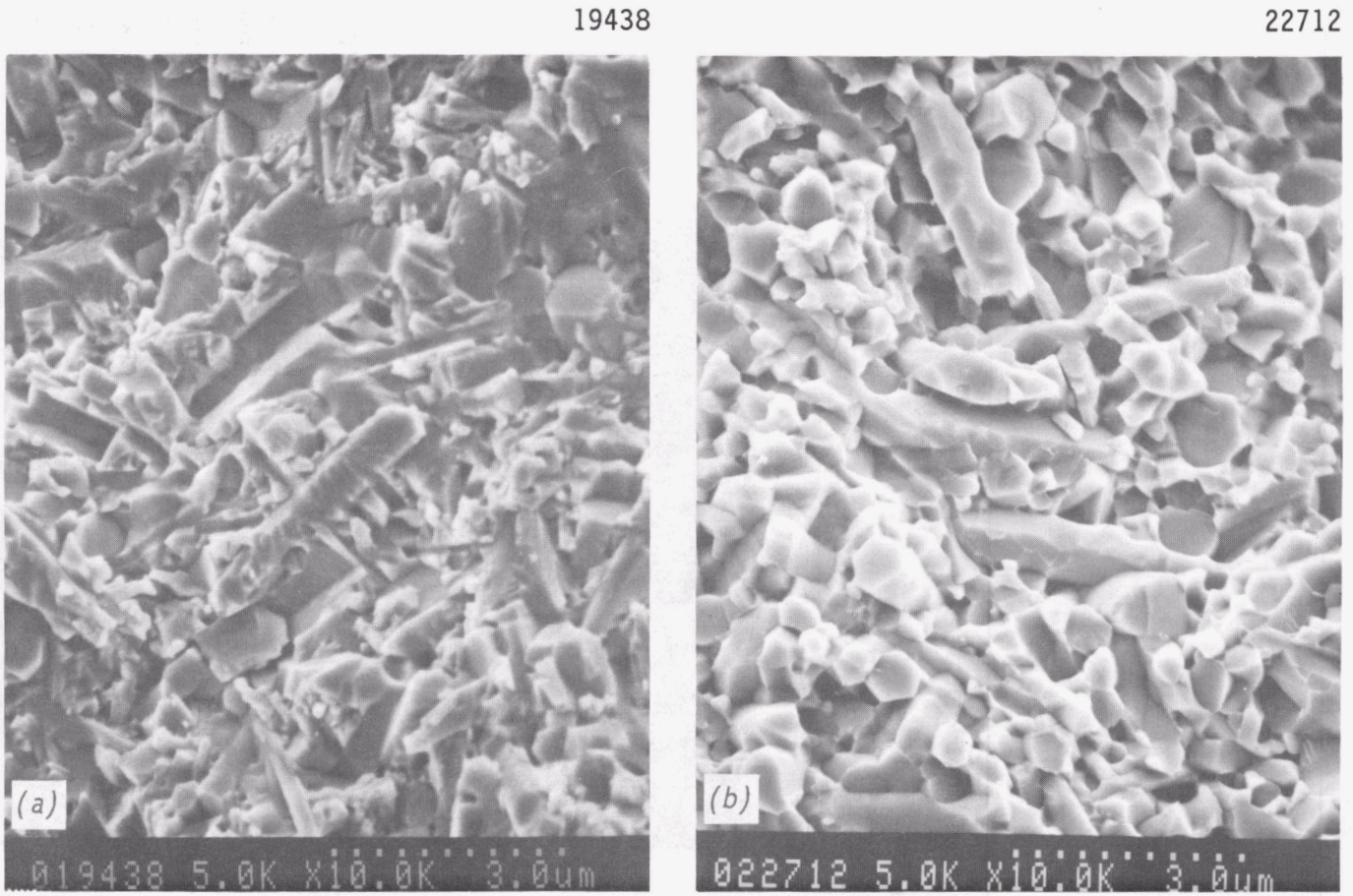

Fig. 14. Fracture surfaces of (*a*) Si_3N_4-4% Y_2O_3-6% La_2O_3 and (*b*) Si_3N_4-4% SiO_2-4% Y_2O_3-6% La_2O_3 samples hot pressed to > 99% T. D. showing elongated grain microstructures produced by refractory grain-boundary phases.

22547

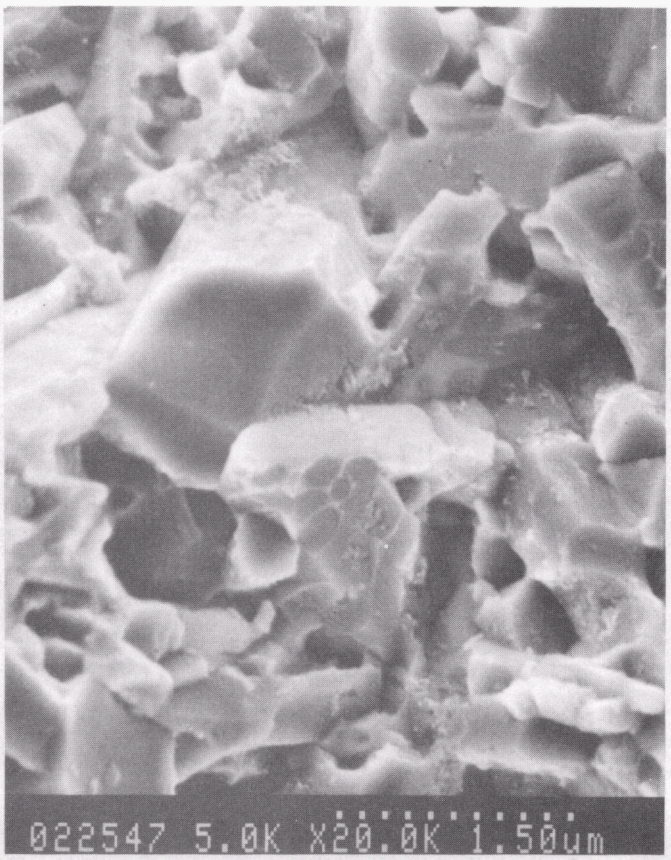

Fig. 15. Fracture surface of Si_3N_4-4% SiO_2-11% La_2O_3 showing degradation of the microstructure caused by poor dispersion of the SiO_2 additive.

Table 5. Series of silicon nitride compositions to examine effect of alternate grain-boundary phases on mechanical properties

Sample	Y_2O_3 Content	La_2O_3 Content	SrO Content	SiO_2 Content
SC-253	6	--	2	--
SC-261	6	--	2	4
SC-262	6	--	1	4
SC-263	--	8	2	--
SC-264	--	8	2	4
SC-265	6	--	1[a]	4

[a]BaO.

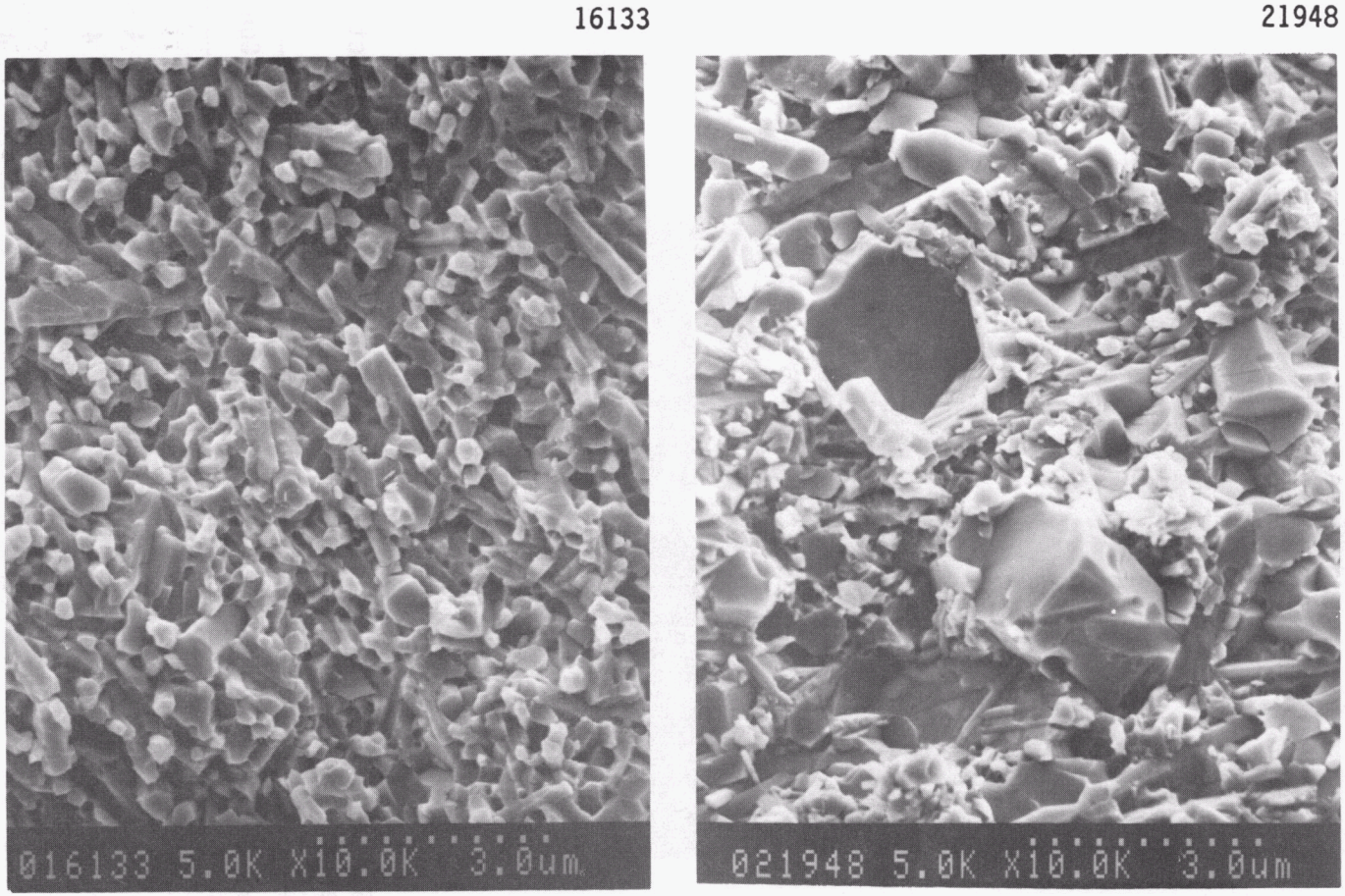

Fig. 16. Fracture surfaces of (*a*) Si_3N_4-8% La_2O_3-2% Al_2O_3 and (*b*) Si_3N_4-8% La_2O_3-2% SrO samples hot pressed to > 99% T. D. showing enhanced grain growth produced by La_2O_3- SrO grain-boundary phases.

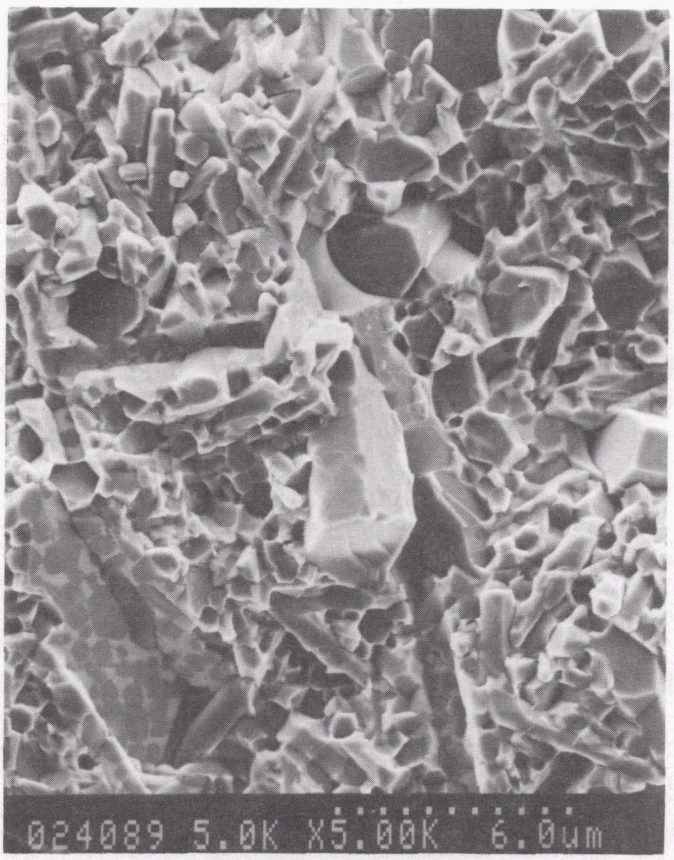

Fig. 17. Fracture surface of hot pressed Si_3N_4-4% SiO_2-8% La_2O_3-1% SrO showing extensive grain growth. Gas-pressure sintered at 1900°C at 20 MPa nitrogen for 4 h.

References

1. T. N. Tiegs, L. F. Allard, P. F. Becher, and M. K. Ferber, "Identification and Development of Optimum Silicon Carbide Whiskers for Silicon Nitride," pp. 167-72 in *Proceedings of Twenty-Seventh Automotive Technology Development Contractors' Coordination Meeting, P-230*, Society of Automotive Engineers, Warrendale, Pa., 1990.

2. I. Berman and C. E. Ryan, "The Growth of Silicon Carbide Needles by the Vapor-Liquid-Solid Method," *J. Cryst. Growth* [9], 314-18 (1971).

3. G. A. Bootsma, W. F. Kippenberg, and G. Verspui, "Growth of SiC Whiskers in the System SiO_2-C-H_2 Nucleated by Iron," *J. Cryst. Growth* [11], 297-309 (1971).

4. R. L. Beatty and F. H. Wyman, "Continuous Silicon Carbide Whisker Production," U.S. patent 4,637,924, January 20, 1987.

5. A. Yamamoto, "Process for Preparing Silicon Carbide Whiskers," U.S. patent 4,500,504, February 19, 1984.

6. M Tanaka, T. Kawabe, and M. Kobune, "Method of Manufacturing Crystalline Silicon Carbide," U.S. patent 4,504,453, March 12, 1985.

7. R. B. Nixdorf and S. Weaver, "Method for Preparing Silicon Carbide Whiskers," U.S. patent 4,873,069, October 10, 1989.

8. N. K. Sharma, W. S. Williams, and A. Zangvil, "Formation and Structure of Silicon Carbide Whiskers From Rice Hulls," *J. Am. Ceram. Soc.* **67[11]**, 715-20 (1984).

9. T. N. Tiegs et al., "Dispersion-Toughened Ceramic Composites," pp. 136-41 in *Ceramic Technology for Advanced Heat Engines Project Semiannual Progress Report for April Through September 1989*, ORNL/TM-11489, Martin Marietta Energy Systems, Inc., Oak Ridge Natl. Lab., 1990.

10. P. D. Shalek et al., "Synthesis and Characterization of VLS-Derived Silicon Carbide Whiskers," pp. 53-62 in *Proceedings of an International Conference on Whisker- and Fiber-Toughened Ceramics*, ed. R. A. Bradley et al., American Ceramic Society, Westerville, Ohio, 1988.

11. D. A. Bonnell, T. Y. Tien, and M. Ruhle, "Controlled Crystallization of the Amorphous Phase in Silicon Nitride Ceramics," *J. Am. Ceram. Soc.* **70[7]**, 460-65 (1987).

12. S. T. Buljan et al., "Ceramix Matrix Composites," pp. 55-67 of *Ceramic Technology for Advanced Heat Engines Project Semiannual Progress Report for October 1988 Through March 1989*, ORNL/TM-11239, Martin Marietta Energy Systems, Inc., Oak Ridge Natl. Lab., 1989.

13. S. T. Buljan et al., "Ceramix Matrix Composites," pp. 93-108 of *Ceramic Technology for Advanced Heat Engines Project Semiannual Progress Report for April 1989 Through September 1989*, ORNL/TM-11489, Martin Marietta Energy Systems, Inc., Oak Ridge Natl. Lab., 1990.

14. E. Tani, S. Umebayashi, K. Kishi, K. Kobayashi, and M. Nishijima, "Gas-Pressure Sintering of Si_3N_4 With Concurrent Addition of Al_2O_3 and 5 wt % Rare-Earth Oxide: High-Fracture Toughness with Fiber-Like Structure," *Am. Ceram. Soc. Bull.* **65[9]**, 1311-15 (1986).

15. C. Li and J. Yamanis, "Super-Tough Silicon Nitride With R-Curve Behavior," *Ceram. Eng. Sci. Proc.* **10[7-8]**, 632-45 (1989).

16. K. Matsuhiro and T. Takahashi, "The Effect of Grain Size on the Toughness of Sintered Si_3N_4," *Ceram. Eng. Sci. Proc.* **10[7-8]**, 807-16 (1989).

17. P. J. Whalen, C. J. Gadsasla, and R. D. Silvers, "Effect of Microstructure on the High-Temperature Deformation Behavior of Sintered Silicon Nitride," *Ceram. Eng. Sci. Proc.* **11[7-8]**, 633-49 (1990).

18. Y. R. Xu, T. S. Yen, and X. R. Fu, "Grain-Boundary Tailoring of High-Performance Nitride Ceramics and Their Creep Property Studies," pp. 739-50 in *Proceedings of 3rd International Symposium on Ceramic Materials and Components for Engines*, ed. V. J. Tennery, American Ceramic Society, Westerville, Ohio, 1989.

19. N. Hirosaki, A. Okada, and K. Matoba, "Sintering of Si_3N_4 With the Addition of Rare-Earth Oxides," *J. Am. Ceram. Soc.* **71[3]**, C-144-147 (1988).

20. H. Okamoto and T. Kawashima, NKK Corporation, Kawasaki, Japan, unpublished results reported in: P. F. Becher, "Microstructural Design of Toughened Ceramics," *J. Am. Ceram. Soc.*, **74[2]**, 255-69 (1991).

21. C. Li, J. Yamanis, and G. Carrasquillo, "High-Fracture Toughness Monolithic Silicon Nitride-Based Ceramics," Patent Application WO 9008113 (1990), CA113[22]:196538a.

22. Y. Tajima, K. Urashima, M. Watanabe, and Y. Matsuo, "Fracture Toughness and Microstructural Evaluation of Silicon Nitride Ceramics," pp. 1034-41 in *Ceramic Transactions, Ceramic Powder Science, II*, B., ed. G. L. Messing, E. R. Fuller, Jr., and H. Hausner, American Ceramic Society, Westerville, Ohio, 1988.

23. K. Homma, T. Tatuno, H. Okada, N. Kawai, and M. Nishihara, "HIP Treatment of Sintered Silicon Nitride," *J. Soc. Mater. Sci. Jpn.* **30[337]**, 1005-11 (1981).

24. M. Mitomo and K. Mizuno, "Sintering Behavior of Si_3N_4 in 10 ATM Nitrogen," pp. 263-70 of *Proceedings of the 2nd International Symposium on Ceramic Materials and Components for Engines*, ed. W. Bunk and H. Hausner, Verlag Deutsche Keramische Gesellschaft, Bad Honnef, Germany, 1986.

25. M. Mitomo, M. Tsutsumi, H. Tanaka, S. Uenosono, and F. Saito, "Grain Growth During Gas-Pressure Sintering of β-Silicon Nitride," *J. Am. Ceram. Soc.* **73[8]**, 2441-45 (1990).

26. Y. Hattori, Y. Tajima, K. Yabuta, J. Matsuo, and T. Watanabe, "Gas-Pressure-Sintered Silicon Nitride Ceramics for Turbocharger Applications," pp. 165-72 in *Proceedings of 2nd International Symposium on Ceramic Materials and Components for Engines*, ed. W. Bunk

and H. Hausner, Verlag Deutsche Keramische Gesellschaft, Bad Honnef, Germany, 1986.

27. I. P Tuersley, G. Leng-Ward, and M. H. Lewis, "High-Temperature Si_3N_4-Based Ceramics," *Brit. Ceram. Proc.* **46**, 231-46 (1990).

28. I. P Tuersley, G. Leng-Ward, and M. H. Lewis, "Silicon Nitride-Based Ceramics For Gas Turbine Applications," pp. 856-70 in *Proceedings of 3rd International Symposium on Ceramic Materials and Components for Engines*, ed. V. J. Tennery, American Ceramic Society, Westerville, Ohio, 1989.

29. D. P. Thompson, "Alternative Grain-Boundary Phases for Heat-Treated Si_3N_4 and β′-Sialon Ceramics," *Brit. Ceram. Proc.* **45**, 1-13 (1990).

Status of milestones

Milestone 123110, "Determine effects of process parameters on flaw generation in SiC whiskers" was completed. Milestone 123111, "Fabricate high-toughness silicon nitride materials with elongated grain microstructures," was not completed due to operational and maintenance problems associated with the GPS furnace.

Publications

L. F. Allard, T. A. Nolan, and T. N. Tiegs, "The Nature of Planer Defects in Silicon Carbide Whiskers," to be submitted to *J. Mater. Res.*

1.2.4 Silicate Matrix

Low Expansion Ceramics for Diesel Engine Applications (VPI)
D. A. Hirschfeld and J. J. Brown

Objective/Scope

Optimize the chemistry, properties, and processing of selected low thermal expansion compositions based on the zircon (NZP) and the β-eucryptite-$AlPO_4$ systems. These materials also exhibit stable properties above 1200°C. The major objective is to demonstrate fabricability and to promote commercialization of these ceramics.

Technical Highlights

Zircon (NZP) System

Dr. Michael Haselkorn, Caterpillar Inc., hot pressed several disks of sol-gel derived $(Ca_{0.6},Mg_{0.4})Zr_4(PO_4)_6$ (CMZP) for 1.5 to 4 h at temperatures of 1250 -1290°C in either Ar or vacuum. The CMZP disks were easily sintered to densities of 99.5% of theoretical indicative of good fabricability. The flexure strength, elastic modulus, and thermal expansion of samples cut from the hot pressed disks are being determined and will be discussed in detail when the study is complete. The maximum modulus of rupture obtained thus far is 136 MPa (±21) with an elastic modulus of approximately 100 GPa as shown in Table 1. The results also indicate that pressing in vacuum at a higher temperature (1290°C) for longer times (4 h) yields higher flexural strengths (Tables 1, 2, and 3).

The effects of zirconia additions on the thermal expansion and grain size of CMZP were investigated. Claussen(1) has shown that additions of ZrO_2 to aluminum titanate reduces microcracking due to crystal anisotropy while maintaining a low coefficient of thermal expansion (CTE). Based on Claussen's results, sol-gel derived CMZP mixed with 1.4 wt% ZrO_2 was cold pressed then sintered at 1250°C for 48 h. An average bulk CTE of -10×10^{-7}/°C (30-1000°C) with a grain size less than 10 μm. Pure CMZP sintered at 1250°C for 24 h yields an average CTE of -16.7×10^{-7}/°C and a grain size of approximately 20 μm. These results indicate that small ZrO_2 additions may allow both a reduction in grain size and a near-zero CTE for CMZP.

Table 1. Effect of Hot Pressing Atmosphere on Flexure Strength and Modulus of CMZP

Atmosphere	Flexural Strength (MPa)	Elastic Modulus (GPa)
	Pressing Conditions (5°C/min to 1250°C, 4 hours at 1250°C, 38.6 MPa)	
Vacuum	Average-100.8 ± 14.7	95.90
Argon	Average-106.86 ± 15	98.94
	Pressing Conditions (5°C/min to 1290°C, 4 hours at 1290°C, 38.6 MPa)	
Vacuum	Average-136.26 ± 21.30	103.14
Argon	Specimen cracked after removal from die	

Table 2. Effect of Time at 1260°C Soak Temperature on Hot Pressed CMZP

(5°C/min to 400°C, 10°C/min to 1260°C vacuum, 38.6 MPa)

Soak Time	Flextural Strength (MPa)		Elastic Modulus (GPa)
2 hours	Average	97.05 ± 7.78	96.53
1.5 hours	Average	78.15 ± 7.69	88.98
0.5 hours	Average	77.60 ± 9.91	97.11

Table 3. Effect of Hot Pressing Temperature on Strength and Modulus of CMZP

(5°C/min to 1250°C, 4 hours soak, vacuum, 38.6 MPa)

Temperature		Flexural Strength (MPa)	Elastic Modulus (GPa)
1250°C	Average	100.8 ± 14.7	95.90
1290°C	Average	136.26 ± 21.30	103.14

Lightweight Ceramics

Lightweight CMZP ceramics were made by coating a polymer substrate using sol-gel techniques to form a more open structure (Figure 1). The reticulated polymers were coated with the gel then dried, pyrolized, and sintered yielding a lightweight ceramic with open cells smaller than 200 μm. The struts between cells are hollow due to pyrolysis of the polymer substrate and have wall thicknesses between 20 and 100 μm as shown in Figure 2. Further development of this processing technique and characterization of the mechanical properties of this lightweight structure is being studied.

To form CMZP for filter applications, sol-gel derived powders are mixed with paraffin wax and a polymer then molded and fired to form an open structure which has both large pores and narrow channels (Figure 3). The large pores are formed by the pyrolysis of the polymer and the channels are formed by the removal of the wax. The processing and properties of this material is under investigation.

Ceramic Composites

The effects of fiber volume fraction and processing on the flexure strength of $(Ca_{0.6},Mg_{0.4})Zr_4(PO_4)_6$ (CMZP) reinforced with either chopped Nicalon-SiC fibers or SiC whiskers was investigated. The CMZP used for this study was prepared by sol-gel synthesis.

Disks 50 mm in diameter were hot pressed in air, N_2, or Ar at the temperature and pressures indicated on Table 4. Three to five specimens approximately 25 mm long were cut from the center of each disk then ground smooth and the edges chamfered. The specimens were broken in three point bending with a span of 20 mm and a crosshead speed of 0.2 mm/min using an ATS universal testing machine with a load

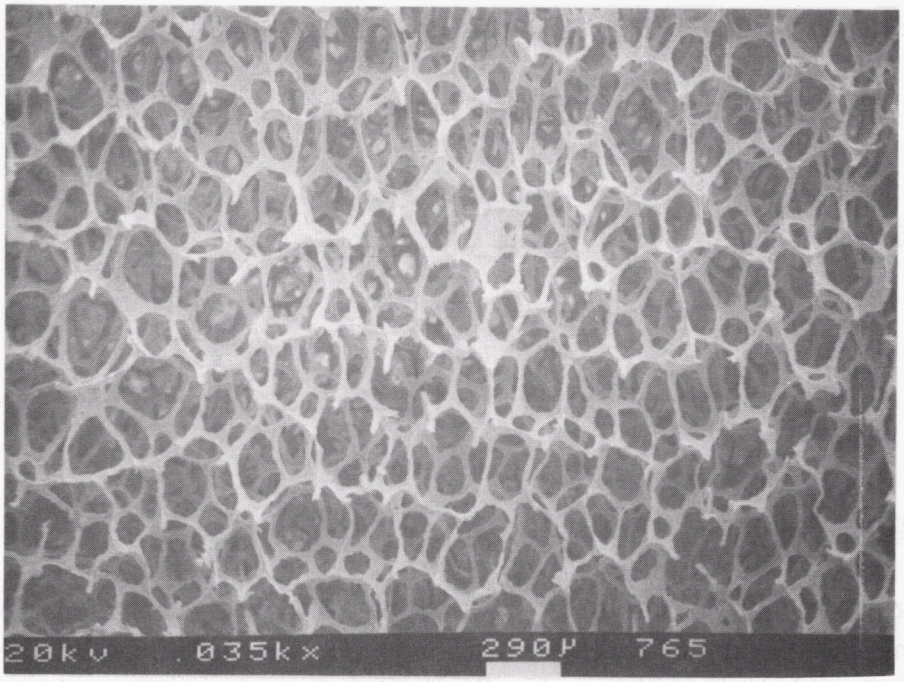

Figure 1. Fracture surface of lightweight CMZP fabricated using a sol-gel coating technique

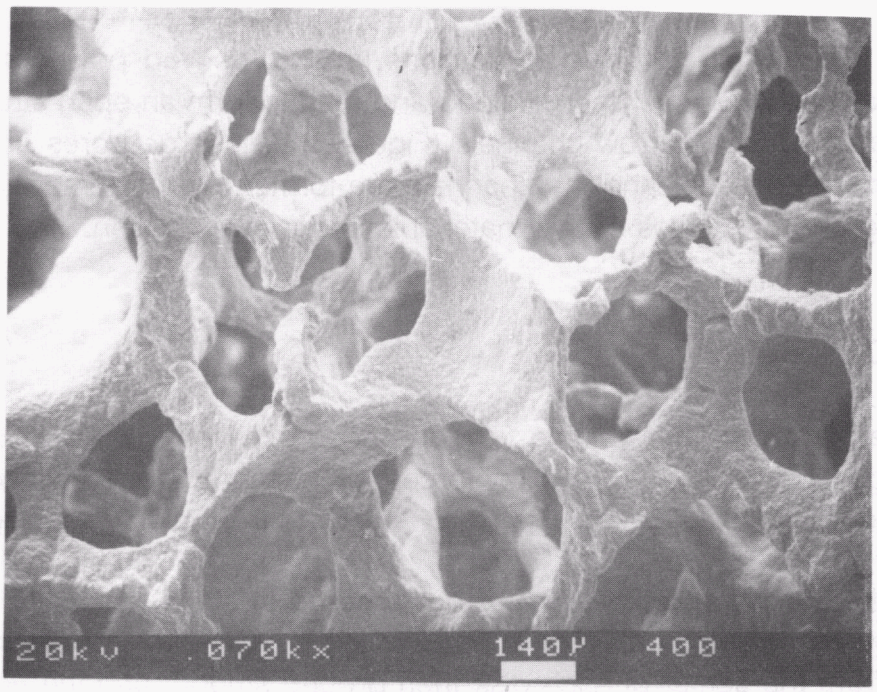

Figure 2. Strut structure of lightweight CMZP

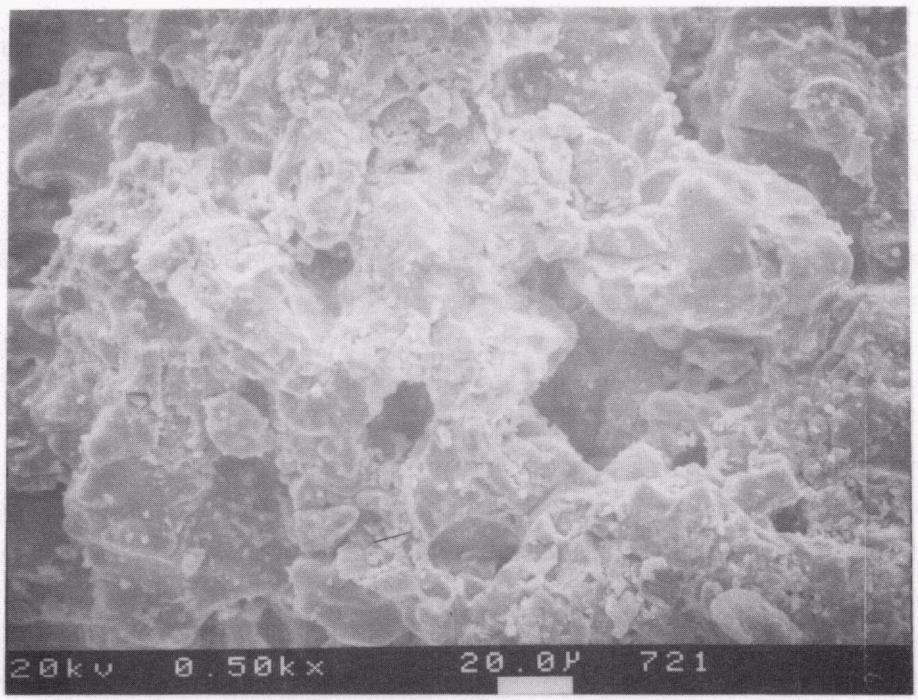

Figure 3. Structure of CMZP for filter applications

Table 4. Fracture Strength of Reinforced CMZP Composites Hot Pressed in Air

Reinforcement Content (vol%)	Processing conditions (Temp./Pressure,Time)	Density (% Theoretical)	MOR (MPa)
5 (Fiber)	1210°C/18 MPa, 2h in Air	97	49.6±9.5
5 (Fiber)	1210°C/18MPa, 8h in N_2	98	47.7±10
10 (Fiber)	1210°C/18 MPa, 2h in Air	97	50.4±10.6
10 (Fiber)	1210°C/27MPa, 6h in Ar	98	48.3±12
10 (Whisker)	1230°C/30MPa, 4h in Ar	97	141.3±11
20 (Fiber)	1230°C/30 MPa, 3h in Air	98	91.3±7.1

capacity of 225 kg. No significant increase in strength was observed by increasing the fiber content from 5 to 10 vol%. Similar to the samples hot pressed in air, no increase in strength was observed for the samples hot pressed in an inert atmosphere by increasing the fiber content from 5 to 10 vol%. These strengths are significantly less than that of hot pressed unreinforced CMZP (approximately 91 MPa) because the chopped fibers act as flaws in the composite. The strength of the composites is significantly increased by adding up to 20 vol% chopped fibers and with higher densities as achieved with higher pressure and temperature during pressing.

Sol-gel derived CMZP powders with 10 vol% SiC whiskers were turbomilled by Dr. Dale Wittmer at Southern Illinois University. A disk of 50 mm in diameter was then made by hot pressing the CMZP powder-SiC whisker mixture with 1.5 wt% ZnO as sintering aid. The processing conditions are listed on Table 4. Densities greater than 97% of theoretical were achieved in the central part of the disk. The average flexure strength of four bars from the center of the composite disk was 141.3 MPa ($\pm$11) measured in three point bending. This strength is much larger than that achieved for chopped fiber reinforced CMZP (Table 4) and hot pressed unreinforced CMZP (approximately 91 MPa). The microstructure of the fracture surface is shown in Figure 4 which exhibits fine grain size, whisker pull outs, and low porosity. An investigation of the effects of whisker content on the toughness and strength at both room temperature and high temperature is underway.

The chemistry of the fiber/matrix interface of Nicalon-SiC/CMZP composites hot pressed in air or in an O_2-deficit atmosphere was further investigated using Auger Electron Scanning (AES) microscopy. An AES microscope (Perkin Elmer Model 610) with a scanning beam size of 3 μm was used to examine both the fiber surfaces and troughs in the matrix where fibers had been removed. The amount of C and Si in the matrix trough for the sample pressed in air was higher than in the sample pressed in Ar as shown in Table 5. Since Si and C are not likely to exist in the form of SiC in the matrix, the presence of Si and C confirms that CMZP reacts with SiC in either Ar or air. In previous reports, this reaction was indicated by energy dispersive x-ray analyses of the fiber surface and trough and by calculations of thermodynamic equilibrium using SOLGASMIX-PV.

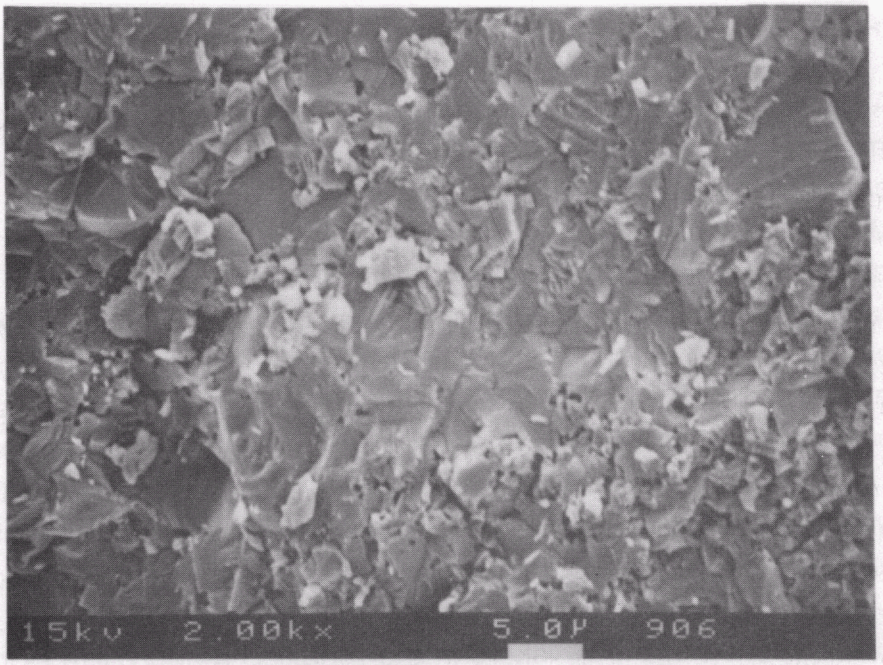

Figure 4. Fracture surface of whisker reinforced CMZP

Table 5 AES Analysis of Fiber Surface and Matrix Trough of Nicalon-Reinforced CMZP

	Hot pressed in air (at%)		Hot pressed in Ar (at%)	
Elements	Fiber	Trough	Fiber	Trough
C	13.7	9.2	11.2	6.4
O	39.2	45.9	35.8	38.1
Si	17.3	15.9	16.7	9.9
Ca	4.0	2.4	2.7	1.7
Zr	4.3	9.3	5.2	17.6
P	1.7	5.0	2.6	16.4

β-Eucryptite System

A process has been developed to form in-situ whiskers in modified β-eucryptite which improves the strength of the material while maintaining a near-zero bulk linear coefficient of thermal expansion (CTE).

Modified β-eucryptite, $(Li_{0.41},Mg_{0.035})Al(P_{0.52},Si_{0.48})O_4$, is prepared using a solid-state reaction method then mixed with up to 12 wt% of either TiO_2 or ZrO_2 and heated at 1600°C to form a glass. The glass melt is quenched in water, ground to a fine powder, then mixed with acetone to form a slurry which is poured into a mold. The acetone is drained leaving a compact. The compact is heat treated at 680°C to allow coalescence of the glass particles and then recrystallized at 1100°C. The resulting ceramic contains randomly oriented whiskers with an aspect ratio of approximately 30 as shown in Figure 5 for a sample containing 6 wt% TiO_2 . Electron microprobe analysis indicates that these acicular grains or whiskers are TiO_2 or ZrO_2, depending on the additive.

The presence of the whiskers in the modified β-eucryptite significantly improves the flexure strength as shown in Figure 6. With up to 12 wt% TiO_2, the MOR determined using three point bending tests show an increase in strength from 53 MPa to 150 MPa (Table 6).

Table 6. Effect of TiO_2 Content on CTE of Modified β-Eucryptite

TiO_2 content (wt%)	Average Bulk CTE (30-1000°C)	MOR (MPa)
0	-7.0×10^{-7}/°C	52.6 ± 1.2
6	-2.5×10^{-7}/°C	99.5 ± 17.4
8	0.5×10^{-7}/°C	117.9 ± 12.2
10	0.9×10^{-7}/°C	113.8 ± 8.8
12	2.8×10^{-7}/°C	150.0 ± 19.5

The presence of the TiO_2 whiskers also affects the thermal expansion behavior of the material. The bulk CTE averaged over 20°C to 1000° increases from -7.0×10^{-7}/°C to $+2.8 \times 10^{-7}$/°C when the TiO_2 content is increased from 0 to 12 wt % as shown in Table 6. From the thermal expansion data it is seen that the incorporation of 8-10 wt% TiO_2 produces a β-eucryptite which exhibits a near zero CTE.

Previously, it was reported that addition of 2 wt% CaO to the $AlPO_4$ modified β-eucryptite, reduced microcrack formation during recrystallization. CaO appears to reduce the viscosity of the glass during recrystallization thus relieving the internal stresses induced by the volume change during the glass to glass-ceramic

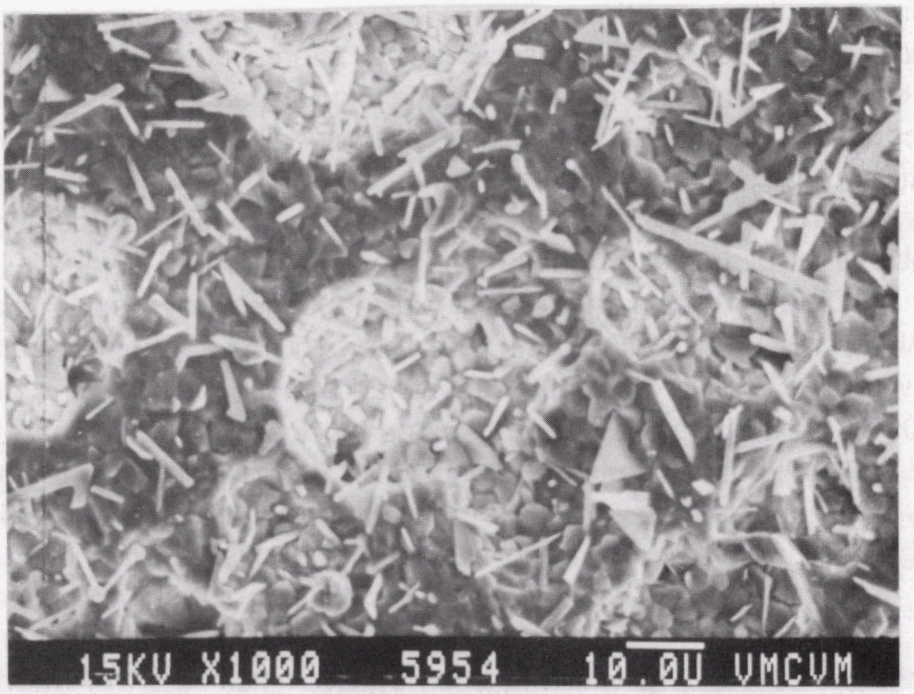

Figure 5. Etched microstructure of modified β-eucryptite with 6 wt% TiO_2

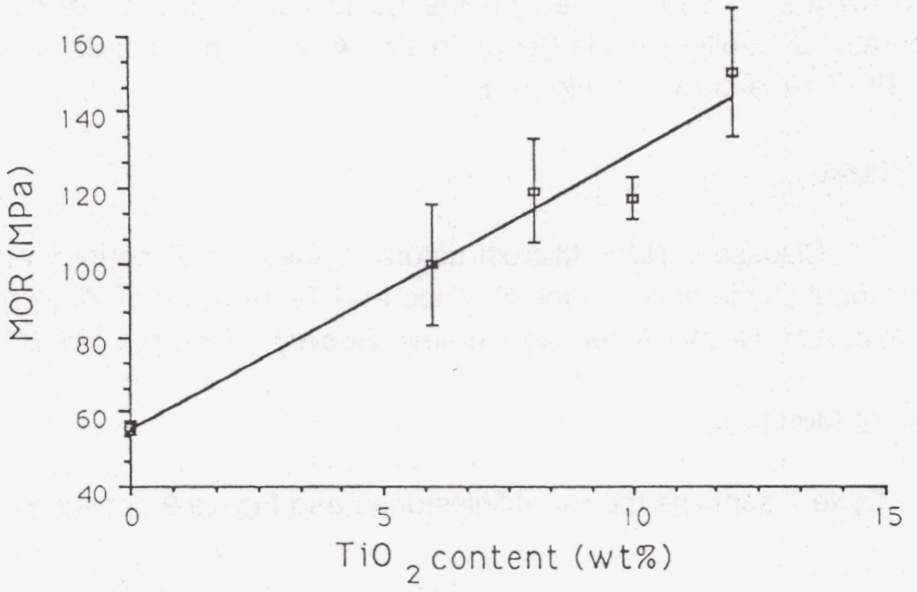

Figure 6. Flexure strength of modified β-eucryptite as a function of TiO_2 content

transformation. However, the melting temperature of recrystallized modified β-eucryptite was reduced to 1000°C as measured using differential thermal analysis (DTA).

One possible way to increase the melting temperature of the modified β-eucryptite is to add silica; hence, a new glass-ceramic which contains higher silica content, $Li_{0.5}Al(P_{0.5},Si_{0.75})O_{4.5}$, hereafter referred to as high silica β-eucryptite, was synthesized by the conventional glass-ceramic processing method. High silica β-eucryptite is a solid solution phase composed of 50 mol% $Li_2O \cdot Al_2O_3 \cdot 3SiO_2$ and 50 mol% $AlPO_4$. This composition was obtained by solid state reaction of $Li_2O \cdot Al_2O_3 \cdot 3SiO_2$ and $AlPO_4$ at 1200°C for 100 hours. The resulting powder was mixed with 4 wt% TiO_2 (nucleating agent) and 2 wt% CaO by dry milling then melted at 1620°C. Next, the glass obtained was annealed at 550°C. The glass-ceramic was formed by heat treatments at 760°C and 1000°C. The melting temperature of high silica β-eucryptite is approximately 1200°C (measured using DTA). The resulting glass-ceramic has a grain size of 2-3 μm with no evidence of microcrack formation. Acicular grains of TiO_2 having an aspect ratio of 10-20 were formed during recrystallization and are shown in Figure 7. The bulk linear coefficient of thermal expansion of high silica β-eucryptite is $-4.3 \times 10^{-7}/°C$ which is less negative than that of modified β-eucryptite ($-7 \times 10^{-7}/°C$). The strength of this ceramic is 134 ($\pm$10) MPa measured in 4 point bending (20mm/40mm spans).

The processing of high silica β-eucryptite glass-ceramic, was also investigated. A mixture of 94 wt% $Li_{0.5}Al(P_{0.5},Si_{0.75})O_{4.5}$. 2 wt% CaO, and 4 wt% TiO_2 was melted at 1620°C, rapidly cooled to temperatures from 600°C to 760°C, and then heated to 900°C for 0.5 h to allow grain growth. The grain size of the resulting glass-ceramic varied from 2 - 15 μm based on the nucleation temperature with higher nucleation temperatures resulting in a larger grain size. A typical microstructure exhibiting a uniform crystallite size is shown in Figure 8.

References

1. Claussen, Nils, "Microstructural Design of Zirconia-Toughened Ceramics," International Conference on the Science and Technology of Zirconia, ed. N. Claussen, M. Ruhle, A.H. Heuer, American Ceramic Society, 1984, pp. 325-351.

Status of Milestones

Table 7 contains the list of Milestones and Figure 9 contains the Milestone Status chart.

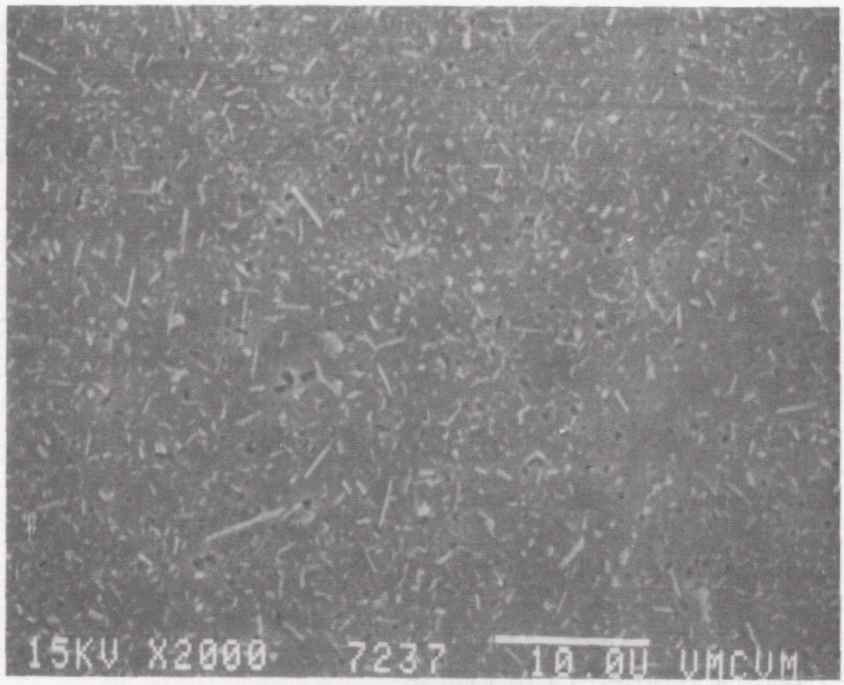

Figure 7. Etched fracture surface of $Li_{0.5}Al(P_{0.5},Si_{0.75})O_{4.5}$

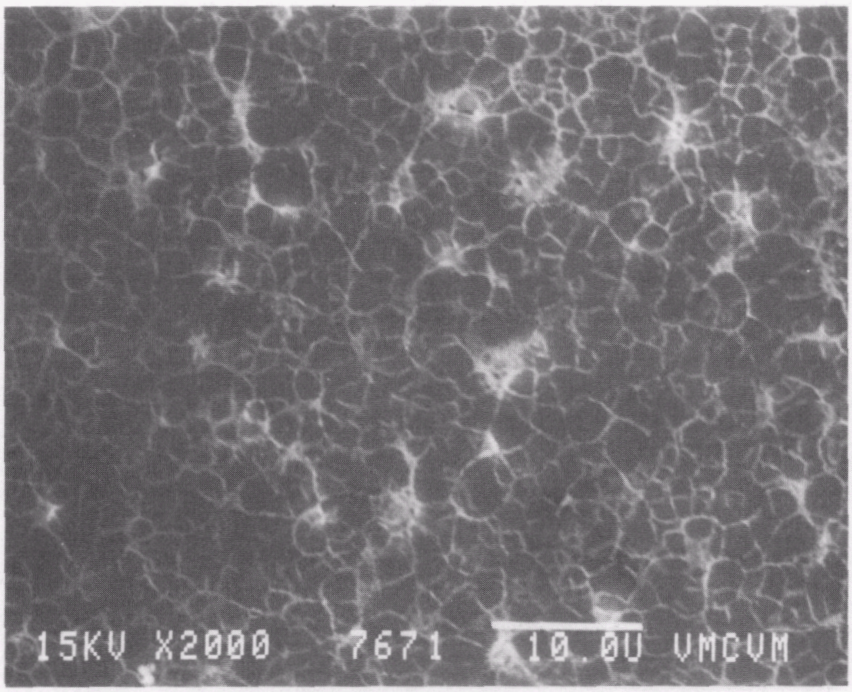

Figure 8. Fracture surface of $Li_{0.5}Al(P_{0.5},Si_{0.75})O_{4.5}$ glass-ceramic heated to 640°C then 900°C.

Table 7. KEY TO MAJOR MILESTONES (WBS ELEMENTS)

		Completion Date
VPI 2.4.1	Property Optimization by Hot Isostatic Pressing	July 31, 1992
VPI 2.4.2	Optimization of Compositions	Mar. 31, 1991
VPI 2.4.3	Mechanical Properties of NZP Ceramics	
	a. Characterization at Room Temperature	Dec. 31, 1991
	b. Characterization at High Temperature	July 31, 1992
VPI 2.4.4	Fiber Reinforced Composites	
	a. Synthesis of SiC/NZP Composities	July 31, 1991
	b. Characterization of Mechanical Properties	July 31, 1992
VPI 2.4.5	Lightweight Insulation	Sept. 30, 1991
VPI 2.4.6	Characterization of In-Situ Toughened Composities	
	a. Modified β-eucryptite Composites	July 31, 1992
	b. NZP Whisker Reinforced Composites	July 31, 1992
VPI 2.4.7	Submit Technical Paper on Research Results for Publication	July 31, 1991
VPI 2.4.8	Final Report	Sept. 30, 1992

Figure 9 Status of milestones

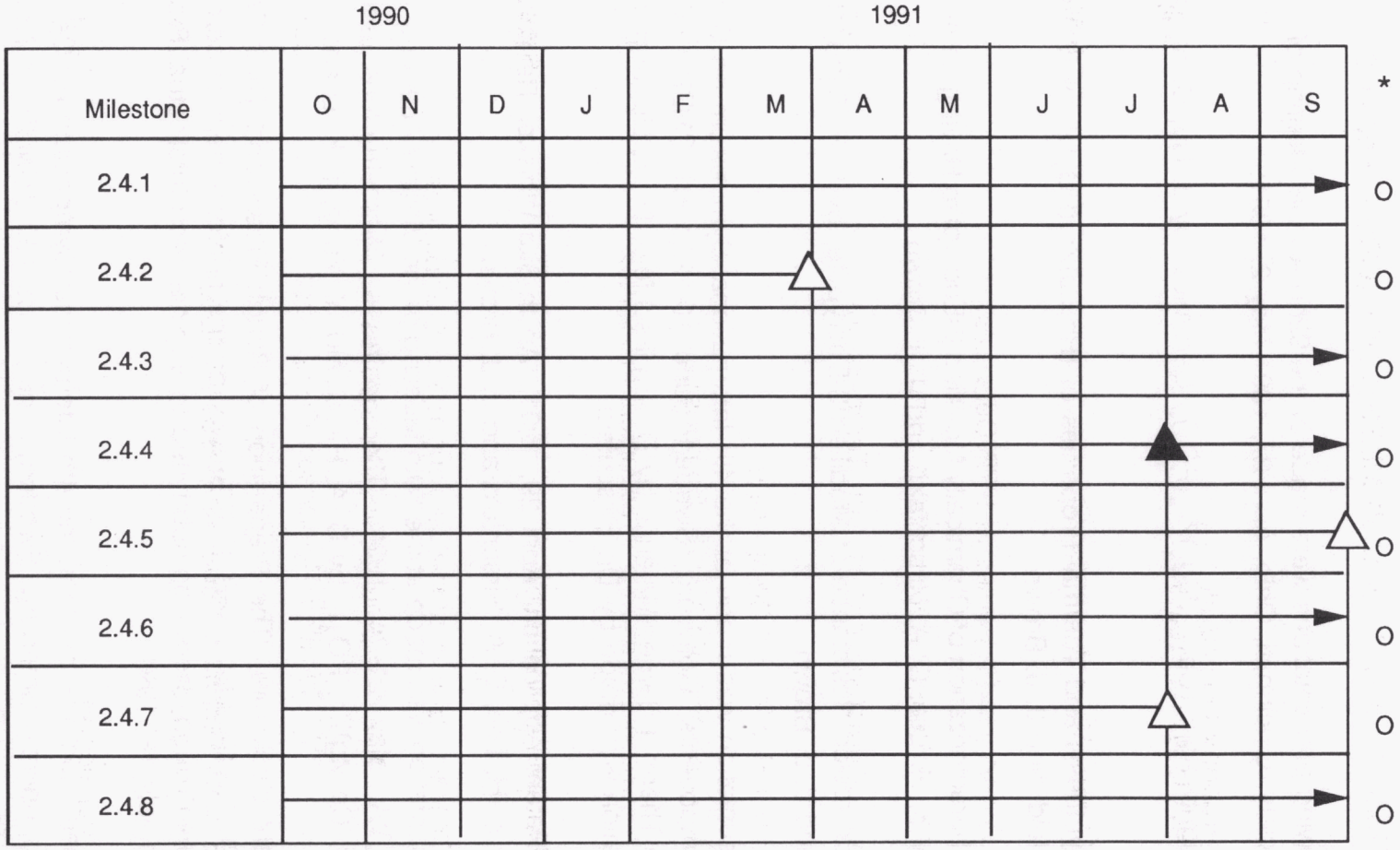

* On, Ahead of, or Behind Schedule

Publications

The following presentations were made at the 92nd Annual Meeting of the American Ceramic Society, Cincinnati, Ohio, April 27, 1991-May 2, 1991:

1. "Lightweight $(Ca_{1-x},Mg_x)Zr_4(PO_4)_6$ Ceramics" by J. Liu, D. A. Hirschfeld, J. J. Brown

2. "Synthesis and Thermal Properties of $(Rb,Cs)Zr_2(PO_4)_3$" by D. Raqué, T. Li, D. A. Hirschfeld, and J. J. Brown

3. "Characterization of Chemically Modified β-Eucryptite Having an Acicular Grain Structure" by K. H. Lee, D. A. Hirschfeld, and J. J. Brown

4. "Corrosion Resistance of Modified β-Eucryptite" by L. P. Battu, D. A. Hirschfeld, and J. J. Brown

A presentation was made at the 4th International Symposium on Ceramics and Ceramic Components, Goteburg, Sweden, June 10-12, 1991,"CMZP - A New High Temperature Thermal Barrier Material" by D. A. Hirschfeld, D. M. Liu, and J. J. Brown. The presentation was made by Dr. Hirschfeld.

U. S. Patent Application, April 29, 1991, "An In-Situ Whisker Reinforced Glass-Ceramic", by K. H. Lee, D. A. Hirschfeld and J. J. Brown

A presentation was made at the 50th Meeting of the Virginia Academy of Science, Blacksburg, VA, May 21-24, 1991, "The Synthesis, Microstructure, and Thermal Properties of $(Ca,Mg)Zr_4(PO_4)_6$ by D. A. Hirschfeld, Y. Yang, T. K. Li and J. J. Brown

A patent disclosure, "The Preparation of Rough Fibers and Their Composites" by T. K. Li, D. A. Hirschfeld, and J. J. Brown, on the reinforcement of ceramic matrix composites with rough fibers was submitted to Virginia Tech Intellectual Properties for evaluation on July 18, 1991.

A presentation was made at the 4th International Symposium on Ceramics and Ceramic Components, Goteburg, Sweden, June 10-12, 1991,"CMZP - A New High Temperature Thermal Barrier Material" by D. A. Hirschfeld, D. M. Liu, and J. J. Brown. The presentation was made by tent on the flexure strength of modified β-eucryptite

1.3 THERMAL AND WEAR COATINGS

Fabrication and Testing of Corrosion-Resistant Coatings
D. P. Stinton, J. C. McLaughlin, and D. W. Graham (Oak Ridge National Laboratory)

Objective/scope

Sodium corrosion of silicon carbide and silicon nitride components in gas turbine engines is a potentially serious problem. The outer surfaces of SiC and Si_3N_4 parts oxidize at high temperatures to form an SiO_2 layer that inhibits further oxidation. However, sodium that is present in high-temperature combustion atmospheres reacts with the SiO_2 layer, such that it is no longer protective. The objective of this program is to develop a coating that will protect the underlying SiC or Si_3N_4 from sodium corrosion and provide simultaneous oxidation protection. To evaluate the behavior of potential materials such as stabilized ZrO_2 or HfO_2, TiO_2, $Al_2O_3 \cdot TiO_2$, and Ta_2O_5 in sodium-containing atmospheres, the corrosion resistance of hot-pressed samples of these materials will first be evaluated. A chemical vapor deposition (CVD) process will be developed for the application of the most promising coatings. The effect of the combustion environment upon coating characteristics such as microstructure, strength, adherence, and other properties will then be evaluated.

Technical highlights

Development of coatings to protect SiC or Si_3N_4 turbine engine components from sodium and steam corrosion continued this period. After an extensive search, a limited number of materials were identified with the potential to protect components from corrosive atmospheres (Table 1). These materials were selected because of their high-temperature stability with respect to sodium and their low coefficients of thermal expansion (CTE). Low CTE's are required to promote good bonding of the coating to the

Table 1. Potential corrosion-resistant oxides

Compound	Density (g/cm^3)	CTE ($\times 10^{-6}/°C$)
Al_2O_3[a]	3.97	8.0
$3Al_2O_3 \cdot 2SiO_2$	2.8	5.7
SiC[a]	3.21	5.5
$ZrTiO_4$	~5	~4
$HfTiO_4$	~5	~4
Ta_2O_5	8.02	3.6
Si_3N_4[a]	3.19	3.0
Al_2TiO_5	3.68	2.2

[a]Included only as a reference and not as a potential coating.

substrate. Previous experience at GTE has shown that the CTE of the coating should be less than that of Al_2O_3 (8×10^{-6}/°C), since their experience indicated the CTE mismatch caused an Al_2O_3 coating to fail to adhere to SiC and Si_3N_4 substrates.

In order to more easily evaluate the corrosion resistance of Al_2TiO_5, $ZrTiO_4$, $HfTiO_4$, and $3Al_2O_3 \cdot 2SiO_2$, specimens were prepared by hot pressing or cold pressing and sintering. Evaluation of these materials by X-ray diffraction revealed that the desired crystalline compounds had been produced. After exposing each of the candidate materials plus a sintered α-SiC specimen to a combustion environment at 1000°C, the pellets were examined metallographically. The α-SiC exhibited a surface layer of glass about 20-μm thick. Significantly better corrosion resistance, which is consistent with the published results of Federer, was exhibited by $3Al_2O_3 \cdot 2SiO_2$, which had a 10-μm glass layer. Further improvements in corrosion resistance are seen by $ZrTiO_4$, $HfTiO_4$, and Al_2TiO_5 since the reaction layers were ~4-μm, 4-μm, and <2-μm thick, respectively.

Corrosion testing was also performed on SiC specimens that had been coated with Ta_2O_5. During coating in an oxidizing environment, the SiC substrate formed a relatively thick crystalline SiO_2 protective layer beneath the Ta_2O_5. Corrosion testing left the Ta_2O_5 coating and the crystalline SiO_2 sublayer unaffected. The Ta_2O_5 coating deposited by CVD nucleated as small equiaxed grains but grew into large columnar grains normal to the substrate surface. Microstructures of this type are not desirable for corrosion protection because grain boundaries provide easy access to the substrate for sodium and oxygen. Varying mor-phologies were produced in a series of coatings produced at different depo-sition temperatures and reactant concentrations. The microstructure of the coatings was whiskerlike at low temperatures and changed to fibrous or columnar at high temperatures. Additional development is needed to optimize the coating process to achieve the small equiaxed grains that are desired. To this end, an experiment has been statistically designed to investigate the effect of deposition temperature, reactant concentration, and total flow rate on the coating morphology. The statistical design should minimize the number of experiments required to determine the optimum coating structure.

SiO_2 layers that form on SiC or Si_3N_4 components are a natural barrier to oxygen, making the material oxidation resistant. SiO_2 is unusual in this regard because most oxides, including the materials being investigated here ($ZrTiO_4$, $HfTiO_4$, Al_2TiO_5, $3Al_2O_3 \cdot 2SiO_2$ and Ta_2O_5), are permeable to oxygen, particularly at high temperatures. Therefore, the natural SiO_2 oxygen barrier present on SiC and Si_3N_4 components will be protective only if it is stable when in contact with the corrosion-resistant oxide coating. Specimens were fabricated this period to test the stability of the substrate-SiO_2-coating interface. Discs of SiC were embedded in pellets of Al_2TiO_5 and $3Al_2O_3 \cdot 2SiO_2$ by hot pressing at 14 MPa and 1600°C for 1 h. Additional specimens are being prepared by cold pressing and sintering from the other potential coating materials. After annealing in air at 1200°C for several weeks, cross sections will be metallographically examined to determine the stability of the SiO_2 layer.

Status of milestones

On schedule

Publications

D. P. Stinton, J. C. McLaughlin, and L. Riester, "Fabrication and Testing of Corrosion-Resistant Coatings," to be published in the *Proceedings of the 4th International Symposium on Ceramic Materials and Components for Engines.*

Development of Adherent Ceramic Coatings to Reduce Contact Stress Damage of Ceramics
- S. Wayne, D. O'Neil, and J.H. Selverian (GTE Laboratories Incorporated)

Objective/Scope

The objective of this program is to develop oxidation-resistant, high-toughness, adherent coatings for silicon-based ceramics for use in an advanced gas turbine engine. These coatings will be deposited by chemical vapor deposition (CVD) onto reaction-bonded Si_3N_4 (RBSN), sintered SiC (SSC), and hot-pressed Si_3N_4 (HSN). The coating will be designed to provide the best mix of mechanical, thermal, and chemical properties for the application.

Technical Highlights

The deposition process of the Al_2O_3+ZrO_2 composite coating has been improved with the use of an Al-10wt%Zr alloy as the metal chloride source material, resulting in a very uniform dispersion of ZrO_2 in the Al_2O_3 matrix.

The room-temperature pin-on-disk sliding wear tests of uncoated and coated RBSN, SSC, and HPSN have been completed. The breakaway and kinetic coefficients of friction have been measured, and microscopic inspection of worn surfaces is underway. The MOR tests from Phase I have been reinterpreted in light of the presence of cracks in the coating.

Uncoated and coated HSN, RBSN, and SSC were scratch-tested. The uncoated SSC sustained the most severe damage compared to uncoated RBSN and HSN. The AlN/Al_2O_3+ZrO_2 coating protected the substrates from damage in the scratch test. Also, the coating had the lowest adherence to SSC.

Microscopic inspection of room-temperature wear-tested specimens has shown that the composite coatings can offer improved resistance to contact stress damage as determined by pin-on-disk and single-point scratch tests. Of the three substrates, the coating was most effective on hot-pressed Si_3N_4, which is thought to be related to higher coating adhesion on this substrate.

Studies were performed on two substrate materials (Si_3N_4 and SiC) with varying numbers and thicknesses of the alumina-zirconia and aluminum nitride coatings. Results were compared to previous finite element studies of the coating system[2] to ensure correct implementation of the composite-plate code.

This report describes the completion of section i of the new milestone added to this contract in June 1991: residual stress in the coating layers due to CVD cycle and thermal expansion mismatch. The residual stresses were calculated by implementing composite plate theory.[1-3] This method readily accommodates modifications to the number of coatings and coating thicknesses, as well as properties of coating and substrate materials.

The propagation of a crack through the Al_2O_3+ZrO_2 composite coating on a silicon nitride substrate was modelled. Initial results suggest that, as a vertical crack propagates through the coating, it is only partially deflected by the interface. Therefore, improvements in the toughness of the interface are expected to have a small influence on these types of cracks.

Coating Development

The deposition process of the Al_2O_3+ZrO_2 composite coating has been improved with the use of an Al-10wt%Zr alloy as the metal chloride source material. Previously, a mixture of Al and Zr particles were used to generate the separate Al and Zr chlorides, which resulted in a coating with an irregular dispersion of ZrO_2. By using an Al-Zr alloy, a uniform dispersion of ZrO_2 was obtained. Figure 1 shows x-ray maps indicating the elemental distribution of Al and Zr.

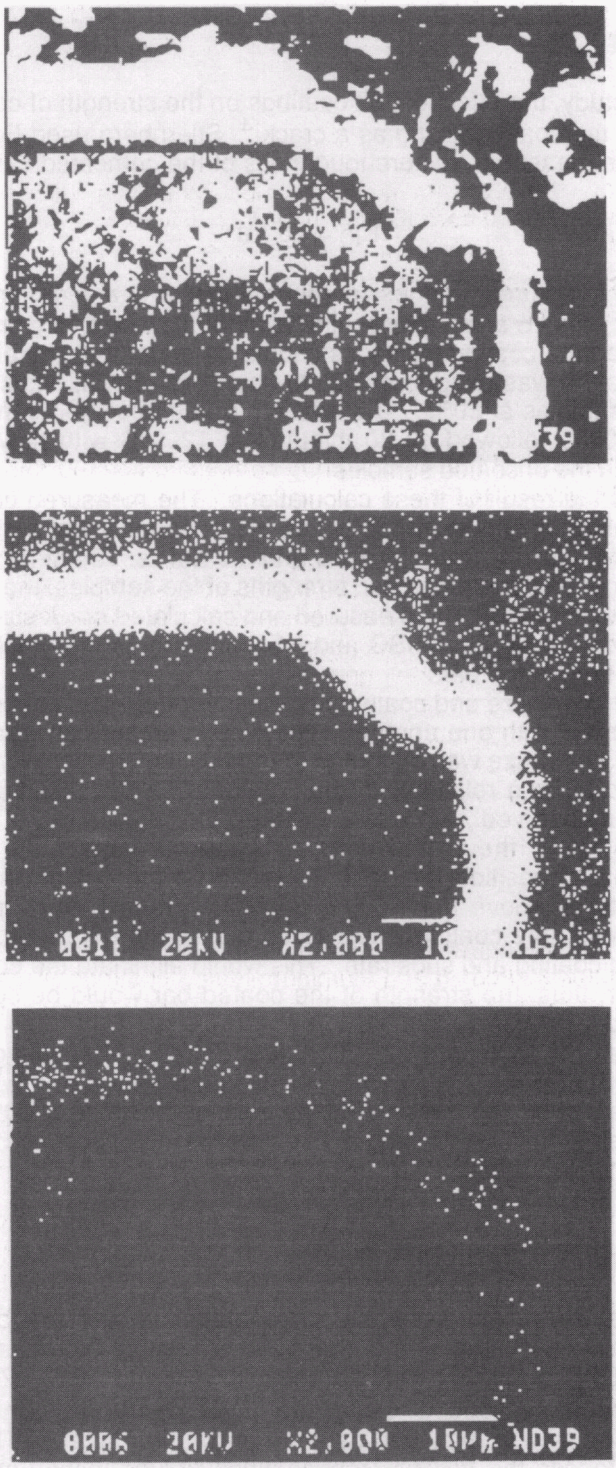

Figure 1. Cross-sections of a Al_2O_3+ZrO_2 coating on SSC. The top image is a backscattered electron image of the coating. The middle image is a Al Kα x-ray map and the bottom image is a Zr L x-ray map. The Al and Zr x-ray maps indicate that the Al and Zr form an intimate mixture.

Phase I MOR Tests

In a previous study, the effect of TiC coatings on the strength of cemented carbides was interpreted in terms of the coating acting as a crack.[4] Stjernberg used Equation 1 to relate the coating thickness to the measured fracture toughness of the cemented carbide:

$$K_{IC} = Y\sigma\sqrt{a} \qquad \text{Eq. 1}$$

where K_{IC} is the mode I fracture toughness of the material, Y is a geometry-dependent constant (Y=1.96 for rectangular bars), σ is the stress, and "a" is the flaw size. If a crack in the coating was regarded as a flaw, then the coating thickness should be equal to the predicted crack size from Equation 1. This equation was used to calculate flaw (e.g., crack) sizes for this study in both uncoated and coated samples at 20°C. The strength of the uncoated samples subjected to the vacuum anneal at 1200°C followed by 20 minutes at 1200°C with flowing HCl was used to calculate the flaw size in the uncoated samples.

Table 1 shows the result of these calculations. The measured coating thicknesses on the SSC and HSN substrates shown in Table 2 agree reasonably well with the calculated crack sizes listed in Table 1 (4.6 μm vs. 7 μm for SSC and 6.5 μm vs. 13 μm for HSN). Unfortunately, due to the amount of scatter in the measured strengths of the samples, the error in the crack size is correspondingly large. However, the measured and calculated crack sizes are the same order of magnitude. This indicates that for SSC and HSN substrates the cracked coating serves to reduce the strength of the coated bars.

The calculated crack size and coating thickness for the RBSN substrate (9.7 μm vs. 146 μm) are in poor agreement with one another. The disagreement between the measured crack size and the calculated crack size was attributed to the coating cracks linking surface flaws in the RBSN, which is known to be a relatively porous material. However, direct evidence of crack linking has not yet been observed.

For SSC and HSN, the calculations in Table 1 explain the observation that at temperatures above the deposition temperature (1000°C) the coating has little effect on the strength. At temperatures above the coating deposition temperature, the coating will be in compression and cracks in the coating would close due to the different coefficients of thermal expansion between the coating and substrate. This would eliminate the cracks as being a weak point in the coated bar; thus, the strength of the coated bar would be controlled by substrate flaws as in the uncoated MOR case.

The magnitude of the strength reduction due to the coating was greater for RBSN and HSN (50%) than for SSC (30%). This can be explained in terms of the coefficient of thermal expansion. SSC has a coefficient of thermal expansion approximately 50% greater than RBSN and HSN. This indicates that the magnitude of the stresses in the coatings play an important role in the observed strength degradation.

Contact Stress/Friction Coefficient Tests

Room-temperature pin-on-disk tests on coated samples are completed. The test procedure being used was described in the April 1990 Bimonthly Progress Report. Sets of pins and disks of RBSN, SSC, and HPSN were coated with AlN and Al_2O_3+ZrO_2 coatings. These coatings were deposited at 1000°C using the CVD operating conditions implemented throughout Phase I. The friction results to date are shown in Table 3. The preliminary results show that in some instances the Al_2O_3+ZrO_2 coatings reduce friction and possibly wear. A significant reduction in kinetic friction value is obtained in the case of HPSN and RBSN, while no apparent benefit is observed with SSC.

Table 1. Crack Size in Uncoated and Coated Ceramics. Calculated from Equation 1. Errors in crack size were calculated based on the error in the measured strengths.

Material	crack size in uncoated material, a_{uc} (μm)	crack size in coated material, a_c (μm)	crack due to coating (a_c - a_{uc}) (μm)
RBSN	48 ± 15	194 ± 70	146 ± 85
SSC	8 ± 2	15 ± 7	7 ± 9
HSN	5 ± 1	17 ± 6	12 ± 7

Table 2. Thickness of Al_2O_3+ZrO_2/AlN Coatings Measured from Fractured Samples

Material	Total coating thickness (μm)
RBSN	9.7 ± 5.0
SSC	4.6 ± 2.9
HSN	6.5 ± 2.4

Table 3. Results from Pin-on-Disk Friction Tests of Uncoated and Coated RBSN, HPSN, and SSC. All tests were done on self-mated samples. Reported values, unless otherwise indicated, are an average of three tests on the same pair of samples.

Material	Test Temperature (°C)	Breakaway Friction Coefficient	Kinetic Friction Coefficient	
			initial	after 500 m
RBSN				
uncoated	25	0.1	0.5	0.8
coated	25	0.17	0.3	0.4
HPSN				
uncoated	25	0.3	---	0.8
uncoated	1000	0.15	0.5	0.9*
coated	25	0.14	0.3	0.4
SSC				
uncoated	25	0.1	---	0.3
uncoated	1000	0.2	0.5	0.7
coated	25	0.17	0.3	0.4

* only 1 sample has been tested at this condition to date.

Wear Test Results

Microscopic inspection of specimens from room-temperature sliding wear tests was completed and results are shown in Figures 2 and 3. Figure 2 contains the worn pin and disk surfaces of uncoated ceramic after 500 meters of sliding contact. The spherical tip of the pins develop a circular wear scar, the extent of which is a measure of wear resistance. Coating the pin and disk materials leads to a noticeable improvement in wear resistance for hot-pressed silicon nitride as seen by reduced wear scar on the pin and the polished wear track surface of the disk. The reaction-bonded silicon nitride and sintered silicon carbide materials were not protected as effectively by the coating, which is in part attributed to the poor adhesion to these substrates. The experimental observations do agree with the previously reported results (see June 10, 1991 Bimonthly Report) insofar as a reduction in kinetic friction was measured with coated HPSN and RBSN. Furthermore, this reduction in kinetic friction was maintained up to 500 meters of sliding contact.

Scratch Tests Results

In a scratch test a diamond indenter (Rockwell C) is drawn over a sample at a constant velocity, while the normal force is monotonically increased (0 to 100 N). An acoustic pick-up is attached to the sample holder, and both the force and acoustic signals are recorded during the test.

The uncoated and AlN/Al_2O_3+ZrO_2 disks of HSN, RBSN, and SSC from the pin-on-disk wear tests were scratch tested. Figures 4 and 5 show the load, acoustic emission, and wear traces for 2 samples (remaining samples are reported in the August bimonthly). Several points can be made from these tests. The force traces of the uncoated and coated samples were similar with the exception of uncoated SSC, which showed several large load drops. In general, the acoustic emission of the coated samples was less than the acoustic emission of the uncoated samples. Acoustic emission is regarded as an indicator of substrate cracking. The scratches themselves are very informative and vary from sample to sample. The individual samples are discussed below.

Cracking of the uncoated SSC disk began at ~40 N. As the force increased, the cracking became massive failure of the SSC disk. The coated SSC disk had a lower acoustic signal than the uncoated SSC disk, indicating that the coating protected the SSC substrate from damage. The scratches on the uncoated and coated SSC are very different. The uncoated SSC showed massive cracking and chipping, while the coated SSC showed no chipping and less cracking. The major damage to the coated SSC was in the form of flaking of the coating in the scratch track beginning at ~30 N, indicating low adhesion of the coating to the SSC.

Vent cracks began to form in the uncoated RBSN disk at ~30 N. As the force increased, the size of the vent cracks increased; however, the RBSN did not chip. The coated RBSN disk had a lower acoustic signal than the uncoated RBSN disk, indicating that the coating protected the RBSN substrate from damage. The scratches on the uncoated and coated RBSN were similar. The major damage to the coated RBSN was in the form of flaking of the coating in the scratch track beginning at very high forces, ~90 N, indicating high adhesion of the coating to the RBSN.

Uncoated HSN behaved differently than the SSC and RBSN (Figure 4). HSN did not exhibit massive chipping (like SSC) or vent crack formation (like RBSN). The uncoated HSN failed at a high force, ~90 N, by small scale chipping at the edge of the scratch track. The coated HSN (Figure 5) was similar to the coated RBSN. The coated began to flake at ~50 N. However, the flaking was not continuous at forces greater than 50 N. The discontinuous nature of the flaking may be related to processing defects in the coating.

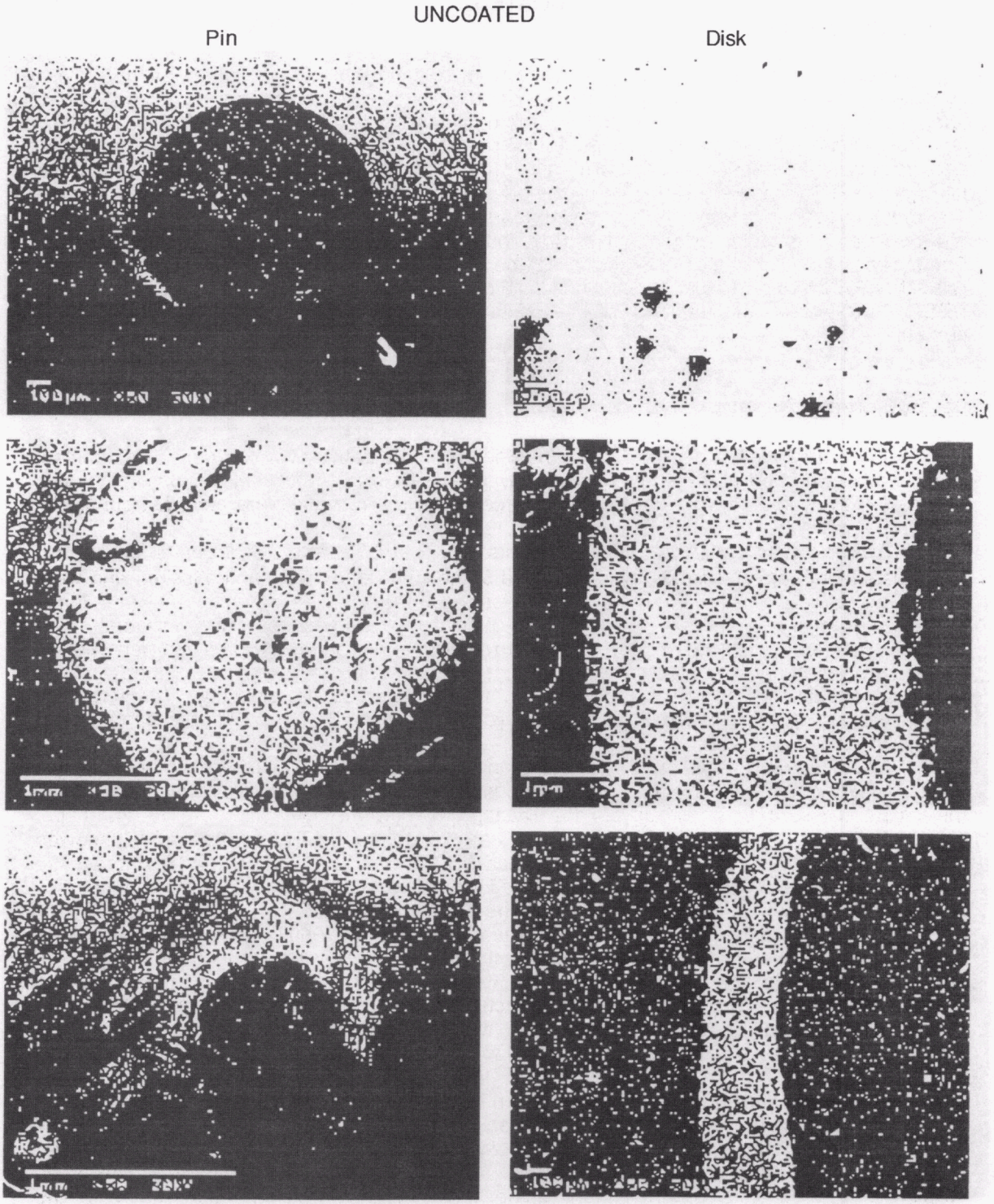

Figure 2. Wear tracks on the pins and disks for uncoated hot-pressed Si_3N_4 (top), reaction-bonded Si_3N_4 (middle), and sintered SiC (bottom), after a sliding distance of 500 meters at a sliding velocity of 0.01 m/s.

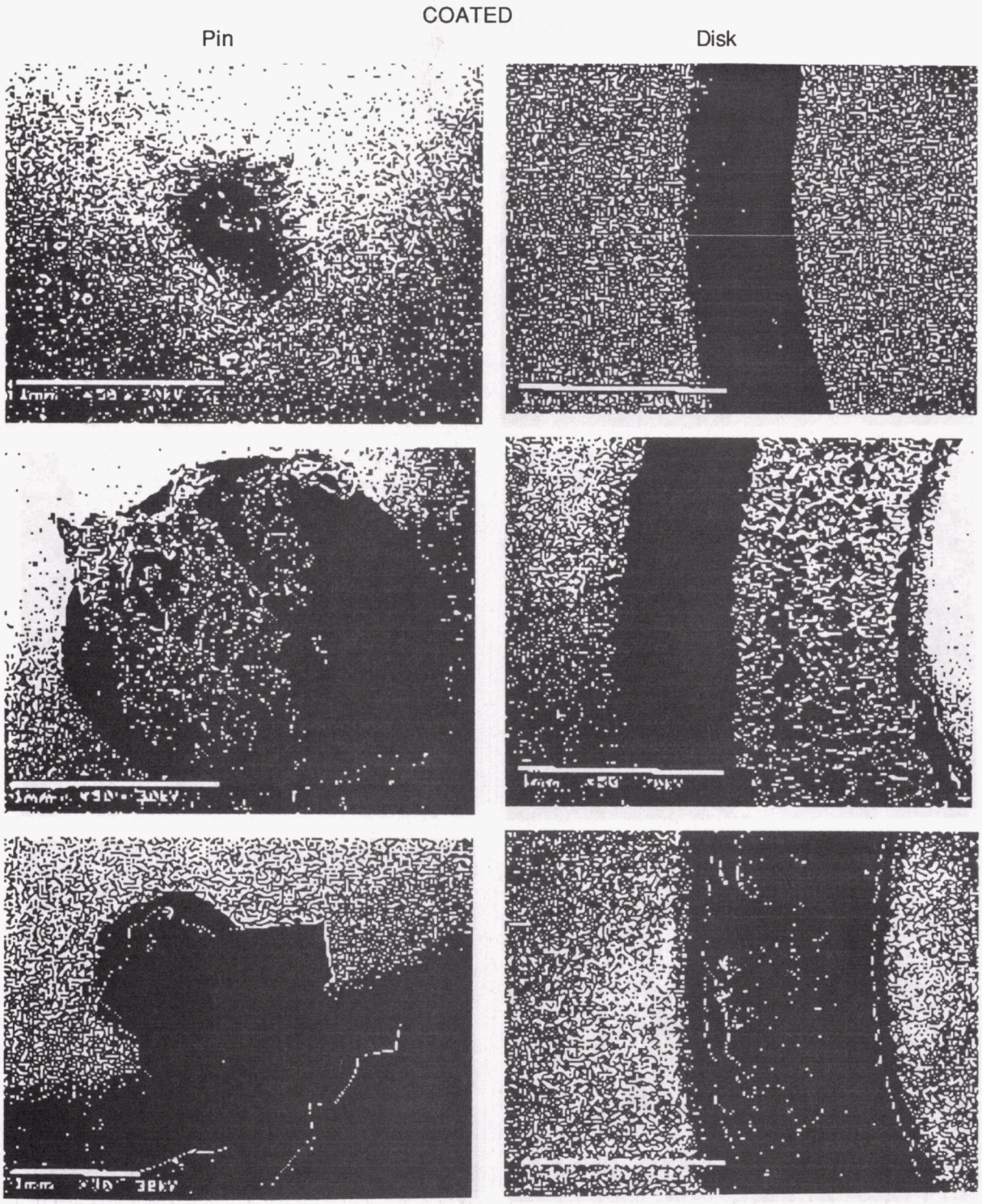

Figure 3. Wear tracks on the AlN/Al_2O_3+ZrO_2-coated pins and disks for hot-pressed Si_3N_4 (top), reaction-bonded Si_3N_4 (middle), and sintered SiC (bottom), after a sliding distance of 500 meters at a sliding velocity of 0.01 m/s.

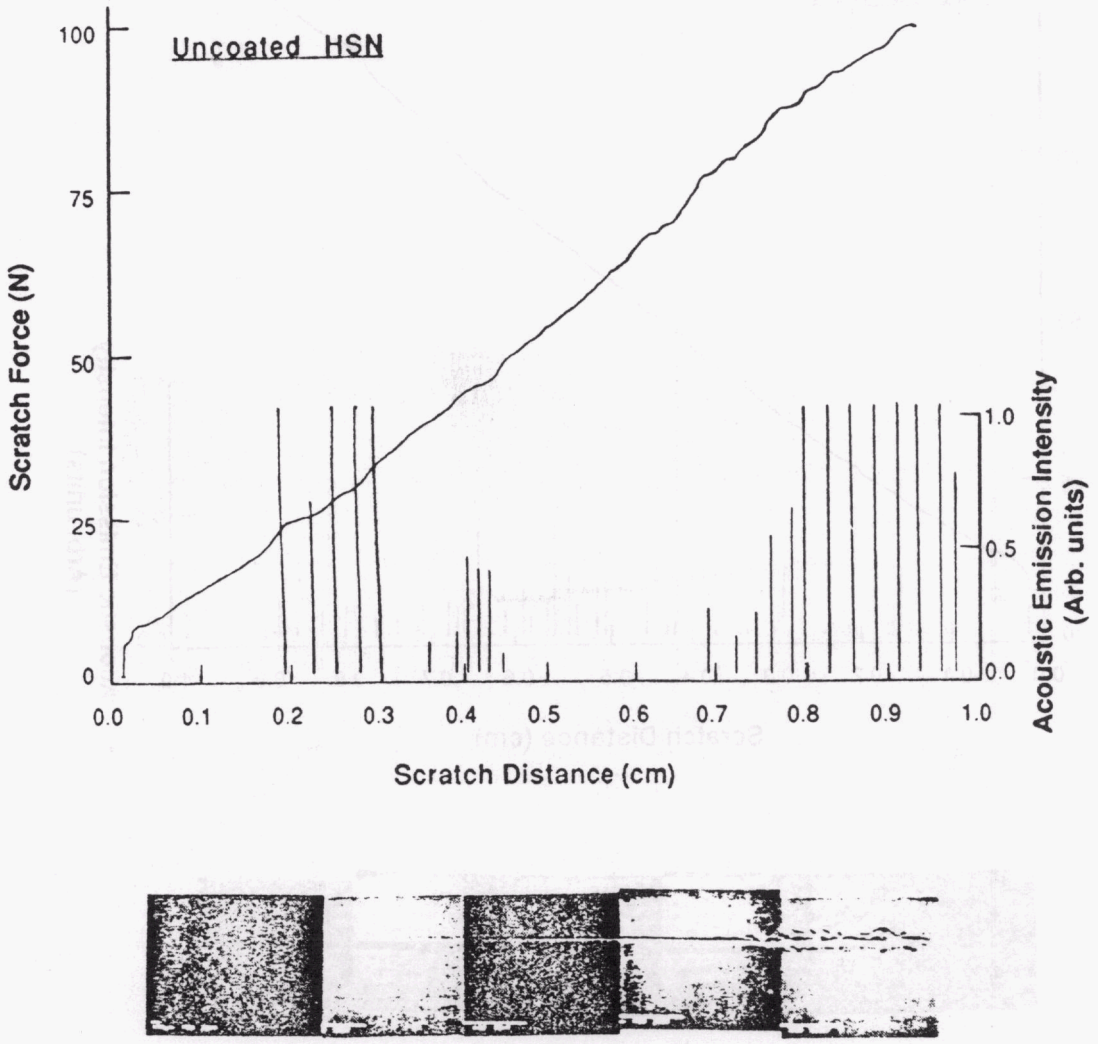

Figure 4. Scratch test results of uncoated HSN. The load trace is the solid line (left axis) and the acoustic signal is represented by the spikes (right axis).

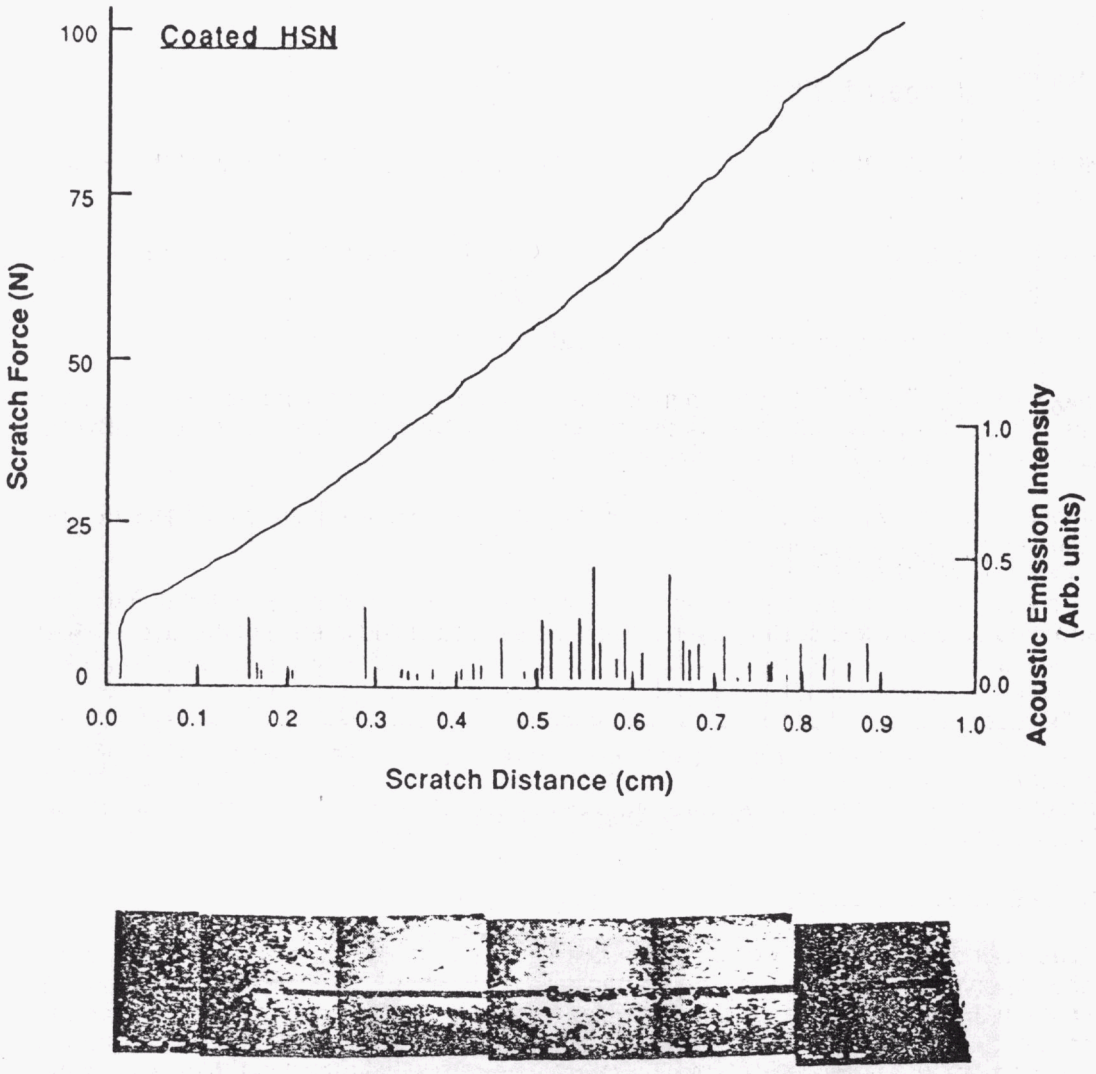

Figure 5. Scratch test results of coated HSN. The load trace is the solid line (left axis) and the acoustic signal is represented by the spikes (right axis).

Computer Simulation of Residual Stress

Summary of Analyses

Based on these studies, our conclusions for brittle ceramic coatings on the above substrates are

- Verifying that coating thickness has *negligible* effect on residual stress in any of the coating layers.
- The *order* (i.e., grading the thermal expansion mismatch in a multilayer-coated system) has *negligible* effect on residual stress in any of the coating layers.
- Modulus of elasticity has almost no effect on residual stress in any of the coating layers.
- Because each of the coatings are thin films relative to the size of the substrate thickness, the strain in the coatings is the same as the strain at the top fiber of the substrate, that zone which has an interface with the first coating layer.
- If material properties vary as a function of temperature, magnitudes of stress will be different, but the above conclusions still hold.

It should be noted that these conclusions apply to brittle thin films, and that simulations were performed on uncracked coating layers. The stresses calculated in each of the layers would be those which induce cracking in any of the layers, and as such are indicators of the tendency for cracking during cooling from the CVD process.

The effect of crack propagation during solid body contact of these elastic layers is not known, so thickness and layer ordering may have an effect in that case. The possibilities for working around the problem inherent to brittle coatings could lie either in the area of controlled brittle fracture using multilayer coating, or by the use of "ductile" layers which would permit stress relief of the ceramic layers when they are bonded to other brittle layers.

Method: Composite Plate Theory

The method follows the flow chart illustrated in Figure 6. Nomenclature is given at the end of the report. The geometry of the coated system is shown in Figure 7, and Figure 8 illustrates the numbering scheme for a multi-coated substrate. In Figure 8, layer 1 could be the substrate, and 5 coating layers could be represented by layers 2 through 6. The method is flexible for describing any number of coating layers. Note that h is the total thickness of the substrate and all the coatings.

Firstly, individual layer stiffnesses are calculated by

$$Q_{11}^k = \frac{E_1^k}{1 - v_{12}^k v_{21}^k} \qquad Q_{12}^k = Q_{21}^k = \frac{v_{21}^k E_1^k}{1 - v_{12}^k v_{21}^k}$$

$$Q_{22}^k = \frac{E_2^k}{1 - v_{12}^k v_{21}^k} \qquad Q_{66}^k = G_{12}^k$$

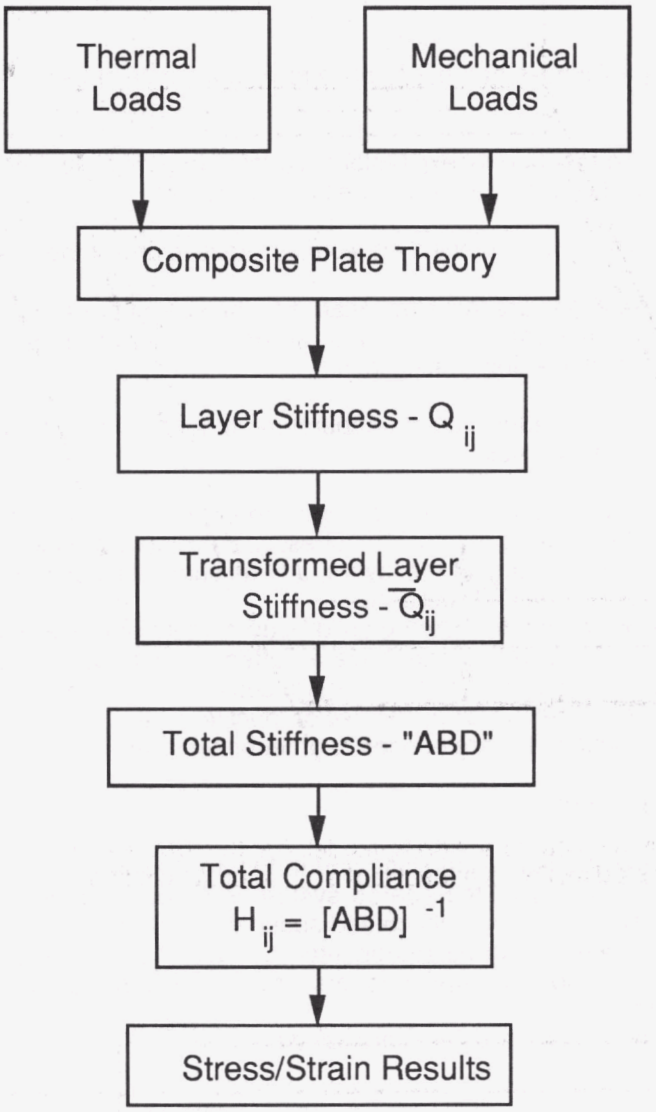

Figure 6. Flow chart for computer code implementation of composite plate theory. Layer properties were used to get transformed stiffnesses for each layer, and these were cumulated into a total stiffness matrix for the entire coated system. Unknown mid-plane strains were then solved for, and stresses in each of the layers recovered.

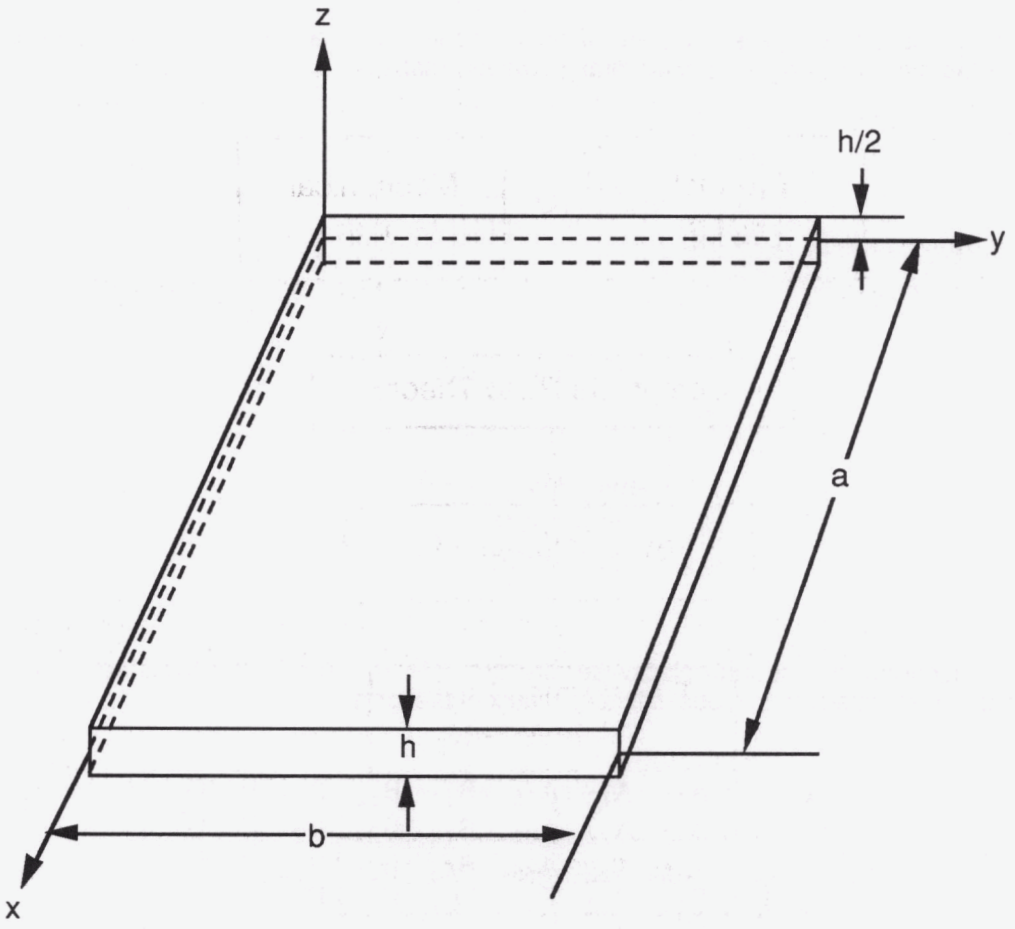

Figure 7. Schematic of the coated substrate model. *h* is the total thickness, and the mid-plane is at *h*/2. The *z* direction is normal to the plane of the coatings.

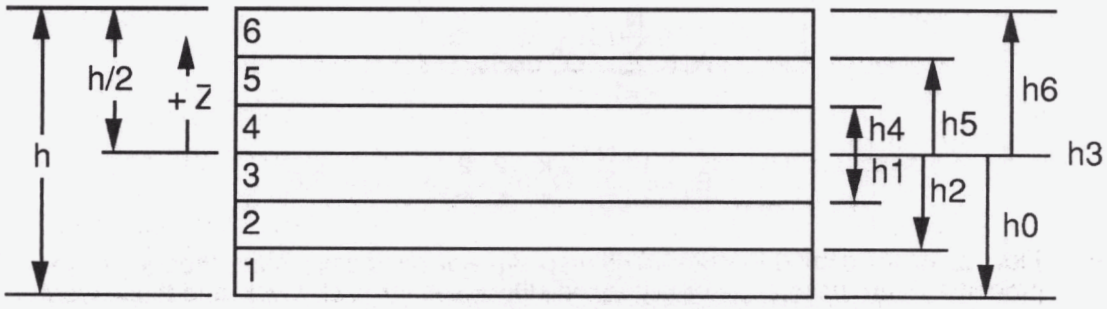

Figure 8. Numbering scheme for a multicoated system. *h* is the total coating thickness, and all interface positions are measured relative to the mid-plane at *h*/2, where the $z = 0$ plane. Note that layers below this plane have negative interlayer position values.

If the layer is anisotropic, the stiffnesses of each of the layers are rotated to the principal directions of the plate by using the tensor rotation transformation

$$\begin{bmatrix} \sigma_x \\ \sigma_y \\ \tau_{xy} \end{bmatrix}_k = [T]^{-1} [Q]_k [T] \begin{bmatrix} \varepsilon_x \\ \varepsilon_y \\ \frac{1}{2}\gamma_{xy} \end{bmatrix}_k$$

$$[T] = \begin{bmatrix} m^2 & n^2 & 2mn \\ n^2 & m^2 & -2mn \\ -mn & mn & m^2-n^2 \end{bmatrix}$$

$$m = \cos\theta$$

$$n = \sin\theta$$

where θ is described in a counter-clockwise direction. Next, each of the transformed layer stiffnesses are assembled into a global stiffness matrix of the form:

$$\begin{bmatrix} N_x \\ N_y \\ N_{xy} \\ M_x \\ M_y \\ M_{xy} \end{bmatrix} = \begin{bmatrix} A_{11} & A_{12} & A_{16} & B_{11} & B_{12} & B_{16} \\ A_{12} & A_{22} & A_{26} & B_{12} & B_{22} & B_{26} \\ A_{16} & A_{26} & A_{66} & B_{16} & B_{26} & B_{66} \\ B_{11} & B_{12} & B_{16} & D_{11} & D_{12} & D_{16} \\ B_{12} & B_{22} & B_{26} & D_{21} & D_{22} & D_{26} \\ B_{16} & B_{26} & B_{66} & D_{61} & D_{62} & D_{66} \end{bmatrix} \begin{bmatrix} \varepsilon_x^o \\ \varepsilon_y^o \\ \gamma_{xy}^o \\ \kappa_x \\ \kappa_y \\ \kappa_{xy} \end{bmatrix}$$

where

$$A_{ij} = \sum_{k=1}^{N} \bar{Q}_{ij}^k (h_k - h_k\text{-}1)$$

$$B_{ij} = \frac{1}{2} \sum_{k=1}^{N} \bar{Q}_{ij}^k (h_k^2 - {}^2_{k-1}) \quad (i,j=1,2,6)$$

$$D_{ij} = \frac{1}{3} \sum_{k=1}^{N} \bar{Q}_{ij}^k (h_k^3 - {}^3_{k-1})$$

The goal is to solve for the mid-plane strain and curvatures of the coated structure, due the applied loads, then to use the strain values to back-calculate for all the stress components

through the thickness of each of the materials in the structure. Thermal forces (due to cooling) are

$$N_x^t = \sum_{k-1}^{N} (\bar{Q}_{11}^k \alpha_x^k + \bar{Q}_{12}^k \alpha_y^k + \bar{Q}_{16}^k \alpha_{xy}^k)(h_k - h_{k-1})\Delta T^k$$

$$N_y^t = \sum_{k-1}^{N} (\bar{Q}_{12}^k \alpha_x^k + \bar{Q}_{22}^k \alpha_y^k + \bar{Q}_{26}^k \alpha_{xy}^k)(h_k - h_{k-1})\Delta T^k$$

$$N_{xy}^t = \sum_{k-1}^{N} (\bar{Q}_{16}^k \alpha_x^k + \bar{Q}_{26}^k \alpha_y^k + \bar{Q}_{66}^k \alpha_{xy}^k)(h_k - h_{k-1})\Delta T^k$$

$$M_x^t = \frac{1}{2} \sum_{k-1}^{N} (\bar{Q}_{11}^k \alpha_x^k + \bar{Q}_{12}^k \alpha_y^k + \bar{Q}_{16}^k \alpha_{xy}^k)(h_k^2 - h_{k-1}^2)\Delta T^k$$

$$M_y^t = \frac{1}{2} \sum_{k-1}^{N} (\bar{Q}_{12}^k \alpha_x^k + \bar{Q}_{22}^k \alpha_y^k + \bar{Q})_{26}^k \alpha_{xy}^k)(h_k^2 - h_{k-1}^2)\Delta T^k$$

$$M_{xy}^t = \frac{1}{2} \sum_{k-1}^{N} (\bar{Q}_{16}^k \alpha_x^k + \bar{Q}_{26}^k \alpha_y^k + \bar{Q})_{66}^k \alpha_{xy}^k)(h_k^2 - h_{k-1}^2)\Delta T^k$$

and the total load on the structure is the sum of any mechanical loads and moments (here zero) with these thermal loads. The global stiffness matrix is then inverted to get

$$\begin{bmatrix} \varepsilon_x^o \\ \varepsilon_y^o \\ \gamma_{xy} \\ \kappa_x \\ \kappa_y \\ \kappa_{xy} \end{bmatrix} = \begin{bmatrix} H_{11} & H_{12} & H_{13} & H_{14} & H_{15} & H_{16} \\ H_{12} & H_{22} & H_{23} & H_{24} & H_{25} & H_{26} \\ H_{13} & H_{23} & H_{33} & H_{34} & H_{35} & H_{36} \\ H_{14} & H_{24} & H_{34} & H_{44} & H_{45} & H_{46} \\ H_{15} & H_{25} & H_{35} & H_{45} & H_{55} & H_{66} \\ H_{16} & H_{26} & H_{36} & H_{46} & H_{56} & H_{66} \end{bmatrix} \begin{bmatrix} N_x \\ N_y \\ N_{xy} \\ M_x \\ M_y \\ M_{xy} \end{bmatrix}$$

and the mid-plane strain and curvature can then be solved for by any matrix solution method. Mid-plane strain and curvatures are used to find the strains through the entire thickness of the coated substrate:

$$\varepsilon_x = \varepsilon_x^o + z\kappa_x$$

$$\varepsilon_y = \varepsilon_y^o + z\kappa_y$$

$$\gamma_{xy} = \gamma_{xy}^o + z\kappa_{xy}.$$

Now that strains have been resolved, stress can be found by

$$\sigma_x^k = \bar{Q}_{11}^k (\varepsilon_x^k - \alpha_x^k \Delta T^k) + \bar{Q}_{12}^k (\varepsilon_y^k - \alpha_y^k \Delta T^k) + \bar{Q}_{16}^k (\gamma_{xy}^k - \alpha_{xy}^k \Delta T^k)$$

$$\sigma_y^k = \bar{Q}_{21}^k (\varepsilon_x^k - \alpha_x^k \Delta T^k) + \bar{Q}_{22}^k (\varepsilon_y^k - \alpha_y^k \Delta T^k) + \bar{Q}_{26}^k (\gamma_{xy}^k - \alpha_{xy}^k \Delta T^k)$$

$$\tau_{xy}^k = \bar{Q}_{61}^k (\varepsilon_x^k - \alpha_x^k \Delta T^k) + \bar{Q}_{62}^k (\varepsilon_y^k - \alpha_y^k \Delta T^k) + \bar{Q}_{66}^k (\gamma_{xy}^k - \alpha_{xy}^k \Delta T^k).$$

Each of the ε_{ij}^k terms vary through the thickness a very small amount relative to the $\alpha\Delta T$ strain terms, thus leading to the sharp discontinuities in the in-plane stress terms when traversing material interfaces.

This theory has been implemented in a FORTRAN computer code, which also includes material properties of the specific material systems used here.

Results: Silicon Nitride and Silicon Carbide Substrates

Numerical experiments were performed to support the above conclusions. Table 4 shows the material properties used in all stress analyses. Each of the systems was cooled from 1000°C to find the residual stress in each of the materials present. The substrate was 6350 microns thick for all studies.

Comparison to Finite Element Results

To ensure that the composite plate theory code was working correctly, the stress results were compared to a finite element solution of a similar problem.[2] The finite element method used in Sham and Sarin[2] was specially formulated to exploit hybrid finite elements because of the relative size of the elements used for the coating and for the substrate.

Results for both substrate materials are shown in Table 5. Excellent comparison between the two methods is shown, thus confirming the applicability of composite plate theory to this problem.

Si_3N_4 Substrate

Three numerical experiments were performed with the silicon nitride substrate. Firstly, residual stress with no interlayer but with varying thickness of the alumina-zirconia coating was calculated. Next an AlN interlayer *between* the alumina-zirconia and Si_3N_4 substrate was varied in thickness and residual stresses found for each material. Lastly, the AlN coating was placed *above* the Si_3N_4 coating to illustrate the irrelevance of thermal expansion grading. All 3 coating configurations resulted in the same coating stresses. One set of results are shown in Figure 9. The results indicate that the presence or absence of an interlayer, thickness of the coating layers, and order of the coatings on the substrate have negligible effect on residual stress in each of the layers.

Table 4. Material Properties Used for All Aubstrate and Coating Layers

Material	Young's Modulus (GPa)	Poisson's Ratio	Thermal Expansion Coeff. (/°C)
Al_2O_3	390	0.22	7.8×10^{-6}
AlN	340	0.24	4.9×10^{-6}
Interface	320	0.255	3.8×10^{-6}
Si_3N_4	296.5	0.27	2.7×10^{-6}
SiC	207	0.22	4.3×10^{-6}

Table 5. Comparison of 2-Dimensional Finite Element Results Using Special Hybrid Elements to the Composite Plate Theory Described Here. Stress values are from reference 2; values in parentheses are results from the composite plate code described here. For both tables, $\Delta T = -1000°C$.

Layer	Young's Modulus (GPa)	Poisson's Ratio	Thermal Expansion Coeff. (/°C)	Residual Stress (MPa) [Layer Thickness, μm]	
				(a)	(b)
Al_2O_3	390	0.22	7.8×10^{-6}	2475 (2527) [10]	2482 (2534) [4]
AlN	340	0.24	4.9×10^{-6}	938 (964) [3]	943 (970) [9]
Interface	320	0.255	3.8×10^{-6}	442 (453) [1]	448 (459) [1]
Si_3N_4 (substrate)	296.5	0.27	2.7×10^{-6}	-16 (-17)	-11 (-12)

Layer	Young's Modulus (GPa)	Poisson's Ratio	Thermal Expansion Coeff. (/°C)	Residual Stress (MPa) [Layer Thickness, μm]	
				(a)	(b)
Al_2O_3	390	0.22	7.8×10^{-6}	1731 (1728) [10]	1740 (1738) [4]
AlN	340	0.24	4.9×10^{-6}	282 (249) [3]	290 (258) [9]
SiC (substrate)	207	0.22	4.3×10^{-6}	-11 (-11.5)	-6 (-6)

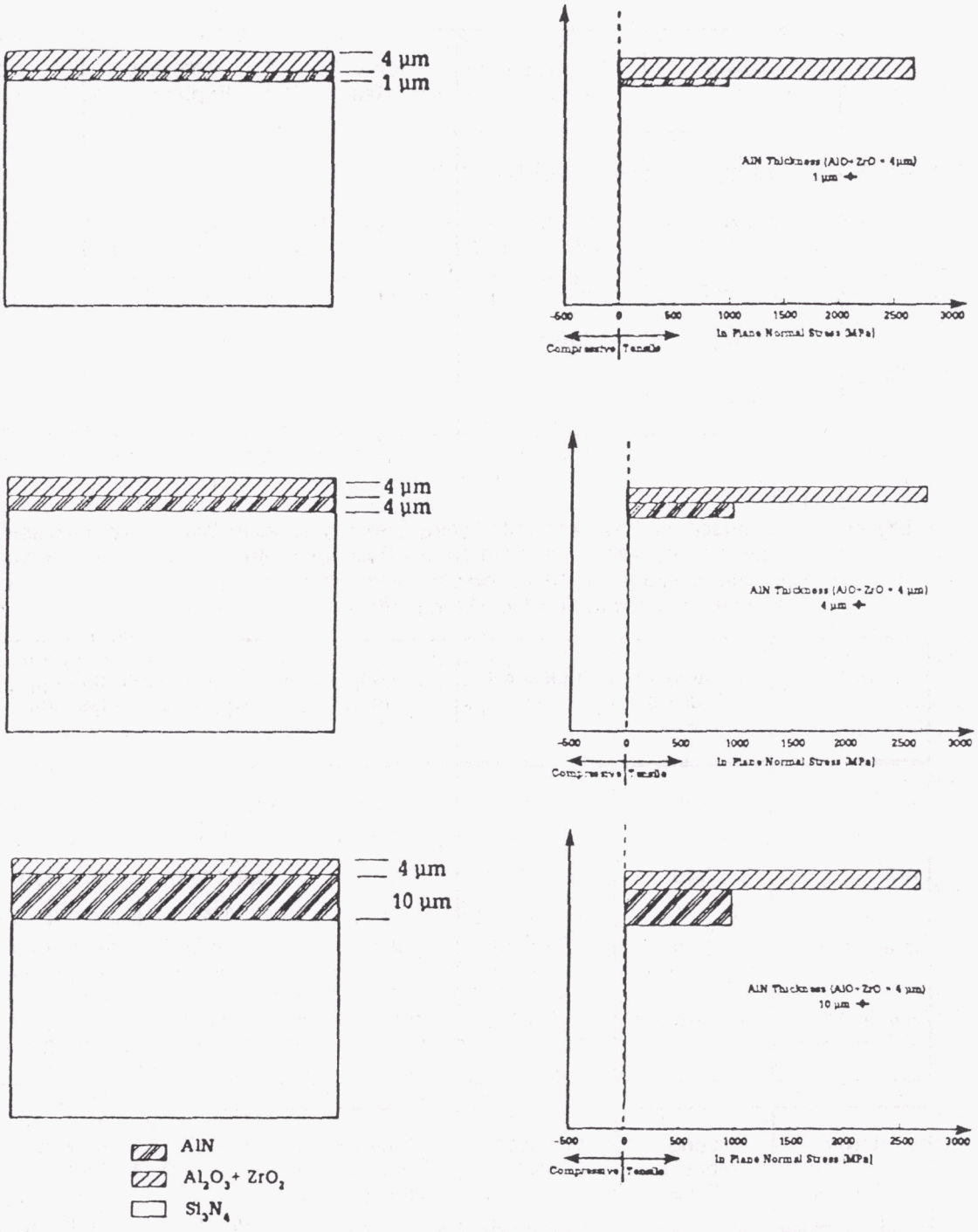

Figure 9. In-plane residual stresses for a silicon nitride substrate coated with alumina-zirconia with an AlN interlayer. Stresses for 1, 4 and 10 micron interlayer thicknesses are shown. Thickness of the interlayer has negligible effect on residual stress.

SiC Substrate

Since it has been shown that coating stresses are not sensitive to thickness or coating order variations, all pertinent stresses for the SiC substrate coating systems can be found with a single residual stress analysis. The stresses shown in Figure 10 are applicable for changes in any layer thickness or order sequence.

Computer Simulation of Crack Propagation

This part of the bimonthly describes modeling work performed on sections (ii) and (iii) of the new milestone added to this contract in June1991. Section (i) of this new milestone has been completed and was described in the August 1991 bimonthly for the contract. We describe here the model and results for numerical simulation of a single-pass scratch test, and crack propagation due to an initial flaw.

Discussion

Studies were performed on a single-layer coating of Al_2O_3-ZrO_2 on a substrate of silicon nitride. Subsequent studies will describe results for a multilayer coated substrate. Loads were imposed on the body in the form of residual thermal stress, and mechanical loads resulting from solid body contact with friction. The finite element model allows automatic changes in mesh topology due to crack growth, and a bimaterial fracture model which takes into account the different fracture toughnesses of the coating, interface, and substrate when the cracks are at or near the interface. Results indicate that, subject to these loads, a vertical flaw in the coating propagates approximately downward until the coating-substrate interface region. Once the crack has entered the interface, it moves away from the contact loads along the interface a distance of approximately half the coating thickness, after which it continues in a direction nearly normal to the net direction of the applied force load. Since the crack did not continue along the interface, improvements in the interface bond strength would not have influenced crack direction significantly.

Geometry

The finite element mesh was created to simulate the cross-section of a wide sample (plane-strain) of a coated substrate. Coating thickness was 2 microns; substrate thickness was arbitrary and assigned a value of 58 microns.

The plane of the mesh is shown in Figure 11. The width of the model was 60 microns. Between the elements describing the coating and the elements describing the substrate, a set of boundary markers exists which describe the location of the bimaterial fracture model. During remeshing, this boundary must lie on element boundaries to keep the interface coherent. The model initially was crack-free. A vertical flaw 0.5 microns long was positioned 1 micron from the mechanical load. As the crack propagated, the model was automatically remeshed to take into account the change in surface, the bimaterial interface, and the stress concentration at the crack tip. Eight noded quadratic elements were used for the original mesh, mesh changes were mapped with 6 noded triangular elements, and the crack tip was modeled with 6 noded singularity elements. When the crack tip was at or near the bimaterial interface, singularity elements were not used. For each crack increment, the next propagation direction was predicted by using a maximum energy release rate criterion, which is also applicable in the region of the interface. The energy release rate was calculated by comparing the energy released by the system for candidate directions in each of the materials the crack tip is near. Once a direction was found, the crack length was increased a small amount and the calculation repeated. This procedure was continued until no significant change in the direction of crack propagation was seen.

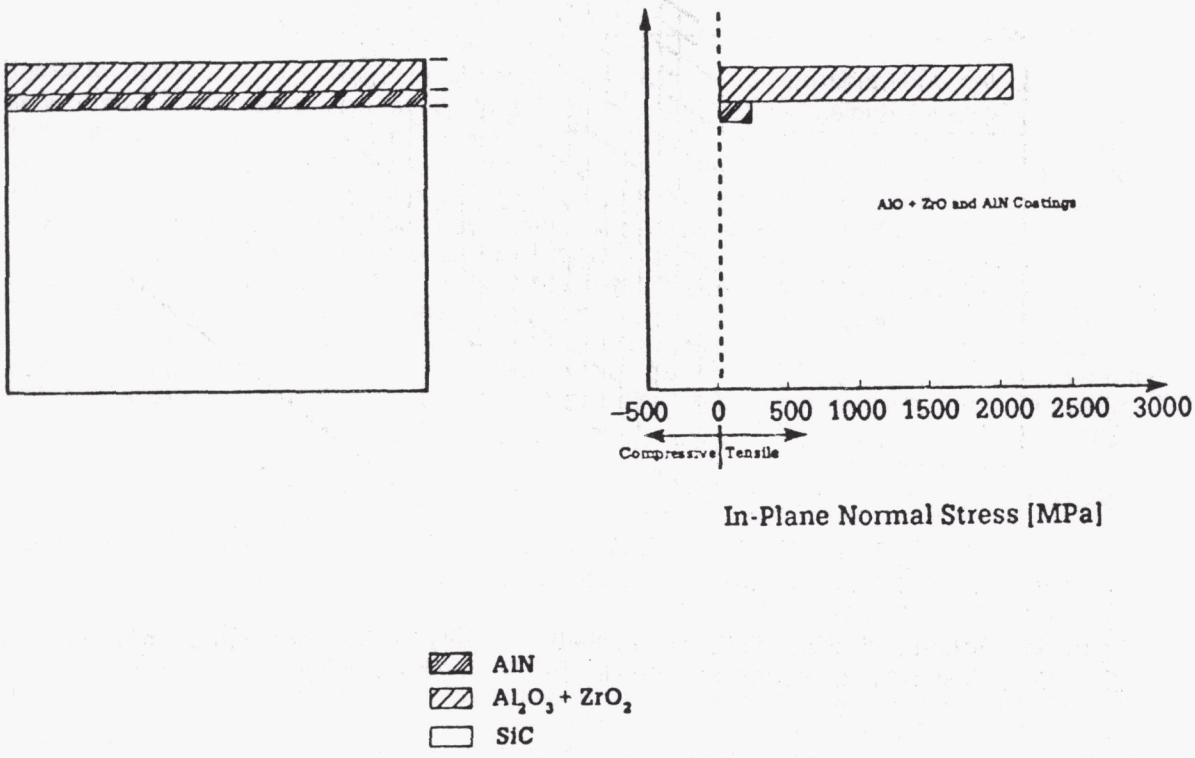

Figure 10. In-plane residual stresses for a silicon carbide substrate coated with AlN and alumina-zirconia. Stresses shown are applicable for a wide range of coating thicknesses.

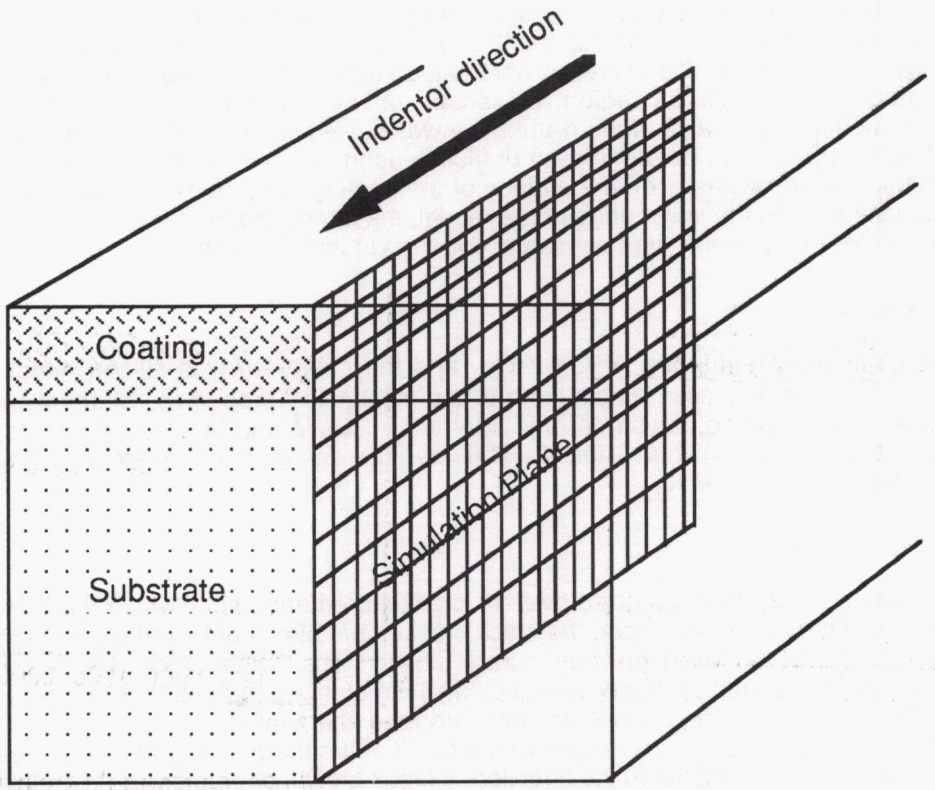

Figure 11. Schematic of the finite element mesh relative to microstructural cross section. Direction and positioning of scratch test indenter are shown.

Boundary Conditions

Thermal loads were applied to the entire body by including a temperature change of -1000°C into the analysis. This temperature is typical of temperatures used in the CVD process for this material system. It was assumed that the coating was applied to the substrate in the CVD chamber in a stress-free state and that stresses were generated in the CVD chamber by thermal expansion mismatch between the coating and the substrate. A mechanical load was also applied to the coating. The mechanical loads represent the load applied by solid body contact. The load was distributed over a 1-micron region; the shape of the distribution was parabolic. The magnitude of the maximum value of the distribution was scaled such that the stress results were normalized from zero to one. The coefficient of friction used was 0.5, resulting in the same form of the distribution of shear stress on the surface of the coating. Figure 12 is a schematic of the boundary conditions. On the lower edge of the model, the central node of the edge was pinned, and all other nodes on the edge were constrained in the vertical direction.

Material Properties

The coating material was Al_2O_3-ZrO_2, and the substrate was silicon nitride. Both materials were modeled as elastic in both thermal and mechanical properties. Material properties were assigned to the coating, substrate, and interface. Elastic and thermal properties for the coating and substrate are shown in Table 6. The interface energy release rate as a function of mode-mixity is shown in Figure 13.

Results

The crack propagation occurred over 14 crack increments, after which the direction of crack growth remained constant. Since the crack crossed the bimaterial interface, the bimaterial interface fracture model was used for several crack growth steps. Other crack growth steps used linear elastic fracture mechanics theory solved using finite element methods. An enlargement of the initial vertical flaw displaying the original and deformed shape of the coated system is shown in Figure 14. Note that the deformed shape was a result of the thermal, normal, and shear loads on the structure. Figure 15 illustrates the direction of crack growth prior to crossing the bimaterial interface. The crack has begun a slight turn away from the applied mechanical loading. Figure 16 shows the deformed shape for the final crack increment. Note that the crack did not remain in the interface, as it would for a material with a lower range of interface fracture toughnesses (lower G_{Ic} curve), and also that the final crack direction is approximately normal to the applied mechanical loading direction. The fracture modeling of coated systems is continuing with a two-layered coated substrate under the same thermal and mechanical loads.

Nomenclature

E_i - Young's Modulus
γ_{ij} - Poisson's Ratio
G_{ij} - Shear Modulus
Q_{ij} - Stiffness Component
T_{ij} - Rotation Transformation Component
ε_i^o - Mid-plane Strain
κ_i - Mid-plane Curvature
N_i - Applied Forces
M_i - Applied Moments

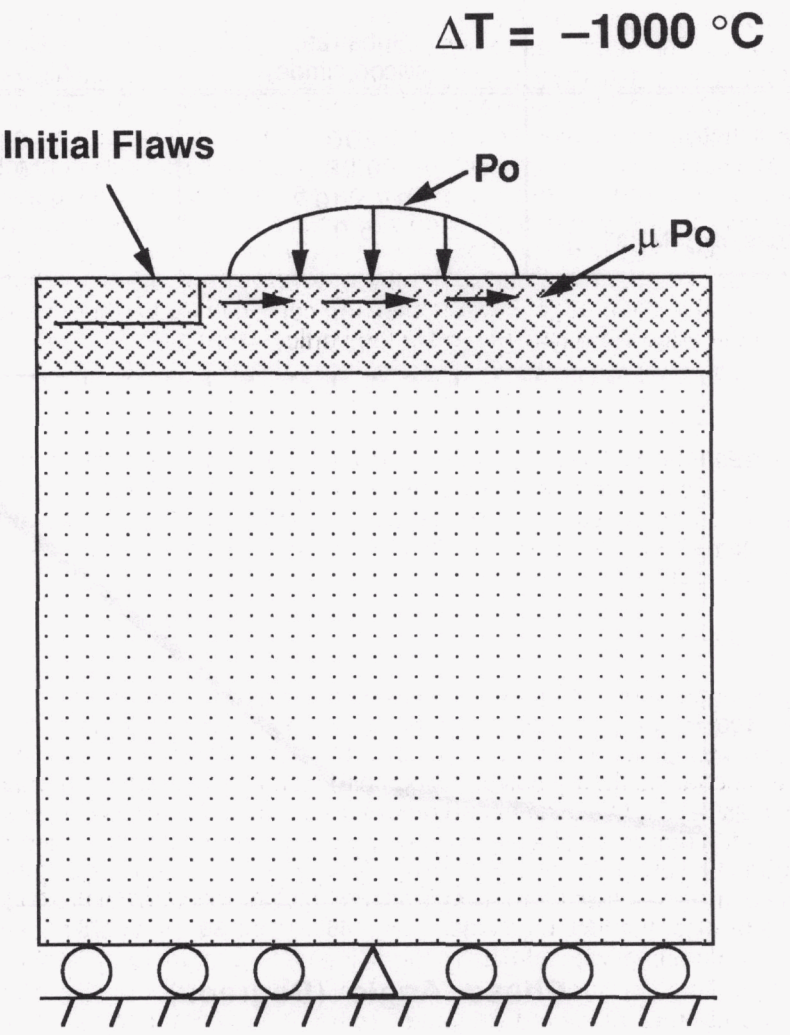

Figure 12. Schematic of the boundary conditions used in the fracture simulation. Coefficient of friction was 0.5. The value of `p' (the maximum magnitude of the load distribution) was assigned a value such that the stress results are normalized.

Table 6. Material Properties Used for the Coating and Substrate

Property	Material	
	Substrate (silicon nitride)	Coating (Al_2O_3+ZrO_2)
Young's Modulus, E (GPa)	300	380
Poisson's Ratio, ν	0.26	0.23
CTE, α (/°C)	2.7×10^{-6}	9.4×10^{-6}
Fracture Toughness, K_{IC} ($MPa\sqrt{m}$)	5.0	3.5

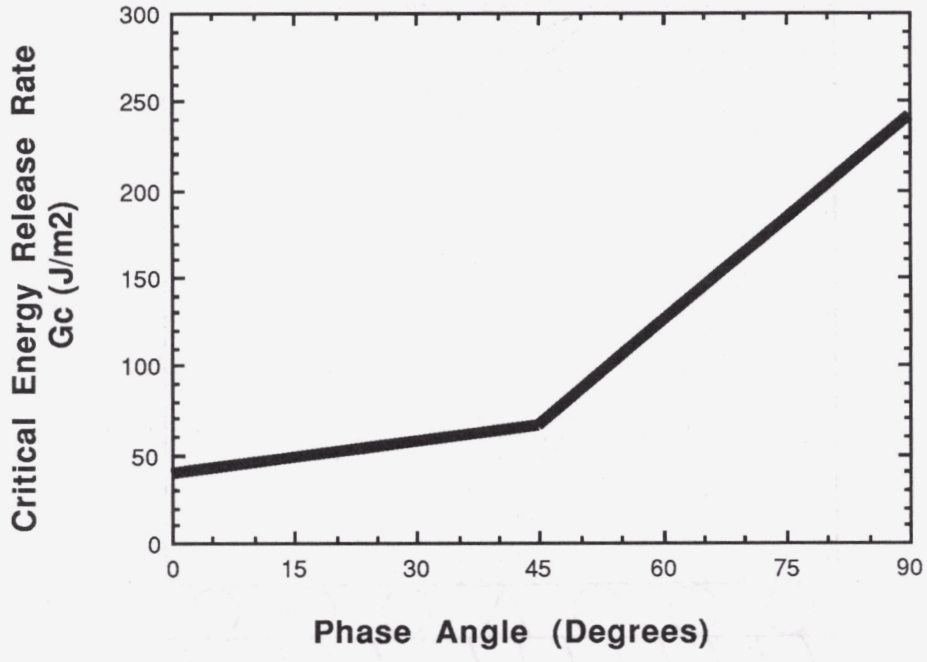

Figure 13. Energy release rate for the interface as a function of mode mixity. A mode-mixity of 0.0 describes pure mode I loading at the crack tip, and a mode-mixity of 90 (degrees) describes pure mode II loading at the crack tip.

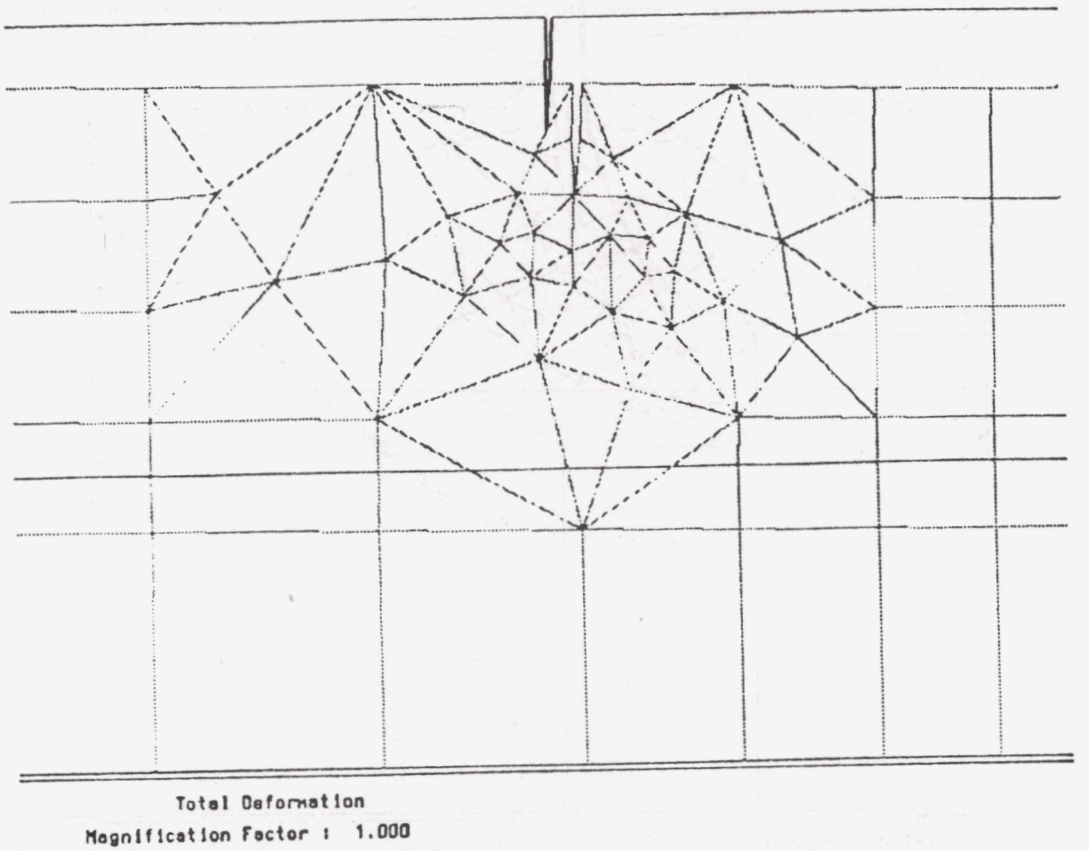

Figure 14. Initial vertical flaw, 0.5 microns long (1/4 coating thickness).

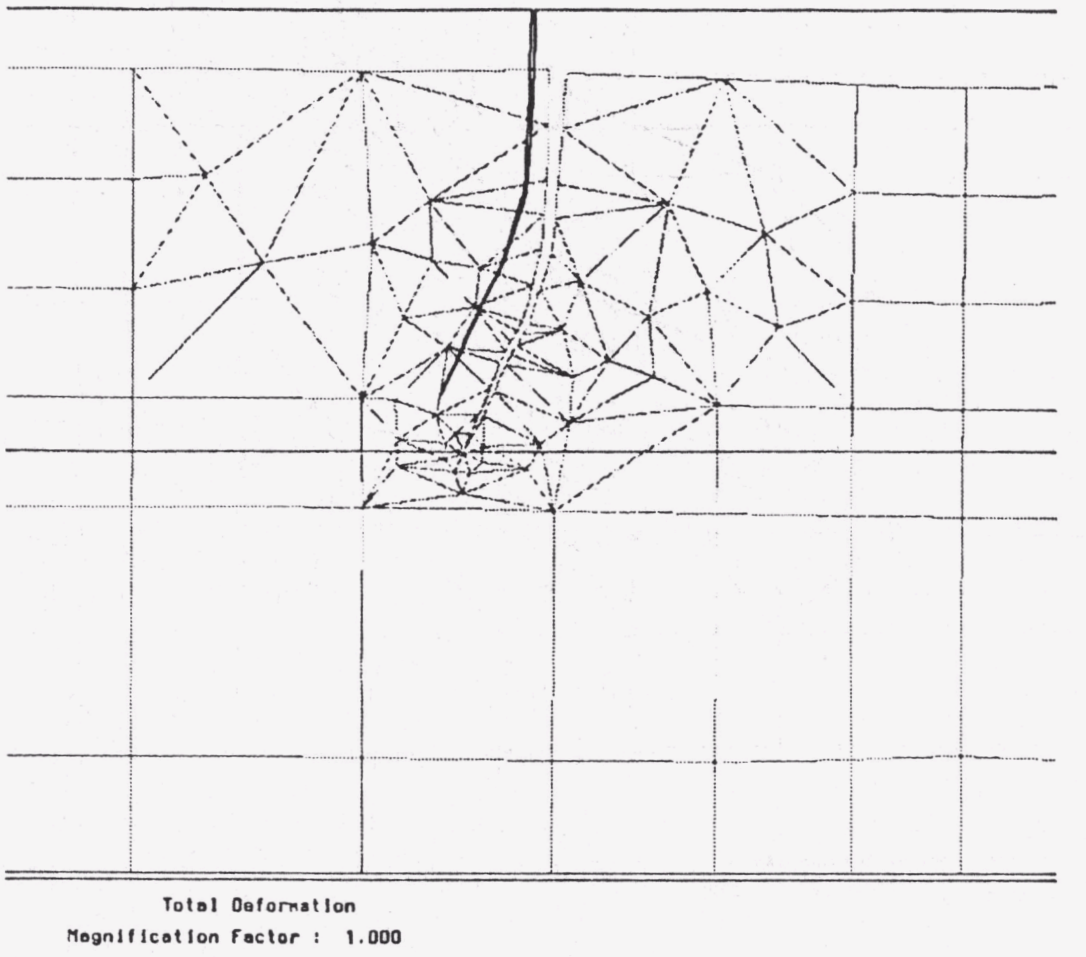

Figure 15. Deformed shape and crack growth direction prior to crossing the bimaterial interface.

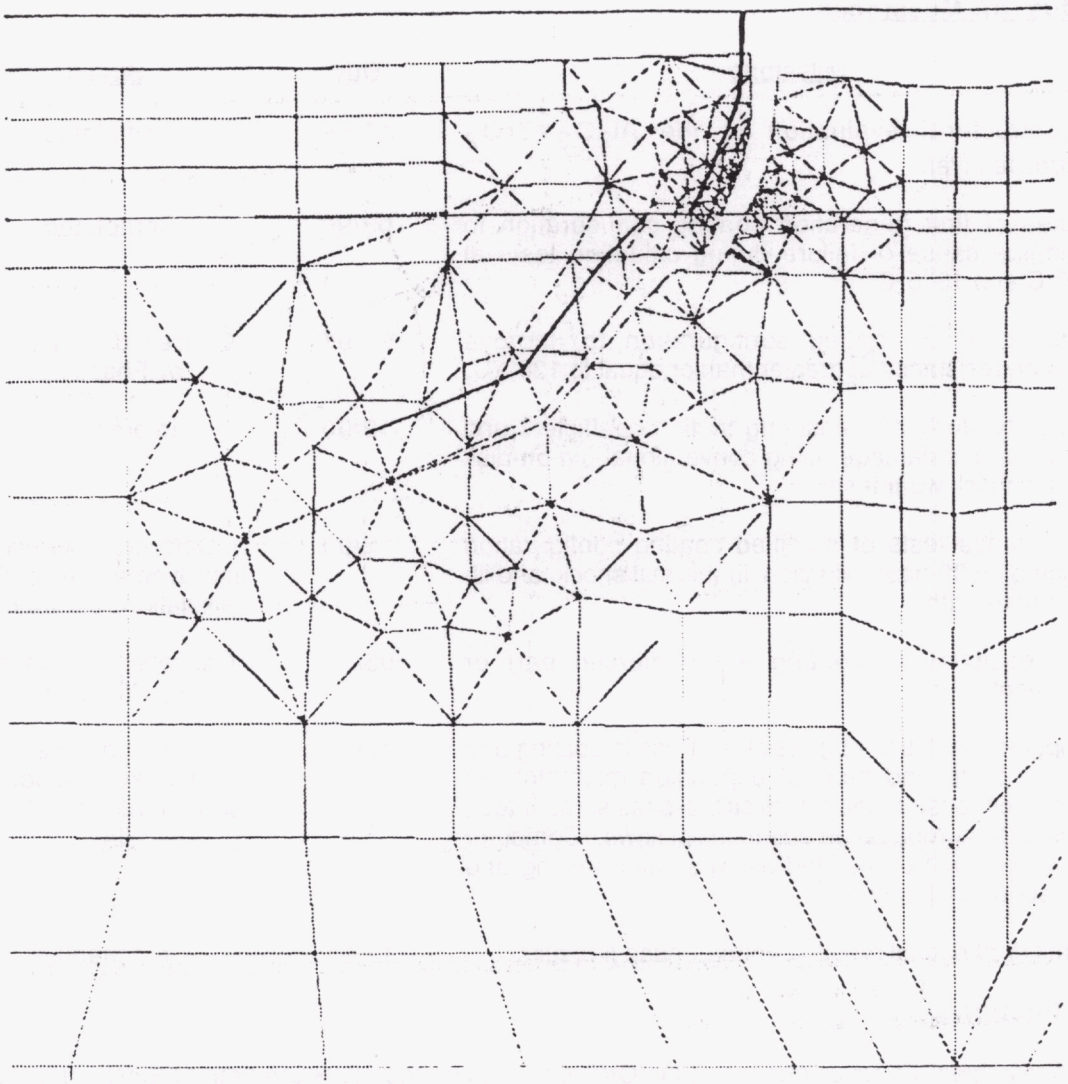

Figure 16. Deformed shape and crack path in final increment.

h - Total Thickness
h_i - Distance from Mid-plane to Interfaces
α_i - Coefficient of Thermal Expansion
ΔT - Temperature Change

Status of Milestones

Milestone	Due	Status
Microstructural evaluation of the Al_2O_3+ZrO_2 composite layer.	12/89	Completed.
Studies of first generation coating configuration to determine cause of failure during oxidation tests at 1200°C and 1375°C.	03/90	Completed.
Modification of coating configuration to improve oxidation resistance at greater than or equal to 1200°C.	06/91	Cancelled. Replaced by Phase IIA.
Feasibility study of measuring friction coefficient and contact stress damage using conventional pin-on-disk or ball-on-disk wear tests.	12/90	In progress.
Performance tests of modified coating configuration including i) 500-hour oxidation, ii) thermal shock, and iii) flexure strength.	12/90	Delayed. Awaiting improvement in coating oxidation resistance.
Test feasibility of coating a commercial part or equivalent.	03/91	Cancelled. Replaced by Phase IIA.
Computer simulation of i) residual stress in coating due to CVD cycle and thermal expansion mismatch, ii) coating response to load from single-pass scratch test, and iii) crack propagation due to initial flaws. Computer calculations will be verified using scratch testing and microscope inspection.	12/91	On schedule. (This new milestone corresponds to Phase IIA).
Submit draft of final report covering Phase II results.	12/91	On schedule.

Publications

1) A talk titled "Effect of Al_2O_3 + ZrO_2 CVD Coatings on the MOR Strength of Si_3N_4 and SiC," was presented by J. Selverian at the 1991 American Ceramic Society Conference.
2) Abstract submitted to the 1991 MRS conference, "Tensile Strength and Weibull Modulus Determination of CVD Ceramic Thin Films on Ceramic Substrates".

References

1. J.C. Halpin, *Primer on Composite Material: Analysis*, Technomic Publishing,1984.
2. T.L. Sham and V.K. Sarin, "Residual Stress Calculations in Coating Configurations Using Finite Element Analysis," *Ceramics Eng. & Sci. Proceedings*, 9 (9, 10), (1988).
3. S.W. Tsai and H.T. Hahn, *Introduction to Composite Materials*, Technomic Publishing, 1980.
4. K.G. Stjernberg, "Fracture Toughness of TiC-Coated Cemented Carbides," *Metal Science*, p. 189-192, (May 1980).

Wear-Resistant Coatings

M. H. Haselkorn (Caterpillar, Inc.)

Objective/scope

The goal of this technical program is to develop wear-resistant coatings for piston ring and cylinder liner components for low heat-loss diesel engines.

Wear resistant coatings will be applied to metallic substrates using plasma spraying, vapor deposition (CVD/PVD), and enameling coating processes. First, the adherence of each coating for each coating process to the metallic substrate will be optimized. Methods which can be used for improving the adherence of these coatings include development of unique substrate preparation methods before application of the coating, grading coating compositions to match thermal expansion; compositional changes; laser or electron beam fusing and/or optimizing coating thickness. Once the adherence of each coating system is optimized, each coating will be screened for friction and wear at 350°C under lubricated conditions. Coatings which show promise after this initial screening will be further optimized to meet the friction and wear requirements. Then, the optimized coating systems will be fully characterized for oxidation resistance, adherence, uniformity, and thermal shock resistance, as well as friction and wear.

Selection of the most promising coatings and coating processes will be made after the characterization task. Criteria for selection will include not only performance (i.e., wear, adhesion, friction coefficient, thermal shock resistance and thermal stability) but also manufacturability and economic factors, as well. Using both criteria a coating system having acceptable cost/benefit relationships will be selected.

Technical progress

Candidate wear resistant piston ring coatings identified from the pin-on-disk friction and wear screening included:

1. Plasma sprayed chromia-silica composite,
2. Plasma sprayed high carbon iron-molybdenum blend,
3. Plasma sprayed, self-lubricating, PS212, and,
4. Mid-temperature chemical vapor deposited Ti(C,N).

Candidate wear resistant cylinder liner coatings also identified from this friction and wear screening included:

1. Low temperature arc vapor deposited (LTAVD) chrome nitride,
2. Plasma sprayed chromia-silica composite, and,
3. Plasma sprayed high carbon iron-molybdenum blend.

Each candidate piston ring/cylinder liner pair was then further optimized for friction and wear using the Hohman A-6 Double Rub Shoe Friction and Wear Test Machine. All tests were run at 350 C, under lubricated conditions. The results of this testing are contained in Tables 1-3. (Note: one of the overall goals of this program is to obtain an average wear coefficient of at least 1.0x10-8 mm^3/N-m for each coating pair.)

Running plasma sprayed high carbon iron-molybdenum coated rub shoes against a plasma sprayed chromia-silica coated disk (Table 1) produced coefficient of friction values below 0.15 and average wear coefficients ranging from 2.3 to 0.4x10-8 mm^3/N-m for the shoes and from 2.43 to 14.2x10-8 mm^3/N-m for the disks. The Hohman test results obtained from this coating pair showed that this piston ring/cylinder liner coating pair would meet the program goals for both friction and wear.

Coefficient of friction values of above 0.2 were obtained running plasma sprayed PS212 rub shoes against a plasma sprayed chromia-silica disk. These high coefficient of friction values, in turn, caused high PS212 wear coefficients and, for this reason, this coating pair ran only 480 hours before the chromia-silica coating completely wore through the PS212. Table 1 lists average wear coefficients of 9.11x10-9 for the chromia-silica and 1.70x10-7 mm^3/N-m for the PS212 coatings.

Running plasma sprayed chromia-silica or mid-temperature chemical vapor deposited titanium carbo-nitride coated rub shoes against the plasma sprayed chromia-silica coated disks produced friction coefficients above 0.2 and average disk wear coefficients ranging from 10-5 to 10-6 mm^3/N-m, respectively. Very little wear was apparent on either set of rub shoes. The friction and average disk wear coefficients for these coating pairs were above the program goals.

Another coating pair which met the program's friction and wear goals is plasma sprayed high carbon iron-molybdenum rub shoes running against a low temperature arc vapor deposited (LTAVD) chrome nitride coated disk (Table 2). This coating pair had coefficient of friction values below 0.15 and, in three tests, had average wear coefficients which ranged from 1.23x10-9 to 7.16x10-8 mm^3/N-m for the high carbon iron-molybdenum coated shoes and from 3.13x10-7 to 1.48x10-8 mm^3/N-m for the chrome nitride coated disk.

Running plasma sprayed chromia-silica or mid-temperature chemical vapor deposited titanium carbo-nitride coated rub shoes against the plasma sprayed chromia-silica coated disks produced friction coefficients above 0.2 and average disk wear coefficients ranging from 10-5 to 10-6 mm^3/N-m, respectively. Very little wear was apparent on either set of rub shoes. The friction and average disk wear coefficients for these coating pairs were above the program goals.

Running either plasma sprayed chromia-silica or mid-temperature titanium carbo-nitride CVD rub shoes against the LTAVD chrome nitride coated disk resulted in coefficient of friction values above 0.20 and very high chrome nitride average wear coefficients (10-6 mm^3/N-m). For this reason, these tests had to be terminated after only 5-30 minutes of testing since none of the chrome nitride coating remained on the surface of the disk.

Average disk wear coefficients of 1.04x10-4 mm^3/N-m were obtained running plasma sprayed PS212 coated rub shoes against a chrome nitride coated disk. This wear

Table 1
Hohman A-6 Friction and Wear Results
Candidate Piston Ring Coatings Run Against a Chromia-Silica Coated Disk

Candidate Piston Ring Coating	Time (Min.)	Average Wear Coefficient (mm3/N-m) Shoe Coating	Chromia-Silica
Chromia-Silica Composite	120	1.7x10-9	3.36x10-6
PS 212	480	7.61x10-7	9.11x10-9
Mid-Temperature Ti(C,N)	55	3.50x10-9	1.52x10-5
High Carbon Iron-Molybdenum	370	2.30x10-8	2.43x10-8
	975	7.56x10-8	1.66x10-8
	960	4.14x10-8	5.91x10-8
	899	4.48x10-9	1.42x10-7

Table 2
Hohman A-6 Friction and Wear Results
Candidate Piston Ring Coatings Run
Against a LTAVD Chrome Nitride Coated Disk

Candidate Piston Ring Coating	Time (Min.)	Average Wear Coefficient (mm3/N-m) Shoe Coating	Chrome Nitride
Chromia-Silica Composite	8	2.17x10-8	8.36x10-7
	5	2.17x10-7	6.95x10-6
Mid-Temperature Ti(C,N)	6	1.72x10-7	1.05x10-6
	5	2.95x10-7	6.35x10-6
	30	4.03x10-9	7.72x10-6
PS 212	120	7.86x10-9	1.04x10-4
High Carbon Iron-	120	1.23x10-9	3.13x10-7
Molybdenum	650	2.85x10-8	1.92x10-8
	375	7.16x10-8	1.48x10-8

Table 3
Hohman A-6 Friction and Wear Results
Candidate Piston Ring Coatings Run Against a
High Carbon Iron-Molybdenum Coated Disk

Candidate Piston Ring Coating	Time (Min.)	Average Wear Coefficient (mm3/N-m) Shoe Coating	High Carbon Iron-Mo
—Mid-Temperature Ti(C,N)	34	9.55x10-8	1.68x10-8
	241	1.42x10-9	1.56x10-8
—Chromia-Silica Composite	120	<10-9	7.72x10-10

coefficient was well above the desired 10-8 mm^3/N-m wear coefficient of this program. High friction coefficients were the probable reason for the poor average wear coefficient for the PS212.

The Hohman friction and wear results for the mid-temperature titanium carbo-nitride, LTAVD chrome nitride and chromia-silica coated rub shoes running against plasma sprayed high carbon iron-molybdenum coated disks are contained in Table 2. Running the mid-temperature titanium carbo-nitride rub shoes against the high carbon iron-molybdenum disk resulted in friction coefficients of below 0.15 and average wear coefficients of 1.42x10-9 to 9.55x10-8 mm^3/N-m for the titanium carbo-nitride coated shoes and 1.56x10-8 to 1.86x10-8 mm^3/N-m for the high carbon iron-molybdenum shoes. These results indicate that this coating pair will meet the friction and wear goals of this program.

Wear testing of the 5 micron thick chrome nitride coated rub shoes against the high carbon iron-molybdenum coated disks could not be completed due to the chrome nitride coating spallation. The first instance of spallation occurred during a heat-up cycle after the test was stopped to obtain an initial set of wear measurements. Prior to the castrophic coating failure the rub shoe and disk had average wear coefficients of 10-9 mm^3/N-m. The second instance of coating spallation occurred prior to testing when the rub shoes were heated to the 350 C test temperature.

Friction coefficients below 0.15 and average wear coefficients of less than 10-9 mm^3/N-m were obtained for the rub shoes and the disk running plasma sprayed chromia-silica rub shoes against a high carbon iron-molybdenum disk. The friction and wear coefficients obtained from this coating pair were similar to those obtained running high carbon iron-molybdenum shoes against a chromia-silica disk (Table 3). These results indicate that this material pair can be interchanged, and either coating can be used for a cylinder liner or piston ring coating.

Wear curves were obtained for the high carbon iron-molybdenum blend running against the chromia-silica composite and the high carbon iron-molybdenum blend running against the LTAVD chrome nitride.

These wear curves were obtained by running the specimens on the Hohman A-6 Double Rub-Shoe machine, at 350 C, with a normal load of 89 N, and a surface velocity of 3.4 m/sec. During the testing, an experimental synthetic lubricant from Lubrizol was used. The lubricant was delivered to each shoe surface using a peristatic pump at a rate of 3mm/min. After every 120 minutes the test was interrupted to measure the wear on the shoe and disk surfaces. Wear curves for each coating pair were then developed from these wear measurements. The wear curves for the high carbon iron-molybdenum running against the chromia-silica are contained in Figures 1A and 1B. Figures 2A and 2B contain the wear curves for the high carbon iron-molybdenum running against the chrome nitride.

Figure 1A
Wear Curve for High Carbon Iron Molybdenum Shoes Running Against a Chromia-Silica Disk

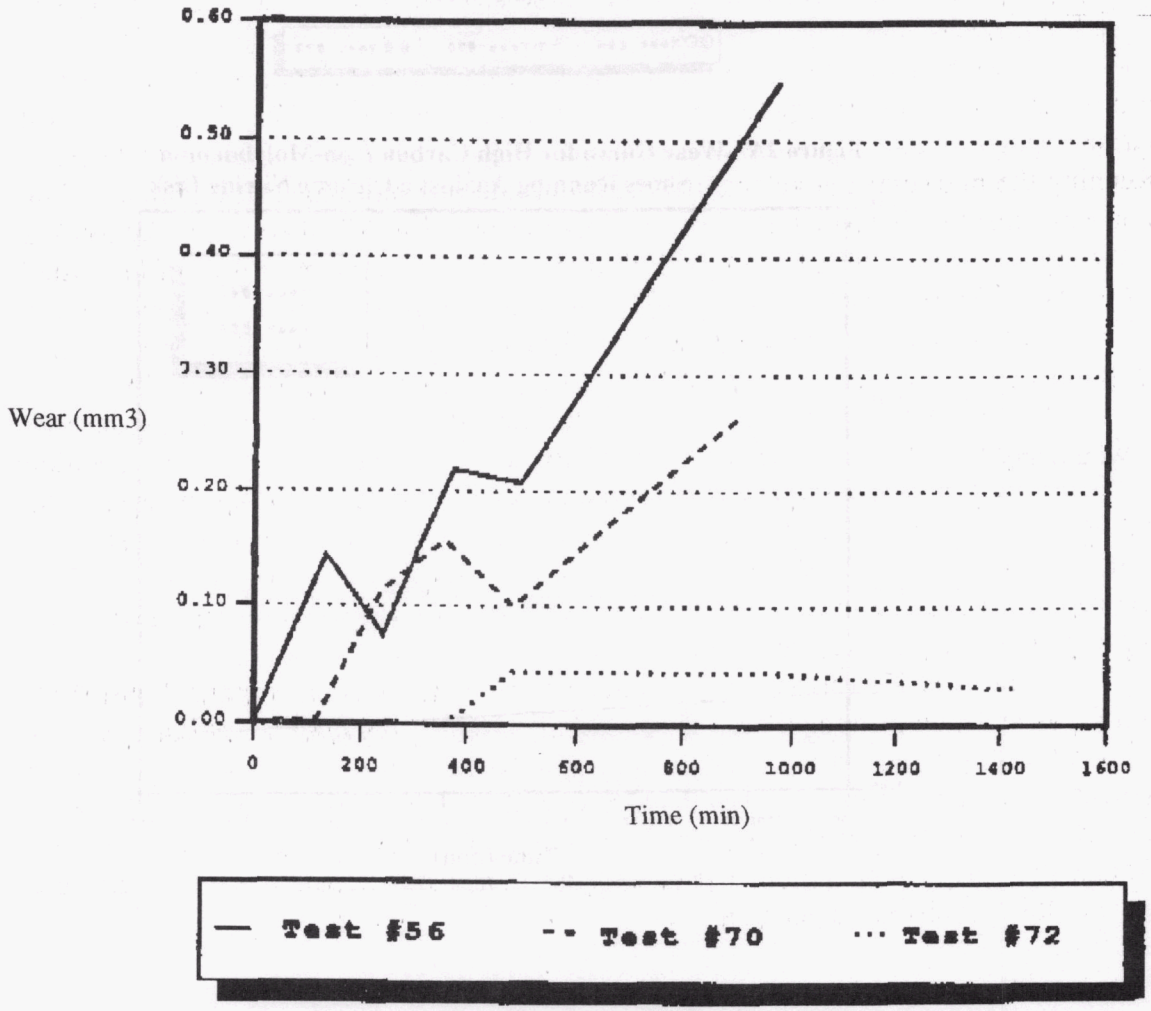

Figure 1B
Wear Curve for Chromia-Silica Disk Run Against High Carbon Iron-Molybdenum Shoes

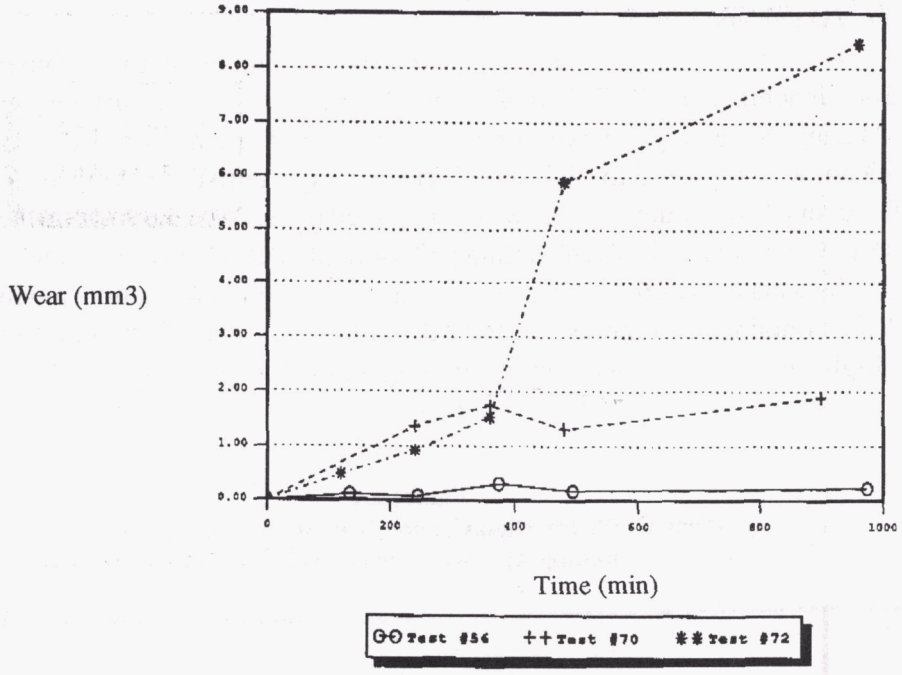

Figure 2A Wear Curve for High Carbon Iron-Molybdenum Shoes Running Against a Chrome Nitride Disk

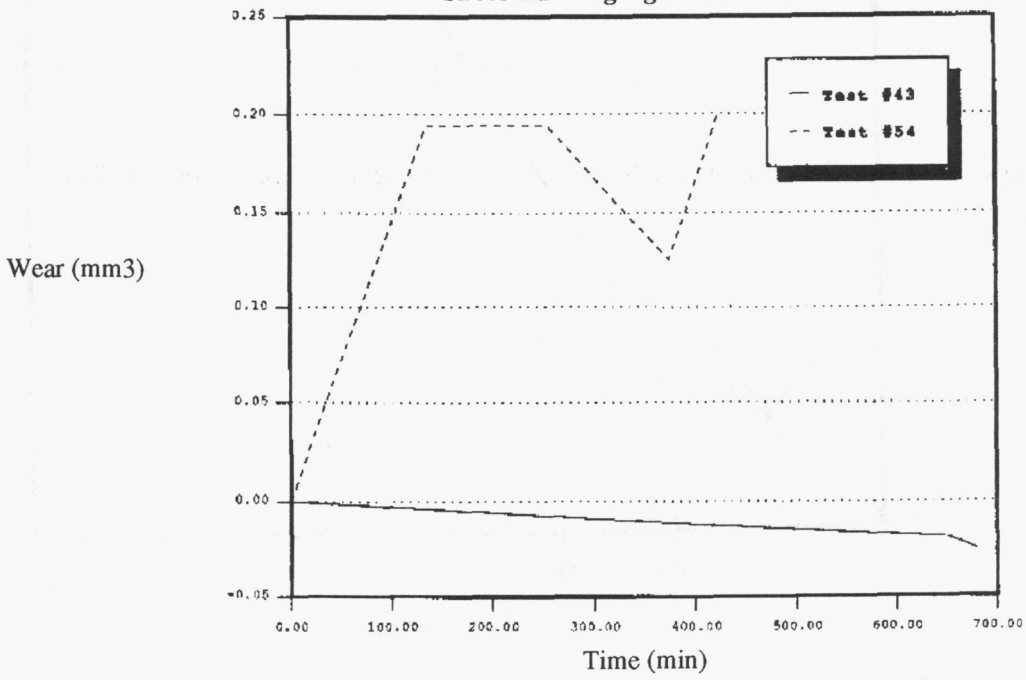

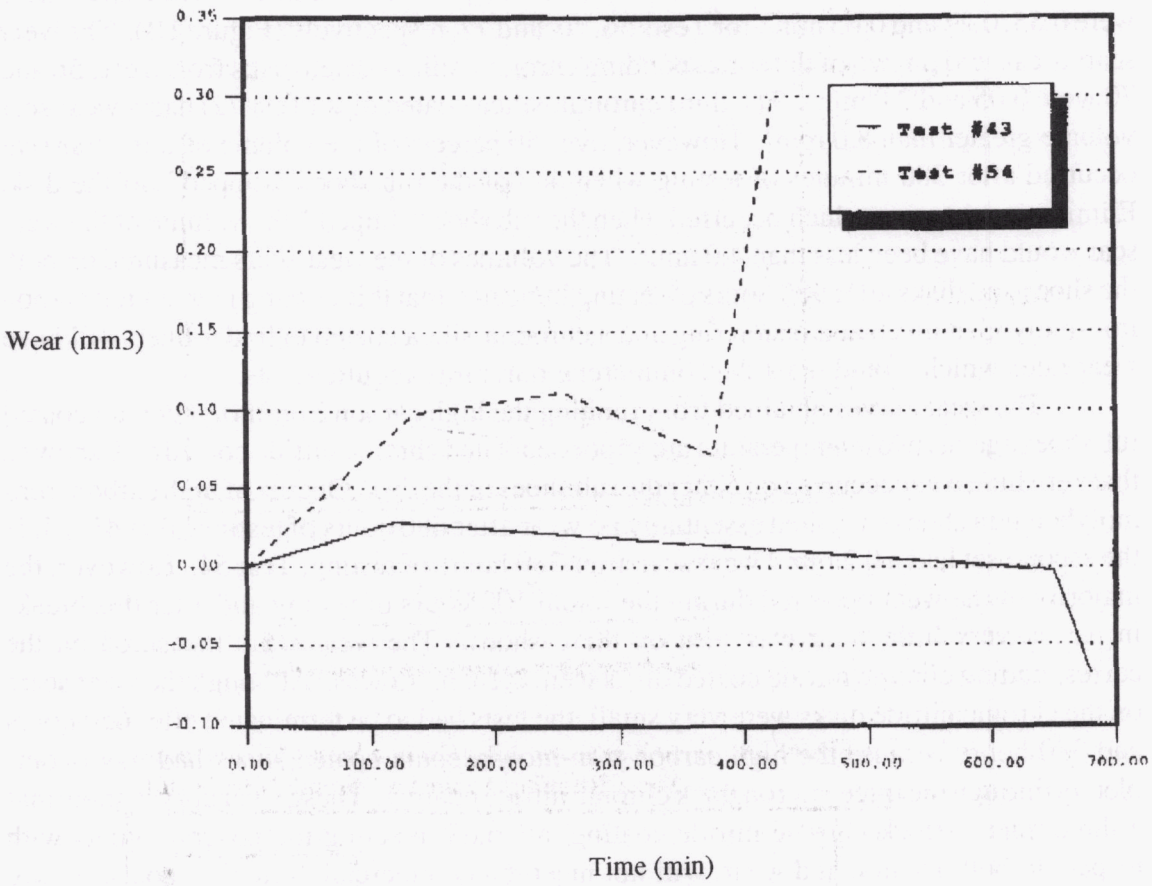

Figure 2B Wear Curve for Chrome Nitride Disk RunningAgainst High Carbon Iron Shoes

The wear scar volumes measured on the high carbon iron-molybdenum coated rub shoes after 980 hours of friction and wear testing against the chromia-silica coated disks were 0.55, 0.27 and 0.05 mm^3, for Tests 56, 70, and 72, respectively (Figure 1B). The wear scars measured on two of the corresponding chromia-silica coated disks from Tests 56 and 70 were 0.05 and 2.0 mm^3. The third chromia-silica coated disk (Test 72) had a wear scar volume greater than 8.0 mm^3. However, over 50 percent of the volume of this wear scar occurred after 380 minutes of testing when one of the rub shoes "slipped" off the disk. Eliminating the wear which occurred when the rub shoe "slipped," the volume of the wear scar would have been less than 4.0 mm^3. The volumes of the wear scars measured on both the shoes and disks after 980 hours of testing indicated that this coating pair, a high carbon iron-molybdenum coated piston ring and a chromia-silica coated cylinder liner, will have wear rates which would meet the commercial durability requirements.

The wear curves obtained from running the high carbon iron-molybdenum coated rub shoes against a low temperature arc vapor deposited chrome nitride coated disk showed that very little wear occurred on either the rub shoes or the disk. One set of high carbon iron-molybdenum shoes exhibited essentially no wear after 680 hours of testing, Test 43, while the second set had a 0.2 mm^3 wear scar after 380 hours of testing, Test 54. However, the majority of the wear occurred during the initial 100 hours of testing and after this break-in period very little wear was seen on these shoes. The wear scars measured on the corresponding chrome nitride coated disks were 0.1 mm^3 or less. Although the wear scars on the chrome nitride disks were very small, the tests had to be terminated after 650 hours and 380 hours because the high carbon iron-molybdenum coated shoes had worn completely through the three micron thick chrome nitride coating. These wear curves show that a three micron thick chrome nitride coating, although meeting the program goals with respect to both friction and wear, will not meet the commercial durability goals. Using these wear curves as a guide, it was calculated that a 15 to 20 micron thick chrome nitride coating is required to meet these commercial durability goals.

The oxidation resistance of the plasma sprayed high carbon iron-Molybdenum and plasma spray chromia-silica coatings was evaluated by exposing these coatings to a simulated diesel exhaust atmosphere, for 500 hours at 400 C, in a tube furnace. The simulated diesel atmosphere was obtained from the mixing of various gases. The composition of this simulated diesel exhaust atmosphere was:

Oxygen (O2) 9.6%
Carbon Dioxide (CO2) 8.3%
Carbon Monoxide (CO) 1439 ppm
Nitric Oxide (NO) 1439 ppm
Hydrocarbons 264 ppm
Water Vapor (H20) 7.3%
Nitrogen (N2) Balance

The plasma sprayed chromia-silica coating was not affected by the simulated diesel exhaust atmosphere. No coating spallation or discoloration was observed on any of the five specimens exposed. In fact, the physical appearance of these specimens was identical to the physical appearance of plasma sprayed chromia-silica specimens which had not been exposed to the simulated diesel exhaust atmosphere.

The high carbon iron-molybdenum plasma sprayed coated discolored during the 500 hour exposure to the simulated diesel exhaust atmosphere. This discoloration was caused by oxidation of the iron on the surface of the specimens which was in direct contact with the atmosphere. The oxidation was limited to the very top surface of the coating and for this reason no significant increase in coating thickness or spallation occurred.

The thermal shock resistance of the plasma sprayed high carbon iron-molybdenum and plasma spayed chromia-silica coatings was determined by quenching plasma sprayed cast iron Falex specimens fifty (50) times from 650 C into boiling water. Each specimen was thermocoupled to assure that it attained a 650 C temperature prior to each quench. The thermocouple also illustrated that it took approximately seven (7) seconds for the Falex disks to be quenched from 650 to 100 C.

Cracks were noticed in both coatings after three thermal shock cycles. Although additional crack propagation occurred during the subsequent thermal shock cycles, no coating disbonding or coating spallation occurred. In addition, no excess oxidation was observed on any of the plasma sprayed coated specimens after completion of the thermal shock testing.

The cracking observed within these plasma spray coatings after the thermal shock testing is not considered a problem since plasma sprayed piston ring coatings used in current production diesel engines exhibit similar crack patterns and these cracks are not detrimental to the friction and wear properties of these coatings.

Wear Resistant Enamel Coating Development

To reduce the coefficient of friction of the enamel and improve its wear properties, one method evaluated was the addition of solid lubricants to the enamel. The solid lubricants evaluated included boron nitride, calcium flouride, barium fluoride, silver flake, and cesium oxythiomolybdate.

Silverflake additions above 5 weight percent were required to reduce the coefficient of friction of the enamel. Additions of 10 weight percent silver flake to the enamel reduced the coefficient of friction for the enamel from 0.036 (no additions) to 0.26. However, even with this coefficient of friction, the enamel had unacceptable wear rates during the initial pin-on-disk screening.

A 5 weight percent barium fluoride addition to the enamel reduced the coefficient of friction of the composition to 0.26. Further barium fluoride additions to the enamel increased the coefficient of friction to above 0.30. For this reason, the barium fluoride did not improve the wear resistance of the enamel.

Up to 10 weight percent additions of boron nitride, calcium fluoride, and cesium oxythimolybdate solid lubricants did not reduce the coefficient of friction and/or reduce the wear properties of the enamel.

The following combinations of solid lubricant additions to the enamel were evaluated:

1. 2.5 weight percent barium fluoride plus 5 or 10 weight percent silver flake, and,
2. 5 weight percent barium fluoride plus 5 or 10 weight percent silver flake.

These combinations of solid lubricants reduced the coefficient of friction of the enamel to 0.26. Again with this coefficient of friction the enamel compositions had unacceptable wear rates.

Examination of the wear surfaces of the enamel compositions after pin-on-disk friction and wear screening showed that the reason for the poor wear characteristics of the enamel was the presence of bubbles in its microstructure which significantly reduced the compressive strength of the enamel.

A program was initiated to determine if the number and size of the bubbles in the enamel could be reduced by changing the firing cycle of the enamel. Fast heating rates (less than one minute to attain temperature), slow heating rates (less than 2 C/minute), as well as long and short soak times at temperature were evaluated.

The fast heating rate resulted in the formation of very large bubbles in the enamel. Reducing the heating rate resulted in the formation of numerous small bubbles evenly dispersed within the enamel's microstructure. Time at temperature or increasing the soak temperature had little affect on the bubbles which developed within the enamel's microstructure. In summary, none of the firing cycle changes were able to produce a bubble free enamel microstructure.

1.4 JOINING

1.4.1 Ceramic-Metal Joints

Joining of Ceramics for Heat Engine Applications
M. L. Santella (Oak Ridge National Laboratory)

Objective/scope

The objective of this task is to develop strong, reliable joints containing ceramic components for applications in advanced heat engines. Presently, this work is focused on the joining of silicon nitride by brazing. The technique of vapor coating ceramics to circumvent wetting problems that was developed for brazing zirconia at low temperatures is being applied to brazing silicon nitride. The emphasis of this activity during FY 1991 was on: (1) high-temperature brazing of silicon nitride and (2) correlating braze joint microstructures with strength data to identify factors that influence joint strength.

Technical highlights

Brazing trials: As previously reported, several Ti-vapor-coated Si_3N_4 joints were made by vacuum brazing at 1250°C with a 60Pd-40Ni wt % commercial foil (25 μm thick), and these joints contained considerable porosity. In a separate experiment, braze joints were made with the 50Au-25Ni-25Pd wt % and the 60Pd-40Ni wt % alloys at 1250°C (about 120°C above the normal brazing temperature for the Au-Ni-Pd alloy). The result was that an acceptable porosity-free joint was obtained only with the Au-Ni-Pd alloy. Standardless microchemical analysis of the joints in a scanning electron microscope (SEM) showed that both braze layers had become enriched to some extent with Si: 2.4 wt % for the Au-Ni-Pd alloy and 9.7 wt % for the Pd-Ni alloy. A cross-sectional view of the microstructure of the Au-Ni-Pd joint, taken in the SEM, is shown in Fig. 1(*a*). The light regions in this braze layer are an Au-rich matrix containing second-phase particles. The darker regions in this braze layer are comprised of grains of an Ni-rich phase and some grains with a composition of $(Pd,Ni)_3Si$. The Ti in this joint remained localized at the Si_3N_4 surfaces. The microstructure of the Pd-Ni joint is shown in Fig. 1(*b*). In this case, the braze layer appears to be primarily a $(Pd,Ni)_3Si$ phase containing small, Ni-rich particles. Several cracks such as the one shown in Fig. 1(*b*) were also found in this braze layer, and these are an indication that the $(Pd,Ni)_3Si$ phase is brittle. Based on composition, it is also likely that the M_3Si-phases found in both braze layers have relatively low melting temperatures since for Ni_3Si, T_M = 1170°C and for Pd_3Si, T_M = 960°C. This experiment also shows that the 50Au-25Ni-25Pd wt % braze filler metal is particularly well suited for brazing Ti-vapor-coated Si_3N_4, and suggests that consideration of high-Au-containing filler metals might permit brazing temperatures to be used.

Based on the above results, a commercially available Au-25Pd wt % alloy was also used to make several joints with Si_3N_4, which was vapor coated with a 2-μm layer of either Ti or Mo. The brazing trials were done at 1425 and 1375°C, which are, respectively, 15°C over and 35°C under the nominal melting temperature (1410°C) of this filler metal. Melting of the filler metal was achieved at both temperatures. Joints were formed for each experimental condition, and those made at 1375°C had good external

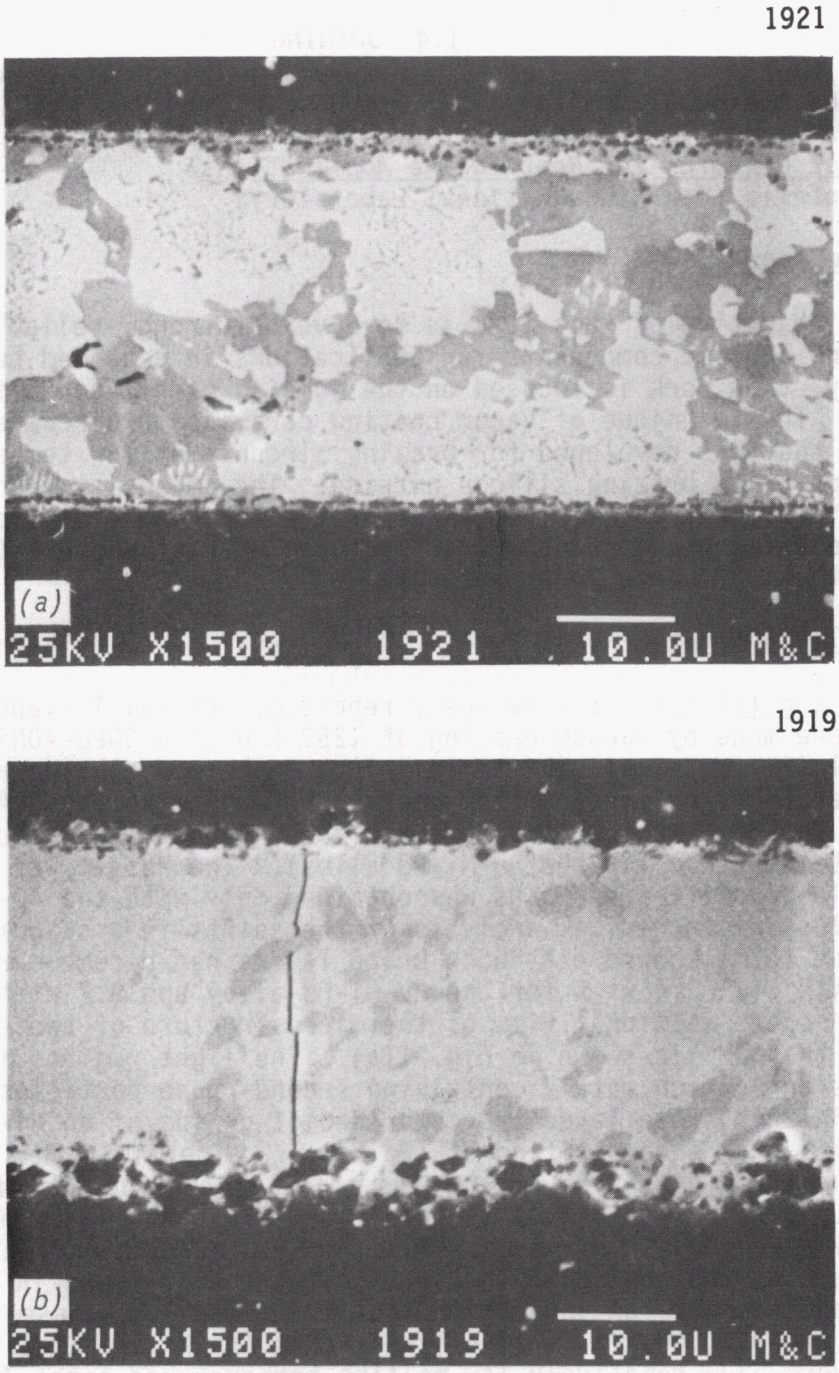

Fig. 1. Cross-sectional views of Ti-vapor-coated Si_3N_4 brazed at 1250°C with (*a*) Au-25Ni-25Pd wt % filler metal and (*b*) Pd-40Ni wt % filler metal.

appearance, but sectioning revealed that all of the joints contained large void areas. The microstructure (as viewed in the SEM) of a joint made at 1375°C using Ti-vapor-coated Si_3N_4 is shown in Fig. 2. In this case, microchemical analysis indicated that the major phase in the braze layer had a composition of 13.6 wt % (36.6 at. %) Si, which suggests that it may be a two-phase mixture of Pd_2Si and PdSi. The high Si level indicates that extensive reaction between Pd and the Si_3N_4 occurred. The minor phase in the braze layer appeared to be Au rich. Figure 2 also shows a large number of particles near the Si_3N_4 surfaces. These particles could not be identified, but some of them were Ti rich and could have been TiN or Ti silicides. It is also clear that the Ti layer did not remain intact and continuous on the Si_3N_4 surfaces and did not inhibit reaction of the braze filler metal with the Si_3N_4. The reaction with Pd is undoubtedly responsible for depression of the filler metal melting temperature and appears to be a significant problem in identifying filler metal compositions, which may permit brazing at temperatures above 1130°C.

Both sets of experiments discussed above indicate that the conditions during the brazing of Si_3N_4 with Ni- and Pd containing filler metals are favorable for the formation of silicide phases. They also indicate that the formation of large quantities of silicide phases in these joints is undesirable because silicides have relatively poor mechanical properties

2527

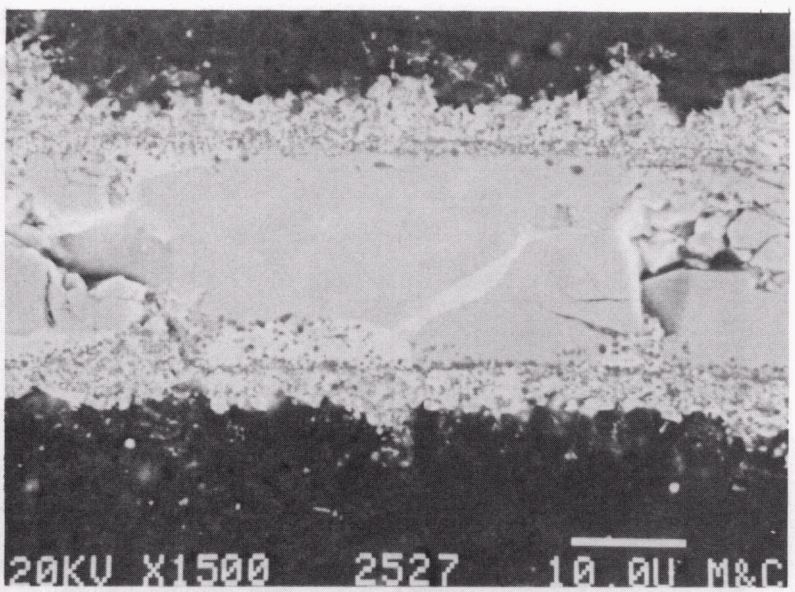

Fig. 2. Microstructure of Ti-vapor-coated Si_3N_4 brazed at 1375°C with a Au-25Pd wt % filler metal.

and possibly low melting points. Also, the formation of silicides in the braze layers involves decomposition of the Si_3N_4 and evolution of nitrogen gas, which then leads to expulsion of filler metal from the joint gaps and the formation of large void regions.

Fractography of Si_3N_4 joint test bars: Specimens of Ti-vapor-coated Si_3N_4 brazed with Au-25Ni-25Pd wt % filler metal and flexure tested at 800°C were examined in the SEM, and a representative fracture surface is shown in Fig. 3. The "knobby" appearance suggests that some liquid phase was present at the test temperature. Microchemical analysis from area scans on this surface indicated that the Si concentration was in the range of 11 wt % (23 at. %). Significant levels of Ni, Ti, and Pd were also present. These observations are consistent with those made on polished cross sections of similar joints, which indicated that high levels of Si and $(Ni,Pd,Ti)_3Si$ phases were produced in the braze layers. The high Si levels probably account for liquation of phases in the braze layers and loss of joint strength near 800°C. Analysis of this problem is continuing.

Thermal analysis of Si_3N_4 brazing: In an effort to learn more about the reactions occurring during brazing of Si_3N_4 and to provide some guidance in selecting brazing alloys with higher temperature capabilities, a group of Si_3N_4 specimens was prepared and submitted for thermal analysis. The specimens were 3-mm-diam by 1-mm-thick discs, some of which are vapor coated with Ti. The test plan includes heating the specimens to elevated

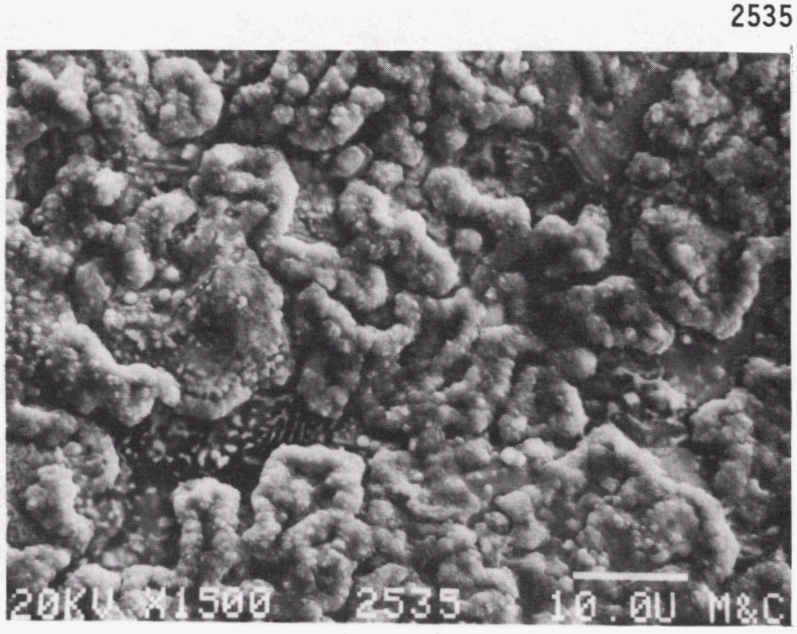

Fig. 3. SEM micrograph of fracture surface from a Si_3N_4 joint specimen brazed with Au-25Ni-25Pd wt % filler metal and flexure tested at 800°C.

temperature alone and in the presence of brazing filler metals. The remelting behavior of the filler metals will also be studied.

Equipment purchase: An electron beam vapor-coating system was purchased and installed. Several problems were encountered with the vacuum system, electron beam power supply, and instrumentation, but the system is now completely operational.

Status of milestones

On schedule

Publications

None

Analytical and Experimental Evaluation of Joining Silicon Nitride to Metal and Silicon Carbide to Metal for Advanced Heat Engine Applications - S. Kang (GTE Laboratories Incorporated)

Objective/Scope

The goal of Phase I is to demonstrate analytical tools for use in designing ceramic-to-metal joints, including the strain response of joints as a function of the mechanical and physical properties of the ceramic and metal, the materials used in producing the joint, the geometry of the joint, externally imposed stresses both of a mechanical and thermal nature, temperature, and the effects of joints exposed for long times at high temperatures in an oxidizing (heat engine) atmosphere. The maximum temperature of interest for application of silicon carbide to metal and silicon nitride to metal-containing joints is 950°C. The initial joint-fabrication work shall include "experimental" joints whose interfacial area is not less than 2 cm^2. The work shall also include demonstration of the potential for scale-up of the joint size to interfacial areas of commercial significance, applicability of the analytical joint modeling tools, and the ability to use these tools to design and predict the mechanical and thermal behavior of larger joints. These joints, referred to as "scale-up" joints, shall have an interfacial area of at least 20 cm^2.

The goal of Phase II is to optimize materials systems and joint designs, building on the results of Phase I. The work shall also include demonstration of the potential for scale-up of the joint size to interfacial areas of commercial significance, applicability of the analytical joint modeling tools, and the ability to use these tools to design and predict the mechanical and thermal stability of the larger joints. These joints, referred to as "scale-up" joints, shall have the ceramic shaft at least 0.8 inches in diameter. The goal is to develop a system which can perform in an engine such as the ATTAP engine. The anticipated environment will be oxidizing and will have joint temperatures of 650°C or higher. Improved joint materials systems shall be developed to optimize the combination of competing properties, which include ductility, yield strength, and creep resistance. The effect of each of these properties on joint performance shall be examined using the FEM model. Finally, a program of mechanical testing shall be carried out to confirm the effectiveness of the modeling program. This shall include torsion tests, thermal and mechanical fatigue, and creep testing. In addition, an analytical and experimental program in service life prediction will be undertaken.

Technical Progress

Materials System Design

Brazing Alloy Development

Development of brazing alloys for ceramic-to-metal joints has been continued. During this period, 4 different alloy systems were investigated: Au-Ni-Cr-Mo-Fe-Nb, Au-Ni-Cr-Fe, Au-Ni-Cu-Cr-Mo-Fe-Nb, and Au-Ni-Cu-Cr-Fe. 140 alloy compositions were produced using an induction melting technique in argon atmosphere and characterized in terms of wetting and ductility. Brazed coupons made of PY6 and Inconel 600 were also produced to see the compatibility of the braze system during and after the brazing process. An effort was made to increase the high temperature strength with a minimum loss of other properties necessary for brazing.

Of those alloys, Au-Ni-Cr-Mo-Fe-Nb alloys, which melt at 1050-1100°C, seemed to meet the processing requirements for high-temperature ceramic-metal joints. Preliminary results from mechanical testing indicated that these alloys had good ductilities and strengths. They wetted well on silicon nitride with various coating materials in the vicinity of 1150°C. However, a major drawback was the limited wetting property of these alloys on Inconel 600 or Ni substrates due to the combined effects of liquation and alloying.

Therefore, the relative effects of Cr and Fe on ductility and the flow property of this system were evaluated by adding Cr, Fe, and Mo systematically to Au-Ni system, and it was determined that (1) addition of Fe to an Au-Ni system did not interfere with the excellent flow property of an Au-Ni system, but it reduced the ductility with an increase of Fe content, (2) high

content of Cr in an Au-Ni system embrittled the braze alloy and reduced the flow characteristics of liquid braze on Inconel 600, (3) excessive addition of Mo to Au-Ni system lowered the flow property significantly, and (4) the presence of Mo and the ratio of Au to Ni appeared to play important roles in enhancing the alloy ductility.

The Fe embrittlement in this system was presumed to be due to the phase segregation or precipitation at low temperature. The reduction of flow property by the addition of Cr can be explained with an Au-Cr phase diagram as well; the melting point increases with the increase of Cr content. The role of Mo on the flow property was closely related to the limited solubility of Mo in Au. Further, the Mo addition caused substrate erosion resulting from liquation, which is attributed to a large gap between solidus and liquidus. The solubility limits of Cr, Fe, and Nb in Au were reported as 20.8, 46.0, and 38.5 (wt.) %, respectively.

Brazing experiments were performed to check the brazability and system compatibility of Au-Ni-Cr-Mo-Fe-Nb and Au-Ni-Cr-Fe alloys. Limited flow property of Au-Ni-Cr-Mo-Fe-Nb braze alloys resulted in spotty bonding between Ti-coated PY6 and Inconel 600, even though these alloys wetted Ti-coated PY6 completely. On the other hand, Au-Ni-Cr-Fe system generally provided excellent wetting and bonding between PY6 and Inconel 600.

In addition, 22 Au-Ni-Cr-Cu-Mo-Fe-Nb and Au-Ni-Cu-Cr-Fe alloys were studied by adding Cu to Au-Ni-Cr-Mo-Fe-Nb and Au-Ni-Cr-Fe systems to improve the flow property. Copper was chosen due to its complete solid solubility with Au. However, addition of Cu did not enhance the wettability of these alloys and raised the melting points of the alloys unexpectedly (>1100°C). These alloys were not able to be processed under 1200°C.

Based on the phase diagram study and the results obtained during this period, two alloy compositions, Au-Ni-Cr-Mo-Fe and Au-Ni-Cr-Fe, were selected for final foil production. These alloys have shown superior wetting and bonding characteristics as well as excellent ductility compared to other compositions studied. These alloys melted in the vicinity of 1000°C and could be brazed at 1050°C, which people in auto industries feel is an upper limit for ceramic-metal joining process. The alloys, even though they have relatively low melting temperatures, are expected to improve high-temperature creep strength by diffusion of Ni, Cr, Fe, and Mo from the adjacent interlayer (Inconel 600).

Braze foil production of two alloy compositions, Au-Ni-Cr-Mo-Fe and Au-Ni-Cr-Fe, was completed at GTE Wesgo. For the production,120 grams of each alloy were melted at 1300-1400°C in a boron nitride crucible by induction heating and cast into a copper mold to produce a 2.0"x0.75"x0.25" bar. The alloy was homogenized at 800°C for 24 hours in an argon atmosphere. The cast bar was rolled into 0.002"-thick foil with intermittent vacuum annealing at 800°C for 2-4 hours. The successful rolling of this alloy was obtained due to its excellent toughness and ductility. It was shown from a microstructural study that these alloys consisted of two or three discrete phases; one is an Au-based solid solution and the other is a Ni-based high-temperature phase, facilitating rolling process. The multiphase microstructures with high-temperature phases have been effective in improving high-temperature creep behavior in general.

Bond strengths of the joints made of PY6 silicon nitride and Inconel 600 was evaluated by shear tests at room temperature. Preliminary results showed that the shear strength of the joints with an Au-Ni-Cr-Mo-Fe alloy was in the range of 2-6.5 ksi, while an Au-Ni-Cr-Fe alloy provided a strength level in the range of 3-17 ksi. The intended bond area was 1 cm^2. Two new alloys exhibited excellent wetting (or bonding) between PY6 and Inconel 600 (50-100% bonding). The joint strength values were found to be a strong function of processing variables. Processing optimization with new alloys was needed in order to control the residual stress resulting from a high percentage of bonding.

Thus, processing parameters were studied for new braze alloys. Performance of the joints was consistently improved in terms of room-temperature shear strength for PY6/Inconel 600 system as the braze thickness increased (3-6 and 6-17 ksi for 0.002" and 0.004"-thick foils, respectively). Also, it was noted that the pressure or weight applied to the samples during the brazing process affected the bond strength significantly. This observation seems to be closely related to the nature of bonding attained from these new alloys and alloy ductility; adhesion of the joint was primarily due to the melting of the Au-based phase. Therefore, the applied pressure and foil thickness have to be determined with discretion, depending on the properties of the braze alloys: i.e., melting phase, the gap between solidus and liquidus, and the viscosity of liquid metal.

Shear strengths of various joints were measured at RT, 500, and 650°C. Joints were made between PY6 and one of the substrate materials such as Inconel 600, Incoloy 909, W, Mo, Ta, and Ni with new braze alloys 0.002" thick. Similar joints were made with Au-Pd-Ni and Nioro (Au-Ni) as shown in Table 1. In general, new alloys outperformed the conventional brazing alloys at high temperature. When they coupled with Ni or refractory metal substrate such as Mo, W, and Ta, the improvement in bond strength was significant. However, the performance with new alloys at RT was found to be low and inconsistent compared to those of conventional alloys, even though it varies depending on the metal substrate used. This implies that at low temperature the joint strength is greatly controlled by the capability of the braze alloy and metal substrate to accommodate the residual stress. At high temperature the multiphase microstructure of new braze alloys and reduced residual stress synergistically enhance the joint strength. The braze alloys of single-phase microstructures like Au-Pd-Ni and Nioro showed somewhat better performance at low temperature and minimal strength at high temperature due to low creep resistance. It was found from this testing that PY6-Ni with these alloys can perform properly without oxidation problems at low and high temperatures. Further evaluation of these systems will be done at 650°C.

Design/Failure Analysis

Prediction of Brazed Joint Strength

Prediction of braze joint strength was made, using the approach described in the February bimonthly, with improved material data, additional experimental data, and 2 different failure theories. The experimental data for the torsion tests of Si_3N_4/Ni/Incoloy 909 brazed joints and torsion tests of Si_3N_4/Mo/Inconel 718 brazed joints are listed in Table 2 and 3.

Two failure theories were used to predict the behavior of the ceramic-to-metal joints for comparison. These were: 1) Shetty criterion with $\bar{C} = 0.82$, a penny-shaped crack, and a shear-insensitive Batdorf crack density coefficient, and 2) Coplanar strain energy release rate with a Griffith crack and a shear-sensitive Batdorf crack density coefficient. For these failure theories, the Weibull modulus (m_V), the normalized Weibull scale parameter (σ_{OV}), and the Batdorf crack density coefficient (k_{BV}) were calculated from 4-point bend tests of the Si_3N_4 material used in the ceramic-to-metal brazed joints. Specimens measuring 2.54 mm x 1.27 mm x 25.4 mm were used with an inner and outer test span of 10.16 mm and 22.86 mm; the tensile surfaces of the test bars were polished to 0.1 μm. Twenty-four samples were tested, and 1 outlier was detected in the data. The data is shown in Figure 1.

A Weibull modulus (m_V) of 21.2 and a normalized Weibull scale parameter (σ_{OV}) of 369.8 $MPa(m)^{3/21.2}$ were used for both failure theories. A shear-insensitive Batdorf crack density coefficient of 43.4 and a shear-sensitive Batdorf crack density coefficient of 22.2 were used for the Shetty and coplanar strain energy release rate theories, respectively. The maximum likelihood method was used to fit the experimental data. The constants described above were required as input variables by CARES and are further described by Nemeth et al.[1]

Figures 2 and 3 show predicted and experimental results of torsion testing of the brazed joints. The predicted strength distributions surrounded the experimental values and intermediate values of P_f, where $P_f = 1 - P_S$. However, at the low and high regions of the probability distributions, the predictions deviated from the experimentally measured strengths. Also, the predicted probability distributions were much steeper than the experimental probability distribution. The difference in the "slopes" of the probability distributions was probably due to defects in the joint introduced during the brazing process.

Table 1: Results of Shear Tests at Various Temperatures

System	Brazing Alloys	RT	Avg* Strength (ksi) 500°C	650°C
PY6* -Incoloy 600	Au-Pd-Ni (Ref)	3.8	3.9	-
-Mo		9.3	21.0	-
-Ni		-	8.5	6.8
PY6 -Inconel 600	Nioro (Ref)	8.9	-	-
(Zr)SNW -Ni		8.9	11.6	-
-Mo		11.7	5.9	-
PY6 -Ni	B Alloy	5.4	14.2	14.5
-Mo		4.1	31.2	25.6
-W		5.1	-	10.5
-Ta		1.9	-	18.0
-PY6				7.5
-Incoloy 909		-	0	-
-Inconel 600		(2-6.5)	-	4.0
PY6 -Ni	C Alloy	5.4	15.2	11.3
-Mo		5.1	32.2	19.9
-W		-	34.2	33.9
-Ta		6.2	30.1	24.6
-PY6			-	6.9
-Incoloy 909		-	0.4	-
-Inconel 600		3-17	4.0	6.4

*Strength values are avg. of min. 2 tests.

Table 2. Results of the Torsion Tests of Si_3N_4/Ni/Incoloy 909 Brazed Joints

Test Temperature (°C)	Torque (N-m)	Shear Strength (MPa)	Bending Moment (N-m)	Rotation	Fracture Mode
25	61	151	7	2.22°	Broke in ceramic
"	97	242	14	3.52°	"
"	53	132	11	1.98°	"
"	30	75	13	1.15°	"
"	60	148	10	1.05°	"
"	49	121	23	2.55°	"
"	64	158	14	3.05°	"
"	90	222	12	4.3°	"
"	45	111	2	2.05°	"

Table 3. Results of the Torsion Tests of Si_3N_4/Mo/Inconel 718 Brazed Joints

Test Temperature (°C)	Torque (N-m)	Shear Strength (MPa)	Bending Moment (N-m)	Rotation	Fracture Mode
25	12	30	25	0.38°	Broke in ceramic
"	40	98	13	1.19°	"
"	23	56	17	0.70°	"
"	51	127	16	0.80°	"
"	41	101	16	0.64°	"

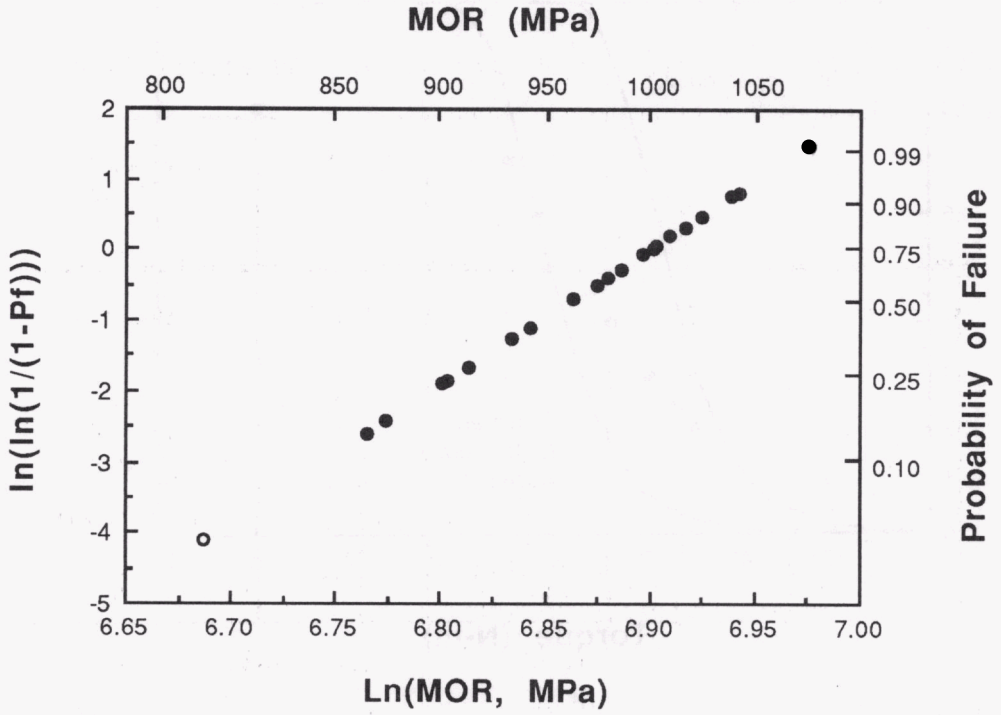

Figure 1. Weibull plot of 4-point bend test data of Si_3N_4 material used in this study. The data point represented by the open circle was considered by CARES as an outlier and was not used to determine the material parameters.

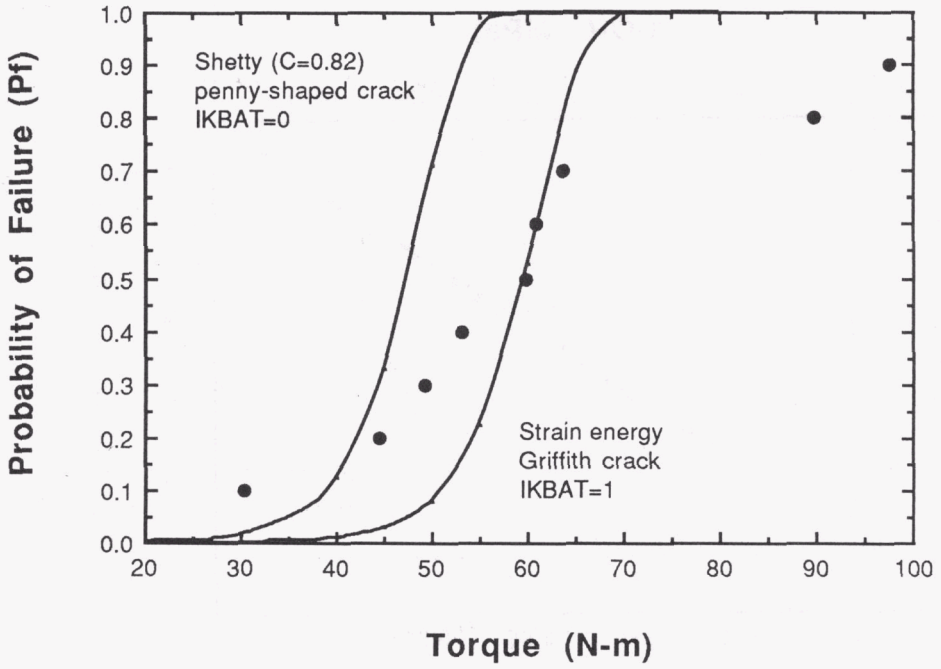

Figure 2. Predicted and experimental values of the brazed joint strength measured in torsion (Si_3N_4/Ni/Incoloy 909). Two failure theories were used: 1) Shetty criterion with $\bar{C}$ = 0.82, penny-shaped crack, and a shear-insensitive Batdorf crack density (IKBAT = 0) and 2) Coplanar strain energy release rate, Griffith crack, and a shear-sensitive Batdorf crack density (IKBAT = 1).

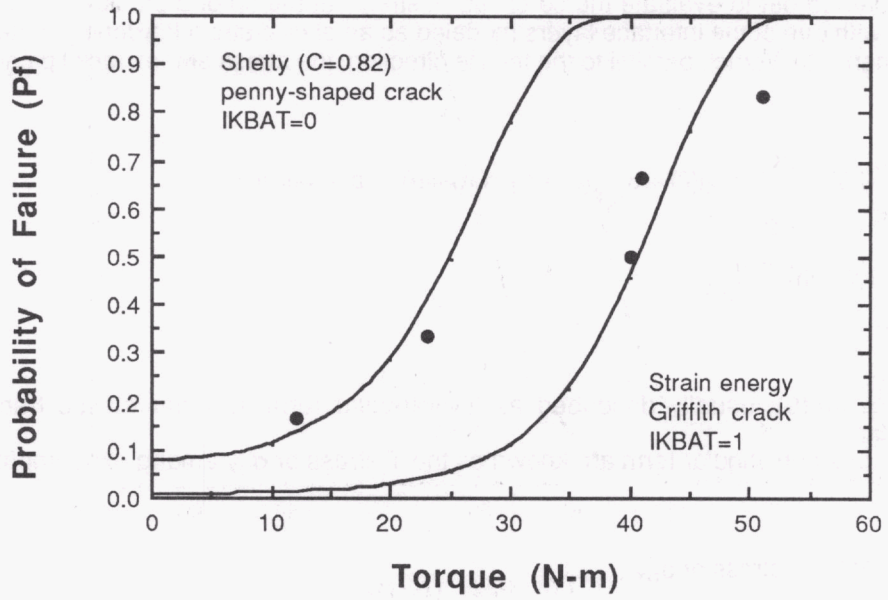

Figure 3. Predicted and experimental values of the brazed joint strength measured in torsion (Si_3N_4/Mo/Inconel 718). Two failure theories were used: 1) Shetty criterion with $\bar{C}$ = 0.82, penny-shaped crack, and a shear-insensitive Batdorf crack density (IKBAT = 0) and 2) Coplanar strain energy release rate, Griffith crack, and a shear-sensitive Batdorf crack density (IKBAT = 1).

Design and Modeling: T-stress

Work was carried out to evaluate the so-called 'T-stress' at the tip of a crack at or near a bimaterial interface with one of the interface layers modeled as an elastic-strain hardening material. For a tensile specimen with a crack parallel to the tensile direction, the stress at the crack tip can be written as

$$\sigma_{\alpha\beta}(r,\theta) = \frac{K_I}{\sqrt{2\pi r}} f_{\alpha\beta}(\theta) + \overset{\circ}{\sigma}_{\alpha\beta}(\theta) + a_1 \sqrt{r} g_{\alpha\beta}(\theta) + a_2 r h_{\alpha\beta}(\theta) + \ldots$$
$$+ a_n (\sqrt{r})^n h^{(n)}_{\alpha\beta}(\theta)$$

The first term, $\frac{K_I}{\sqrt{2\pi r}} f_{\alpha\beta}(\theta)$, usually described as the singular term in linear elastic fraction mechanics, and the first nonsingular term are known as the T-stress or σ_{ox} among experimentals, so

$$\overset{\circ}{\sigma}_{\alpha\beta}(\theta) \equiv \text{T-stress or } \sigma_{ox}.$$

Otteral and Rice have shown that the instability of the crack path depends on the T-stress term. In addition, it has been speculated that the nonsingular term may play a significant role in crack branching. For design of the ceramic-to-metal braze joint, the description of the instability of the crack path due to the T-stress term will permit numerical study of the fracture surface by following crack propagation and allow joint design that takes into account the effect of this nonsingular term coupled to the elasto-plastic interface (the ceramic-braze interface).

The method used to find the nonsingular stress term (the T-stress) at the crack tip uses application of an energetic force on a point load in the development of an interaction (or mutual) integral to extract this term.

A description of the general method for study of an interaction integral of a point load follows. The conservation force on an object such as an inclusion, a crack tip, a dislocation or a point force is referred to as an *energetic force* or an *energy release rate*. The energetic force, G, is defined as the negative gradient of the potential energy of a body with respect to a virtual displacement of the object. Denoting the virtual displacement of the object by $\rho\mathbf{e}$, for which $\mathbf{e}$ is a unit vector, the definition of the energetic force is expressed as

$$G = -\lim_{\rho \to o} \frac{\Pi(\mathbf{r}+\rho\mathbf{e}) - \Pi(\mathbf{r})}{\rho}\mathbf{e},$$

where Π represents the potential energy of the body. The energetic force often can be calculated by the **J** integral. Provided the mechanical response function, i.e., the elastic property, is invariant in the direction of G, the energetic force, G, can be evaluated by a surface integral (or a contour integral for two-dimensional cases) in terms of the field quantities. The elastic equilibrium field surrounding the object is represented by the field quantities of the stress, σ, the strain, ε, and the displacement, u. Denoting the equilibrium field (σ,ε;u) by S, the surface integral is depicted by $\mathbf{J}_\Gamma(S)$, where Γ indicates the integrating surface (or contour). A Cartesian component of the **J** integral is expressed as

$$J_i = \int_\Gamma (Wn_i - \sigma_{kj} n_k u_{j,i}) d\Gamma,$$

where the summation convention is assumed on the repeated indices, the strain energy density function is represented by W, and the out normal of the surface, Γ, is indicated by **n**.

The energetic forces of various singular objects have many interesting properties. Those of dislocations, point defects and cracks have been applied to many engineering problems in plasticity, diffusion, and fracture mechanics. However, not much attention has been paid to those of point forces.

The stress state around a point load in a linear elastic medium can be separated into two parts. One is the singular stress field corresponding to the point load in an infinite medium, denoted by superscript p, e.g., S^p. The remaining stress field corresponds to the image effect of the limited geometry and other sources of stresses. This remaining field is denoted without superscripts, e.g., S. In order to get a useful expression of the energetic force of a point load in such a superposed field, an alternative expression of the **J** integral of a general superposed field is derived first, and then some properties of the **J** integral related to the energetic force of a point load will be discussed next.

Consider the superposition of two general equilibrium fields, S^A and S^B. Substituting the field quantities of the total field, $S^A + S^B$, into Eq.(2), the J integral of the total field over a Γ is expressed as

$$\mathbf{J}_r(S^A + S^B) = \mathbf{J}_r(S^A) + \mathbf{J}_r(S^B) + \mathbf{J}^{int}_\Gamma(S^A, S^B),$$

where the superscript 'int' indicates the interaction integral. A Cartesian component of the interaction integral is given by

$$J^{int}_i(S^A S^B) = \int_\Gamma (W^{int}_{n_i} - \sigma^A_{kj} n_k u^B_{j,i} - \sigma^B_{kj} n_k u^A_{j.i}) d\Gamma,$$

where the interaction strain energy, W^{int}, has the relationship of

$$W^{int} = \frac{1}{2}(\sigma^A_{ij}\varepsilon^B_{ij} + \sigma^B_{ij}\varepsilon^A_{ij}) = \sigma^A_{ij}\varepsilon^B_{ij} = \sigma^B_{ij}\varepsilon^A_{ij}.$$

The last two equalities hold, due to the symmetry of the elastic moduli tensor. Therefore, the interaction integral can be expressed in a convenient form,

$$J^{int}_i(S^A S^B) = \int_\Gamma (\sigma^B_{kj}\varepsilon^A_{k,j} - \sigma^B_{kj} n_i - \sigma^B_{k,j} n_k u^A_{j.i}) d\Gamma - \int_\Gamma \sigma^A_{kj} n_k u^B_{j,i} d\Gamma.$$

In subsequent reports, the evaluation of J^{int} to the solution of the nonsingular T-stress component will be described.

Interaction Integrals for Extracting Stress Intensity Factor and T-Stress

In order to extract the complex stress intensity factor, *K*, and T stress, the interaction integral based on the path-independent J-integral (June 91 bimonthly) was used by many investigators.[2,3] To define the interaction integral, consider two general equilibrium fields, S^A and S^B. The J-integral of the superposed field, $S^A + S^B$, over a contour Γ can be expressed as

$$J(S^A + S^B) = J(S^A) + J(S^B) + J^{int}(S^A,S^B) \tag{1}$$

where the superscript "int" indicates the interaction integral. Then, the interaction integral $J^{int}(S^A,S^B)$ is defined by

$$J^{int}(S^A,S^B) = \int_\Gamma (W^{int}\delta_{1k} - \sigma^A_{kj}\frac{\partial u^B_j}{\partial x_1} - \sigma^B_{kj}\frac{\partial u^A_j}{\partial x_1})\, ds \tag{2}$$

where the interaction strain energy, W^{int}, has the relationship of

$$W^{int} = \frac{1}{2}(\sigma^A_{ij}\varepsilon^B_{ij} + \sigma^B_{ij}\varepsilon^A_{ij}) = \sigma^A_{ij}\varepsilon^B_{ij} = \sigma^B_{ij}\varepsilon^A_{ij} \tag{3}$$

due to the symmetry of the elastic moduli tensor.

First, to extract the complex stress intensity factor K near an interface crack, consider an interaction integral between the actual field S and the auxiliary field $S^{\tilde{K}}$ which is the $(1/\sqrt{r})$ singular field and whose strength is $\tilde{K} = |\tilde{K}|e^{i\phi}$. Then by calculating each j-integral in Eq. (1), the interaction integral $J^{int}(S,S^{\tilde{K}})$ can be expressed in terms of two stress intensity factors, K and $\tilde{K}$, as

$$J^{int}(S,S^{\tilde{K}}) = \frac{|\tilde{K}|h_{22}}{2\cosh^2\pi\varepsilon}(K_1\cos\phi + K_2\sin\phi) \tag{4}$$

for an anisotropic bi-material interface crack where h_{22} is defined by Eq. (A.10) in Choi et al.[4] Therefore, the complex stress intensity factor can be completely obtained (i.e., K_1 and K_2 separately) by applying Eq. (4) twice with the different mode, ϕ, of the auxiliary field $S^{\tilde{K}}$, and then by solving for K_1 and K_2. In each case, the interaction integral, $J^{int}(S,S^{\tilde{K}})$, is calculated by Eq. (2).

Now, to extract the T stress at an interface crack, consider an interaction integral between the actual field S and the auxiliary field $S^{\tilde{T}}$, which is the (1/r) singular field of the point force, $\tilde{T}$, located at a crack tip and directed to the x-axis. Noting that, for the in-plane problem, only the nonsingular stress at the crack tip is σ^o_{xx}, Kim et al.[2] have shown that the interaction integral between the S and $S^{\tilde{T}}$ field is reduced to

$$J^{int}(S,S^{\tilde{T}}) = \tilde{T}\varepsilon^o_{xx}. \tag{5}$$

Once ε^o_{xx} is obtained through the above equation, the nonsingular stress term σ^o_{xx} can be easily calculated using Hookes's law. Note that for the interface cracks the T stress can have a jump across the interface. The jump quantities are determined from the compatibility condition that the corresponding strain, ε^o_{xx} should be continuous across the interface.

Both fundamental fields of S^{R} and S^{T} in the above were presented in Choi et al.[4] for an interface crack between an anisotropic bi-material, but they can also be used for the isotropic cases.

Toughening of the Brazing Structure

These results have been implemented into a two-dimensional finite element program and results obtained for the material system specific to the ceramic-to-metal joint. The geometry of the metal-braze-ceramic region is shown in Figure 4. Material properties of each of the materials were

(1) Structural Alloy: Incoloy 909
E_s = 158.6 GPa, v_s = 0.34

(2) Braze Material: 30Au-34Pd-36Ni
E_b = 32.4 GPa, v_b = 0.3
Yield stress σ_o = 626.0 MPa

(3) Ceramic: PY6 (Si_3N_4)
E_c = 296.5 GPa, v_c = 0.2

Typical results for a crack parallel to the ceramic-braze interface are shown in Figure 5. Figure 5a shows the increasing energy release rate when the crack gets closer to the interface. Note also the energy release rate increases as fracture tends to mode II loading. The change in the T-stress factor for the same cases of mode mixity and crack position are illustrated in Figure 5b.

In summary, we have seen that not only is the interface tougher in mode II loading (as it is near an elastic-elastic interface), but also the plastic deformation of braze material acts as a toughening agent, particularly in mode II loading. The result is a failure model for ceramics which is significantly different from existing models.

Detailed Description of Implementation

The correction factor for stress can be estimated using energy release data obtained from finite element calculations. Data was obtained for cracks at different distances *h* from the interface (with a constant brazing thickness *t*) under various far-field loading conditions. The ratio of the total energy release rate due to far-field loading G^{∞} to the actual energy release rate calculated at the crack tip *G* is a measure of the amount of energy consumed by plastic yielding in the brazing layer. The behavior of this ratio was plotted as a function of $\frac{t}{h}$ for various angles of far-field loading incidence Ψ . These plots were made for different loading magnitudes $|K|$, where the magnitude has been normalized as follows (Figures 1-3).

$$|K^{\infty}| \equiv \frac{K_{IC}}{\sigma_o \sqrt{t}}$$

This data shows the dependence of $\frac{G^{\infty}}{G}$ on $|K^{\infty}|$ and *t*/*h* for each angle of incidence. Thus, the effective stresses which we seek should assume this form:

$$\sigma_{yy}^{eff} = \frac{\sigma_{yy}}{\sqrt{f_c}} \qquad (1)$$

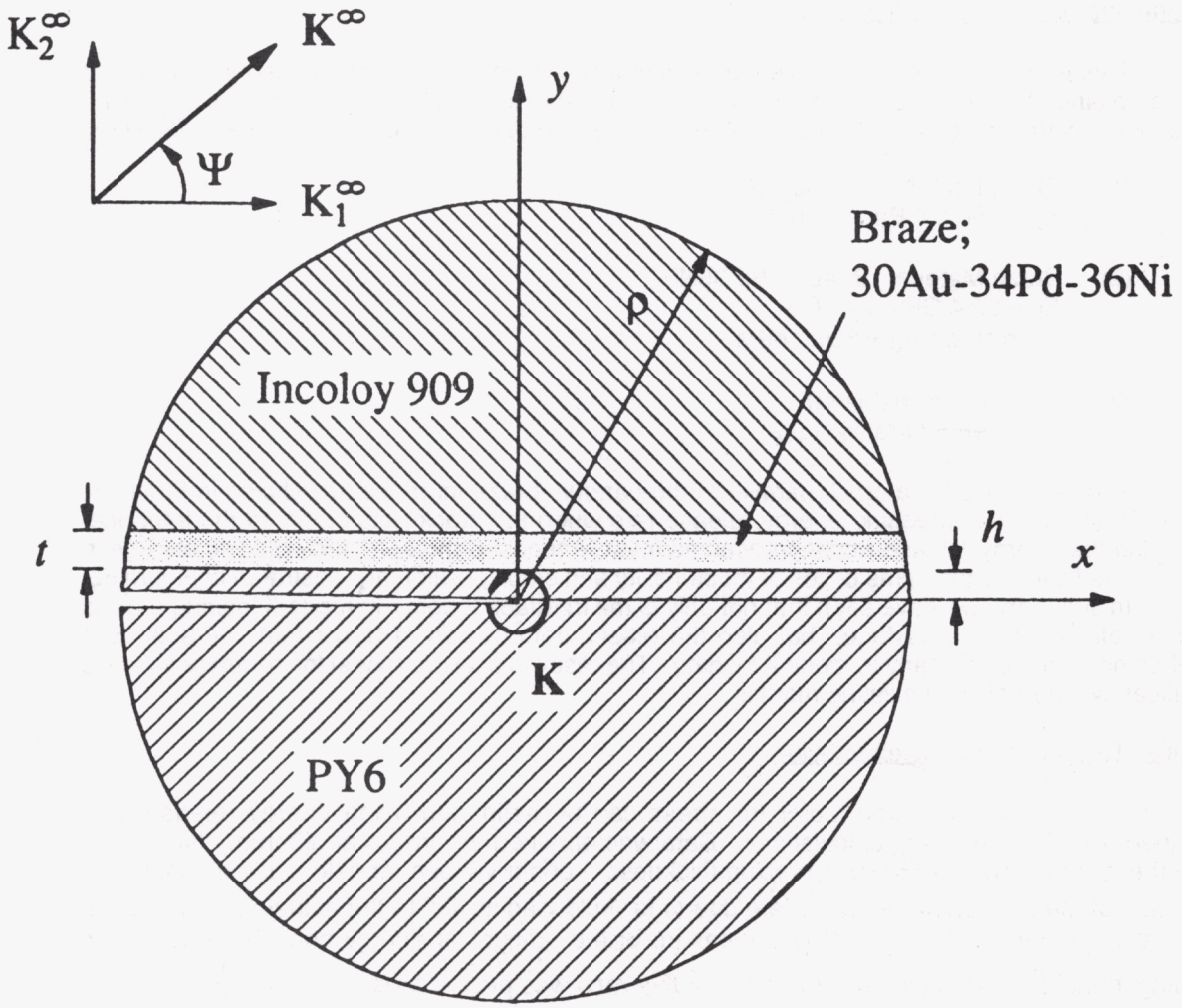

Figure 4: Geometry of the model used to find the effect of a plastic region on bi-material fracture in the ceramic-to-metal braze joint. Note material system studied and definition of *h* and *t*.

In the figures, $\bar{\sigma}^o_{zz} = \sqrt{\rho}\sigma^o_{zz}/|K^\infty|$, and $|\bar{K}^\infty| = |K^\infty|/(\sigma_o\sqrt{\rho})$.

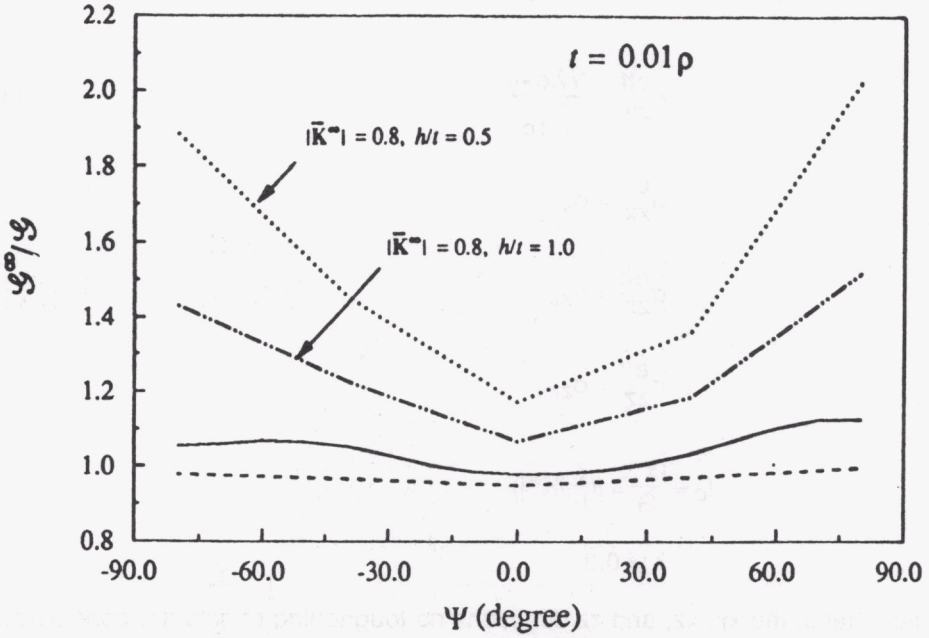

(a) Mode-dependent Toughening

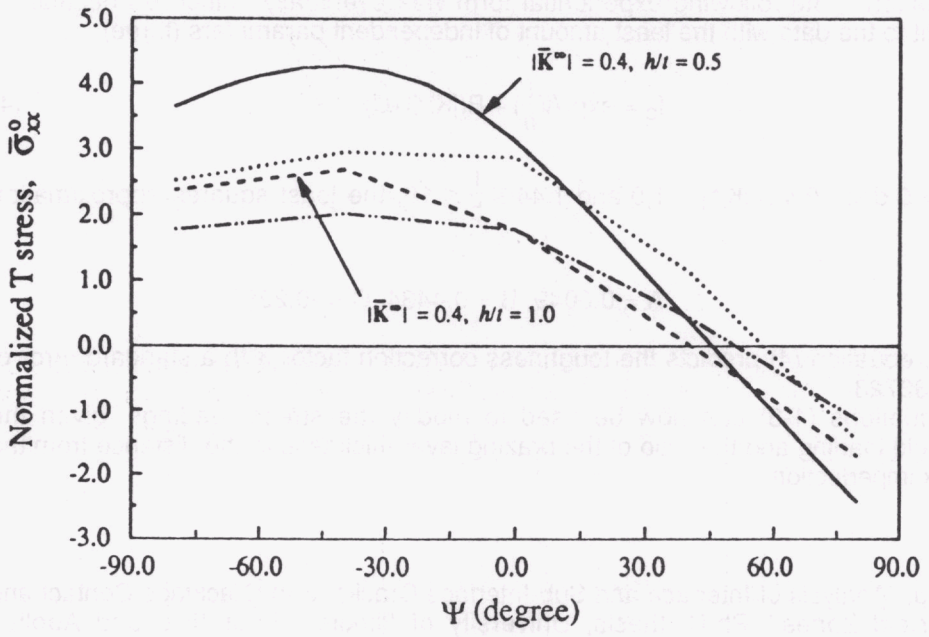

Figure 5: Toughening effect of plastic interlayer (a), and T-stress component values as a function of mode mixity and distance of crack tip from interface (b).

$$\sigma_{xy}^{eff} = \frac{\sqrt{\lambda}\sigma_{xy}}{\sqrt{f_c}} \tag{2}$$

$$\sigma_{zy}^{eff} = \frac{\sqrt{\lambda}\sigma_{zy}}{\sqrt{f_c}} \tag{3}$$

$$\sigma_{xx}^{eff} = \sigma_{xx}$$

$$\sigma_{zz}^{eff} = \sigma_{xz}$$

$$\sigma_{zz}^{eff} = \sigma_{zz}$$

where $$f_c = \frac{G^{\infty}}{G} = f(\frac{t}{h}, |K^{\infty}|)$$

and $$\lambda = 0.3$$

Notice that in the xx, xz, and zz directions no toughening effects are considered, since metal plasticity model affects shear coupons only.

To find f_c, numerous function forms were assumed and tested using a least squares approximation. The following exponential form was eventually settled on because it provided the best fit to the data with the least amount of independent parameters (three):

$$f_c = \exp(A(\frac{t}{h}) + B(|K^{\infty}|) + C) \tag{4}$$

Using data for $\psi = 0$ deg., $0.4 \le |K^{\infty}| \le 1.0$ and $1.44 \le \frac{t}{h} \le 10$, the least squares approximation yields:

$$A = 0.0049,\ B = 0.4434,\ C = -0.2287$$

With these values, equation (4) predicts the toughness correction factor with a standard error of approximately 0.032723.

Equations (1-3) can now be used to modify the stress readings, given the magnitude of far-field loading and the ratio of the brazing layer thickness to the distance from the interface to a crack imperfection.

Publications

Minfa Yang, "Analysis of Interface and Sub-Interface Cracks, with Crackface Contact and Interface Shear Yield Zones," Ph.D. thesis, University of Illinois, Theoretical and Applied Mechanics Dept., Urbana, IL (May 1991) funded in part through subcontract to the University of Illinois.

References

1. N.N. Nemeth, J.M. Mandersheid, and J.P. Gyekenyesi, *Ceramic Analysis and Reliability Evaluation of Structures (CARES) - Users Guide*, NASA Technical Paper 2916, 1989.

2. K.-S. Kim, U. Stigh, and H.C. Choi, "A Study on the Energetic Force of a Point Load," submitted to *Journal of Applied Mechanics*, 1991.

3. B. Moran and C.F. Shih, "Crack Tip and Associated Domain Integrals from Momentum and Energy Balance," *Engineering Fracture Mechanics*, 27, pp. 615-642 (1987).

4. H.C. Choi, K.-S. Kim, and C.F. Shih, "A Study on the Interlayer Effect of the Interface Toughness: Part I, Elasticity Effect," preparing for publication, 1991.

Status of Milestones

On schedule.

Publications

None.

2.0 MATERIALS DESIGN METHODOLOGY

INTRODUCTION

This portion of the project is identified as project element 2 within the work breakdown structure (WBS). It contains three subelements: (1) Modeling, (2) Contact Interfaces, and (3) New Concepts. The subelements include macromodeling and micromodeling of ceramic microstructures, properties of static and dynamic interfaces between ceramics and between ceramics and alloys, and advanced statistical and design approaches for describing mechanical behavior and for employing ceramics in structural design.

The major objectives of research in Materials Design Methodology elements include determining analytical techniques for predicting structural ceramic mechanical behavior from mechanical properties and microstructure, tribological behavior at high temperatures, and improved methods for describing the fracture statistics of structural ceramics. Success in meeting these objectives will provide U.S. companies with methods for optimizing mechanical properties through microstructural control, for predicting and controlling interfacial bonding and minimizing interfacial friction, and for developing a properly descriptive statistical data base for their structural ceramics.

2.1 MODELING

2.1.1 Modeling

Microstructural Modeling of Cracks - J.A.M. Boulet (University of Tennessee, Knoxville)

Objective/scope

The goal of the study is to develop mathematical procedures by which existing design methodology for brittle fracture could accurately account for the influence of protrusion interference on fracture of cracks with realistic geometry under arbitrary stress states. To predict likelihood of fracture in the presence of protrusion interference, a simulation will be developed. The simulation will be based on a three-dimensional model of cracks with realistic geometry under arbitrary stresses.

Technical progress

During the past six months, equations necessary for merging the computer codes BINTEQ[1] and DDID[2, 3] have been put in final form.

BINTEQ performs elastic stress analysis for an *uncracked, finite* domain using a boundary element method (BEM) based on Somigliana's identity[4, 5]. For a *cracked, finite* domain, Somigliana's identity is

$$u_j = \int_S U_{ij}\, t_j\, dS - \int_S T_{ij}\, u_j\, dS - \int_\Gamma T_{ij}\, \Delta u_j\, d\Gamma \qquad (1)$$

where S is the domain's external boundary, u_j is the displacement vector, t_j is the traction vector, T_{ij} and U_{ij} are well-known fundamental solution tensors of linear elasticity, and Γ is the domain's internal boundary (the crack). Through the use of discrete boundary elements, one can transform (1) into

$$[A]\{u_S\} + [E]\{\Delta u_\Gamma\} = [B]\{t_S\} \qquad (2)$$

where $[A]$, $[E]$, and $[B]$ are computed from material properties and the given geometry, $\{u_S\}$ and $\{t_S\}$ are the displacement and traction components, respectively, at element nodes on S, and $\{\Delta u_\Gamma\}$ is the set of displacement discontinuity components at element nodes on Γ. The row dimension of (2) equals the dimension of $\{u_S\}$ and $\{t_S\}$, so that $[A]$ and $[B]$ are square. But the dimension of $\{\Delta u_\Gamma\}$ is, in general, different from that of $\{u_S\}$ and $\{t_S\}$. Thus, $[E]$ is not square. For prescribed boundary tractions, the number of unknowns in (2) is the sum of the dimensions of $\{u_S\}$ and $\{\Delta u_\Gamma\}$. Hence, (2) has more unknowns than equations. When there is no crack (as in BINTEQ), the second term of (2) is absent. Then (2) is a square system and readily solved by standard methods.

DDID performs elastic stress analysis for a *cracked, infinite* domain using a traction boundary integral equation (BIE)[4], rather than Somigliana's identity. For a *cracked, finite* domain, the traction BIE is

$$\sigma_{i3} = \int_S U^{\sigma}_{ki3}\, t_k\, dS - \int_S T^{\sigma}_{ki3}\, u_k\, dS - \int_\Gamma T^{\sigma}_{ki3}\, \Delta u_k\, d\Gamma \qquad (3)$$

where σ_{i3} is the traction vector on Γ, U^{σ}_{ki3} and T^{σ}_{ki3} are well-known fundamental solution tensors of linear elasticity, and all else is as before. Through the use of discrete boundary elements, one can transform (3) into

$$[G]\{u_S\} + [C]\{\Delta u_\Gamma\} = [F]\{t_S\} + [D]\{t_\Gamma\} \qquad (4)$$

where $[G]$, $[C]$, $[F]$, and $[D]$ are computed from material properties and the given geometry, $\{t_\Gamma\}$ is the set of traction components at element nodes on the crack, and all else is as before. The row dimension of $[C]$ and $[D]$ equals that of $\{\Delta u_\Gamma\}$ and $\{t_\Gamma\}$, so that $[C]$ and $[D]$ are square. But since, as noted above, the dimension of $\{u_S\}$ and $\{t_S\}$ is not the same as that of $\{\Delta u_\Gamma\}$ and $\{t_\Gamma\}$, $[G]$ and $[F]$ are not square. For prescribed boundary tractions, (4) has more unknowns than equations. When there is no external boundary (as in DDID), the terms involving $\{u_S\}$ and $\{t_S\}$ are absent. Then (4) is a square system and readily solved by standard methods.

For a *cracked, finite* domain, (2) and (4) together become

$$\begin{bmatrix} [A] & [E] \\ [G] & [C] \end{bmatrix} \begin{Bmatrix} \{u_S\} \\ \{\Delta u_\Gamma\} \end{Bmatrix} = \begin{bmatrix} [B] & [0] \\ [F] & [D] \end{bmatrix} \begin{Bmatrix} \{t_S\} \\ \{t_\Gamma\} \end{Bmatrix} \qquad (5)$$

Equation (5) is a square system and should be solvable by standard methods. Since BINTEQ computes $[A]$ and $[B]$, and DDID computes $[C]$ and $[D]$, it remains to compute $[E]$, $[F]$, and $[G]$. A computer code that does that is under development.

References

1. J. A. M. Boulet, " Microstructural Modeling of Cracks," pp. 254-255 in *CTAHE Project Semiannual Progress Report for October 1990 through March 1991*, ORNL/TM-11859, Oak Ridge National Laboratory, Oak Ridge, Tennessee, 1991.

2. T. A. Cruse and G. Novati, "Traction-BIE Solutions for non-planar and surface cracks," presented at 22nd National Symposium on Fracture Mechanics, June 26-28, Atlanta, Georgia, 1990.

3. J. A. M. Boulet, " Microstructural Modeling of Cracks," pp. 189-192 in *CTAHE Project Bimonthly Technical Progress Report to DOE Office of Transportation Systems, April-May, 1991*, ORNL/CF-91/281, Oak Ridge National Laboratory, Oak Ridge, Tennessee, 1991.

4. T. A. Cruse, *Boundary Element Analysis in Computational Fracture Mechanics*, Kluwer Academic Publishers, The Netherlands, 1988.

5. C. A. Brebbia, et al., *Boundary Element Techniques*, Springer-Verlag, 1984.

Status of milestones

Work is behind schedule.

2.2 CONTACT INTERFACES

2.2.1 Static Interfaces

Elastic Properties and Adherence of Thin Films and Coatings

Debra Joslin (Department of Materials Science and Engineering,
The University of Tennessee)

Objective/Scope

The objective of this research is the examination of the effects of ion bombardment on the structure of thin ceramic films on ceramic substrates. The material combinations will include oxide films that have (a) no solid solubility, (b) limited solid solubility, and (c) complete solid solubility with the substrate material (also an oxide). Techniques for determination of elastic and plastic properties of thin films or coatings on ceramic substrates and for the determination of the strength of the bond between the film and substrate, which are currently being developed, will be used to determine the hardness, elastic modulus, and adherence of each material combination. The main testing techniques will be the ultra-low load microindentation tester (Nanoindenter), and thermal cycling tests.

Technical Highlights

Several.samples.of oxide films (Cr_2O_3 or ZrO_2) were grown on sapphire (Al_2O_3) by rf sputter deposition. The films were all between 80 and100 nm thick. Implantations of 4.7×10^{16} Cr^+ were made at three different temperatures: room temperature, 800°C, and 900°C. The samples were implanted in pairs, one ZrO_2/Al_2O_3 and one Cr_2O_3/Al_2O_3 at each temperature. Rutherford backscattering spectroscopy (RBS) was done on each of the samples to look for mixing of the oxide film and the Al_2O_3.

No mixing of the ZrO_2 was observed at any temperature. For the room temperature implantation, no mixing of the Cr_2O_3 was observed. However, mixing of the Cr_2O_3 was definitely observed at 900°C. Additional RBS spectra on the 800°C implantation were taken at glancing angle to take advantage of the improved depth resolution made possible by tilting the sample. By this technique, it was found that the Cr_2O_3 mixed with the Al_2O_3 at this temperature as well. Samples for transmission electron microscopy are being prepared from these specimens.

Several samples of metal films (Cr or Zr) were grown on sapphire (Al_2O_3) to thicknesses of approximately 50 nm by electron beam evaporation. These samples were implanted at room temperature with 45 keV oxygen ions to a fluence of 5×10^{16} ions-cm^{-2}. The energy was chosen so that the oxygen would be located mostly at the film/substrate interface, maximizing the possibility of chemical mixing of the film and substrate. To retain a portion of unimplanted film, an area of each sample was masked during the implantation. The RBS was performed on each of the samples to look for mixing of the metal film and the Al_2O_3.

No mixing of either film was observed in the initial RBS analysis. The films were then etched off the Al_2O_3 to determine whether ballistic mixing took place. Ballistic mixing can be a very small effect occurring within 10 nm of the interface; this is beyond the resolution of RBS of the film on the substrate. However, etching the film away and analyzing both the implanted area and the unimplanted area for the presence of the metal from the film provides a way to determine whether ballistic mixing took place. If no metal is present on the unimplanted portion, but metal

is present on the implanted portion, ballistic mixing has occurred. Analysis via this technique shows that ballistic mixing did not occur.

In the next report period, Kr will be implanted into similar samples to determine if larger energy deposition at the interface will induce mixing in these systems.

Status of Milestones

N/A

Publications

None

2.2.2 Dynamic Interfaces

Studies of Dynamic Contact of Ceramics and Alloys for Advanced Heat Engines

P. A. Gaydos and K. F. Dufrane (Battelle)

Objective/Scope

The objective of the program is to develop an understanding of the friction and wear processes of ceramic interfaces based on experimental data. The supporting experiments are to be conducted at temperatures to 650 C under reciprocating sliding conditions reproducing the loads, speeds, and environment of the ring/cylinder interface of advanced engines. The test specimens are to be carefully characterized before and after testing to provide detailed input to the model. The results are intended to provide the basis for identifying solutions to the tribology problems limiting the development of these engines.

Technical Highlights

Apparatus

The apparatus developed for this program primarily uses specimens of a flat-on-flat geometry, which facilitates specimen procurement, finishing, and testing. The apparatus reproduces the important operating conditions of the piston/ring interface of advanced engines. The specimen configuration and loading is shown in Figure 1. A crown with a 32 mm radius is ground on the ring specimen to ensure uniform contact. The ring specimen holders are pivoted at their centers to provide self-alignment. A chamber surrounding the specimens is used to control the atmosphere and contains heating elements to control the temperature. The exhaust from a 4500 watt diesel engine is heated to the specimen temperature and passed through the chamber to provide an atmosphere similar to that of actual diesel engine service. A summary of the testing conditions is presented in Table 1.

M.S.U. Ion Implantation

Michigan State University (M.S.U.) has demonstrated the feasibility of implanting ^{7}Be and ^{22}Na ions in ceramic materials for the purpose of wear studies. The intensity of low-level γ radiation emitted from the wear surface of the ion-implanted material can be correlated to the depth of wear. This method is said to be capable of resolving wear as low as 50 nm.

Wear tests were conducted to determine if the implantation itself would influence the wear rate of the material. M.S.U. supplied a number of control Si_3N_4 ring specimens as well as some that were implanted with six doses of 10^{12} particles of ^{20}Ne. This non-radioactive ion is similar in size to ^{22}Na and should produce similar

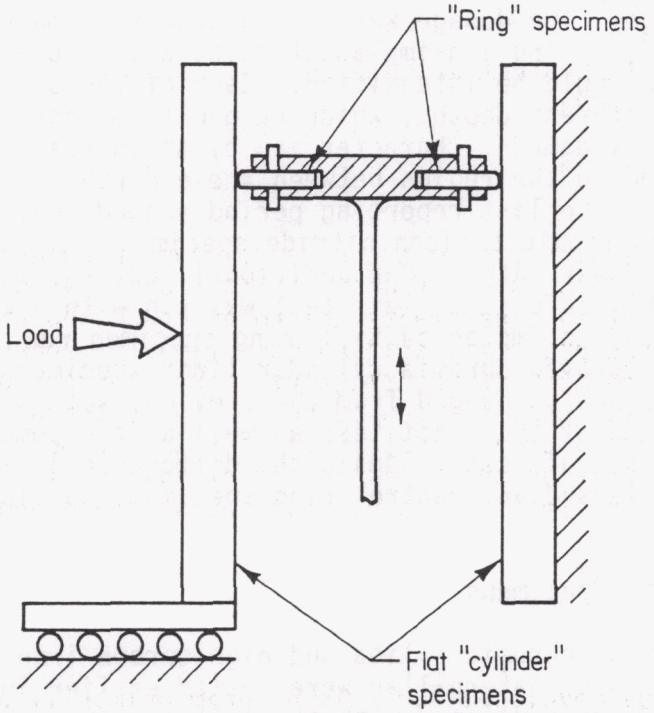

FIGURE 1. TEST SPECIMEN CONFIGURATION AND LOADING

TABLE 1. SUMMARY OF TESTING CONDITIONS

Sliding Contact:	Dual flat-on-flat
"Cylinder" Specimens:	12.7 x 32 x 127 mm
"Ring" Specimens:	3.2 x 19 x 19
"Ring" crown radius:	32 mm
Motion:	Reciprocating, 108 mm stroke
Reciprocating Speed:	500 to 1500 rpm
Average Specimen Speed:	1.8 x 5.4 m/s
Load:	to 950 N
Ring Loading:	to 50 N/mm
Atmosphere:	Diesel exhaust or other gases
Measurements:	Dynamic friction (during test) Specimen wear (after test)

radiation damage. The dosage was 2 to 3 orders of magnitude higher than required for using ion-implantation as a wear diagnostic tool so that any damage would be intensified. Each of the six doses was implanted to different depths, which ranged from less than 5 μm to about 10 μm. Any damage, characterized by an increase in wear rate, would be located in the region between these depths.

Results from the last reporting period showed that the implanting ^{20}Ne ions in monolithic silicon nitride specimens had no measurable effect on their wear rates. One additional test was run to gather more wear data on this material. This test was run with a control Si_3N_4 ring specimen and an implanted Si_3N_4 ring specimen run simultaneously against plasma sprayed chromia cylinder liner specimens. The test conditions remained unchanged from the previous set of tests. Table 2 shows the results of this last test as well as the compiled results from the first set of tests. Again the difference in wear factors between the implanted and control ring specimens was insignificant.

Caterpillar Wear Specimens

Plasma sprayed chromia-silica and high carbon iron-molybdenum coatings supplied by Caterpillar were tested earlier in this program. These coatings were developed with the criteria that they not only be wear resistant but also be viable from a manufacturing standpoint. Before presenting the most recent results, a summary of these previous tests will be given.

In past tests with the Caterpillar coatings, ring specimens made from the chromia-silica were run against high carbon iron-molybdenum cylinder liner specimens and were shown to have excellent wear resistance. Ring wear rates were as low as 4×10^{-9} $mm^3/N\text{-}m$ for some test portions. Other material pairs tested in this program came close to this wear performance, but many were not materials one would consider using in production engines.

The target baseline wear rate is that of conventional hard chrome and cast iron sliding pairs tested at current engine operating temperatures (i.e. increase the top ring reversal temperature without sacrificing wear life). When hard chrome ring specimens and cast iron cylinder liner specimens were tested in the Battelle wear apparatus, a ring wear rate of 3×10^{-9} $mm^3/N\text{-}m$ was obtained. Considering the normal variability in the wear data can be a half an order of magnitude or more, the Caterpillar specimens had met the baseline goal. More importantly, the specimens had met the wear goal at a top ring reversal temperature of 260 C, which is higher than the baseline temperature in today's engines.

TABLE 2. WEAR RATES OF SILICON NITRIDE RING SPECIMENS AGAINST PLASMA SPRAYED CHROMIA CYLINDER SPECIMENS (mm^3/N-m)

(SDL-1 lubricant, room temperature, 12.3 N/mm ring load, 500 cpm)

^{20}Ne Ions?	Test Number & Portion	Run Duration Min.	Wear of Specimen in Left Position	Wear of Specimen in Right Position	Average Wear of all Test Portions
No	92a	60		8×10^{-8}	4×10^{-8}
	b	120		1×10^{-8}	
	c	120		2×10^{-8}	
Yes	92a	60	6×10^{-8}		3×10^{-8}
	b	120	6×10^{-9}		
	c	120	2×10^{-8}		
Summary of Test Numbers 88-91					
Average Wear of all Control Specimens					2×10^{-8}
Average Wear of all Implanted Specimens					2×10^{-8}

Recent Tests - Caterpillar coatings showed unusually good performance even though they are based on a plasma sprayed chromia-silica ring coating very similar to a plasma sprayed chromia coating that had been used in this program for several years. The difference seemed to be in the use of a more conventional mating cylinder liner material. The high carbon iron-molybdenum is not quite as hard as other ceramic coatings tested in the past and would not be expected to wear the ring coatings as quickly. To evaluate this possibility, two ring materials that performed very well in the past against plasma sprayed chromia cylinder liner coatings were tested against the high carbon iron-molybdenum liner specimens. The ring materials tested were plasma sprayed chromia (Cr_2O_3) and a monolithic silicon carbide whisker reinforced alumina (Al_2O_3 + SiC).

Table 3 shows the results of the wear tests. Test Numbers 84-86 were the earlier tests with the Caterpillar coatings, test Number 93 was with Al_2O_3 + SiC ring specimens, and test Number 94 was with plasma sprayed Cr_2O_3 rings. The wear rates of all of the ring materials against the high carbon iron-molybdenum cylinder liners are about the same. On this basis, the wear performance of the Caterpillar chromia-silica coatings was similar to that measured with the previously tested coatings.

TABLE 3. WEAR RATES OF VARIOUS RING MATERIALS AGAINST HIGH CARBON IRON AND MOLY CYLINDER LINER SPECIMENS (mm^3/Nm)
(SDL-1 LUBRICANT*, 12.3 N/mm RING LOAD, 500 cpm)

Test Number & Portion	Ring Material	Test Temperature °C	Run Duration Min.	Friction Coefficient Range	Average Ring Wear Rate During Test
84 a		25	60	0.10 - 0.14	2×10^{-8}
b	Cr_2O_3 + Si	260	240	0.08 - 0.11	4×10^{-9}
c	(Caterpillar)	260	240	0.09 - 0.13	2×10^{-8}
85 a		25	60	0.11 - 0.13	1×10^{-8}
b	Cr_2O_3 + Si	260	240	0.10 - 0.13	4×10^{-9}
c	(Caterpillar)	260	240	0.07 - 0.10	2×10^{-8}
86 a	Cr_2O_3 + Si	25	60	0.09 - 0.10	4×10^{-9}
b		260	240	0.13 - 0.20	7×10^{-9}
c	(Caterpillar)	315	240	0.11 - 0.13	1×10^{-8}
d		315	240	0.10 - 0.13	2×10^{-8}
93 a	SiC whisker	25	60	0.08 - 0.09	5×10^{-9}
b	Reinforced	260	240	0.07 - 0.10	6×10^{-9}
c	Al_2O_3	260	240	0.07 - 0.09	2×10^{-8}
d	(ACMC)	260	480	0.07 - 0.10	6×10^{-9}
94 a	Cr_2O_3	25	60	0.08 - 0.09	5×10^{-9}
b		260	240	0.08 - 0.10	7×10^{-9}
c	(Battelle)	260	480	0.08 - 0.10	6×10^{-9}

*Test 86 was run with Lubrizol OS-80001H lubricant in order to reach the higher operating temperatures.

Lastly, the friction of the Caterpillar chromia-silica rings tended to be slightly higher, with coefficients typically above 0.1. The friction coefficients of the other two materials under the same conditions were typically less than 0.1.

Curved Caterpillar Wear Specimens - In order to better duplicate the ring and cylinder interface in actual engines, Caterpillar also supplied wear specimens that were cut from engine components. Ring sections coated with aluminum titanate (KP123) and cermet (KP107E) were supplied, as well as cylinder liner sections coated with Kaman Science SCA. These curved specimens were intended to be wear tested in Battelle's engine simulation rig without much modification.

When the specimens were undergoing initial test preparation, it was discovered that the curvatures of the ring and cylinder liner sections did not match. The ring sections had a radius of curvature equal to that of the component ring in the relaxed state. Because this radius of curvature was larger than that of the cylinder liner specimens, the only points of contact between the wear specimens were at the ends of the ring sections.

Several approaches were considered to correct the mismatch. Plastically bending the ring sections to a smaller curvature was not possible due to the brittle nature of the ring material. Heating the sections and then plastically bending them was not considered feasible because of the possibility it would affect the microstructure of the base material and/or the coating. Relief slots cut into the back side of the ring to reduce the stresses during bending were found to close the ring curvature enough (presumably from internal stresses) so that it matched the liner section. However, subsequent welding of the slotted ring section to a backing (which could then be clamped in the engine rig) returned the ring section to its original mismatched curvature.

To hold the slotted ring specimens without welding, a properly sized piston will be obtained from Caterpillar. A holder will then be cut from a portion of the piston that contains the ring groove, as shown in Figure 3. The piston section and end plates and will simply capture the ring section, and the normal load applied to the ring specimens will hold them in place during the tests as shown in Figure 2. Wear tests will be conducted during the next reporting period.

Status of Milestones

The study is progressing in accordance with the overall milestone schedule.

Publications

None.

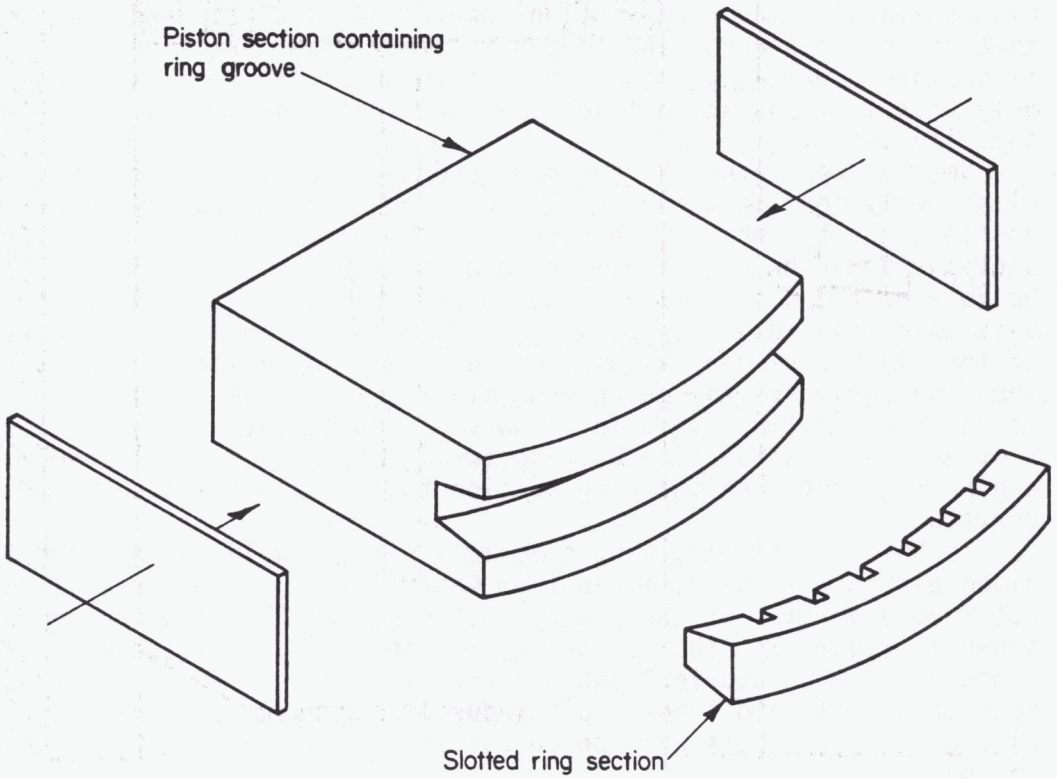

FIGURE 2. PROPOSED RING SPECIMEN HOLDER

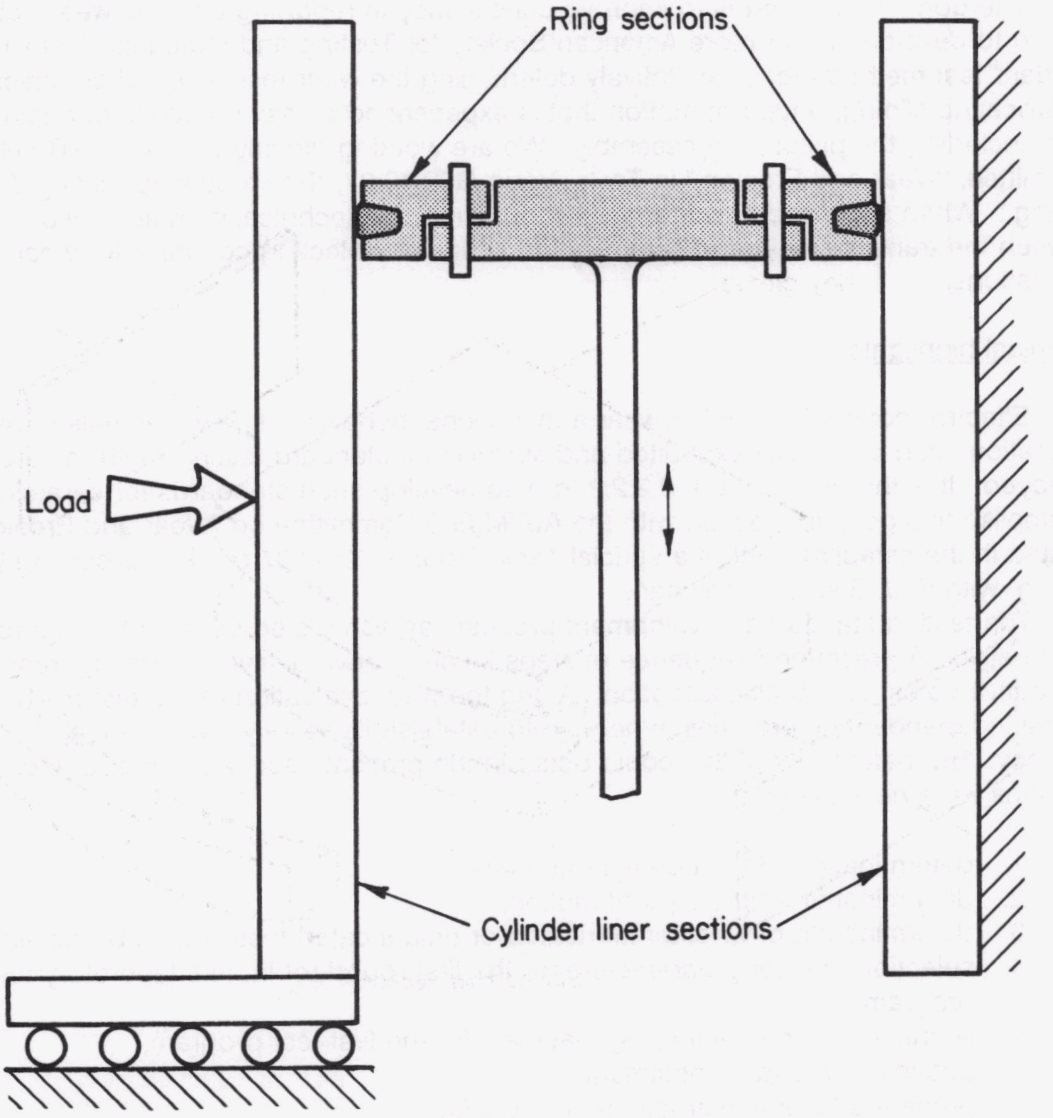

FIGURE 3. PROPOSED CONFIGURATION FOR CURVED RING AND CYLINDER SPECIMENS

Development of Standard Test Methods for Evaluating the Wear Performance of Ceramics

P. J. Blau (Oak Ridge National Laboratory)

Objective/scope

The goal of this effort is to improve consistency in reporting ceramic wear data by helping to develop one or more American Society for Testing and Materials (ASTM) standard test methods for quantitatively determining the wear resistance of ceramics in reciprocating sliding, a type of motion that is experienced by several types of engine wear parts, including the piston/ring assembly. We are working directly with the ASTM G-2 Committee, "Wear and Erosion," in Task Group G02.40.07, "Reciprocating Sliding Wear Testing." When approved, this standard should improve technical communication between the transportation and ceramics industries on selecting ceramics for wear applications.

Technical highlights

Effective comparison of the wear and frictional behavior of new materials for engine applications can be greatly expedited and simplified if standard testing methods are employed. It is the goal of Task 2.2.2.2 to help develop such standards for ceramics. To accomplish this goal, interaction with the ASTM G-2 Committee on "Wear and Erosion" resulted in the establishment of a special Task Group G02.40.07 on "Reciprocating Wear Testing" with P. J. Blau as Chairman.

The testing standards development process, as conducted by ASTM, is rigorous and iterative. A prescribed sequence of steps involves several levels of voting, resolution of negative votes, and finally, adoption. Along the way, evaluation of the test method in several independent laboratories is needed to establish its validity, precision, and accuracy. But before any of this could occur in the present case, a number of technical decisions were necessary:

1. determination of the contact geometry,
2. determination of the type of motion,
3. determination of whether lubricated or unlubricated tests would be developed,
4. selection of testing parameters for the first round-robin, interlaboratory test program,
5. securing and characterizing materials for the first test program,
6. obtaining testing commitments,
7. preparing testing instructions (protocols),
8. conducting the round-robin tests,
9. collecting and analyzing data according to valid statistical methods, and
10. obtaining subcommittee approval on major decisions.

In the last six months, the ball-on-flat test geometry and reciprocating motion was selected. The test will be a reciprocating type because many engine components experience this type of motion. We have chosen to use our commercial testing machine (Cameron-Plint TE-77) as the basis for the procedure because there are more than 60 machines of that type in use all over the world. More importantly, several of the major

engine companies like Cummins Engine Company and Caterpillar, Inc., own such machines.

A diagram of the Cameron-Plint machine is shown in Fig. 1. The basic geometry is ball-on-flat. The ball is clamped on the moving holder. Oscillating speeds typically range from 5 to 50 Hz, and stroke lengths can be varied from about 1 to 10 mm. A survey of Task Group participants was conducted to determine the range of capabilities of their own machines. Some potential participants own Cameron-Plint machines, but others have homemade reciprocating testers than might fall within the range of our testing conditions. Initial testing protocols will be for unlubricated testing, but the manufacturer of the machine is planning a concurrent lubricated testing program, and we will coordinate with that effort to some degree.

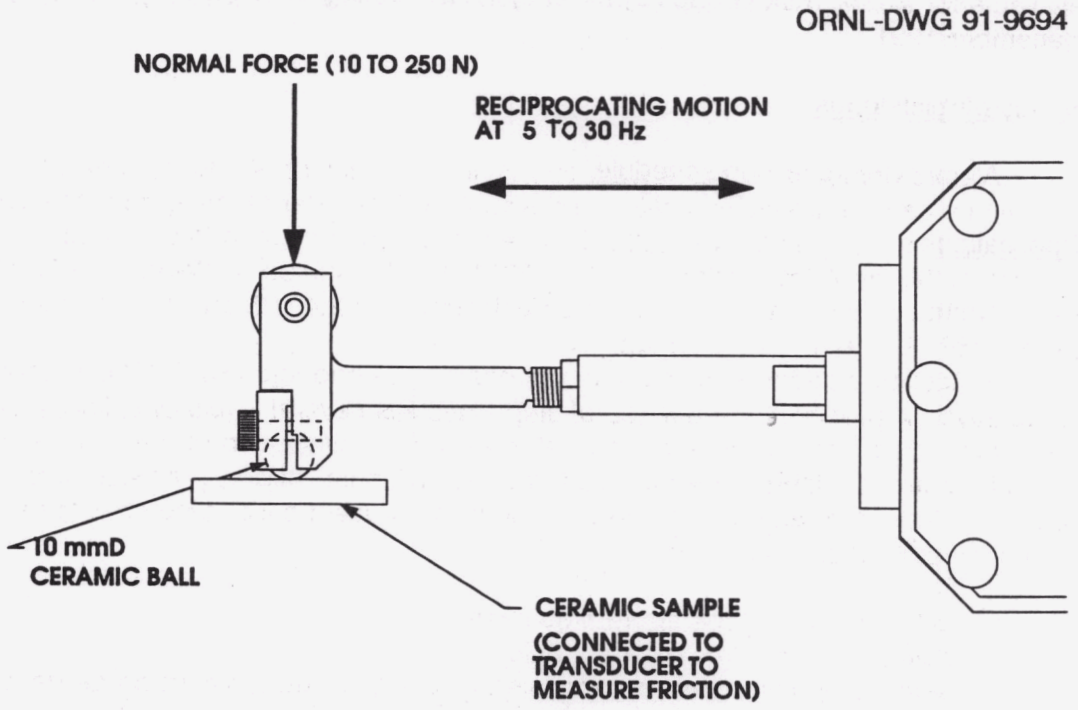

Fig. 1. Schematic drawing of the Cameron-Plint TE-77 fixture showing typical operating conditions. Initial tests at Oak Ridge National Laboratory will help determine the conditions for the first round-robin test program with steel and silicon nitride ball and flat specimens. Preliminary studies suggest that 5 Hz with a 10-mm stroke is in the range of most Task Group members' equipment. A 25-N load will be used as the first for unlubricated tests. Lubricated tests may require higher loads.

The acquisition of well-characterized wear test specimens for beginning a round-robin testing program is continuing. Efforts to locate a commercial source of M-50 tool steel, flat-specimen materials were unsuccessful. Therefore, it was decided to purchase a more readily available material for the flat specimen. D-2 tool steel was felt to be a good

candidate material, and a supply was ordered. M-50 steel balls are readily available, and several hundred are already on hand.

Silicon nitride spheres will be obtained, as will silicon nitride modulus of rupture (MOR) bars. These will be used as ceramic test specimens. The number of specimens per set and the number of tests per material per laboratory are yet to be determined. These numbers will in part be affected by the number of organizations involved and the amount of material available.

Several companies, including Caterpillar, Inc., and Cameron-Plint, have expressed an interest in participating in the round-robin testing program. Once specimens have been procured and prepared as packages, with protocols included, final commitments to participate will be obtained.

The development of a simple set of test protocol instructions (e.g., specimen cleaning, handling, recording of data, etc.) to be included with the specimen sets will be available for ASTM Task Group review at the G-2 meeting in Philadelphia, Pennsylvania, in December 1991.

Status of milestones

All milestones are on schedule.

Publications

None.

2.3 NEW CONCEPTS

Advanced Statistical Concepts of Fracture in Brittle Materials

C. A. Johnson and W. T. Tucker (General Electric Corporate Research and Development, Schenectady, NY 12301

Objective/Scope

The design and application of reliable load-bearing structural components from ceramic materials requires a detailed understanding of the statistical nature of fracture in brittle materials. The overall objective of this program is to advance the current understanding of fracture statistics, especially in the following four areas:

- Optimum testing plans and data analysis techniques.
- Consequences of time-dependent crack growth on the evolution of initial flaw distributions.
- Confidence and tolerance bounds on predictions that use the Weibull distribution function.
- Strength distributions in multiaxial stress fields.

The studies are being carried out largely by analytical and computer simulation techniques. Actual fracture data are then used as appropriate to confirm and demonstrate the resulting data analysis techniques.

Technical Highlights

During this reporting period, work has continued on assessing the effects of the equivalence, as shown in recent semiannual contract reports, of the Batdorf-Heinisch (B-H) (Ref. 1) and Lamon-Evans (L-E) (Ref. 2) approaches to multiaxial stress states. In these reports, it has been further shown that by employing this equivalence, a "size" factor, denoted by I, can be determined for general loading geometry, specimen geometry, and choice of multiaxial failure criterion. This size factor, I, can be shown to be the multiaxial counterpart of the size factor, k, that is conventionally used in the exponent of the uniaxial size-scaled Weibull distribution function. The product of k times volume (or surface area, if appropriate) is often referred to as the effective volume under uniform tensile stress. The product of I times volume (or area) can now be interpreted in an analogous fashion as the volume that is effectively in a "standard" stress state. The standard stress state in the uniaxial case is almost universally defined as the maximum principal tensile stress anywhere in the structure. The standard stress state in the multiaxial case could be any of several possible choices that are being considered.

When finite element stress analysis is used for components with complex geometries, non-uniformly stressed elements result in more accurate results than a comparable number of constant stress elements. The benefit from non-uniformly

stressed elements is even greater in the case of multiaxial probabilistic effects. The equivalence of B-H to L-E shows that effects due to geometry, loading, and multiaxial stress can all be accounted for by a generalized size factor. This size factor can be applied on an elemental basis or to the component structure as a whole.

The remainder of this semiannual report will discuss the definition, interpretation and importance of the multiaxial size factor, I. This will include the relationship to k and potential uses of I.

A General Size Factor

As shown in earlier reports, another way to determine the probability of failure for a component under multiaxial loading is from

$$P_f = 1 - \exp\left[-I(m)V\sigma_M^m/\sigma_0^m\right], \tag{1}$$

where

$$I(m) = \frac{1}{2\pi V}\int_0^{\pi/2}\int_0^{2\pi}\int_V (\sigma_e/\sigma_M)^m dv \cos\phi d\phi d\psi. \tag{2}$$

In (1) and (2) V is the component size, m is the Weibull modulus (shape factor), σ_0 is the inherent strength (scale factor), σ_e is a stress function defined by the selected failure criterion, and σ_M is the maximum value of σ_e in the component. Also σ_e is a function of the local principal stresses (and hence location) and the orientation of the principal plane of a potential failure producing flaw; this accounts for the limits of integration in (2). The importance of (1) lies in the fact that all methods developed to date for combining data and obtaining confidence bounds (via bootstrapping and likelihood methods) have a direct application in (1). This follows since for a given loading, geometry, and failure criterion, the I factor given by (2) is only a function of m. Thus, at worst, for a particular problem (2) need be determined only once. Evaluation of (2) may be laborious and the best way to proceed in the case of non-uniformly stressed elements is open at this point.

$I(m)$ as defined by (2) has some interesting properties. Since σ_M is defined here as the maximum of σ_e for any orientation and position in the component, then the ratio σ_e/σ_M must be less than or equal to one. Therefore the maximum possible value of $I(m)$ is unity in this setup. It is clear that the lower bound of (2) is zero, so that $0 \le I(m) \le 1$. While any other value of the effective stress that is in a one-to-one relationship to σ_M could be employed in (2), the maximum is an obvious choice and is consistent with the physical mechanism of failure. Furthermore, suppose that the component is in a state of equal triaxial loading. Then with all presently proposed forms for σ_e the ratio σ_e/σ_M is unity, since there is no shear component in any orientation. In this case $I(m)$ achieves its upper bound of unity with σ_M as defined. However, note that with this definition, $I(m)$ may not reduce directly to k, as will be shown below.

Orientation Independent Models

By assuming appropriate forms for σ_e, it can be shown that (2) is consistent with the usual failure models developed by Weibull (Ref. 3). The first model studied by Weibull was for a uniform stress state. In extending this model to non-uniform stress states Weibull tacitly assumed that the failure criterion was independent of the angles ϕ and ψ in (2). (See Ref. 3, Eq.'s 49-57.) With this assumption, (2) reduces to

$$I(m) = \frac{1}{V}\int_V (\sigma_e/\sigma_M)^m dv . \tag{3}$$

Possibly, the simplest form for σ_e for use in (3) is $\sigma_e = \sigma_1$ for $\sigma_1 \geq 0$, and zero otherwise, which was studied in some detail by Weibull. By further approximating σ_1 with the longitudinal tensile stress it can be shown that (3) gives the standard evaluations of k for 3-point and 4-point bending, etc. For example, in the case of uniform axial tension it is straightforward to show that the value of (3) is unity. In the case of three point bending with a volume failure mode, (3) becomes

$$I(m) = 1/(2(m+1)^2) \tag{4}$$

where the integration is carried out only over that portion of the specimen that is in a state of tension.

Moreover, any of the classical failure models, that are orientation independent, (e.g., it is assumed that the critical flaw is in the worst orientation) can be used in the context of (3). Indeed as noted by Nadai (Ref. 4), the model given by

$$\sigma_e = \frac{1}{2}[\sigma + \sqrt{\sigma^2 + Q^2\tau^2}], \tag{5}$$

(where σ is the stress component normal to the crack surface, τ is the shear component parallel to the crack surface, and Q is a "material" constant), can be reformulated as a functional relationship only involving the principal stresses σ_1 and σ_3. In the notation of (5) where σ_e is set equal to σ_c, (the critical stress that just produces failure), Equation (5) can be solved by finding the conditions at which the largest principal Mohr's circle just touches the parabola resulting from the failure criterion of (5) when plotted as σ versus τ. The result is

$$\left(\frac{\sigma_1 - \sigma_3}{2}\right)^2 = \frac{4}{Q^2}\sigma_c^2\left(1 - \frac{1}{Q^2}\right) - \frac{4}{Q^2}\sigma_c\left(\frac{\sigma_1 + \sigma_3}{2}\right), \tag{6}$$

when $\sigma_1 - \sigma_3 \geq (4/Q^2)\sigma_c$. Otherwise, a set of solutions exists with $\sigma_c = \sigma_1$ which are given by all σ_3 such that

$$\frac{4}{Q^2}\sigma_c > \sigma_c - \sigma_3 . \tag{7}$$

When (6) and (7) are used in (3), a failure criterion is produced that is shear sensitive but, at the same time, is independent of orientation. The model given by (5) is based on the assumptions that fracture does not occur in a state of equal triaxial

compression and that fracture does occur for some states of compressive loading driven by non-zero shear stresses. All of this is discussed in great detail by Nadai, (Ref. 4, Chapter 15). Also an in depth study of failure criteria is given by Nadai in Chapter 15.13 in which various theories are discussed and compared.

Orientation Dependent Models

The second model studied by Weibull is given by $\sigma_e = \sigma$ for $\sigma \geq 0$, and zero otherwise. This is the so called normal stress model or criterion. For the normal stress model and a loading of uniform axial tension, $\sigma_e = \sigma_1 \cos^2(\phi)$. Then, since the volume terms integrate out, (2) becomes

$$I(m) = \frac{2}{\pi}\int_0^{\pi/2} \cos^{2m+1}(\phi) d\phi \int_0^{\pi/2} \cos^{2m}(\psi) d\psi$$

$$= 1/(2m+1). \tag{8}$$

This is in effect Eq. 36 of Ref. 3. In the situation of biaxial loading σ_3 is zero so that the failure criterion is $\sigma_e = \sigma = \cos^2(\phi)(\sigma_1 \cos^2(\psi) + \sigma_2 \sin^2(\psi)$. Again the size terms integrate out, but the remaining integral cannot be obtained in closed form. The final result is

$$I(m) = \frac{1}{2\pi}\int_0^{\pi/2}\int_0^{2\pi} \cos^{2m+1}(\phi)\left[\cos^2(\psi) + \frac{\sigma_2}{\sigma_1}\sin^2(\psi)\right]^m d\phi d\psi, \tag{9}$$

which is essentially Eq. 39 of Ref. 3. Equations (8) and (9) (and Eq.'s 36 and 39 of Ref. 3) show that this failure model is not independent of orientation. Indeed I is $1/(2m+1)$ for uniform axial tension and not unity as is the case for the maximum principal stress model. Thus, if one were to employ the normal stress criterion and wished that I were unity under uniaxial loading, then a rescaling of (2) is required. As previously indicated, determination of the standard stress state for situations of multiaxial loading is under study.

Concluding Remarks

Careful study of these two models (or model forms) indicates that the essential difference is in the way orientation effects are considered. For example, models such as maximum principal stress that are orientation independent have the property that failure *always* occurs when the σ_e just reaches a cutoff value. This is shown clearly by (6) and (7). On the other hand, orientation dependent models, such as the normal stress criterion or (5) applied directly in (2), can have values of σ_e at which failure occurs for some orientations and not for others. This latter situation is much more satisfying from a physical viewpoint, since a failure model that is orientation independent requires that the critical flaw is always in the worst orientation, (i.e. there are an infinite number of flaws of non-zero size, or that the flaws are spherical in nature). While these conditions might be appropriate for certain special situations, it is doubtful that any can hold in general.

References

1. S.B. Batdorf and H.L. Heinisch (1978), "Weakest Link Theory Reformulated for Arbitrary Fracture Criterion," *J. Am. Ceram. Soc.,* **61,** 7-8, 355-58.

2. J. Lamon and A.G. Evans (1983), "Statistical Analysis of Bending Strengths for Brittle Solids: A Multiaxial Fracture Problem," *J. Am. Ceram. Soc.,* **66,** 3, 177-82.

3. W. Weibull, "A Statistical Theory of the Strength of Materials," *Royal Swedish Academy of Eng. Sci. Proc.,* **151,** 1-45, 1939.

4. Nadai, A. (1950), *Theory of Flow and Fracture of Solids,* Vol. I, Engineering Societies Monographs, McGraw-Hill Book Company, New York.

Status of Milestones

All milestones are on schedule.

Publications

None.

3.0 DATA BASE AND LIFE PREDICTION

INTRODUCTION

This portion of the project is identified as project element 3 within the work breakdown structure (WBS). It contains five subelements, including (1) Structural Qualification, (2) Time-Dependent Behavior, (3) Environmental Effects, (4) Fracture Mechanics, and (5) Nondestructive Evaluation (NDE) Development. Work in the Structural Qualification subelement includes proof testing, correlations with NDE results and microstructure, and application to components. Work in the Time-Dependent Behavior subelement includes studies of fatigue and creep in structural ceramics at high temperatures. Research in the Environmental Effects subelement includes study of the long-term effects of oxidation, corrosion, and erosion on the mechanical properties and microstructures of structural ceramics. Work in the Fracture Mechanics subelement includes development of techniques for measuring the tensile strength and creep resistance of ceramic materials at high temperatures, and testing ceramic materials at high temperatures under uniaxial tension. Work in the NDE Development subelement is directed at identifying approaches for quantitative determination of conditions in ceramics that affect their structural performance.

Major objectives of research in the Data Base and Life Prediction project element are understanding and application of predictive models for structural ceramic mechanical reliability, measurement techniques for long-term mechanical property behavior in structural ceramics, and physical understanding of time-dependent mechanical failure. Success in meeting these objectives will provide U.S. companies with the tools needed for accurately predicting the mechanical reliability of ceramic heat engine components, including the effects of applied stress, time, temperature, and atmosphere on the critical ceramic properties.

3.1 STRUCTURAL QUALIFICATION

Microstructural Analysis of Structural Ceramics

B. J. Hockey and S. M. Wiederhorn
(National Institute of Standards and Technology)

Objective/Scope

The objective of this part of the program is to identify mechanisms of failure in structural ceramics subjected to mechanical loads at elevated test temperatures. Of particular interest is the damage that accumulates in structural ceramics as a consequence of high temperature exposure to stresses normally present in heat engines.

Design criteria for the use of ceramics at low temperature differ from those at high temperature. At low temperature ceramics are elastic and brittle; failure is controlled by a distribution of flaws arising from processing or machining operations, and the largest flaw determines the strength or lifetime of a component. By contrast, at high temperature where ceramics are viscoelastic, failure occurs as a consequence of accumulated, or distributed damage in the form of small cavities or cracks that are generated by the creep process. This damage effectively reduces the cross-section of the component and increases the stress that must be supported. Such increases in stress are autocatalytic, since they increase the rate of damage and eventually lead to failure as a consequence of loss in cross section. When this happens, the individual flaw loses its importance as a determinant of component lifetime. Lifetime now depends on the total amount of damage that has occurred as a consequence of the creep process. The total damage is now the important factor controlling lifetime.

Recent studies of high temperature failure of the non-oxide ceramics intended for use for heat engines indicates that for long term usage, damage accumulation will be the primary cause of specimen failure. Mechanical defects, if present in these materials, are healed or removed by high temperature exposure so that they have little influence on long term lifetime at elevated temperature. In this situation, lifetime can be determined by characterizing the damage and the rate of damage accumulation in the material at elevated temperatures. In ceramic materials such as silicon nitride and SiAlON, such characterization required high resolution analyses because of the fine grain size of these materials: hence the need for transmission electron microscopy as an adjunct to the mechanical testing of ceramics for high temperature applications is apparent.

In this project, the creep and creep-rupture behavior of several ceramic materials will be correlated with microstructural damage that occurs as a function of creep strain and rupture time. Materials to be studied include: SiAlON; hot-pressed silicon nitride; sintered silicon carbide. This project will be coordinated with WBS 3.4.1.3, Tensile Creep Testing, with the ultimate goal of developing a test methodology for assuring the reliability of structural ceramics for high temperature applications.

Technical Highlights

During the past six months microstructural analyses studies were initiated on Garrett GN-10 silicon nitride to determine the effect of microstructure on tensile creep behavior. As tensile creep invariably results in cavitation, an emphasis is being placed on characterizing cavitation damage and on describing the cavity nucleation and growth processes. Although the study of this material is still in its initial stages, results have been obtained on three different creep samples tested to failure at 1250°C (100 and 150 mPa) and at 1375°C (75 mPa) under Task 2. These results, Summarized in this report, allow a generalized description of the microstructure and the cavitation process.

Experimental Technique

The bulk of the results described in this report were obtained by analytical transmission electron microscopy. So far, observations have been limited to three tensile creep rupture samples, whose test temperatures, supplied stresses, and failure times, respectively were: 1250°C, 100 mPa, ~1000h; 1250°, 150 mPa, 220h; 1375°, 75 mPa, 1.5h.

In each case, multiple slices were made parallel to the tensile stress axis to obtain sections from the interior and from the near-(exposed) surface. Prior to final TEM specimen preparation, these polished sections were examined optically for evidence of creep cracks.

Results and Discussion

Examination of GN-10 revealed a silicon nitride matrix of variable grain size and morphology, Fig. 1. Grain shapes could be broadly classified as either equi-axed or acicular (typically with aspect ratios exceeding 3); grain dimensions generally ranged from ~0.2 to 3 microns, although acicular grains of 5 microns or more in length were not uncommon. The microstructure of crept samples also contained a relatively high volume fraction of a crystalline second phase grains, generally of irregular morphology and sub-micron size, Fig. 2. The presence of this second phase is clearly a result of devitrification of intergranular glass, originally present within multi-grain junctions, due to high temperature exposure either during creep testing or post processing annealing. Identification of the second phase has not been completed, however, EDS results indicate a yttrium-strontium-calcium silicate(s). In most cases, these results suggest a mole ratio of 1:1 for Y_2O_3:SiO_2, the primary constuients. While no estimate can yet be made on the strontia content, the calcia concentration is estimated to be $\lesssim$ 2 wt%.

Preliminary analyses of interfaces separating both adjacent silicon nitride grains and adjacent silicon nitride and second phase grains suggest the presence of a narrow, glassy interfacial layer. For adjacent silicon nitride interfaces, EDS spectra invariably show detectable intensity peaks for oxygen, strontium, and yttrium.

Figure 1. Representative view of microstructure of GN-10 silicon nitride illustrating varied ß-Si_3N_4 grain morphology and size.

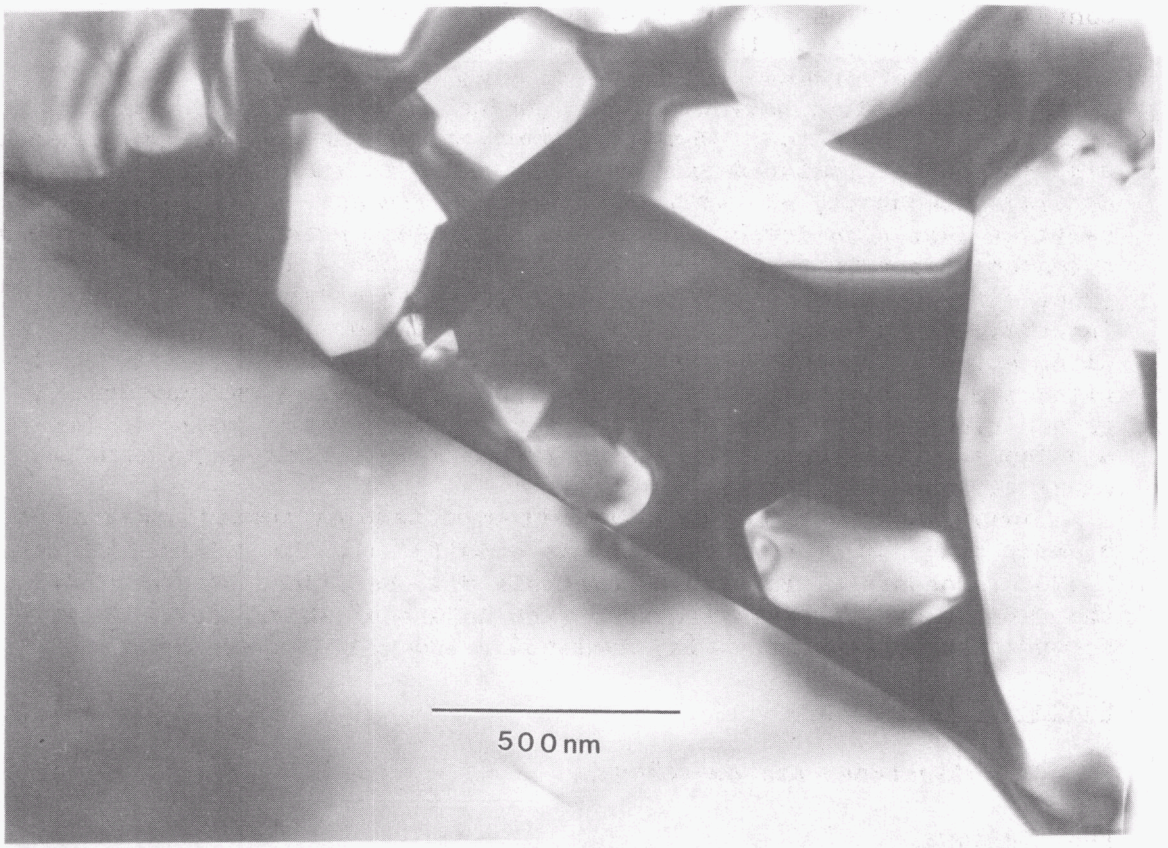

Figure 2. Region of GN-10 containing high concentration of similarily-oriented second phase crystallites (dark contrast), produced by devitrification of glass originally present during sintering.

Significantly, the strontium to yttrium kα peak ratios from these interfaces are roughly three times larger than that for the crystalline second phase, suggesting a relative enhancement of strontia (or alternatively, depletion of yttria) occurs within the glass phase upon devitrification. In addition to these general microstructural features, examination also revealed the presence of carbon/graphite inclusions. While these were generally of sub-micron dimensions (~250 nm) and widely dispersed, one region was found to contain clusters of these inclusions and covered an area several microns in diameter. At the surface, such clusters conceivably can act as sites of premature failure at high temperatures.

More generally, however, creep rupture occurs as a result of interfacial cavitation. While all samples examined so far contained a distribution of isolated cavities-most often at small triple junctions and less frequently at two Si_3N_4 grain interfaces - crack-like cavities were also found. In most cases, these precursor creep cracks appeared to result from cavity nucleation within small triple junctions and rapid cavity growth along the intersecting two-grain interfaces, Fig. 3a. Full-facet cavity growth was particular evident along acicular grains (oriented normal to the tensile stress axis) to effectively from a segmented creep crack, Fig. 3b. Continued cavity growth along the surface of such large grains clearly leads to the development of macroscopic size creep cracks which can propagate to cause rupture.

Future efforts call for examination of samples tested under a broader range of creep conditions to clarify both the deformation and rupture processes. Particular emphasis will be placed on describing the details of the microstructure (the nature of interfaces and the second phases) and the cavity nucleation and growth processes.

Status of Milestones

All milestones are on schedule.

Publications

1. D. C. Cranmer, B. J. Hockey, S. M. Wiederhorn and R. Yeckley, "Creep and Creep-Rupture of HIP-ed Si_3N_4", Ceram. and Eng. Sci. Proc. 12[9-10] 1862-1872 (1991).

2. S. M. Wiederhorn, B. J. Hockey and T.-J. Chuang, "Creep and Creep Rupture of Structural Ceramics", pp. 555-576 in *Toughening Mechanisms in Quasi-Brittle Materials*, S.P. Shah, ed., Kluwer Academic Publishers, 1991.

References

None

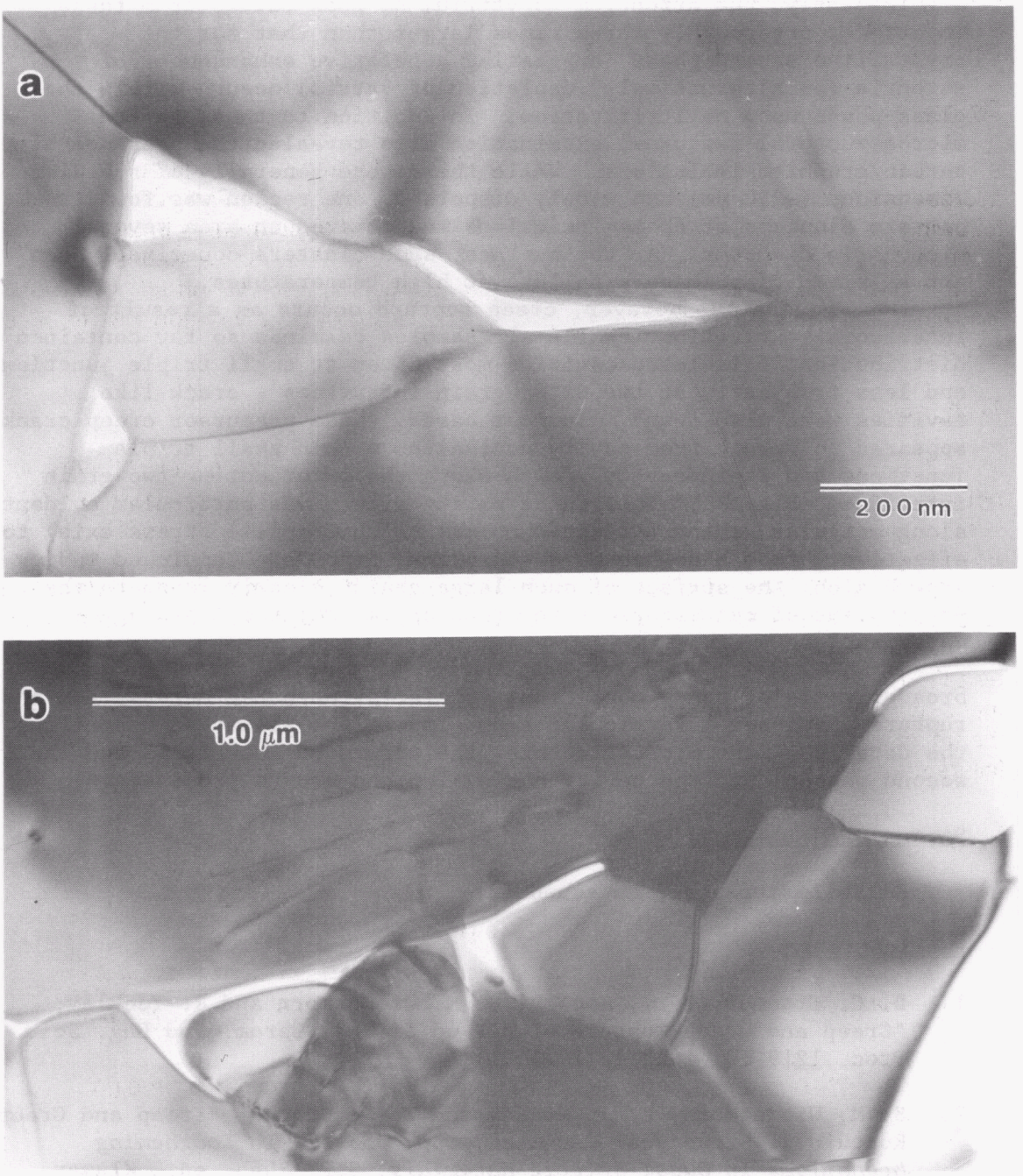

Figure 3. Intergranular cavitation produced in GN-10 during tensile creep. a) initial stage: cavities appear to initiate within small triple grain junctions and grow along two grain interfaces. b) Crack development: continued interfacial cavity growth in direction normal to tensile stress eventually results in joining of individual grain segments to form creep cracks.

Mechanical Properties and Microstructural Characterization of Si_3N_4 Ceramics

Karren L. More (Oak Ridge National Laboratory)

Objective/scope

The objective of the research is to use analytical and high-resolution electron microscopy to characterize the microstructure of a Norton NT-154 Si_3N_4 ceramic material following mechanical strength (tensile) testing at elevated temperatures in air. This work represents a collaboration with The University of Dayton. Work has also been started on the microstructural characterization of a similar material, as well as Garrett's GN-10 Si_3N_4, following high-temperature tensile creep in air and is a collaborative effort with K. Liu of ORNL.

Technical highlights

The material under investigation in collaboration with the University of Dayton is a hot-pressed Si_3N_4 supplied by Norton (NT-154 designation) containing 4.0 wt % Y_2O_3 intentionally added as a sintering aid. The material was annealed to crystallize the grain-boundary phase as part of the Norton processing procedure. Tensile rods were fabricated from the bulk NT-154 and subjected to tension/tension (10% of maximum load/maximum load) cyclic fatigue (TCF) testing or tensile stress rupture (TSR) in air at a temperature of 1300° C. The mechanical test matrix for the samples received for microstructural characterization are given in Table 1. Longitudinal TEM and "new" transverse fracture SEM specimens have been prepared from the hot zone of both the TCF and TSR specimens close to the fracture surface from each tensile rod to evaluate microstructural changes and/or failure mechanisms occurring during high-temperature cyclic testing.

Table 1. Tensile cyclic fatigue and stress rupture specimens supplied for microstructural characterization (NT-154, University of Dayton)

Sample No.	Temperature (° C)	Load (MPa)	Time (h)	Cycles
18 (TCF)	1300	20 to 200	100.0	450,000
67 (TSR)	1300	200	71.2	--
74 (TSR)	1300	200	100.0	--
33 (TCF)	1300	30 to 300	--	30,239
36 (TCF)	1300	30 to 300	100.0	450,000
113 (TSR)	1300	300	1.2	--
8 (TCF)	1300	35 to 350	--	4,617
30 (TCF)	1300	35 to 350	--	246,381
21 (TCF)	1300	40 to 400	--	190

The results given in Table 1 show that the TSR experiments were designed such that if the specimen did not fail after 100 h, it was fast fractured in tension. Likewise, the TCF experiments were designed such that if the specimen did not fail after 450,000 cycles (~ 100 h), the specimen was fast fractured in tension.

An SEM image of sample 18 (1300°C, 20 to 200 MPa) is shown in Fig. 1(*a*). Extremely small, shallow voids were found at many Si_3N_4/Si_3N_4 two-grain junctions, as arrowed in Fig. 1(*a*). These voids were difficult to image using the SEM, even at low voltages. The TEM image shown in Fig. 1(*b*) clearly shows these small voids present at Si_3N_4/Si_3N_4 grain boundaries aligned perpendicular to the tensile axis. Similar voids have also been observed in NT-154 subjected to tensile stress rupture at 1300°C and 200 MPa (sample 67) as shown in the SEM and TEM images of Figs. 2(*a*) and (*b*), respectively. The voids following TCF (20 to 200 MPa) and TSR (200 MPa) at 1300°C clearly did not reach a critical size or number to ultimately cause failure as a result of damage accumulation since each was ultimately fast fractured in tension after 100 h. The voids form within the residual glass film present at most Si_3N_4/Si_3N_4 grain boundaries, as shown in the high-resolution TEM image of Fig. 3. The voids grow via diffusion at the elevated temperatures until failure. This phenomenon is currently being investigated.

Larger voids were found at Si_3N_4/Si_3N_4 boundaries in sample 36 (1300°C, 30 to 300 MPa), as shown in the SEM and TEM images of Figs. 4(*a*) and (*b*), respectively. This specimen also lasted 450,000 cycles. Thus, a critical size and/or number of voids was not reached during TCF under these conditions to result in sufficient damage accumulation for failure. Results for specimen 113 (TSR at 1300°C and 300 MPa) are shown for comparison in Figs. 5(*a*) and (*b*). Relatively large voids were also observed in this sample. Specimen 33 (1300°C, 30 to 300 MPa) was also examined in the SEM, but no voids were found. This specimen failed after only ~ 30,000 cycles under TCF conditions similar to those used for specimen 36. It is clear from these results that the voids do not form in the early stages of testing, and, thus, premature failure of these specimens does not occur as a result of damage accumulation. No voids were found in specimen 21 (1300°C, 40 to 400 MPa). Specimen 30 (1300°C, 35 to 350 MPa) has not yet been examined.

Samples for TEM and SEM examination have also been prepared from tensile creep specimens of both NT-154 and Garrett's GN-10 Si_3N_4 (in collaboration with K. Liu, ORNL). The samples received thus far are summarized in Table 2. Both longitudinal and transverse TEM specimens were prepared from each tensile rod close to the fracture surface. New transverse fracture surfaces were created close to the original oxidized fracture surface in order to view Si_3N_4/Si_3N_4 grain boundaries lying perpendicular to the direction of applied stress.

The creep behavior of the "precycled" NT-154 specimen was superior to that of as-received and the annealed (100 h at 1370°C) NT-154 material at 1370°C (see Fig. 6). Both the precycled and annealed NT-154 had much better creep resistance than the as-received NT-154; thus, a direct comparison between these two specimens was undertaken. Two SEM images of new fracture surfaces comparing the annealed and the precycled specimens are shown in Figs. 7(*a*) and (*b*), respectively. Clearly, voids are present at grain boundaries perpendicular to the tensile axis in both specimens and are qualitatively just as numerous and in the same size range in both. The reason for the superior behavior of the precycled specimen is as yet unclear.

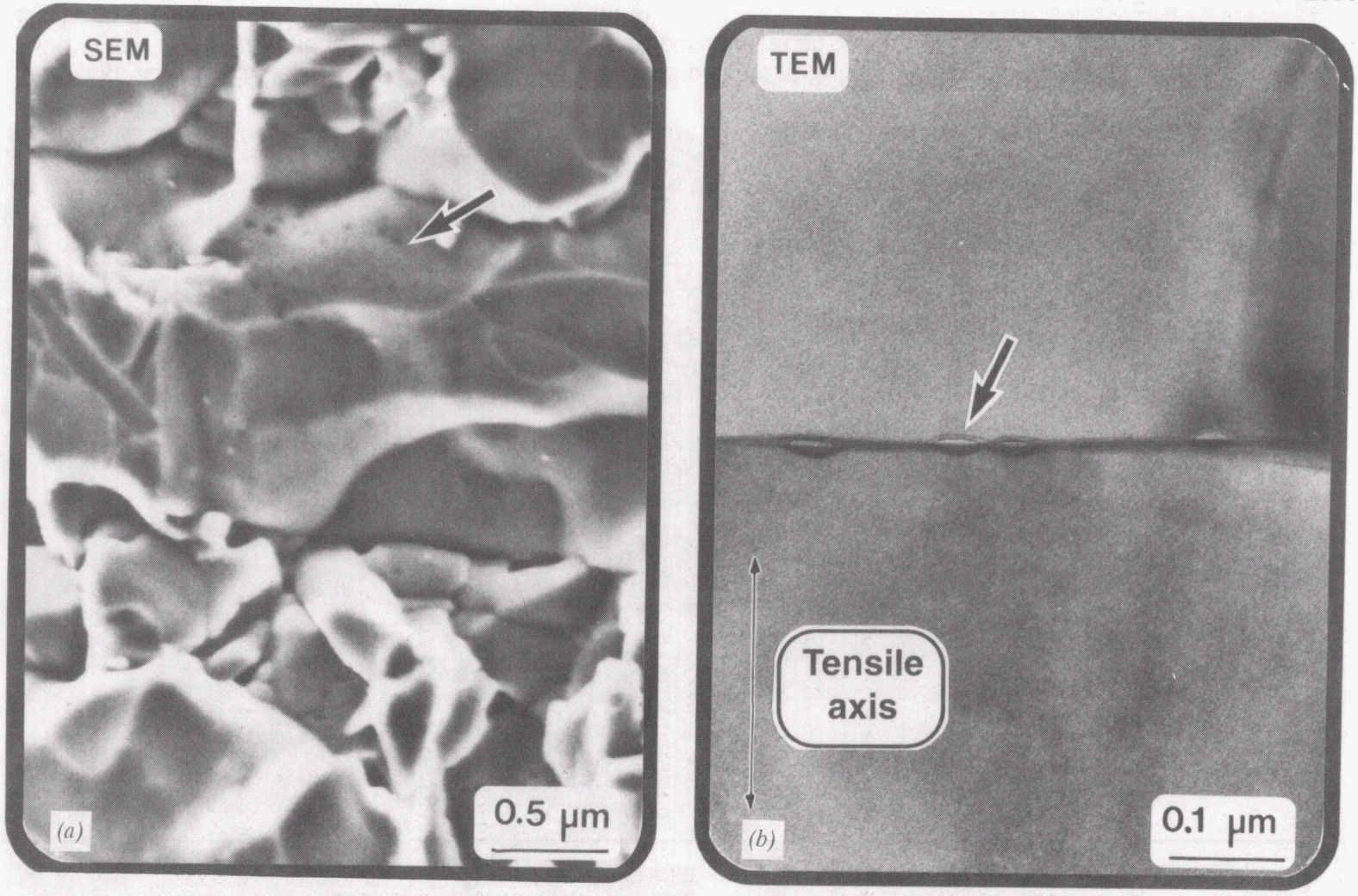

Fig. 1. (*a*) SEM image showing small, shallow voids present at Si_3N_4/Si_3N_4 grain boundaries following TCF at 1300°C and 20 to 200 MPa; and (*b*) TEM image of multiple voids at an Si_3N_4/Si_3N_4 grain boundary aligned perpendicular to the tensile axis (TCF at 1300°C and 20 to 200 MPa).

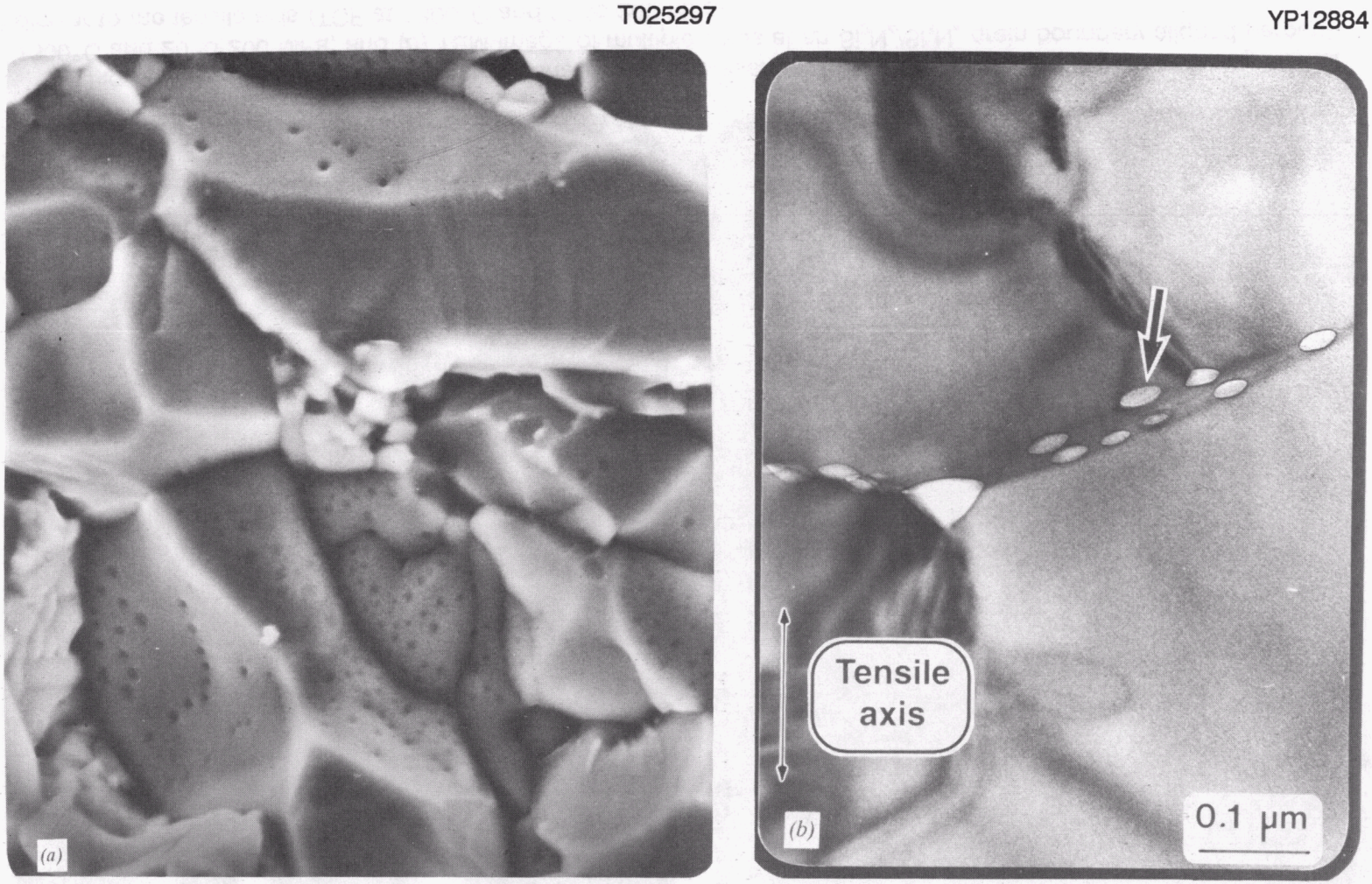

Fig. 2. (*a*) SEM image showing small, shallow voids present at Si_3N_4/Si_3N_4 grain boundaries following TSR at 1300°C and 200 MPa; and (*b*) TEM image showing multiple voids at an Si_3N_4/Si_3N_4 grain boundary aligned perpendicular to the tensile axis (TSR at 1300°C and 200 MPa).

YP12891

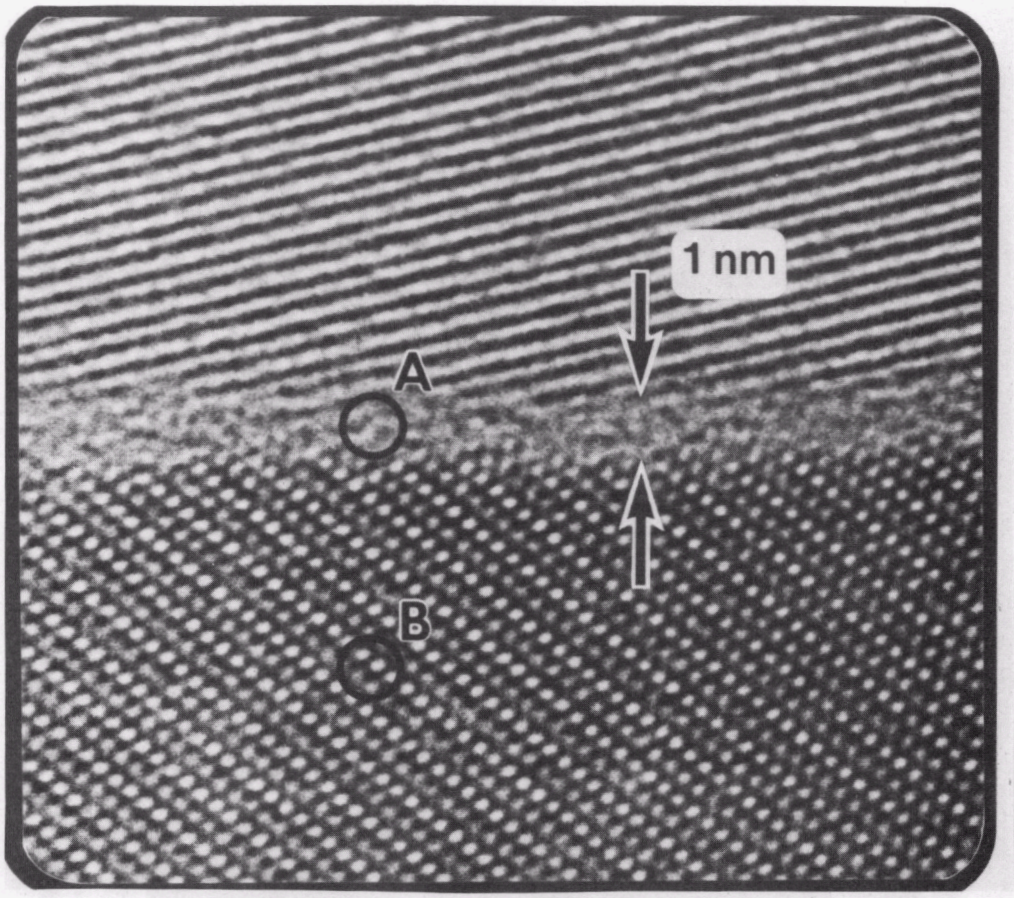

Fig. 3. High-resolution TEM image of a Si_3N_4/Si_3N_4 grain boundary in NT-154.

Status of milestones

Program on schedule.

Publications

1. K. L. More, D. A. Koester, and R. F. Davis, "Microstructural Characterization of a Creep-Deformed SiC Whisker-Reinforced Si_3N_4 Composite," presented at the Frontiers of Electron Microscopy in Materials Science Meeting, Oak Brook, Ill., May 20-24, 1990; also in *Ultramicroscopy* **37**, 263 (1991).

2. K. L. More, D. A. Koester, and R. F. Davis, "The Role of Interfaces in the Creep-Deformation of a SiC Whisker-Reinforced Si_3N_4 Composite," p. 382 in *Electron Microscopy 1990*, Vol. 4, ed. L. D. Peachey and D. B. Williams, San Francisco Press, San Francisco, 1990.

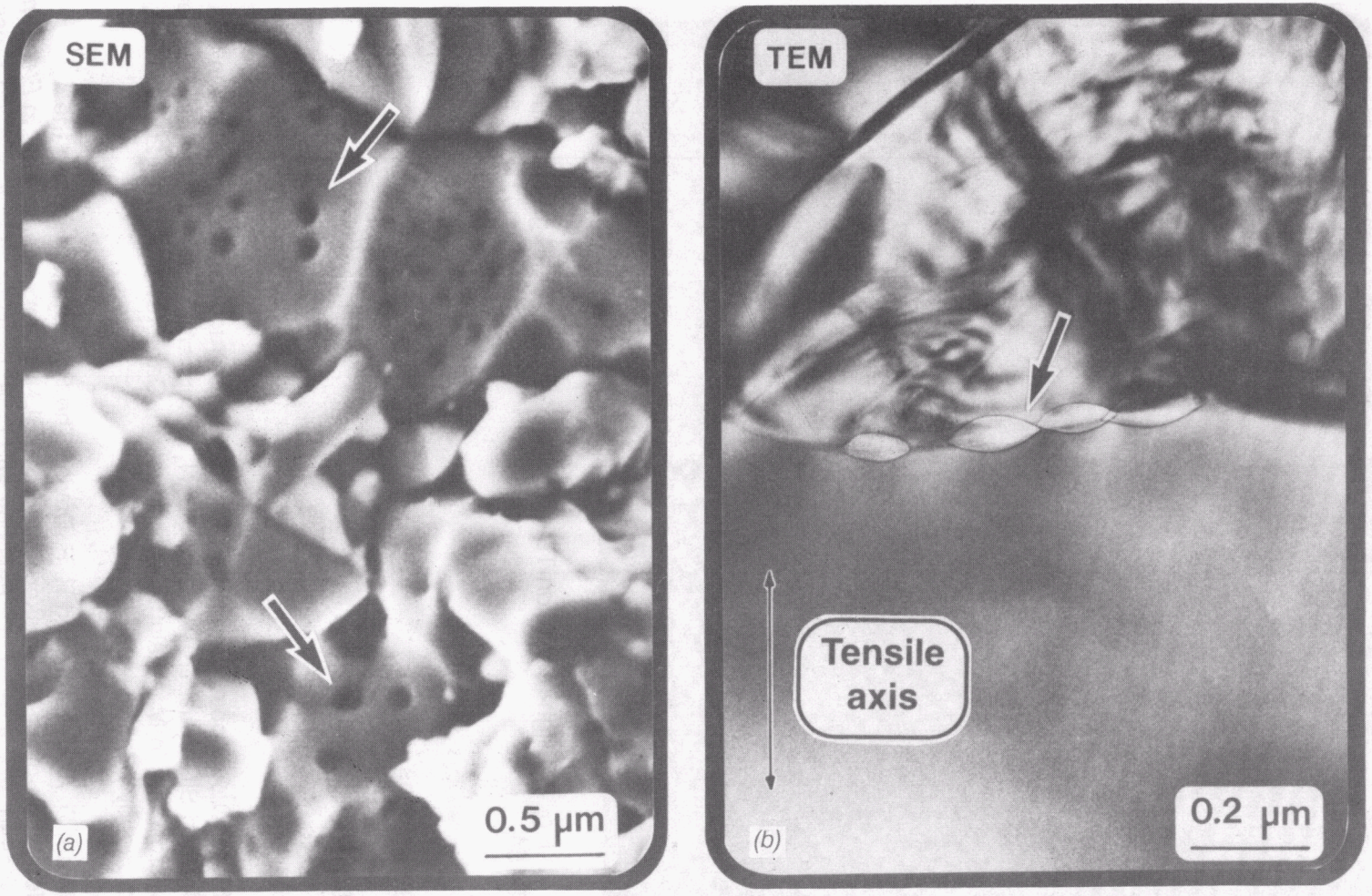

Fig. 4. (*a*) SEM image showing voids found at Si_3N_4/Si_3N_4 grain boundaries following TCF at 1300°C and 30 to 300 MPa; and (*b*) TEM image of multiple voids at an Si_3N_4/Si_3N_4 grain boundary aligned perpendicular to the tensile axis (TCF at 1300°C and 30 to 300 MPa).

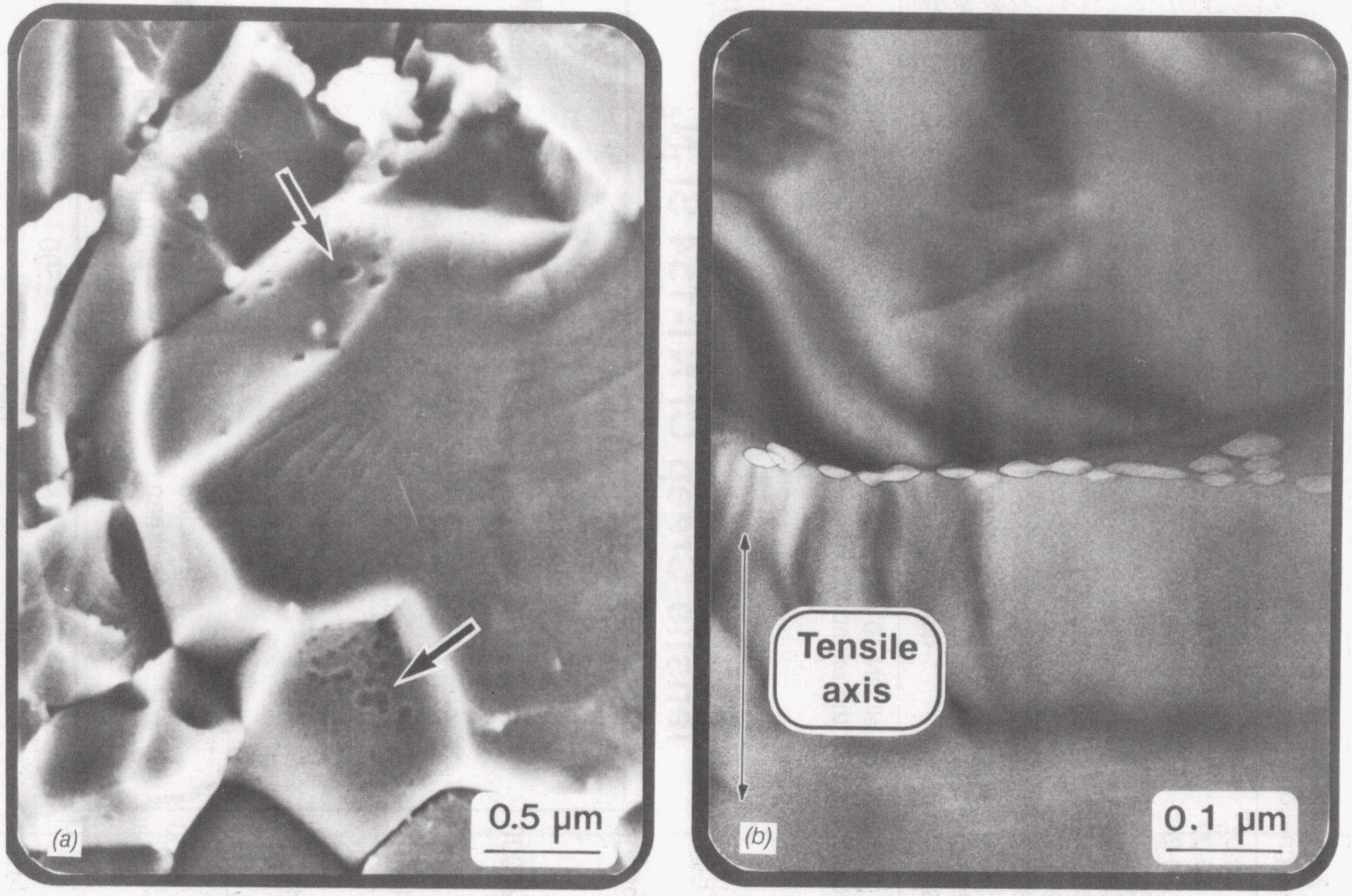

Fig. 5. (*a*) SEM image showing extensive void formation at Si_3N_4/Si_3N_4 grain boundaries following TSR at 1300°C and 300 MPa; and (*b*) TEM image of multiple voids at an Si_3N_4/Si_3N_4 grain boundary aligned perpendicular to the tensile axis (TSR at 1300°C and 300 MPa).

Table 2. Tensile creep specimens supplied for microstructural characterization

Sample designation	Manufacturer	Creep conditions
20-07[a]	Norton	unannealed
20-09	Norton	precycled, 1370°C, 100 MPa
20-24	Norton	1370°C, 100 MPa
89360F-1	Garrett	1150°C, 250 MPa
89333-4	Garrett	1200°C, 150 MPa
89360F-5	Garrett	1200°C, 225 MPa
89360A-1	Garrett	1250°C, 175 MPa
89360A-4	Garrett	1300°C, 125 MPa
89340-1-2	Garrett	aged 1370°C-150 h, 1250°C, 175 MPa
89340-1-3	Garrett	aged 1370°C-150 h, 1250°C, 225 MPa
89340-1-1	Garrett	aged 1370°C-150 h, 1300°C, 125 MPa

[a]Note that all GN-10 and NT-154 materials are annealed as part of processing with the exception of sample 20-07.

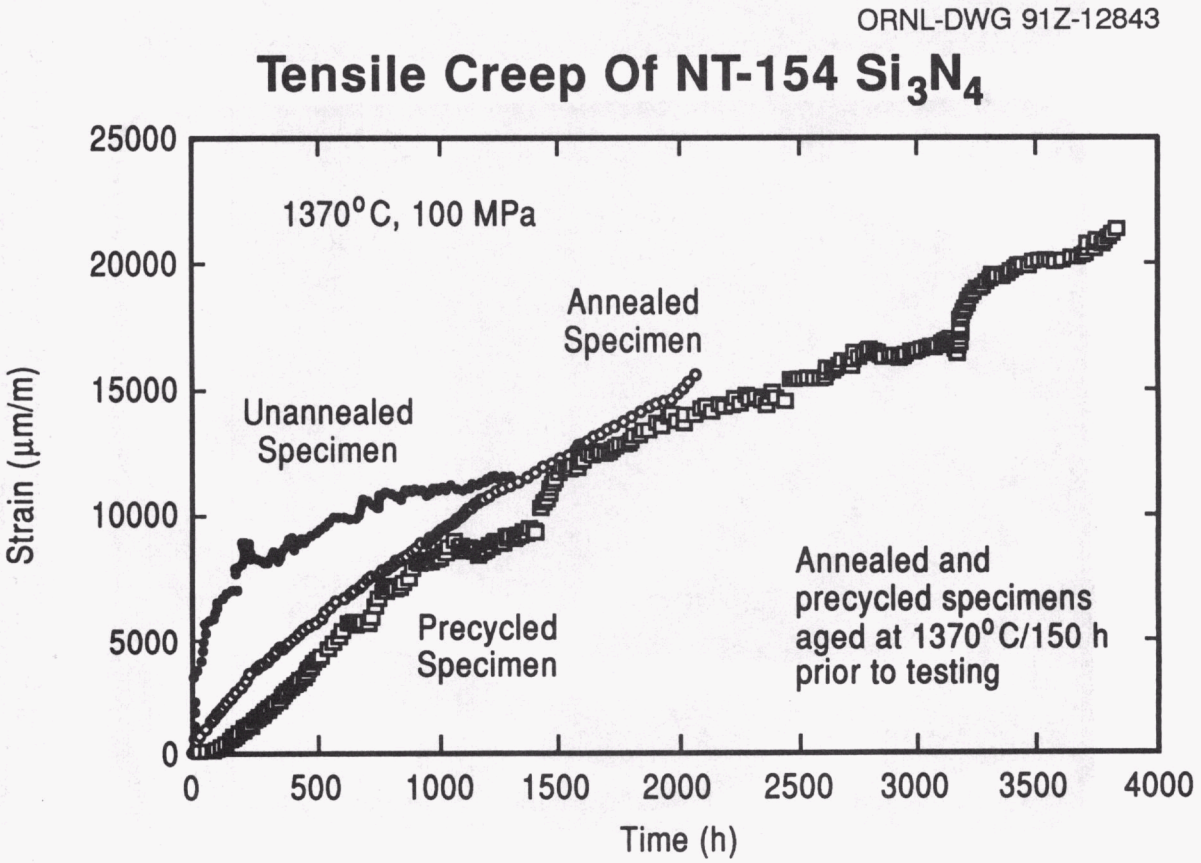

Fig. 6. Strain versus time curve comparing the tensile creep behavior of as-received, annealed, and precycled NT-154.

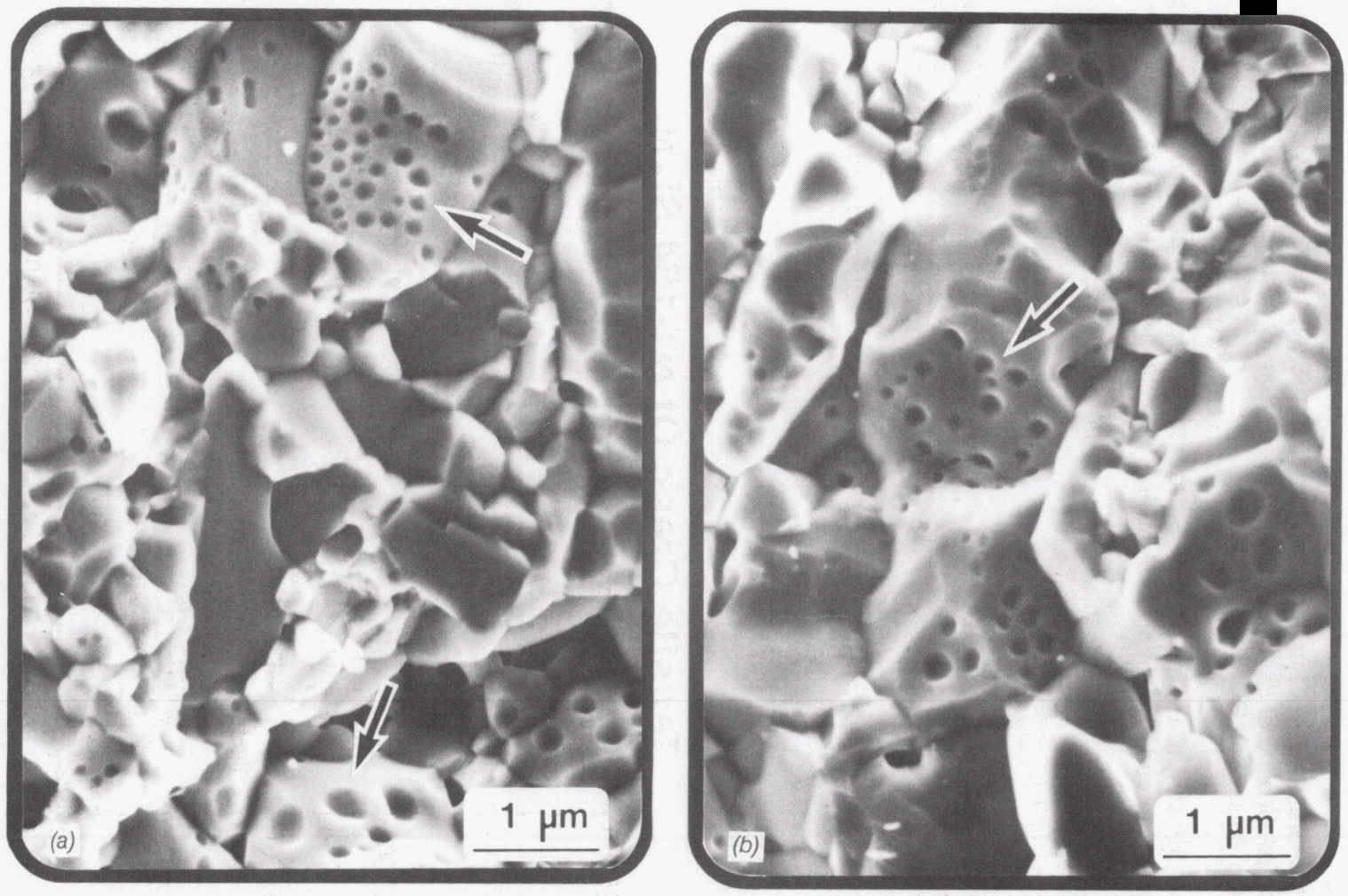

Fig. 7. (*a*) SEM image showing voids at Si_3N_4/Si_3N_4 boundaries in a "precycled" NT-154 specimen subjected to tensile creep testing at 1370°C and 100 MPa; and (*b*) SEM image showing voids at Si_3N_4/Si_3N_4 boundaries in an annealed NT-154 specimen subjected to tensile creep testing at 1370°C and 100 MPa.

3. D. A. Koester, K. L. More, and R. F. Davis, "Deformation and Microstructural Changes in SiC Whisker-Reinforced Si_3N_4 Composites," *J. Mater. Res.* **6**[12], 2735 (1991).

4. K. L. More, "Defect Charaterization in a CVD $\propto$-Si_3N_4," p. 936 in *Proceedings of the 49th Annual Meeting of the Electron Microscopy Society of America*, ed. G. W. Bailey, San Francisco Press, San Francisco, 1991.

5. D. A. Koester, K. L. More, and R. F. Davis, "The High Temperature Creep of a SiC Whisker-Reinforced Si_3N_4 in an Air Ambient," submitted to *J Mater. Res*.

Project Data Base
B. L. Keyes (Oak Ridge National Laboratory)

Objective/scope

The objective of this task is to develop a comprehensive computer data base containing the experimental data on properties of ceramic materials generated in the total effort. This computer system should provide a convenient and efficient mechanism for the compilation and distribution of the large amounts of data involved. The data base will be available in electronic form to all project participants. In addition, periodic hard copy summaries of the data, including graphical representation and tabulation of raw data, will be issued to provide convenient information sources for project participants.

Technical highlights

The Ceramic Technology for Advanced Heat Engines data base presently contains 6309 test results on 27 different types of tests, 338 material characterizations, 13 lubricant characterizations, 101 coating characterizations, and 1953 other associated records. A more detailed description is shown in Table 1.

Recent efforts have centered around collecting and storing tribology data generated by the project and analyzing each work breakdown structure by facility from program beginning to present. Analyses and storage of wear data from Battelle Columbus, Caterpillar, and Cummins Engine Company have been completed.

Tribology test characterization proved to be quite intricate, often involving several materials. The simplest test involved two specimens of the same monolithic material; the most complicated, so far, involved multicoated substrate disks abraded by pins of other materials. Accurately defining the multicoated surfaces and the various substrates required adding new files to handle this special situation.

The entire structure of the existing tribology information file was reworked to provide more information to the user. Better test definition, more material fields, distinguishing between a coated and a monolithic sample, and adding new files to accommodate the coating characteristics were just a few of the improvements accomplished during this reporting period. Although these additions were included for the wear data, data base personnel plan to expand them to other test data as time permits.

Wear test data records now offer four material fields rather than only one: two coating fields and two substrate fields. When monolithic, alloys, or uncoated materials are tested, the coating fields will be blank, leaving the substrate fields to identify the monolithics used. All entries in the substrate fields will be further characterized in the main material characterization file, MATLCHAR, and the coatings will be defined in a new file appropriately named COATINGS. Multilayered coatings will be named according to their component materials and will be defined as unique coatings in the COATINGS file. For example, a coating named "M461/ZIRCOA-2L" is actually a two-layer coating (the "2L" composed of a METCO 461 base coat and a ZIRCOA Zr_2O_3 top coat). "M461/ZIRCOA-3L" is a METCO 461 base coat, followed by a 50:50 coat of METCO 461 and ZIRCOA,

Table 1. CTAHE Data Base Summary as of September 30, 1991

Material class	Brazed specimens					Creep	Cyclic fatigue	Density	Dynamic fatigue	Elasticity
	MOR 4	Shear str.	Toughness	Torsion	Tor fatigue					
Alumina							15		9	28
Alumina + reinforcing fibers								7		
Alumina + zirconia										
Mullite										2
Mullite + reinforcing fibers										11
Silicon carbide		12						10	13	15
Silicon nitride	69	48		15	7	37	19	28	16	24
Silicon nitride + reinforcing fibers							15	2		16
Zirconia	160	58	2				51	158		119
Zirconia + reinforcing fibers										
Other				6				4		
Totals	229	118	2	21	7		100	209	38	215

Material class	Fracture toughness	Hardness	Interrupted fatigue	MOR 3-Pt. bend	MOR 4-Pt. bend	Oxidation rate	Poisson's ratio	Shear modulus	Tensile	Thermal conductivity
Alumina	39	4			411				28	3
Alumina + reinforcing fibers	39				144				11	34
Alumina + zirconia					7					
Mullite	1			1	4					
Mullite + reinforcing fibers	12			9	22					
Silicon carbide	29	27			236					
Silicon nitride	94	112		10	647	1	2	1	75	9
Silicon nitride + reinforcing fibers	53				144	3	17	16	86	9
Zirconia	347	24	239		1554				50	
Zirconia + reinforcing fibers					2				36	
Other	3	39			59					
Totals	617	206	239	20	3230	4	19	17	286	55

Table 1 (continue)

Material class	Thermal contraction	Thermal diffusivity	Thermal expansion	Thermal shock	Torsion	X-Ray diffraction	Material char.	Chemistry
Alumina			1	2			13	14
Alumina + reinforcing fibers		18	4	6			94	
Alumina + zirconia	23		21				8	
Mullite							2	
Mullite + reinforcing fibers							24	
Silicon carbide			23			17	9	57
Silicon nitride		10	44		3	49	56	7
Silicon nitride + reinforcing fibers		17	14				53	
Zirconia						72	38	44
Zirconia + reinforcing fibers							5	
Other			35		4		36	17
Totals	23	45	142	8	7	138	338	139

Material class	Wear resistance	Coatings	Lubricants	
Alumina based	9	3		
Alumina + reinforcing fibers	1			
Silicon carbide	3			
Silicon nitride	22			
Chromia based	98	20		
Zirconia based	13	15		
Enamels	5	10		
Other	126	53	13	
Totals	277	101	13	
Grand total (characterization data)				452
Grand total (test data only)				6309

followed by a top coat of ZIRCOA. Four coatings would be defined in the COATINGS file: "METCO 461," "ZIRCOA ZrO2," "M461/ZIRCOA-2L," and "M461/ZIRCOA-3L." (Note: "METCO" was shortened to "M" because of space limitations.)

Another problem with tribology data has been determining which one of the numerous types of test rigs was used. A brief literature survey revealed that everything from complex engine emulation systems to relatively simple roller-to-disk rigs are being used to determine a material's coefficient of friction and/or wear resistance. Each test data record now contains a TEST_RIG field that points to a description of the particular test rig used.

Ceramics lack a standard identification system available for other materials, such as the Unified Numbering System (UNS) for metals. A given ceramic may be known by several different names (Z-191 is also called PSZ, ZrO2, and zirconia), each one correct but all different as far as a computer query is concerned. The MATNAMES file was created to facilitate choosing a material name for use in a data base query. This file contains a list of material names used in the data base cross-indexed to composition, manufacturer's, and generic designations all indicating the same material. This file will be useful for locating the aliases for each material.

As the data base grows, accessing specific data becomes more complicated because of the shear number of records involved and the possible combinations of search criteria needed. Data base personnel usually collect and store the data by tracing a facility's research on a particular work breakdown structure (WBS) from its origin to present. Accessing all the data for that WBS has been difficult for everyone except the person who input the data initially. With the new WBS_STUDY field, each facility's work on a WBS is coded for easier retrieval. The data may still be searched using material, test type, and a variety of other parameters. Eventually, a computerized interface to facilitate this task even more will be available, possibly for both Apple Macintosh and IBM-compatible computers.

Status of milestones

The seventh data base summary has been completed through the first draft and will go into review soon.

Publications

The Ceramic Technology for Advanced Heat Engines Project Data Base: September 1990 Summary Report is in revision.

The Ceramic Technology for Advanced Heat Engines Project Data Base: March 1990 Summary Report is in revision.

The Ceramic Technology for Advanced Heat Engines Project Data Base: September 1991 Summary Report is completed through first draft and will soon go into review.

3.2 TIME-DEPENDENT BEHAVIOR

Characterization of Toughened Ceramics

Jeffrey J. Swab and Michelina O'Day
(U.S. Army Materials Technology Laboratory)

Objective/scope

To evaluate and characterize toughened ceramic matrix composite (CMC) materials for potential high temperature structural applications. This includes all classes of CMC materials. There will be no CMC materials produced as part of this project. At the present time four-point flexure testing is being used to determine the high temperature performance of these CMCs.

Technical highlights

Ceramatec, Inc. of Salt Lake City, UT provided flexure bars of SiC-fiber reinforced silicon nitride for elevated temperature evaluation. Some of the bars which were received were coated with a CVD coating of SiC in an attempt to improve the oxidation resistance of the material. Uncoated bars were subjected to flexural stress rupture testing at 1000°C and 1100°C in air while the coated bars were tested only at 1000°C in air.

The stress rupture results for the uncoated bars are shown in Figures 1 and 2. At 1000°C this material was able to survive 1000 hours under a 400 MPa applied stress without failure and minimum plastic deformation. Above 400 MPa, as the applied stress approached or exceeded the matrix cracking stress of 460 MPa, the time-to-failure was significantly reduced and brittle fracture dominated. Similar results were observed at 1100°C where the material was able to survive 1000 hours under a 300 MPa applied stress without failure and a minimum amount of plastic deformation. Above 300 MPa, as the applied stress increased brittle failure dominated and the time-to-failure was reduced.

The stress rupture results at 1000°C for the CVD bars were very different from the uncoated bars. These bars failed in a brittle manner with minimal fiber pull-out, at very short times-to-failure over the same stress range as the uncoated bars. The reason for this reduction in time-to-failure is unknown at this time.

A sintered A4Y13-Si_3N_4 monolithic ceramic manufactured using a new continuous belt furnace process was obtained from Dale Wittmer at Southern Illinois University. Materials processed in this manner have demonstrated a higher average strength than identical materials processed using conventional batch furnace methods. Dale is obtaining funding from DoE for the processing of this material while MTL was providing the evaluation, also through DoE funding. Room and high temperature fast

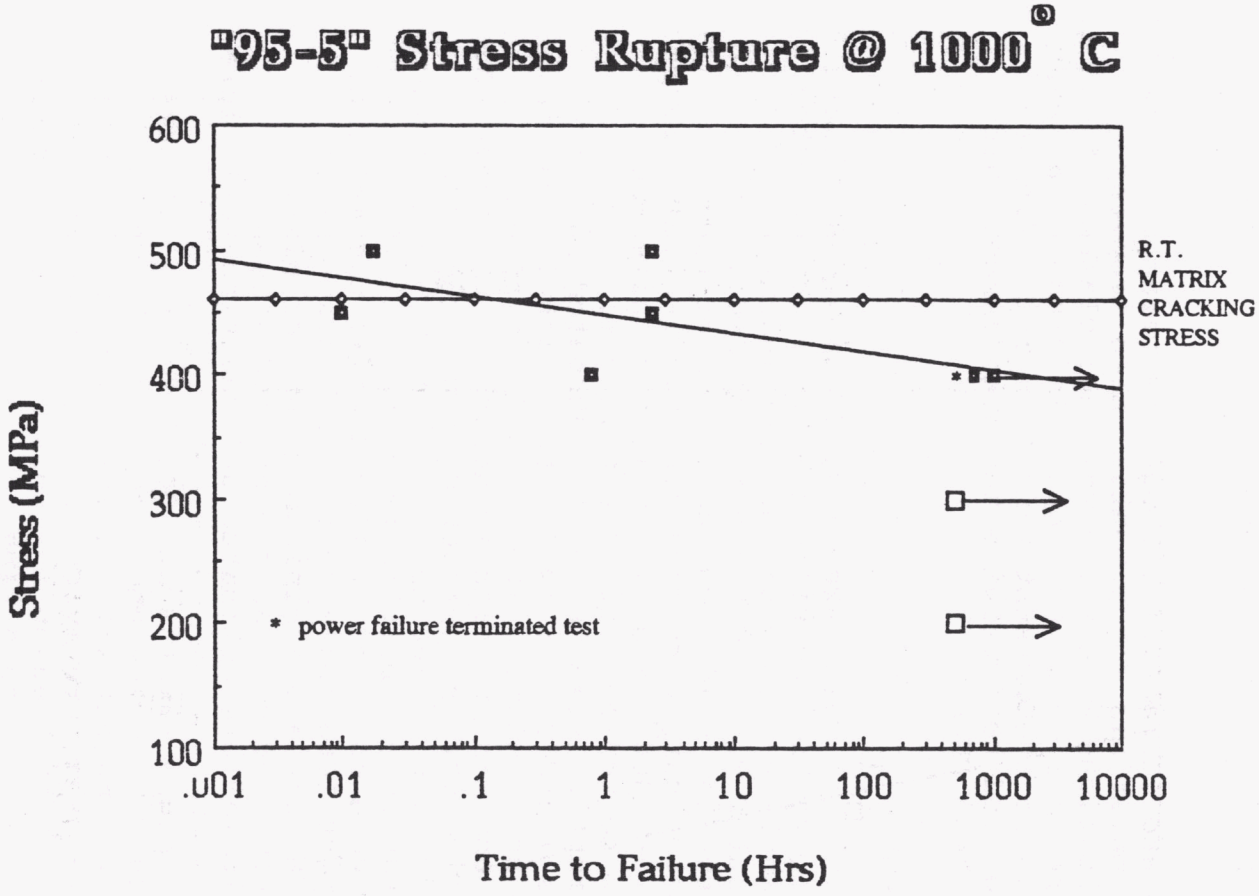
"95-5" Stress Rupture @ 1000° C
600
500
400
300
200
100
Stress (MPa)
R.T.
MATRIX
CRACKING
STRESS
* power failure terminated test
.001
.01
.1
1
10
100
1000
10000
Time to Failure (Hrs)

FIGURE I

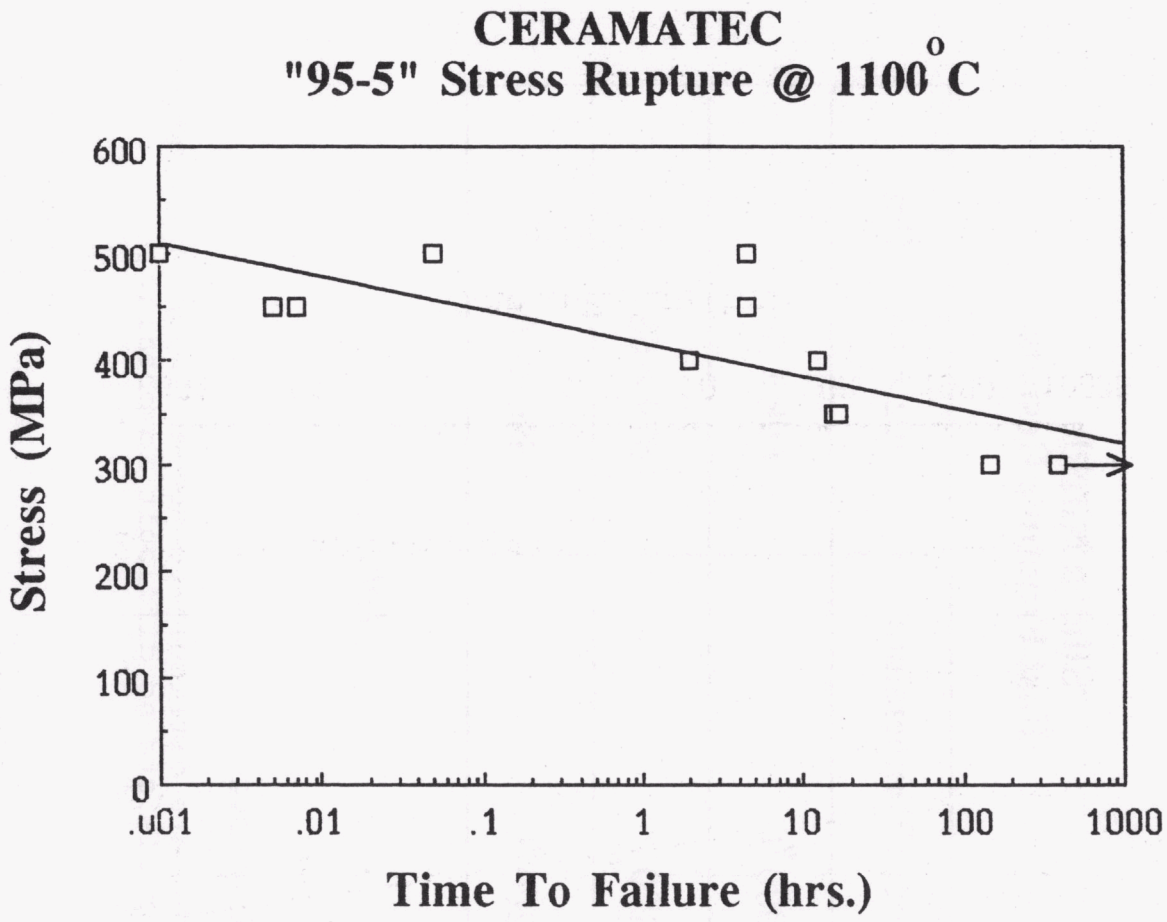
CERAMATEC
"95-5" Stress Rupture @ 1100°C
Stress (MPa)
600
500
400
300
200
100
0
.001
.01
.1
1
10
100
1000
Time To Failure (hrs.)

Figure 1

fracture tests were done and the results are shown in Table 1.

Further testing of this material (as well as testing of a self-reinforced silicon nitride, processed in the same manner) was scheduled, but DOE has terminated this project. This will be the last report.

Silicon Nitride
Fast Fracture Results

Room Temperature	702 ± 148 MPa
1000 °C	698 ± 50
1100 °C	579 ± 68
1200 °C	586 ± 79

Table 1

Status of milestones

Milestones are difficult to set and keep on schedule when CMC materials are so difficult to obtain.

Publications

None

Fracture Behavior of Toughened Ceramics

H. T. Lin, P. F. Becher, and W. H. Warwick (Oak Ridge National Laboratory)

Objective/scope

Ceramic composites, such as fiber- and whisker-reinforced ceramics, particulate phase composites, and ceramics with similar grain structures, offer important advantages for heat engine applications. Chief among these is the improved fracture toughness that can be achieved by appropriate design of microstructural and material parameters. Previous studies show that these materials often exhibit substantial improvements in damage, thermal shock, and slow crack growth resistances. However, design of such systems must also consider those factors influencing their performance at elevated temperatures.

In response to these needs, studies are conducted to determine the mechanical properties (e.g., creep, delayed failure, strength, and toughness) at elevated temperatures for these toughened ceramics. Particular emphasis is placed on understanding how microstructure and composition influence the mechanical performance at elevated temperatures and the stability of these properties for extended periods at these temperatures. The knowledge gained from these studies provides input on how to modify materials to optimize their mechanical properties for the temperature ranges of interest.

Technical highlights

Over the past six months, the research efforts were primarily directed on (1) the compressive creep behavior of polycrystalline fine-grained alumina and 20 vol % SiC whisker-reinforced alumina composites and (2) the strength and toughness behavior of *in-situ* reinforced silicon nitride ceramics that contain elongated grain structures. The objective of the compressive creep study is to develop a data base for the comparison of creep behavior in flexure and compression. This will provide an insight into the effect of the stress state on the creep response and on creep life of monolithic ceramics and ceramic composites. Finally, it can also provide some insight as to the tensile creep response.

Compressive Creep of Al_2O_3 and Al_2O_3-SiC_w Materials

The compressive creep tests at temperatures from 1200 to 1400°C were conducted on polycrystalline fine-grained alumina (1.5 μm) and alumina composites reinforced with 20 vol % SiC_w (2 μm) in air. Figure 1 shows the creep data in both flexure and compression for polycrystalline alumina at 1200 and 1300°C. The applied stress for flexure creep ranges from 37 to 150 MPa, and that for compressive creep ranges from 25 to 75 MPa. Results indicate that the creep rates in compression are slightly higher than those in flexure for polycrystalline alumina. However, the creep stress exponent, n, is independent upon the applied stress state. The creep stress exponent is approximately 2 in both flexure and compression under the applied stress ranges in this study. The stress exponent of 2 was attributed

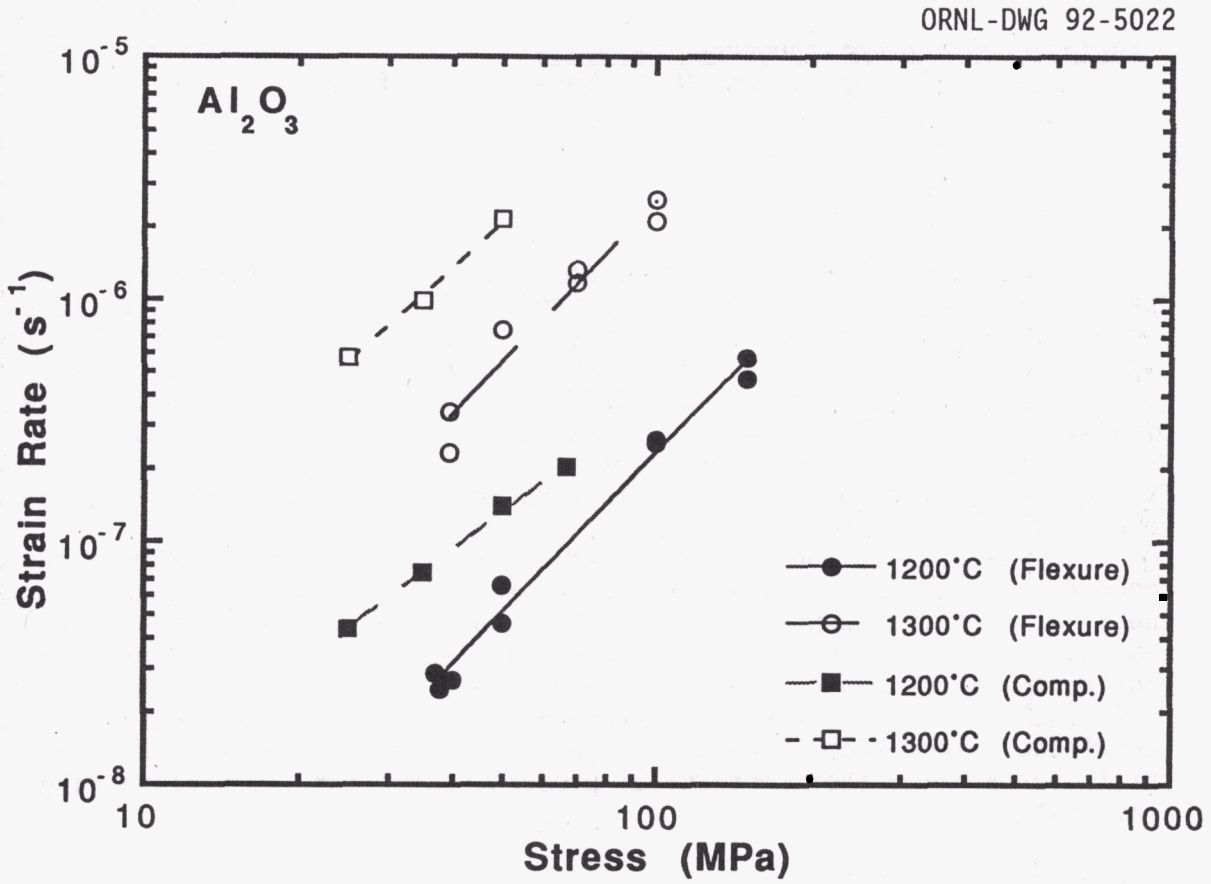

Fig. 1. Strain rate versus stress curves for polycrystalline fine-grained aluminas under flexural and compressive loading, respectively.

to the grain-boundary sliding mechanism.[1] It is emphasized that the behavior of alumina grains sliding out of the specimen surface due to grain-boundary sliding is observed in the compressive creep specimens in this study.

Figure 2 compares the creep data of alumina composites reinforced with 20 vol % SiC whiskers at temperatures of 1300 and 1400°C. The applied stress range for compression is from 37 to 110 MPa, and that for flexure is from 50 to 275 MPa. The results indicate that the stress state has only a minor influence on the creep rates of this whisker-reinforced alumina under the applied stress ranges at both 1300 and 1400°C. However, the creep stress exponent, n, is altered by changing the stress state at 1300°C. Regression analysis of compressive creep data at 1300°C reveals n of approximately 1, while that at 1400°C is approximately 2, which is the same as that for flexure creep. Previous studies have shown that polycrystalline fine-grained aluminas exhibited essentially the same creep rates and exponents (n = 2) in both tension and compression tests.[2,3] The difference in creep rates between flexure and compression tests of fine-grained alumina in the present study results from the difficulty of attaining alignment with small compression specimens, which introduces an

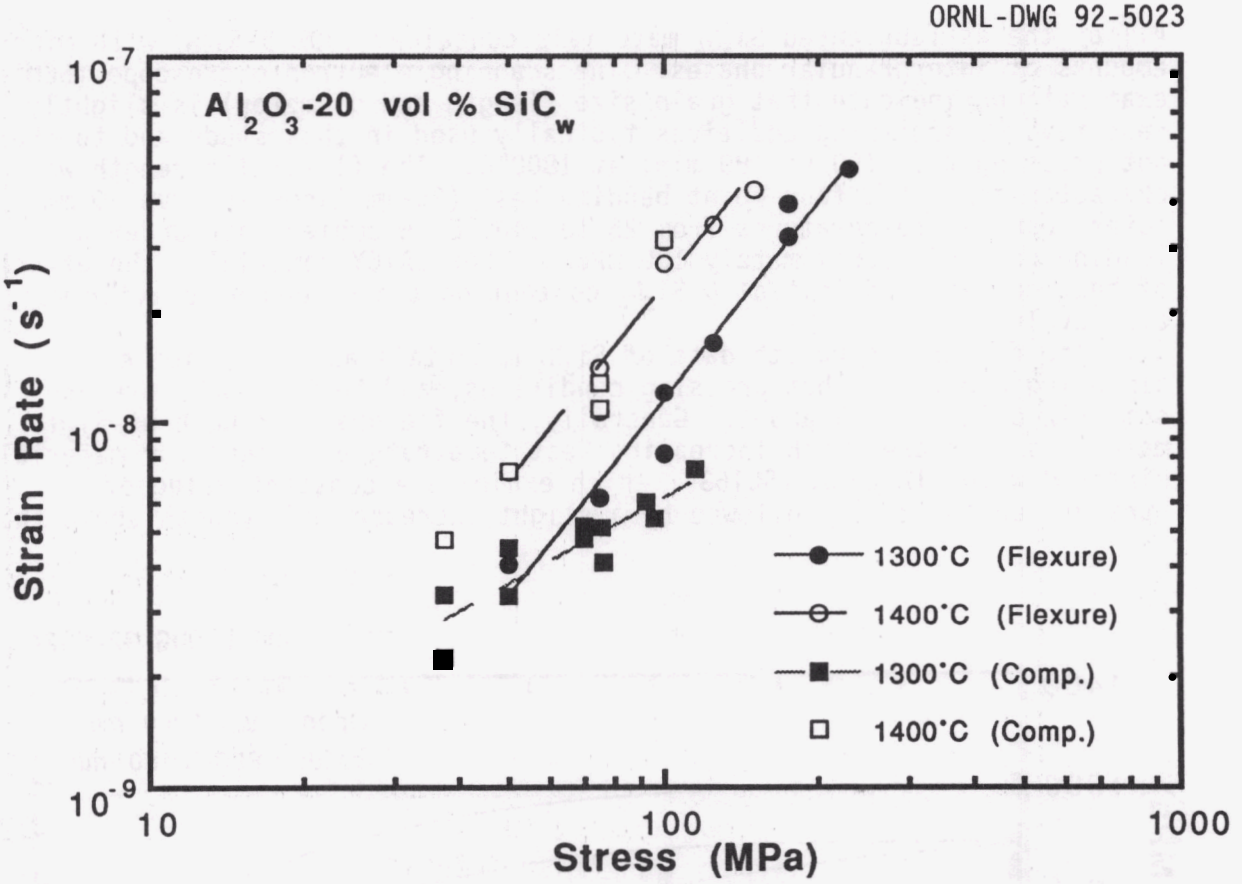

Fig. 2. Strain rate versus stress curves for 20 vol % SiC whisker-reinforced aluminas under flexural and compressive loading, respectively.

additional bending moment on the compressive specimens, leading to higher deformation rates in compression. On the other hand, the change in stress exponent for alumina composites at 1300°C may be due to the alteration of creep-controlling mechanisms and/or suppression of the creep cavitation in compression.

Strength and Toughness Behavior of Si_3N_4 Ceramics

Evaluation of the effects of the sintering additives and microstructures on strength and toughness behavior of *in-situ* reinforced silicon nitride ceramics that contain elongated grain structures was one of the primary efforts in this reporting period. The *in-situ* reinforced Si_3N_4 ceramics were fabricated under work breakdown structure (WBS) Element 1.2.3.1 by hot pressing at 1800°C for 90 and 180 min to > 99.5% theoretical density. The starting silicon nitride powder is UBE E10. The sintering additive systems (in wt %) used in the present study are 2.0% SrO-6.0% Y_2O_3 (2Sr6Y), 1.95% Al_2O_3-8.43% La_2O_3 (2Al8La), 1.97% Al_2O_3-2.96% Y_2O_3-4.27% La_2O_3 (2Al3Y4La), 3.93% Y_2O_3-5.67% La_2O_3 (4Y6La), 11.14% La_2O_3 (11La), 4% Y_2O_3 (4Y), 1.5% Al_2O_3-6% Y_2O_3 (2Al6Y), and 2%BaO-6% Y_2O_3 (2Ba6Y).

All of the as-fabricated Si_3N_4 materials contained 100% β-Si_3N_4 with minor amounts of intergranular phases. The scanning electron microscope (SEM) examinations indicate that grain size (length and diameter) is slightly sensitive to sintering additives typically used in this study and to the hot-pressing time (90 vs 180 min) at 1800°C. The flexural strength was characterized via a four-point bending test (20-mm inner span vs 40-mm outer span) at temperatures from 25 to 1400°C in ambient air under a loading rate of approximately 100 MPa/s. For 2Al6Y materials, the effects of heating rate and initial β-Si_3N_4 content on the strength behavior were also evaluated.

The flexural strength data of Si_3N_4 materials as a function of sintering additives, hot-pressing conditions, and test temperature are summarized in Figs. 3 and 4. Generally, the flexural strength of Si_3N_4 materials decreases with increasing test temperature, except for materials sintered with 11% La_2O_3 (SC163), which exhibits a constant value of strength up to 1200°C followed by a slight increase in strength above that.

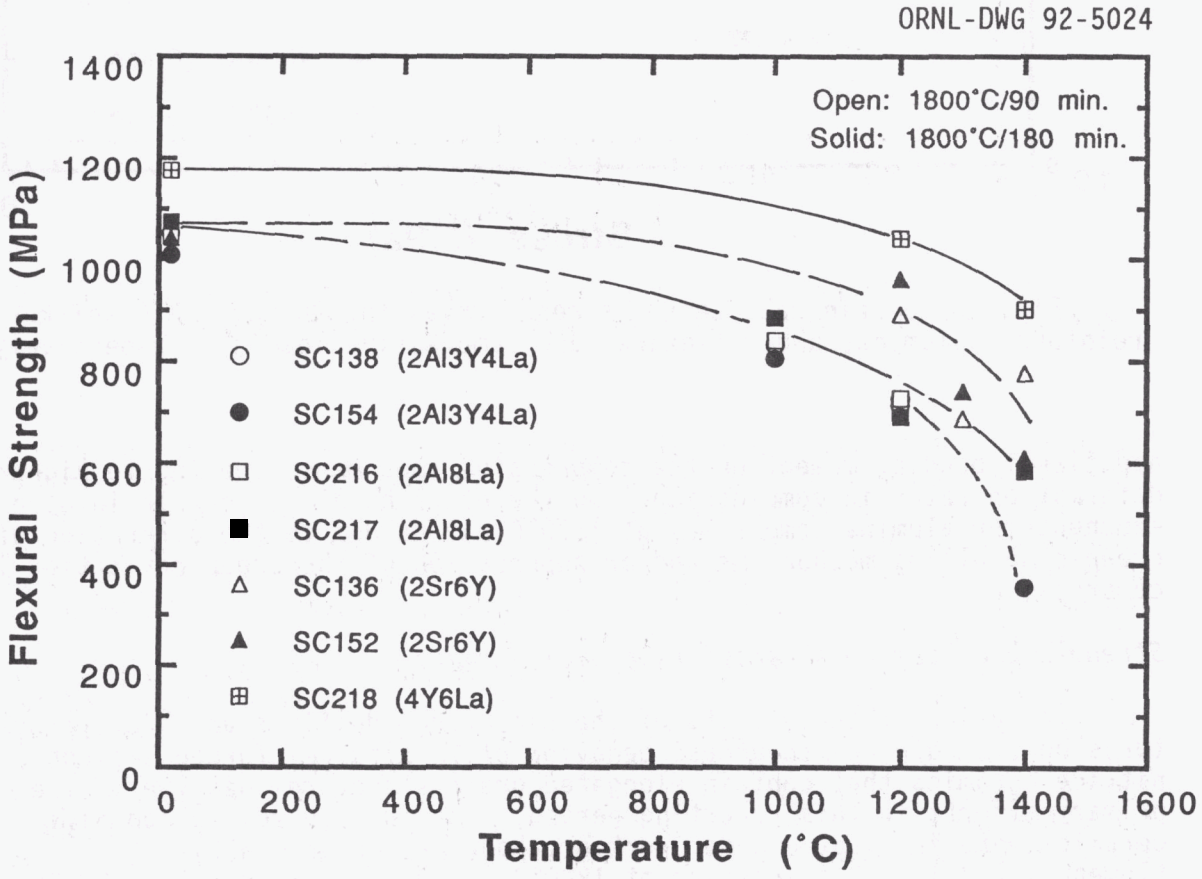

Fig. 3. Flexural strength as a function of test temperature for Si_3N_4 ceramics with sintering systems of 2Al3Y4La, 2Al8La, 2Sr6Y, and 4Y6La.

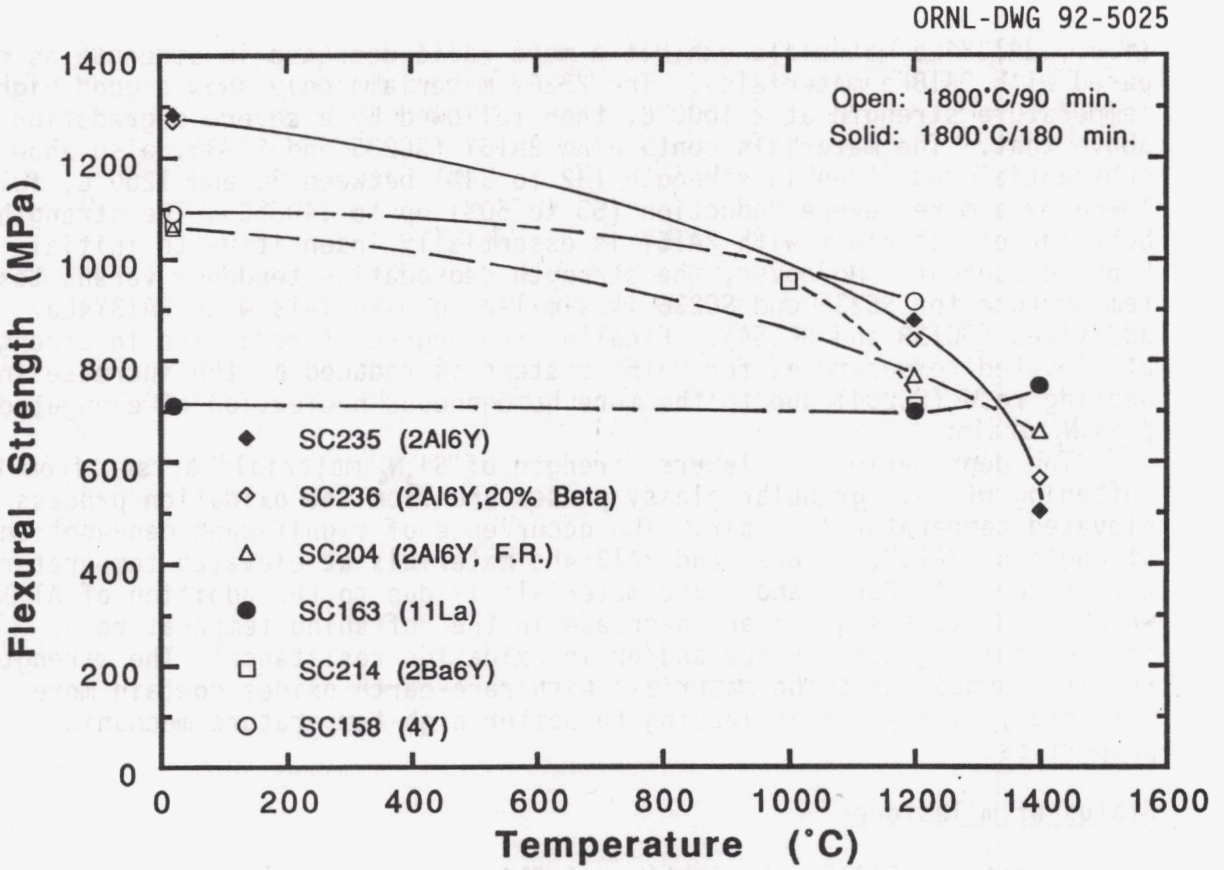

Fig. 4. Flexural strength as a function of test temperature for Si_3N_4 ceramics with sintering systems of 2Al6Y, 11La, 2Ba6Y, and 4Y.

In addition, the strength of Si_3N_4 materials is insensitive to hot-pressing time (90 vs 180 min) at 1800°C, which may be attributed to their similarity in grain size. The 2Al6Y materials (SC235) exhibit the highest room-temperature strength among the materials investigated in the present study, while the 11La materials (SC163) exhibit the lowest strength. Note that the materials sintered with 4Y, 2Sr6Y, 2Al8La, 2Al3Y4La, and 2Ba6Y exhibit similar strength at room temperature.

Both the 4Y6La (SC218) and 2Sr6Y (SC136 and SC152) materials exhibit a slight reduction (8 to 15%) in strength between room temperature and 1200°C in air followed by a marked decrease in strength above that. The 4Y material also reveals a better retention of high-temperature strength up to 1200°C, which is similar to materials with 4Y6La and 2Sr6Y additives. On the other hand, both the 2Al8La (SC216 and SC217) and 2Al3Y4La (SC138 and SC154) materials reveal more of a reduction (28 to 36%) in strength between room temperature and 1200°C as compared with 4Y6La and 2Sr6Y materials. In addition, there is no apparent difference in flexure strength between 2Al8La and 2Al3Y4La materials at temperatures $\leq$ 1200°C; however, the strength curve reveals a significant division at temperatures > 1200°C

(i.e., 2Al3Y4La materials exhibit a more rapid decrease in strength as compared with 2Al8La materials). The 2Ba6Y materials only show a good high-temperature strength at ≤ 1000°C, then followed by a severe degradation above that. The materials containing 2Al6Y (SC235 and SC236) also show a substantial reduction in strength (32 to 34%) between 20 and 1200°C, followed by a more severe reduction (55 to 60%) up to 1400°C. The strength behavior of materials with 2Al6Y is essentially insensitive to initial β phase content. Moreover, the strength degradation tendency versus test temperature for SC235 and SC236 is similar to materials with 2Al3Y4La additives (SC138 and SC154). Finally, the degree of reduction in strength at elevated temperatures for 2Al6Y systems is reduced by the increase in heating rate (SC204) due to the more homogeneous nucleation of elongated β-Si_3N_4 grains.

The degradation in flexure strength of Si_3N_4 materials arises from the softening of intergranular glassy phases and from the oxidation process at elevated temperatures in air. The occurrence of significant degradation in strength of 2Al6Y, 2Al8La, and 2Al3Y4La materials at elevated temperatures with respect to 2Sr6Y and 4Y6La materials is due to the addition of Al_2O_3, which leads to a significant decrease in the softening temperature of intergranular glassy phases and/or in oxidation resistance. The strength results suggest that the materials with rare-earth oxides contain more refractory glassy phases leading to better high-temperature mechanical properties.

Status of milestones

Milestone 321310: Evaluation of flexural versus compressive creep for Al_2O_3 and Al_2O_3-20 vol % SiC whiskers was completed.

Milestone 321311: Evaluation of strength and toughness behavior for Si_3N_4 ceramics containing elongated grain structures was completed.

Publications

H. T. Lin and P. F. Becher, "High-Temperature Creep Deformation of Alumina-SiC Whisker Composites," *J. Am. Ceram. Soc.* **74**(8), 1886–93 (1991).

References

1. H. T. Lin and P. F. Becher, "Creep Behavior of a SiC Whisker-Reinforced Alumina," *J. Am. Ceram. Soc.* **73**(5), 1378–81 (1990).

2. A. G. Robertson, D. S. Wilkinson, and C. H. Cáceres, "Creep and Creep Fracture in Hot-Pressed Alumina," *J. Am. Ceram. Soc.* **74**(5), 915–21 (1991).

3. S. M. Wiederhorn of National Institute of Standards and Testing, personal communication.

Cyclic Fatigue of Toughened Ceramics

K. C. Liu, J. L. Ding, H. Pih, C. O. Stevens, and C. R. Brinkman
(Oak Ridge National Laboratory)

Objective/Scope

The objective of this task is to develop, design, fabricate, and demonstrate the capability to perform tension-tension dynamic fatigue testing on a uniaxially loaded ceramic specimen at elevated temperatures. Three areas of research have been identified as the main thrust of this task: (1) design, fabrication, and demonstration of a load train column that truly aligns with the line of specimen loading; (2) development of a simple specimen grip that can effectively link the load train and test specimen without complicating the specimen geometry and, hence, minimize the cost of the test specimen; and (3) design and analysis of a specimen for tensile cyclic fatigue testing.

Technical progress

Cyclic fatigue behavior of SiC (Hexoloy-SA)

It was reported previously and shown in Fig. 1 (ref. 1) that the 1300°C fatigue data obtained from ORNL specimens (excluding specimens 7-1 and 7-2, which were tested during this reporting period) were generally

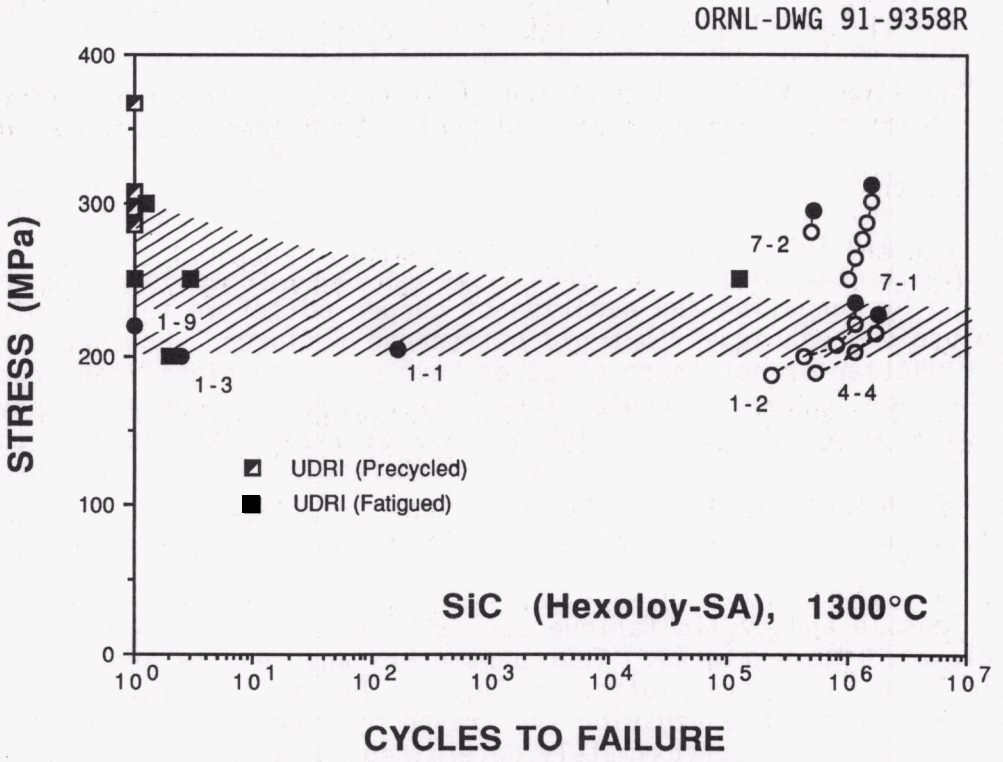

Fig. 1. Comparison of UDRI and ORNL cyclic fatigue data of SiC (Hexoloy-SA) tested at 1300°C.

lower than those obtained from University of Dayton Research Institute (UDRI) specimens. Closed symbols in Fig. 1 indicate the specimens were fractured at the test condition; open symbols indicate the test condition was changed at the number of cycles indicated to the next higher cyclic stress amplitude until failure occurred. A careful review indicated that all of the ORNL specimens except specimen 4-4 were tested in the as-machined condition. It was thought that the residual machining flaws might be a detriment to the fatigue life of unannealed specimens because buttonhead failures occurred in several tests. However, no significant enhancement in fatigue resistance was observed when the fatigue performance of unannealed specimen 1-2 was compared with that of specimen 4-4, which was annealed at 1500°C for 100 h in air.

In light of all successful utilization of copper collets in subsequent tests at 1400°C with no buttonhead failures, two additional tests were performed on specimens 7-1 and 7-2 at 1300°C. Both specimens were annealed, side by side, with specimen 4-4 in the same batch, except that the specimens were made from two different plates, which are identified by the prefix of specimen numbers.

Specimen 7-1 was initially cycled to 250 MPa for the purpose of comparison with UDRI 250-MPa tests, in which two tests fell far short from the target number of 0.45 megacycles, as shown in Fig. 1. In contrast, specimen 7-1 survived far beyond the UDRI target life in excess of one megacycle. Subsequently, the applied stress was increased successively in steps of about 14 MPa after each intermittent step completing a block of about 150,000 cycles until failure occurred at 313 MPa with a total number of cycles to failure at 1.56 megacycles. Specimen 7-2 was tested with a starting cyclic stress of 281 MPa, which was about two 14-MPa steps higher than that of specimen 7-1. After successfully completing the target number of cycles with no indication of imminent failure, the peak stress was increased by a step of 14 MPa at 0.503 megacycles. The specimen subsequently failed at 515,507 cycles in total. The reason for inability of specimen 7-2 to attain the same level of fatigue strength as specimen 7-1 is not known, but it may be related to the amplitude of starting peak stress used. Test results and parameters are summarized in Table 1, and data are plotted in Fig. 1.

Additional results obtained from the above tests indicate that flaw healing by annealing and adoption of copper collet in the gripping fixture were useful techniques to avoid buttonhead failures. However, it is not clear whether or not these measures have made any significant contributions to the high fatigue strength of both specimens. A general observation of the data suggests that the high fatigue strengths exhibited by these two specimens may be attributed to some differences in microstructure of plate samples investigated.

Cyclic fatigue testing of GN-10 Si_3N_4

Tensile and cyclic fatigue strengths were investigated for GN-10 Si_3N_4 at elevated temperatures. Test parameters and results are summarized in Table 2, and data are plotted in Fig. 2. Due to the limited number of test results, the fatigue behavior (portrayed by broken lines and shaded band) of GN-10 Si_3N_4 was approximately determined based on the 1200°C fatigue data[2] obtained previously for NT-154 Si_3N_4, also plotted in Fig. 2 to

Table 1. Summary of tensile and cyclic fatigue tests of Hexoloy-SA SiC tested at elevated temperatures

Specimen	Tensile strength (MPa)	Cyclic stress to failure (MPa)	Intermediate cyclic stress (MPa)	Number of cycles at intermediate cyclic loading	Number of cycles to failure	Locations of fractures
			Temperature = 1300°			
1 - 9	220				1	
1 - 3		199			2	
1 - 1		204			165	
1 - 4			189	239,361	(239,361)[a]	BH & SHNK[b]
1 - 2			187	231,000	(231,000)	
			200	193,800	(424,800)	
			208	394,000	(818,800)	
			222	352,513	(1,171,313)	
		235			1,171,415	
4 - 4			189	551,960	(551,960)	
			202	596,901	(1,148,861)	
			215	567,000	(1,715,861)	
		228		75,647	1,791,508	
7-1			250	1,004,570	(1,004,570)	
			265	133,930	(1,138,500)	
			278	167,270	(1,305,770)	
			289	123,470	(1,429,240)	
			302	5,206	(1,558,110)	
		313		5,206	1,563,316	
7-2			281	503,382	(503,382)	
		295		12,125	515,507	

[a]Number of cycles accumulated at the end of intermediate loading.

[b]BH = Buttonhead failure; SHNK = shank failure.

Table 2. Results of tensile and cyclic fatigue tests of GN-10 Si_3N_4 at elevated temperatures

Specimen	Temp. (°C)	Tensile/cyclic stress to fracture [MPa, (ksi)]	Intermediate cyclic stress [MPa, (ksi)]	Number of cycles to failure	Number of cycles at intermediate loading
357-2	1150	585.6, (84.9)		1	
350-1-2	1200	514.2, (74.6)		1	
340-2-5	1200	350, (50.8)		41,845	
350-2-4	1200		300, (43.5)	(1,139,464)	1,139,464
			313, (45.4)	(1,198,796)	59,332
			326, (47.3)	(1,286,018)	87,222
		337, (48.9)		1,329,464	43,446
338-1-2	1250	472.5, (68.5)		1	
331-1-1	1250	285, (41.3)		59,308	
350-2-5	1250	250, (36.3)		221,774	

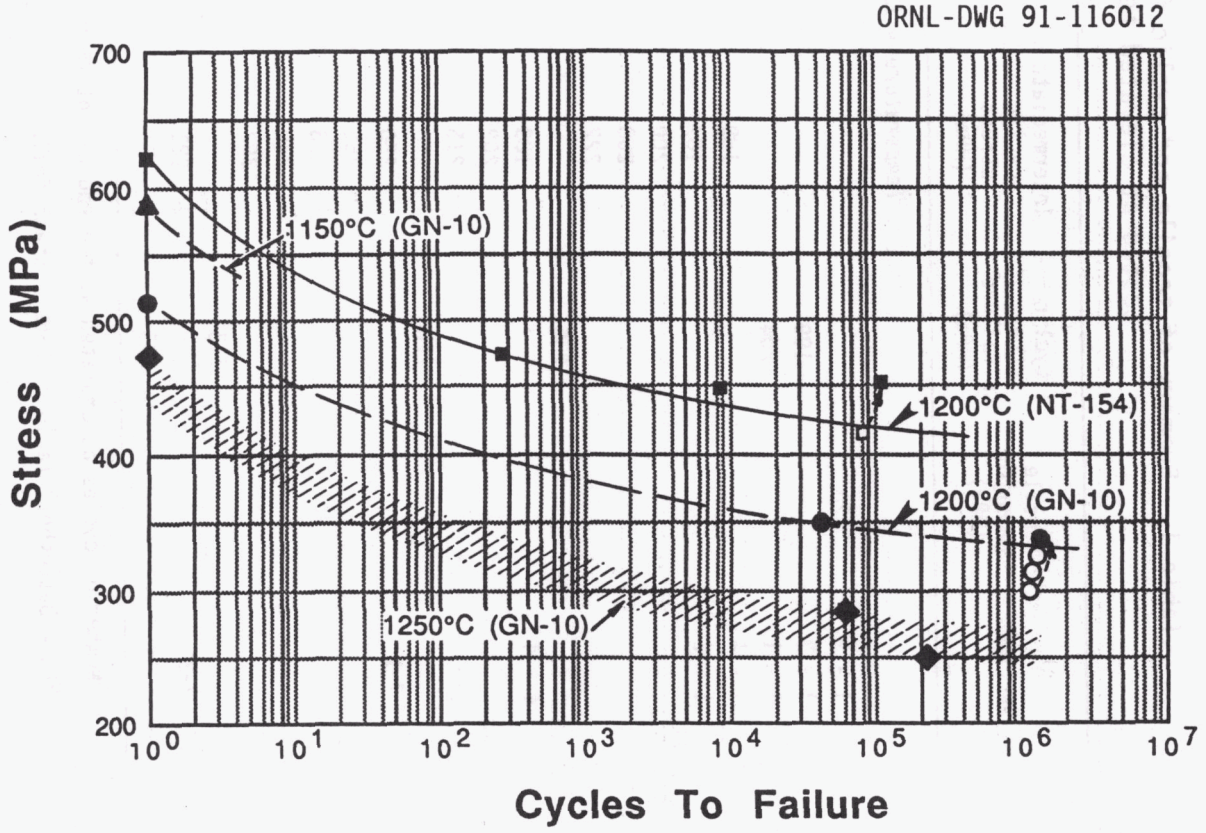

Fig. 2. Tensile fracture and cyclic fatigue behavior of GN-10 Si_3N_4 tested at 1150, 1200, and 1250°C. Cyclic fatigue data of NT-154 Si_3N_4 tested at 1200°C are also included for comparisons.

facilitate comparison. Test results at 1200°C show that both the tensile and cyclic fatigue strengths of GN-10 were lower than those of NT-154 by about 20%. The tensile strength of GN-10 tested at 1150°C hints that the cyclic fatigue strength of GN-10 at 1150°C would be comparable to or slightly lower than those of NT-154. Although not compared in Fig. 2, the tensile and cyclic fatigue strengths of GN-10 at 1200°C and those of NT-154 at 1300°C were about the same, indicating NT-154 was one notch better than GN-10 in terms of temperature.

Acoustic emission studies of ceramic fatigue

Progressive damage in three different ceramic materials subjected to tension-tension cyclic fatigue was monitored using acoustic emission (AE) technique. Silicon nitride, alumina, and SiCw/Al_2O_3 matrix composite were chosen to vary in microstructure, composition, and flaw sizes in order to investigate the effects of these variables on the ability of the AE technique to detect failure before it occurs and locate the potential failure sites.

Figure 3 shows the energy versus time plot for a silicon nitride specimen that was cycled initially to a peak stress of 442 MPa for 14,200 cycles and subsequently raised to 480 MPa, upon which failure occurred after 11,100 cycles. The spike at the end of the test indicates high intensity of AE energy at failure time, as expected. However, this graph did not show an increase in energy rate (warning that failure is imminent)

ORNL-DWG 91-16658

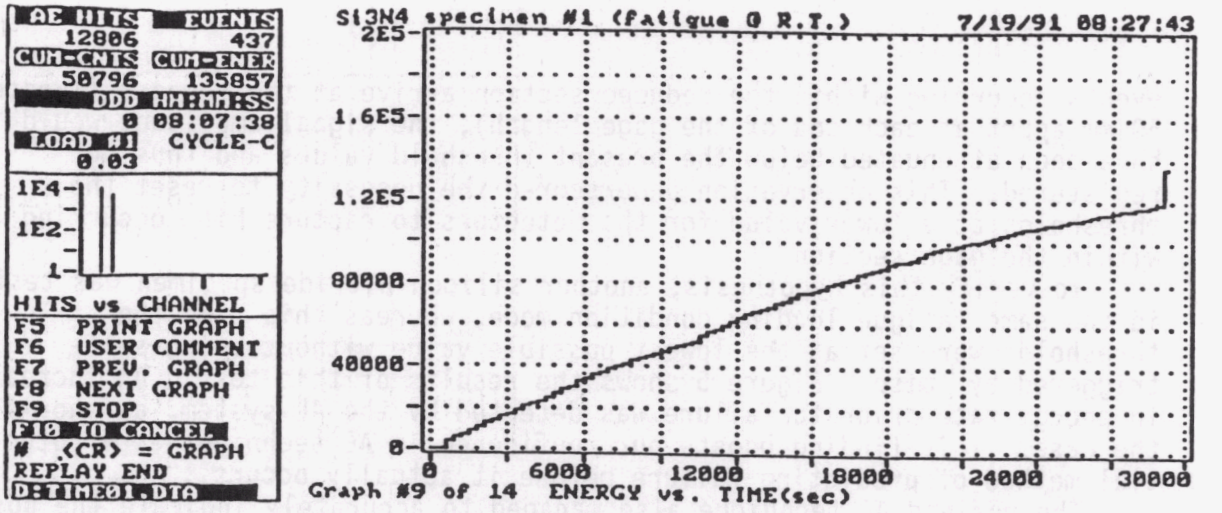

Fig. 3. Plot of energy versus test time for silicon nitride (SNW-1000) tested in tension-tension with a peak stress of 480 MPa and the thresholds set at 50 dB.

prior to fracture. Upon further study and by filtering the AE data to maintain only the relatively high-amplitude hits (50 dB and greater), it was found that no events were registered within the reduced gage section of the specimen except the final AE event that occurred at failure (see Fig. 4). This observation led to the conclusion that by the time the

ORNL-DWG 91-16659

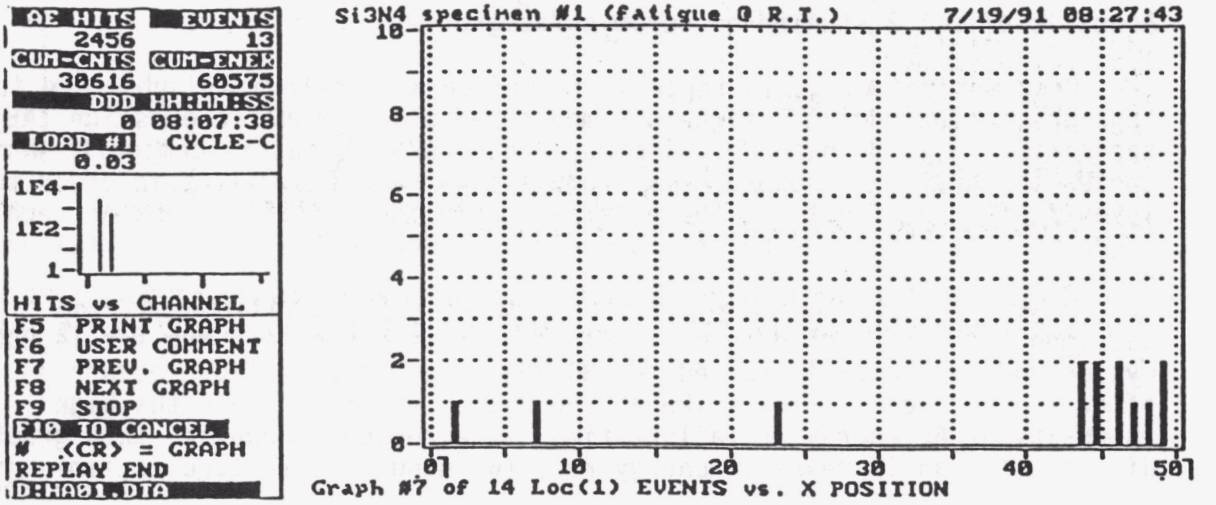

Fig. 4. Plot shows few events occurring within the gage section, when the thresholds were set at 50 dB.

events occurring within the reduced section arrive at the sensors (located 50 mm apart at each end of the gage length), the signal amplitude would have been attenuated below the present threshold values and thus not registered. This observation underscored the necessity to reset the thresholds at a lower value for the detectors to capture hits occurring within the gage section.

To verify this hypothesis, another silicon nitride specimen was tested in the same fatigue loading condition mode, whereas this time the thresholds were set at the lowest possible value without being self-triggered by noise. Figure 5 shows the results of this test. An increase in energy rate prior to failure was detected by the AE system, as should be the case. This finding boosts our confidence in AE technique as a potential method of predicting failure before it actually occurs.

The refined AE technique also managed to accurately indicate the position of the failure sites in both specimens. Figure 6 shows the counts versus position for one of the silicon nitride specimens tested. The spike at x = 15mm seen in this graph coincides with the location of failure in this specimen.

Similar analyses are currently underway for specimens made of the alumina and SiCw/Al_2O_3. Preliminary studies indicate that the AE system also accurately predicted the locations of failure in these two specimens.

ORNL-DWG 91-16660

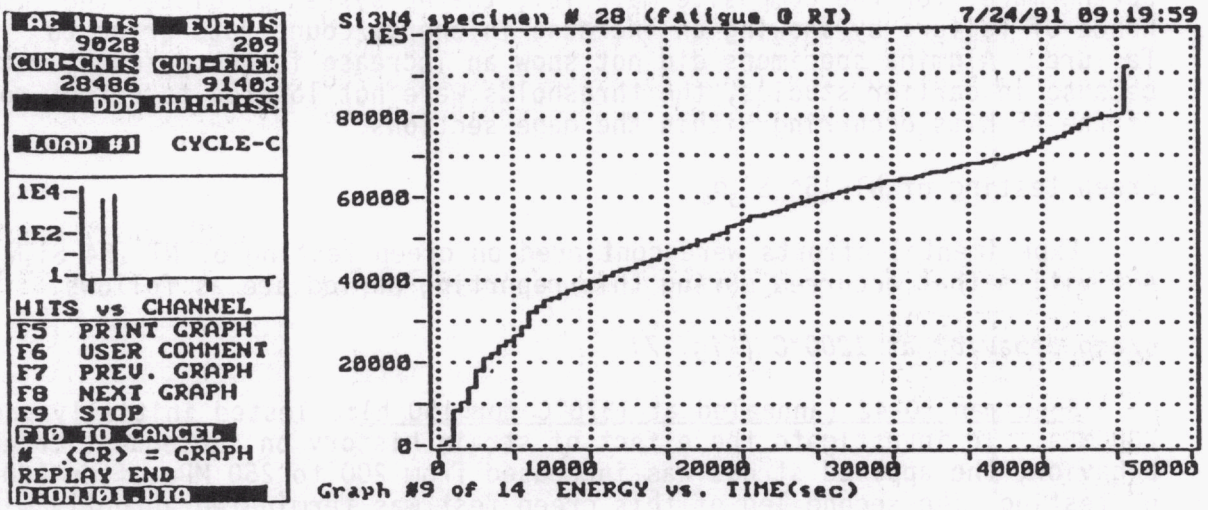

Fig. 5. Plot of energy vs test time for the second specimen tested in the same condition as the first specimen, except the thresholds were set at 42 dB.

ORNL-DWG 91-16661

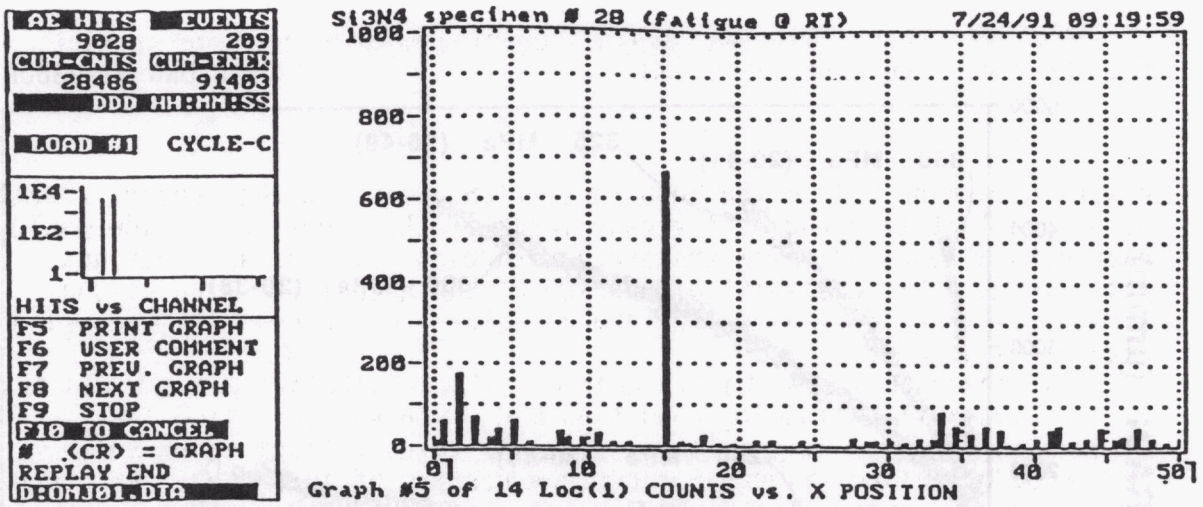

Fig. 6. The highest peak indicates high frequency of events and the location of specimen failure.

Furthermore, for the composite material, the AE system predicted the imminence of failure by showing an increase in energy/count rate prior to failure. Alumina specimens did not show an increase in energy/count rate because in earlier studies, the thresholds were not lowered to detect most of the AE hits occurring within the gage sections.

Creep testing of NT-154 Si_3N_4

Experimental efforts were continued on creep testing of NT-154 Si_3N_4. Activities that occurred during this reporting period are as follows.

Creep behavior at 1200°C (Fig. 7)

Specimen 20-42 (annealed at 1370°C for 150 h): Tested initially under 200 MPa. To investigate the effect of strain history on subsequent creep behavior, the applied stress was increased from 200 to 250 MPa after 1600 h of testing. The second leg of this creep test was terminated abruptly with a premature specimen failure that occurred outside the gage section due to a general power outage. The open arrowhead shown at the end of the creep curve indicates the test would have continued if the premature failure had not occurred.

Specimen 20-48 (annealed): Tested under a constant stress of 250 MPa. This specimen also failed prematurely due to the power outage after 1440 h of testing (Fig. 7). The creep behavior of specimen 20-48 and that of

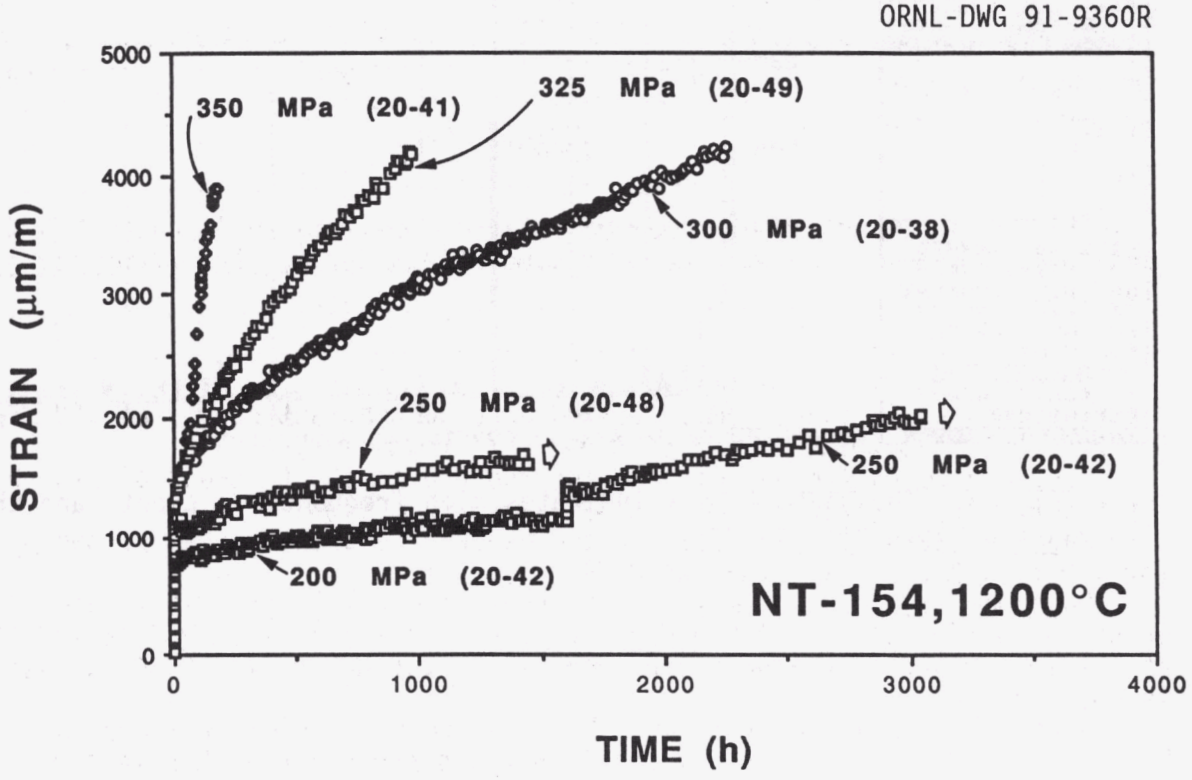

Fig. 7. Creep curves of NT-154 Si_3N_4 tested at 1200°C under indicated applied stresses.

specimen 20-42 subjected to the second leg of loading are compared in Fig. 8. They have been replotted such that both start at zero time to facilitate comparison. Both creep curves are about the same, except that specimen 20-48 crept more than specimen 20-42 by about 200 microstrain during the first 5 h. This observation suggests that the material may have weak memory of previous strain history at the temperature or the applied stress might be too low to have stimulated the material memory.

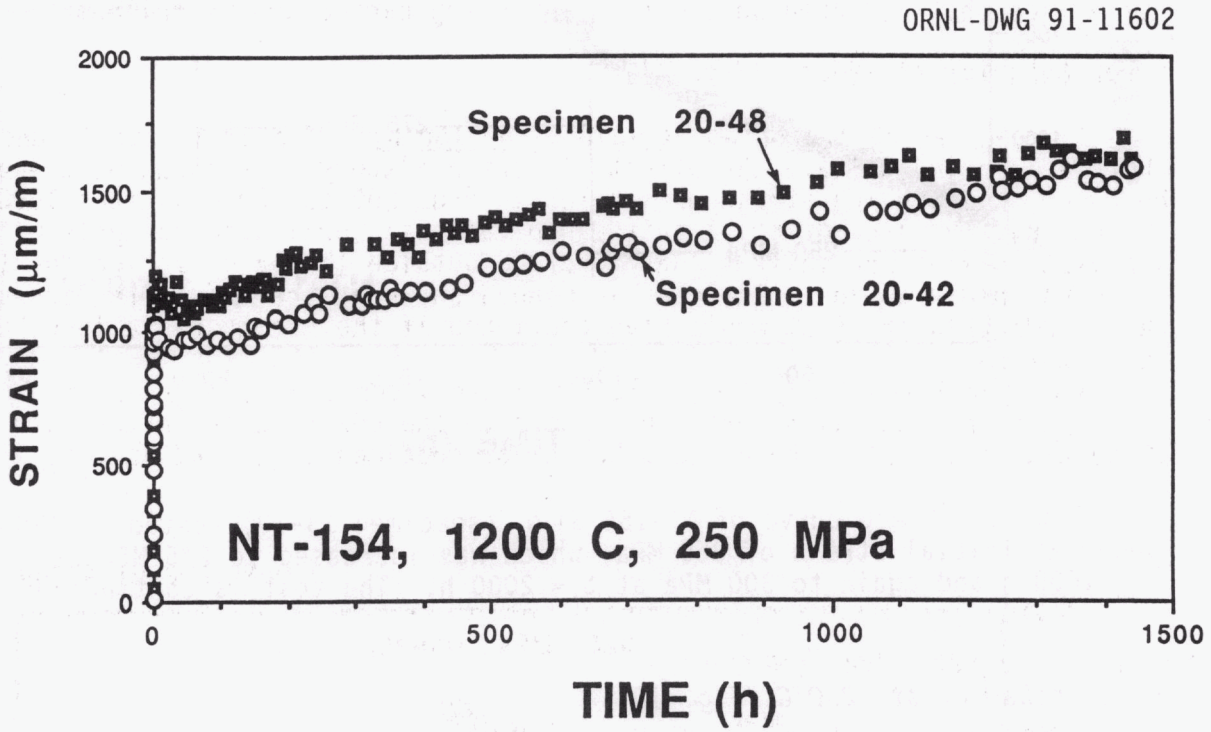

Fig. 8. Comparison of creep behavior of specimen 20-48 under 250 MPa and that of specimen 20-42 under the same stress during the second leg of loading.

Specimen 20-38 (annealed): Tested under a constant stress of 300 MPa for 2257 h with a total strain of 0.4%; test completed.

Specimen 20-49 (annealed): Tested under a constant stress of 325 MPa for 979 h with a total strain of 0.42%; test completed.

Specimen 20-41 (annealed): Tested under a constant stress of 350 MPa for 150 h with a total strain of 0.39%; test completed.

Specimen 13-10 (annealed): Test (Fig. 9) was initiated at 1200°C under an initial stress of 250 MPa, which was increased from 250 to 275 MPa at t ~ 1000 h and increased again from 275 to 300 MPa at t ~ 2000 h; test is continuing.

General observations indicate that the creep behavior of annealed NT-154 at 1200°C was reasonably consistent and predictable when tested under constant loading conditions.

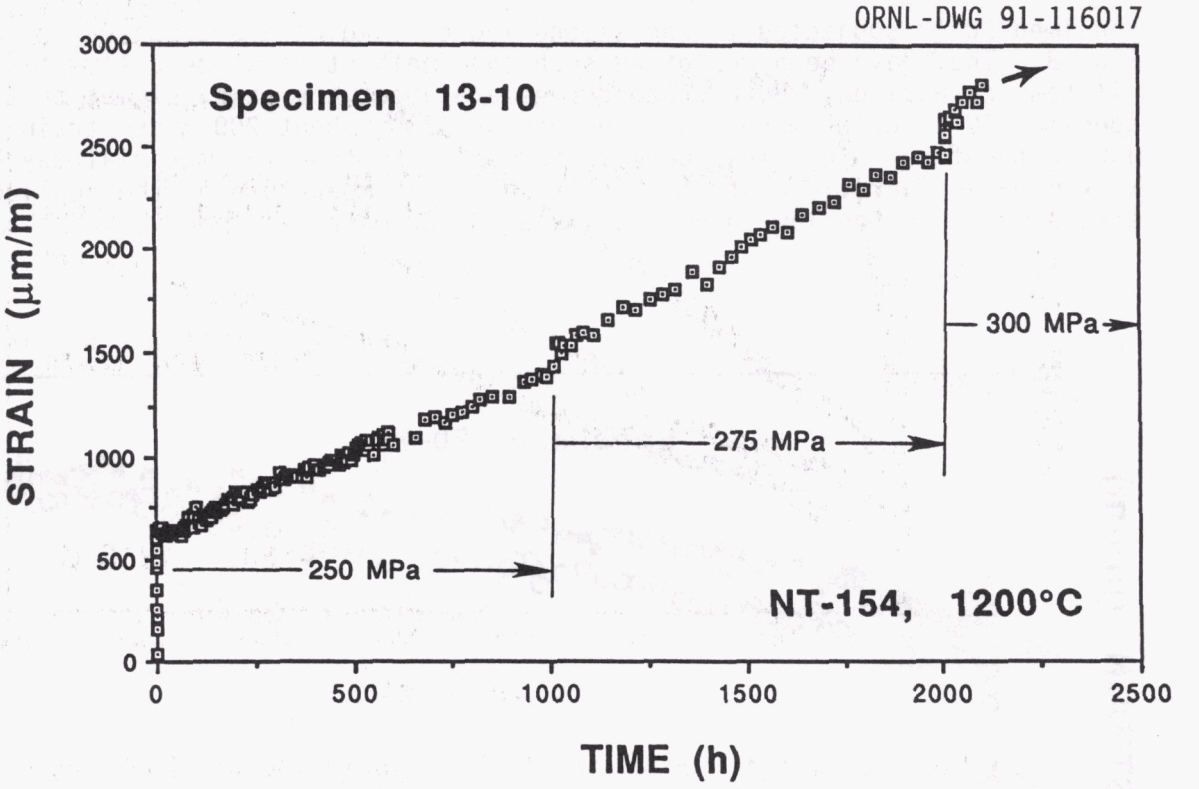

Fig. 9. Creep curve of NT-154 Si_3N_4 (specimen 13-10) tested at 1200°C under an initial stress of 250 MPa, which was increased to 275 MPa at t = 1000 h and again to 300 MPa at t = 2000 h. The test is continuing.

Creep behavior at 1250°C (Fig. 10)

Specimen 20-62 (annealed): Tested under a constant stress of 275 MPa for 100 h with a total strain of 0.33%; test completed.

Specimen 20-57 (annealed): Tested under a constant stress of 250 MPa for 340 h with a total strain of 0.49%; test completed.

Specimen 20-59 (annealed): Tested under a constant stress of 225 MPa for 2153 h with a total strain of 0.46%; test completed.

Specimen 20-56 (annealed): Test is continuing under a constant stress of 175 MPa with a total strain of 0.3% accumulated to this date.

Specimen 13-04 (annealed): Test began initially under 150 MPa, which was increased to 175 MPa at t ~ 1000 h. A comparison of the creep behavior of the first 1000 h shows that this specimen is less creep resistant than specimen 20-56. The creep strain rate of specimen 13-04, after increased to 175 MPa, was also higher than that of specimen 20-56. A plausible explanation is the lot variation as the prefix of the specimen numbers indicates. Until microstructural analyses are completed, no conclusive remarks can be made at this time.

Specimen 13-14 (annealed): Test (Fig. 11) was initiated under an applied stress of 175 MPa at 1200°C, which was increased to 1250°C at t = 1000 h. Although the furnace power was shut down at t = 777 h due to a

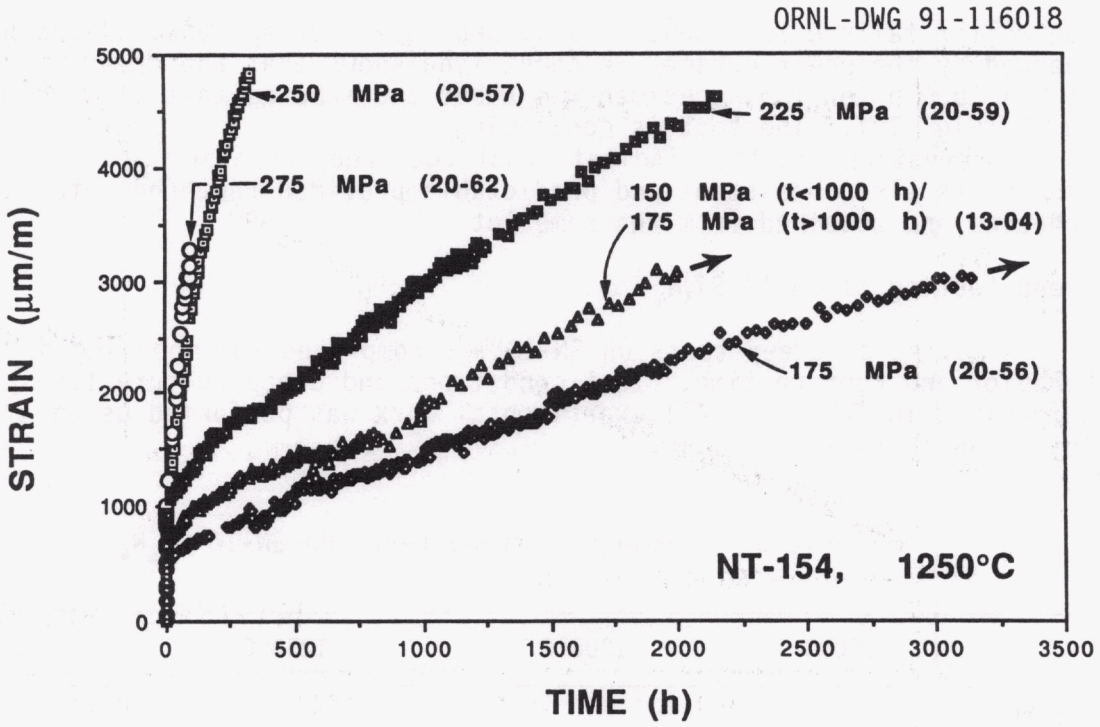

Fig. 10. Creep curves of NT-154 Si_3N_4 tested at 1250°C under indicated applied stresses.

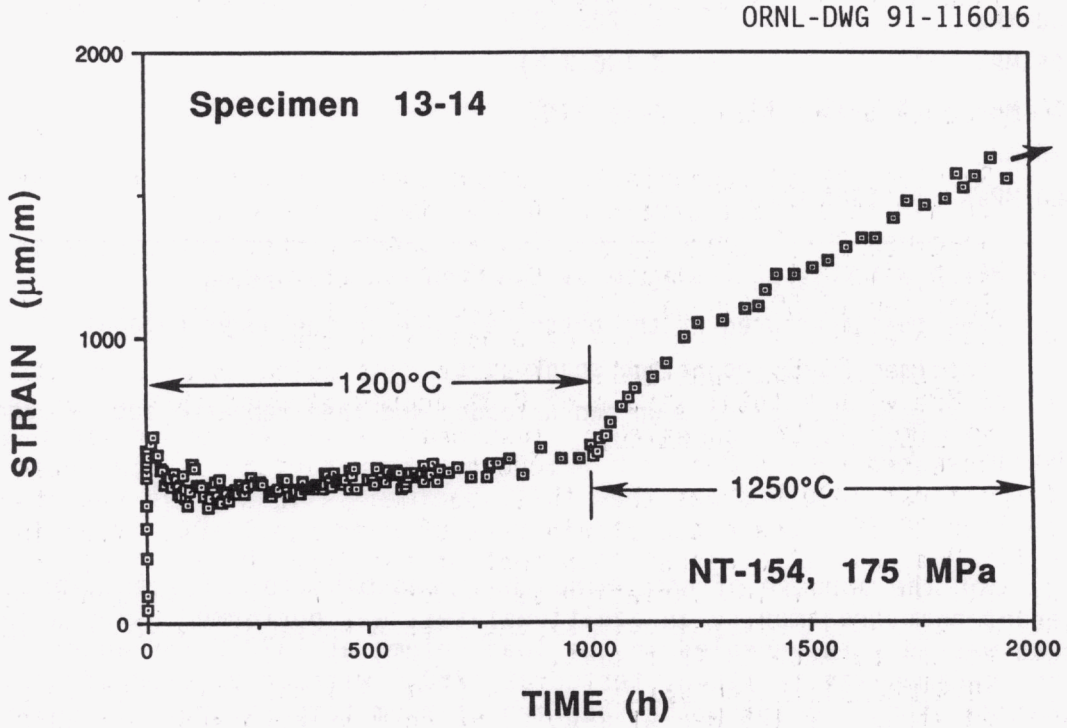

Fig. 11. Creep curve of NT-154 Si_3N_4 (specimen 13-14) tested under an applied stress of 175 MPa at 1200°C, which was increased to 1250°C at t = 1000 h. The test is continuing.

controller failure for about 2 days, subsequent creep behavior was not changed by the power outage. A comparison shows that the creep strain rate at t = 2000 h for this specimen was about the same as that of specimen 20-56 (Fig. 10). The test is continuing.

Observations further indicate that the creep behavior of NT-154 at 1250°C was also consistent and predictable provided that the material is annealed and obtained from the same lot.

Creep testing of GN-10 Si_3N_4

A series of creep tests on GN-10 was completed for modeling of creep behavior and rupture time. Test conditions and creep rupture times are summarized in Table 3. All experimental work was performed using a single lot of GN-10 Si_3N_4.

Table 3. Summary of creep tests on GN-10 Si_3N_4

	1150°C	1200°C	1250°C	1300°C
75 MPa				X[d] (> 936.9 h)
100 MPa			X[c] (> 1029.5 h)	X (1721.33 h)
125 MPa		X[a] (> 1030.9 h)	X (2996.35 h)	X (15.2 h)
150 MPa		X (1203.6 h)	X (135.9 h)	X (0.2 h)
175 MPa		X[b] (> 3405.2 h)	X (25.5 h)	
200 MPa		X (203.13 h)		
225 MPa		X (96.3 h)		
250 MPa	X (733.8 h)	X (7.5 h)		
275 MP				
300 MPa	X (365.4 h)			

[a]Stress increased to 225 Mpa after 1030.9 h of testing.

[b]Specimen fractured at the buttonhead due to the power outage.

[c]Specimen fractured at the shank part.

[d]Specimen was cooled down and unloaded and then reheated and reloaded at the end of 936.9 h.

For the purpose of comparing the creep behavior of specimens with different heat treatments, an additional test was performed using a specimen that was in-situ annealed in the load column at 1370°C for about 150 h. The specimen was, in turn, tested at 1250°C with an applied stress of 175 MPa without cooling the specimen to room temperature. In contrast, a specimen annealed in a laboratory furnace under stress-free conditions must

be reheated from room temperature to the test temperature. To maintain a good alignment in the load column during in-situ annealing, the specimen was lightly loaded with a stress of 16.6 MPa. Despite the light loading, a significant amount of creep deformation was measured, as shown in Fig. 12. The subsequent creep test was very short, indicating that the specimen might have failed prematurely. This creep curve and those obtained previously for two specimens tested in the as-received and furnace-annealed conditions are compared in Fig. 13. The hardening characteristic of the material in the as-received condition was clearly different from that of annealed material. However, the hardening effects introduced by different annealing methods remained unclear due to the incomplete information obtained from the short test.

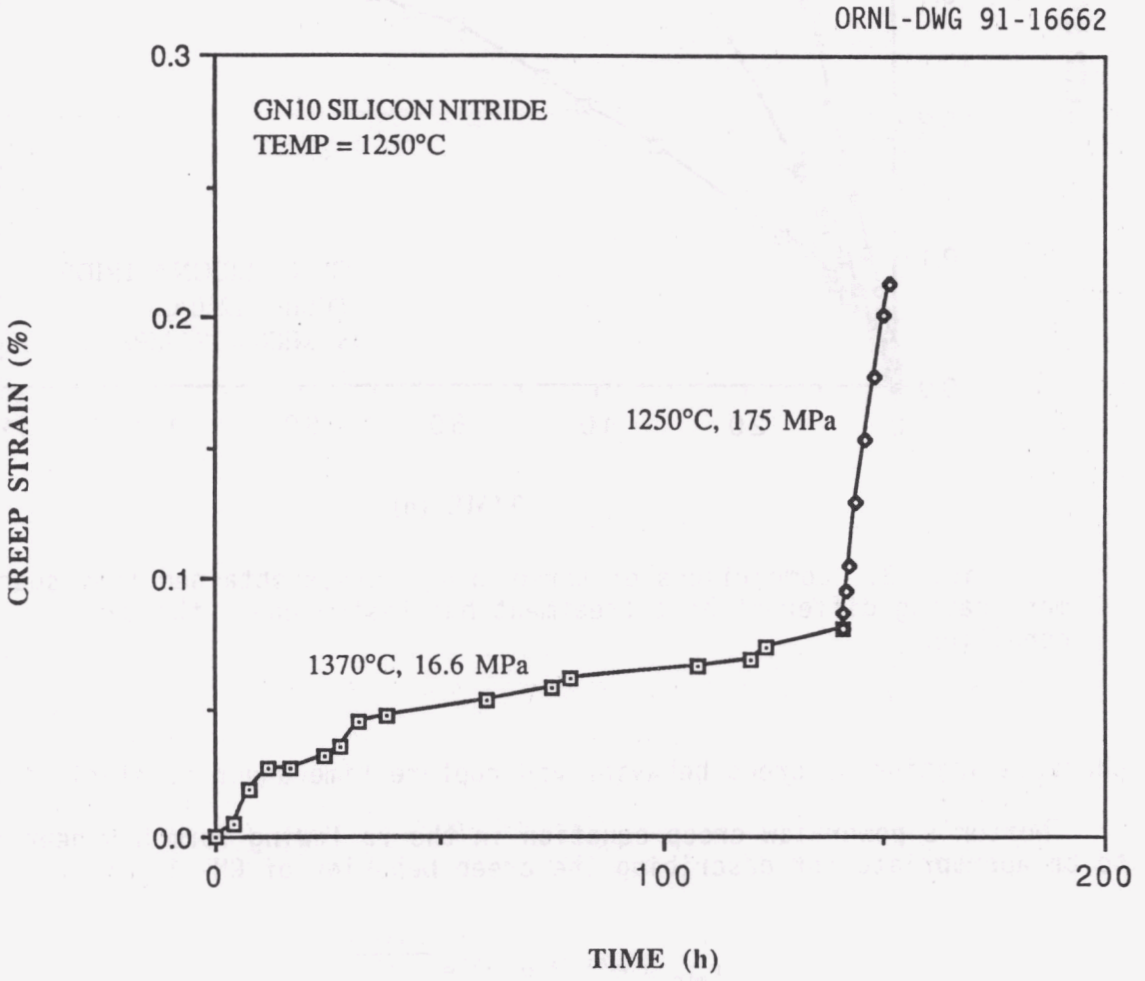

Fig. 12. Creep curve of GN-10 annealed at 1370°C with a tare stress of 16.6 MPa followed by a change in test condition to 1250°C with an applied stress of 175 MPa.

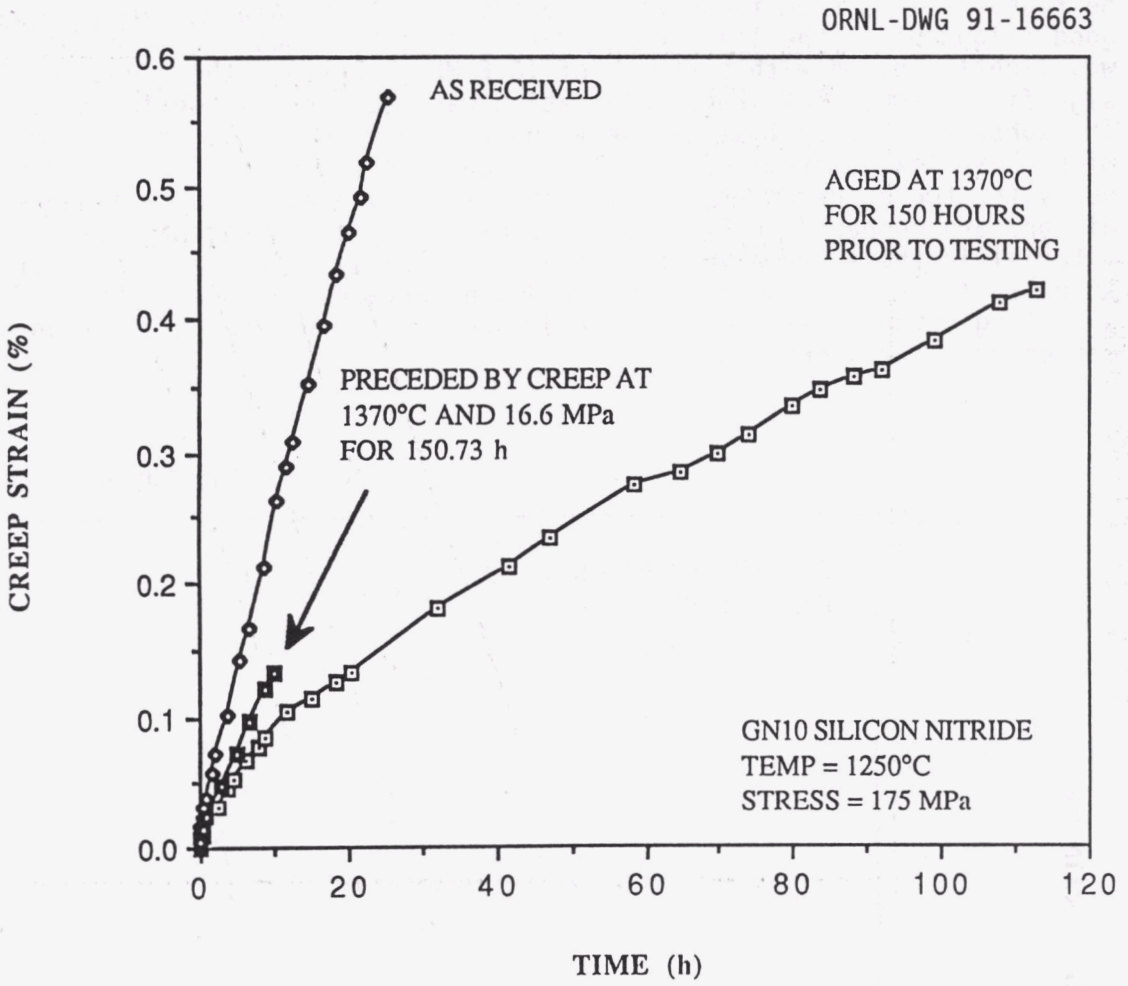

Fig. 13. Comparisons of three creep curves obtained from specimens having different heat treatment but tested under the same condition.

Characterization of creep behavior and rupture time under constant stresses

Norton's power-law creep equation in the following form has been shown to be appropriate for describing the creep behavior of GN-10:

$$\dot{\varepsilon}_{min} = e^{61.73}\, \sigma^{11.31} e^{\frac{-1631.7}{RT}}, \qquad (1)$$

where $\dot{\varepsilon}_{min}$ is the minimum creep rate in h^{-1}, σ the stress in MPa, T the absolute temperature in K, and R the gas constant. The stress exponent and activation energy are estimated to be 11.31 and 1631.7 kJ/mole, respectively. Experimental data and predictions by Eq. (1) are compared in Fig. 14.

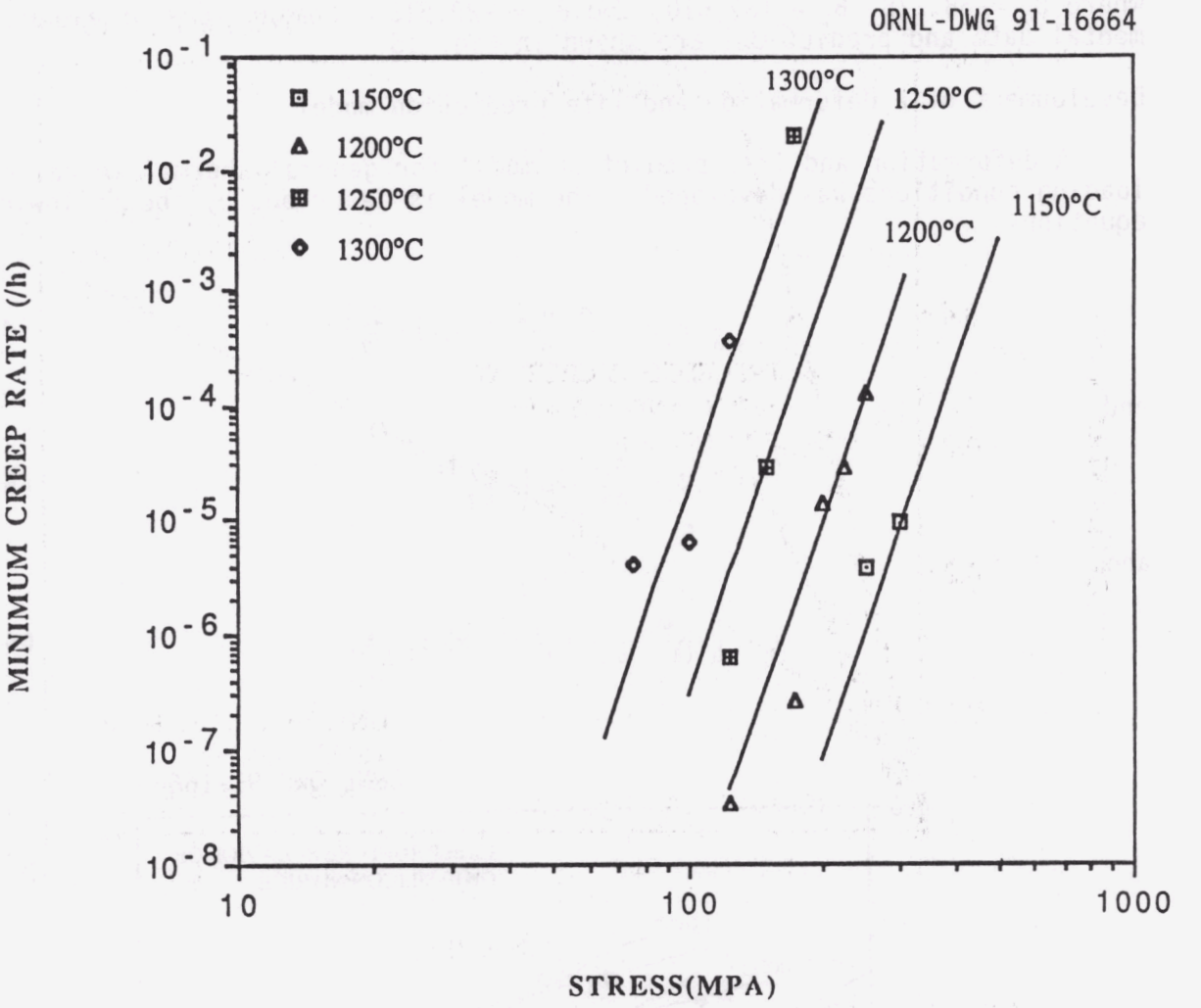

Fig. 14. Comparisons of measured minimum creep rates and predicted. Symbols are experimental data, and the solid lines are generated from Eq. (2).

In order to predict the rupture time as a function of T and σ, two empirical equations were developed based on the minimum-commitment (MC) model and the Larson-Miller (LM) model. The MC mode is described by

$$\log t_r + [R_1 (T-T_m) + R_2 (1/T - 1/T_m)] = B + C \log\sigma + D/\sigma + E\sigma^2 , \quad (2)$$

where t_r is the rupture time in hours and T_m the middle temperature, which is 1498 K, of the test temperature range used. The constants were determined to be: R_1 = 0.17312, R_2 = 303,720, B = 87.238, C = -45.689, D = 0.11559, and E = -0.97325×10^{-4}. The LM model is described by

$$\log t_r = B_0 + B_1/T + B_2 \log\sigma/T , \quad (3)$$

where B_0 =-58.278, B_1 = 136,610, and B_2 = -20,513. Comparisons of experimental data and predictions are shown in Fig. 15.

Development of a deformation and life prediction model

A deformation and life prediction model for general thermal mechanical loading conditions was developed. The model is described by the following equations:

$$\epsilon = \frac{\epsilon_o}{\delta} \sinh \left(\frac{\sigma - \sigma_{th}}{100}\right)^2 \exp\left(-\frac{Q_\epsilon}{RT}\right), \tag{4}$$

and

$$\delta = \frac{\delta_o}{\delta^m} \exp\left(-\frac{Q_\delta}{RT}\right), \tag{5}$$

and

$$\omega = \frac{\omega_o}{\delta\ (1 - \omega)} \left(\frac{\sigma}{\sigma_o}\right)^v \exp\left(-\frac{Q_\epsilon}{RT}\right), \tag{6}$$

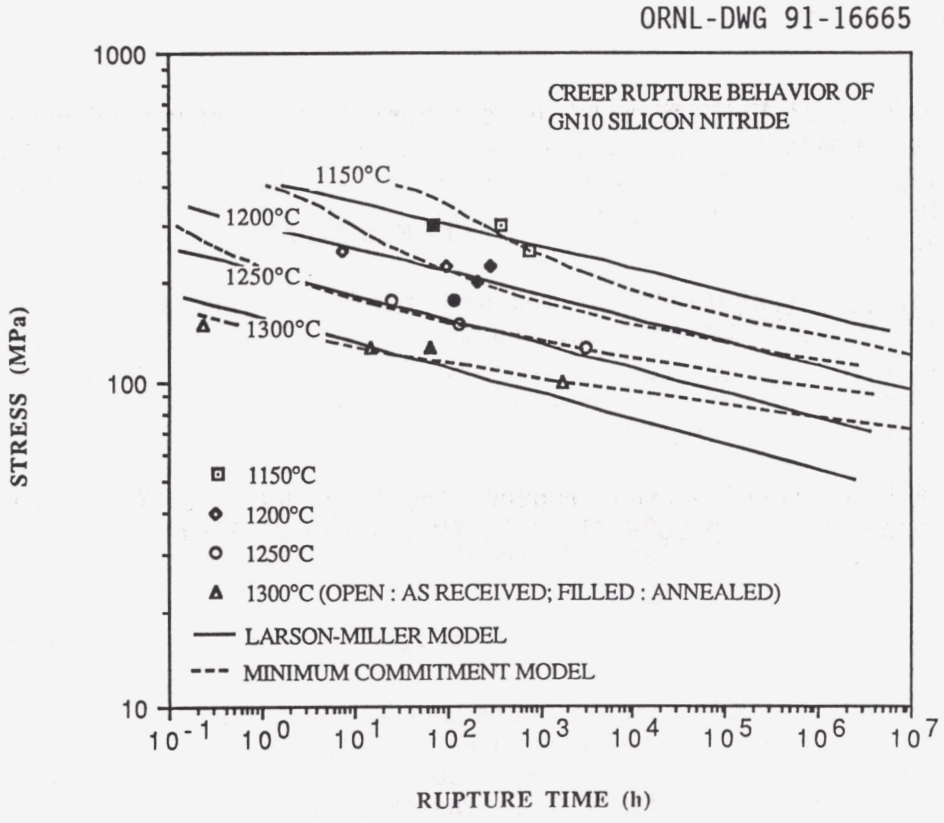

Fig. 15. Comparisons of experimental data and model predictions for the creep-rupture time of GN-10 Si_3N_4.

where ε is the creep strain, δ is a devitrification variable that takes an initial value equal to 1 but increases as devitrification prevails in the grain-boundary phase, ω is a creep damage variable that takes a value ranging from 0 to 1 with 0 corresponding to the initial state and 1 to the ruptured state, and σ_{th} is the threshold stress in MPa:

$$\varepsilon_o = e^{62.259} \text{ for } T \leq 1200°C \text{ and } = e^{36.455} \text{ for } T \geq 1200°C ,$$

$$\sigma_{th} = 2.8342 \times 10^{-6} \times 10^{11069/T} \text{ MPa} ,$$

$$Q_\varepsilon = 711.34 \text{ kJ/mole for } T \leq 1200°C \text{ and } = 395.51 \text{ kJ/mole for } T \geq 1200°C ,$$

$$m = 0.43 ,$$

$$\delta_o = e^{78.8} \text{ for } T \leq 1200°C \text{ and } = e^{2.62} \text{ for } T \geq 1200°C ,$$

$$Q_d = 997.12 \text{ kJ/mole for } T \leq 1200°C \text{ and } = 64.65 \text{ kJ/mole for } T \geq 1200°C ,$$

and

$$\omega_o = e^{110.74} \; V = 10.86 \text{ and } Q_\omega = 1510 \text{ kJ/mole} .$$

Comparisons between model predictions and the creep behavior under constant temperature and constant stress are shown in Figs. 16 to 19; the annealing effects are compared in Figs. 20 to 23, the creep behavior under variable loadings are compared in Figs. 24 and 25, and the rupture behavior is compared in Fig. 26.

Status of milestone

Completed a matrix of tensile and fatigue tests on advanced silicon carbide and cyclic/static fatigue tests on NT-154 silicon nitride at high temperatures (Milestone 321412).

Completed tensile creep rupture tests for GN-10 Si_3N_4 tested at elevated temperatures by July 31, 1991 (Milestone 321506).

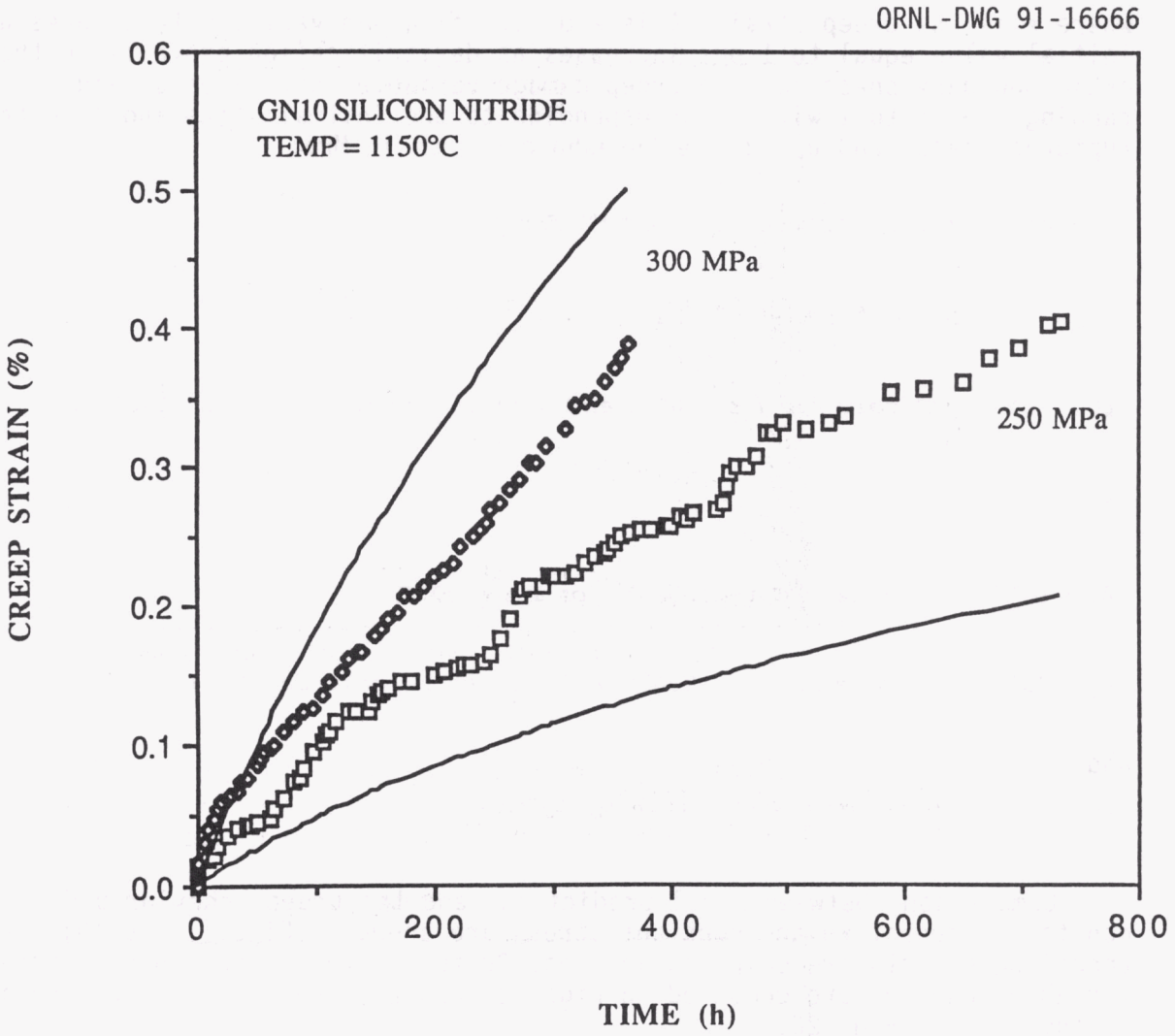

Fig. 16. Comparisons of creep curves of GN-10 tested at 1150°C. Symbols are experimental data, and solid lines are predicted from the model.

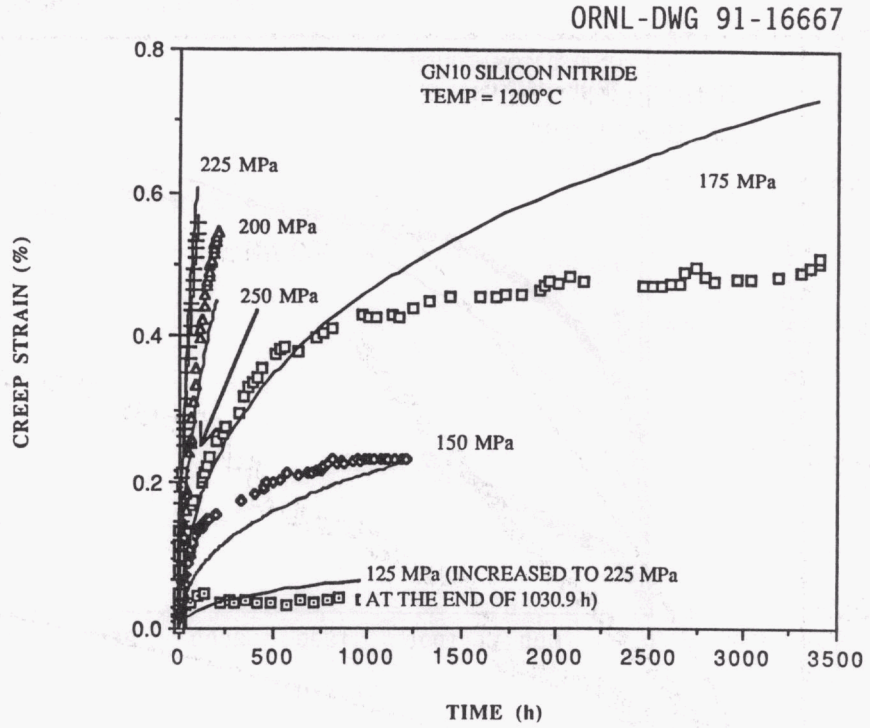

Fig. 17(*a*). Comparisons of creep curves of GN-10 tested at 1200°C. Symbols are experimental data, and solid lines are predicted from the model.

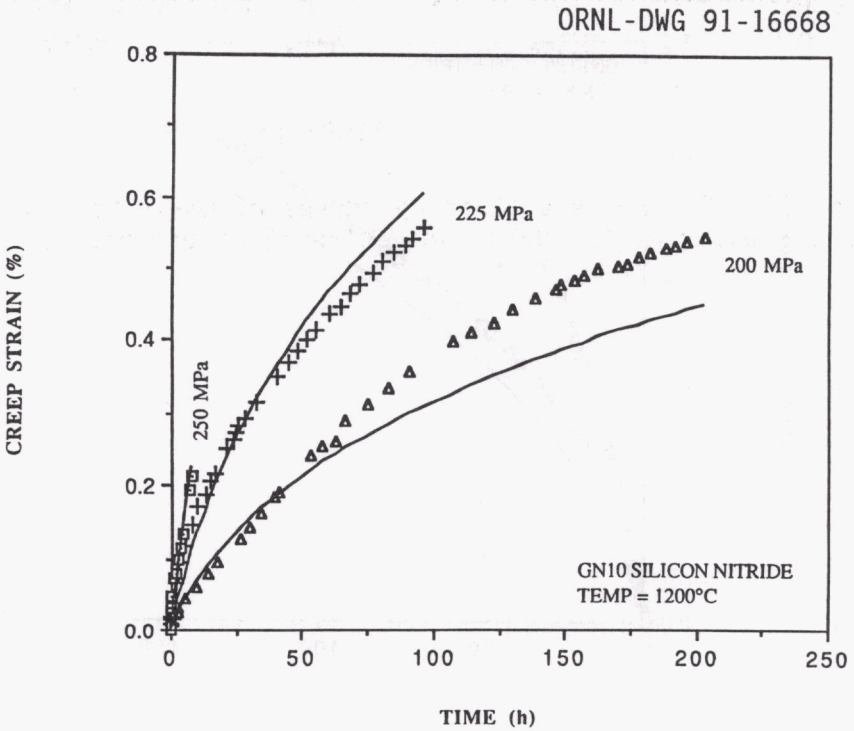

Fig. 17(*b*). A close-up of initial transient creep curves shown in Fig. 6(*a*).

ORNL-DWG 91-16669

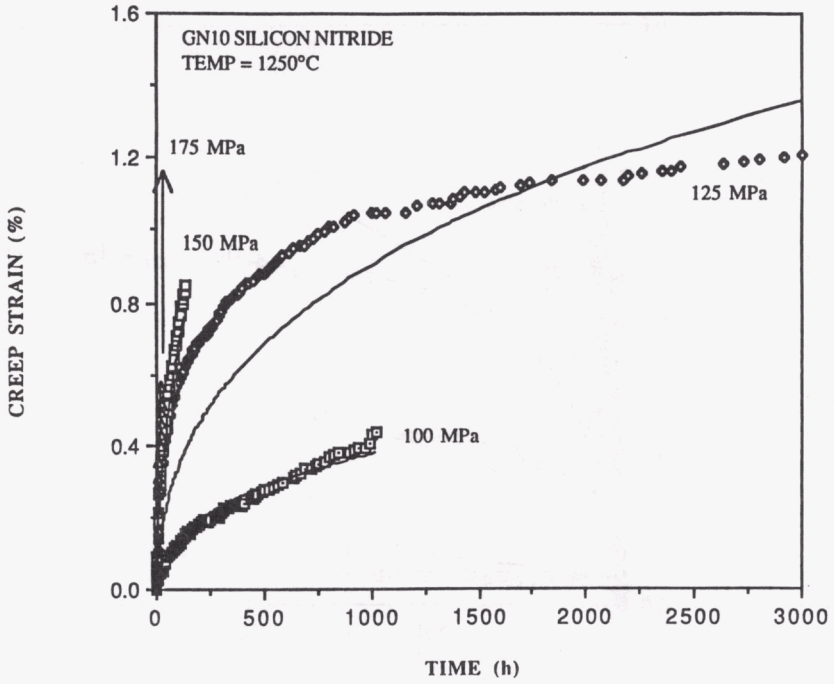

Fig. 18(*a*). Comparisons of creep curves of GN-10 tested at 1250°C. Symbols are experimental data, and solid lines are predicted from the model.

ORNL-DWG 91-16670

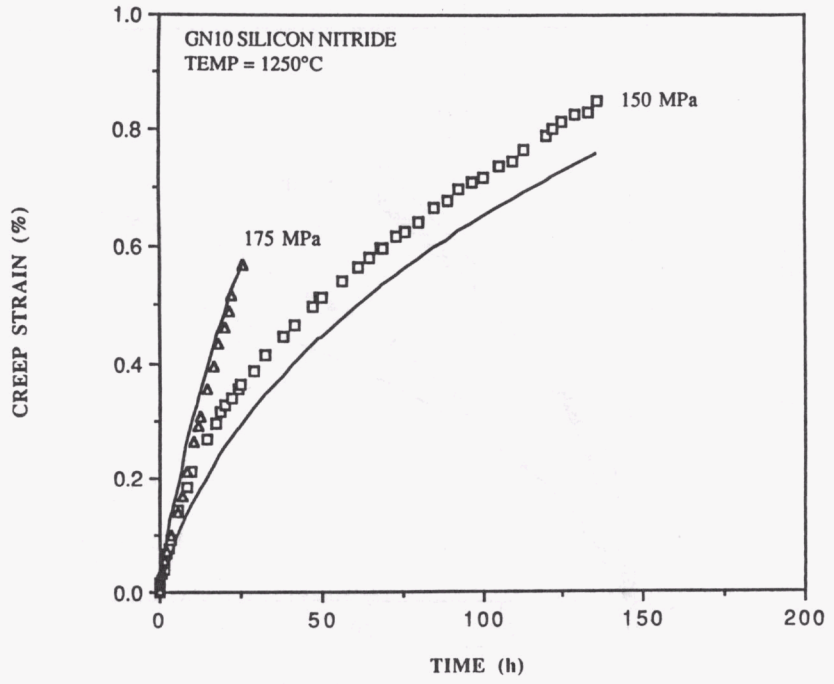

Fig. 18(*b*). A close-up of initial transient creep curves shown in Fig. 7(*a*).

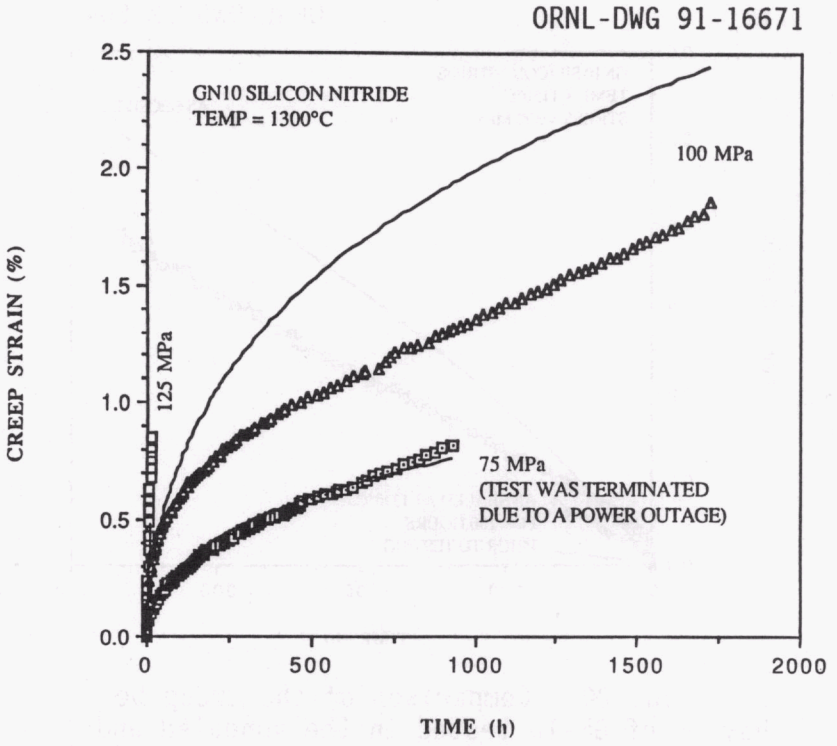

Fig. 19(*a*). Comparisons of creep curves of GN-10 tested at 1300°C. Symbols are experimental data, and solid lines are predicted from the model.

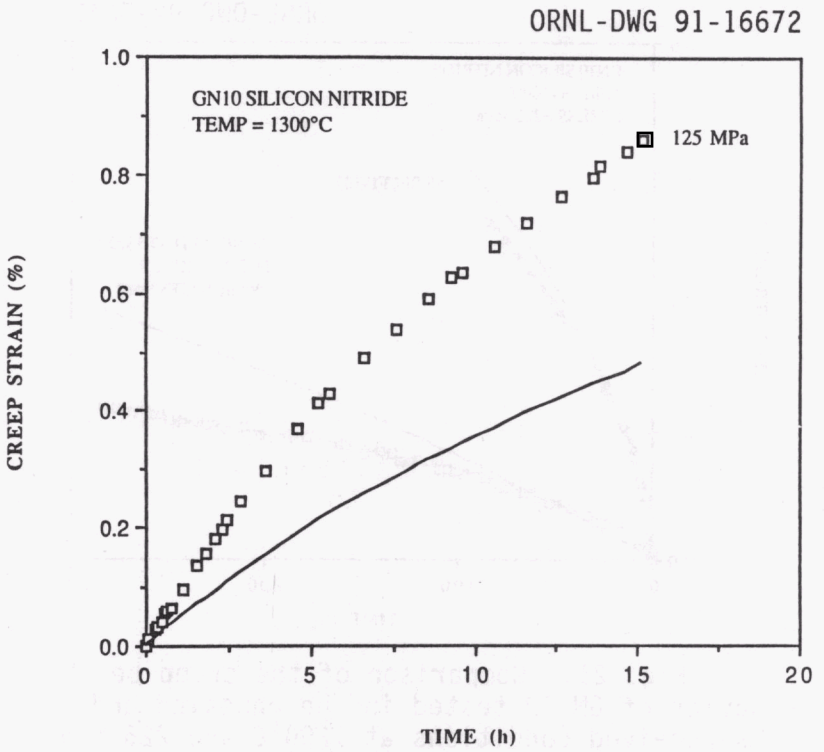

Fig. 19(*b*). A close-up of initial transient creep curves shown in Fig. 8(*a*).

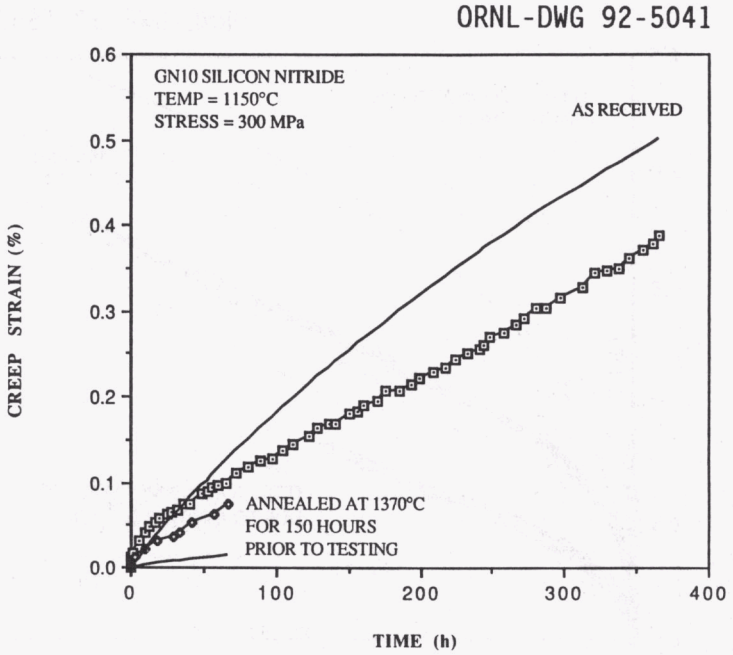

Fig. 20. Comparison of the creep behavior of GN-10 tested in the annealed and as-received conditions at 1150°C and 300 MPa. Symbols are experimental data, and lines are predictions from the model.

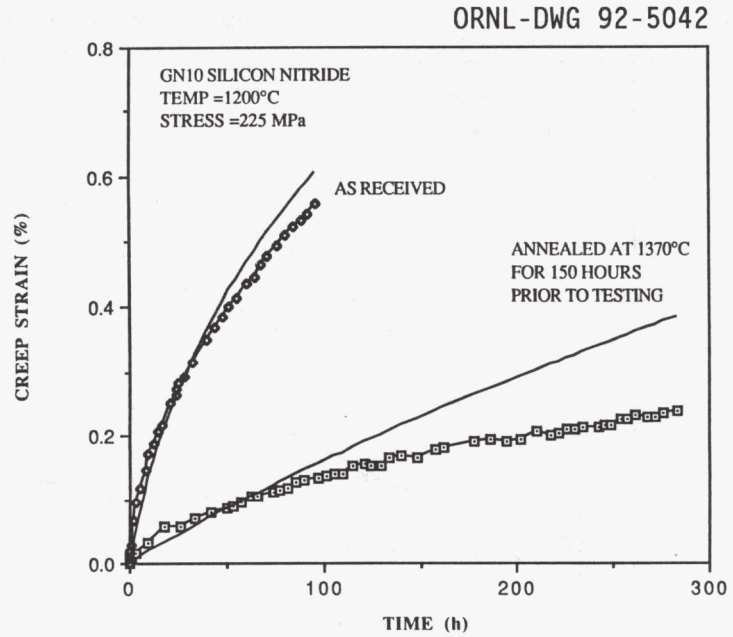

Fig. 21. Comparison of the creep behavior of GN-10 tested in the annealed and as-received conditions at 1200°C and 225 MPa. Symbols are experimental data, and lines are predictions from the model.

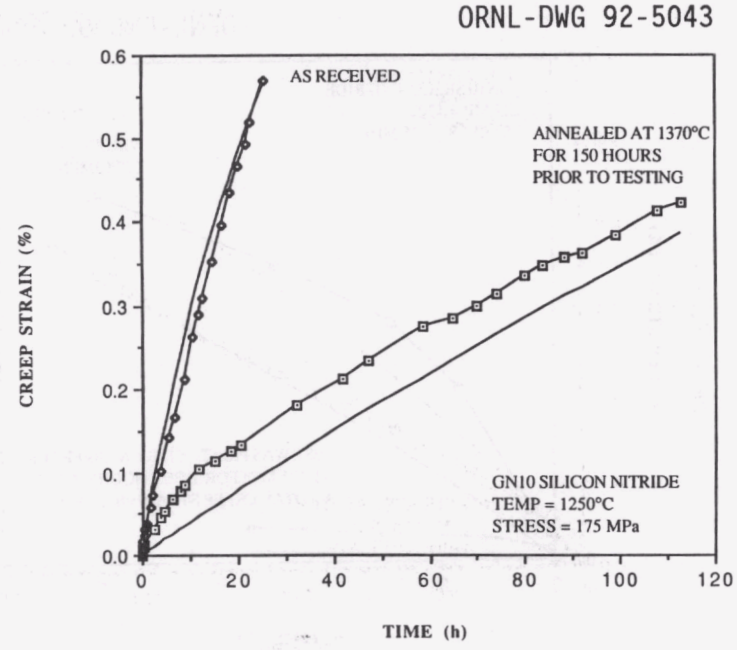

Fig. 22. Comparison of the creep behavior of GN-10 tested in the annealed and as-received conditions at 1250°C and 175 MPa. Symbols are experimental data, and lines are predictions from the model.

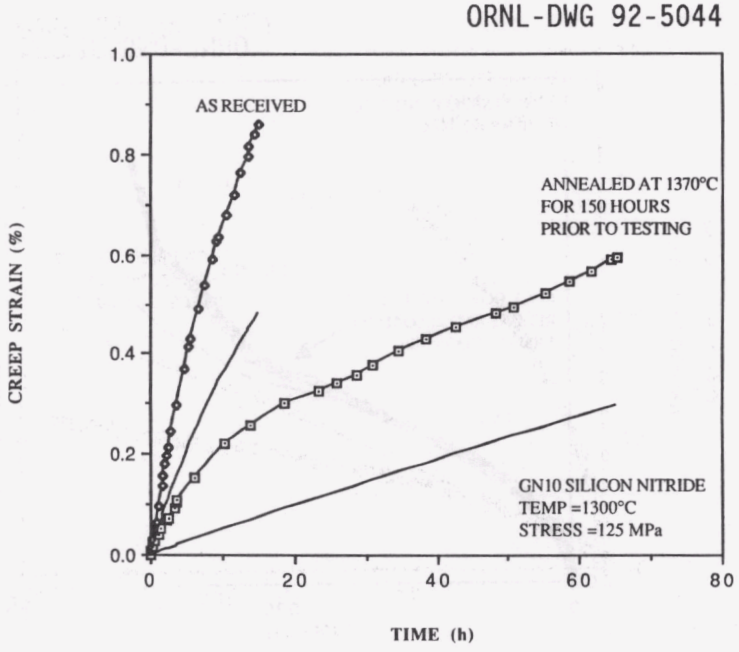

Fig. 23. Comparison of the creep behavior of GN-10 tested in the annealed and as-received conditions at 1300°C and 125 MPa. Symbols are experimental data, and lines are predictions from the model.

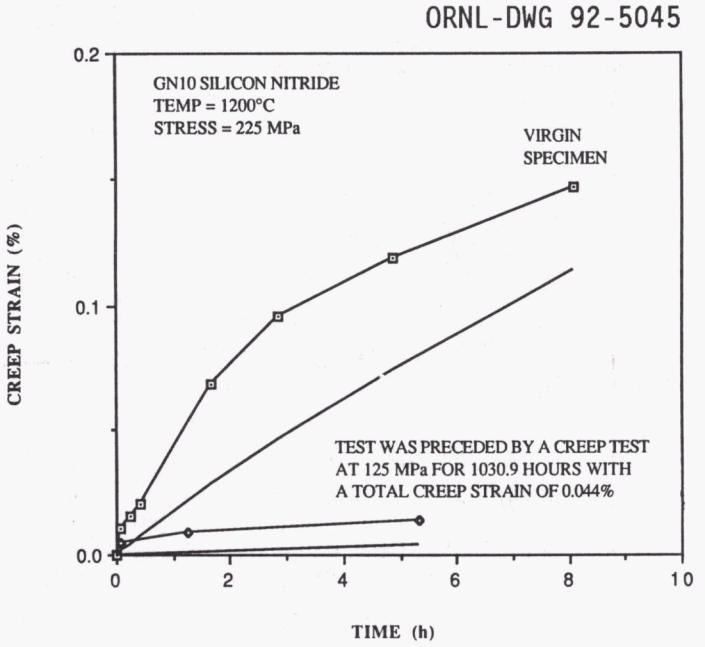

Fig. 24. Comparison of initial transient creep behavior of an uncrept specimen and that of a specimen precrept at 125 MPa for 1030.9 h. Symbols are experimental data, and lines are predictions from the model.

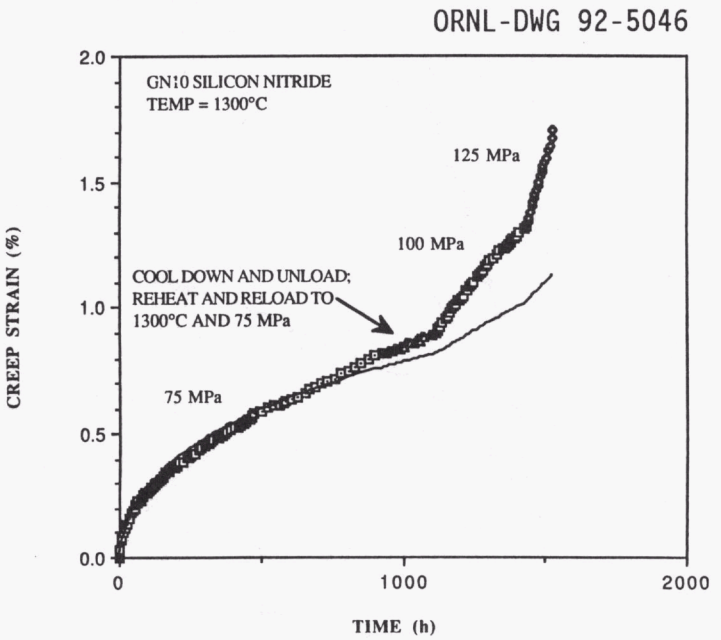

Fig. 25. Comparison between measured creep curve of a specimen tested under incremental step loading at 1300°C and a theoretical prediction shown by a solid line.

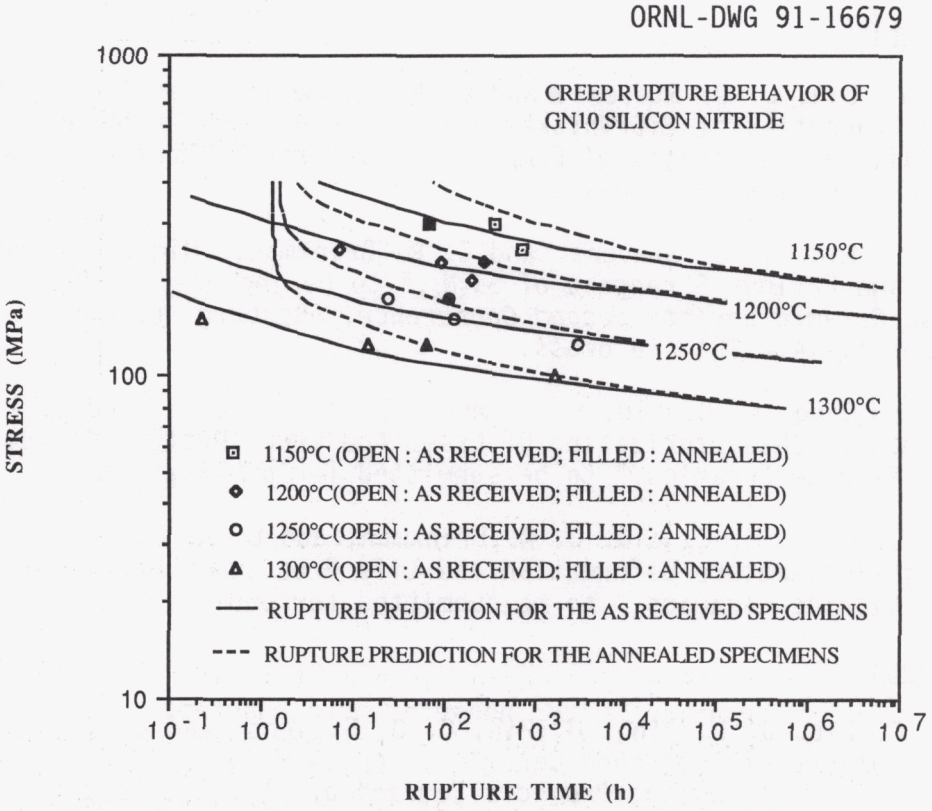

Fig. 26. Comparison between observed creep-rupture times and theoretical predictions.

Publications

1. K. C. Liu, C. O. Stevens, and C. R. Brinkman, "Tensile and Cyclic Fatigue Properties of SiC Whisker-Reinforced Al_2O_3," in *Proceedings of the First Canadian International Composites Conference*, Montreal, Canada, September 4-6, 1991, in press.

2. K. C. Liu, C. O. Stevens, and C. R. Brinkman, "High-Temperature Tensile and Fatigue Strengths of Si_3N_4," to be included in *Proceedings of European Ceramic Society Second Conference*, Augsburg, Germany, September 11-14, 1991, in press.

3. J. L. Ding, K. C. Liu, K. L. More, C. R. Brinkman, and D. R. Johnson, "Experimental Characterization Of Creep And Creep Rupture Of Advanced Silicon Nitride Ceramics," to be submitted for publication.

4. J. L. Ding, K. C. Liu, C. R. Brinkman, and D. R. Johnson, "Development of A High-Temperature Deformation and Life Prediction Model for Advanced Silicon Nitride Ceramics," to be submitted for publication.

References

1. K. C. Liu, J. L. Ding, H. Pih, C. O. Stevens, and C. R. Brinkman, "Cyclic Fatigue of Toughened Ceramics," pp. 319-39 in *Ceramic Technology for Advanced Heat Engines Projects Semiannual Progress Report for October 1990 Through March 1991*, ORNL/TM-11859, Martin Marietta Energy Systems, Inc., Oak Ridge Natl. Lab., July 1991.

2. K. C. Liu and C. R. Brinkman, "High-Temperature Tensile and Fatigue Strength of Silicon Nitride," pp. 235-44 in *Proceedings of the 27th Automotive Technology Development Contractors' Coordination Meeting*, P-230, Society of Automotive Engineers, Inc., Warrendale, Pa., April 1990.

Rotor Data Base Generation

M. K. Ferber and M.G. Jenkins (Oak Ridge National Laboratory)

Objective/scope

The goal of the proposed research program is to systematically study the tensile strength of a silicon nitride ceramic as a function of temperature and time in an air environment. Initial tests will be aimed at measuring the statistical parameters characterizing the strength distribution of three samples types (two tensile specimens and one flexure specimen). The resulting data will be used to examine the applicability of current statistical models as well as sample geometries for determining the strength distribution.

In the second phase of testing, stress rupture data will be generated by measuring fatigue life at a constant stress. The time-dependent deformation will also be monitored during testing so that the extent of high-temperature creep may be ascertained. Tested samples will be thoroughly characterized using established ceramographic, scanning electron microscopy (SEM), and transmission electron microscopy (TEM) techniques. A major goal of this effort will be to better understand the microstructural aspects of high-temperature failure including:

1. extent of slow crack growth,
2. evolution of cavitation-induced damage and fracture,
3. transition between brittle crack extension and cavitation-induced growth, and
4. crack blunting.

The resulting stress rupture data will be used to examine the applicability of a generalized fatigue-life (slow crack growth) model. If necessary, model refinements will be implemented to account for both crack blunting and creep damage effects. Insights obtained from the characterization studies will be crucial for this modification process. Once a satisfactory model is developed, separate stress-rupture (confirmatory) experiments will be performed to examine the model's predictive capability. Consequently, the data generated in this program will not only provide a critically needed base for component utilization in automotive gas turbines but also facilitate the development of a design methodology for high-temperature structural ceramics.

Technical progress

Studies of the high-temperature mechanical properties of a high-performance silicon nitride (PY6) were continued this reporting period.* The PY6 material is fabricated by hot isostatic pressing (HIP) using 6 wt % yttria as the densification aid. The microstructure typically consists of 1- to 6-μm-long acicular grains surrounded by equiaxed grains 0.1 to 1.0 μm in diameter. This morphology leads to a relatively dense microstructure. The silicon nitride grains, which are generally in the form of β-Si_3N_4, are separated by relatively thin layers of an amorphous yttrium silicate. The intergranular phase is also present in the triple points as a crystalline yttrium silicate. The exact phase composition of these intergranular compounds depends upon the HIP conditions.

*PY6 silicon nitride, GTE Laboratories, Inc., Waltham, Massachusetts.

Testing of this material involved the measurement of (1) the fast fracture strength as a function of temperature and (2) the creep/fatigue behavior at temperatures in the range of 1150 to 1400°C. Data were generated using both four-point flexure (3 × 4 × 50 mm) and button-head tensile specimens (6.35-mm gage diameter and 35-mm gage length). The majority of the flexure specimens were machined from injection-molded and HIPed bars having approximate fired dimensions of 4 × 6 × 50 mm. The tensile specimens were machined from isopressed and HIPed rods 160 mm long and 22 mm in diameter. In order to examine the effect of green state processing (i.e., injection molding versus isopressing) upon mechanical behavior, a limited number of flexure specimens were also machined from the as-received tensile rods.

During this reporting period, the microstructural analysis of the the PY6 creep/fatigue tensile specimens was completed. These specimens were tested at 1150, 1260, and 1370°C. Additional details are given in Ref. 1. Low-power optical microscopy of the tensile fracture surfaces revealed a transition in the fracture markings as the test temperature increased from 1150 to 1370°C. At 1150°C the fracture surfaces contained well-defined mirror, mist, and hackle regions (Fig. 1). A region of apparent slow crack growth was also identified within the mirror region. SEM of this area showed the presence of microcracks, which were presumably involved in the slow crack growth process. At 1260°C, the fracture surface was characterized by a relatively small creep damage zone (region of high surface roughness) originating from the gage-section surface. This zone contained numerous microcracks extending over many grain facets and lenticular-shaped cavities located predominantly at two-grain junctions. Additional details of these cavities, which were also observed throughout the gage section, are given below. Finally, as indicated in Fig. 1, the mirror size at 1260°C was significantly larger than that at 1150°C, while the hackle region was smaller.

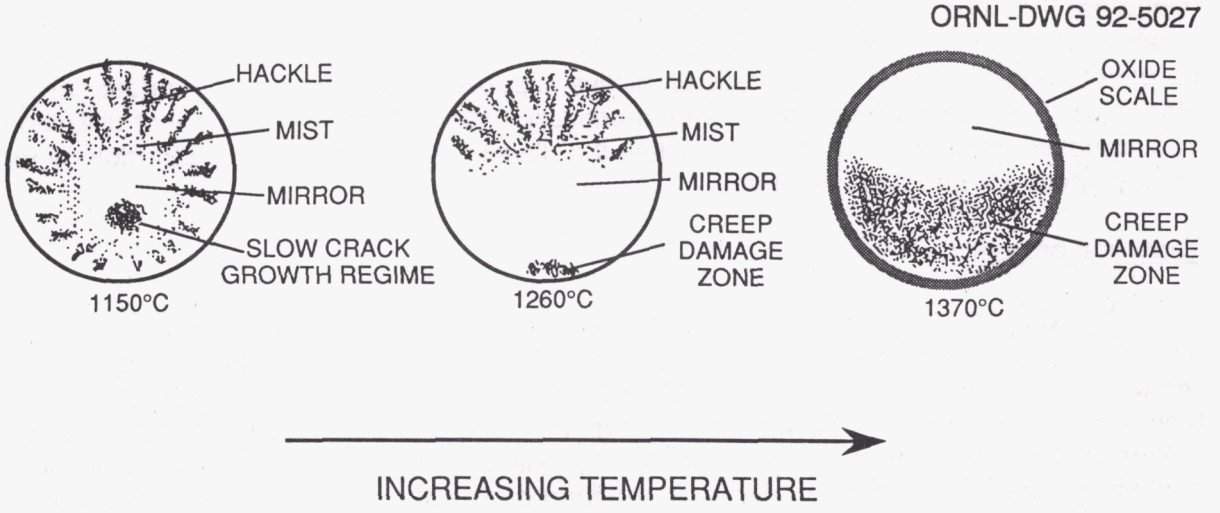

Fig. 1. Schematic representation of key fracture markings observed along the fracture surfaces of button-head tensile specimens.

At 1370° C, the creep damage zone, which also appeared to originate from the surface, covered as much as 50% of the fracture surface with the mirror region comprising the remainder (Fig. 1). The fact that no hackle markings were present suggests that the true mirror size exceeded the specimen dimensions. The creep damage zone was similar to that observed at 1260° C in that both cavitation and microcracking were predominant features. In addition, the size of creep damage zone increased slightly with decreasing stress thus indicating a slight stress dependency of the damage accumulation process. These results are in agreement with those reported in other studies[2,3] of the creep deformation behavior of silicon nitride.

An important difference in the failure behavior at 1260 and 1370° C concerned the presence of multiple cracks in the gage sections of the 1370° C specimens. Therefore, as the temperature increased, the damage coalescence process became active throughout the gage section. This behavior may have resulted from the increased oxidation at 1370° C. As indicated in Fig. 1, a 0.5- to 1-mm-thick oxide scale was present along the outer surface of the 1370° C specimens. As discussed in the next section, surface oxidation may provide preferred sites for damage coalescence. This would also explain why the creep damage zone at 1260 and 1370° C appeared to originate from the gage-section surface.

Detailed SEM examination of the cavities observed along the fracture surface of specimens tested at 1260 and 1370° C was prohibited by the oxide scale. However, these cavities could be readily observed by generating a secondary fracture at room temperature. As shown in Fig. 2, extensive cavitation was found along two-grain junctions. These cavities, which were lenticular in shape, were present throughout the gage-section volume. Furthermore, the extension of the cavities into the silicon nitride grains suggests that the growth mechanism involved solution/precipitation rather than viscous flow [Fig. 3(*a*)]. The fact that no cracklike cavities were found indicates that the rate of surface diffusion was relatively high.[4] Finally, there was a tendency for the number of cavities in the 1370° C specimens to decrease dramatically as the the applied stress was lowered to 50 MPa. This result is consistent with a critical threshold for cavity nucleation.[5]

A second, fairly common feature observed along the 1260 and 1370° C secondary fracture surfaces was the skeletal pattern of the intergranular phase outlining the interfaces between small grain clusters and a single, large grain (Fig. 2). As shown in Fig. 3(*b*), the formation of this pattern may have been a consequence of grain separation by viscous flow of the boundary phase. Such deformation would lower the local fracture resistance of the intergranular phase, thereby providing a preferred failure path during secondary fracture. This viscous flow process, which is discussed in detail in Refs. 3 and 4, would ultimately lead to the formation of facet-sized microcracks. As shown in Fig. 2, the size of these microcracks was significantly greater than the average cavity diameter. However, the total damage generated by this viscous flow process may have been limited, due to the fact that potential damage sites were restricted to interfaces between large and small grains. Finally, the absence of extensive creep damage at 1150° C was a consequence of the increased viscosity of the intergranular phase.

The damage mechanism illustrated in Fig. 3(*b*) has been observed for other silicon nitride ceramics containing a bimodal grain size.[6] Based upon these observations, one may conclude that the deformation rate of the large grain regions was lower than the surrounding fine-grain matrix. This behavior is expected for diffusion-controlled creep since the diffusion distances are shorter for small grains. Similar arguments have been

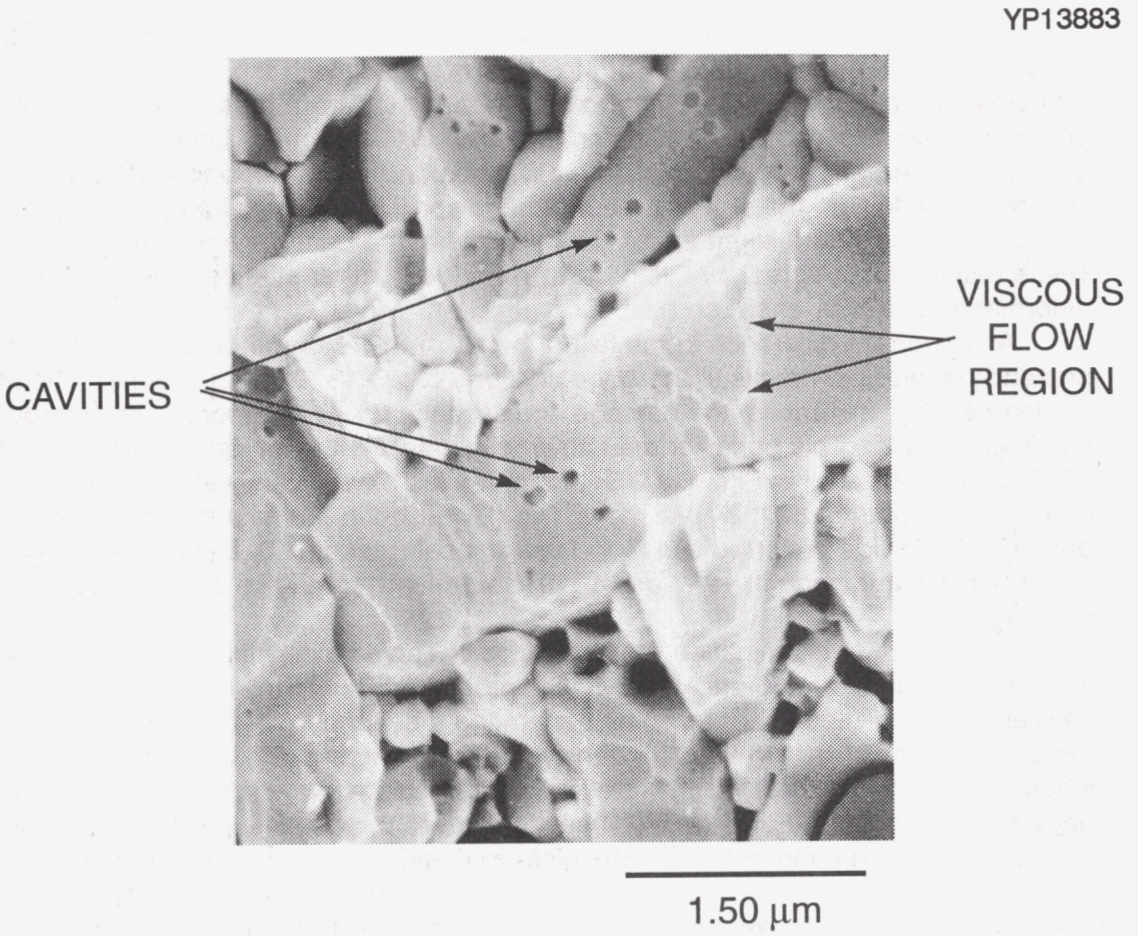

Fig. 2. SEM micrograph of cavities generated in specimens tested at 1260° C. Similar cavities were observed at 1370° C.

used to describe the creep and fatigue responses of ceramics containing large inhomogeneities.

Finally, samples taken from the gage sections of specimens tested at all three temperatures were ground and polished for metallographic examination. Observations of the 1370° C specimens made at low magnification (< 10X) under polarized light revealed a spotted microstructure. These spots, which were 0.5 to 1.0 mm in diameter, were attributed to preferred recrystallization of the intergranular phase over large regions of the microstructure. In particular, the X-ray diffraction peaks associated with yttrium disilicate compound (a major component of the intergranular phase) became sharper and larger following the creep exposure at 1370° C. Similar changes were absent in the 1150 and 1260° C specimens. In order to better quantify possible time-dependent variations in grain-boundary crystallography, TEM will be performed upon selected specimens. Results will be reported at a later date.

As reported previously,[1] the creep studies of the PY6 revealed a number of active deformation mechanisms. For example, the accommodated creep deformation in the PY6

ORNL-DWG 92-5028

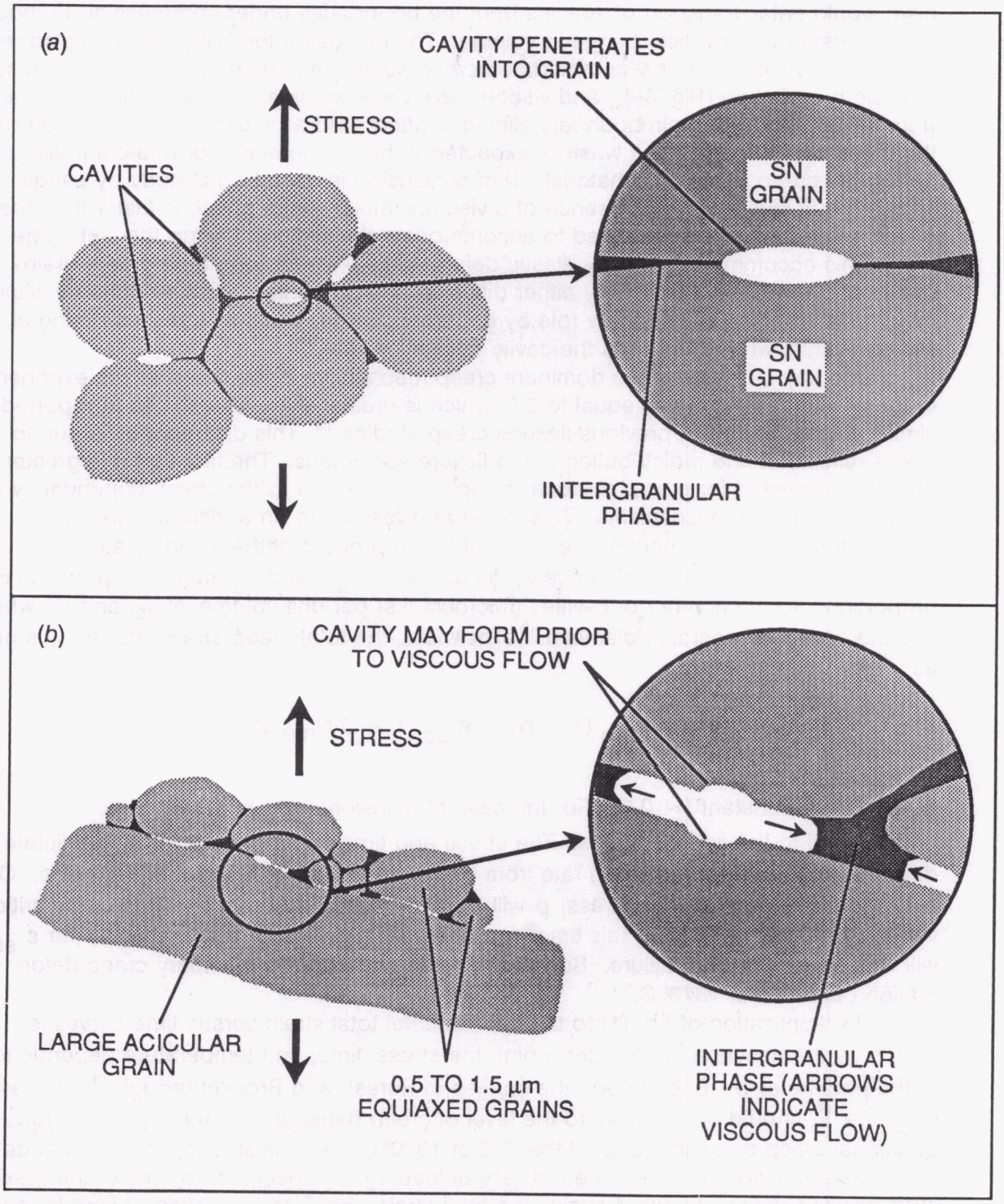

Fig. 3. Schematic representation of the two dominant creep damage modes: (*a*) cavitation and (*b*) viscous flow between small and large SN grains.

at 1260 and 1370° C was apparently controlled by grain-boundary diffusion. This mechanism would entail transport of species from the boundaries under compression to those under tension with no net change in volume. The microstructural observations also revealed the presence of unaccommodated creep strain (i.e., creep damage), which resulted from both cavitation [Fig. 3(*a*)] and viscous flow between small and large grain interfaces [Fig. 3(*b*)]. Although grain-boundary sliding is often cited as a deformation mechanism in the creep of silicon nitride, it was not expected to be the dominant or rate-controlling step during the creep of the PY6 material. This conclusion is based on a study by Lange[7] showing that sliding in the presence of a viscous intergranular phase is faster than the rate of grain deformation required to accommodate the sliding. During the first stage of creep, this accommodation is by elastic deformation while for long-term creep, grain deformation will be controlled by either diffusion or viscous flow. Grain-boundary sliding may, however, play a secondary role by generating large, transient stresses during abrupt sliding events, which increases the cavity nucleation rate.[5]

One key indicator of the dominant creep mechanism is the creep stress exponent, n. In the present study, n was equal to 5.0, which is greater than values (1 to 3) reported for similar silicon nitrides in previous flexural creep studies.[8,9] This discrepancy is due to stress relaxation and redistribution in the flexure specimens. The fact that n is greater than that expected for pure diffusional creep (n = 1) is due to the stress dependency of the creep damage mechanisms. This damage gives rise to an additional (unaccommodated) strain rate component, $\dot{\varepsilon}_c$, equal to the product of the steady-state creep rate measured in the absence of the cavities, $\dot{\varepsilon}_{so}$, and a parameter, ρ, which is proportional to the number of cavities (microcracks) per unit volume, N_{mc}, and d^3, where d is the cavity (microcrack) diameter.[10] Therefore, the total creep strain rate, $\dot{\varepsilon}_{st}$, is given as

$$\dot{\varepsilon}_{st} = \dot{\varepsilon}_{so}(1 + \rho) = \dot{\varepsilon}_{so}(1 + D\, N_{mc}\, d^3), \tag{1}$$

where D is a constant ($\sim$ 0.5). For the case of diffusional creep, $\dot{\varepsilon}_{st}$ is directly proportional to the applied stress. The stress and time dependencies of ρ will dictate the deviation of the measured strain rate from that expected for diffusional creep alone. One may assume that at a given stress, ρ will increase from 0 (at time, t = 0) to some critical value, ρ_c, at failure. During this time, if ρ becomes significantly larger than 1, the $\dot{\varepsilon}_{st}$ will exceed $\dot{\varepsilon}_{st}$ prior to failure. Such behavior is consistent with tertiary creep deformation observed at 1370° C.

The application of Eq. (1) to the experimental total strain versus time curves is limited by the absence of data describing the stress, time, and temperature dependencies of the parameter ρ. Based upon the studies of Suresh and Brockenbrough,[11] the elastic modulus, E, should be sensitive to the level of creep damage and, thus, ρ. Consequently, additional creep measurements of the PY6 at 1370° C were initiated in which E was determined as a function of time by periodically unloading the specimen to 20% of the maximum applied stress. Figure 4 shows the total strain and E as a function of time for an applied stress of 62 MPa. For times less than 250 h, E decreased slightly, which is consistent with the expected evolution of creep damage. However, E increased as the test time exceeded 250 h. It is possible that changes in the degree of crystallinity of the

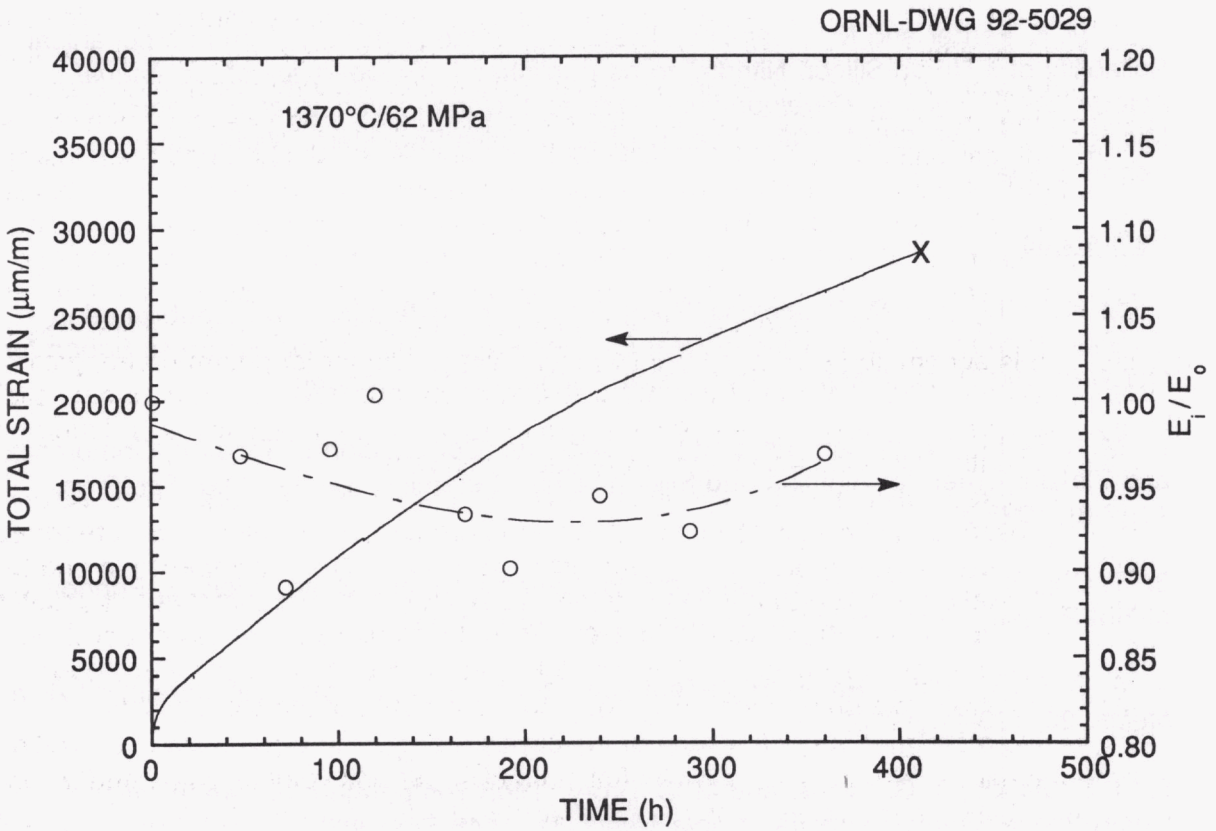

Fig. 4. Time dependence of total strain and elastic modulus for specimen tested under a 62-MPa applied stress at 1370° C.

intergranular phase were responsible for this behavior. The crystallinity of the intergranular phase is currently being examined using X-ray diffraction. A second interesting finding is that the strain versus time curve in Fig. 2 exhibited no evidence of tertiary creep. Previous data[1] revealed a strong tertiary strain component preceding failure. Reasons for this discrepancy are under investigation.

Status of milestones

None.

Publications

M. K. Ferber and M.G. Jenkins, "Evaluation of the High-Temperature Mechanical Reliability of a HIPed Silicon Nitride," submitted to *J. Amer. Ceram. Soc.* for publication.

M. K. Ferber and M.G. Jenkins, "Evaluation of the High-Temperature Mechanical Reliability of a HIPed Silicon Nitride," to be published in *Proceedings of the Annual Automotive Technology Development Contractors' Coordination Meeting*, Dearborn, Michigan, October 28-31, 1991, Society of Automotive Engineers, Warrendale, Pennsylvania.

References

1. M. K. Ferber and M. G. Jenkins,"Rotor Data Base Generation," to be published in *Ceramic Technology for Advanced Heat Engines Project Semiannual Progress Report for October 1990 Through March 1991*, ORNL Technical Memorandum.

2. M. K. Ferber, M. G. Jenkins, and V. J. Tennery, "Comparison of Tension, Compression, and Flexure Creep for Alumina and Silicon Nitride Ceramics," *Ceram. Eng. Sci. Proc.* **11** [7-8], 1028-37 (1990).

3. T. Ohji, S. Sakai, M. Ito, Y. Yamauchi, W. Kanematsu, and S. Ito, "Yielding Phenomena of Hot-Pressed Si_3N_4," *High Temp. Tech.* **5** [3], 139-44 (1987).

4. A. G. Evans and A. Rana, "High-Temperature Failure Mechanisms in Ceramics," *Acta Metall.* **28**, 129-41 (1980).

5. J. E. Marion, A. G. Evans, and M. D. Drory, "High-Temperature Failure Initiation in Liquid Phase Sintered Materials," *Acta Metall.* 31, 1445-57 (1983).

6. M. K. Ferber, T. N. Tiegs, and M. G. Jenkins, "Effect of Post-Sintering Microwave Treatments Upon the Mechanical Performance of Silicon Nitride,"to be published in *Proceedings of the 15th Annual Conference on Composites and Advanced Ceramic Materials*, American Ceramic Society, Westerville, Ohio.

7. F. F. Lange, "Non-Elastic Deformation of Polycrystals with a Liquid Phase," pp. 361-81 in *Deformation of Ceramic Materials*, ed. R. C. Bradt and R. E. Tressler, Plenum Press, New York, 1975.

8. J. A. Todd and Zhi-Yue Xu, "The High-Temperature Creep Deformation of Si_3N_4-$6Y_2O_3$-$2Al_2O_3$," *J. Mater. Sci.* **27**, 4443-52 (1989).

9. A. E. Pasto, W. C. Van Schailkwyk, and F. M. Mahoney, "Creep Behavior of Yttria- and Alumina-Doped Silicon Nitride," pp 776-85 in *Third International Symposium on Ceramic Components and Materials for Engines*, ed. V. J. Tennery, American Ceramic Society, Westerville, Ohio, 1988.

10. H. Riedel, *Fracture at High Temperatures*, Springer-Verlag, Heidelburg, Berlin, 1987.

11. S. S. Suresh and J. R. Brockenbrough, "A Theory for Creep by Interfacial Flaw Growth in Ceramics and Ceramic Composites," *Acta Metall. Mater.* **38** [1], 55-68 (1990).

TOUGHENED CERAMICS LIFE PREDICTION

Jonathan A. Salem and Sung R. Choi (NASA-Lewis Research Center)

Objective/Scope

The purpose of this research is to understand the room temperature and high temperature [>1370°C (2500°F)] behavior of toughened ceramics as the basis for developing a life prediction methodology. A major objective is to understand the relationship between microstructure and mechanical behavior within the bounds of a limited number of materials. A second major objective is to determine the behavior as a function of time and temperature. Specifically, the room temperature and elevated temperature strength, reliability, fracture toughness, slow crack growth and the creep behavior will be determined for the as-manufactured material. The same properties will also be evaluated after long-time exposure to various high temperature isothermal and cyclic environments. These results will provide input for parallel materials development and design methodology programs. Resultant design codes will be verified.

Technical Highlights

The slow crack growth and creep behavior of a hot-pressed Si_3N_4 was determined in flexure in air at 1200 and 1300°C. The slow crack growth data determined from dynamic fatigue was compared with that evaluated from static fatigue. Steady-state creep data were obtained as a function of applied stress, and the validity of bend data was evaluated from neutral axis shift determinations.

Experimental Procedures

The material used in this study was a hot-pressed Si_3N_4 with 1% MgO (Ceralloy 147A Si_3N_4, fabricated by Ceradyne, Inc.). Typical mechanical properties of the test material are presented in Table 1. This material was chosen because it exhibits moderate fatigue and creep susceptibilities at high temperatures, enabling the comparison of life prediction results from various testing methods. The nominal dimensions of the test bar specimens were 3.2x4.2x50 mm.

Dynamic and static fatigue testing for the as-received specimens was conducted in ambient air at 1200 and 1300°C using a SiC four-point bend fixture in an Instron testing machine (Model 8562). The inner and outer spans of the test fixture were 20 and 40 mm, respectively. The loading rates for the dynamic fatigue testing varied from 2 to 2000 N/min at each test temperature. Stress levels in the static fatigue tests were 120 to 320 MPa, and 80-260 MPa, respectively, at 1200 and 1300°C. During the static fatigue testing, the deflection at the midspan of each specimen was monitored using a LVDT to obtain creep strain data. Each test specimen was preloaded with 20 N to maintain good alignment relative to the test fixture, and held at test temperature for 20 min prior to testing.

In addition, creep strain measurements across the specimen height were made for short specimens (3.2x4.2x25 mm) at various applied stresses. These tests were carried out to examine the location of the neutral axis during creeping. This was done by putting three scratch lines (≈2 mm between adjacent lines) within the inner span on a polished side surface of the specimen (see Fig. 1). The scratch marks were made with a Vickers microhardness indenter. A similar method was used by Chen and Chuang [1] to measure neutral axis shift by placing the rows of Vickers impression marks ≈ 2 mm apart. But, it should be noted that the post-creep visibility was better for line scratches than for impression marks. Applied moments resulted in calculated stresses of 100 and 130 MPa at 1200°C, and 60 and 85 MPa at 1300°C. After some time interval under steady-state creep condition, the testing was interrupted, the furnace cooled and the specimen removed. The specimen was then immersed into 20%HF-20%H_2SO_4-60%H_2O solution for ≈15 minutes to the remove oxide layer and enhance visibility of the scratch lines. The distances, L_1' and L_2', between two adjacent lines were measured along the specimen height at 0.2 mm spacing using a machinist microscope. The corresponding strains, ϵ_1 and ϵ_2, were calculated and the average stain at each point along the specimen height was obtained by averaging ϵ_1 and ϵ_2 ($\epsilon = (\epsilon_1+\epsilon_2)/2$).

Results and Discussion

For most ceramics and glasses, slow crack growth can be expressed by the empirical relation $V = AK_I^n$, where A and n are the fatigue constants associated with material and environment, and K_I is the Mode I SIF. For dynamic fatigue testing which employs constant loading ($\dot{P}$) or constant stress rate ($\dot{\sigma}$), the corresponding fatigue strength, σ_f, is expressed [2]

$$\sigma_f = \alpha\ [\dot{\sigma}]^{1/n+1} \tag{1}$$

where α is a value associated with A, n, toughness, inert strength, and crack geometry. The slow crack growth parameters, n and α, can be obtained from the intercept and slope, respectively, of the linear fit of Log σ_f versus Log $\dot{\sigma}$. In the same way, for static fatigue testing where constant stress is applied, the time to failure (t_{fs}) can be derived easily in terms of applied stress (σ_a) as follows [3]:

$$t_{fs} = \beta\ \sigma_a^{-n} \tag{2}$$

where ß is a value related to A, n, toughness, inert strength and crack geometry. Likewise, the fatigue parameters n and ß in static fatigue can also be evaluated by a linear regression analysis from the slope and intercept of the static fatigue curve when time to failure (Log t_{fs}) is plotted against applied stress (Log σ_a). However, it should be noted that there are several statistical approaches to estimate the fatigue parameters based on static and dynamic fatigue data. Currently, statistical approaches such as median value, bivariant and trivariant are being reviewed using room-temperature fatigue data obtained from soda-lime glass.

The relationship in fatigue life between dynamic and static fatigue is [4]

$$t_{fs} = t_{fd}/(n+1) \tag{3}$$

where t_{fd} is the time-to-failure in dynamic fatigue, which corresponds to $t_{fd} = \sigma_f/\dot{\sigma}$. By substituting t_{fs} in Eq. (3) into Eq. (2) with $\sigma_a=\sigma_f$, the dynamic fatigue curve can be converted a into static fatigue curve as follows:

$$t_{fd} = \gamma\beta\ \sigma_f^{-n} \tag{4}$$

where γ is the value associated with n and ß.

A summary of the dynamic fatigue results is presented in Fig. 2, where fatigue strength (Log σ_f) was plotted as a function of applied stress rate (Log $\dot{\sigma}$) at temperatures of 1200 and 1300°C. The solid lines in the figure represent the best-fit lines based on Eq. (1). The decrease in fatigue strength with decreasing stress rate, which represents fatigue susceptibility, was evident at both temperatures, as shown in Fig 2. The fatigue parameters n and α, which were determined by a linear regression of Log σ_f versus Log $\dot{\sigma}$, are included in Table 2. Also, included in Table 2 are the fatigue parameters obtained from static fatigue which will be described in the next section. Both the fatigue parameters n and α decreased with temperature: n = 16.1 at 1200°C and n = 13.7 at 1300°C, and log α = 2.3025 at 1200°C and log α = 2.1552 at 1300°C. Hence, fatigue susceptibility is greater at 1300°C than at 1200°C. The low value of n is indicative of higher susceptibility to slow crack growth. This value of n is considerably lower than that (n = 40-46) previously obtained for GN-10 silicon nitride [5]. It should be noted that an appreciable creep deformation was observed for the specimens subjected to the very low stressing rates ($\dot{\sigma} \leq 5$ MPa/min) at 1300°C. Typical fracture surfaces of the specimens tested at different stress rates are shown in Fig. 3. As shown in the figure, the presence of slow crack growth zones is dominant as the stress rate decreases, consistent to the results shown in Fig 2. One complication evident from the fractography is the shape of the crack developed in the test specimens, especially at long time-to-failure. The cracks, though initially half-pennies in configuration, develop into corner and straight-through cracks as the crack size approaches the specimen size. This may effect the values of the measured fatigue parameters.

The results of the static fatigue tests are shown in Fig. 4, where constant applied stress (Log σ_a) was plotted in terms of time-to-failure (Log t_f) at 1200 and 1300°C. The arrow marks in the figure represent the specimens that did not break before 187 and 141 hours, respectively, at 1200 and 1300°C. Also, the solid lines in the figure represent the best-fit lines based on Eq. (2). The fatigue constants n and ß, evaluated from the fatigue data in Fig. 4 using a linear regression analysis, are presented in Table 2. The fatigue constants n decreased from n = 14.5 at 1200°C to n = 12.3 at 1300°C with corresponding log ß = 36.379 and 29.818

values, respectively, at 1200 and 1300°C. It was observed that creep deformation became significant at low applied stresses ($\leq$ 120 MPa) with ϵ > 0.5 % at 1300 °C. In that case, the specimen failure was mainly associated with creep deformation. To the contrary, at the moderate applied stress levels a combination of slow crack growth and simultaneous creep resulted in specimen failure. The higher the applied stress the greater the tendency for slow crack growth failure. Similar failure phenomena has been observed elsewhere for silicon nitride materials [6,7]. It is noteworthy, however, that the value of n obtained from dynamic fatigue is in excellent agreement with that obtained from static fatigue. Figure 5 shows typical examples of the fracture surfaces of the specimens failed at different stress levels at both temperatures. As mentioned before, slow crack growth is dominant at higher applied stress; whereas, creep associated failure is noted at low applied stress and verified by observation of many microcracks in the tensile surface. As with the dynamic fatigue cracks, the static fatigue cracks develop into corner and straight-through configurations. The development of data for component life prediction may require larger specimens, shorter test times or adjustments in crack geometry factors.

As aforementioned, excellent agreement exists between dynamic and static fatigue behaviors. This can be seen more readily by converting the dynamic fatigue data into a static fatigue curve by using Eqs. (3) and (4). The resulting plots are shown in Fig. 6, where the converted data are compared with the static fatigue data. Notwithstanding a little variation in data and the small number of test specimens, overall agreement is excellent. Therefore, based on these results it is possible to calculate slow crack growth parameters from either static or dynamic testing techniques. It should be noted that dynamic fatigue testing is preferable since time-to-failure is shorter in dynamic fatigue than in static fatigue. However, care should be taken when dynamic fatigue data is extrapolated to predict fatigue behavior in the low applied stress regime.

The results of the creep strain-rate measurements as a function of applied stress are summarized in Fig. 7. Assuming a $\dot{\epsilon} \alpha \sigma_a^N$ relation (Norton's law) with no neutral axis shift, the stress exponent (N) was evaluated to be N = 6.0 and 5.0, respectively, at 1200 and 1300°C. For a given applied stress, creep rate at 1300°C is about 10 times greater than that at 1200°C. The high N indicates that creep was associated with cavitational damage.

In constructing Figure 7 it was assumed that creep deformation is symmetric between the tension and compression sides and that no neutral axis shift takes place during creeping. However, it has long been observed that ceramics normally creep faster in tension than in compression, resulting in shift of the neutral axis and an asymmetric stress distribution. The results of the neutral axis determinations, based on the scratch mark technique described in the Experimental Procedure section, are presented in Fig. 8. The strains as a function of location along the y axis are presented for different conditions of

applied stress, sustained time and temperature.

The results in Figure 8 show clearly that the neutral axis shifted to the compression side for Si_3N_4 at all the test conditions. By contrast, the neutral axis of a stainless steel test bar that was subjected to creep with σ_a = 250 MPa at a temperature of 700°C remained almost unchanged, indicating that tensile and compressive creep are identical to each other, as noted previously [8]. These results suggest again that the stress exponent (N) as well as any of the other creep parameters determined in bending creep should be accepted with some caution. Therefore, in view of the ambiguities and uncertainties related with bend bar creep data, individual tensile and compressive creep testing must be performed, as emphasized previously (for example, [9]). Currently, results of flexural creep (Figs. 7 and 8) obtained by the scratch mark technique are being analyzed with the analysis of Chen and Chuang [1] to predict tension and compression creep parameters.

Conclusions

The dynamic and static fatigue behaviors of Ceralloy Si_3N_4 with 1 % MgO material are in excellent agreement at 1200 and 1300°C, notwithstanding some creep deformation at low applied stress or low stress rates at 1300°C. Although creep behavior in bending follows Norton's law, neutral-axis shift occurred at all the test conditions. Individual uniaxial tension and compression testing is thus desirable for complete characterization of creep behavior of a ceramic material.

Status of Milestone

Milestones are on time.

Publications

1. S. R. Choi, J. A. Salem, and J. P. Gyekenyesi, "Dynamic Fatigue Properties of Silicon-Carbide Whisker-Reinforced Silicon Nitride," Ceram. Eng. Sci. Proc., 12[7-8] pp. 1537-1536 (1991).

2. V. Tikare and S.R. Choi, "Influence of the Si_3N_4 Microstructure on Its R-Curve and Fatigue Behavior," ibid. 12[7-8] pp. 1437-1447 (1991).

References

1. C. F. Chen and T. J. Chuang, "Improved Analysis for Flexural Creep with Application to Sialon Ceramics," J. Am. Ceram,. Soc., 73 [8] 2366-73 (1990).

2. A. G. Evans, "Slow Crack Growth in Brittle Materials under Dynamic Loading Conditions," Int. J. Fract. 10 251-59 (1974).

3. J. E. Ritter, "Engineering Design and Fatigue Failure of Brittle Materials," pp. 667-86 in Fracture Mechanics of Ceramics, Vol.4 , R. C. Bradt, D. P. H. Hasselman, and F. F. Lange, eds., Plenum Publishing Co., New York (1978).

4. R. W. Davidge, J. R. McLaren, and G. Tappin, "Strength-Probability-Time (SPT) Relationship in Ceramics," J. Mater. Sci., 8 1699-1705 (1973).

5. S. R. Choi and J. A. Salem, "Comparison of Dynamic Fatigue Behavior Between SiC Whisker-Reinforced Composite and Monolithic Silicon Nitrides," NASA TM 103707 (1991).

6. P. K. Khandalwal, J. Chang, and P. W. Heitman, "Slow Crack Growth in Sintered Silicon Nitrides," Pp 351-362 in Fracture Mechanics of Ceramics, Vol. 8, R. C. Bradt, D. P. H. Hasselman, and F. F. Lange, eds., Plenum Publishing Co., New York (1983).

7. G. D. Quinn, "Fracture Mechanisms Maps for Advanced Structural Ceramics, Part I: Methodology and Hot-Pressed Silicon Nitride," J. Mater. Sci., 25 4361-76 (1990).

8. Metals Handbook, ninth edition, Vol. 8, pp. 306.

9. K. Jakus and S. M. Wiederhorn, "Creep Deformation of Ceramics in Four-Point Bending," J. Am. Ceram. Soc., 71[10] 832-36 (1988).

Table 1. Mechanical properties of Ceralloy Si_3N_4 at room temperature.

Toughness[1] K_c (MPa$\sqrt{m}$)	Hardness[2] H (GPa)	Young Modulus[3] E (GPa)	Density[4] (g/cm^3)
5.78 (0.10)*	14.7 (0.9)	313	3.21

Notes:
1. By the SEPB method
2. By Vickers microhardness indenter, $H=P/2d^2$.
3. By strain gaging
4. By the buoyancy method
* The parenthesis indicates one standard deviation.

Table 2. Summary of fatigue parameters determined from dynamic and static fatigue for Ceralloy Si_3N_4 at temperatures of 1200 and 1300°C in air.

Temp (°C)	Dynamic fatigue $\sigma_f = \alpha\,[\dot{\sigma}]^{1/n+1}$	Static Fatigue $t_f = \beta\,\sigma_a^{-n}$
1200	Log α = 2.3025 n = 16.1 r_{coef} = 0.8146 Log β = 38.14*	Log β = 36.379 n = 14.5 r_{coef} = 0.8639 Log α = 2.424*
1300	Log α = 2.1552 n = 13.7 r_{coef} = 0.8687 Log β = 30.51*	Log β = 29.818 n = 12.3 r_{coef} = 0.9550 Log α = 2.327*

Notes :
1. Units are: $\dot{\sigma}$:MPa/min; σ_f and σ_a:MPa; t_f:sec
2. r_{coef} represents the correlation coefficient of the regression analysis.
* Calculated from the relation $n+1 = \alpha^{n+1}/\beta$.

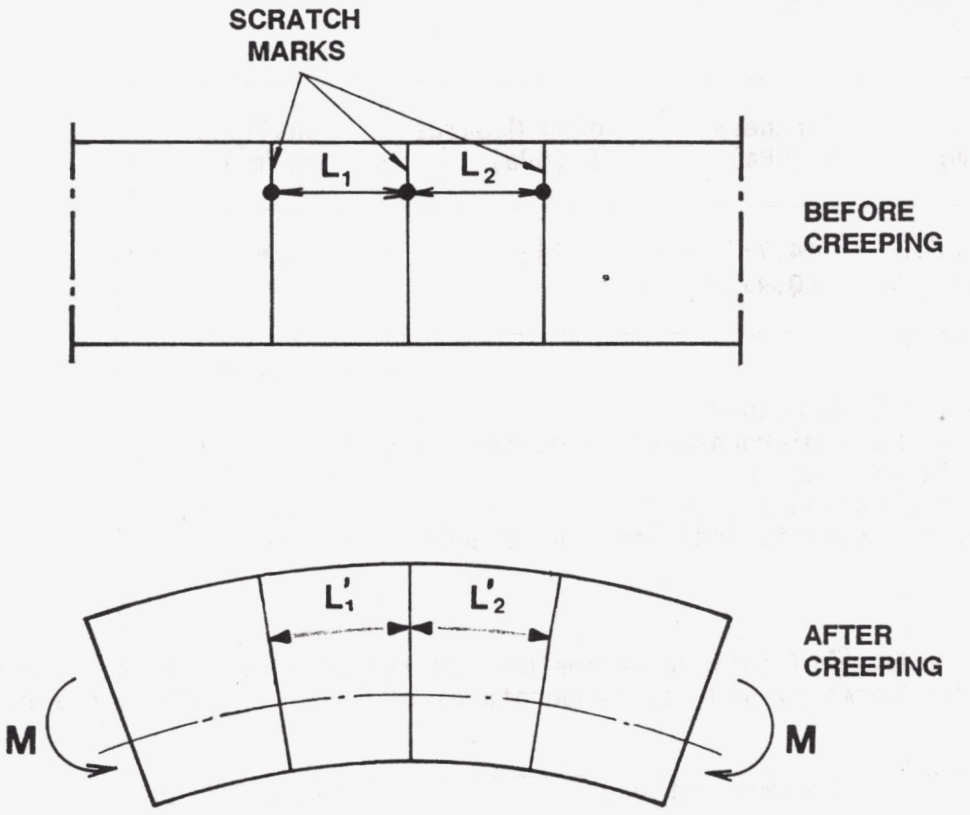

Figure 1. Schematic of scratch lines made on a flexure creep specimen.

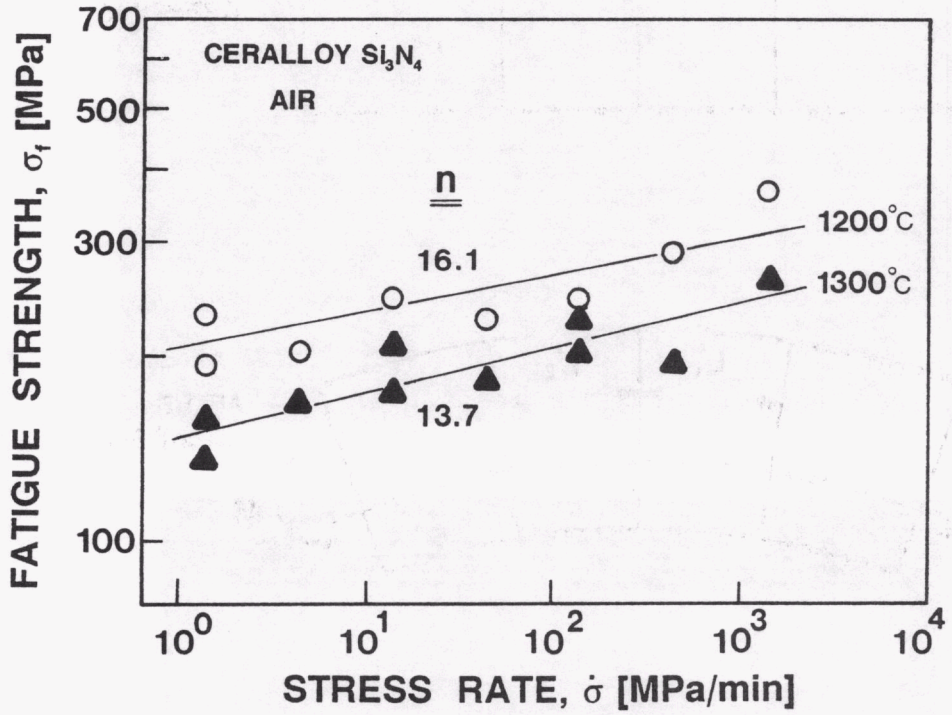

Figure 2. Dynamic fatigue results of as-received Ceralloy Si_3N_4 flexure specimens at 1200 and 1300°C in air.

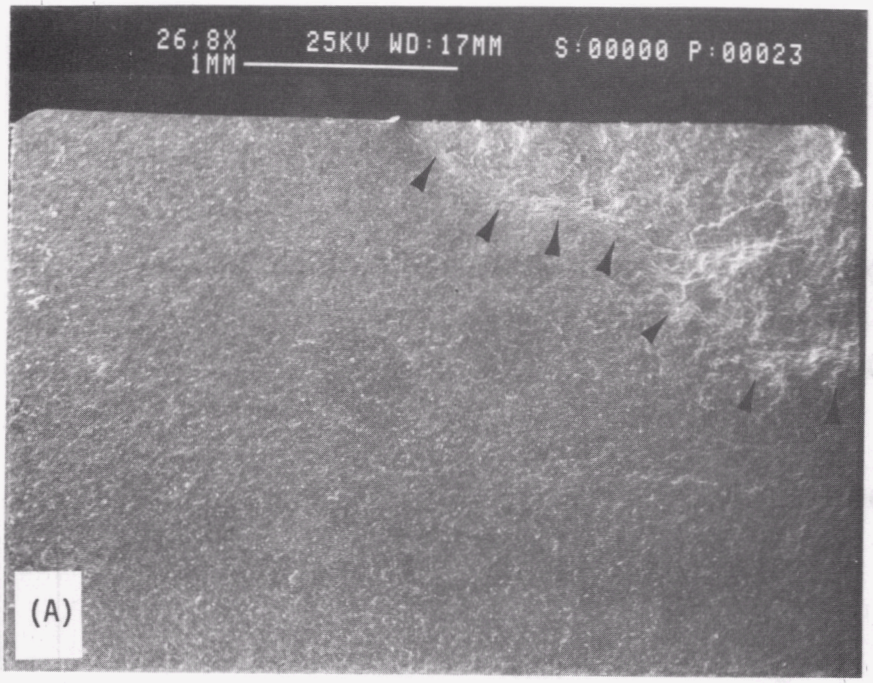

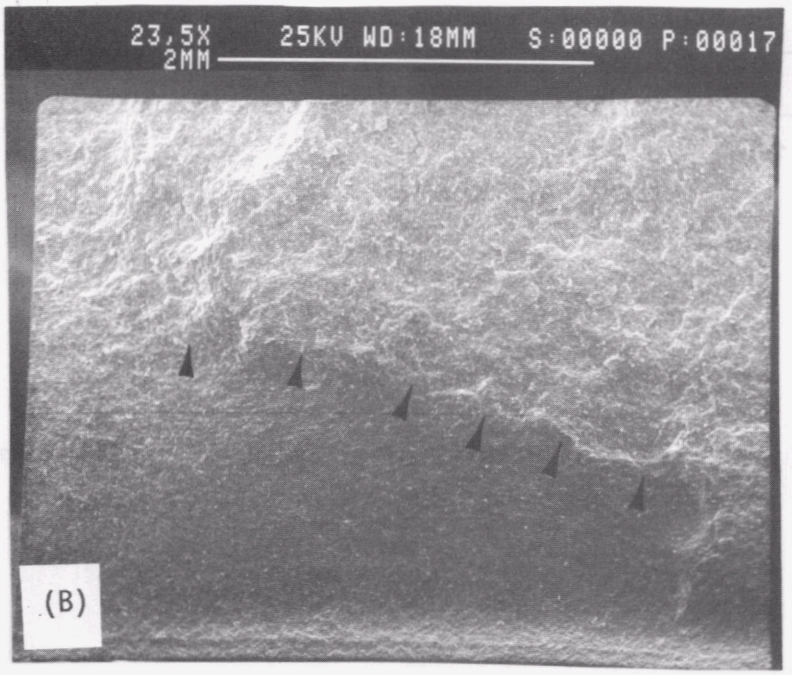

Figure 3. Fracture surfaces of test specimens subjected to dynamic fatigue at (A) 2000 N/min and (B) 2 N/min in 1300°C air.

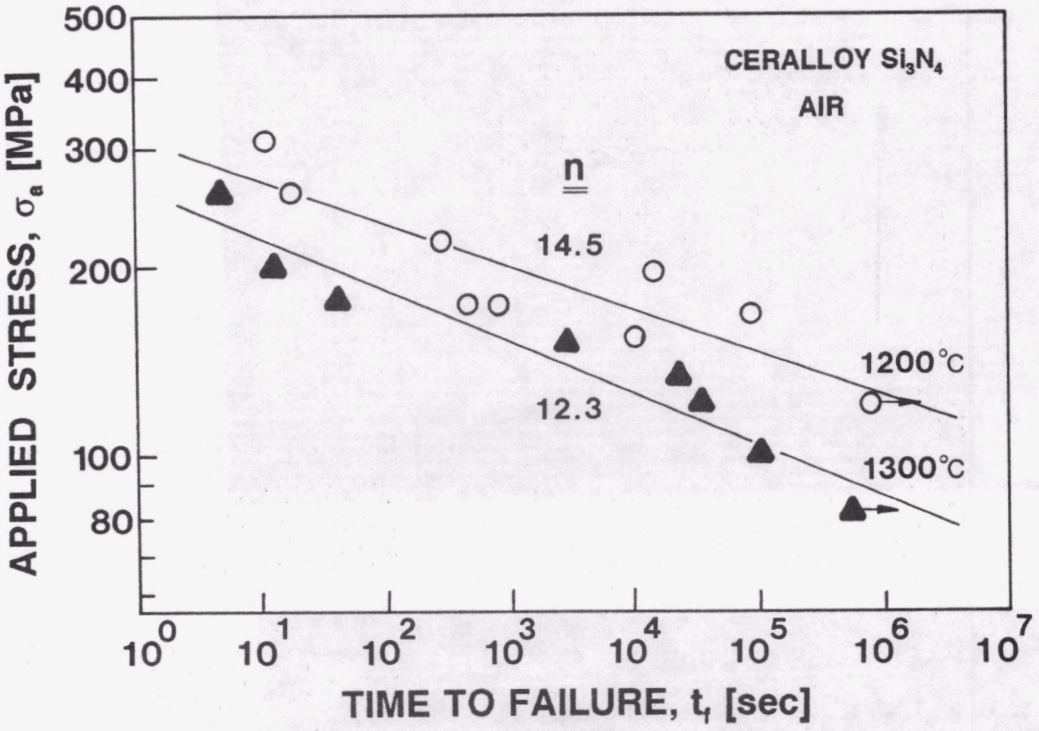

Figure 4. Static fatigue results of as-received Ceralloy Si_3N_4 flexure specimens at 1200 and 1300°C in air.

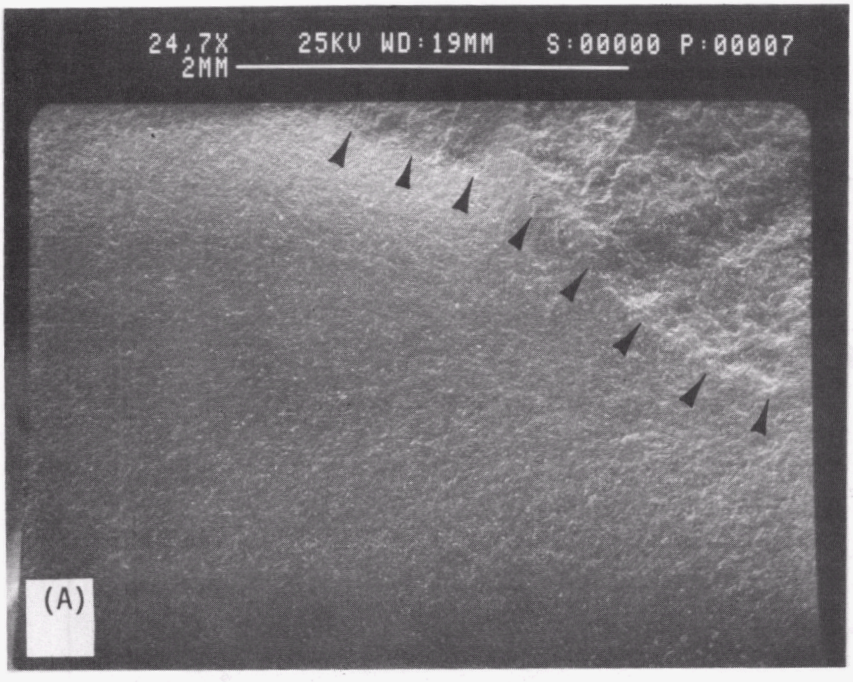

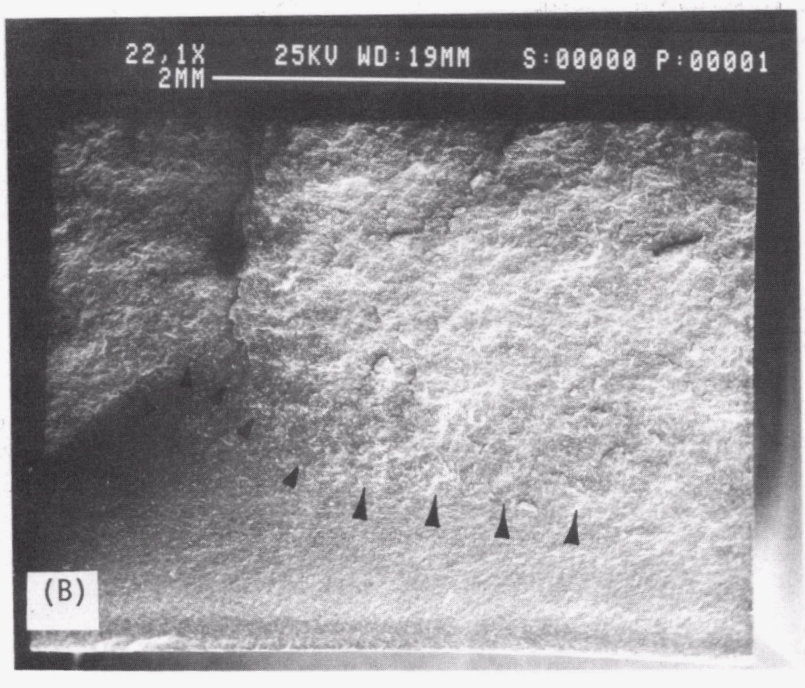

Figure 5. Fracture surfaces of test specimens subjected to static fatigue in 1300°C in air at loads of (A) 357 N and (B) 165 N.

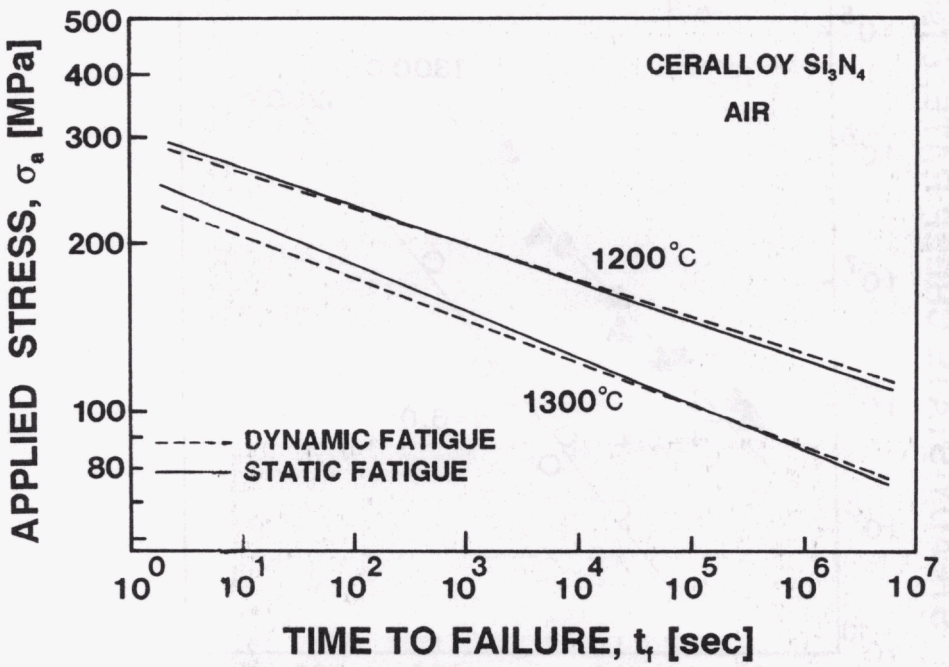

Figure 6. Comparison of static and dynamic fatigue data obtained for Ceralloy Si_3N_4 flexure specimens at 1200 and 1300°C in air. The dynamic fatigue data were converted to the static fatigue curve using Eqs. (3) and (4).

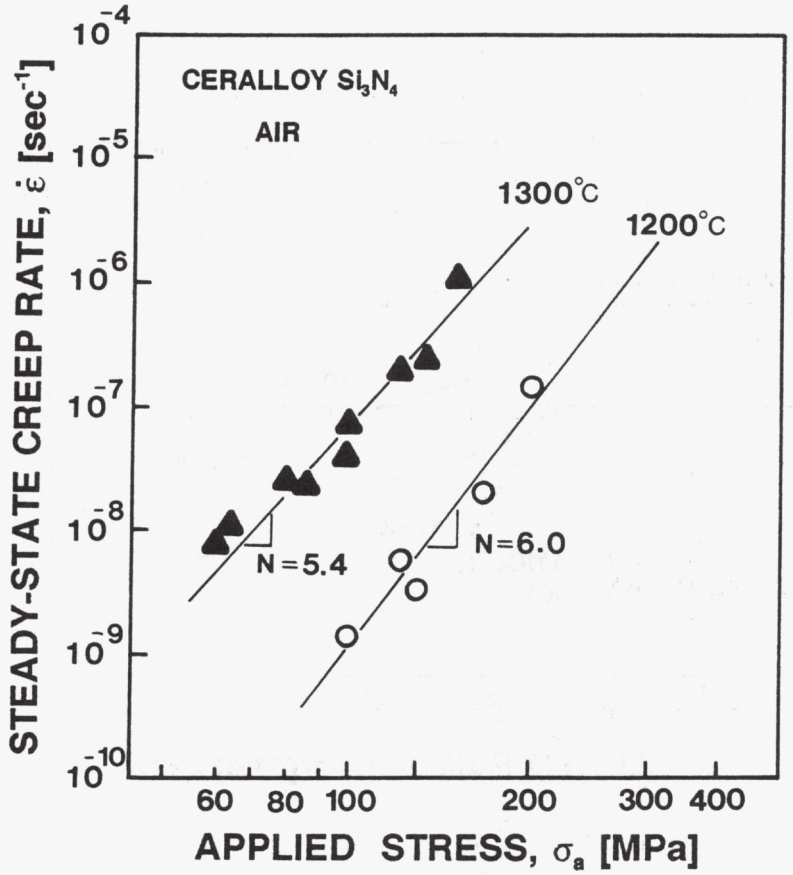

Figure 7. Flexure steady-state creep rate as a function of applied stress of Ceralloy Si_3N_4 at 1200 and 1300°C in air. The stress exponent (N) is shown for each temperature.

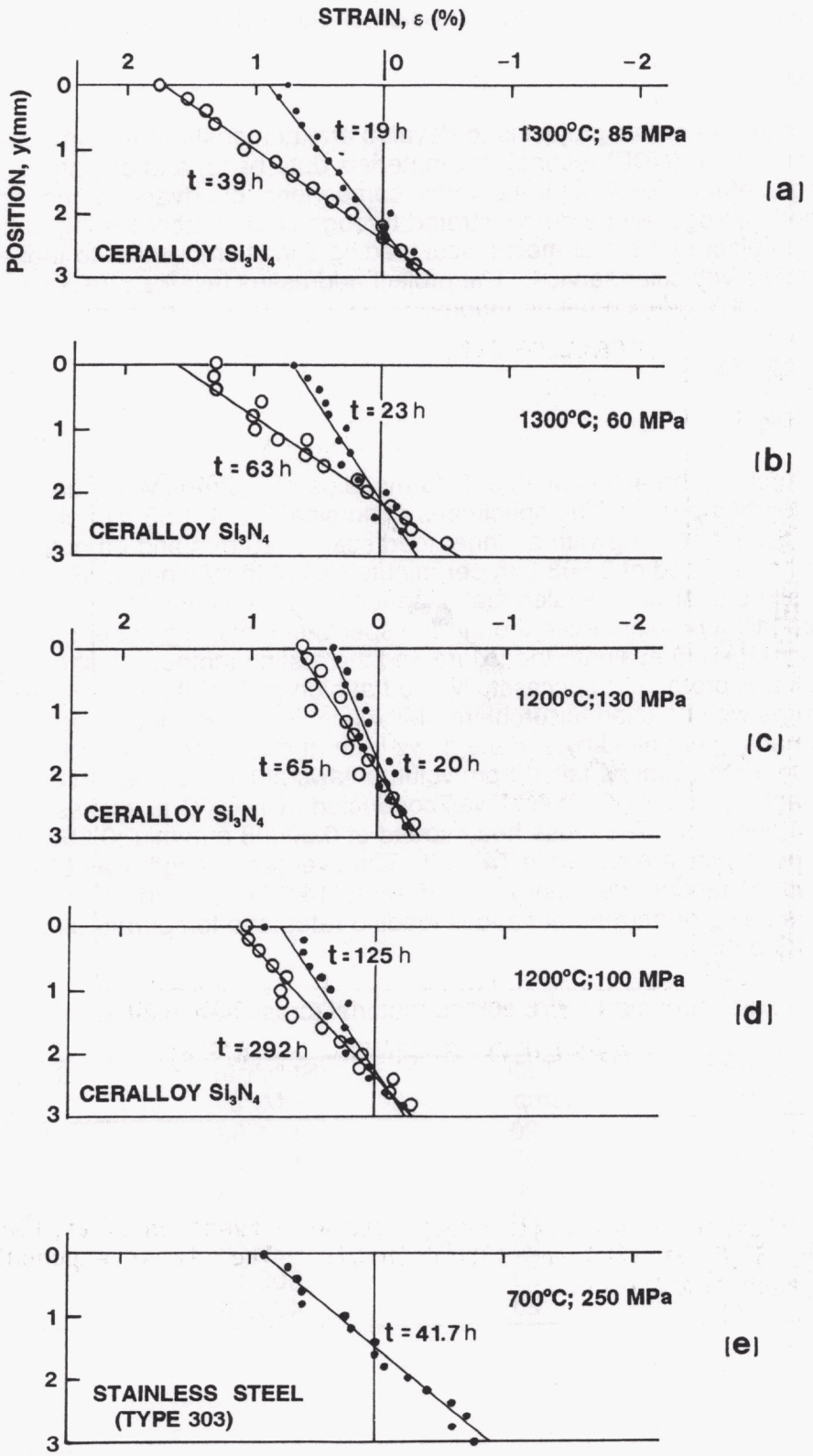

Figure 8. Flexural creep strain as a function of specimen height for Ceralloy Si_3N_4 and stainless steel.

Life Prediction Methodology

P. K. Khandelwal (Allison Gas Turbine Division of General Motors Corporation)

Objective/Scope

The objective of this project is to develop and demonstrate the necessary nondestructive examination (NDE) technology, materials data base, and design methodology for predicting useful life of structural ceramic components of advanced heat engines. The analytical methodology will be demonstrated through confirmatory testing of ceramic components subject to thermal-mechanical loading conditions similar to those anticipated to occur in actual vehicular service. The project addresses fast fracture, slow crack growth, creep, and oxidation failure modes.

Technical Progress

Flexural Testing

Fast fracture characterization of PY6 modulus-of-rupture (MOR) bars continued during this reporting period. The specimens of nominal 3 X 4 X 50 mm dimensions were evaluated in 4-point bending with an inner load span of 20 mm and an outer span of 40 mm at cross-head speed of 0.508 mm per minute (0.020 inch/minute). Results are shown in Table I. Failure analysis revealed that chamfer or near chamfer failures at room temperature were still a problem even though the specimens had high strength. A specimen is being strain gaged to evaluate the fixture and the testing method. It should be noted that the same test protocol is successfully used at high temperatures using elevated temperature fixtures with no chamfer problem. Microscopic analysis indicated that the failure was predominantly controlled by surface flaws both at room and elevated temperatures. Limited number of specimens failed from volume flaws at high temperatures. Dynamic fatigue evaluation of the PY6 material was conducted at 1200°C to assess the slow crack growth (SCG) behavior. The cross-head speed of 0.00508 mm/min (0.0002 inch/min) was used. The results are shown in Table II. The average strength was 601.78 MPa (79.78 ksi) with a standard deviation of 20.85 MPa (14.67 ksi). Additional dynamic fatigue testing is being performed at various loading rates and temperatures to explore the material's SCG behavior.

Table I. Flexural strength of PY6 HIP'ed material (cross head speed = 0.5 mm/min).

Specimen number	Test temp--°C	Strength --MPa	Strength --ksi
34.1596	20	961.88	139.50
34.1598	20	978.67	141.94
34.1599	20	731.63	106.11
34.1600	20	550.00	77.77
34.1601	20	820.08	118.94
34.1602	20	502.15	72.83
34.1603	20	486.56	70.57

Table I. (cont.)

Specimen number	Test temp--°C	Strength --MPa	Strength --ksi
34.1604	20	750.37	108.83
34.1605	20	604.51	87.67
34.1465	1000	772.66	112.06
34.1466	1000	728.15	105.61
34.1467	1000	720.50	104.50
34.1468	1000	739.18	107.21
34.1469	1000	707.07	102.55
34.1436	1100	545.50	79.12
34.1437	1100	576.29	85.58
34.1438	1100	622.52	90.29
34.1439	1100	944.38	78.95
34.1475	1100	547.54	79.42
34.1431	1200	460.74	66.82
34.1432	1200	662.97	95.15
34.1433	1200	648.01	93.98
34.1434	1200	505.04	73.25
34.1435	1200	585.35	84.89
34.1460	1200	666.92	96.72
34.1461	1200	559.58	81.16
34.1462	1200	621.74	90.17
34.1463	1200	571.70	82.92
34.1464	1200	587.23	83.86
34.1981	1400	481.15	69.78
34.1982	1400	431.21	62.54
34.1983	1400	511.93	74.25
34.1984	1400	510.10	73.98
34.1985	1400	472.30	68.50
34.1986	1400	454.76	65.96
34.1987	1400	782.98	70.05
34.1988	1400	485.23	70.37
34.1989	1400	475.30	68.90
34.1990	1400	481.04	69.77

Table II. Dynamic fatigue behavior of PY6 HIP'ed material (cross head speed = 0.00508 mm/min).

Specimen number	Test temperature--°C	Strength --MPa	Strength --ksi
34.1966	1200	666.55	96.09
34.1967	1200	617.44	89.55
34.1968	1200	578.00	83.83
34.1969	1200	584.69	54.80
34.1970	1200	627.00	90.94

Dog Bone Tensile Testing

One hundred machined dog bone tensile specimens were received from the National Institute of Science and Technology (NIST) for NDE and characterization prior to creep/stress rupture testing. The specimens were characterized using visual, fluorescent penetrant (FPI), microfocus X-ray and ultrasonic techniques to detect surface and volume flaws. The specimens were evaluated both for the surface and volume flaws since creep rupture can occur from both type of defects. The specimens were shipped back to NIST during this period to initiate monotonic creep and stress rupture testing.

Fracture Toughness (KIc)

Fracture toughness of the PY6 material was measured using Vickers microindentation method. Indents were made in a circular disk from 10 Kg to 40 Kg loads in 5 Kg increments. This method provided a fracture toughness (KIc) of 5.8 MPa$\sqrt{m}$. This is in good agreement with Battelle's measured toughness of 6.4 MPa$\sqrt{m}$ using the thru-crack specimens and 6.7 MPa$\sqrt{m}$ using the controlled flaw (CF) method . Further measurement of KIc is planned using the chevron-notch method at room and elevated temperatures.

Uniaxial Tensile Testing (Buttonhead Specimen)

Fast Fracture uniaxial tensile testing continued at Southern Research Institute (SoRI) both at room temperature and 1400°C. The measured strength of each specimen is shown in Table III. The average room temperature strength was measured to be 407.9 MPa (59.16 ksi) with a standard deviation of 62.53 MPa (9.07 ksi). The Weibull modulus (m) was calculated by maximum likelihood method to be 6.53. The average 1400°C strength was measured to be 317.9 MPa (46.1 ksi) with a standard deviation of 90.9 MPa (13.19 ksi). The Weibull modulus (m) was determined by the maximum likelihood method to be 4.68. Failure at room temperature was generally controlled by volume inclusions, Figures 1 and 2. Energy dispersive analysis indicated that these flaws are iron based compounds. One specimen also showed presence of nickel and chrome indicating abrasion of process equipment components such as compounder, injection molding parts, etc. by hard silicon nitride powder. The majority of the failures at 1400°C occurred from volume inclusions, Figure 3. There were some failures, however, from surface defects. The testing is continuing as planned to characterize the material.

Multiaxial Testing

Biaxial fast fracture strength at room temperature was measured at Battelle Laboratories, Columbus, Ohio, using a ball-on-ring arrangement at a loading rate of 0.25 mm/min (.01 in/min). The average measured strength was 701 MPa (101.67 ksi) for eight (8) specimens. The Weibull modulus (m) was calculated to be 18.8 with a characteristic strength of 719 MPa. Fractographic analysis revealed that the failure originated from the machining damage and propagated parallel to the grinding marks, Figure 4. The large value of Weibull modulus may be an aberration due to small sample population, the type of test, or the machining direction. Flexural specimens with transverse grinding are currently being machined at Battelle to assess the transverse strength of the material.

NDE Development

The development and application of NDE techniques namely film microfocus radiography and ultrasonic imaging continued during this reporting period. Reference

standards with laser drilled surface holes in MOR bars, button-head tensile specimens, and biaxial disks were evaluated. The hole diameters varied from 25 to 100 microns. Microscopic examination of the holes revealed them to be irregular shape and size. The depth of the 25 micron diameter holes varied between 10-20 microns. The microfocus X-ray detection sensitivity of the surface holes, assuming the nominal dimensions, is shown in Table IV. The 25 micron diameter holes were not detected because of their shallow depth and lower than anticipated effective volume. In the past, however, Allison has demonstrated detection of simulated 25 micron surface and internal voids in silicon nitride MOR bars fabricated by NASA-Lewis Research Center using the M-film and Feinfocus X-ray system which is also used in the present study. It was also observed that the X-ray detection of the holes in button-head cylindrical specimens depend on their radial orientation and location with respect to the X-ray beam because of their irregular shape, size and cumulative geometrical effects.

Table III. Uniaxial tensile strength of PY6M HIP'ed material (stress rate = 600 ksi/min).

Specimen number	Test temp--°C	Strength-- MPa	Strength-- ksi
92B	20	479.2	>*69.50
243B	20	373.02	>54.1
163B	20	445.21	>64.57
229B	20	488.30	>70.82
142B	20	446.72	>64.79
166B	20	487.61	>70.72
233B	20	547.04	79.34
168A	20	387.77	56.24
174A	20	516.22	74.87
308B	20	378.60	54.91
243A	20	494.85	>71.77
159B	20	402.80	58.42
327B	20	423.90	61.48
325B	20	328.54	47.65
229A	20	427.49	62.00
324A	20	527.39	76.49
348A	20	312.41	45.31
72A	20	382.74	55.51
179A	20	455.55	>66.07
167B	20	276.55	40.11
236B	20	447.20	64.86
372B	20	377.08	54.69
363A	20	310.61	45.05
371B	20	442.59	64.19
372A	20	414.52	60.12
370A	20	434.38	63.00
369B	20	451.20	65.44
96A	20	575.24	86.43
177B	20	369.02	53.52
325A	20	386.39	56.04
182A	20	490.71	71.17
337B	20	395.01	57.29
182B	20	380.60	55.20
363B	20	335.78	48.70

Table III. (cont.)

Specimen number	Test temp--°C	Strength--MPa	Strength--ksi
368A	20	486.92	70.62
276A	20	346.61	50.27
282A	20	359.09	52.08
286A	20	413.70	60.00
291A	20	383.49	55.62
366B	20	421.28	61.10
360A	20	411.49	59.68
298A	20	320.96	46.55
273A	20	438.93	63.66
362B	20	337.85	49.00
291B	20	419.42	60.83
366A	20	408.04	59.18
279B	20	392.94	56.99
297B	20	369.64	53.61
292A	20	408.94	59.31
274B	20	444.38	64.45
274A	20	373.70	54.20
373A	20	386.94	56.12
370B	20	383.98	55.69
369A	20	487.95	70.77
368B	20	464.86	67.42
374B	20	394.46	57.21
373B	20	390.87	56.69
172B	1400	338.13	51.07
328B	1400	352.12	51.07
232A	1400	411.90	59.74
172A	1400	291.17	42.23
157B	1400	387.22	56.16
156B	1400	348.68	50.57
158A	1400	111.49	16.17
232B	1400	179.27	26.00
248A	1400	388.05	56.28
329B	1400	296.27	42.97
71B	1400	203.95	29.58
178A	1400	383.22	55.58
159A	1400	387.84	56.25
161B	1400	368.05	53.38
234B	1400	363.15	52.67
176A	1400	408.25	59.21
154A	1400	173.47	25.16
244A	1400	391.56	56.79
175B	1400	347.92	50.46
245A	1400	348.54	50.55
161A	1400	236.63	34.32
240B	1400	398.73	57.83
179B	1400	356.05	51.64

• Denotes head failures

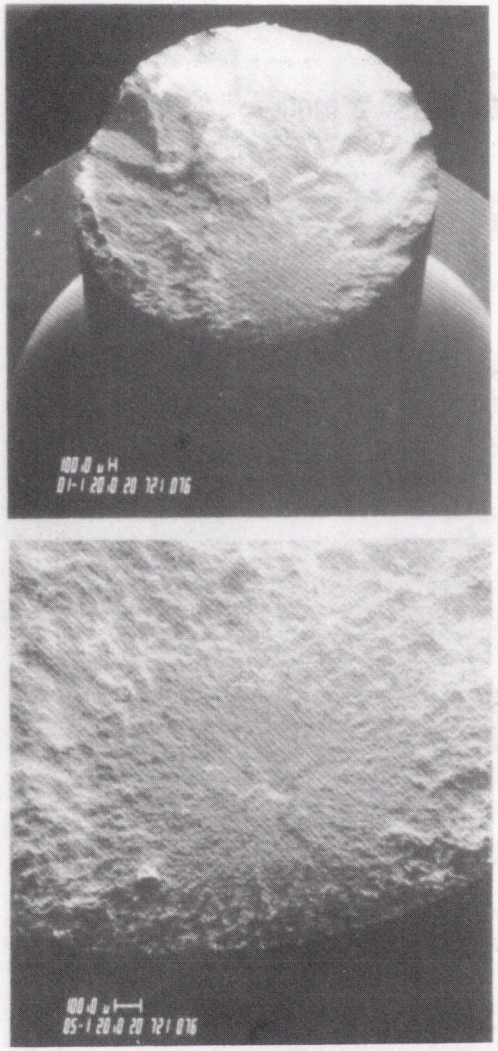

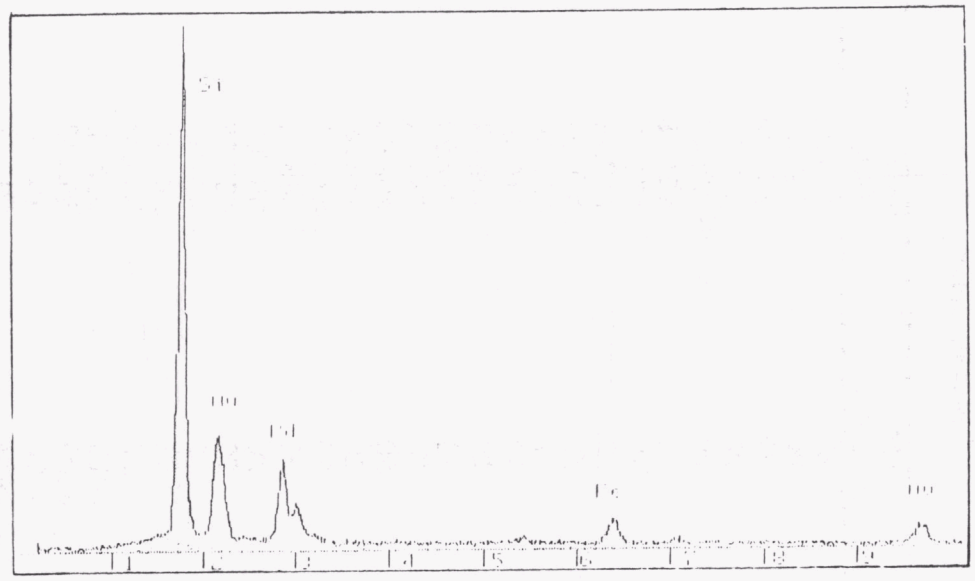

Figure 1. SEM fractography and energy dispersive analysis of room temperature tensile specimen.

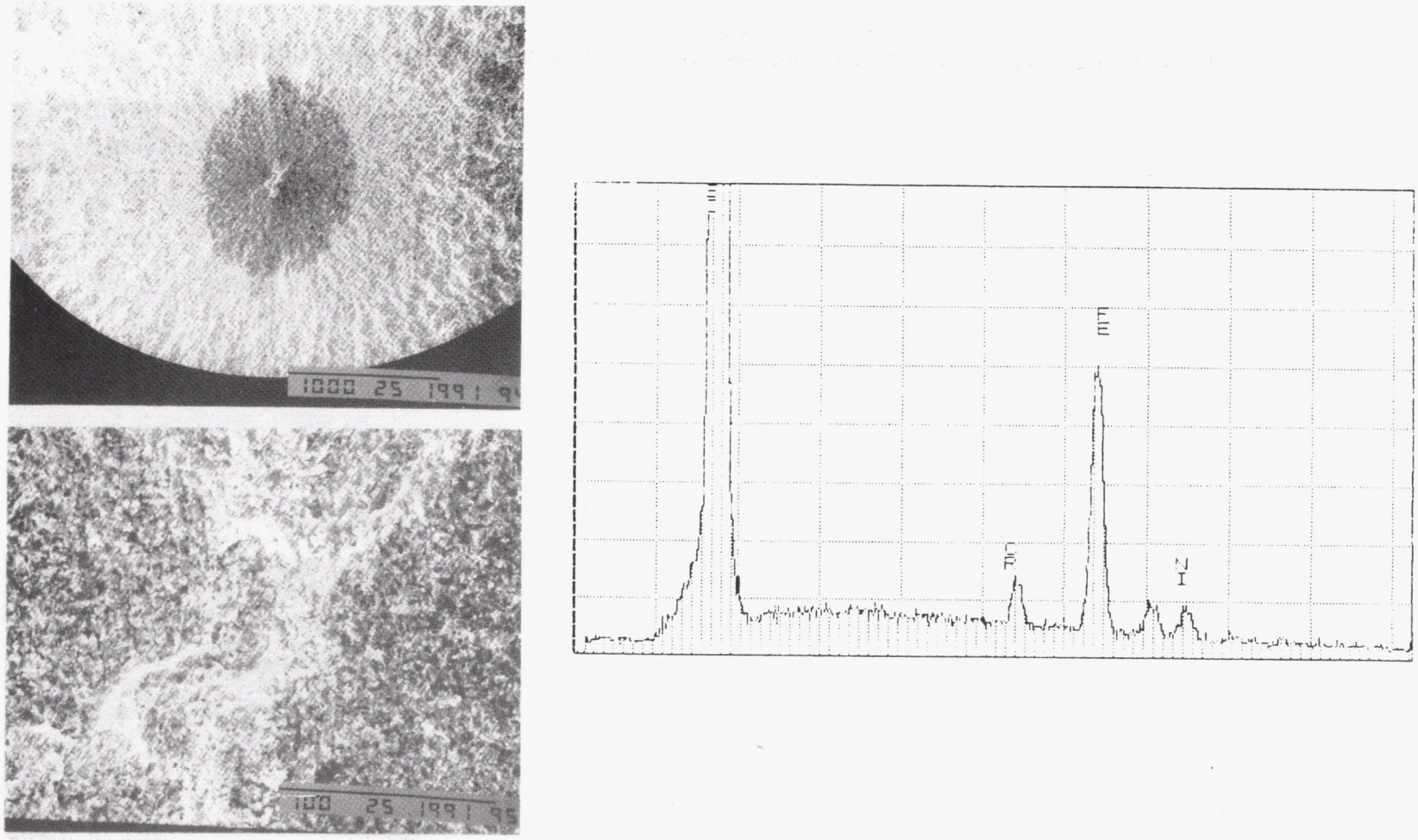

Figure 2. SEM fractography and energy dispersive analysis of room temperature tensile specimen showing Fe, Cr, and Ni present at fracture site.

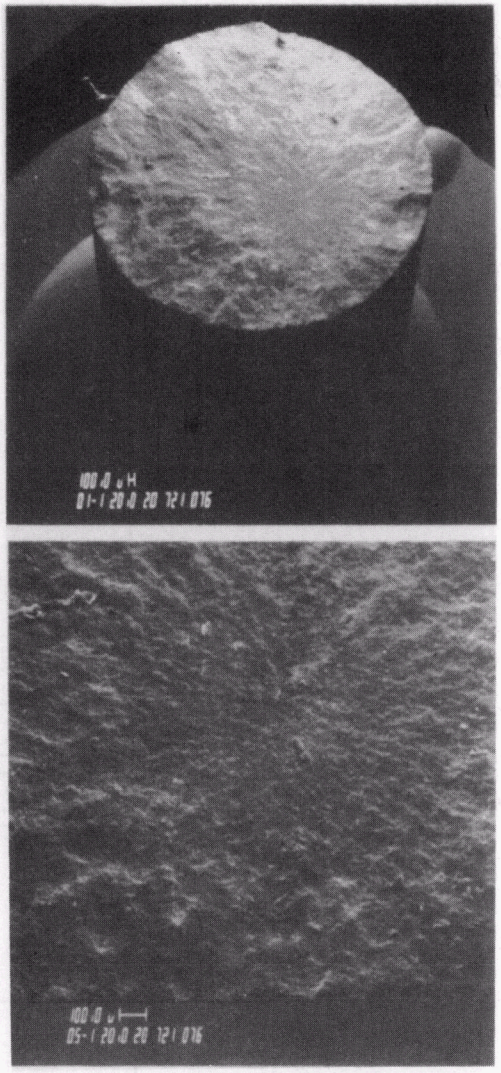

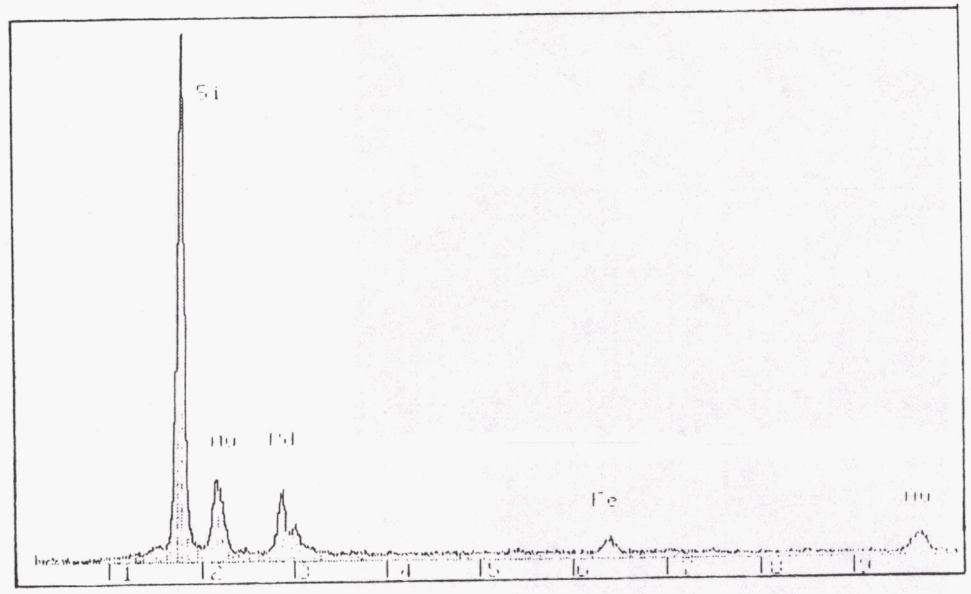

Figure 3. SEM fractography and energy dispersive analysis of a tensile specimen tested at 1400°C.

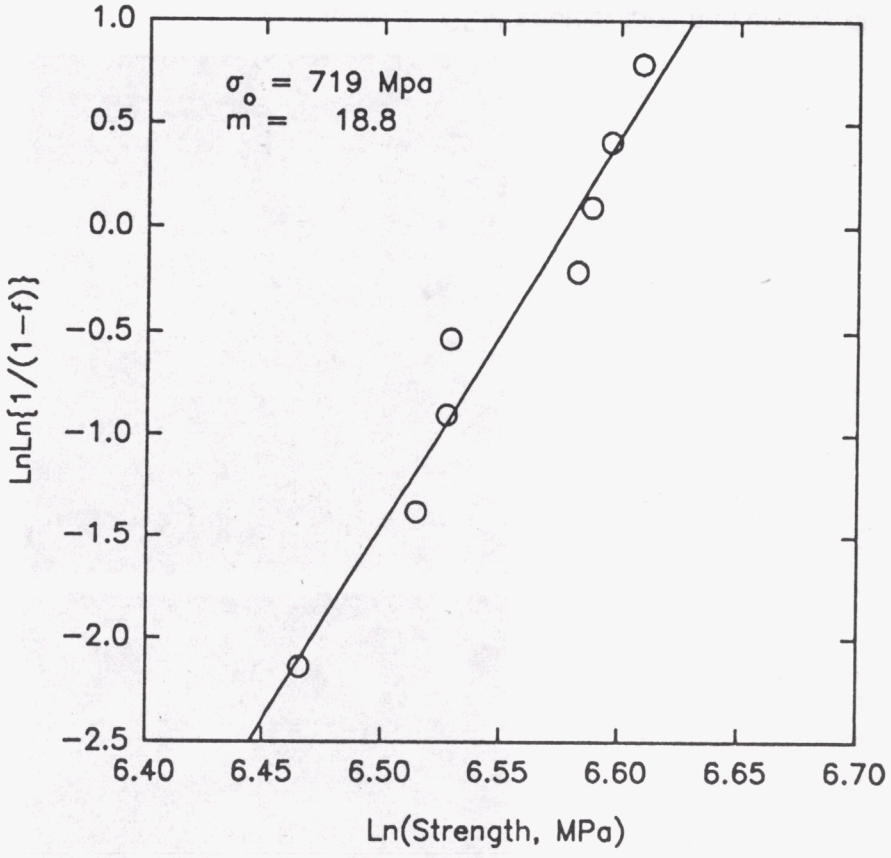

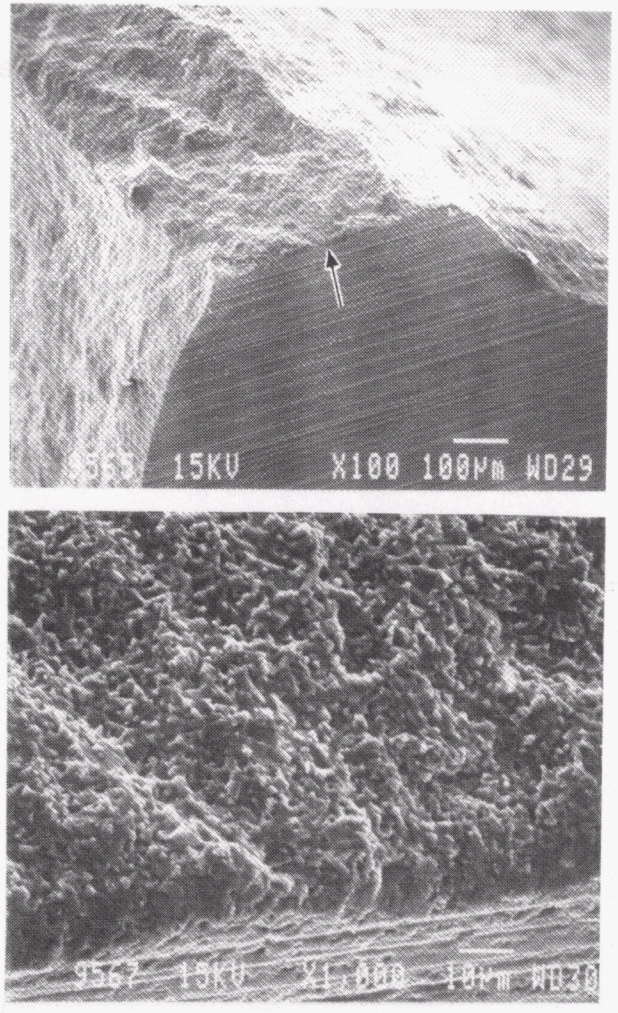

Figure 4. Strength distribution and fractography of biaxial disk specimen characterized at room temperature.

Ultrasonic examination of the aforementioned surface hole specimens was conducted to optimize the experimental parameters using the 100 MHz imaging systems assembled at Allison. Optimum inspection parameters were developed to detect surface flaws. Table V summarizes the results. The radial resolution in button head specimen was measured to be 6 micron and the axial resolution was better than 76 micron.

Table IV. Detection of surface holes by microfocus radiography.

Specimen type	Nominal flaws* Diameter --μm	Depth --μm	Number of flaws Present	Detected	Percent thickness sensitivity
MOR bar					
T**=3mm	100	100	100	100	3.38
	50	50	50	43	1.69
Tensile					
T=4.76mm	100	100	50	36	2.13
Biaxial Disk					
T=3.5mm	100	100	50	50	2.85
	50	50	50	32	1.42

*Actual holes: not flat bottom, shallow depth, angular, irregular
**Thickness of specimen

Table V. *Ultrasonic detection of surface holes.**

Specimen type	Nominal hole size** Diameter	Depth	Number of flaws Present	Detected
MOR bar	100	100	100	100
	50	50	100	50
	25	25	50	49
Tensile	100	100	50	50
	50	50	50	50
	25	25	50	50
Biaxial disk	25	25	49	49

*Transducer: 50MHz, F#0.8
**Actual flaw shape/size were uncontrolled

Status of Milestones

322201: Computer Implementation of Initial Failure Models–complete
322202: Initiation of MOR Testing–complete
322203: Initiation of Tensile Testing–complete
322204: Initiation of Biaxial Testing–complete
322205: Initiation of Confirmatory Testing–slipped due to vendor delivery problems
322206: Completion of All Specimen Testing–on schedule
322207: Finalization/Verification of Computer Code–on schedule
322208: Draft Final Report–on schedule
322209: Final Report–on schedule

Publications

None

Life Prediction Methodology

J. Cuccio
(Garrett Auxiliary Power Division, Allied-Signal Aerospace Company)

Objective/Scope

Garrett Auxiliary Power Division (GAPD) has defined a program to develop the methodology required to adequately predict the useful life of ceramic components used in advanced heat engines. GAPD's approach to ceramic life prediction consists of comprehensive testing of various specimen geometries under both uniaxial and multiaxial loads at different environmental conditions to determine the strength-controlling flaw distributions and to identify various failure mechanisms. This information will be used to develop the flaw distribution statistical models and material behavior models for fast fracture, slow crack growth, creep deformation, and oxidation. As sub-routines, these models will be integrated with stress and thermal analyses into a failure risk integration analytical tool to predict the life of ceramic components. The methodology developed will be verified (for completeness and accuracy) by analytically predicting the life of several ceramic components and testing these components under stress and temperature conditions encountered in ceramic turbine engines.

Technical Highlights

Material Testing and Analysis
H. Fang, N. Menon, and T. Strangman

Material Testing

Test specimen deliveries from Norton/TRW Ceramics (NTC) are on track, per the revised NTC delivery schedule. Table 1 summarizes the specimens ordered and their current status. All specimens are NT154 silicon nitride, processed under identical conditions and finish machined and heat treated by NTC. Selected specimens will be notched and precracked for testing. All specimens will be subjected to visual inspection, laser marking, and NDE (which may include fluorescent penetrant, radiography, and ultrasonic inspection) before testing.

GAPD is continuing tensile creep and tensile slow crack growth testing as a User at the ORNL High Temperature Materials Laboratory (ORNL-HTML) under the direction of Drs. M.G. Jenkins and M.K. Ferber of the Mechanical Properties User Center. The specimens are of the ORNL cylindrical buttonhead geometry with a 6.35 mm diameter by 35 mm length gage section. The specimens are loaded in uniaxial tension in Instron screw-driven machines using the ORNL/Instron Supergrips. Instron extensometers with SiC probes are being used to monitor the strain deformation of the gage sections during testing.

TABLE 1. ORNL LIFE PREDICTION CERAMIC TEST SPECIMEN STATUS

Type of Test	Specimen Size	Surface Machining Direction	Specimens Received	Specimen Status
4-Point Bend	MIL-STD-A	Longitudinal	Yes	Ready for Testing
4-Point Bend	MIL-STD-B	Longitudinal	Yes	NDE
4-Point Bend	MIL-STD-B	Transverse	Yes	Ready for Testing
4-Point Bend	MIL-STD-B	45 degrees	Yes	NDE
4-Point Bend	0.35 x 0.72 x 6 in	Longitudinal	Yes	NDE
Chevron Notch	--	--	Yes	Ready for Testing
Diametral Compression	--	--	Yes	Ready for Testing
Plate Bending	--	--	Yes	NDE
Tensile (Fast Fracture and S/R)	--	--	Yes	NDE, Ready for Testing
Pre-cracked Tension/Torsion	--	--	Yes	Ready for Testing
Unnotched Tension/Torsion	--	--	Yes	NDE
Notched Tensile	--	--	Yes	Visual Inspection
Notched Tensile	--	--	Yes	Visual Inspection
Rectangular Flaw Growth	--	--	No	On Order
Square Flaw Growth	--	--	No	On Order
Spin Disk	--	--	No	On Order

8491(05)-1

Fifteen specimens have been tested at temperatures between 1204C to 1400C. Table 2 summarizes the test temperature, load, time to failure, and strain to failure data for these specimens. Strain versus time curves for four of the test temperatures are presented in Figures 1-4. GAPD will use 21 specimens to establish the load and temperature regime best suited to characterize creep and slow crack growth in planned tests using additional specimens.

Specimens 1-9, 2-66, 1-2, and 1-20 were examined for cavitations using the scanning electron microscope (SEM). Test conditions for these specimens are listed in Table 2. A special sample preparation technique developed by M. Ferber and M. Jenkins of ORNL-HTML was adopted to facilitate observation of the cavities in these specimens. The gage sections of the specimens were partially notched in the transverse plane, i.e. parallel to the fracture surface, and then broken in a low-energy mode to create a clean fracture surface. All of the specimens examined showed voids or cavities at the grain boundaries. A typical fracture surface showing these distinct cavities is shown in Figure 5.

TABLE 2. SUMMARY OF PRELIMINARY TENSILE CREEP TEST RESULTS

Specimen ID	Test Temp, C	Applied Stress σ_0, MPa	Minimum Strain Rate $\dot{\varepsilon}_{ss}$, $\mu\varepsilon$/sec	Time to Failure t_f, hrs.	Total Strain to Failure ε_f, $\mu\varepsilon$
1-21	1400	140	3.3×10^{-8}	96	18,270
1-4	1400	125	1.3×10^{-8}	341	22,820
2-68	1400	100	1.3×10^{-8}	>212	>14,300
2-55	1371	210	4.6×10^{-7}	1.4	3510
1-9	1371	190	2.3×10^{-8}	68	10,920
1-20	1371	160	1.3×10^{-8}	209	14,410
2-121	1371	125	6.3×10^{-9}	>210	>7500
1-2	1315	250	2.2×10^{-8}	24	3640
1-15	1315	225	2.2×10^{-9}	>675	10,300
1-11	1295	375	3.8×10^{-7}	0.35	2231
1-23	1295	300	2.2×10^{-7}	0.40	788
2-66	1295	200	--	>530	--
2-56	1204	415	1.1×10^{-8}	1.3	1378
2-71	1204	350	4.4×10^{-8}	2.3	1190
1-3	1204	300	1.8×10^{-10}	>517	>1580

Uniaxial tension, gage section 6.35 mm diameter, 35 mm length.

8491(05)-2

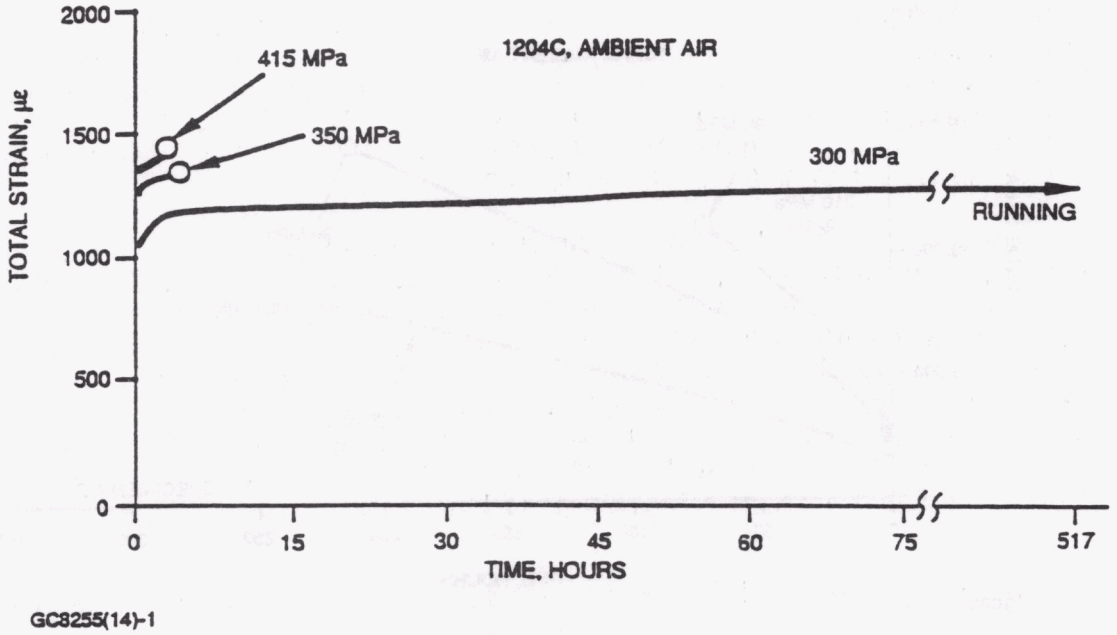

Figure 1. Strain Versus Time Data at 1204C.

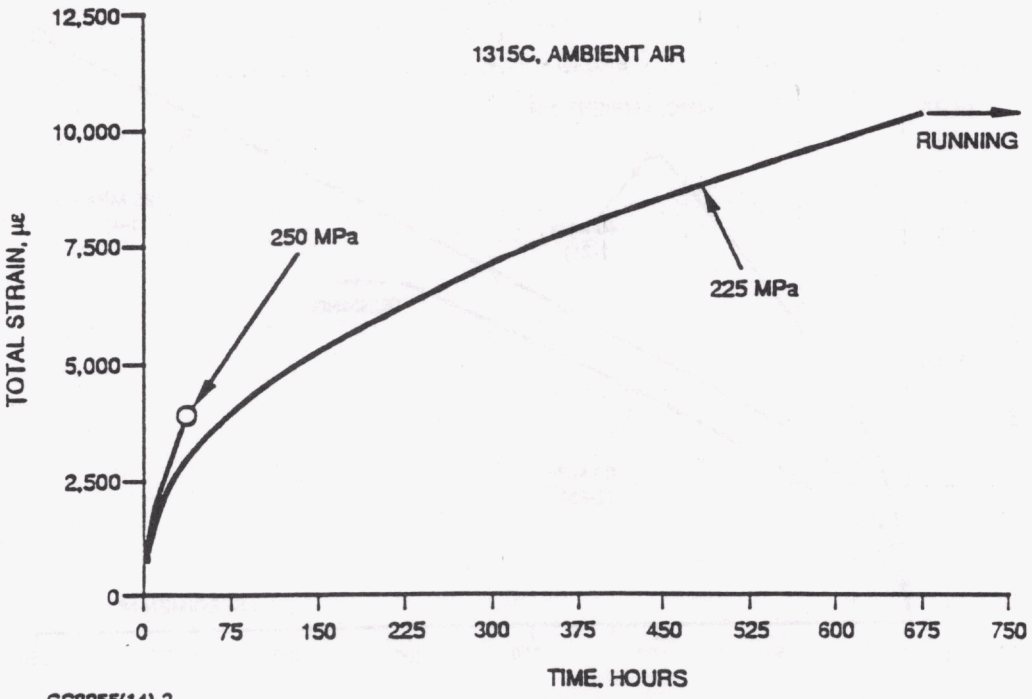

Figure 2. Strain Versus Time Data at 1315C.

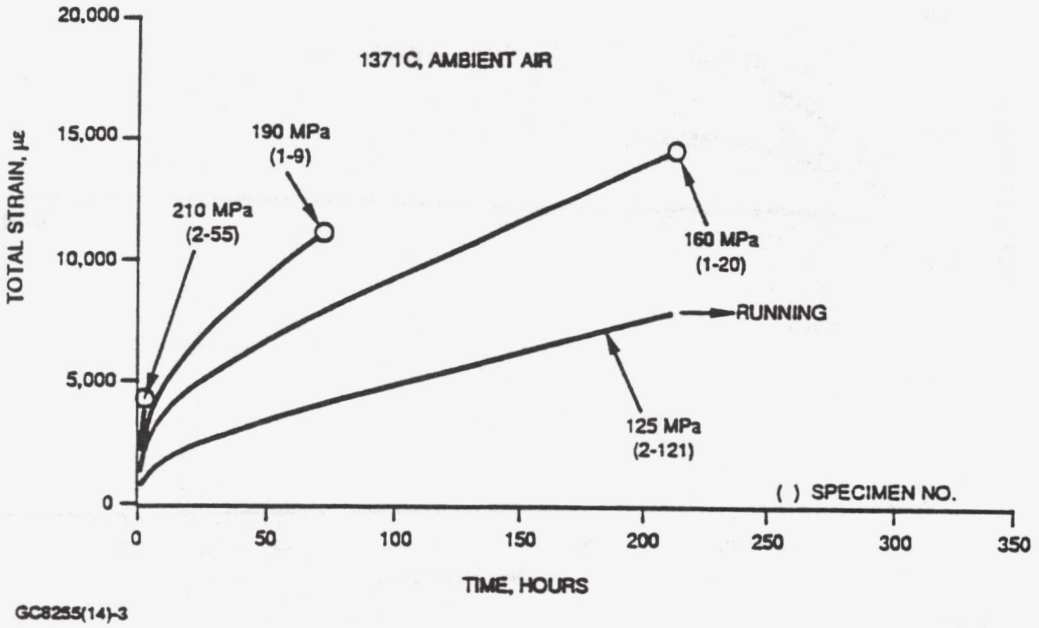

Figure 3. Strain Versus Time Data at 1371C.

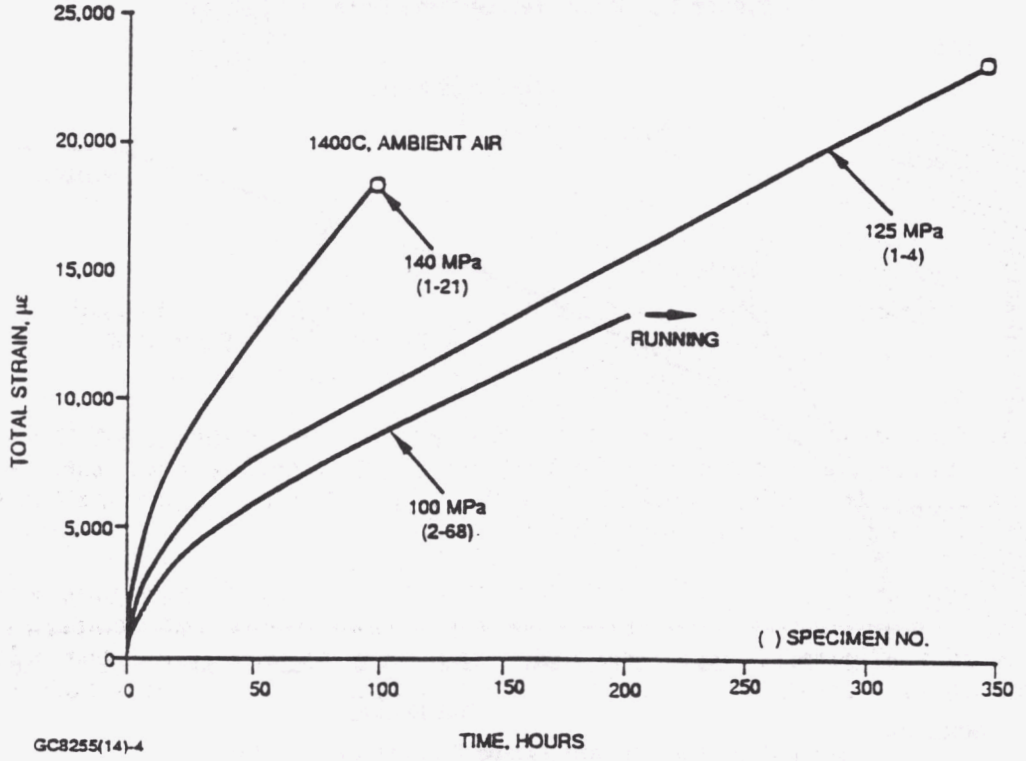

Figure 4. Strain Versus Time Data at 1400C.

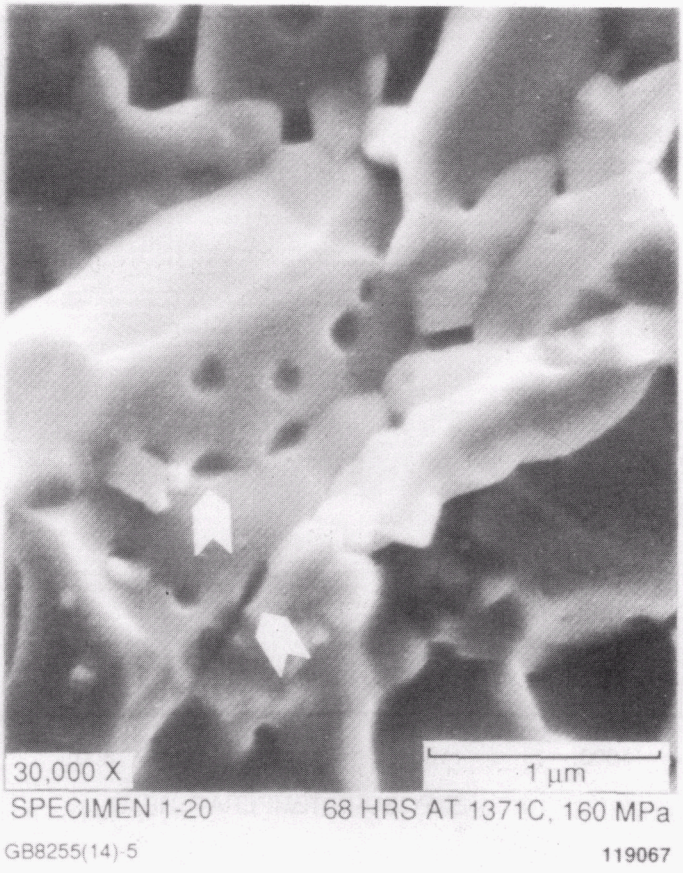

Figure 5. Cavities (Indicated by Arrows) Formed at the Grain Boundaries of an NT154 Tensile Creep Specimen Tested at 1371C and 160 MPa for 68 Hours.

The surface strength of silicon nitride components is dependent upon the severity of the gas turbine oxidation environment, which can modify critical surface flaws. Consequently, the overall Ceramic Life Prediction Model must include the effects of oxidation on the strength of NT154.

In this oxidation testing program, 180 MIL STD-B size flexure bars are being exposed in an electric furnace in air for various times and temperatures as indicated in Figure 6. The distribution of specimens will permit the effects of oxidation on strength and surface flaw size to be analyzed as functions of:

- o Temperature (between 1000 and 1400C)
- o Time (between 1 and 1000 hours)
- o Time and temperature

The oxidized bars will be flexure tested in four-point bending at room temperature. Following testing, lines of constant strength will be superimposed on Figure 6.

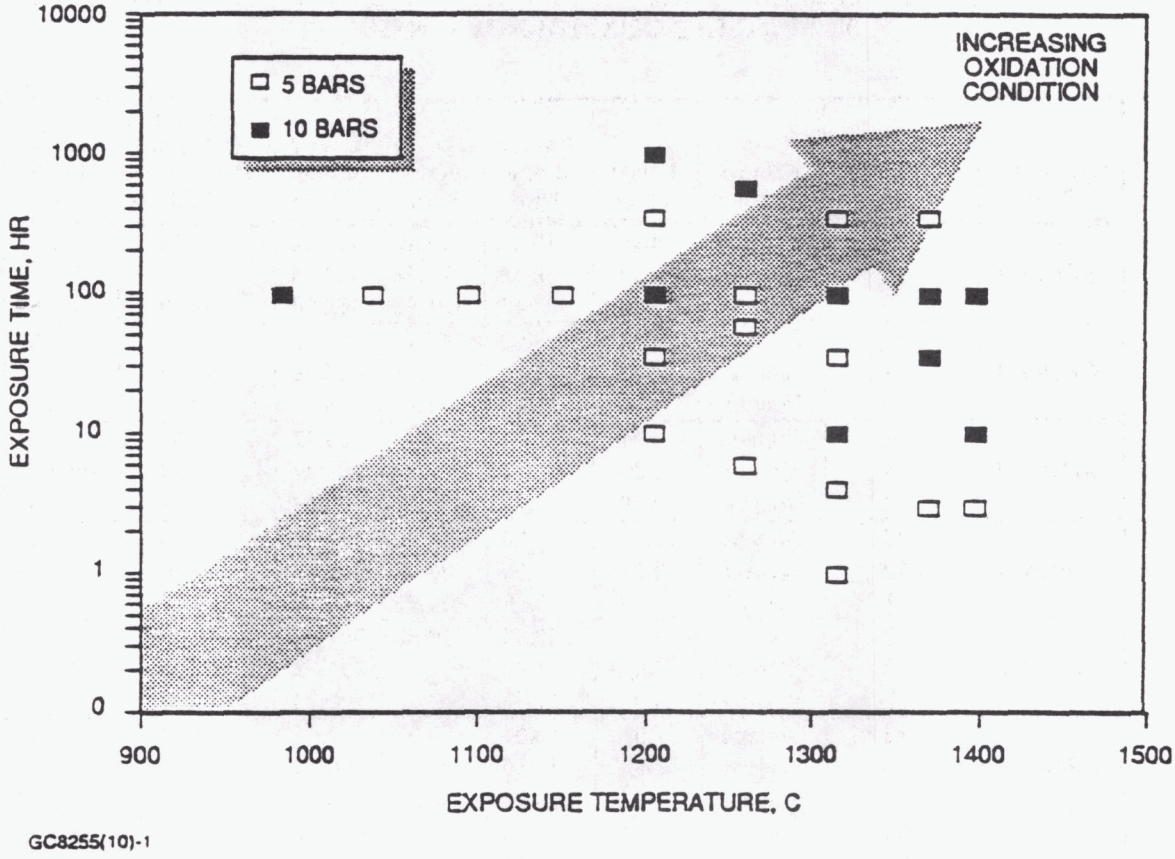

Figure 6. Oxidation Exposure Test Conditions.

Detailed fractography and microstructure characterization, including SEM/WDX and X-ray diffraction, will then be used to quantify the oxide scale thickness and the size of any oxidation-induced pit(s) that initiated fracture. The results will be presented as lines of constant oxidation (oxide scale thickness) and superimposed on Figure 6.

Data Analysis and Methodology Development
A. Peralta, P. Brehm, J. Cuccio, J. Song, and D. Wu

A computer code is being developed to implement the statistical methods to analyze ceramic material test data. The code will predict confidence intervals for Weibull parameters, design stress, and reliability. The code will also treat test data from specimens of different sizes and different loading conditions with multiple failure modes.

The computer code has been evaluated using data for silicon carbide (SiC) obtained by Drs. C. Johnson and W. Tucker of the General Electric Corporate Research Center (GE-CRC). In this data (Table 3) there are a total of six specimen types: 3-point and 4-point flexure test specimens, in three different sizes (A, B, and C). Estimates of the Weibull parameters and the corresponding confidence limits generated from this data set are listed in Table 3.

TABLE 3. SILICON CARBIDE DATA ANALYSIS SUMMARY WITH 95 PERCENT CONFIDENCE LIMITS

Specimen Type	Number of Specimens	Failure Location	Lower Limit	Weibull Slope MLE	Upper Limit	Lower Limit (MPa)	Second Weibull Parameter MLE (MPa)	Upper Limit (MPa)
	11	Surface	8.98	15.25	23.46	421.62	443.06	500.26
3-Point A	6	Corner	5.58	12.19	21.82	434.33	480.25	674.37
	1	Volume	4.24	34.45	101.53	382.16	403.18	816.59
	16	Surface	6.42	9.59	13.41	420.35	459.85	545.55
4-Point A	1	Corner	0.55	7.31	23.48	438.38	732.04	*
	0	Volume	N/A	N/A	N/A	N/A	N/A	N/A
	12	Surface	8.01	12.78	18.48	423.27	459.30	552.88
3-Point B	4	Corner	3.97	10.44	19.69	425.47	504.99	1063.53
	2	Volume	3.06	12.78	28.42	383.88	442.19	1786.53
	35	Surface	10.94	14.26	17.92	412.23	440.04	486.87
4-Point B	12	Corner	9.27	14.85	21.43	402.92	444.30	545.46
	1	Volume	0.66	9.46	30.53	380.30	610.55	*
	9	Surface	12.71	20.58	29.63	387.47	412.63	480.52
3-Point C	6	Corner	5.08	11.33	19.78	391.78	458.94	786.15
	3	Volume	6.09	17.48	32.72	366.24	410.70	810.90
	12	Surface	7.91	13.07	19.57	407.17	474.19	650.45
4-Point C	4	Corner	4.68	12.40	24.06	380.23	472.89	1060.41
	2	Volume	21.09	59.23	136.22	326.28	336.99	398.25
	95	Surface	12.67	14.28	15.89	430.17	443.87	462.28
All Data	33	Corner	9.00	11.51	14.13	453.97	488.24	548.63
	9	Volume	12.87	18.68	24.45	389.81	413.01	473.14

N/A — Failure mode not present in the data; no analysis could be performed.

* — Program could not converge on a solution

8491(05)-3

The combination of different specimen sizes and loading conditions produces Weibull parameters that are not representative of any particular specimen size or loading condition. Instead, they represent material properties that can be thought of as parameters representative of specimens of unit size and uniform stress. The significance of pooling together data points from specimens of different types and sizes is that the confidence limit is much narrower for both parameters. Figures 7(a) and (b) illustrate this, using the data for silicon carbide listed in Table 3.

The following statistical analysis capabilities have been derived and added to the computer code:

(1) Maximum likelihood estimates for censored and uncensored data.

(2) Maximum likelihood estimates of the reliability and the design stress level. The estimate of the reliability is shown in Figure 8; the plot is scaled to a component of unity effective size. The figure shows the reliability for only the surface failure mode.

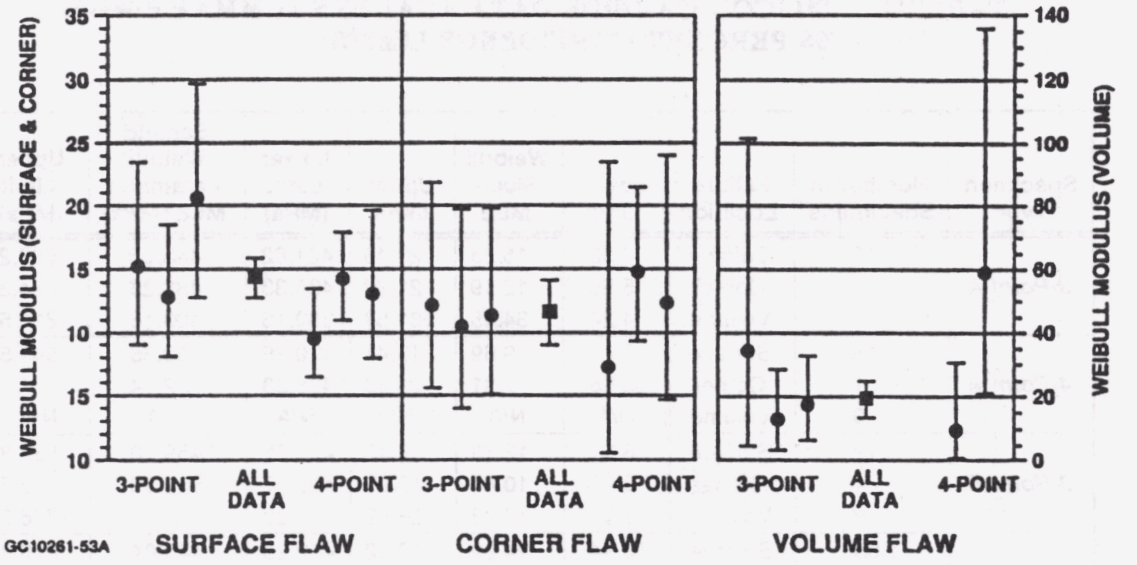

Figure 7(a). Method for Combining Data Significantly Improved the Confidence Limit on Weibull Modulus Estimate.

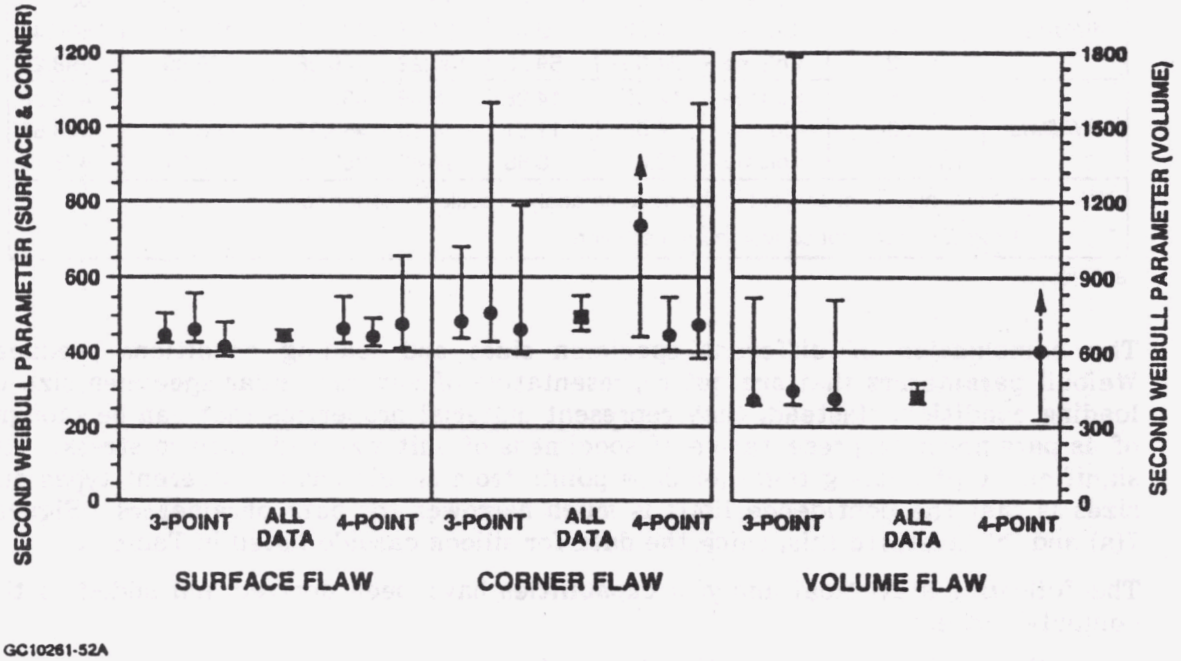

Figure 7(b). Method for Combining Data Significantly Improved the Confidence Limit on Second Weibull Parameter Estimate.

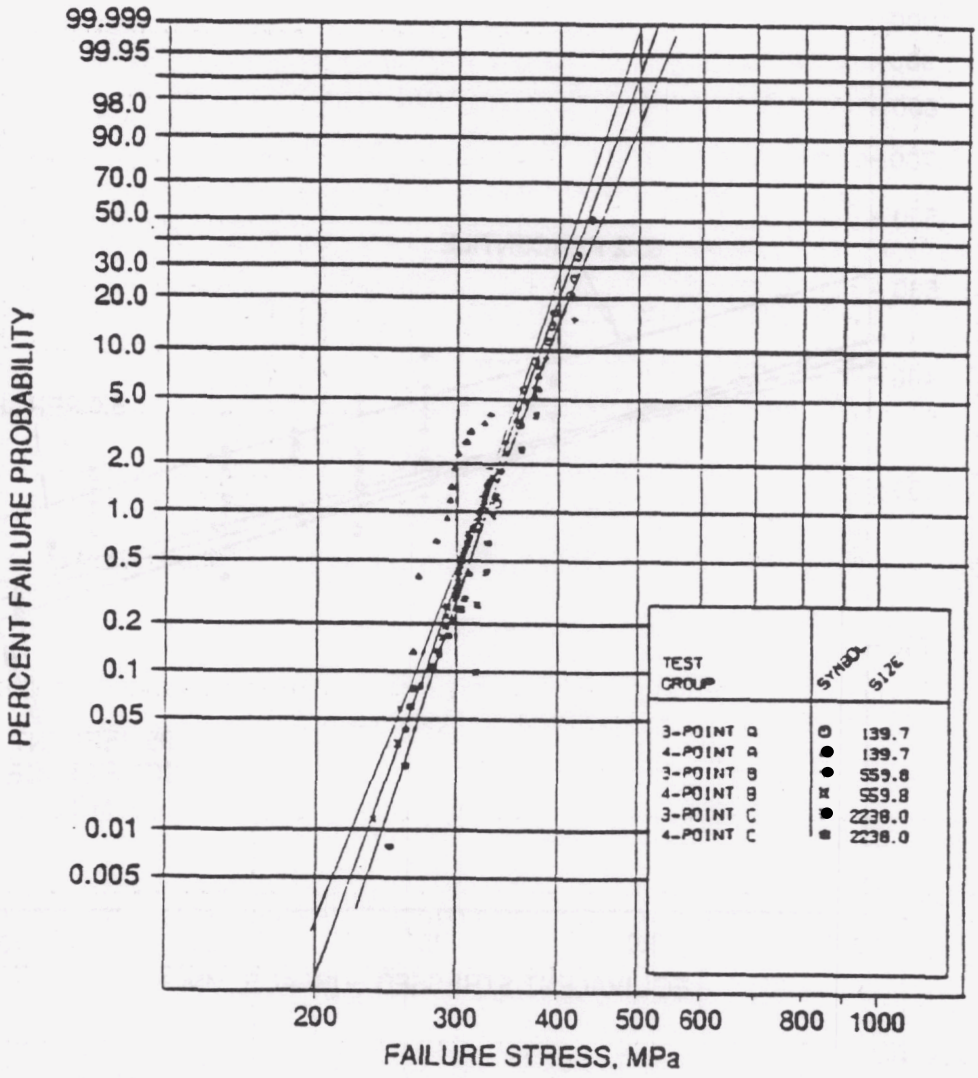

Figure 8. Reliability Plot of Silicon Carbide Data With 95 Percent Confidence Limits.

(3) Likelihood ratio confidence limit estimates for the Weibull parameters for both uncensored and censored data. Confidence limits for m and σ_o listed in Table 3 were generated using this method.

(4) Likelihood ratio confidence limit estimates for the reliability and design stress level for both uncensored and censored data. Figure 8 shows the reliability confidence limits for the 95th percentile; and Figure 9 shows the 95th percentile confidence limits for the design stress level.

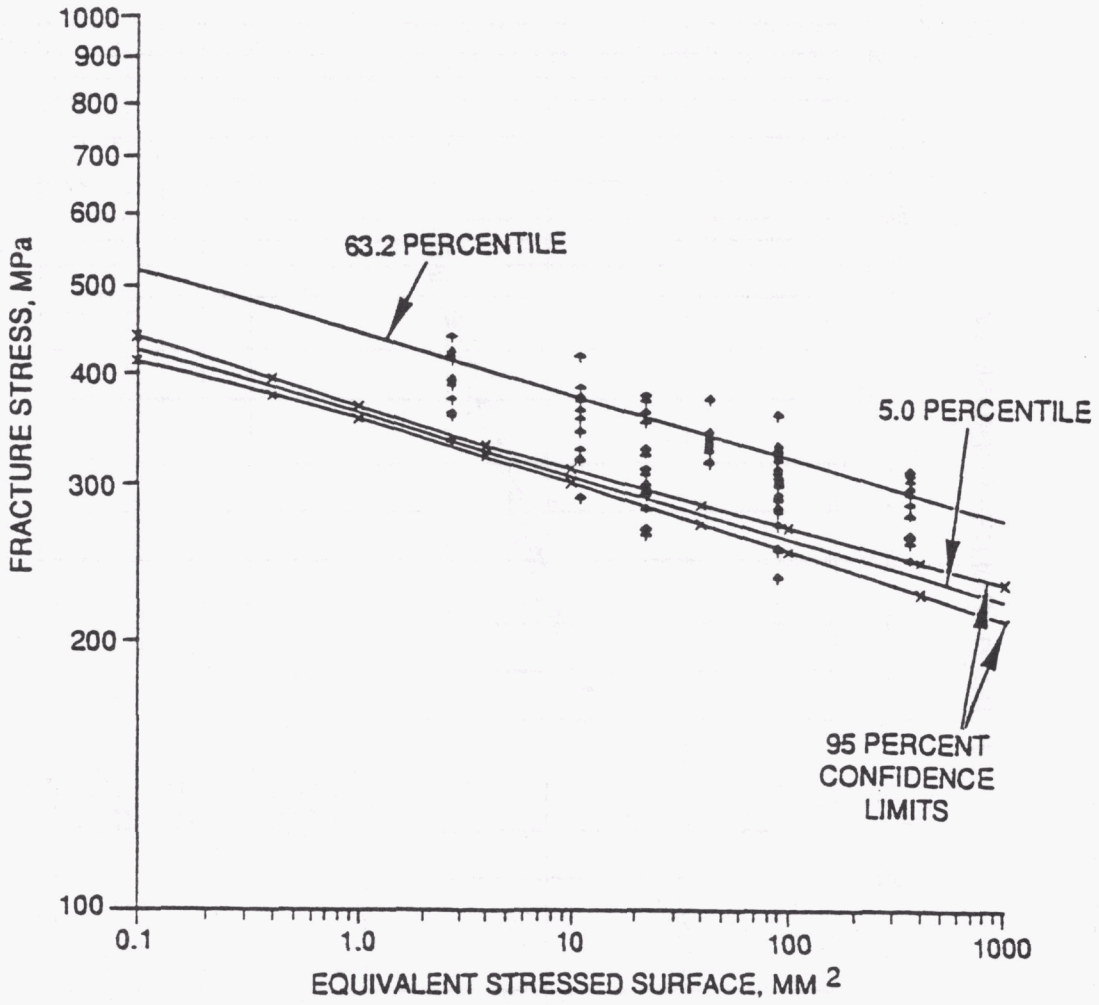

G88255(14)-7

Figure 9. Size Versus Strength Plot of Silicon Carbide Data, 63.2 Percentile and 5.0 Percentile With 95 Percent Confidence Limits.

(5) Bootstrap confidence limit estimates for the Weibull parameters for both uncensored and censored data. The method of treating censored data with a single failure mode is still to be developed. Table 4 shows a confidence limit comparison for the pooled data set between likelihood ratio and bootstrap methods with 99 simulations. The confidence levels are 95 percent for the likelihood ratio method and 96 percent for the bootstrap method. The group of 99 simulations is used in the bootstrap method to save computation time during the code development. To achieve more reasonable accuracy, 1000 simulations are required.

(6) Bias correction using the bootstrap approach for the Weibull parameters for uncensored data. Results for the 3-point A bend specimen data is shown in Table 5.

TABLE 4. LIKELIHOOD RATIO VERSUS BOOTSTRAP CONFIDENCE LIMIT COMPARISON FOR THE POOLED DATA SET (137 SPECIMENS)

Failure Mode	Weibull Parameter	Level	Likelihood Ratio 95% C.L.	Bootstrap 96% C. L.
Surface	m	U.L. L.L.	15.89 12.67	15.76 12.57
	σ_o (MPa)	U.L. L.L	462.28 430.17	461.98 428.01
Corner	m	U.L. L.L.	14.13 9.00	14.73 8.16
	σ_o (MPa)	U.L. L.L	48.63 453.97	566.67 446.96
Volume	m	U.L. L.L.	24.45 12.87	29.93 12.33
	σ_o (MPa)	U.L. L.L	473.14 389.81	499.88 383.73

U.L. = Upper Limit
C.L. = Confidence Limit
L.L. = Lower Limit

8491(05)-4

TABLE 5. COMPARISON OF BIASED VERSUS UNBIASED WEIBULL PARAMETERS FOR THE UNCENSORED 3-POINT A BEND SPECIMEN DATA

Wiebull Parameter	Biased	Unbiased
m	14.56	13.65
σ_o (MPa)	402.64	403.29

8419(05)-5

At present, the methods development effort is proceeding in the following areas:

- Confidence limit predictions for combined reliability with multiple failure modes, using the likelihood ratio method
- Application of the bootstrap method to the single failure mode with censored data
- Bias correction factors for the confidence limit predictions, using the bootstrap method
- Bias corrections using liklihood ratio methods

The technical approaches to be used, to develop the capabilities to treat anisotropic cracking and to model time-dependent processes such as slow crack growth (SCG), were identified in detail during the semiannual meeting with Drs. W. Tucker and C. Johnson of GE-CRC. Development work in these two important areas will be initiated in the next reporting period.

NDE Methods Development and Application
J. Wade and B. Meade

Acoustic Microscopy

Inspection procedures for each of the specimen geometries listed in Table 1 have been established, and specimen inspection has started. Table 1 lists the inspection status by specimen type.

Alternate sources for computed tomography (CT) and acoustic microscopy of the tensile rods were evaluated. General Electric was selected to perform CT inspection services and some acoustic microscopy services. The acoustic microscopy services will complement acoustic microscopy performed in-house at GAPD.

An additional source, Precision Acoustic Devices, is still under evaluation for internal acoustic microscopy inspection of the tensile rods. Preliminary results have not been as promising as initially thought; none of the 25 or 50 micron holes in the calibration standards have been detected with transducers used for inspection of tensile rods under a different program. Surface finish of the specimens has been identified as a possible cause for lack of detection. The tensile rods for the GAPD test matrix have a surface finish typical of engine components (Ra $\leq$ 16 microinches), while the tensile rods evaluated previously by Precision Acoustic Devices had optically polished surfaces.

Acoustic microscopy inspections of the tensile rods continue to show some transverse indications on the surface in the gage section that cannot be verified visually at magnifications up to 40X. Figure 10 shows a typical ultrasonic scan on a tensile rod with no unusual indications; Figure 11 shows a tensile rod with transverse indications in the gage section, which could not be verified visually. (Note: both scans show a white horizontal line, which is a printer artifact.) Tensile rods having suspect indications are being identified prior to testing, but are still included in the test matrix, as planned. All B-size flexure bars for oxidation testing have been inspected. A group of 15 bars was inspected before and after oxidation exposure, and showed significant differences in the surface inspection results.

Status of Milestones

Milestone No. 4, All Specimens Delivered, has been delayed five months, due to a revised specimen delivery schedule from Norton/TRW Ceramics.

Communications/Visits/Travel

Periodic telephone and written correspondence has taken place with Drs. C. Johnson and W. Tucker from the General Electric Corporate Research Center (GE-CRC) dealing with implementation of the confidence interval methods development work.

During October, 1991, Mr. H. Fang of GAPD visited the Norton/TRW Ceramics Co. facilities in Northboro, Massachusetts and Salem, New Hampshire, to discuss and review the Norton/TRW modified spin disk machining procedure. Mr. Fang also inspected the first article spin disk machined using the modified procedure. Mr. Fang also visited Brown University in Providence, Rhode Island, to discuss scheduling and testing of notched and smooth tension/torsion specimens.

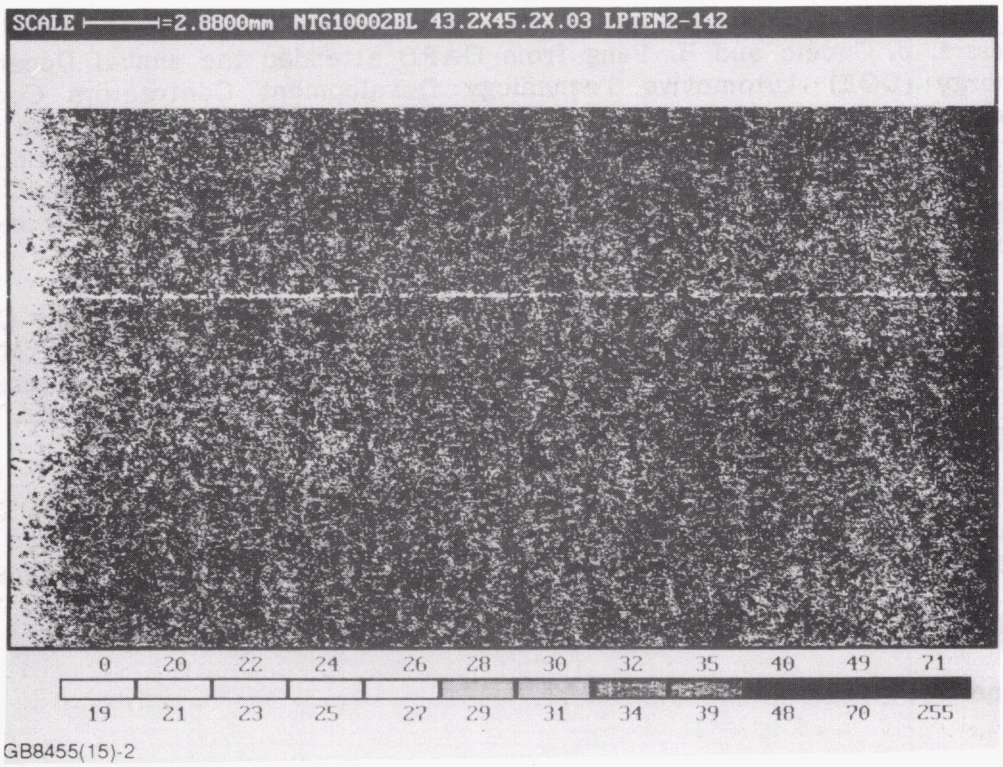

Figure 10. Acoustic Scan of Tensile Rod Showing No Unusual Indications.

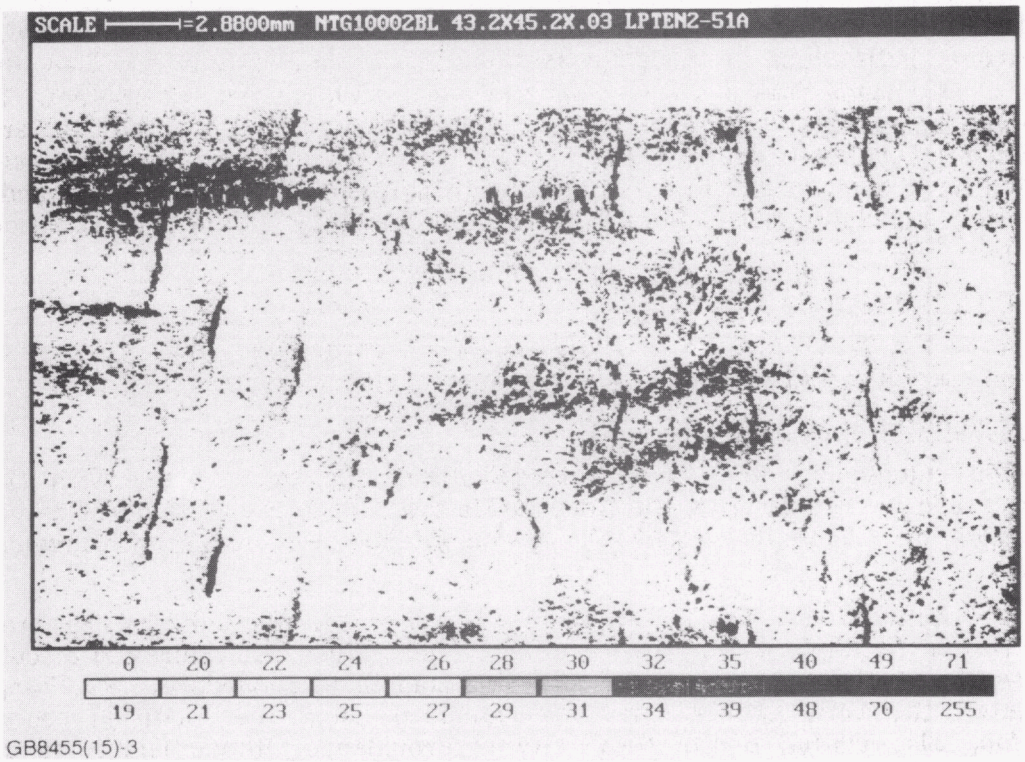

Figure 11. Acoustic Scan Showing Transverse Indications, Not Verified by Visual Inspection.

Messrs. J. Cuccio and H. Fang from GAPD attended the annual Department of Energy (DOE) Automotive Technology Development Contractors Coordination Meeting in Dearborn, Michigan on October 28-30, 1991. A presentation was given by Mr. Fang summarizing GAPD's progress in the ceramic life prediction program during the past year. Messrs. Cuccio, Fang, and Mrs. J. Wade and C. McCormick of GAPD also attended the semi-annual life prediction program review meeting on November 1, 1991, in Dearborn, Michigan.

In June, 1991, Dr. N. Menon and Mr. J. Hartman of GAPD visited the Oak Ridge National Laboratory High Temperature Materials Laboratory (ORNL-HTML) in Oak Ridge, Tennessee to set up an extensometer test apparatus and begin tensile creep testing, under the ORNL-HTML User Program. Dr. Menon and Mr. Hartman returned to ORNL-HTML to continue tensile creep testing in July.

Dr. J. Song and Mr. A. Peralta of GAPD visited the General Electric Corporate Research Center (GE-CRC) in Schenectady, New York on September 23, 1991 for a semiannual review of progress in data analysis and methodology development.

Publications

None.

3.3 ENVIRONMENTAL EFFECTS

Environmental Effects in Toughened Ceramics
Norman L. Hecht (University of Dayton)

Objective/scope

Since December 1984, the University of Dayton has been involved in a five-phase project to investigate the effects of environment on the mechanical behavior of commercially available ceramics being considered for heat engine applications. In the first phase of this project, the effects of environment on the mechanical behavior of transformation-toughened ZrO_2 ceramics were investigated. In the second phase, two Si_3N_4 ceramics (GTE PY6 and Norton/TRW XL144) and one SiC ceramic (Hexoloy SA) were evaluated. In the third phase, the tensile, flexural, and fatigue strength of three SiC and six Si_3N_4 ceramics were evaluated at temperatures ranging from 20 to 1400°C. Microstructure, chemistry, and physical properties were also investigated. In the fourth phase, the flexural strength and fatigue behavior of two additional Si_3N_4 ceramics (Kyocera SN-260 and Garrett GN-10) were investigated. In addition, the fatigue behavior of one Si_3N_4 ceramic (NT-154) was investigated. Efforts to study the tension/compression cyclic fatigue behavior of NT-154 have been delayed because of problems with the Instron test fixture. In phase five, three newly developed SiC and three newly developed Si_3N_4 ceramics will be investigated. In addition, the effects of different machining processes on the mechanical behavior of selected SiC/Si_3N_4 ceramics will also be studied.

During the past six months (April 1991 through September 1991), the fatigue behavior of NT-154 was investigated, the Raman microprobe was used to analyze NT-154 flexural specimens, and a new grip system for measuring the tensile strength of buttonheadless tension specimens was evaluated. In addition, during this reporting period this project was extended 24 months (phase V).

Technical progress

Fatigue Testing of NT-154

During this reporting period the fatigue behavior of a newly received batch of NT-154 tensile specimens was evaluated. Six specimens were tested in tensile stress rupture (TSR) at an assumed temperature of 1300°C. Stress levels of 200 and 250 MPa were used. Specimens surviving 50 hours were stressed to

---

*Research sponsored by the U.S. Department of Energy, Assistant Secretary for Conservation and Renewable Energy, Office of Transportation Systems, as part of the Ceramic Technology for Advanced Heat Engines Project of the Advanced Materials Development Program under Contract DE-AC05-840R21400 with Martin Marietta Energy Systems, Inc., Work Breakdown Structure Subelement 3.3.1.4.

failure using the rapid loading rate (crosshead speed of 0.004 cm/s). Tensile stress rupture was conducted on the buttonhead cylindrical tensile specimens using an Instron Model 1361 Electro-Mechanical Test System equipped with the "Super-Grip" specimen holders and Instron short furnace. The results of the TSR tests are compiled in Table 1. Only one specimen survived the desired 50 hour test time. The other five specimens failed after very short exposure times (0.05 to 1.6 hours). The five samples that failed at short exposure times all appeared to have failed from flaws at or very near the surface of the test specimens. The single specimen that survived the 50 hour test time failed from an inclusion containing iron (Fe), nickel (Ni), and chrome (Cr) (see Figure 1). Micrographs of the fractured surface of five tested specimens are presented in Figure 2(a-e).

Table 1. Interrupted Tensile Stress Rupture Test Results, Norton/TRW NT-154 [desired test temperature: 1300°C (2372°F), corrected test temperature 1328°C(2422°F)]

Specimen Number	Stress Level (MPa)	Desired Test Time (hrs)	Time to Failure (hrs)	Failure Stress (MPa)	Fracture Origin
300-29	250	50	1.6	250	surface
300-35	250	50	0.1	250	surface
300-36	200	50	0.1	200	surface
300-27	200	50	50.0	507	vl. incl.
300-37	200	50	0.05	200	surface
300-13	200	50	0.8	200	surface

The TSR results obtained from this set of specimens were considerably different from the set of specimens tested earlier at 1300°C. The TSR results from the earlier set of specimens are presented in Table 2 for purpose of comparison. As shown in Table 2 five of the six specimens survived for 70 or more hours, and all six specimens failed from volume initiated flaws (pore nucleation and agglomeration).

Table 2. Interrupted Tensile Stress Rupture Test Results, for the Initial Batch of Norton/TRW NT-154 [test temperature: 1300°C (2372°F)]

Specimen Number	Stress Level (MPa)	Time to Failure (hrs)	Failure Stress (MPa)	Fracture Origin
96	200	117.6	450	volume
63	200	8.4	200	volume
74	200	100.0	470	volume
71	200	100.0	469	volume
77	200	114.3	506	volume
67	200	71.2	200	volume

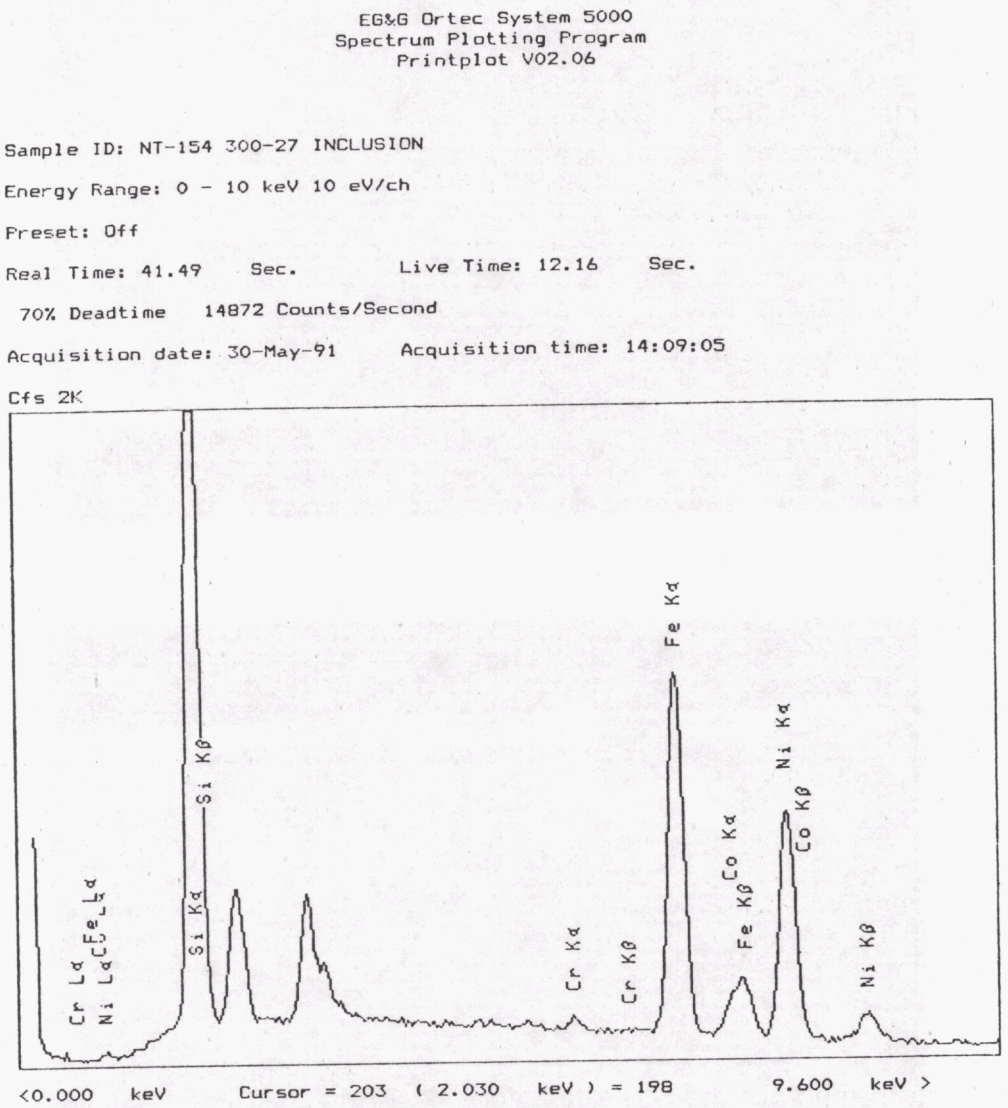

Figure 1. EG&G Ortec System 5000 spectra of the inclusion in specimen NT-154, #300-27.

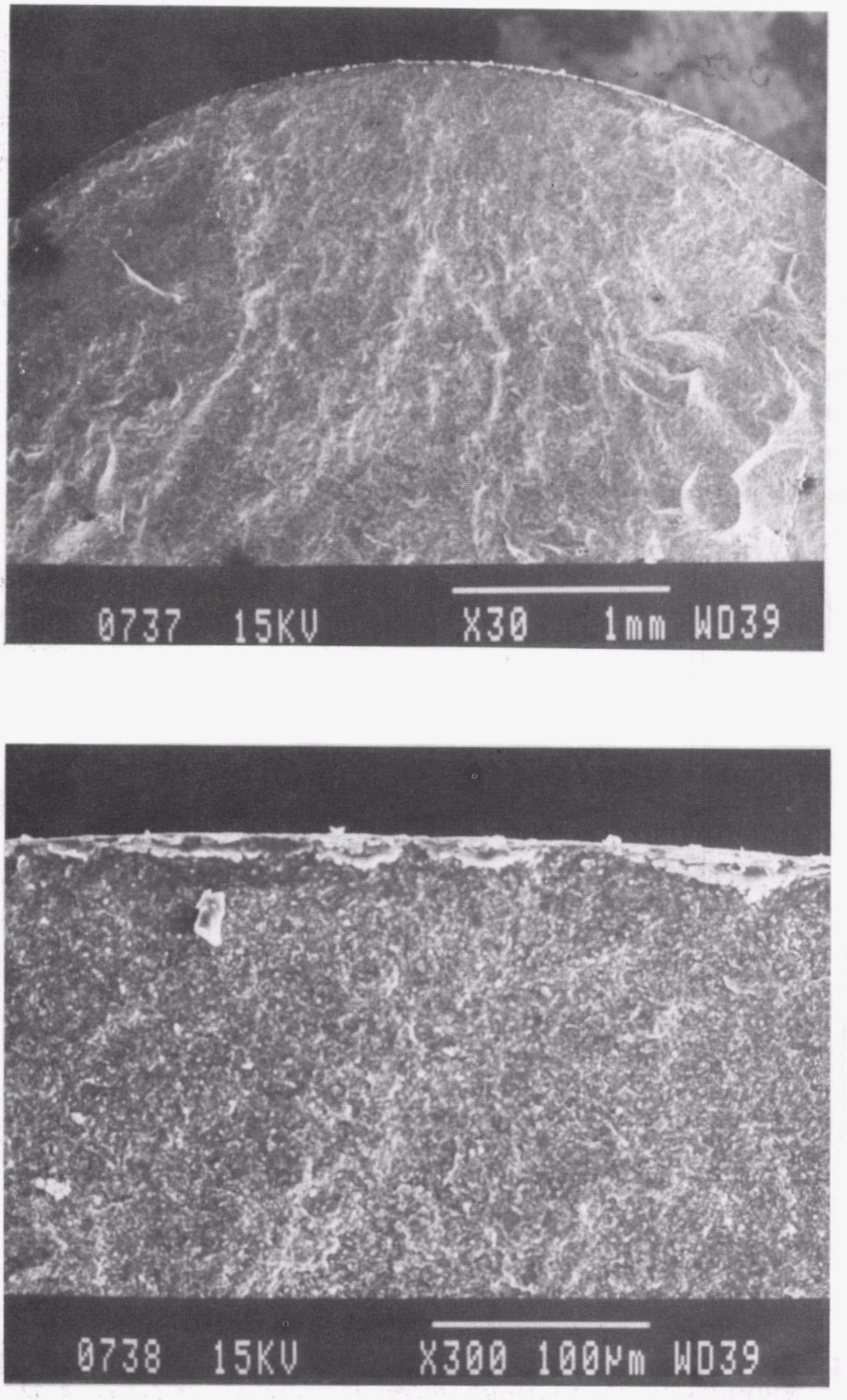

Figure 2a. Fracture surface of NT-154 specimen #300-36 subject to tensile stress rupture at 1328°C.

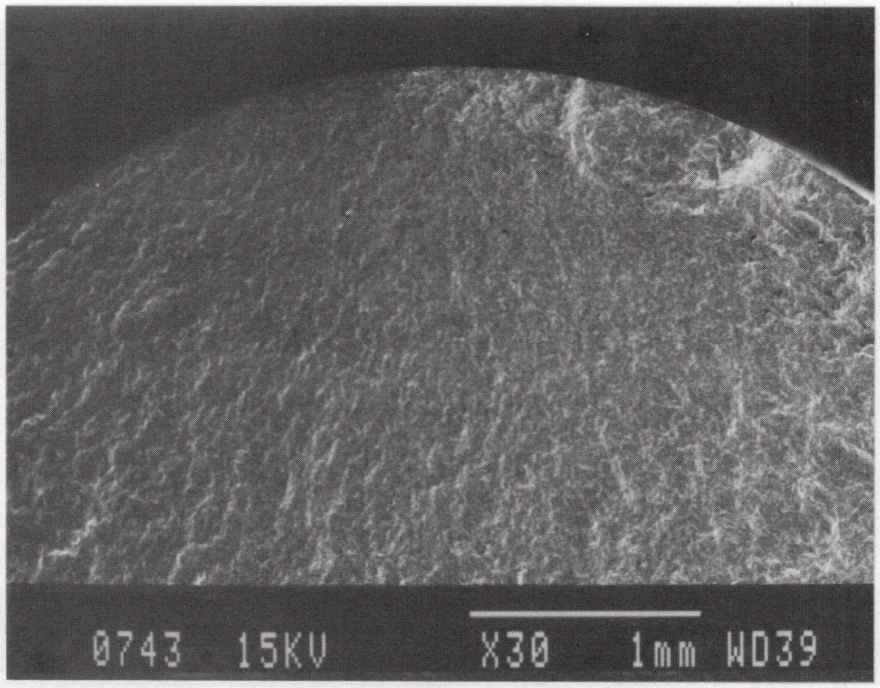

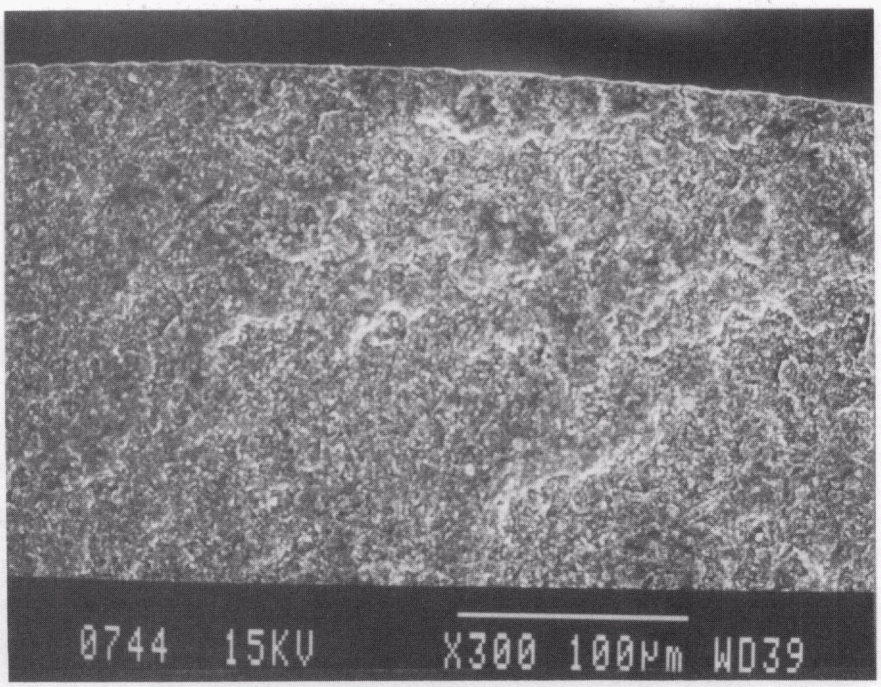

Figure 2b. Fracture surface of NT-154 specimen #300-37 subject to tensile stress rupture at 1328°C (continued).

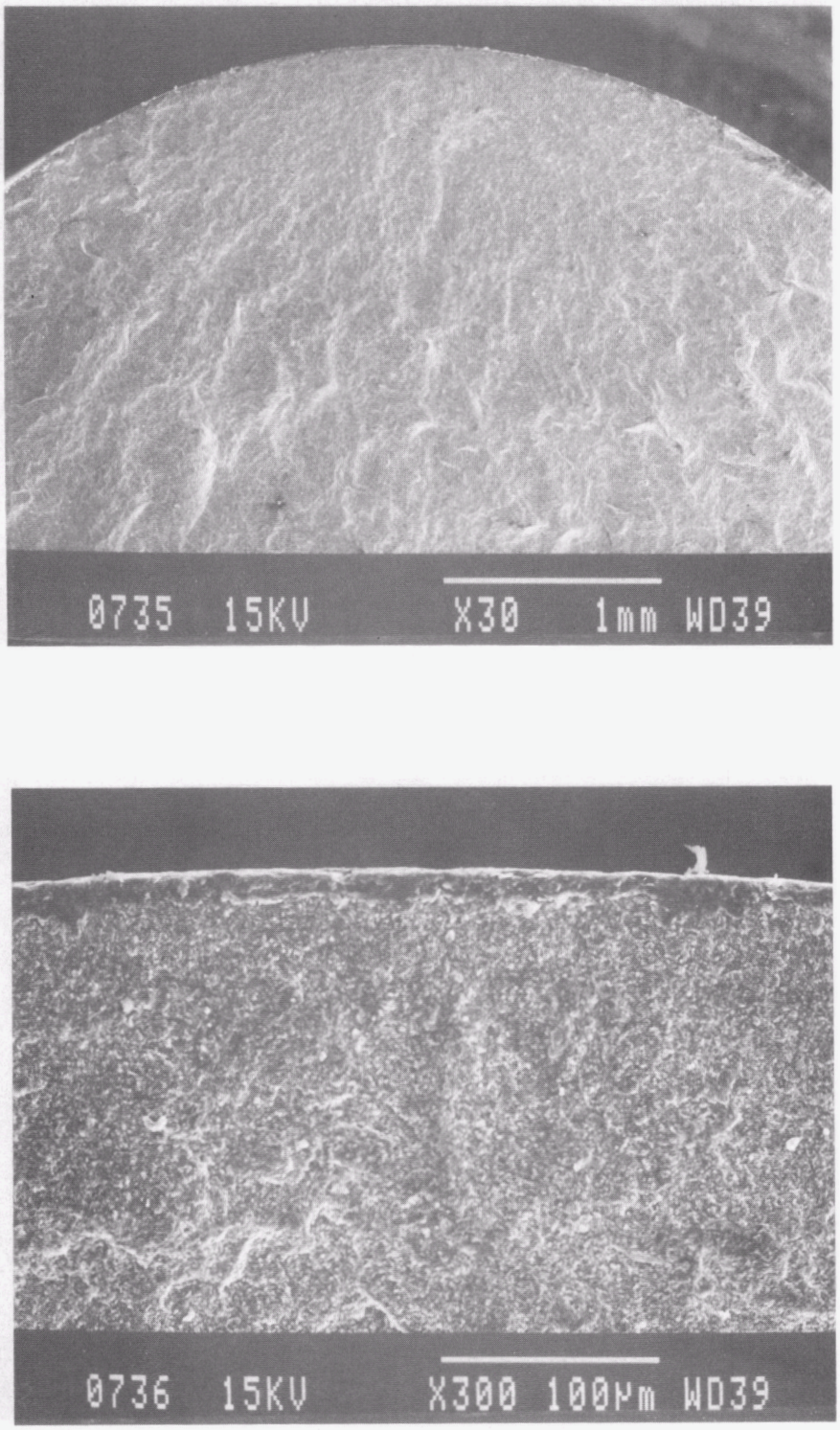

Figure 2c. Fracture surface of NT-154 specimen #300-35 subject to tensile stress rupture at 1300°C 1328°C (continued).

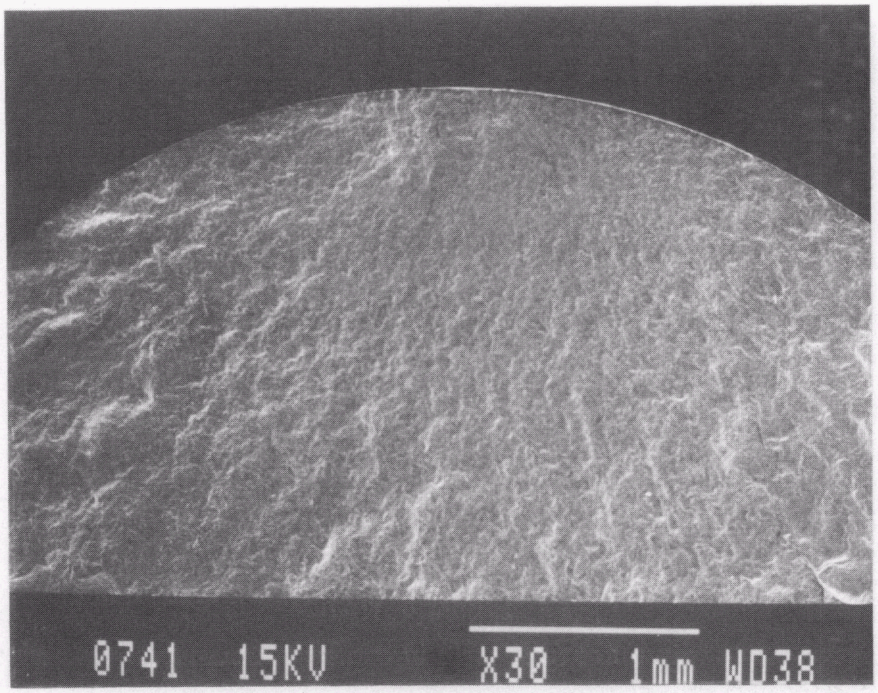

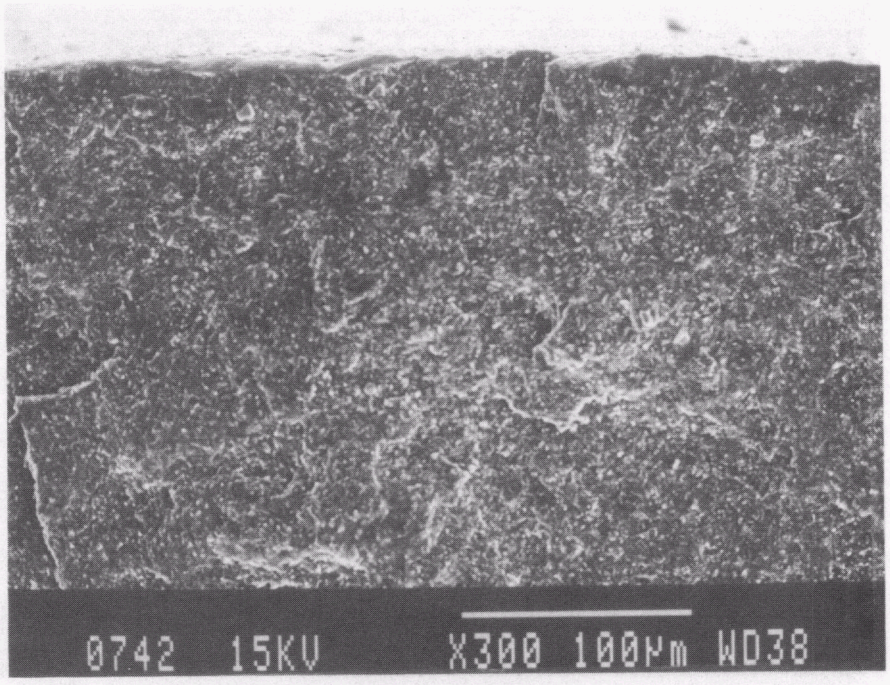

Figure 2d. Fracture surface of NT-154 specimen #300-29 subject to tensile stress rupture at 1300°C 1328°C (continued).

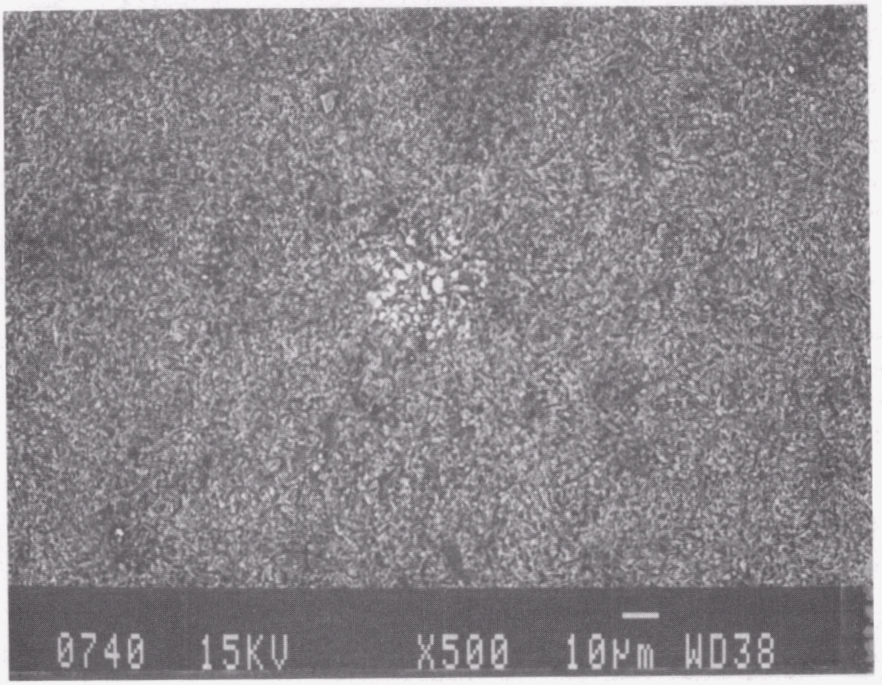

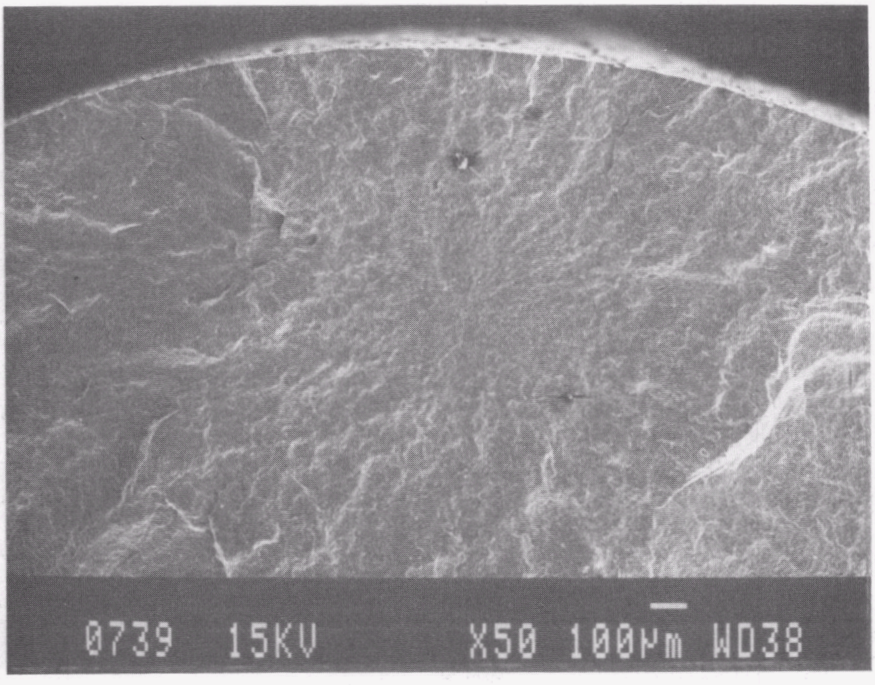

Figure 2e. Fracture surface of NT-154 specimen #300-27 subject to tensile stress rupture at 1300°C 1328°C (concluded).

Four tensile specimens from this new batch of NT-154 were tested in dynamic fatigue at what we also assumed was 1300°C. Two specimens were tested at the rapid loading rate (cross-head speed of 0.004 cm/s) and two specimens were tested at the slow loading rate (crosshead speed of 0.00004 cm/s). The results of these tensile dynamic fatigue tests are presented in Table 3. Included in Table 3 are the tensile dynamic fatigue results obtained from the initial shipment of NT-154 specimens (May 1990). The two specimens tested under the rapid loading rate failed at an average strength value that was 16% below the May 1990 test results. The two specimens tested under the slow stressing rate failed at an average strength value that was 25% below the May 1990 test results.

The results of the static and dynamic fatigue test for this new batch of NT-154 were troubling in comparison to the results obtained with the initial batch of NT-154 (May 1990). Based on our results it was concluded that this new batch of specimens was subject to some processing defect.

Table 3. Tensile Dynamic Fatigue Results for NT-154 [desired test temperature 1300°C (2372°F); corrected test temperature1328°C (2422°F)]

Specimen Number	Actuator Speed (cm/s)	Tensile Strength (MPa)	Fracture Origin	Mirror Radius (mm)
300-15	0.004	322 $\bar{x} = 335$	Volume (pore)	620
300-22	0.004	349	Volume	610
Average May 1990 Results		399 ± 54 MPa	Volume	-
300-2	0.00004	253 $\bar{x} = 240$	Surface	1500
300-18	0.00004	228	Surface	1300
Average May 1990 Results		322 ± 27 MPa	Surface	-

Six of the tensile specimens from this new batch of NT-154 were returned to Norton/TRW for their analysis. The six specimens returned were tested by Norton/TRW in dynamic fatigue at 1300°C (three in rapid loading and three in slow loading) using "identical" testing procedures. As shown in Table 4, the average tensile strength measured by Norton/TRW was significantly higher than those measured by UDRI during July 1991 and somewhat higher than the UDRI May 1990 data. As a result, Norton/TRW concluded that the low strengths obtained by UDRI for the July 1991 set of specimens were not due to a material difference in this batch.

Table 4. Summary of NT-154 Tensile Dynamic Fatigue Testing by Norton/TRW

Specimen ID No.	Data Source	Temp. °C	Loading Rate	Tensile Strength
300-4	Norton 9/91	1300	.1"/min	505 MPa
300-17	Norton 9/91	1300	.1"/min	447 MPa $\bar{x} = 472$
300-26	Norton 9/91	1300	.1"/min	466 MPa
300-19	Norton 9/91	1300	.001"/min	431 MPa
300-20	Norton 9/91	1300	.001"/min	392 MPa $\bar{x} = 415$
300-8	Norton 9/91	1300	.001"/min	422 MPa

This conclusion would suggest that the low strengths measured were due to the experimental procedures employed. As a result, the UDRI has (a) reviewed the testing procedures used and the monitoring procedures used to validate the test equipment for the 1989-90 tests, and (b) reviewed our current test procedures and rechecked all monitoring equipment.

In the 1989-1990 tensile test procedures no anomalies were found. At the time these tests were conducted the load train alignment and load cell calibration were verified by Instron on a regular maintenance basis. During testing the specimens were also monitored by speckle interferometry to determine if off-axis bending occurred. Temperature of the gauge section was periodically monitored by optical pyrometer. It is our conclusion that the 1989/1990 data is valid and reliable.

The load train alignment and load cell calibration continue to be verified by Instron and are in good order. The two thermocouples used to measure hot zone temperature in the short furnace were also found to be in good agreement. However, a 26-28°C temperature difference was observed when a third thermocouple or an optical pyrometer were used to measure the gage section temperature of a tensile specimen at 1300°C. Six separate test runs were conducted at 1300°C with a newly prepared thermocouple. The temperature variation between the two furnace thermocouples and the new thermocouple ranged from 27-30°C and averaged 28°C. Two additional test runs were made using the optical pyrometer and a temperature variance of 26°C was recorded. These results demonstrated that the test temperature we reported for our recent evaluation of the tensile strength of NT-154 at 1300°C was in error. We apologize for reporting an incorrect test temperature of 1300°C and have revised the test temperature listed in Tables 1 and 3 to 1328°C.

From a plot of the 1989-1990 data (Figure 3) the projected fast loading rate tensile strength at 1328° should be approximately 384 MPa and the slow loading rate tensile strength at 1328° should be approximately 300 MPa. These strengths are still significantly higher than measured in July 1991 (335 MPa and 240 MPa, respectively). We cannot explain the very large strength difference between the UDRI measurements and the Norton/TRW measurements even allowing for our temperature difference. We hope further analysis will enable us to clarify these differences.

Raman Microprobe Analysis of NT-154 Flexural Specimens

During this reporting period seven NT-154 flexure bars (3 x 4 x 50mm) (1990 vintage) were studied by Raman microprobe while they were under stress in a four-point bend fixture. When a crystalline solid is subjected to stress, changes in the crystallite structure occur which can have a dramatic effect on the observed Raman spectrum. The most prevalent change in the Raman spectra is a shift of the Raman mode frequency. In most cases these modes shift linearly with strain. It is expected that the Raman frequency shift will provide insights into the nature and magnitude of the stress effects at the microscopic level on crystalline materials such as β-Si_3N_4.

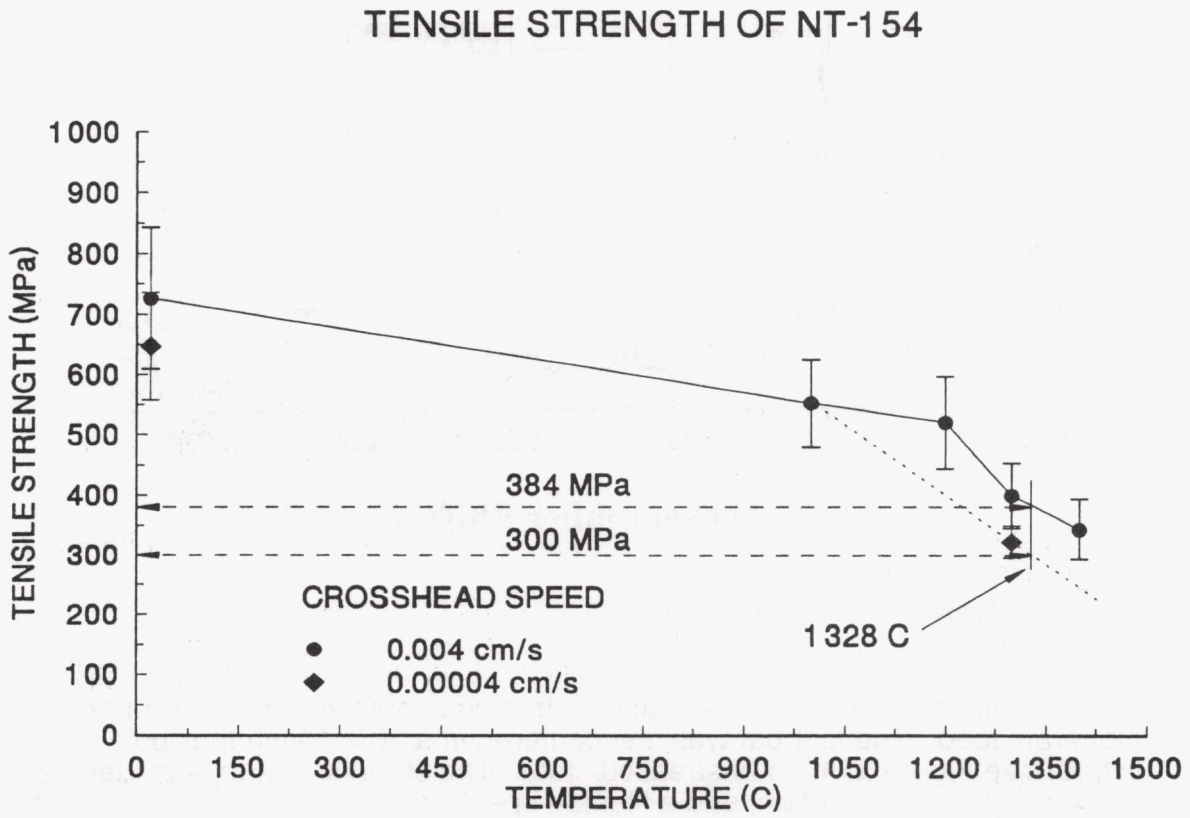

Figure 3. Plot of the tensile strength measurements of NT-154 in 1989/1990.

Norton/TRW NT-154 is primarily a β-phase polymorph. This β-phase polymorph has C^2_{6h} symmetry and 14 atoms per unit cell. Analysis of these symmetry properties and application of group theoretical methods predict 11 first order Raman lines in the Norton/TRW NT-154 Si_3N_4 spectrum composed of four A9 symmetry, five E_{2g} symmetry, and two E_{1g} symmetry.

Figure 4 shows a typical Raman spectrum obtained for a Norton/TRW NT-154 Si_3N_4 specimen. The spectrum agrees with that expected for β-Si_3N_4, and 10 of the 11 Raman lines were observed in the spectrum. A preliminary loading study of one of the test bars showed noticeable shifts in the Raman frequencies for seven of the 10 observed Raman lines. The 862 cm^{-1} Raman line showed the largest change, and it was selected for further analysis.

The Si_3N_4 Raman spectra obtained with the microprobe is due to the normal, vibrational modes of the individual Si_3N_4 grains. The microprobe provides a measure of the microscopic changes in strain for the accumulated Si_3N_4 grains scanned.

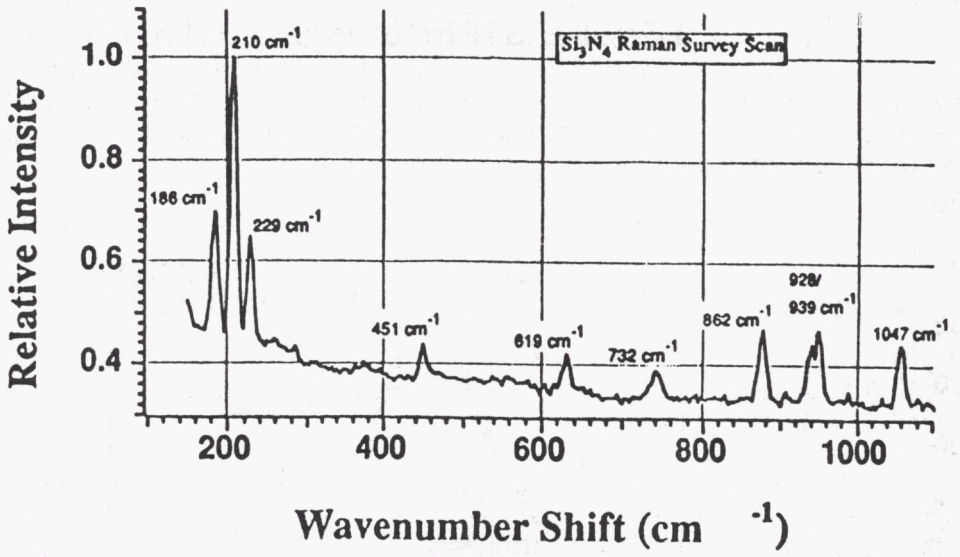

Figure 4. Si3N4 Raman spectrum.

In the initial study the Raman spectrum was obtained for a bar under a moderate load. The test bar was first centered in a 20 x 40mm four-point bend fixture (see Figure 5) in an unstressed state. The strain indicator was then zeroed and checked for calibration, and a Raman spectrum of the 862 cm^{-1} line was taken using the CCD detection system.

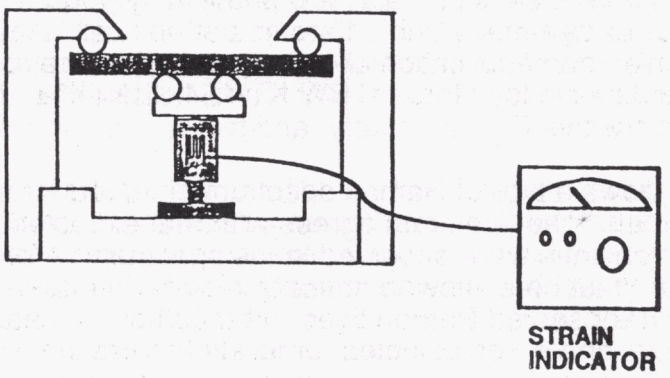

Figure 5. Four-point bending apparatus for Raman microprobe analysis.

Due to the very weak Raman signal levels from Si_3N_4, a 1½ hour integration time was needed to obtain an adequate signal-to-noise ratio. After the unstressed 862 cm^{-1} scan was completed, the test bar was subjected to a 70-lb flexural load. This load corresponds to an applied stress of 261 MPa. A 1½-hour long Raman spectrum was then taken at the 862 cm^{-1} line. The two spectra are plotted for comparison in Figure 6. A shift of 2 cm^{-1} was observed for the stressed versus the unstressed condition. The load remained constant (no relaxation of the Si_3N_4 bar in the bend fixture) throughout the 1½-hour long run time.

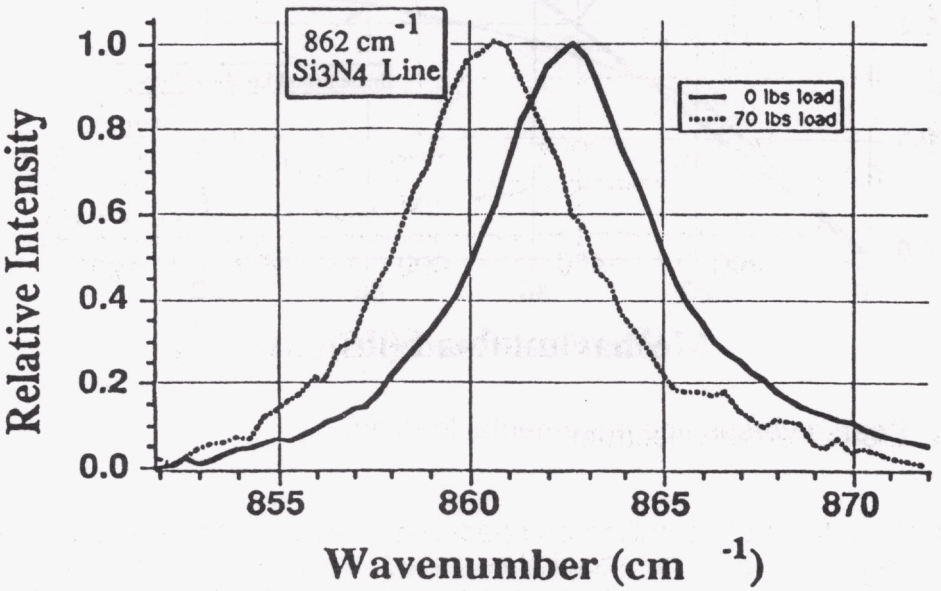

Figure 6. Shift of Raman lines due to mechanical loading.

A second study involved fine 20-lb incremental loading of the test bar instead of the course 70-lb step load. The spectrum for each 20-lb load level required 1½ hours to obtain. A plot of the Raman frequency shift comparing the course step load, and the fine incremental loading condition is presented in Figure 7. As shown in Figure 7, the different loading conditions show fairly good agreement in Raman frequency shift at loads below 30-lbs. Above a 30-lb load (112 MPa), a nonlinear behavior was observed. This phenomenon may be due to a relaxation or fatiguing of the grain boundary glassy phase at loads above 112 MPa. This phenomena is being investigated further.

The third study involved cyclic loading of the test bar from 0 lbs to 70 lbs. The same general procedure was followed for setup and loading the Si_3N_4 test bar. The first loading sequence showed a 2 cm^{-1} shift in Raman frequency. It was expected that when the load was removed the Raman frequency would shift back to its original unstressed value. However, this was not the case. The frequency shifted to an intermediate position approximately halfway between the 0-lb and 70-lb load positions. A second 70-lb loading resulted in a shift to almost the same frequency position as the first 70-lb load position. The sequence of events is shown graphically in Figure 8. This behavior is typical of a hysteresis phenomenon and also may be due to a relaxation of the glassy grain boundary phase. These results were repeated with all of the NT-154 flexural bars tested. All three studies were repeated with the other six test bars with similar results, and additional experiments are in progress to further investigate these findings.

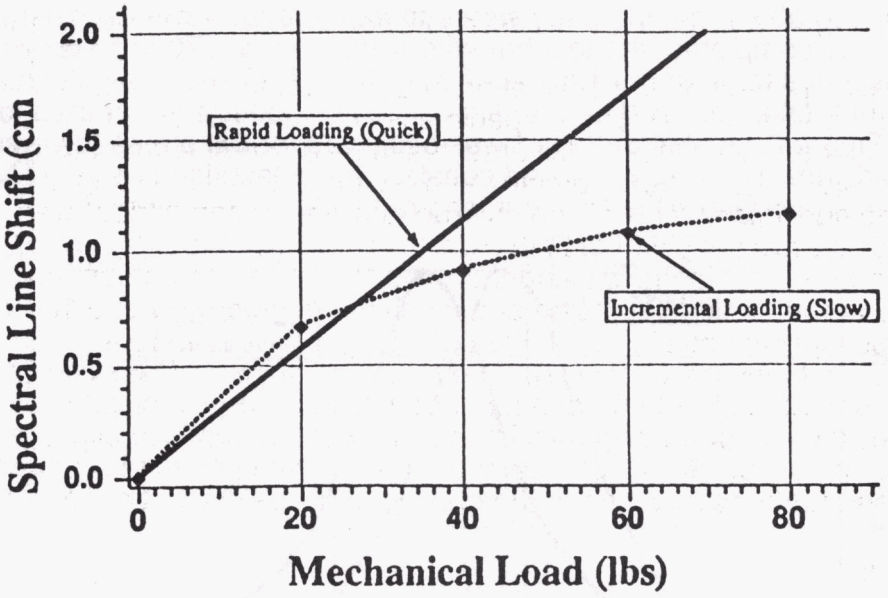

Figure 7. Course versus fine incremental loading.

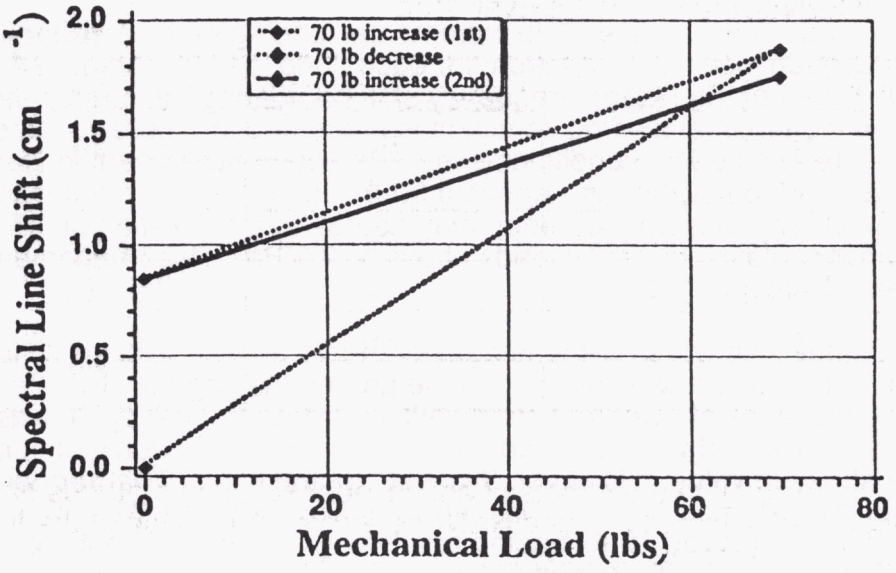

Figure 8. Repeated loading showing residual strain.

Evaluation of a Grip System for Testing Buttonheadless Tensile Specimens.

During this reporting period evaluation of a proprietary grip system for testing straight shank (buttonheadless) tensile specimens was conducted. The grips were mounted in the Instron Model 1361 Universal testing machine. Alignment of the gripping system proved to be very complex and tedious. Tensile testing of three straight-shanked specimens (two silicon carbide and one silicon nitride) was attempted. The first two specimens, both Hexoloy SA silicon carbide, tested in this gripping system were held in place using the manufacturer's recommended gripping pressure and loaded in tension at a machine actuator rate of 0.1in/min. Both of these test specimens slipped in the shank grips prior to tensile fracture (1180-lb and 860-lb loads, respectively). The third specimen, a PY6 silicon nitride, was held in the grip at 125% of the recommended gripping pressure and loaded at the same rate as the two preceding specimens. This specimen also slipped in the shank grips before failing. Repeated attempts to eliminate specimen slippage were unsuccessful, and further evaluation of the grip system was discontinued.

Project Renewal

During this reporting period, our project was extended 24 months to continue our investigation of SiC and Si_3N_4 ceramics (Phase V). In Phase V, three tasks (XII, XIII, and XIV) will be initiated to extend our investigation of the effects of environment on the mechanical behavior of new generation Si_3N_4 and SiC ceramics. The first two tasks are to investigate the flexural and tensile strength and the fatigue behavior of newly developed Si_3N_4 and SiC ceramics (see Table 5).

Table 5. SiC and Si_3N_4 Ceramics to be Evaluated

Material Supplier	Designation	Flexure Specimens	Tensile Specimens
Norton/TRW	NT-230 SiC	69	-
Norton/TRW	NT-164 Si_3N_4	69	10
Carborundum	Hexoloy SX SiC	69	65
Kyocera	SN-260 Si_3N_4	69	65
Dow Corning	SiC	69	-
Sullivan Mining	Si_3N_4	69	-

The third task is to investigate the effects of advanced machining methods on the mechanical behavior of selected SiC and Si_3N_4 ceramics. An outline of the test matrix for Phase V is presented in Table 6.

Table 6. Proposed Material Test Plan for Phase V

Tasks XII and XIII Characterization of SiC/Si_3N_4

1. Flexural Strength Measurement Matrix - 50 Specimens

Machine Loading Rate (cm/s)	Test Temperatures (°C) 20°C	1250°C	1350°C
0.004	10	10	10
0.0004	-	-	5
0.00004	5	5	5

2. Flexural Stress Rupture (FSR) Measurement Plan - 10 Specimens
   Test Duration - 100 hrs.
   Load - 1/2 and 2/3 the rapid loading rate strength (σ_f)
   Test Temperature - 1350°C (5 specimens/σ_f)

3. Physical Property Characterization - 9 specimens

   Density @ 20°C and Young's Modulus 20-1350°C - 3 specimens
   Coefficient of Thermal Expansion 20-1350°C - 3 specimens
   Hardness and Fracture Toughness by Microindent at 20°C - 3 specimens

Items 1, 2, and 3 above will require 69 flexural test bars 3 x 4 x 50 mm for each of the 6 candidate materials.

4. Tensile Strength Meausrement Matrix - 45 specimens

Machine Loading Rate (cm/s)	Test Temperatures (°C) 20°C	1250°C	1350°C
0.004	10	10	10
0.00004	5	5	5

5. Tensile Stress Rupture (TSR) Measurement Plan - 10 Specimens
   Test Duration - 100 hours
   Loads - 1/2 and 2/3 σ_f (5 specimens/σ_f)
   Test Temperature - 1350°C

6. Tensile/Tensile Cyclic Fatiuge - 10 Specimens
   Test Duration - 450,000 (~100 hours)
   Rate - I cycle/sec
   Loads - 1/2 and 2/3 σ_f (5 specimens/σ_f)

Items 4, 5, and 6 above will require 65 specimens for two candidate materials.

Table 6. Proposed Material Test Plan for Phase V (concluded)

Task XII - Investigate the Effects of Machining Methods on Flexural Strength

7. Flexural Strength Test Matrix - 20 specimens

Machine Loading Rate (cm/s)	Test Temperatures (°C) 20°C	1350°C
0.004	5	5
0.00004	5	5

Item 7 will be used to evaluate 10 different machining conditions.

Note: Weibull analysis will be employed to evaluate the strength data for sets of 10 or more test points. The S test will be used for smaller data sets. Optical microscopy and SEM will be used to evaluate fractured surfaces and the microstructure of the newly developed SiC/Si_3N_4 ceramics. Plasma etching will be used to determine microstructure.

3.4 FRACTURE MECHANICS

Testing and Evaluation of Advanced Ceramics at High Temperature in Uniaxial Tension

J. Sankar, A. D. Kelkar, B. Wang, and S. Krishnaraj
(Department of Mechanical Engineering, North Carolina A & T State University, Greensboro, NC 27411)

Objective/scope

The purpose of this effort will be to test and evaluate advanced ceramic materials at temperatures up to 1200 ^{0}C in uniaxial tension. Testing may include fast fracture strengths, stepped static fatigue strength, and creep strength along with the analysis of fracture surfaces by scanning electron microscope. This effort will comprise of the following tasks:

Task 1. Specifications for testing machine and controls + (procurement) for creep testing.
Task 2. Identification of test material (s) for the present year + (procurement of specimens).
Task 3. Identification of test specimen configuration.
Task 4. Identification and procurement of test grips, high temperature extensometer, and furnace for the creep machine.
Task 5. High temperature fatigue creep interaction study and tensile testing.
Task 6. Reporting (periodic).
Task 7. Final Report.

It is anticipated that this program will help in understanding the behavior of ceramic materials at very high temperatures in uniaxial tension.

Technical highlights

During the reporting period, the internal porosity characterization of both the creep tested and untested SNW-1000 Si_3N_4 samples continued. We were using both SEM and Energy Dispersive Spectrum(EDS) analyzer to do the analysis of the composition distribution. The EDS analysis was used to understand the microchemical changes in and around the pores of both the untested and creep tested samples.

A chemical analysis was also done, in addition to the pore on both the left and right sides of a said pore. Number of pores were analyzed and the pores were taken far apart from each other(Table 1 & 2). In addition, a general chemical analysis across the cross-section of the gage area was done for both the untested and creep tested sample(Table 3). The result here showed that there is very little difference in the chemical distribution between these two conditions.

EDS analyses indicate that there is difference in chemical compositions especially in the Yttrium and Silicon contents of the pores in the untested and the creep tested specimens(Fig. 1 & 2) at 1200° C over a prolonged period of time. The Yttrium content is higher and the Silicon content is lower in and around the pores in the creep tested specimen as compared to the untested specimens, but varied little from that of the general chemical composition mentioned earlier.

Table 1.

EDS Results of Pores in Si_3N_4 Samples

	Pore #1 Creep Tested	Spectrum Number Across Pores														
		1	2	3	4	5	6	7	8	9	10	11	12	13	14	15
	Si	81.46	83.93	79.42	72.66	80.49	51.63	70.48	84.05	86.59	74..33	82.27	76.76	79.19	82.63	84.33
	Al	2.87	2.59	3.03	2.28	1.83	1.18	1.22	1.83	1.95	9.23	2.63	3.10	2.70	2.87	0.66
	Y	15.66	13.48	17.55	25.05	17.68	47.19	28.30	14.11	11.46	16.44	15.10	17.15	17.32	14.49	12.97
	Pore #2 Creep Tested															
Creep Tested	Si	80.96	78.47	82.19	77.60	77.30	82.06	82.05	79.67	79.67	83.07	83.67	81.37	79.14	83.49	83.98
	Al	3.04	3.38	2.47	3.53	2.94	1.54	1.55	1.63	1.62	1.72	2.10	2.69	2.81	2.69	2.82
	Y	16.06	18.15	15.34	18.87	19.75	16.40	16.40	18.70	18.71	15.22	19.23	15.05	18.05	13.83	13.20
	Pore #3 Creep Tested															
	Si	81.36	80.00	83.09	78.33	78.35	76.70	77.01	65.64	82.03	80.28	82.84	81.99	83.26	83.24	83.24
	Al	2.91	2.97	2.92	2.81	2.80	1.35	2.17	8.79	2.64	2.64	2.69	3.10	2.13	3.07	3.07
	Y	15.73	15.73	14.49	18.85	18.86	221.95	20.82	25.57	15.13	17.08	14.47	14.90	14.60	13.66	13.66
	Pore #1 Untested Sample	1	2	3	4	5	6	7	8	9	10	11	12	13	14	15
	Si	94.37	94.87	94.45	94.14	94.14	90.10	92.83	93.15	91.99	87.86	93.36	92.05	93.70	94.43	94.43
	Al	2.83	2.77	3.46	2.80	2.80	2.94	3.02	3.26	3.41	3.76	3.57	3.34	2.97	2.39	2.32
	Y	2.79	2.36	2.00	3.06	3.06	6.96	4.15	3.59	4.59	8.38	3.07	4.61	3.33	3.18	3.25
	Pore #2 Untested Sample															
	Si	94.00	93.70	94.35	94.13	92.66	93.71	93.06	91.76	84.78	80.32	77.72	69.77	73.59	60.88	58.84
Untested	Al	2.90	3.26	3.15	2.95	3.70	2.58	2.79	3.01	3.84	1.73	3.50	4.42	2.47	0.00	3.69
	Y	3.11	3.04	2.51	2.92	3.64	3.71	4.15	5.23	11.39	17.95	18.78	25.81	23.94	39.12	37.48
	Pore #3 Untested Sample															
	Si	93.00	92.78	91.89	91.46	92.55	89.49	93.23	92.71	93.21	92.91	93.03	92.73	94.34	93.20	92.16
	Al	2.91	3.29	4.22	4.09	2.89	7.12	3.48	3.42	2.77	3.72	3.62	3.58	3.05	3.28	4.63
	Y	4.09	3.93	3.89	4.05	4.56	3.39	3.29	3.87	4.02	3.37	3.35	3.69	2.62	3.52	3.20

Left of The Pore — Pore Area — Right of The Pore

Table 2.

EDS Results of Pores in Si_3N_4 Samples
Average Values

		Spectrum Number Across Pores														
	Tested Sample	1	2	3	4	5	6	7	8	9	10	11	12	13	14	15
Creep Tested	Si	81.22	80.80	81.57	76.20	78.71	70.13	76.51	76.45	82.76	79.23	82.93	80.04	80.53	83.12	83.85
	Al	2.94	2.98	2.81	2.87	2.52	1.36	1.65	4.08	2.07	4.53	2.47	2.96	2.55	2.88	2.19
	Y	15.82	47.36	15.79	20.92	18.76	28.51	21.84	19.46	15.10	16.27	16.27	15.70	16.66	13.99	13.28
	Untested Sample	1	2	3	4	5	6	7	8	9	10	11	12	13	14	15
Untested	Si	93.97	93.78	93.59	93.24	93.12	91.10	93.04	92.54	89.99	87.03	88.04	84.85	87.21	82.81	81.81
	Al	2.88	3.11	3.57	3.28	3.13	4.21	3.10	3.23	3.34	3.07	3.56	3.78	2.83	1.89	3.55
	Y	3.33	3.11	2.80	3.34	3.75	4.69	3.86	4.23	6.67	9.90	8.40	11.37	9.96	15.27	14.64

Left of The Pore ← Pore Area → Right of The pore

Table 3.

EDS Results of Cross Section in Si_3N_4 Samples

		Spectrum Number Across Samples														
	Tested Sample	1	2	3	4	5	6	7	8	9	10	11	12	13	14	15
Creep Tested	Si	81.54	82.95	81.90	80.61	81.46	81.12	80.73	80.75	81.28	82.98	82.11	82.84	81.99	83.26	81.10
	Al	2.36	2.41	2.87	3.03	2.18	2.84	3.17	2.70	2.58	2.41	2.76	2.69	3.10	2.13	2.02
	Y	16.10	14.64	15.23	16.36	16.36	16.04	16.10	16.55	16.14	14.60	15.13	14.47	14.90	14.60	16.80
	Untested Sample	1	2	3	4	5	6	7	8	9	10	11	12	13	14	15
Untested	Si	82.06	83.21	82.36	82.37	80.65	80.17	80.16	80.13	79.85	79.27	78.10	72.71	80.93	78.12	73.45
	Al	2.46	2.44	2.76	2.96	2.83	2.52	2.80	2.69	2.64	2.67	2.38	2.66	2.45	2.92	2.80
	Y	15.47	14.35	14.87	14.67	16.52	17.31	17.04	17.18	17.50	18.06	19.52	24.63	16.63	18.97	23.76

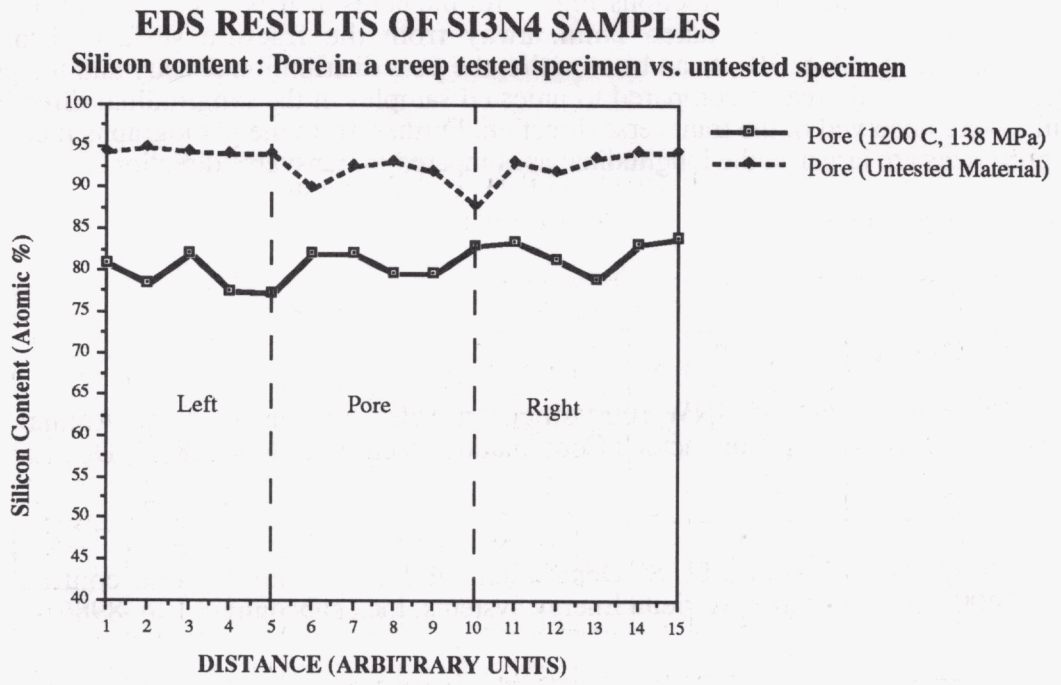

Figure 1. COMPOSITIONAL VARIATION ACROSS A PORE

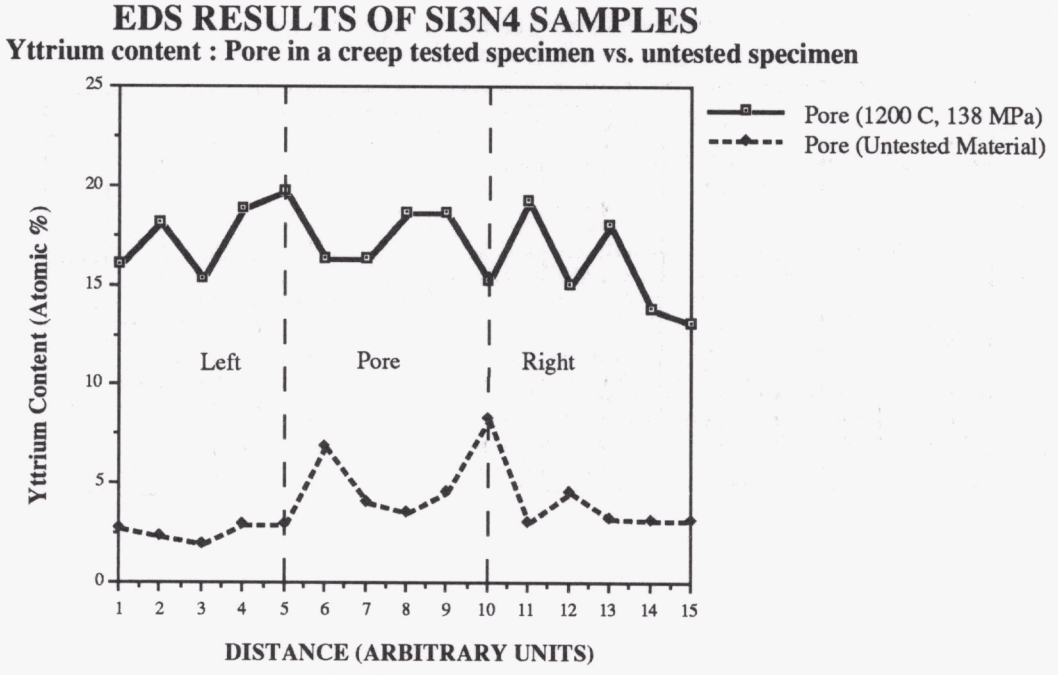

Figure 2. COMPOSITIONAL VARIATION ACROSS A PORE

The untested and creep tested samples were analyzed using optical microscope both in the longitudinal and transverse directions(Fig. 4) for the pores distribution. The sections for analyses in the gage section were taken 2mm. away from the fracture surface. From the SEM photographs(Fig. 3A & 3B) it can be seen that the pore distribution density and the pore sizes are larger in the tested area as compared to untested samples in the longitudinal directions. Similar results were observed in the transverse direction. Further, from the photographs it can be seen that the pore sizes are larger in the longitudinal as compared to transverse direction.

Status of milestones

On schedule.

Publications & presentations

"Creep Testing of SNW-1000 silicon nitride", presented at the Annual Automotive Technology Development Contractor's Coordination meeting, October 28-31, Dearborn, Michigan.

Research sponsored by the U. S. Department of Energy under prime contract DE-AC05-840R21400 with the Martin Marietta Energy systems, Inc., subcontract 19X-89867C.

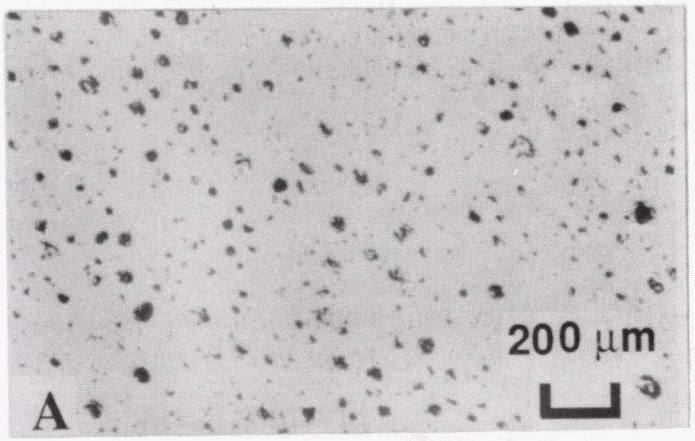

Figure 3A. Polished Microstructure of the untested GTE SNW-1000 Specimens, longitudinal direction showing pores.

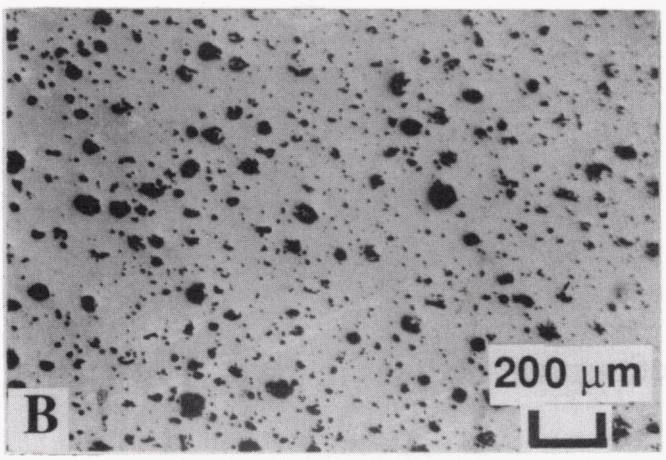

Figure 3B. Polished microstructure of the GTE SNW-1000 specimens creep tested at 1200 ^{0}C, 60 % σ_F, 138 MPa, showing pores in the longitudinal direction. Pore distribution density and the pore sizes are larger in the tested area. Similar pattern was observed in the Transverse direction.

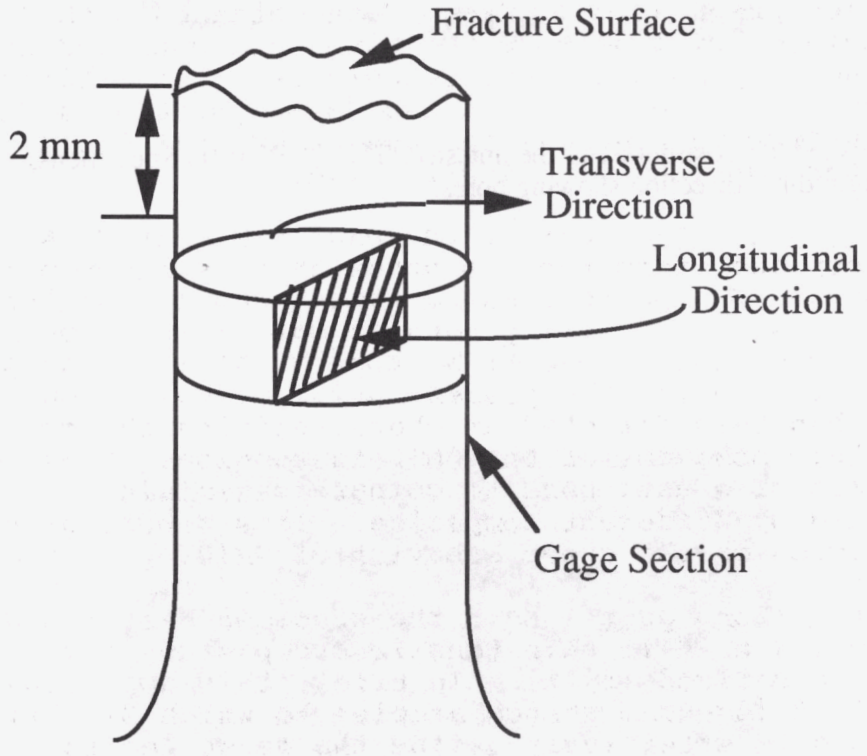

Figure 4. Sections for Analyses in the Gage Section

Standard Tensile Test Development

S. M. Wiederhorn, D. C. Cranmer, R. F. Krause, Jr., and D. E. Roberts
(National Institute of Standards and Technology)

Objective/Scope:

This project is concerned with the development of test equipment and test procedures for measuring the tensile strength and creep resistance of ceramic materials at elevated temperatures. Inexpensive techniques for measuring the creep behavior and strength of structural ceramics have been developed and are being used to characterize the mechanical behavior of these materials. The test methods use self-aligning fixtures, and simple grinding techniques for specimen preparation. Creep data obtained with tensile test techniques will be compared with data obtained using flexure and compressive creep techniques. The ultimate goal of the project is to assist in the development of a data base and a test methodology for the structural design of heat engines for vehicular applications.

Technical Highlights - During the past six months, studies on the creep and creep rupture behavior of silicon nitride as a function of applied tensile stress and temperature were continued. Two commercial grades of material are being investigated on this project: Norton/TRW NT-154, and Allied-Signal GN-10. During the present period, most of our attention has been directed at characterizing the creep and creep rupture behavior of the GN10 in tension. These data will be part of a data base to compare materials manufactured by different companies. This report presents data collected on the creep behavior of GN10.

Experimental Techniques - Both the specimen design and the test apparatus used in this tensile creep study have been previously described in [1]. In brief, this apparatus utilized flat dog-bone shaped samples to which SiC "flags" are attached to effectively define the gauge length. During tensile testing, relative displacements of the flags are continuously monitored by a laser extensometer to an accuracy of ± 1 μm at temperature. To assure thermal stability, the specimens were heated at the test temperature for approximately 20 hours before testing. Tests were made over a temperature range of 1200°C to 1350°C and a stress range 75 to 150 MPa. For most tests, the applied stress was maintained until the specimen failed. In this way, both the creep and creep rupture behavior of the material could be characterized.

The microstructure of tested specimens was studied by transmission electron microscopy (TEM). TEM sections were taken from the gauge section after the conclusion of most tests. To differentiate between the effects of creep and annealing on the microstructure, these TEM sections were compared with TEM sections from the unstressed ends of selected tensile specimens and with TEM sections from as-received material. Microstructural analyses were conducted on specimens that failed during creep and on specimens from tests that were interrupted before failure. Specimens from interrupted tests were cooled under load to prevent stress relaxation. The gauge sections of crept specimens were cut parallel to the stress axis to obtain both near-surface and mid-plane TEM sections. Prior to final preparation, these sections were examined optically for evidence of distributed creep cavitation or crack damage.

Results

A summary of the creep behavior of GN10 is shown in figure 1 for a temperature of 1300°C, and stresses of 75, 100 and 150 MPa. Creep in this material is characterized by a relatively short primary stage and an extended secondary stage of creep. On some specimens a slight upward curvature is observed in the latter part of the secondary stage. However, unlike many metallic alloys, extensive tertiary strain prior to rupture is not observed. As with other ceramics, the strain to failure depends on the minimum strain rate, the higher the minimum strain rate, the smaller the strain to failure. For this material, the failure strain ranges from about 0.5 to 1.5 percent.

The stress and temperature dependence of the creep behavior was determined by expressing the logarithm of the strain rate, $\dot{\varepsilon}$, as the sum of the inverse absolute temperature, $1/T$, and the logarithm of the applied stress, σ, for the entire data set.

$$\log(\dot{\varepsilon}) = A + n \cdot \log(\sigma) + \Delta H/RT \qquad (1)$$

Where n is the stress exponent, ΔH is the apparent activation energy and R is the universal gas constant. A least squares analysis of the data yielded a stress exponent of ≈6 and an apparent activation energy of 1230 kJ/mol for this material. Graphical representations of the data for the GN10 are given in figures 2 and 3. In figure 2 the data are temperature compensated to show the stress dependence of the data, whereas in figure 3 the data are stress compensated to illustrate the temperature dependence of the data. For both figures, the data tend to cluster about straight lines, suggesting that the assumed functionality provides a reasonable fit of the minimum creep rate.

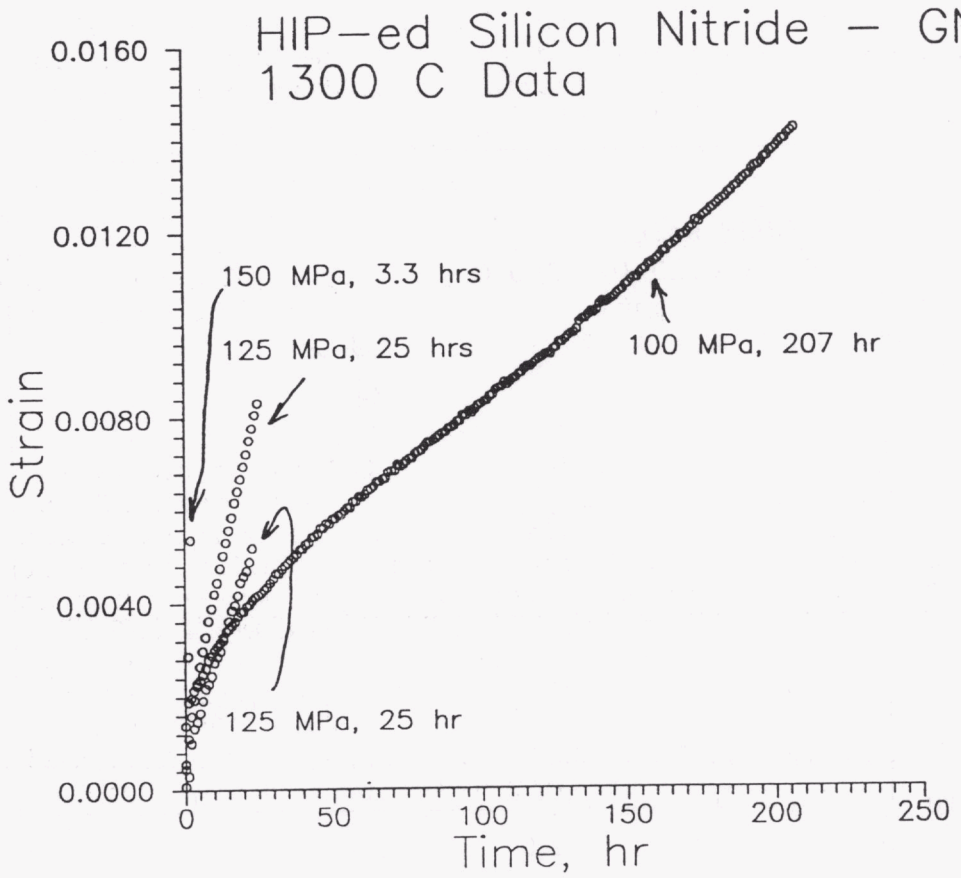

1. A summary of the creep behavior of GN10. Tests conducted at 1300°C.

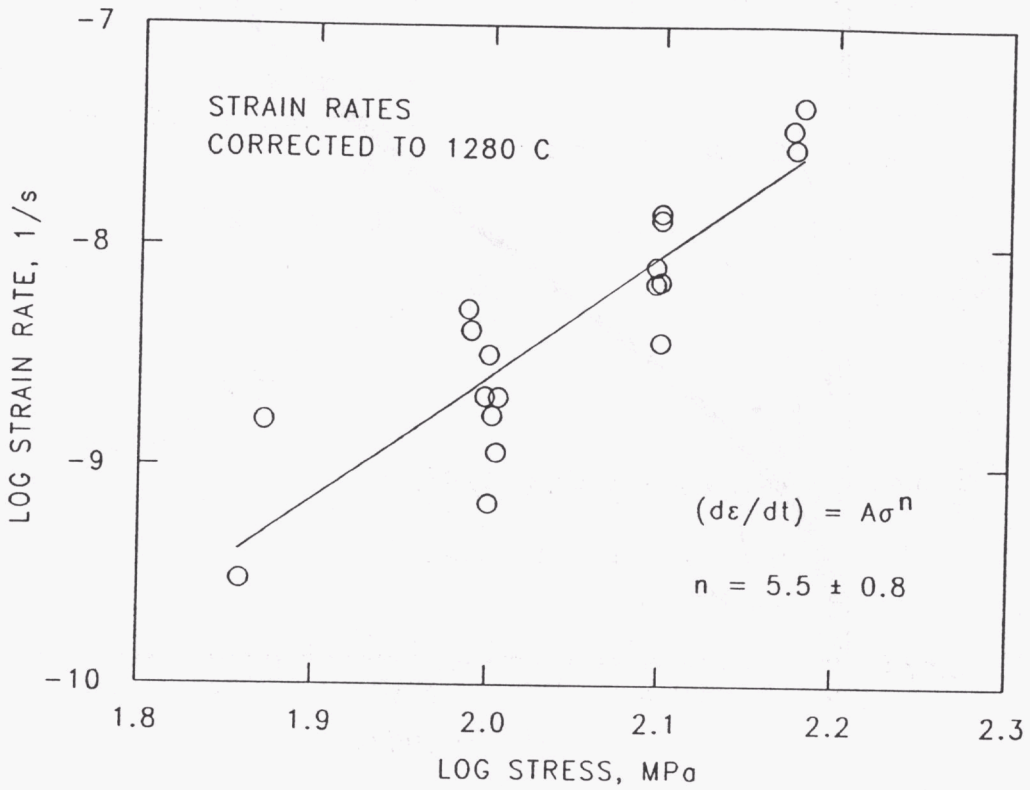

2. Stress dependence of the creep rate. Corrected to a temperature of 1280°C.

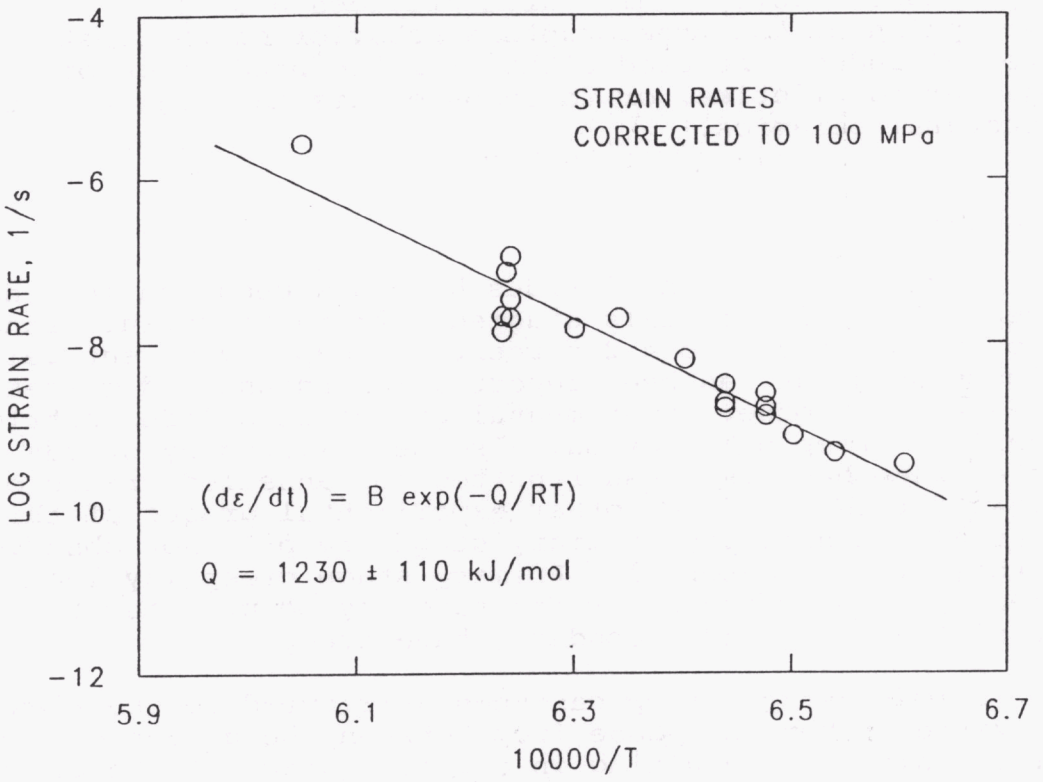

3. Temperature dependence of the creep rate. Corrected to a stress of 100 MPa.

The rupture dependence of the GN10 is illustrated in figure 4, where the logarithm of the minimum creep rate is plotted as a logarithmic function of the rupture time. The data cluster about a common straight line, with a slope of -0.96, regardless of test temperature or applied stress. Known as a Monkman-Grant plot, this type of curve is commonly used to describe the creep rupture behavior of high temperature alloys. This curve provides a simple description of the creep rupture behavior of the test material and can be used either for the prediction of engineering lifetime, or to compare this material with other structural ceramics.

Discussion

A variety silicon nitrides have now been run in tensile creep. For all materials studied, strain to failure ranges from ≈ 0.5 percent to ≈ 2 percent. Creep may be entirely primary stage as has been reported for unannealed grades of NT154 and for other experimental grades of silicon nitride. Transient creep behavior may also be followed by steady state creep has also been reported for annealed grades of NT154, for GN10 and for other experimental grades of this material. Generally, tertiary stage creep is not observed in this type of material. Primary stage creep may lead directly into fracture, or fracture may occur after the material has entered secondary stage creep.

Primary stage creep has been attributed to the flow of the vitreous bonding phase from between the grains of silicon nitride, resulting in direct contact of the grains. Primary stage creep can occur either as a consequence of devitrification of the bonding phase, or because the pathways between the grains decrease as a function of time. Devitrification increases the effective viscosity of the bonding phase and hence reduces the rate of creep for a given stress and temperature. The rate of creep is also decreased when the bonding phase is forced to flow between narrower passage-ways. This latter mechanism also leads to a difference in creep in tension and compression.

Secondary stage creep in silicon nitride is often observed to occur in concurrence with the formation of cracks or cavities in this material. In the GN10 cavity and crack formation in tension was confirmed by TEM studies, which are reviewed in Section 3.1 of this report under Microstructural Analysis of Structural Ceramics. Cavity formation provides the stress relief required to modify the creep behavior of the silicon nitride. Because of the volume increase consequent upon cavitation, the rate

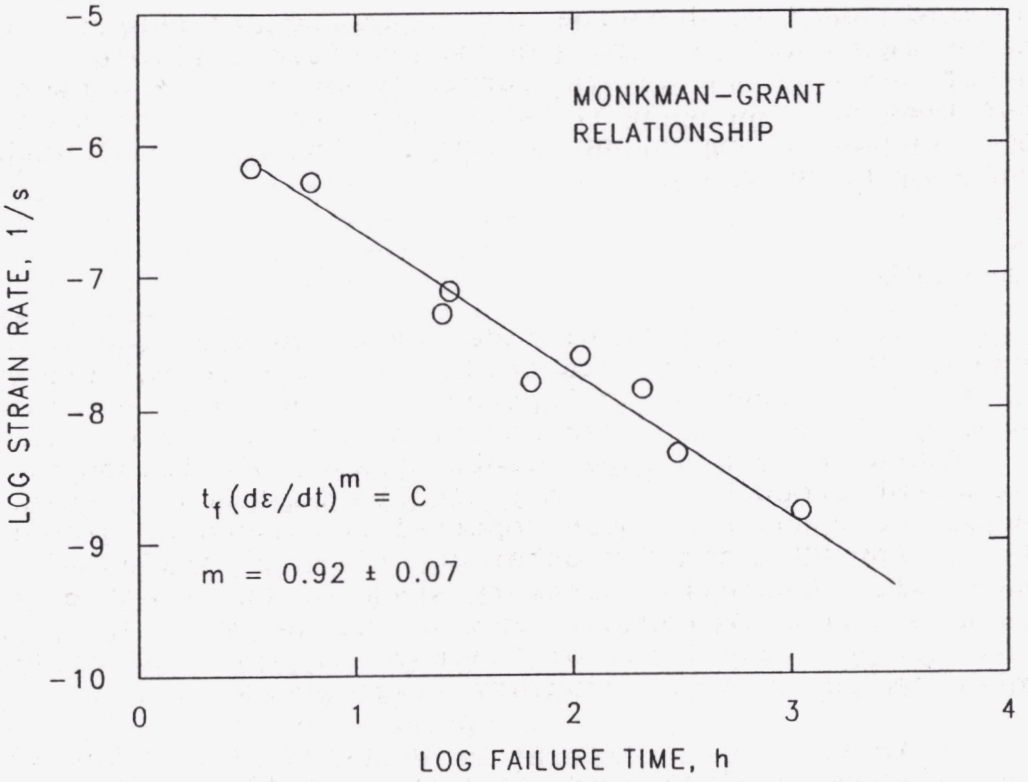

4. Monkman-Grant curve for GN10.

displacement of the ends of the specimen must also increase, thus, increasing the creep rate in the material. For the GN10, the creep rate due to cavitation must be relatively constant for steady state creep to have been observed. This same behavior was reported earlier in Si/SiC which cavitates extensively during creep.

If the flow of the bonding phase plays a major role in the deformation process, then the viscosity or the diffusivity of the bonding phase along the grain interfaces will also be important to the creep process. As noted by Raj and Morgan [2], such transport processes often depend on a number of different factors that determine the apparent activation energy. The rate of creep will depend on the rate of transport of silicon nitride along the grain interface, which in turn depends on the mobility and concentration of the silicon nitride in the glass at the interface. The temperature dependence of the mobility and the concentration together determine the measured value of the apparent activation energy.

In their discussion of the reasons for the high activation energies for creep, densification and grain boundary sliding in hot-pressed silicon nitride, Raj and Morgan [2] suggest that the Gibbs free energy controlling the concentration of silicon nitride in the interfacial glass of a magnesia-doped silicon nitride was approximately equal to the heat of solution of the silicon nitride in the glass, ΔH_s. From densification experiments reported by Bowen et al. [3], they estimate the heat of solution as ΔH_s=400 kJ/mol. The temperature dependence of the mobility can be estimated from the activation energy for the viscosity of oxynitride glasses (assuming the applicability of the Stokes-Einstein equation). Rouxel et al. [4] measured the viscosity of an oxynitride glass (Y, 17.3; Si, 34.7; Al, 9.9; O, 31.9; N, 6.2 w/o) over the temperature range 850°C to 980°C. The activation energy for viscosity ranged from 335 kJ/mol at 880°C to about 1000 kJ/mol at 940°C, and slowly decreased to 850 kJ/mol at 980°C. These values were consistent with measurements by Hampshire et al. on a similar glass [5]. If oxynitride glasses containing only yttria behave in a similar manner, then the activation energy for viscosity plus the heat of solution of silicon nitride in glass are sufficient to account for the high activation energy, 1,230 kJ/mol, for creep measured in the current study.

In the coming months, additional studies will be conducted on NT-154 in order to determine the effect of annealing on the creep behavior. This work is being conducted in collaboration with Ho Fang at Allied-Signal. The objective of the work will be to determine if annealing

is a viable procedure for improving creep resistance in silicon nitride. A similar program will be started later in the year with Bernie Busavne of the Garrett Processing Division. In this research, we will be investigating GN-10 instead of NT-154. A second program will be started to characterize the creep and creep rupture behavior of PY6, a grade of silicon nitride made by GTE. This work is being done in collaboration with Pramod Khandelwal of Allison Gas Turbine. In this program we hope to obtain a complete evaluation of the creep and creep rupture behavior of PY6. Studies on the NT-154 and PY6 are being conducted as part of the DOE Reliability program.

Status of Milestones

All milestones are on schedule.

Publications

1. D. C. Cranmer, B. J. Hockey, S. M. Wiederhorn and R. Yeckley, "Creep and Creep-Rupture of HIP-ed Si_3N_4," Ceram. and Eng. Sci. Proc. 12[9-10] 1862-1872 (1991)

2. S.M. Wiederhorn, B.J. Hockey and T.-J. Chuang, "Creep and Creep Rupture of Structural Ceramics," pp. 555-576 in *Toughening Mechanisms in Quasi-Brittle Materials*, S.P. Shah, ed., Kluwer Academic Publishers, 1991

3. Ching-Fong Chen, Sheldon M. Wiederhorn and Tze-jer Chuang, "Cavitation Damage During Flexural Creep of SiAlON-YAG Ceramics," J. Am. Ceram. Soc. 74[7], 1658-62 (1991).

References

1. D. F. Carroll, S. M. Wiederhorn and D. E. Roberts, J. Am. Ceram. Soc., 72 [9] 1610-1614 (1989).

2. R. Raj and P.E.D. Morgan, "Activation Energies for Densification, Creep and Grain-Boundary Sliding in Nitrogen Ceramics," J. Am. Ceram. Soc. 64, C143-C145 (1981).

3. L.J. Bowen, R.J. Weston, T.G. Carruthers and R.J. Brook, "Hot-Pressing and the α-ß Phase Transformation in Silicon Nitride," J. Mater. Sci., 13 [2] 341-50 (1978).

4. T. Rouxel, J.-L. Besson, C. Gault, P. Goursat, M. Leigh and S. Hampshire, "Viscosity and Young's Modulus of an Oxynitride Glass," J. Mater. Sci. Let. 8 1158-1160 (1989).

5. A. Hampshire, R.A.L. Drew and K.H. Jack, "Viscosities, Glass Transition Temperatures and Microhardness of Y-Si-Al-O-N Glasses," J. Amer. Ceram. Soc. 67 [3] C46-C47 (1984).

Development of a Fracture Toughness Microprobe

G. M. Pharr and D.S. Harding (Rice University)

Objective/scope

The objective of this study is to develop a technique for measuring fracture toughness in thin films and small volumes on a spatially resolved basis using the Mechanical Properties Microprobe at ORNL (MPM or Nanoindenter). The MPM is currently used to measure both hardness and elastic modulus with a spatial resolution of better than 1 μm. Once developed, the technique will be useful in probing toughness at the scale of the microstructure and thus in establishing important relations between microstructure and fracture behavior. The method will be applied to ceramic systems of importance to the Ceramic Technology Program.

Technical progress

The method we are pursuing is based on the cracking which occurs when brittle materials are indented by a sharp indenter, such as a Vickers diamond. The indentation cracking method has been developed by several investigators over the last 15 years [1-12]. A critical review of its predictive capabilities has been presented by Anstis et al. [7], who have applied the method to a wide variety of ceramics and glasses and found its accuracy to be better than 40%. The basis of the method is to compute the fracture toughness, K_C, from the length of the cracks, c, through the semi-theoretical relation [7]

$$K_C = \alpha \left(\frac{E}{H}\right)^{1/2} \left(\frac{P}{c^{3/2}}\right) \qquad (1)$$

Here, α is an empirically determined geometric constant (for a Vickers indenter, its value is about 0.016 [7]), P is the indentation load, and E and H are the elastic modulus and hardness of the material, respectively. One attractive feature of applying this method with the MPM is that, in addition to being able to produce very small indentations with very precise positioning, the load-displacement data provided by the instrument can be used to establish the local modulus and hardness. Since a knowledge of both these quantities is needed for the computation of toughness, the MPM provides a simple and convenient means for obtaining *all* the data needed to measure toughness on a spatially resolved basis.

Earlier in this research, we showed that an indenter with a cube corner geometry can be used to substantially reduce the cracking threshold in most ceramic materials, thus paving the way for implementation of the method to

micron-sized indentations. During the past 6 months, most of our work has concentrated on establishing how well Eqn.1 works for the cube corner diamond, and what the value of the geometric constant α might be.

To this end, we have acquired a number of brittle materials and determined their toughnesses either by direct measurement or by consultation of the literature. An apparatus for conducting fracture toughness testing using the chevron notch method was completed, calibrated, and used to establish the toughness of soda-lime glass, fused quartz, and pyrex. A notch geometry was found which produces stable crack growth in all three materials and good results were obtained. The measured toughnesses were 0.70 ± 0.02 MPa$\sqrt{m}$ for soda lime glass, 0.59 ± 0.01 MPa$\sqrt{m}$ for fused quartz, and 0.63 ± 0.01 MPa$\sqrt{m}$ for pyrex, all of which compare favorably with values in the literature. We have thus developed a good method for assessing toughness for comparison with results from the indentation testing. Interestingly, previous attempts by other investigators to measure toughness in these same glasses using the chevron notch method met with very little success; valid tests could not be performed because stable crack growth could not be achieved. Our success is due to a careful choice of the notch geometry.

Indentation testing was subsequently performed in each of the three glasses as well as in NC-132 silicon nitride and single crystals of silicon and sapphire, both in (111) orientations. The majority of indentations were made in a conventional microhardness tester using both the Vickers and cube corner indenters in the load range 1 to 10 N (100 to 1000 gms). A few Berkovich indentations were also made, and some of the materials were indented in the Nanoindenter at much lower loads. The materials are shown in Table 1 along with their moduli, hardnesses, and toughnesses. The moduli were taken directly from the literature. The hardnesses are averages based on the Vickers indentations. The toughnesses were either directly measured using the chevron-notch method or extracted from reliable sources in the literature.

Table 1. Mechanical properties of materials used in this study.

Material	E (GPa)	H (GPa)	Kc (MPa$\sqrt{m}$)
Soda-Lime Glass	70	5.5(1)	0.70(2)
Fused Quartz	72	8.9(1)	0.58(2)
Pyrex Glass	63	6.2(1)	0.63(2)
Silicon	168	9.3(1)	0.7(3)
Sapphire	403	21.6(1)	2.2(3)
Si_3N_4 (NC132)	300	16.3(1)	4.0(3)

1. Average of all Vickers indentations.
2. Measured with chevron-notch method.
3. Anstis et al. [7].

As we expected, the threshold loads for cracking for the Vickers indenter were relatively high. The threshold for both soda-lime glass and fused quartz was in the range 1-2 N (100 to 200 gms), and that for pyrex was slightly higher in the range 2-4 N (200-400 gms). Both sapphire and silicon nitride cracked at loads of 1 N (100 gms), but because of their high hardnesses, the indentations were small, and the threshold, which has been reported to be about 0.25 N (25 gms) [13,14], could not be established by optical observation. The threshold in silicon is well documented to be in the range 0.1-0.5 N (1-5 gms) [15].

When indented with the cube corner indenter, all of the materials cracked over the entire load range, consistent with our earlier observations that cracks are produced in sapphire, fused quartz, soda-lime glass, and silicon at loads as low as 0.005 N (0.5 gms). Pyrex and silicon nitride have not yet been tested at low loads in the Nanoindenter with the cube corner diamond.

Some notable behaviors were observed in some of the materials when indented at relatively high loads with the cube corner indenter. In silicon and sapphire, indentation at 10 N (1000 gms) results in complete removal of large portions of material around the indentation, probably from the formation of extensive lateral cracks. Because of this, the indentation size and therefore the hardness cannot be measured. In pyrex glass, the crack mode appears to change at loads greater than 6 N (600 gms) from radial cracking (at low loads) to cracking which is dominated by either cone cracks or laterals (at high loads). The significance of this is that since the toughness measurement method relies on the formation of radial cracks, some caution must be exercised in using the cube corner indenter at high loads. At low loads, on the other hand, the cube corner indenter performs extremely well; radial cracks form consistently in all the materials at loads well below the threshold for the Vickers indenter.

To test the applicability of Eqn.1, crack lengths for both the Vickers and cube corner indenters are plotted as a function of load in Fig.1. To be consistent with the form of Eqn.1 , the crack lengths are plotted in normalized form as $K_c[H/E]^{1/2}c^{3/2}$, where the values of K_c, H, and E are those in Table 1. If Eqn.1 is valid, then data from all the materials should group about a single line, the slope of which is the geometric constant α. While the plots show that this is more or less the case for both indenters, the data are much more tightly grouped for the cube corner indenter than for the Vickers indenter. This is a very significant result in that it implies that in this load range, not only can the cube corner indenter be used in the measurement of fracture toughness, but it gives significantly better results as well.

To examine what happens at loads lower than 1 N , the data for the cube corner indenter are replotted in Fig.2 along with results obtained in nanoindentation experiments. The data, which extend over 4 orders of magnitude in load, again group nicely about a single line. When fit to a power law relation of the form $y = ax^n$, the best fit power law exponent is $n = 1.05$, thus implying that the assumed relation between P and $c^{3/2}$ is correct. The value of the geometric constant resulting from the fit is $\alpha = 0.0319$, roughly

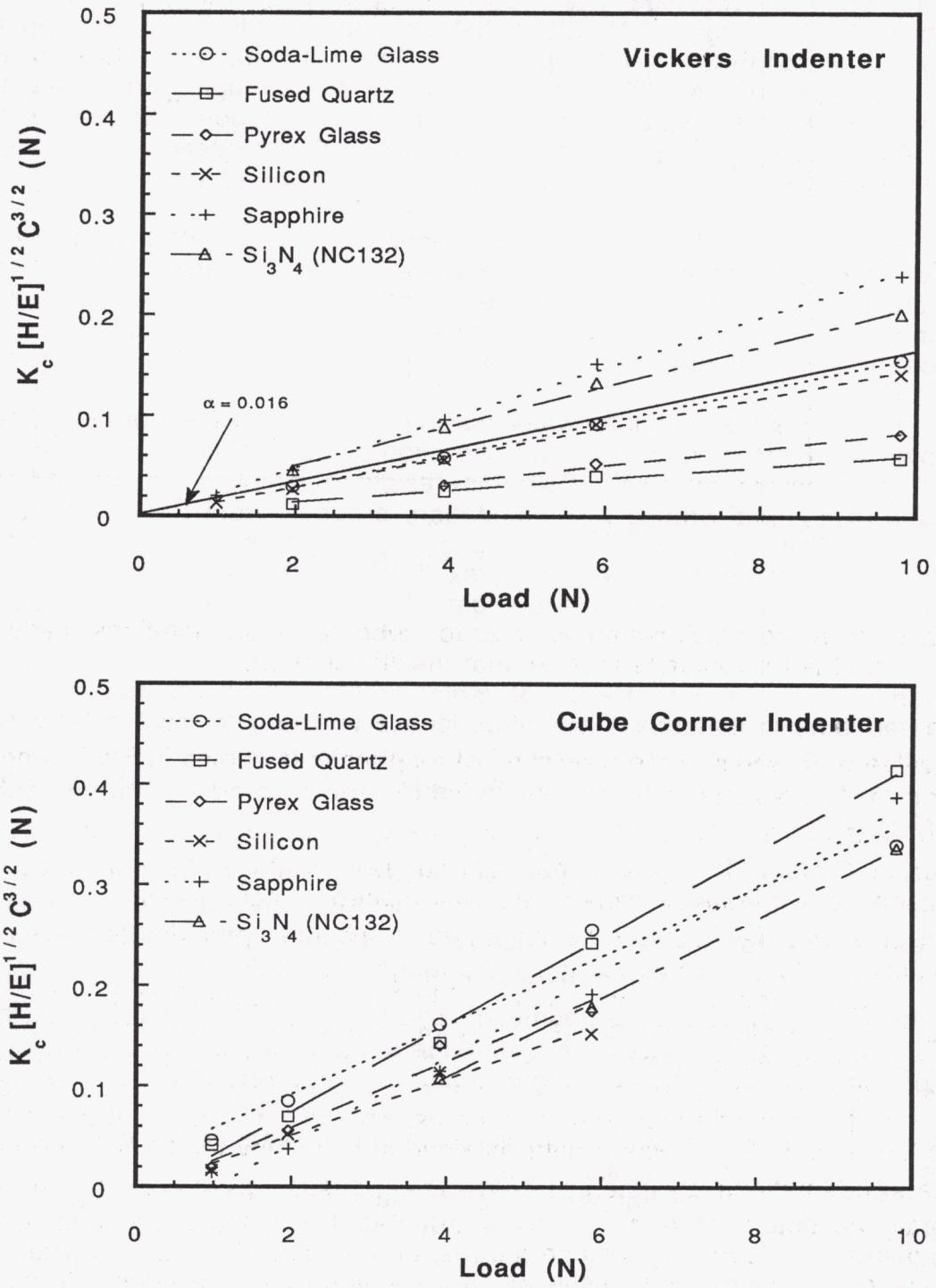

Fig.1. Plots of normalized crack length vs. load for the Vickers and cube corner indenters. The load range is 1-10 N (100 to 1000 gms).

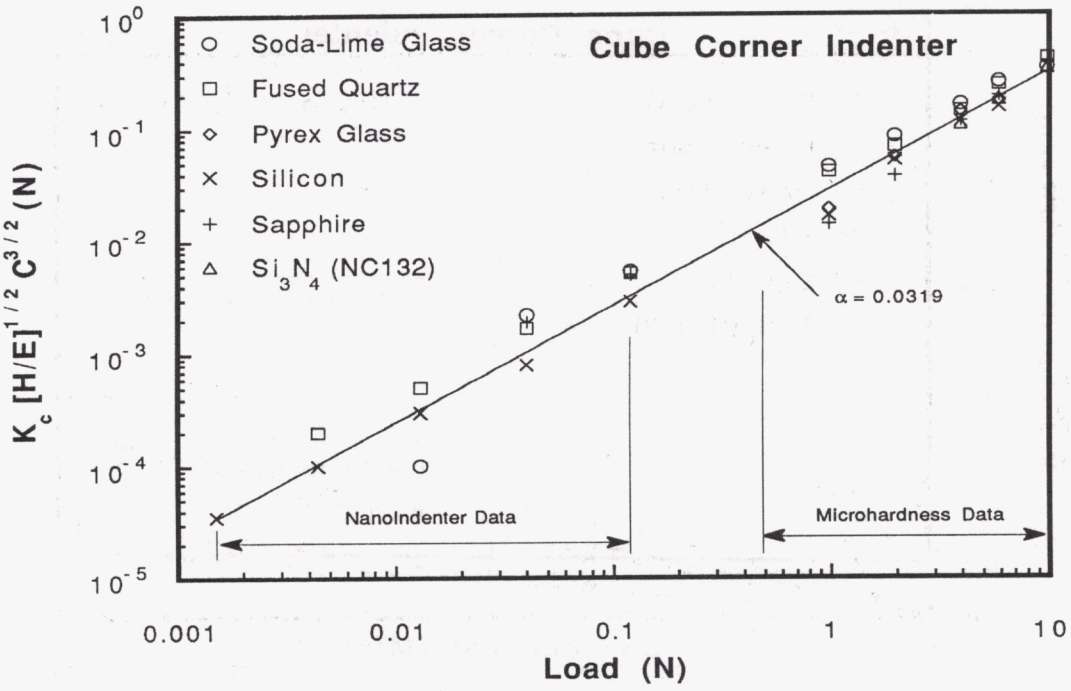

Fig.2. Normalized crack length vs. load for cube corner indentations made in both the microhardness tester and the Nanoindenter.

twice the value reported by Anstis et al. for the Vickers indenter [7]. How well this value of α works in the prediction of toughness is shown in Fig.3, where values of K_c predicted from measured crack lengths produced by the cube corner indenter at a load 4 N (400 gms) are plotted against the values of K_c shown in Table 1. The good agreement suggests that the method based on the cube corner indenter works very well indeed. Before settling on a final value of α, the data set will be extended to include approximately 4 more materials with toughnesses varying in the range 1 to 4 MPa$\sqrt{m}$.

Another significant observation in Fig.3 is that the predictions for fused silica and pyrex glass compare favorably with the values determined from the chevron notch measurement. This is somewhat surprising since it is well known that these materials behave anomalously when indented with a Vickers indenter - the computed toughnesses are usually too high [16]. That this is the case is shown in Fig.4, where data obtained in this study for 10 N (1000 gm) Vickers indentations are used to compute K_c assuming that α = 0.016, the normally accepted value for a Vickers indenter. The fused quartz and pyrex data points are clearly higher than the rest of the data. Also shown in the plot are the data obtained by Anstis et al. for a variety of materials [7] which demonstrate that their results are generally similar to ours. Anstis et al. did not include fused quartz or pyrex in their data set, presumably due to the poor agreement. The point we wish to make is that the anomalous behavior which exists for the Vickers indenter does not appear to occur for the cube corner

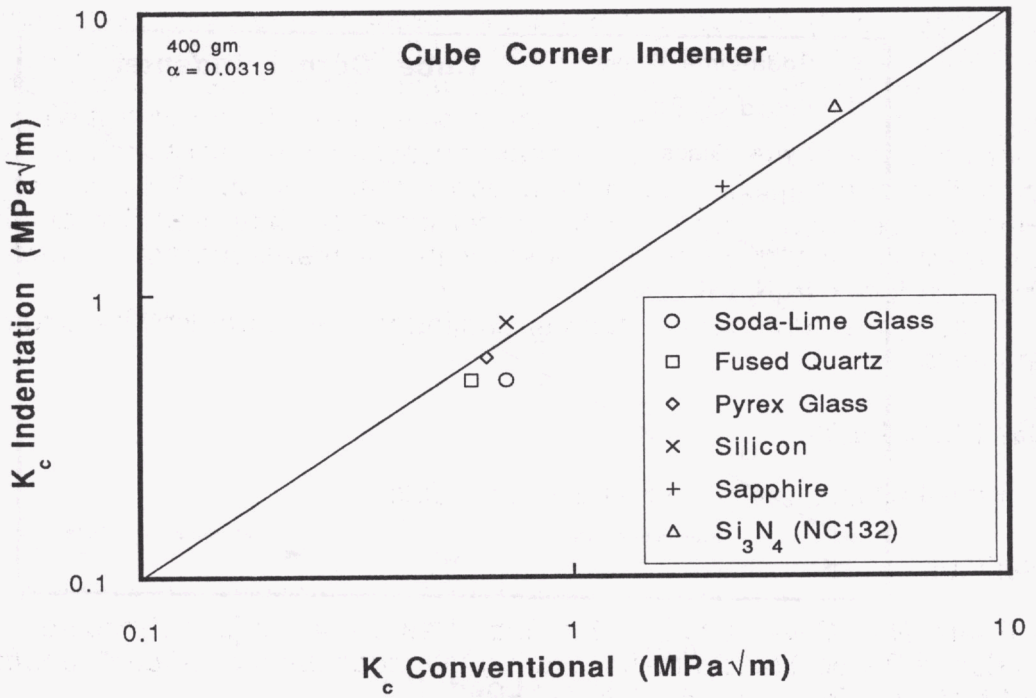

Fig.3. Values of K_c predicted from data from the cube corner indenter at a load of 4 N vs. values of K_c determined by more conventional means.

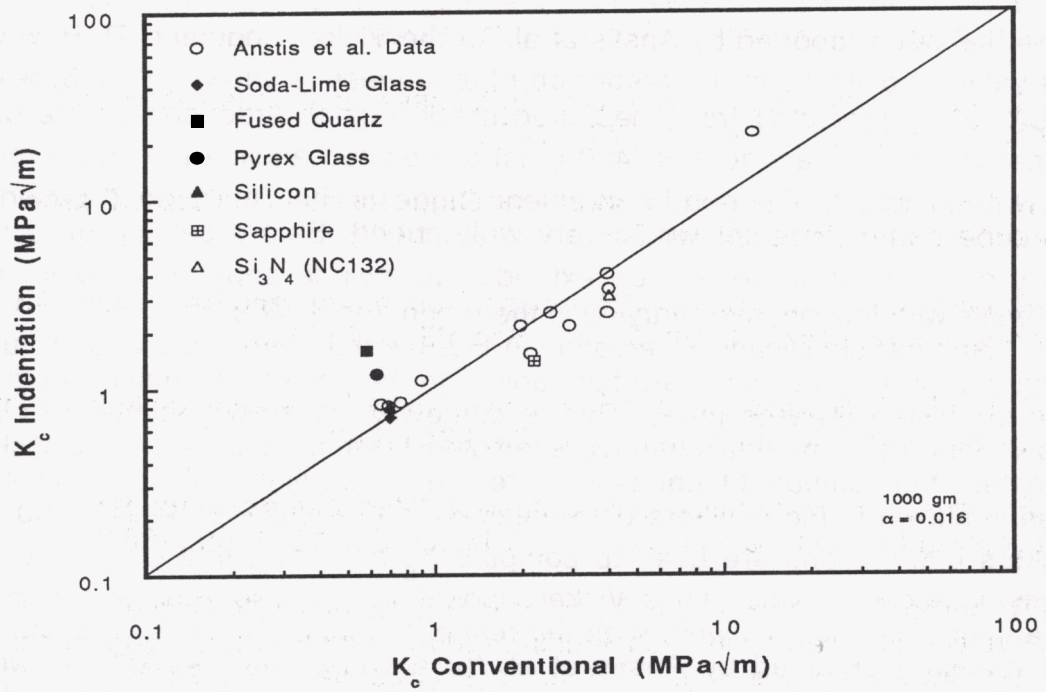

Fig.4. Values of K_c predicted from data from the Vickers indenter at a load of 10 N vs. values of K_c determined by more conventional means. The data of Anstis et al. are also shown [7].

indenter (see Fig. 3). We speculate that the reason for the better performance of the cube corner indenter has to do with a difference in cracking mode. Last year, we found that the predominant cracks which form in fused quartz during loading with a cube corner indenter are radials, while those with a Vickers indenter are cone cracks. This is important because cone cracks interfere with the formation of the radials and thus influence their lengths. Cone cracks do not form in fused quartz for the cube corner indenter, thus providing another reason to prefer the cube corner indenter in the measurement of fracture toughness at low loads.

In sum, the cube corner indenter continues to perform well beyond our expectations.

Status of milestones

All milestones are proceeding on schedule.

Publications

G.M. Pharr, W.C. Oliver, and D.S. Harding, "New Evidence for a Pressure-Induced Phase Transformation During the Indentation of Silicon", *Journal of Materials Research* **6**, 1129 (1991).

References

1. A.G. Evans and E.A. Charles, "Fracture Toughness Determinations by Indentation", J. Am. Ceram. Soc. **59**, 371 (1976).

2. B.R. Lawn, T. Jensen, and A. Arora, "Brittleness as an Indentation Size Effect", J. Mater. Sci. Let. **11**, 573 (1976).

3. B.R. Lawn and A.G. Evans, "A Model for Crack Initiation in Elastic/Plastic Indentation Fields", J. Mater. Sci. **12**, 2195 (1977).

4. B.R. Lawn and D.B. Marshall, "Hardness, Toughness, and Brittleness: An Indentation Analysis", J. Am. Ceram. Soc. **62**, 347 (1979).

5. T.P. Dabbs, D.B. Marshall, and B.R. Lawn, "Flaw Generation by Indentation in Glass Fibers", J. Am. Ceram. Soc. **63**, 224 (1980).

6. B.R. Lawn, D.B. Marshall, and P. Chantikul, "Mechanics of Strength-Degrading Contact Flaws in Silicon", J. Mater. Sci. **16**, 1769 (1981).

7. G.R. Anstis, P. Chantikul, B.R. Lawn, and D.B. Marshall, "A Critical Evaluation of Indentation Techniques for Measuring Fracture Toughness: I, Direct Crack Measurements", J. Am. Ceram Soc. **64**, 533 (1981).

8. P. Chantikul, G.R. Anstis, B.R. Lawn, and D.B. Marshall, "A Critical Evaluation of Indentation Techniques for Measuring Fracture Toughness: II, Strength Method", J. Am. Ceram Soc. **64**, 539 (1981).

9. J. Lankford, "Indentation Fracture in the Palmqvist Regime: Implications for Fracture Toughness by the Indentation Method", J. Mater. Sci. Let. **1**, 493 (1982).

10. K. Niihara, "A Fracture Mechanics Analysis of Indentation Induced Palmqvist Crack in Ceramics", J. Mater. Sci. Let. **2**, 221 (1983).

11. M.T. Laugier, "Palmqvist Cracking in WC-Co Composites", J. Mater. Sci. Let. **4**, 207 (1984).

12. M.T. Laugier, "Palmqvist Indentation Toughness in WC-Co Composites", J. Mater. Sci. Let. **6**, 897 (1987).

13. J. Lankford and D.L. Davidson, "The Crack-Initiation Threshold in Ceramic Materials Subject to Elastic/Plastic Indentation", J. Mater. Sci. **14**, 1662 (1979).

14. J. Lankford, "Threshold-Microfracture During Elastic/Plastic Indentation of Ceramics", J. Mater. Sci. **16**, 1177 (1981).

15. G.M. Pharr, W.C. Oliver and D.R. Clarke, "The Mechanical Behavior of Silicon During Small-Scale Indentation", Journal of Electronic Materials **19**, 881 (1990).

16. A. Arora, D.B. Marshall, B.R. Lawn, and M.V. Swain, "Indentation Deformation/Fracture of Normal and Anomalous Glasses", J. Non-Cryst. Sol. **31**, 415 (1979).

3.5 NONDESTRUCTIVE EVALUATION DEVELOPMENT

Nondestructive Characterization
D. J. McGuire (Oak Ridge National Laboratory)

Objective/scope

The purpose of this program is to conduct nondestructive evaluation (NDE) development directed at identifying approaches for quantitative determination of conditions (including both properties and flaws) in ceramics that affect the structural performance. Those materials that have been seriously considered for application in advanced heat engines are all brittle materials whose fracture is affected by structural features whose dimensions are on the order of the dimensions of their microstructure. This work seeks to characterize those features using high-frequency ultrasonics and radiography to detect, size, and locate critical flaws and to measure nondestructively the elastic properties of the host material.

Technical progress

Ultrasonics - W. A. Simpson, Jr., and K. V. Cook

We continued to receive and evaluate large (41-cm^2, 7.6-cm-thick) ceramic blocks, primarily alumina, for flaws and cracks. In addition, the elastic moduli of the samples were determined nondestructively at several points in order to estimate the homogeneity of the material. The blocks have averaged about 85% of theoretical density and thus contain a relatively large volume fraction of voids. Each of the samples is to undergo thermal cycling, following which they will be retested to determine if prejudicial flaws have developed or if the elastic properties have been affected.

One of these large alumina blocks was sectioned to provide suitable specimens for more detailed NDE. Two of these sections were received and are approximately 21.5 by 17.5 cm in area and approximately 2.5-cm thick. One of the samples was taken from the upper one-third of the original block, and the second was cut from the center one-third. The samples were derived from different quadrants of the original block and were ground on the opposing through-thickness faces to provide adequate entry surfaces for the ultrasonic energy. Both samples were subjected to 25-MHz, pulse-echo ultrasonic testing to determine the presence of cracks, voids, or density variations. At this frequency, discrete voids or inclusions smaller than about 100 μm would not be detected reliably, but both cracks and density variations can usually be discerned quite readily.

Figure 1 shows the results obtained by monitoring the back-surface reflection on the sample derived from the middle one-third of the original block. One of the more obvious features of this scan is the series of concentric circles superimposed on the pattern. These circles can be matched with faint grinding marks visible on the back surface of the sample, even though these marks appear to have no significant height and can only be seen under oblique illumination. No such marks could be discerned on the front (entry) surface of the sample. However, the white

ORNL-PHOTO 7131-91

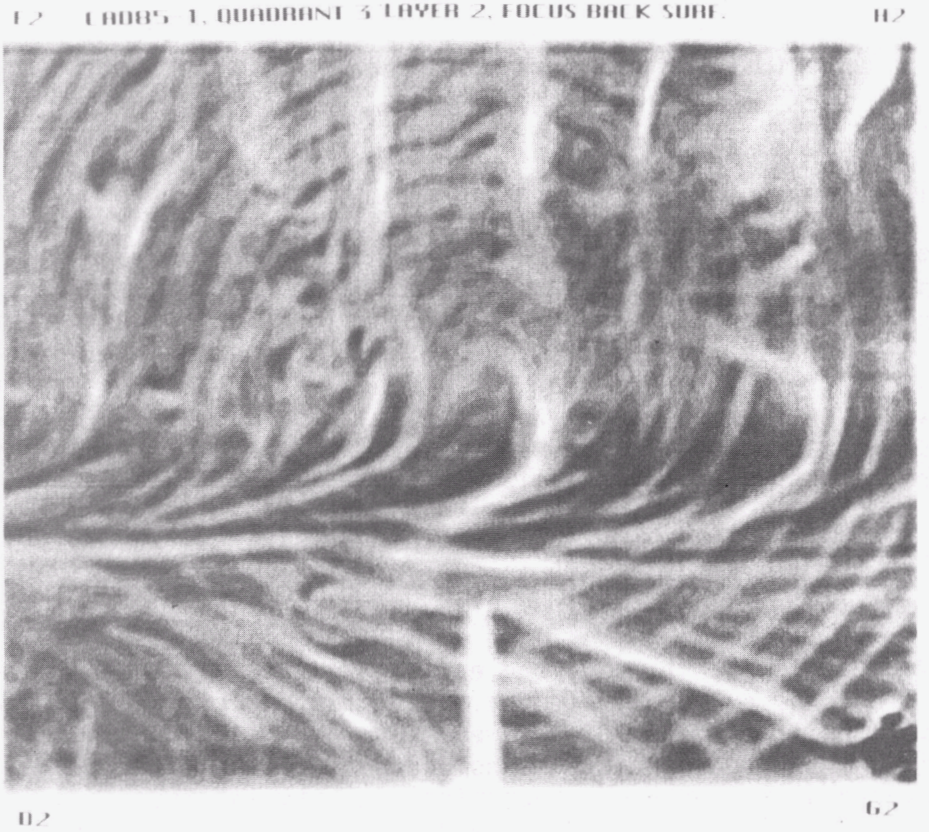

Fig. 1. Ultrasonic back-surface reflection image of an alumina block showing density variations and circular grinding marks.

vertical feature near the bottom center of the figure is caused by a deep gouge in the entry surface.

The remaining, rather striking features evident in Fig. 1 appear to be internal variations. The most likely source for these features is variation in the local material density. This conclusion is supported by the backscattering data, which are shown in Fig. 2. Here, the ultrasonic transducer was focused approximately 10-mm deep in the sample, or very near the midplane. The energy scattered from a small volume centered on this focal point was digitized and assigned a gray-scale value. Since this information comes from the midplane of the sample and is unaffected by the properties of the back surface, it is representative of the conditions existing only in the vicinity of the midplane. Although the variations recorded are much less intense than those seen in the back-surface data, they clearly exhibit the same spatial distribution, with the exception of the concentric circles, which are associated only with the back surface. In addition, dark regions in the backscattering data should correlate with lighter regions in the back-surface data, and this is seen to

ORNL-PHOTO 7133-91

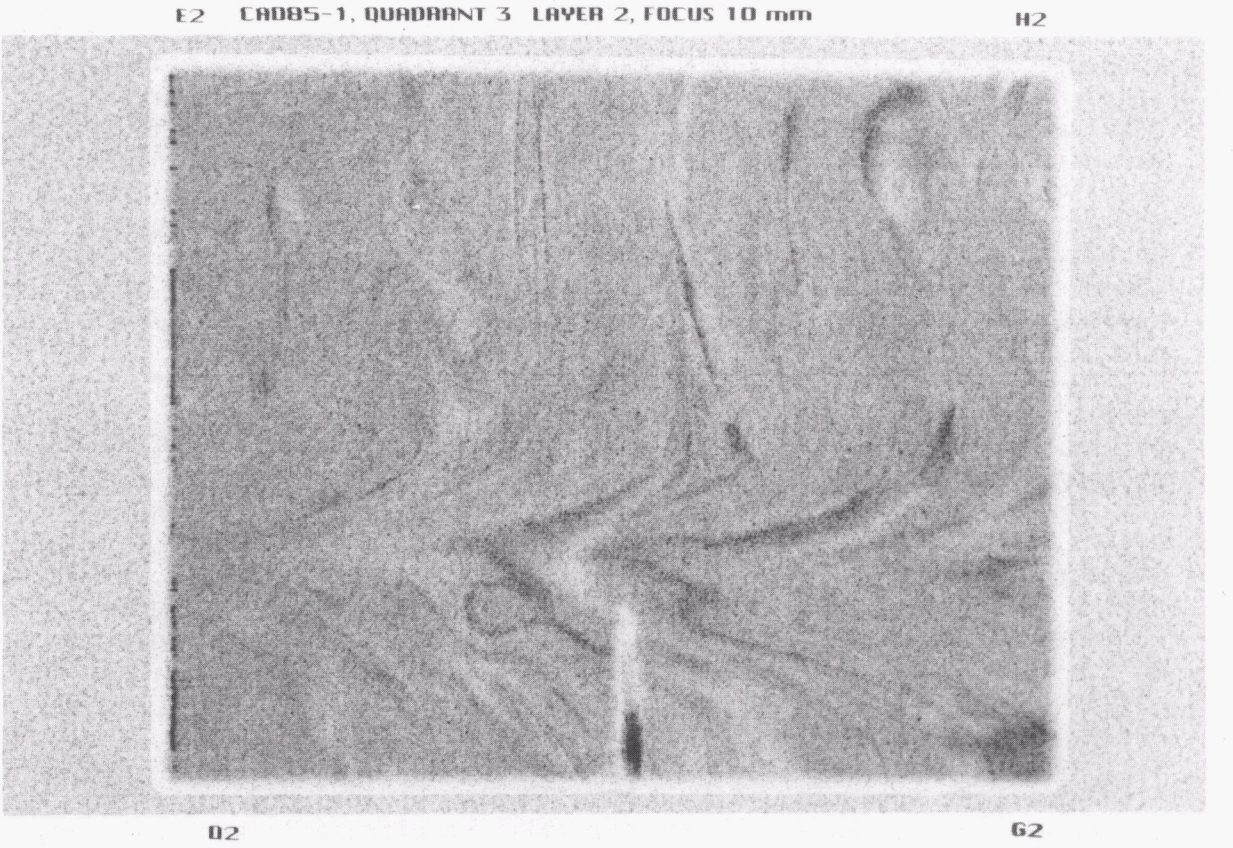

Fig. 2. Ultrasonic backscattering image of the alumina block of Fig. 1 showing density variations.

be the case. In the backscattering case, the recorded variations definitely originate from small changes in the local void fraction, i.e., material density. This conclusion has now been supported by destructive analysis, which showed that the regions of anomalous scattering contained clusters of small voids.

The data acquired on the second sample exhibited the same correlation between the back-surface echo amplitude variations and those produced by midplane backscattering. In this sample as well, therefore, the recorded indications are likely caused by local density variations.

We also completed interfacing a commercial ultrasonic scan tank assembly to a high-speed, PC-based data acquisition system. This work was completed in time to scan the alumina samples described above with the new hardware. The data display is in color rather than gray scale, and we have incorporated a few image processing primitives in the software that allow us to expand the amplitude range under consideration. The results on both alumina samples are identical to the gray-scale information, and

the use of color allows us to see adjacent-level variations (i.e., variations of only one level in the digitizer output), which were not discernible in the gray-scale results. We have tested the new system at inspection speeds up to 10 in. (25.4 cm) per second, which is five times the speed obtainable with an earlier minicomputer interface and twice the maximum speed of our commercial primary inspection system. Both the scan hardware and software of the new configuration are capable of higher-speed operation, but the pulse repetition rate of the ultrasonic exciter limits the inspection speed to the stated value. Above this speed, data dropout begins to occur and is quite serious at the maximum scan speed of 20 in. (50.8 cm) per second. The pulser can be clocked externally at twice the maximum internal rate, but an inspection speed of 10 in. per second seems adequate for the present.

A specification was written and submitted for an upgrade to our primary high-frequency ultrasonic evaluation system for ceramics. The heart of this improvement is an 8-bit peak detector/digitizer to replace the present 4-bit hardware. This change will increase the dynamic range of our system from 24 to 48 dB as well as provide greatly enhanced image processing capabilities. The new system will be color based with computer storage of data files up to 3200 by 3200 image points and will possess a number of sophisticated enhancement algorithms including histogram equalization, contrast enhancement, low- and high-pass filtering, zoom, and pan. In addition, digital time-of-flight information will be provided for up to eight software gates for generating velocity versus position scans of ceramic specimens. This latter capability will be used to map subtle density variations in structural ceramics. Three-dimensional (3-D) color display of the acquired C-scan data will also be included in the operating software. This package will use our existing ultrasonic and scan tank hardware, replacing only the controller and gray-scale recorder.

Based on the specification described above, we purchased a commercial upgrade for our primary high-frequency ceramic inspection system. W. A. Simpson, Jr., delivered our hardware to the vendor's plant; oversaw the installation of an 8-bit, high-speed digitizer and its associated software; received operator training on the use of the new equipment; and returned the upgraded system to Oak Ridge. In addition to greatly improved amplitude resolution, the new package provides time-of-flight information for delineating regions of varying density in ceramic materials via changes in the elastic wave velocity, color display of the resulting images, and storage of data files up to the limit of the hard disk drive. The digitizer is a real-time 100-MHz unit and may be operated in equivalent-time sampling modes at rates of 200, 400, 800, 1600, and 3200 MHz. At the 200- and 400-MHz sample rates, the speed of the software is such that no reduction of the scan velocity of several inches per second appears to be required. At all rates up to the 100-MHz real-time limit, the full radio frequency (rf) waveform may be acquired and stored; at the higher sample rates, only the peak amplitude and time of flight are recorded.

In addition to the features described above, the new system has several capabilities that should prove very useful for ceramic evaluation. A number of image enhancement functions, including data smoothing, high- and low-pass filtering, histogram equalization, zoom, and 3-D color plotting have been included. A test of these functions on an alumina sample, which

we have previously characterized repeatedly, revealed several indications not seen before. We also examined with high-frequency surface waves several silicon nitride modulus of rupture (MOR) bars, which contained laser-drilled holes of 20-μm diam and 20-μm depth and 10-μm diam and 10-μm depth. We examined these samples with our old hardware and were able to detect the holes on the A-scan but could not record their presence because of the limited amplitude resolution of the 4-bit digitizer. Figures 3 and 4 show the results obtained on the 20-μm hole. In Fig. 3, the unprocessed ultrasonic data are shown with the full 256-level ampli-tude resolution on a VGA monitor in 256-color mode. The 20-μm flaw is the bull's-eye feature shown near the center of the figure. This distinctive pattern is easily explained from the properties of the radially propa-gating surface wave and the nature of the laser-drilled hole. The semi-circular features shown at the top and bottom edges of the MOR bar are small specks of paint used to mark the location of the drilled hole. Figure 4 shows the same data with contrast enhancement to accentuate the presence of the flaw.

Figure 5 shows the contrast-enhanced surface-wave result obtained on the sample containing a 10-μm-diam, 10-μm-deep laser-drilled hole. In this case, there was only a single dot of paint used to locate the hole,

YP13369

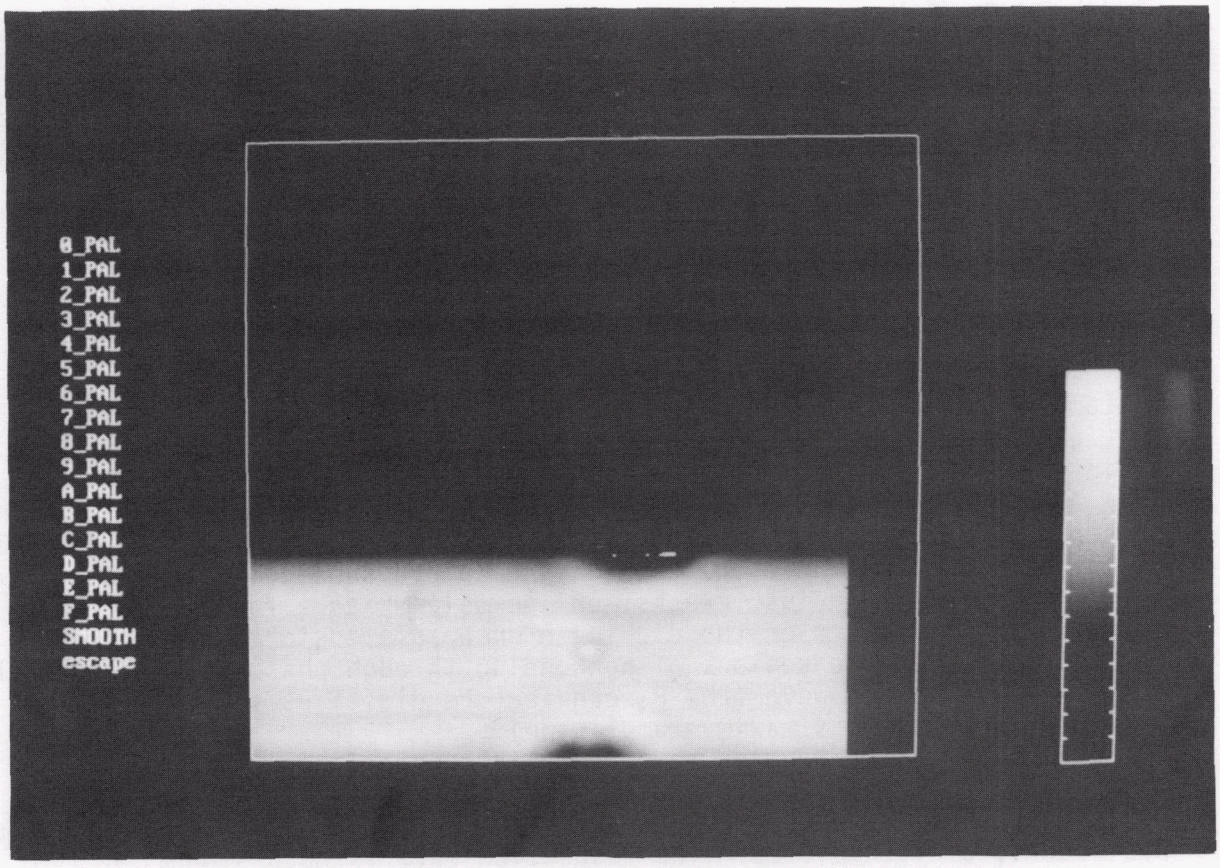

Fig. 3. Unprocessed ultrasonic surface-wave image of a 20-μm-diam, 20-μm-deep flaw (circular indication).

YP13368

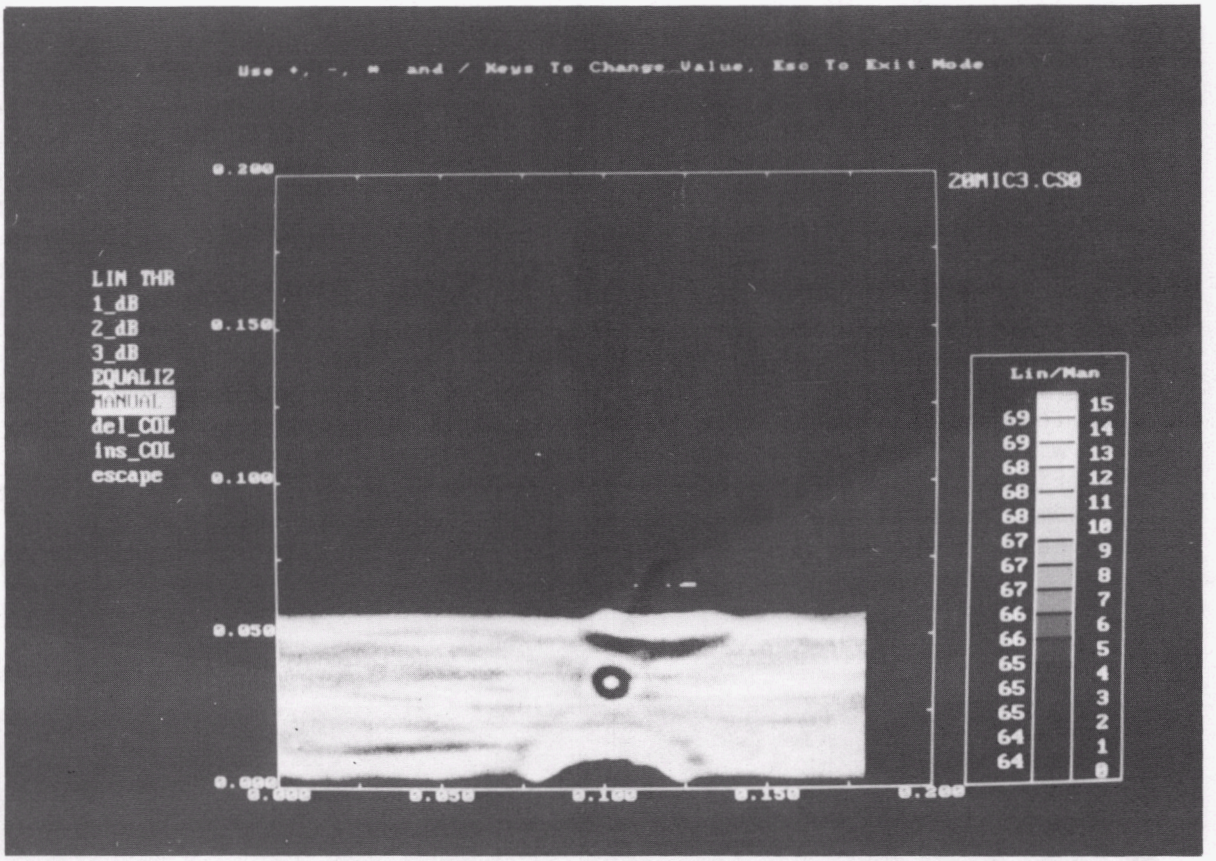

Fig. 4. Contrast-enhanced image of the 20-μm flaw of Fig. 3.

and the response from this dot is the semicircular indication at the top of the figure. The 10-μm hole is the dark circular feature seen at the bottom edge of the paint indication. The linear indications running left to right on the figure are the response from surface grinding marks. Only a hint of the flaw can been seen in the unprocessed data.

Another feature that is present on the new system is the ability to generate B-scan presentations of ultrasonic data. These presentations are essentially vertical sections through the sample showing the response from scattering centers (voids, cracks, or inclusions) as a function of depth. A test of this feature on the die in an encapsulated integrated circuit was able to delineate regions of nonbonding through phase reversals in the scattered ultrasonic wave (the B-scan feature digitizes the entire rf waveform, not just its maximum amplitude).

We continued to develop an ultrasonic synthetic aperture system for evaluation of planar ceramic specimens. The in-house modified interface described above was used for this purpose, and a test of the entire system was successfully completed. The inspection rate is much slower, of course, since the full analytic signal must be acquired at each aperture point, which is approximately every half wavelength. The advantage

YP13365

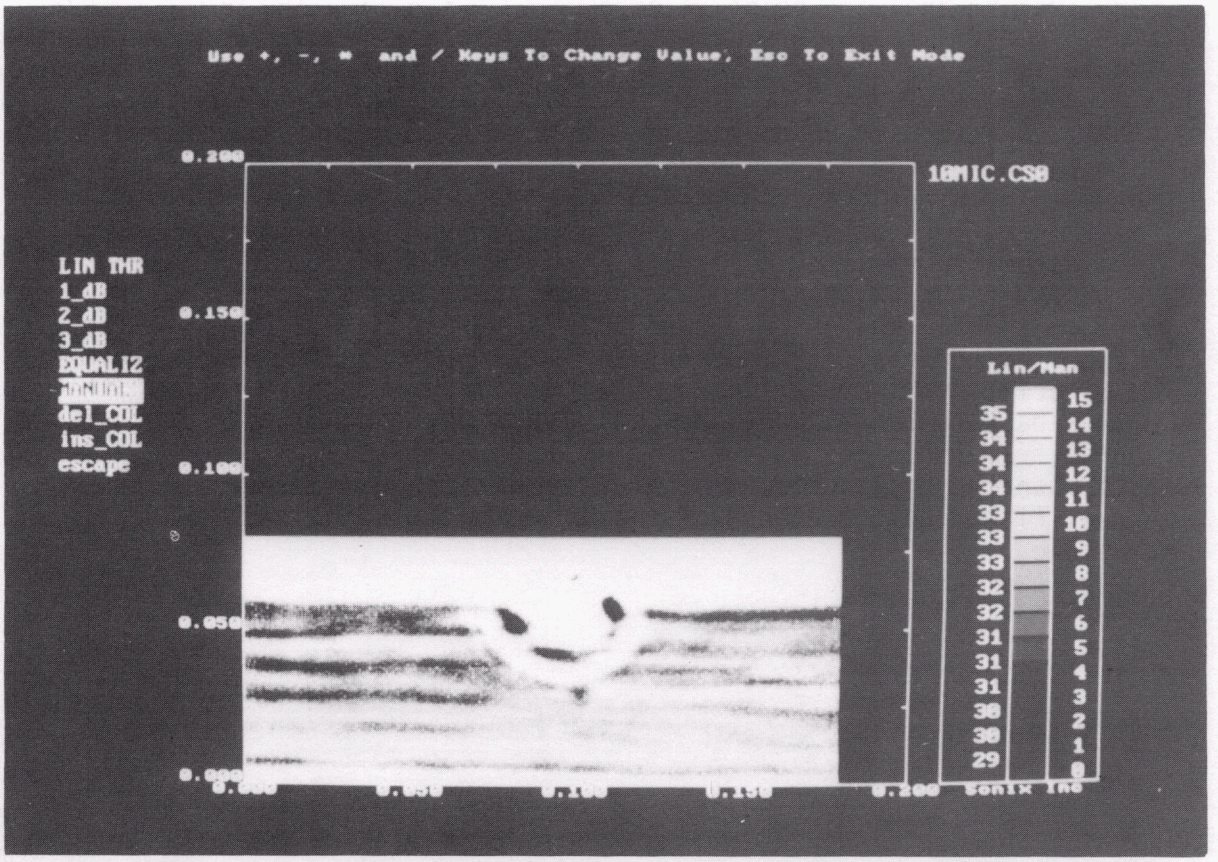

Fig. 5. Contrast-enhanced ultrasonic surface-wave image of a 10-μm-diam, 10-μm-deep flaw (circular indication near center of image).

gained, however, is that the inspection depth is limited only by the signal-to-noise ratio obtainable with the hardware available. All required hardware modifications were completed as well as the software changes necessary to implement the synthetic aperture algorithms on our system. A preliminary, one-dimensional synthetic aperture scan was successfully tested using the new hardware. The commercial system upgrade described above is also somewhat compatible with the synthetic aperture approach in that data which we have acquired can be imported to the B-scan program for display in both the raw and processed forms.

With the completion of these changes, we have a functioning, automatically controlled system to implement synthetic aperture processing of ultrasonic ceramic data. Given the characteristics (elastic wave velocity, etc.) of the target material, the nominal operating frequency, and the desired total area to be examined, our system will determine the optimum aperture for a point scatterer, move the transducer over the total scan area, and collect the complete rf scattering record from throughout the sample thickness at each aperture point. These data are written to

disk as one record of the entire aperture file. As there are 512 points per waveform and each point is encoded as a 4-B floating point number (this is modified to an 8-bit integer when the data are presented to the commercial B-scan program), each point of the synthetic aperture generates a 2-KB record. Thus, for a 100 by 100 array of aperture points, more than 20 MBs of data will be generated. Our software has been written to perform the appropriate processing of these records over the optimum aperture for each point of the resulting image.

Figure 6 shows the data obtained by a single synthetic aperture scan line across an artificial flaw (a drilled hole) in aluminum. The vertical features at the right of the figure are the rf oscillations of the back-surface signal, while the curved pattern is the signal from the tip of the flaw. The quadratic phase delay characteristic of a point scatterer can be clearly seen in this figure. Two similar curved responses to the right of the back-surface signal are caused by reflection of the ultrasonic energy from the sides of the drilled hole. These signals occur later in time than the back-surface signal and would not be present in the case of a real flaw. Note the loss of the back-surface signal in the region of the hole.

YP13372

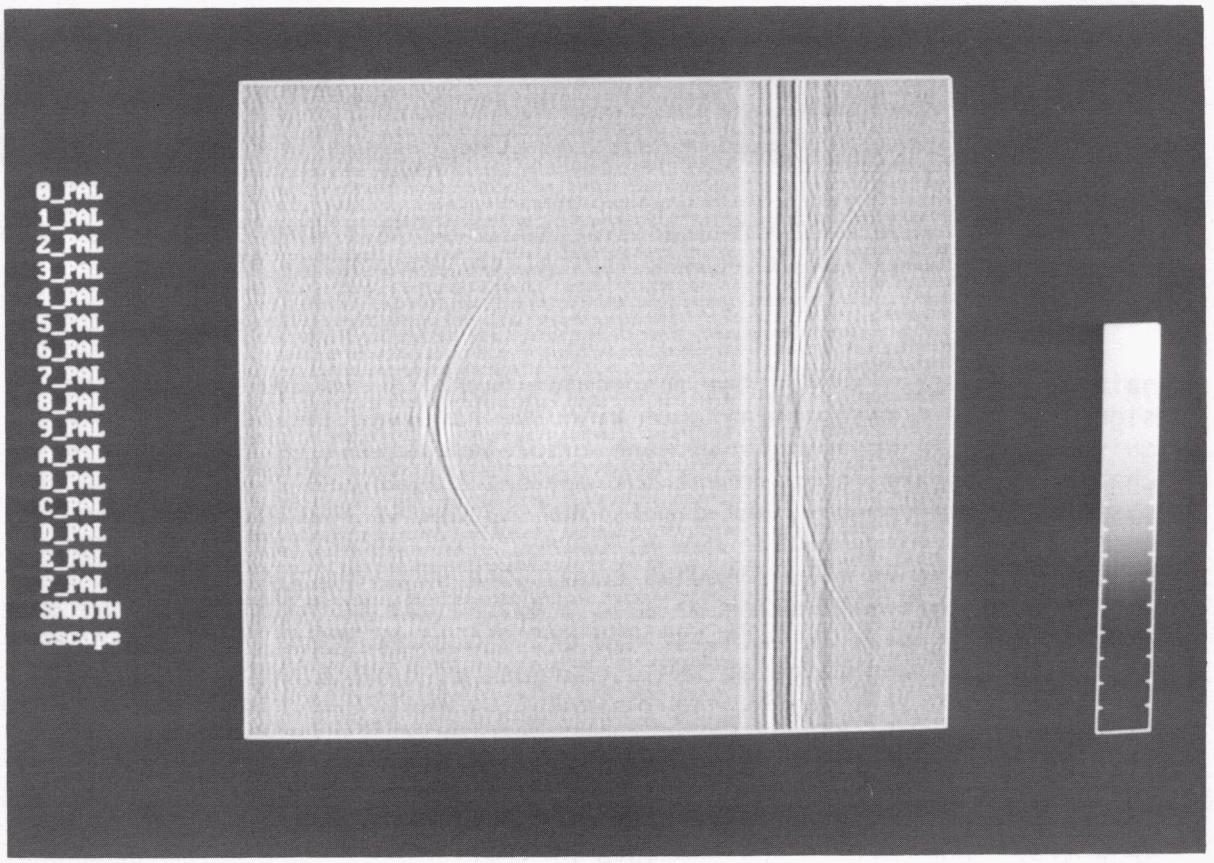

Fig. 6. Unprocessed synthetic aperture scan showing back-surface signal (vertical lines at right of figure) and the response from a point source flaw (curved indication left of center of figure) in aluminum.

Figure 7 shows the contrast-enhanced response from a flaw in a zirconia MOR bar. The vertical features at the left and right of the figure are the front- and back-surface signal, respectively, while the curved response to the right of center is caused by the flaw, which is approximately 250 μm in diameter and located about 3-mm deep. These are raw data that have not been processed to yield a "focused" image of the flaw.

Computed Tomography - B. E. Foster

A purchase requisition was issued for several ceramic samples to be used for beam-hardening corrections and standards. One of the samples is a 12-mm-thick SiC wedge with approximate dimensions (150 x 250 x 300 mm) for establishing beam-hardening correction tables. The remaining six samples are SiC and Si_3N_4 discs (12-mm thick) with diameters of 25, 50, and 110 mm. Anticipated delivery was originally late July or early August 1991, but fabrication and delivery delays at the vendor's plant have moved

YP13371

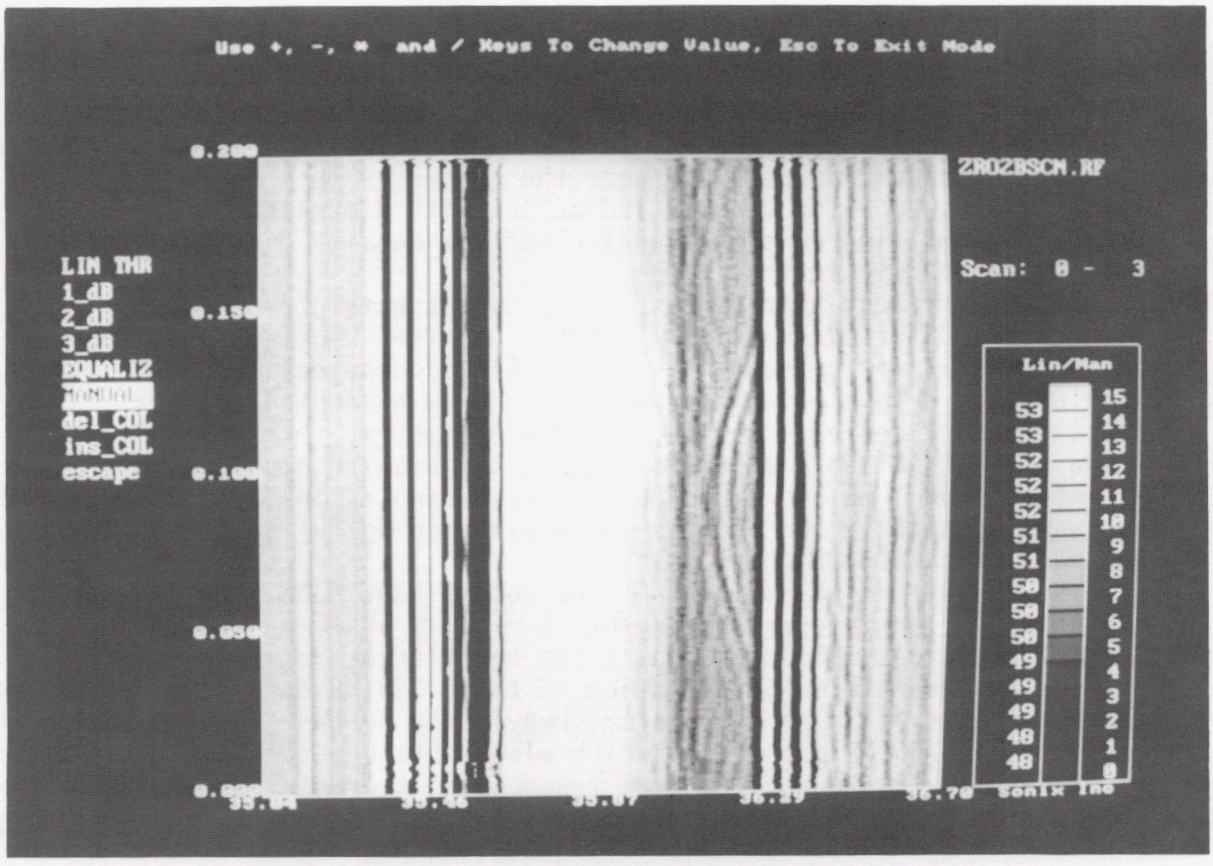

Fig. 7. Unprocessed synthetic aperture scan showing front- and back-surface signals (vertical lines at left and right of figure) and response (curved indication) from a 250-μm flaw in zirconia.

this date to late November or December 1991. The discs will subsequently have different diameter and depth holes (25- to 250-μm range) placed in them.

A Si_3N_4 tensile specimen with hole diameters ranging from 25 to 100 μm in the 6-mm-gauge block portion was available for a brief time period. A rather hurried calibration of the CT System in the high-resolution mode was done and the sample scanned. Indications in the vicinity of the 100-μm-diam holes were noted during our necessarily brief examination, which established the need for a better calibration. The specimen was subsequently returned to us for further evaluation. In addition, a similar tensile specimen without holes was also received. Since the CT system was temporarily unavailable for scanning these small samples in the high-resolution mode (it was being used for some larger diameter ceramic rotors), we radiographed the samples with our conventional X-ray equipment. Several of the 100-μm and a few of the 50-μm (diameter and depth) holes were imaged. The sharpness of the hole images was less than anticipated. Further evaluation of the holes in the sample with the aid of a metallurgical microscope showed that the holes were tapered. The quoted 100-μm holes were indeed that at the surface but were only about 70 μm at the bottom. The film radiography of the second sample showed several cracks. Some of these cracks were visible at the surface.

Three other silicon nitride tensile samples were scanned using the digital radiograpy mode. A linear-type indication was noted in the 6-mm-gauge block portion of one of the samples. There were no indications noted in the other two samples. A 0.25-mm-thick CT slice was then taken across the gauge thickness and near the center of the linear indication. This scan showed a low-density indication with dimensions of approximately 0.2 by 0.5 mm. There were several other low-density circular indications (less than 0.2 mm) in that image.

Thirty silicon nitride tensile specimens with a 6-mm-gauge block have been received for evaluation with the CT system. Digital radiography will be done on all of the samples with CT slices on selected areas. These samples will be evaluated as soon as the beam-hardening calibration, precise object center location, and the parameters for sharpening the image reconstruction are determined for the high-resolution (small sample diameter) mode. We had expected to begin scanning in early August 1991 but were delayed by the efforts on beam-hardening calibration and image sharpness reconstruction algorithms.

Seven 50-mm-diam silicon nitride rotors have been received for CT evaluation. The interest is in the 15-mm-diam shaft of the rotor. Several CT slices will be taken in the shaft area.

We have completed installation of three 760-MB hard-disk drives and expansion chassis in the CT system. Previously we had a 380-MB system disk and a single 760-MB data disk (which also contained some system files). The limited data storage required fragmenting the data for a single 100-mm-diam rotor onto magtape and disk, which was very labor intensive, for later image review and analysis. Now, we have three data disks, each with a 760-MB capacity, in addition to about 400 MBs available for data on the system disk. The original 380-MB disk drive was removed.

While waiting for the beam-hardening calibration standards, we received and installed new software from Scientific Measurement Systems (SMS), Inc. (the manufacturer of the CT unit), for picture reconstruction,

which is supposed to reduce some of the annoying artifacts that were being observed. In addition, SMS personnel realigned and centered the X-ray tube (the change was approximately 0.5 mm) and replaced a circuit board in the array processor for further reduction of artifacts in the final image. These changes are presently being evaluated.

Milestones

Milestone 351105 was completed on schedule.

Publications

W. A. Simpson, Jr., and R. W. McClung, "An Ultrasonic Evaluation of Silicon Carbide Whisker-Reinforced Ceramic Composites," accepted for publication in *Mater. Eval.*

R. W. McClung, W. A. Simpson, Jr., and D. R. Johnson were invited contributors to a chapter entitled "Ultrasonic Tests for Advanced Structural Ceramics," *Section 15, UT Applications in Advanced Materials and Processes*, which has now been published in the American Society for Nondestructive Testing (ASNT) Handbook on Ultrasonic Testing.

B. E. Foster and F. Hopkins, "High-Resolution Imaging of Ceramic and Other Materials with Computed Tomography," presented at the Industrial Computed Tomography II Topical Conference, San Diego, May 20-23, 1991. The paper summary is to be printed in the conference proceedings.

NDE STANDARDS FOR ADVANCED CERAMICS

R. W. McClung (Oak Ridge National Laboratory)

The development of standards is important for the establishment of reliability and acceptance of advanced structural materials. Committee C-28, on Advanced Ceramics, is organized in the American Society for Testing and Materials (ASTM) to address this issue. One of the activities of the C-28 committee is nondestructive examination (NDE). The Task Group is reviewing existing standards on NDE (primarily developed for metals) to determine potential applicability for ceramics, as well as preparing original standards. Use of existing or modified standards is more efficient than generation of new documents and will ensure the input of a large body of NDE expertise. Close liaison is established with ASTM Committee E-7 on Nondestructive Testing, and documents are in various stages of review, recommendations for change modification, and balloting. R. W. McClung is a member of both committees and the official liaison.

Liaison and technical support have been continued between ASTM Committees C-28 and E-7. To date, 31 NDE standards have been reviewed in detail with recommendations made to E-7 for modifications to identified documents. Successful action is complete on 13 documents, E-7 balloting action is in progress on 8 items, and the others require action by C-28. A table of ultrasonic velocities in typical ceramic materials, prepared by C-28 and submitted to E-7 for incorporation in an existing NDE standard, had a successful E-7 subcommittee ballot, and a full committee ballot was approved on this item. A document on fabrication of seeded voids in pressureless sintered ceramics balloted in C-28 at the subcommittee level is being revised for a concurrent ballot at both committee and subcommittee levels. A guideline document that describes available approved standards and their applicability for examination of ceramics was approved by ASTM as C-1175 and is to be published in Vol. 15.01 of the *ASTM Book of Standards*. Comments received from a Task Group advisory ballot conducted on five new E-7 standards covering specific techniques of liquid penetrant examination were submitted to E-7 for recommended modifications. At the E-7 meeting in June 1991, appropriate contacts were made to ensure ongoing activity in response to C-28 requests on documents on radiography, ultrasonics, and liquid penetrants. Plans are being made in C-28 for potential procedures for (1) fabricating reference specimens containing seeded inclusions and laser-drilled holes and (2) ultrasonic examination and radiographic equivalence factors in ceramic materials.

X-ray Computed Tomographic Imaging – W. A. Ellingson,
N. Gopalsami (Argonne National Laboratory) and J. P. Pollinger,
(Garrett Ceramic Components of Allied-Signal Aerospace Corporation)

Objective/scope

The objective of this program is to develop X–ray computed tomographic (CT) imaging technology for application to structural ceramic materials. This technique has the potential for mapping short–range (<5 mm) and long–range (>5 mm) density variations (to perhaps 0.5–1%), detecting and sizing high– and low–density inclusions, and detecting and sizing (within limits) cracks in green–state and densified ceramics. Use of 3-D CT (volume CT) imaging allows the capability of interrogating the full volume of a component and is noncontacting. It is also relatively insensitive to part shape and thus can be used to inspect components with complex shapes, such as turbocharger rotors, rotor shrouds, and large individual turbine blades.

Technical progress

The work this reporting period covers application work relative to X-ray computed tomography using Argonne National Laboratories 3-D microfocus system on phase III of this research program relative to detection of whisker distributions (likely to be manifested and detected as density variations) in as-cast pressure slip-cast SiC(w)/Si_3N_4 (Garrett's GN-10 material). This a continuing joint project between Argonne National Laboratory and Garrett Ceramic Components of Allied-Signal Aerospace Corporation of Torrance, California.

We have now received all of the first set of SiC(w)/Si_3N_4 billets (length/diameter ratio = 1.5) made by pressure slip-casting and all are in good condition for NDE characterization. The decision was made during this reporting period to air-dry the remaining specimens prior to shipping to ANL. Originally, for the Garrett Ceramic Processing companion NMR studies, we had attempted to retain the maximum amount of water in the billets. This proved to be a problem both in transportation and in maintaining dimensional stability during NDE analysis. Table 1 below gives the identification of the air-dried billets which will be used in this study. The data for casting of these billets are given in Table 2.

Table 1. Identification of first set of as-received billets

Billet ID	Whisker Content wt.%
91A–013	20
S–910002	23
S–91036–2	27
S–910373	30

Table 2. Casting parameters for First set of billets

Billett Identification	Whisker Content Wt.%	Slip Solids Content wt.%	Slip viscosity cps	Bulk density at demolding g/cc
91A–013	20	69.8	135	2.07
S–910002	23	68	93	2.47
S–910362	27	65	105	2.15
S–910373	30	63	362	2.30

In all cases the casting pressure was 40 psi and the mold type was plaster of paris. The configuration of the casting is shown in Fig. 1. Note that the dewatering was in 2 directions: radially and axially (bottom only).

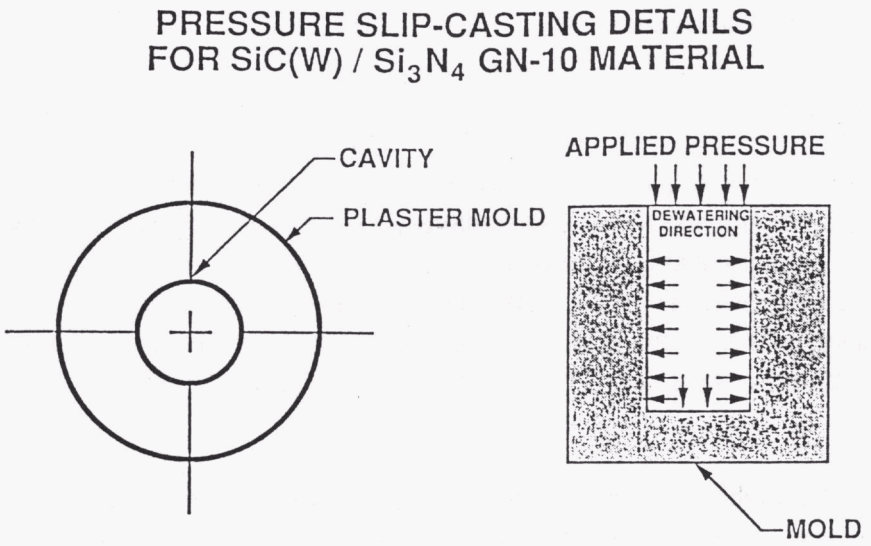

Fig. 1. Schematic diagram of dewatering/mold configuration for pressure-slip-cast SiC(w)/Si_3N_4 GN-10 ceramic materials

23 wt.% billet

We further studied the 23 wt.% billet for changes in density distribution axially as well as radially. Figure 2 shows a series of tomographic sections at different axial locations for the 23 wt.% specimen.

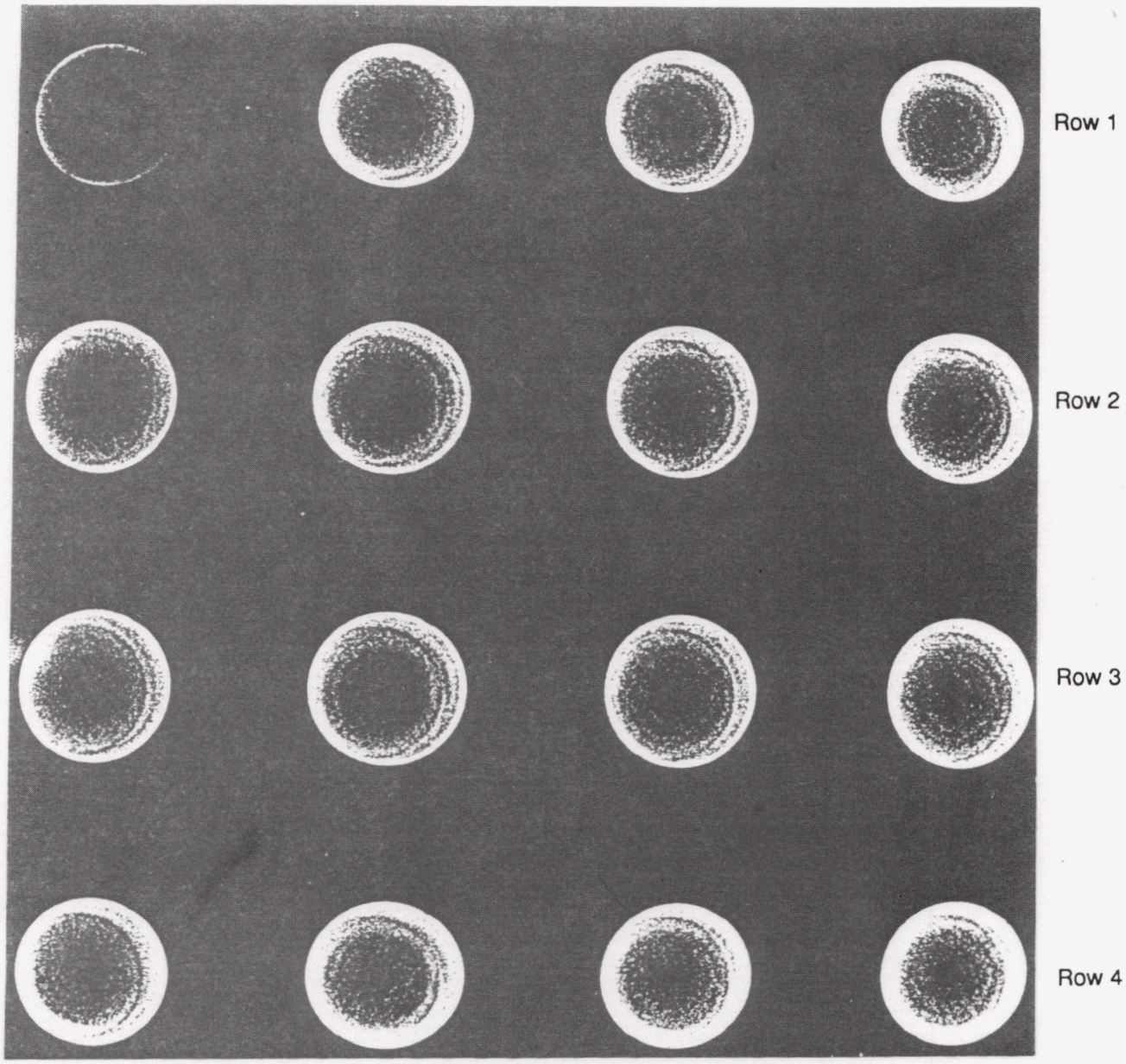

Fig. 2 X-ray tomograms from volume CT scan of 23 wt.% whisker specimen. The series of images goes left to right for rows 1-4. These are top to bottom in order, about 3 mm per slice

20, 23, 27, 30 wt.% billets

We obtained this period, complete volumetric X-ray CT data on all billets with L/D = 1.5. The initial volumetric cross-sections are shown in Fig. 3. The images were reconstructed using 260 X 260 reconstruction data. The pixel sizes are 141 μm for the X-direction and 111 μm for the Y-direction.

After inspection of the axial cross-sections, we noted there appears to be columnar density variations. That is, there appears to be distinct "rings" of varying density at any axial position. Because of limits in destructive sectioning size, we choose to select rings of 2 mm increments to establish relative density from the X-ray CT scans. We choose a section 2 mm thick at each of three axial locations, L/4, L/2, 3L/4. These are the quarter points and mid point. We measured from the top of the specimen which we had oriented in the CT scanner in a "top up" orientation. Figures 4-6 show the variation in X-ray CT image gray scale (related to density) as a function of axial position for each of the four specimens. We will correlate these data to destructive density measurements during the next reporting period.

In order to further examine the variations in gray scale, we tabulated the difference in CT image gray scale between the 2 mm wide "rings," measuring the step-height between "rings". These are given in Table 3.

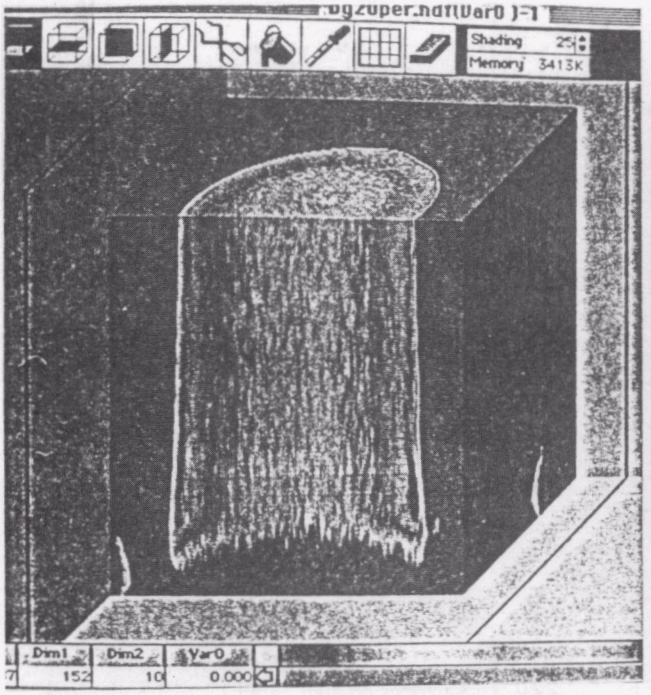

(a)
20 wt.%

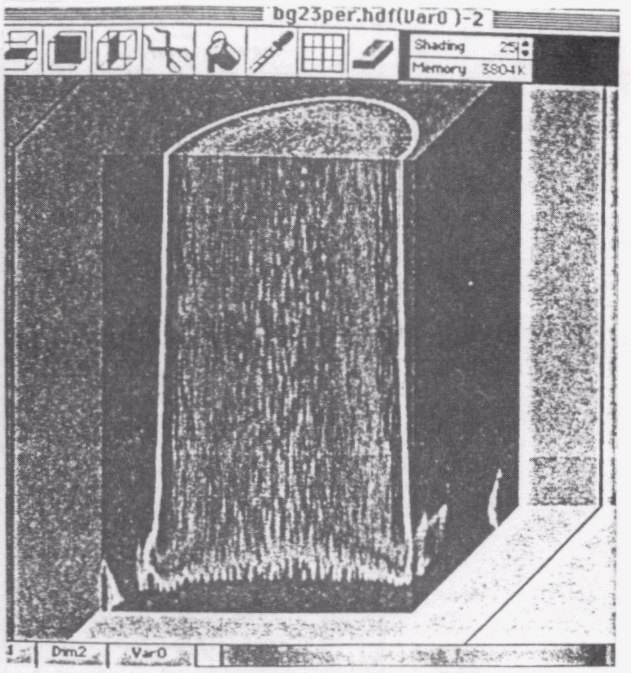

(b)
23 wt.%

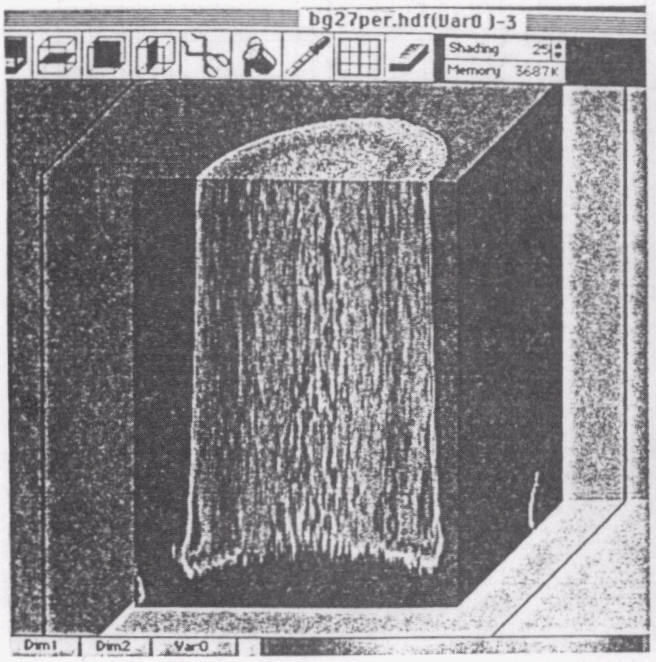

(c)
27 wt.%

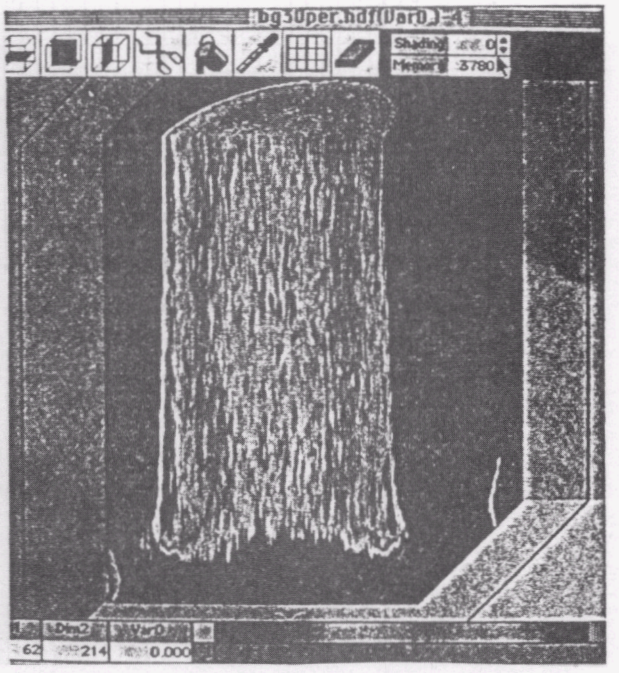

(d)
30 wt.%

Fig. 3. Axial volumetric X-ray CT images of 20, 23, 27 and 30 wt.% whisker specimens

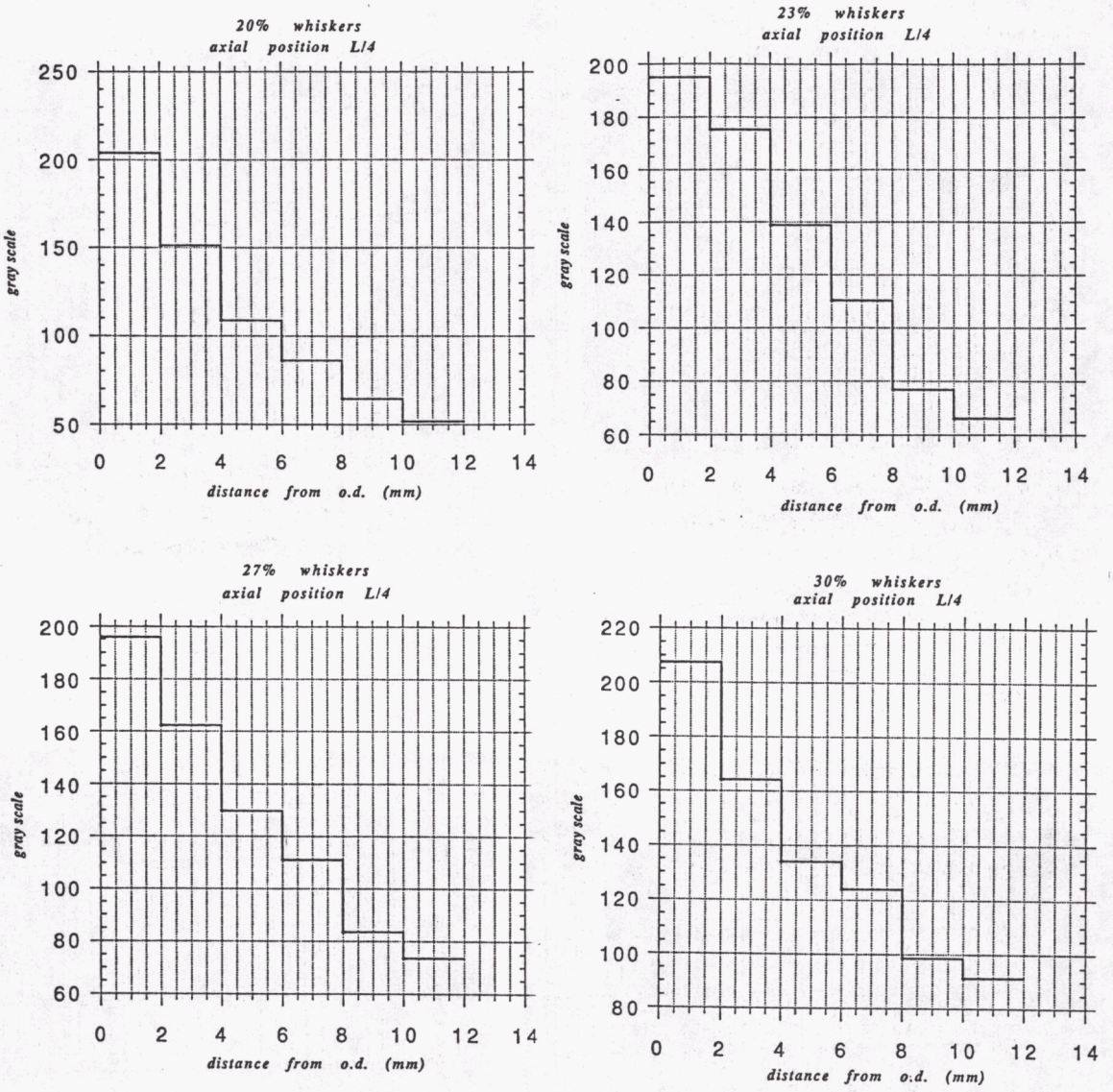

Fig. 4. Apparent radial density variation of pressure slip-cast SiC(w)/Si_3N_4 at elevation L/4

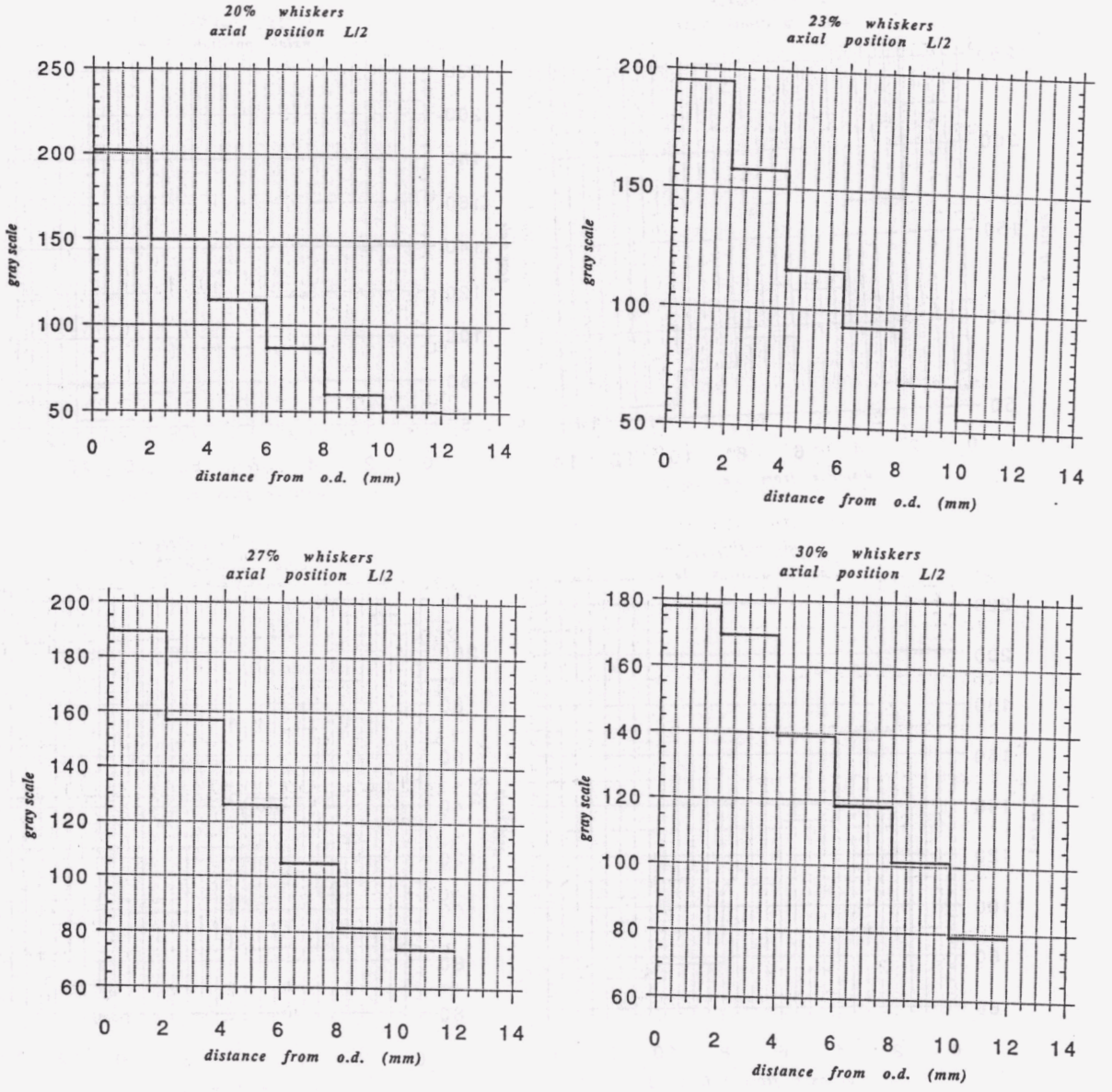

Fig. 5. Apparent radial density variation of pressure slip-cast SiC(w)/Si_3N_4 at elevation L/2

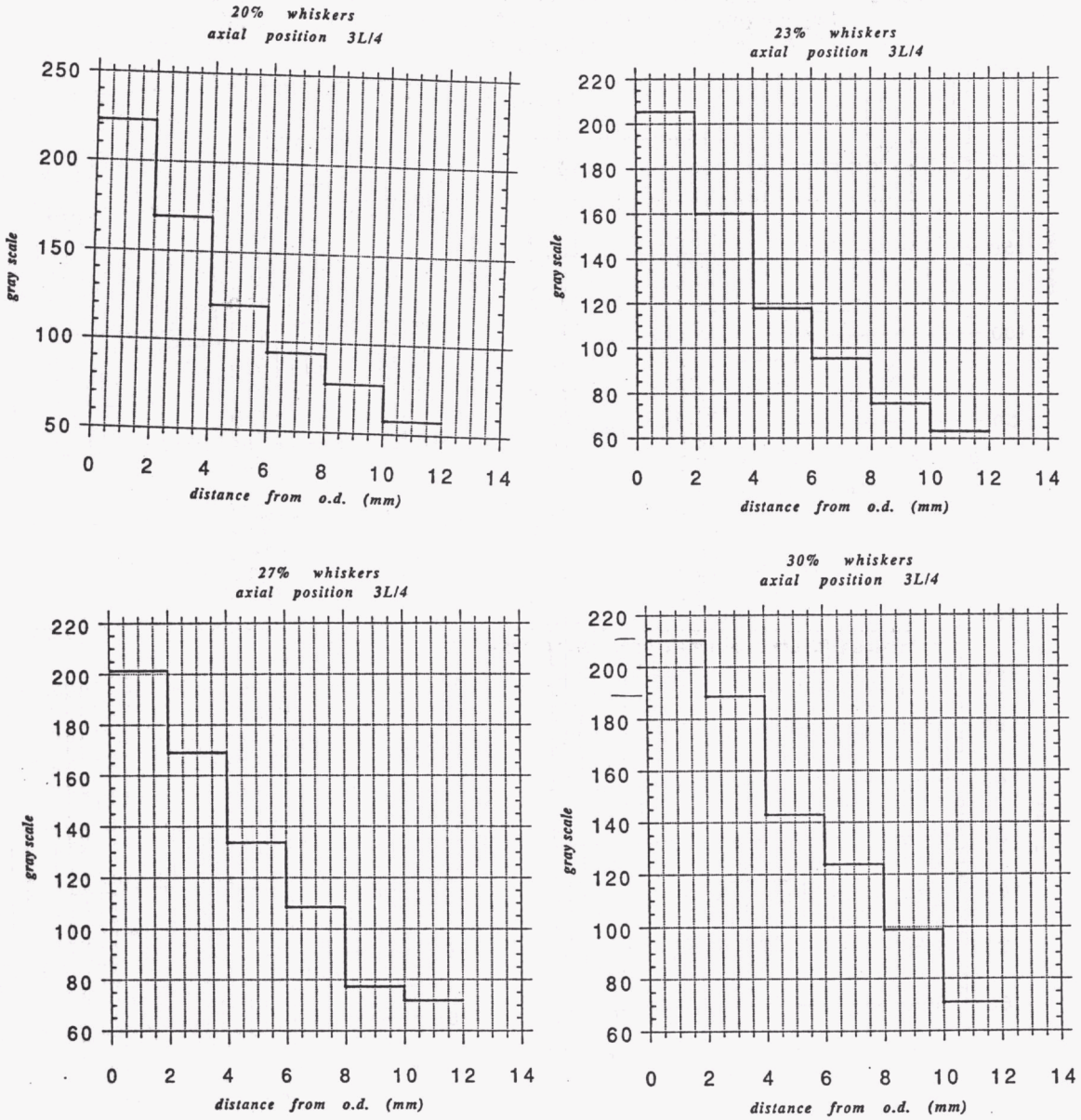

Fig. 6. Apparent radial density variation of pressure slip-cast SiC(w)/Si_3N_4 at elevation 3L/4

Table 3. Difference in X-ray CT image gray-scale density as a function of radial position and axial position for pressure slip-cast $SiC(w)/Si_3N_4$*

Axial position	Whisker concentration (wt.%)			
	20	23	27	30
L/4	52.9	19.8	33.5	43.4
	42.6	36.4	32.5	30.0
	22.4	28.6	18.8	10.1
	21.4	33.3	27.5	25.3
	12.8	10.8	10.0	7.4
L/2	52.2	37.2	32.2	8.3
	35.2	41.8	30.6	30.5
	27.6	23.2	21.4	20.9
	26.8	23.7	23.3	16.8
	9.7	13.8	7.5	22.4
3L/4	53.5	45.3	32.2	21.8
	49.3	42.2	35.4	45.7
	26.0	22.6	25.2	19.0
	16.9	19.8	31.2	25.0
	19.9	12.3	5.5	28.0

*These differences are measured starting from O.D.

Nuclear Magnetic Resonance Imaging – S. L. Dieckman
A. C. Raptis, W. A. Ellingson (Argonne National Laboratory),
and H. Yeh and J. P. Pollinger (Garrett Ceramic Components
of Allied-Signal Aerospace Corporation)

Objective/Scope

The objectives of this task are to: (1) utilize NMR imaging techniques to study the distribution of whiskers and other possible variations in composite pressure slip-cast green-state (as cast) billets; (2) conduct destructive analysis of the same billets (to be performed by Garrett Ceramic Components a Division of Allied Signal Corp.); (3) correlate the results obtained from the NMR imaging techniques with those obtained from both the 3-D X-ray and the optical microscopy.

Technical Highlights

In the previous reporting period, images of a small section of an as-cast benzene-imbibed composite specimen was acquired using 3-D back-projection techniques. These techniques can generally provide high spatial resolution, approaching 5 μm for materials with narrow spectroscopic NMR line widths. Additionally, the technique provides cubic voxels and can be advantageously applied to both narrow and broad line width materials. However, while it was possible to image rather small specimens in ANL's current imaging system using the 3-D back-projection technique, physical limitations in both the magnet bore size and the available sampling time prohibit the application these techniques to large specimens. Since the green-state as-cast specimens (produced by Garrett Ceramic Components, a division of Allied-Signal Aerospace Corp.) are cylindrical shaped 25 mm in diameter and 41 mm long, they approximate an infinite sample when compared to the region of high magnetic field homogeneity.

To circumvent this difficulty, a 3-D planar (slice-selected) gradient recalled echo imaging sequence, generally implemented for medical diagnostic purposes, was implemented. The pulse technique provides the ability to electronically select a planar region of interest (a slice) to be imaged. This technique has several rather significant advantages over 3-D back-projection imaging by providing increased spatial resolution in the 2-D plane of interest while significantly reducing data acquisition times. Additionally, the acquired and reconstructed data sets are much more compact, and they require a relatively simplistic reconstruction algorithm to obtain the final image. However there are several disadvantages of the gradient recalled technique. These main disadvantages include providing lower resolution in the slice selected direction, providing data only from within the plane, and requiring that the specimen have moderate to narrow NMR spectroscopic line widths (generally less than 1 KHz).

The gradient echo recalled pulse sequence was implemented to provide slice selection along the longitudinal axis of the specimens (along Z), while phase and frequency encoding were performed along the X and Y gradient directions respectively, see Fig. 1. The effectiveness of the slice selection methodology was demonstrated by imaging a cylindrical phantom consisting of water filled holes which were drilled to varying depths, see schematic diagram in Fig. 2A. A planar slice selected from a region near the top of the phantom shows all the holes with fluid (Fig. 2B), while a slice selected from within the center of the phantom shows fewer water filled holes (Fig. 2C).

The GRE pulse technique provides the ability to acquire data in the form of a series of narrow 2-D slices from the 3-D object. This is performed by electronically selecting the planar region of interest (the slice), then encoding the selected plane both in frequency and phase. Accurate selection of plane thickness to and its location will be critical for correct sampling and the ultimate interpretation of the data. A key area of concern is thus establishing the ability to select of the planar excitation.

Planar excitation is performed by application of a selective, shaped RF pulse (with a narrow excitation bandwidth) in the presence of a magnetic field gradient. An ideal excitation pulse would excite only a narrow frequency range and thus a thin spatial region within the specimen. Previously reported image data were acquired using square RF pulses. These pulses provides a excitation response similar to a sinc function in the spatial domain. The signal from the excited sinc side lobes blur the image by folding into the 2-D plane of interest. This results is a loss of contrast and sensitivity in the imaged plane.

In this period, Gaussian shaped RF pulses were evaluated for slice selectivity. These pulses provide a Gaussian RF excitation response in the frequency domain, which is void of unwanted side lobes. The excitation bandwidths of the pulses were empirically determined by the measurement of the NMR signal intensity after the RF selection pulse as a function of difference between the nuclear resonance frequency of the specimen and the excitation frequency. Evaluations were performed for three Gaussian RF pulses with peak widths of 2, 4, and 6 ms. A plot of integrated signal amplitude as a function of frequency for three experiments shown in Fig. 3. Using the Gaussian excitation pulse, excitation bandwidths can be narrow with little fold-over from outside the desired slice. Currently, image slices of 1 mm thick can be obtained using this technique.

Additionally, significant effort was expended to increase the signal-to-noise ratio in the images. The benzene-imbibed specimen has an intrinsic fwhm ^{1}H NMR spectral line width (Δf) of approximately 500 Hz. Since the observable magnetization decays as a first order exponential, with a decay rate of $1/(\pi\Delta f)$, long delay times between the RF pulse and data acquisition significantly decrease the amount of observable signal. Efforts were made to shorten the delay time by decreasing the time allocated for phase encoding (X gradient) and echo dephasing pulses (Y gradient). This delay time was reduced from 2.8 to 0.75 ms.

Gradient recalled echo (GRE) imaging techniques were implemented and demonstrated on the benzene-imbibed as-cast composite specimens. These preliminary results showed that there appears to be a radial porosity variation with lower porosity near the outer boundary. This qualitatively agrees with the X-ray CT results which show lower density near the center of the 25 mm diameter specimen and higher density near the specimen. However, upon repair of the local Vax computer system, and the reconstruction of additional images, it was evident that little sensitivity to internal benzene was achieved. Acquisition of data with this technique resulted in images of the benzene existing on the surface (on the surface of the specimen) rather than images of benzene existing in the open porosity within the sample. This is evident from Fig. 4B which was acquired from the interior portion of the cylinder.

It was determined that the main cause of the discrepancy between the expected signal and the experimental measurement is due to the difference in the magnetic susceptibility of the benzene and the solid Si_3N_4. These susceptibility differences cause intense (approximately 1 Gauss) and but localized differences in the magnetic field seen by the protons on the benzene. Since the spectral frequency is dependent upon the static magnetic field, this effect results in a broadening in the benzene spectral linewidth and a much quicker decay of the signal. The quicker decay resulted in a loss of benzene signal except in areas where the benzene is free of the localized magnetic field distortions (i.e. on the surface of the specimen). This phenomena is known and has been observed in other solution/solid systems, such as benzene-imbibed alumina, but generally several orders of magnitude less severe.

While the quick decay of the signal is a problem, a the signal can be recovered by refocussing the magnetization with a 180 degree RF inversion pulse. This is effective because the magnetization is dephased in a coherent manor. Note that this is effective when the refocussing inversion pulse occurs before natural benzene diffusion moves the molecule into a difference magnetic environment. Spectroscopic (RF generated spin-echo) experiments which were performed to attempt to refocus the magnetization were effective. Imaging experiments incorporating the spin-echo sequence are currently underway using this technique. Attempts to correlate these results with those obtained from X-ray CT and destructive testing will be performed in the months ahead.

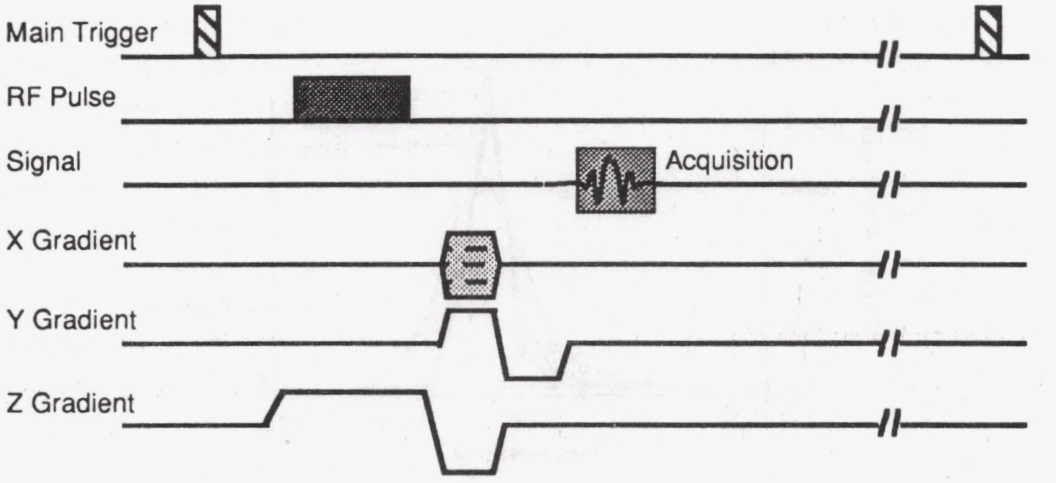

Fig. 1. Schematic drawing of the gradient recalled echo imaging sequence employed in this work.

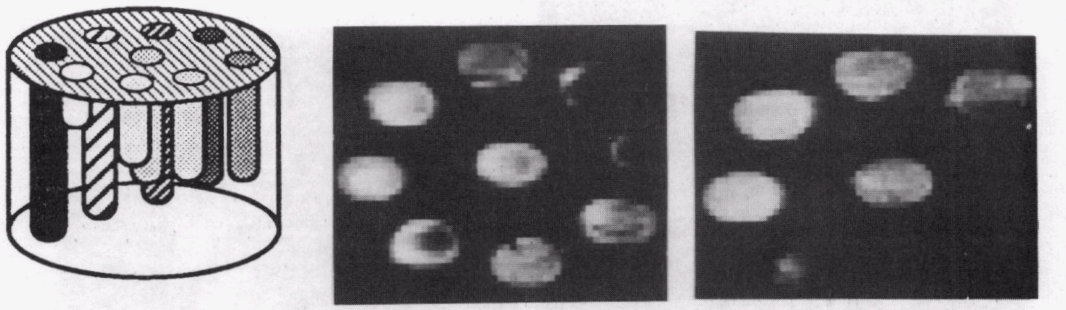

(A) (B) (C)

Fig. 2. (A) Schematic drawing of slice selection phantom showing holes of various depths filled with water, and two-dimensional NMR gradient recalled images acquired from (B) the top and (C) middle of the phantom respectively

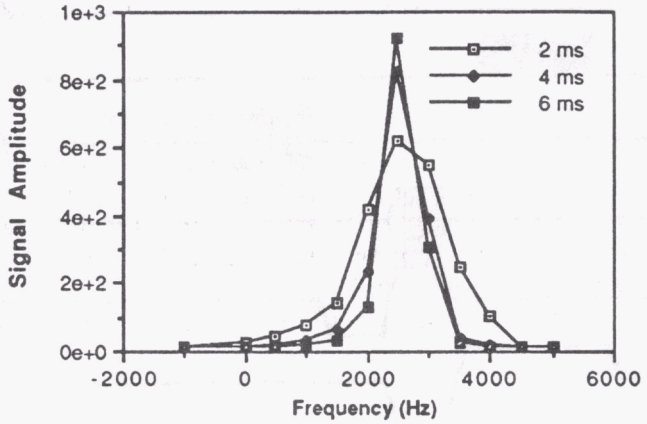

Fig.3. Plots of ^{1}H NMR integrated signal amplitude as a function of the frequency difference between the intrinsic nuclear resonance frequency and RF excitation frequency

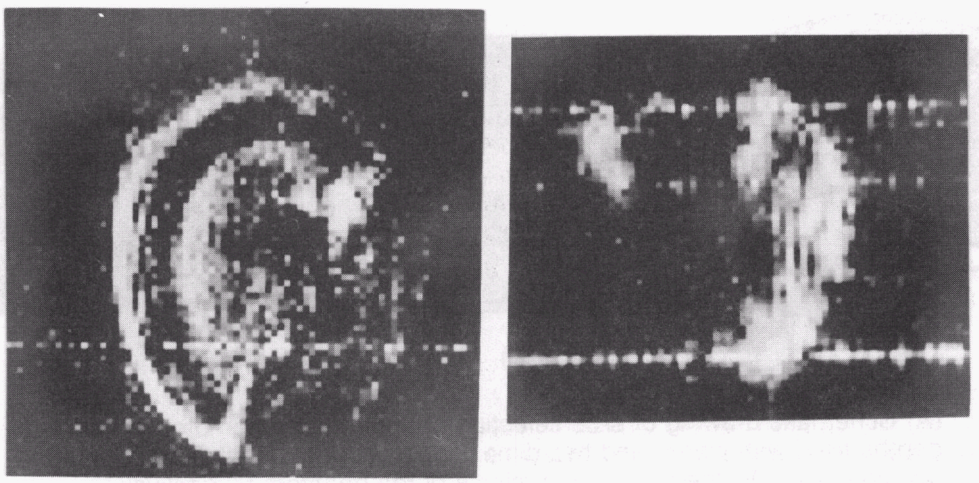

(A) (B)

Fig. 4. Two-dimensional slice selected NMR images of the 20 wt% whisker composite benzene-imbibed as-cast billet acquired at ambient conditions using the gradient recalled echo sequence shown in Fig. 1. The slices were acquired (A) near the specimens end, and (B) near the center of the cylinder

PHYSICOCHEMICAL CHARACTERIZATION AND SURFACE MODIFICATION OF SILICON NITRIDE CERAMIC POWDERS - Prof. Marc A. Anderson (University of Wisconsin - Madison)

Objective/scope

This project is designed to fulfill two primary objectives:

1. characterization of the aqueous surface chemistry of silicon nitride, which also requires the development of a standard for mobility measurements and participation in a round-robin characterization of this standard; and
2. spectroscopic characterization of aqueous suspensions of silicon nitride.

Technical highlights

Our work in the past six months has focused on two areas:

1. perform round robin investigations of the electrophoretic mobility of silicon nitride suspensions; and
2. continue investigating the kinetics of hydrolysis for silicon nitride powder (Ube E-10) as a function of pH.

Round Robin Analysis of Mobility Measurements:

Two Si_3N_4 Electrophoretic Mobility Studies (SEMS 1 and 2) were performed using experimental protocols similar to those developed for the earlier mobility studies of phosphated goethite. In SEMS 1, aqueous suspensions of silicon nitride powder (Ube E-10) were prepared at Rutgers Univ. and distributed to all participants. Five separate sets of measurements were performed on these suspensions. Results within each individual set of measurements could be compared. These results suggest that reasonable agreement in measurement values was obtained by the participants for acidic suspensions. However, the mobilities of alkaline suspensions appeared to differ significantly among the participants. Variations were observed that were on the order of 3 to 4 x 10^{-8} $m^2V^{-1}sec^{-1}$, some ten times larger than the variations observed in acidic suspensions. It was not possible to compare these variations across the different sets of measurements because the suspensions aged rapidly.

A modified protocol was developed for performing SEMS 2 that was designed to minimize measurement variations caused by the aging of the suspensions. Thus, pre-measured samples of silicon nitride powder were shipped from Rutgers to all the participants. Each participant was responsible for preparing all suspensions needed for each set of measurements, following a set of guidelines that were provided. (These guidelines should be described in the report submitted by Rutgers Univ.) Since each suspension was prepared about 24 h before

use, suspension aging effects were significantly minimized. Thus, it was possible to directly compare all the measurements performed in SEMS 2. Although the data are still being analyzed, it appears that the variations in mobility that were noted above are valid. We still cannot explain the large differences that we observed in the measured mobilities in alkaline suspensions.

Aging of Aqueous Suspensions of Silicon Nitride:

Studies for the past few months have focused on investigating the kinetics of dissolution as a function of pH, especially attempting to clarify the reactions that occur at the surface of Ube E-10 silicon nitride powder during hydrolysis and dissolution. In particular, potentiometric titrations of silicon nitride suspensions were conducted to monitor the development of charge on the surface of the powder as a function of pH, ionic strength and pretreatment conditions. The suspensions were treated in two ways. In one case, an aqueous suspension (pH 8) of the dry powder (stored under air in a closed container for ca. 2 years) was prepared. In the other case, the dry powder was washed in an alkaline medium (about pH 10) several times before the washed powder was suspended in water (pH 9.7). Both potentiometric titrations were performed under nitrogen using the Matec ESA 8000 (Electrokinetic Sonic Amplitude) System. Each titration lasted about one hour and involved measurements made at three different ionic strengths, leading to a set of three titration curves for each system. Some titration hysteresis was observed, so that neither set of curves intersected exactly at one point. However, the intersection points were no more than 0.4 pH units apart. Thus, we refer to an average of these intersection points as a common intersection point (CIP).

Earlier electrophoretic mobility studies of similarly prepared suspensions indicated that alkaline washing of the powder shifted the isoelectric point (IEP) of the powder to a higher pH value (from about 6.6 to about 8.6). The CIP for the untreated suspension was about 6.5, and the CIP for the washed suspension was about 8.5. Since the CIP and the IEP for the untreated suspension were very close, no specific adsorption of cations or anions occurred on the surface of the powder. Thus, one could state that the zero point of charge (ZPC) for the untreated powder was about 6.6 (see J. Lyklema, "Adsorption of Small Ions", Chap. 5 (pp. 223-246) in Adsorption at the Solid/Liquid Interface (G.D. Parfitt and C.H. Rochester, Eds.), Academic Press, New York, 1983 for further discussion). Similarly, the ZPC for the washed suspension was about 8.5 with no specific adsorption of cations or anions. The change in ZPC that was observed on washing is attributed to a change in the actual surface rather than specific adsorption of some ion. We had earlier suggested that alkaline washing of the silicon nitride surface was removing silica and leaving a more pristine silicon nitride. These titration experiments further corroborate that earlier hypothesis.

CIR-FTIR Spectroscopy of Silicon Nitride Suspensions:

No further work has been performed because no silicon nitride powder with an acceptably high surface area is available. Efforts to find a suitable powder are continuing.

Status of milestones

1. Complete round robin characterization of "benchmark" colloid. Complete.
2. Complete initial round robin mobility testing of silicon nitride. Complete.
3. Complete round robin mobility testing of silicon nitride. Expected completion: Dec. 31, 1991. Further delayed to allow possible industrial participation in at least one round robin.
4. Complete peak assignments for CIR-FTIR spectra of aqueous suspensions of silicon nitride. Since a supplier of high surface area ($> 25\ m^2/g$) silicon nitride powder has not been located, we do not expect to be able to perform a peak assignment study of CIR-FTIR spectra of aqueous suspensions of silicon nitride during the remainder of this project. Thus, we will probably not be able to complete this milestone.

Publications

None.

Surface Adsorption

James H. Adair (Materials Science and Engineering, University of Florida)

Objective/scope

This project represents a coordinated effort among ORNL and three university laboratories (WBS Elements 3.5.1.7, 3.5.1.8, 3.1.5.9, and 3.5.2.0). The purpose of this project (WBS 3.1.5.9) is to study the surface chemical interaction of silicon nitride powders in aqueous and non-aqueous enviroments and to study surface chemical modification of the material, and, in particular, to understand the acid - base nature of the silicon nitride - solvent interface.

Background

As a heat resistant material, silicon nitride has applications or potential applications in ceramic engines, heat exchangers, turbine blades, and high frequency combustion crucibles. The variety of current and potential applications for silicon nitride require a range of forming operations to fabricate the specific components. Most of the forming processes to achieve the range of shapes for silicon nitride components require the use of organic additives. For example, precombustion chambers for diesel engines and turbine blades are usually injection molded using highly filled thermoplastic polymers while tubular heat exchangers are extruded with less polymer as binder and usually the binder is significantly different in terms of functional groups and properties than those polymers used for injection molding.

Ceramic processing often involves the suspension of ceramic powders in an organic solvent rather than water to promote separation or dispersion of the ceramic particles during forming operations. The use of non-aqueous solvents is particularly important in the processing of nonoxide ceramics such as silicon carbide, silicon nitride, and aluminum nitride because these compounds are subject to reactions with water to form oxides or hydroxides surface groups or, in the case of aluminum nitride, uniform transformation to the hydroxide. Yet little fundamental data exists on the interaction of ceramic particle surfaces with the organic species in organic solvents. Furthermore, the role that the surface composition of the ceramic particle plays in the dispersion and interaction of particles in solvents is not well established. The current study is designed to determine the nature of the surface interactions of silicon nitride with organic solvents and solutes.

Approach

There are four participants in the overall project: ORNL and three universities, the University of Florida (UF), the University of Wisconsin, and Rutgers University.

The UF project is composed of two distinct elements:

1. Participation in a round robin characterization of electrophoretic mobility and acid-base character in aqueous suspension to be conducted by all participants.

2. Special projects at UF composed of the following activities:

The UF workplan is based on five tasks: Task 1 to participate in round-robin particle electrophoretic mobility measurements, Task 2 to determine the nature of reactive sites on the silicon nitride surface, Task 3 to modify the chemistry of the silicon nitride interface using organic species, Task 4 to determine the rheological and dispersion properties of the non-aqueous silicon nitride suspensions, and Task 5 to ensure transfer technology to ORNL via meetings and reports.

Technical progress

FY 1989

Round Robin - Electrophoresis - Goethite standards prepared at Wisconsin were evaluated as part of the UF participation in the round robin.

Reactions at the Silicon Nitride - Solution Interface - A study was conducted to determine the extent of aqueous reactions at the silicon nitride - water interface. It was demonstrated that up to 27 days are required to stabilize reactions at the interface as indicated by pH and particle electrophoresis measurements. A semi-automatic titrator was also purchased and set-up to use acid - base titrations to study the silicon nitride - solvent interface. A particular emphasis of this work was on the non-aqueous potentiometric and conductometric titration to determine the relative strength of acid and base sites on the silicon nitride surface.

FY 1990

Round Robin - Electrophoresis and pH measurements - The round robin electrophoresis on the goethite standards prepared at Wisconsin indicated several interesting features. The isoelectric points determined by each of the participants in the round robin were similar, but measured pH values displayed considerable scatter at higher pH (e.g., pH 8). The suspected influence of dissolved CO_2 and adducts and methods to overcome the effect of these dissolved species are currently under investigation at UF.

Reactions at the Silicon Nitride - Solution Interface - The use of potentiometric titrations in non-aqueous solvents indicates that there are several different kinds of acid and base sites on the silicon nitride depending on the prior enviromental history of the powder. The results are generally consistent with potentiometric titrations used to evaluate the silicon dioxide surface. However, potentiometric titrations could not be reproduced because of a variety of problems inherent to the technique.

FY 1991

Round robin - The first test of the silicon nitride powders was completed and evaluated. The University of Florida team did not participate in this round because of instrument problems. A second and third round of tests on silicon nitride have been conducted and have been evaluated at Rutgers. The final, approved test procedure will be written. Industrial participation will be invited.

Reactions at the Silicon Nitride - Solution Interface - The strengths of the acid and base sites at the silicon nitride surface are being estimated based on calculated relative bond strengths and the non-aqueous titrations. The surface of silicon nitride is also being modified using metal oragnic coatings and polymeric grafting techniques selected to simultaneously ensure both dispersion and inhibition of oxidation reactions.

Potentiometric titrations of silicon nitride powder in non-aqueous suspension are difficult to reproduce for a variety of reasons. The glass pH electrodes are difficult to stabilize in the non-aqueous environment and miilivolt drift is a continual problem. The relatively low surface area of the silicon nitride powder requires a characterization technique with greater sensitivity than the non-aqueous potentiometric titration. Similar to aqueous titrations, powders with specific surface areas greater than 50 $m^2 \cdot g^{-1}$ are required to provide enough surface groups to ensure rapid response to acid or base additions and minimize the influence of drift in electrode response created by dehydration of the electrode's glass membrane. Therefore, while potentiometric titrations of non-aqueous solutions will continue to provide insight into reactions among solution species, attempts to titrate surface groups have been suspended in lieu of more reliable and reproducible electrokinetic techniques.

Particle electrophoresis in isopropanol indicates that measureable surface charge is present on the surfaces of as-received silicon nitride in as-received isopropanol. The initial particle electrophoresis of as-received silicon nitride (UBE E-10) indicated that the particles are positively charged with zeta potentials of approximately 3 mV. This indicates that there are some basic groups on the surface of the silicon nitride basic enough to attract the proton generated by the autoprotolysis of the isopropanol (pK=20.6).

Current work has evaluated the zeta potentials and corresponding state of dispersion of silicon nitride suspensions in 1,4 dioxane (a neutral solvent) and isopropanol, a solvent capable of disassociation into isopropoxide and a proton. The dioxane is generally an undesirable solvent for ceramic processing because of environmental concerns, but has been used in the present work to determine the effect of a neutral solvent that does not contain any reactive protons. Perchloric acid and pyridine have been used to provide protons and act as a Lewis base, respectively to react with groups on the silicon nitride surface. Potassium nitrate in a 10^{-3} M concentration was used as an indifferent electrolyte.

Zeta potentials in isopropanol for a given set of conditions are greater in magnitude than values in the dioxane. The zeta potentials seen in Figure 1 for the suspensions containing pyridine are relatively small up to 0.1 M pyridine where a positive surface charge is indicated. It is uncertain at the present how a positive surface charge is obtained at the elevated pyridine concentration. However, the modest electrophoretic mobilities at lower pyridine concentrations may be due to

either the pyridine being a weaker base than the corresponding surface base or indicate that there are relatively few acidic groups on the as-received silicon nitride surface. In contrast to the relatively weak effects seen with pyridine additions, perchloric acid imparts a relatively large positive charge to the surface of the silicon nitride surfaces. This indicates that the protons provided by the acid interact with a relatively strong basic surface site(s) to create a relatively large surface charge. Electrophoretic mobility measurements are continuing with a variety of acidic and basic additives with a range of acid and base strengths to create a data base and hierarchy of acid and base strength to determine the relative strength of surface sites on silicon nitride.

The relative state of dispersion for the silicon nitride particles in the non-aqueous solvents was estimated based on the particle size distribution determined using a sedimentation particle sizing method (Horiba CAPA 700). As expected from DLVO theory, the suspensions with the highest magnitude of zeta potential had the smallest median particle size as shown in Figure 2. However, the particles in suspension in the isopropanol had the greatest dispersion in all cases regardless of whether perchloric acid or pyridine was present. Thus, the initial data indicate that solvent selection is critically important in controlling the state of dispersion of the powder with the the solvent capable of proton and alkoxide generation providing the greatest inherent stability in this preliminary evaluation. Other effects such as solvent dieletric contant on relative particle dispersion will be evaluated in future studies.

The contribution of the electrostatic forces toward dispersion of the silicon nitride in this non-aqueous solvent are currently being estimated as are the effects that trace amounts of water have on the formation of surface charge in the non-aqueous solvents. A general computer program, DLVO, designed in its current version to operate on personal computers, will be used to calculate the theoretical state of dispersion to be compared against experiemntally determined values. These studies combined with novel dispersion techniques are being used to develop guidelines for the dispersion of silicon nitride particles in non-aqueous solvents.

Status of milestone

The program is on schedule.

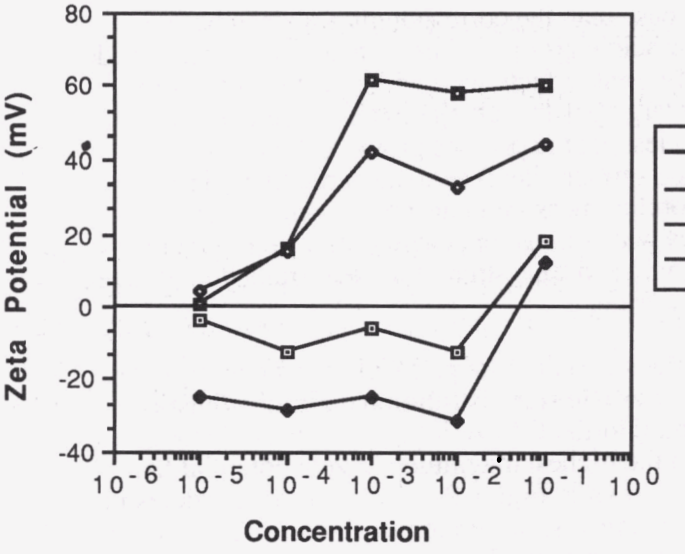

Figure 1

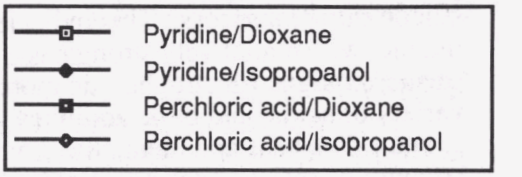

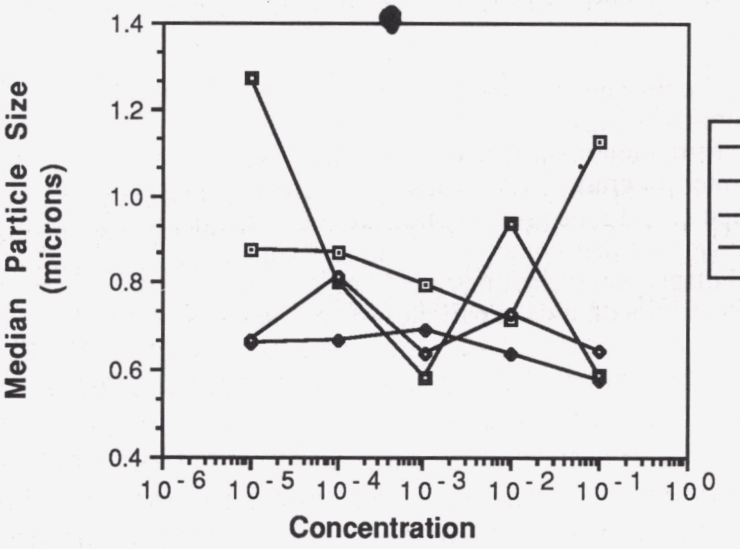

Figure 2

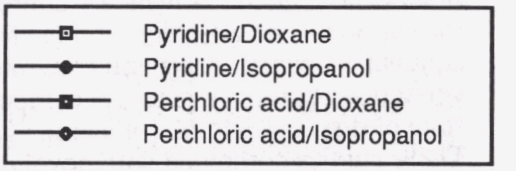

Physicochemical Characterization and Surface Modification of Silicon Nitride Ceramic Powders

J.-F. Wang, R. E. Riman, and D. J. Shanefield (Rutgers University, Piscataway, NJ)

Objective/scope

The purpose of this effort is to (1) identify and characterize those aspects of the chemistry and physics of the ceramic powder and powder/solvent interface that control processing, (2) develop standard methods of analysis for item (1), and (3) develop procedures for writing specifications for ceramic powders to include any methods of analysis developed in this project.

Technical highlights

The work that has been done or under investigation in the past six months is summarized as follows:

(1) The first and second electrophoretic mobility round robin studies on UBE SN E-10 silicon nitride powder (SEMS1 and SEMS2) were completed. There were four participants involved in these two round robin studies, namely, Oak Ridge National Laboratory, University of Florida, University of Wisconsin, and Rutgers University.

Highly scattered electrophoretic mobility (μ) data was obtained for SEMS1. That was due to the inadequate control of solids loading during the sample preparation, and subsequently followed by the strong aging effect of silicon nitride powder in aqueous solution. The pH and μ measurements, therefore, were influenced by the above causes greatly.

SEMS2 was designed to understand the reproducibility of the instrumentation and to minimize the solids loading and aging effects on the pH and μ measurements of silicon nitride powder in aqueous solution. The pH measurements were found to be more consistent than that in SEMS1. However, highly scattered μ data were measured for the samples at high pH values. This could be attributed to instrumental factors, because the Zetasizer II consistently gave a higher value than other instruments, especially at a high pH range.

(2) Five ball milled silicon nitride slips with different sintering aids and dispersant addition conditions were prepared and characterized using microelectrophoresis. The uniformity of the coating was characterized using transmission electron microscopy (TEM) and energy dispersive spectroscopy (EDS).

First silicon nitride electrophoretic mobility study (SEMS1):

The SEMS1 started from 3/20 (sample prepared at Rutgers University) and ended on 5/7/91. In total, four simultaneous measurements, on various aging times (i.e., 2, 3, 4, and 7 weeks) among four participating laboratories were taken. The aging effect on pH and μ measurements for UBE SN E-10 powder was found to be strong in either 0.01 or 0.05M KNO_3 solution. Scattered pH and μ values were obtained for SEMS1, especially in 0.01M KNO_3 solution.

The sample preparation of the concentrated (5 vol%) UBE SN E-10 suspension and the reconstitution procedure of its dilute (0.01 vol%) suspension for EM measurement were described in the last semi-annual report dated 5/7/91. Although the 5 vol% UBE SN E-10 could be completely homogenized using high shear mechanical mixing, the suspension was unstable. This instability led to a solids loading variation among samples. Since the solution pH increases with increase in solids loading of UBE SN E-10 suspension, the deviation of the solids loading would cause a spread of both pH and μ measurements.

Several referencing points using GEMS3 goethite sample in 0.01M KNO_3 solution were taken prior to the μ measurement on UBE SN E-10 suspensions (Figures 1 & 2). The distribution of the pH measurement on referencing points from three laboratories at various aging times was 3.41 ± 0.12 and that for the μ was $2.47\pm0.15\times10^{-8}m^2/Vs$. Upon comparison of this data with that obtained from GEMS3 (i.e., $pH=3.41\pm0.08$ and $\mu=2.35\pm0.12\times10^{-8}m^2/Vs$), we observed a significant disagreement on μ measurement. Therefore, the experimental factors could be contributing a great deal of variation in this round robin study.

Figure 1 shows that the scattered μ data of UBE SN E-10 suspension in 0.01M KNO_3 was a function of pH, aging time, instrumentation, and probably the solids loading. The range of isoelectric points (IEP) of aged UBE SN E-10 suspensions observed from Figure 1 was wide (e.g., from 4.1 to 7.7). However, the very top curve represented by a thick broken line and with solid squares in Figure 1 was obtained at a different condition than the others. The sample was reconstituted after one week of aging but measured seven weeks later. Its solution chemistry was quite different from the other samples which were reconstituted only one day prior to the μ measurement.

The sample aged as a dilute suspension would leach out more silica from its surface than those concentrated suspensions aged in the same time period. A higher IEP was therefore expected for UBE SN E-10 with less solids loading, which was in good agreement with our early study. If we leave this curve out and treat the data obtained from the University of Florida after 3 weeks of aging of nominal pH=3.5 sample as an outlier, then the IEP range observed was from 5.4 to 6.8, which falls within the

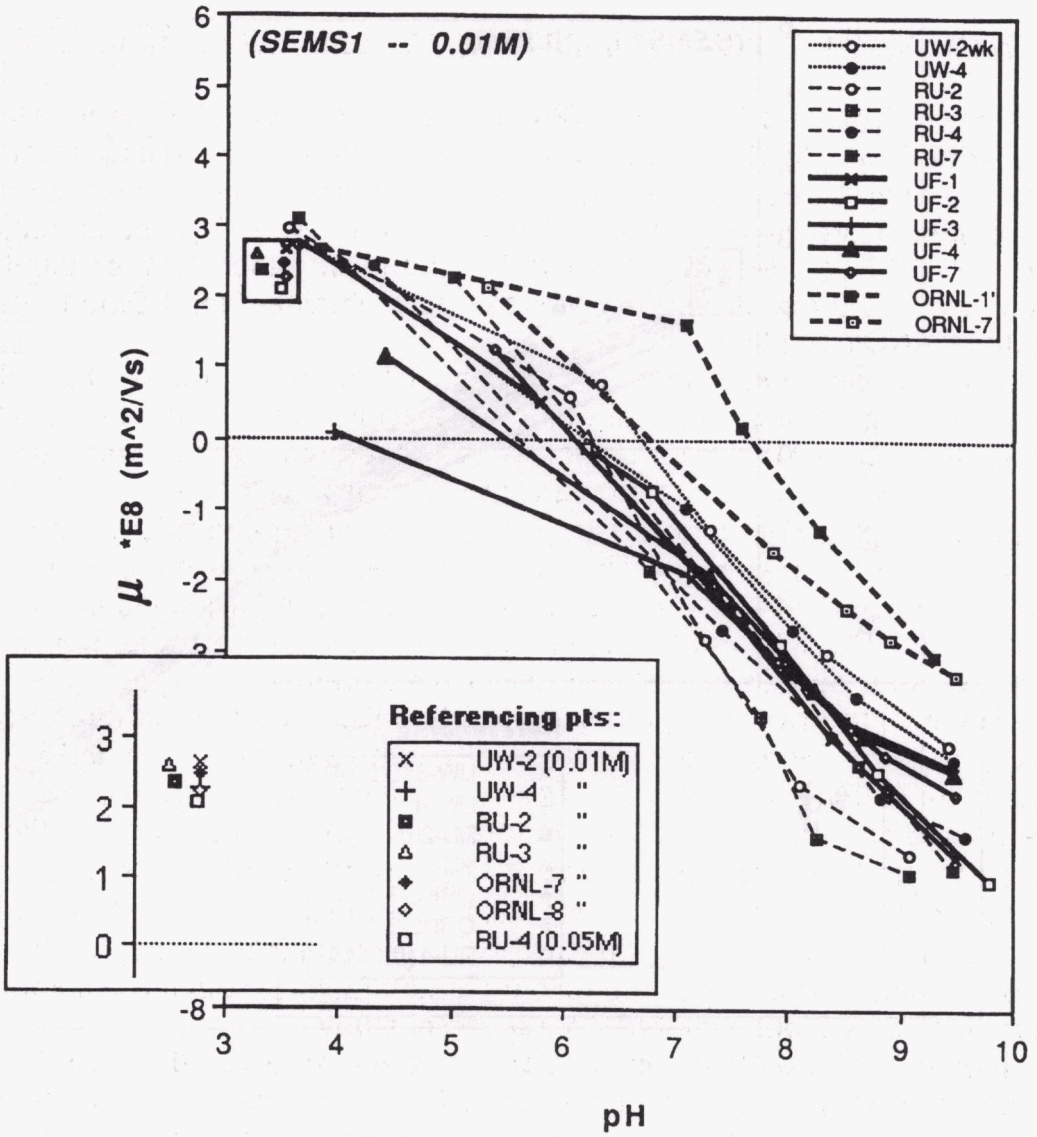

Figure 1. First electrophoretic mobility round robin study on UBE SN E-10 powder in 0.01M KNO_3 solution as a function of aging time and pH.

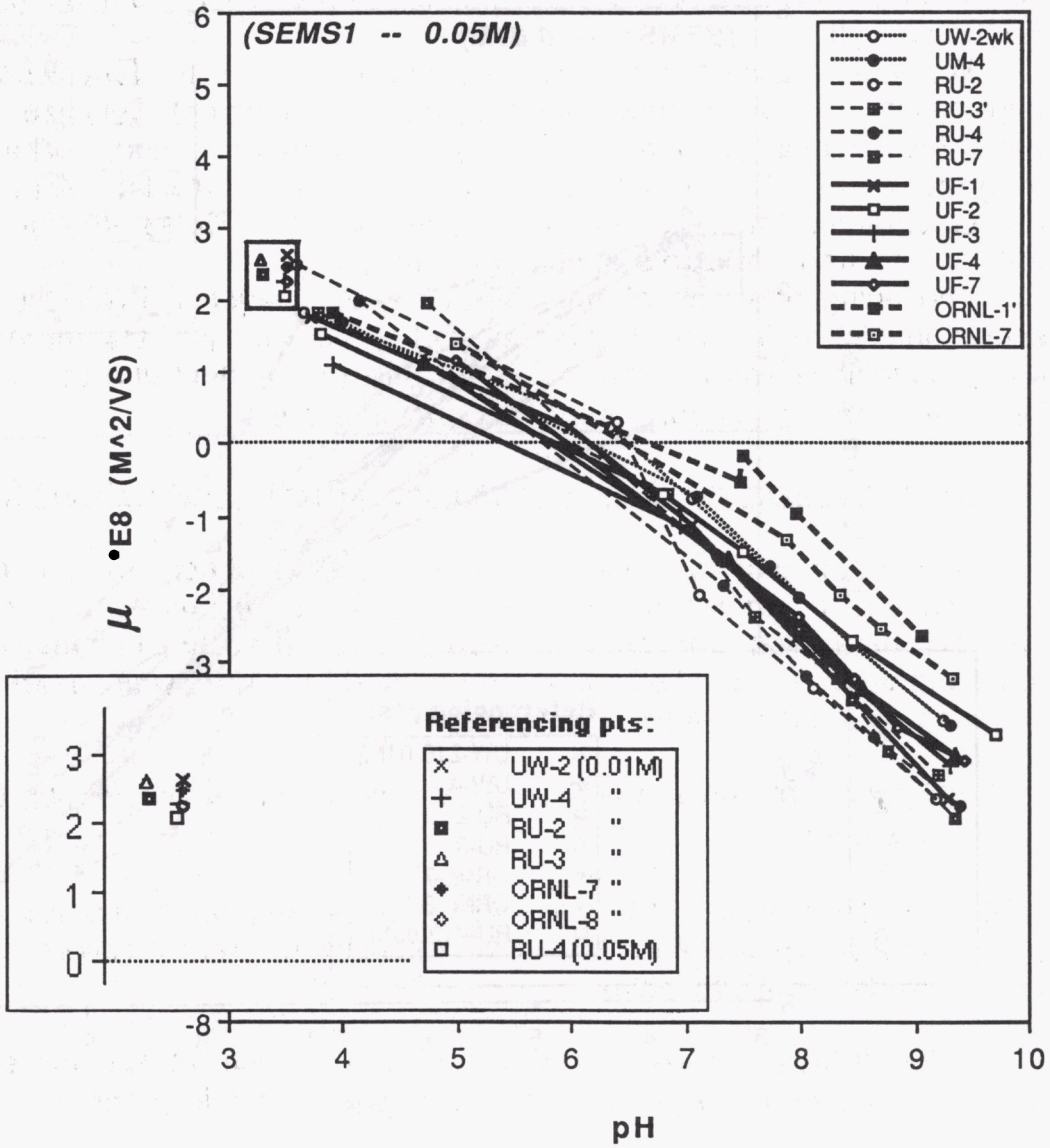

Figure 2. First electrophoretic mobility round robin study on UBE SN E-10 powder in 0.05M KNO_3 solution as a function of aging time and pH.

same range as UBE SN E-10 aged in 0.05M KNO_3 solution (i.e., 5.4 to 6.7)(Figure 2).

We also noticed that the magnitude of the μ data was strongly dependent on the instrumentation used. The Malvern Zetasizer II always gave the highest μ data, especially in the basic media. The order of magnitude of the μ observed at the basic media from different instrumentations was as follows: Zetasizer II > Delsa 400 > Pen Kem 3000. The trend in acidic media was not clear.

The aging effect on pH of UBE SN E-10 powder in KNO_3 solution was shown in Figure 3. The lower the starting solution pH, the more important aging conditions were. This could be due to the neutralization of the Si_2-NH groups on the silicon nitride powder surfaces.

Second silicon nitride electrophoretic mobility study (SEMS2):

Due to the strong aging and solids loading effects for the distributed suspensions, a significant problem in obtaining reliable silicon nitride EM and pH data was observed in SEMS1. In order to demonstrate better reproducibility in SEMS2, dry and riffled powder was used and the following guidelines were employed:

1. Rutgers distribute dry UBE E-10 powder riffled in the appropriate quantities.

2. We, as a group, collectively agree on a preparation method where each group prepares their own suspensions from received powder on given dates.

3. For SEMS2, we examine 3 pH points so we can rapidly assess the direction we are going in the final phase of this program.

The SEMS2 started from 7/15 and ended on 7/30/91. In total, three simultaneous measurements, on three given dates (7/16, 7/23, and 7/30) among four participating laboratories were taken.

The SEMS2 was designed to understand the reproducibility of the instrumentation and to minimize the solids loading and aging effects on the pH and μ measurements of silicon nitride powder in aqueous solution. Those effects had given inconsistent results in the previous study, SEMS1. Due to the better control of powder aging time and solids loading in SEMS2, the pH measurements were found to be more consistent than that in SEMS1.

By viewing the clusters of open circles (SEMS2) versus the highly scattered solid circles (SEMS1) in Figure 4, the pH measurements in SEMS2 for samples at specific aging time and pH range were found to be

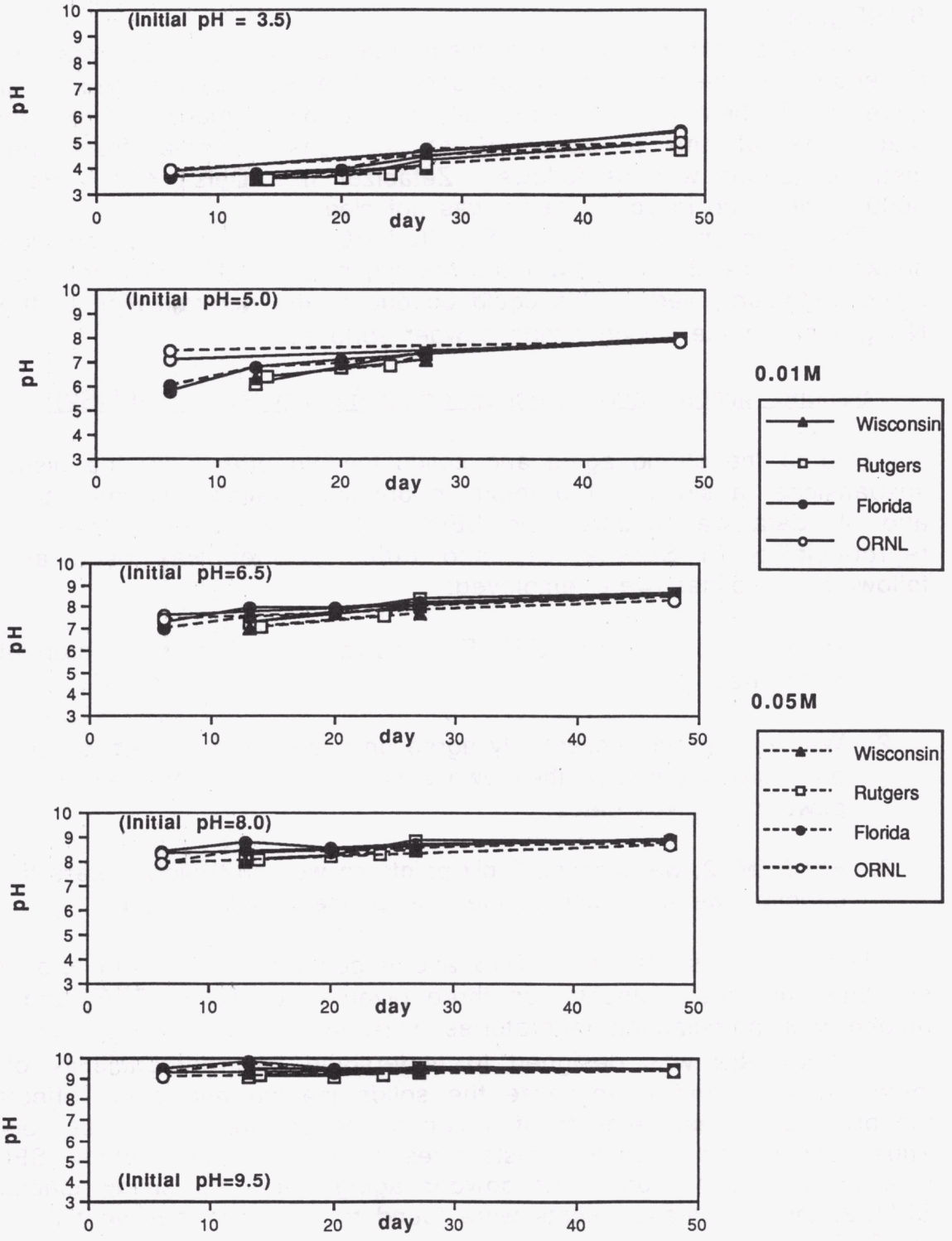

Figure 3. Aging effect on pH of UBE SN E-10 powder in KNO3 solution.

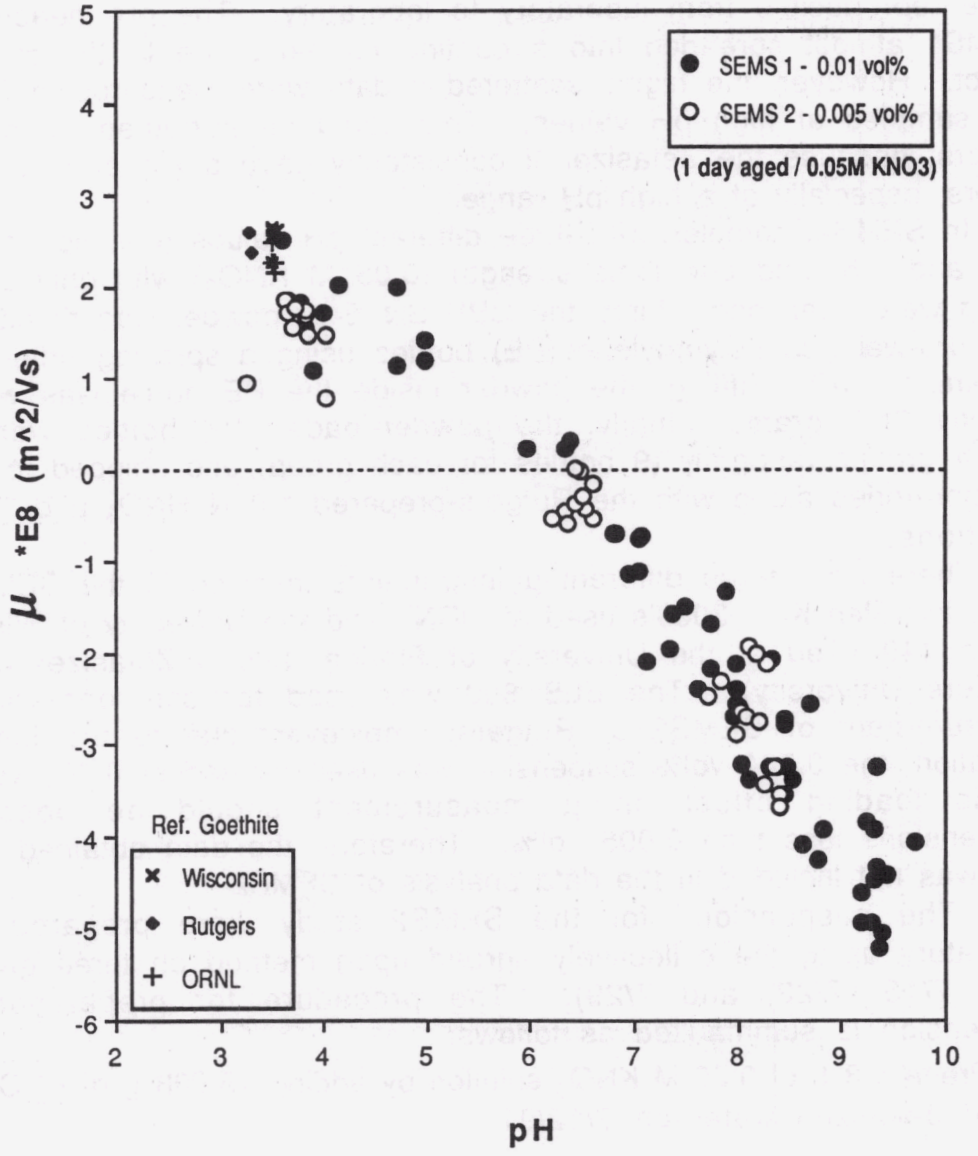

Figure 4. Overall electrophoretic mobility data for SEMS1 and SEMS2 studies of UBE SN E-10 powder in 0.05M KNO_3 solution.

more reproducible from laboratory to laboratory. The pH measurement of SEMS1 almost spreaded into a continuous band due to the strong aging effect. However, the highly scattered μ data were measured in SEMS2 for the samples at high pH values. This could be attributed to instrumental factors, because the Zetasizer II consistently gave a higher value than the others, especially at a high pH range.

In SEMS2, samples with three different pH values (i.e., nominal pH 3.5, 6.0, and 8.5) and one ionic strength (0.05 M KNO_3) with only one day of aging were examined. First, the UBE SN E-10 powder was riffled to empty and pre-weighed polyethylene (PE) bottles using a spinning riffler made by Brinkmann. After riffling, the powder inside the PE bottle was weighed at exactly 31.6 grams. Finally, the powder-loaded PE bottles were divided into 4 groups randomly (9 bottles for each group) and shipped to the other 3 laboratories along with the Rutgers-prepared 1.0 N HNO_3 and 1.0 N KOH solutions.

There were three different μ instruments involved in the SEMS2 study (e.g., two Pen Kem 3000's used at ORNL and the University of Wisconsin, a Delsa 440 used at the University of Florida, and a Zetasizer II used at Rutgers University). The ELS 800 was used for only one round robin measurement of SEMS2 at Rutgers; however, due to the instrumental limitation, the 0.001 vol% suspension was used instead of 0.005 vol%. The solids loading effect on μ measurement should be observed for suspensions less than 0.005 vol%. Therefore, the data obtained from ELS 800 was not included in the data analysis of SEMS2.

The suspensions for the SEMS2 study were prepared in each laboratory using the collectively agreed upon method on three given dates (i.e., 7/15, 7/22, and 7/29). The procedure for preparation of the suspension is summarized as follows:

1. Prepare 3 L of 0.05 M KNO_3 solution by adding 15.203 g of KNO_3 to 3 L of deionized water on 7/12/91.

2. ***Mornings of 7/15, 7/22, & 7/29*** -- **5 vol% suspension preparation:**
   i) add 190 mL of 0.05 M KNO_3 solution to three powder-loaded bottles to prepare 5 vol% suspension and add 1.0 N HNO_3 (A) or 1.0 N KOH (B) solution to prepare suspension at pH 3.5, 6.0, and 8.5, respectively; (i.e., 260 μL of A for pH 3.5, 90 μL of A for pH 6.0, and 110 μL of B for pH 8.5)
   ii) magnetically stir the suspension in the capped PE bottle for 20 min followed by bath sonication for another 15 min; and
   iii) repeat the procedure ii) until 3 bottles of suspensions with different pH values are dispersed.

3. ***Mornings of 7/16, 7/23, & 7/30*** -- **Reconstitution of 0.005 vol% suspension:**
   i) redisperse the three 5 vol%, sonicated suspensions in the sequence of pH 3.5, 6.0, and 8.5 by magnetic stirring for 10 min with bottle cap closed;
   ii) take 0.15 mL of the above redispersed suspension while stirring and store it in an empty, clean, and capped PE bottle;
   iii) centrifuge the remaining suspension from i) at 7,000 rpm for 20 min to obtain the supernatant for reconstitution work; and
   iv) reconstitute a 0.005 vol% suspension by adding 150 mL of the centrifuged supernatant obtained from iii) to the concentrated suspension from ii). --- **Allow 4 hours between reconstituting suspension and making the μ and pH measurements for each sample.**

4. ***Afternoons of 7/16, 7/23, & 7/30*** -- **μ and pH measurements:**
   i) redisperse the 0.005 vol% suspensions in the same sequence of reconstitution using bath sonication for 15 min and then wait for another 10 min prior to the μ and pH measurements;
   ii) measure μ for 5 times and pH for one time for each sample;
   iii) save the remaining sample for later possible aging effect study; and
   iv) Ross Sure-Flow electrode must be used.

Figure 5 shows the overall result of the SEMS2 study, which was similar to that of the GEMS3 study except for a few outliers found at nominal pH 3.5. (The lower the solution pH, the better the consistency, either in pH or μ measurement.) If we neglect those outliers, the IEP data obtained from the three round robins fell in the pH range from 5.72 to 6.18. The magnitude of the μ was heavily dependent on the instrumentation applied, especially at the basic media (Table 1). The different reading of μ for two Pen Kem's used at Wisconsin and ORNL was noted. The higher absolute μ data was found consistently for the University of Wisconsin for both the goethite reference and the silicon nitride powder used in the SEMS2 study (e.g., $\mu_{goethite}=2.60\pm0.03\times10^{-8}m^2/Vs$ from Wisconsin and $\mu_{goethite}=2.22\pm0.06\times10^{-8}m^2/Vs$ from ORNL) (Figure 5).

The Ross electrode was used for every participant and the solids loading was tightly controlled. The deviation in pH measurements could be due to the different amount of acid or base addition. The micropipette used in Rutgers seems to have larger capacity than that used in the other laboratories -- the lowest and highest averaged pH values were obtained at Rutgers for the acidic samples (i.e., pH 3.5 and 6.0) and for the basic samples (i.e., pH 8.5), respectively (Table 2).

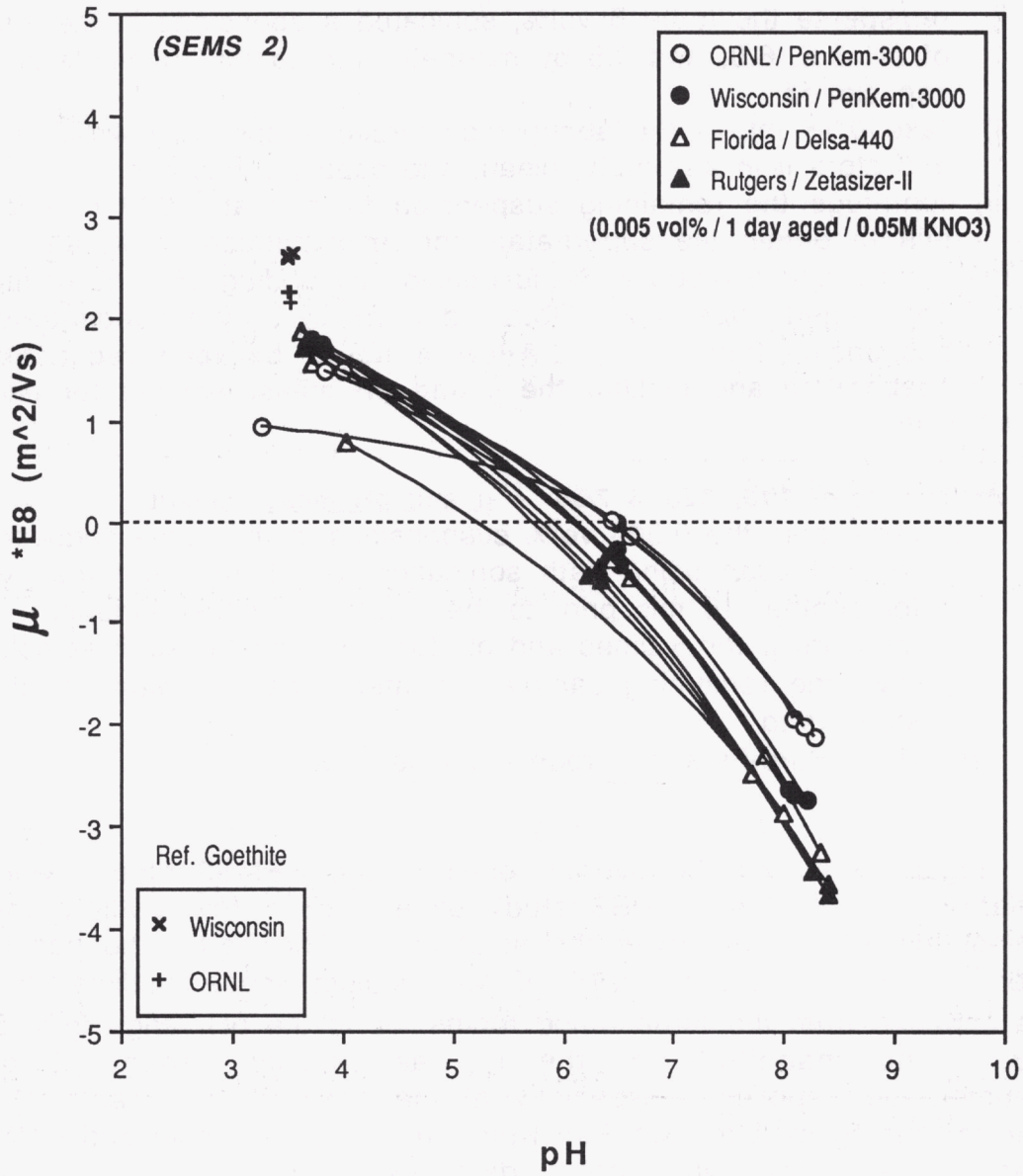

Figure 5. Electrophoretic mobility data for SEMS2 study of UBE SN E-10 powder in 0.05M KNO_3 solution.

Table 1. Instrumental dependency on μ measurement -- SEMS2.

	pH3.5	pH6.0	pH8.5
		$\mu \times 10^8 m^2/Vs$	
Zetasizer II	1.75±0.04	-0.52±0.06	-3.54±0.13
Delsa 440	1.71±0.22	-0.45±0.13	-2.81±0.47
Pen Kem 3000 (UW)	1.73±0.05	-0.35±0.07	-2.69±0.06
Pen Kem 3000 (ORNL)	1.48±0.01	-0.04±0.08	-2.02±0.10
Overall	1.68±0.14*	-0.33±0.21	-2.77±0.60

(* outliers excluded)

Table 2. Pipette capacity dependency on pH measurement -- SEMS2.

	Nominal pH		
	3.5	6.0	8.5
Rutgers	3.68±0.04	6.30±0.07	8.34±0.08
Wisconsin	3.79±0.06	6.48±0.05	8.10±0.09
ORNL	3.93±0.11*	6.51±0.09	8.19±0.09
Florida	3.67±0.06	6.53±0.12	8.05±0.26
Overall	3.76±0.11*	6.44±0.12	8.17±0.17

(* outliers excluded)

Dr. Omatete from ORNL suggested that the use of lower concentration (e.g., 0.2N) of acid or base could reduce the experimental error introduced from the pipette addition for the oncoming SEMS3 study.

The comparison on pH and μ results obtained from SEMS1 and SEMS2 was shown in Figure 4. Due to the well controlled solids loading and fixed aging time used in SEMS2, the spread in pH and μ data was significantly reduced for samples at lower pH. The scattered μ data observed for samples at high pH was suspected to be attributed to instrumental factors.

Having studied the μ data shown in Table 1, the standard deviation observed for each instrument was not so large at nominal pH 8.5 except for the one obtained from Delsa 440. This means that the reproducibility of each instrument was good. But the overall standard deviation was found to be significantly high. The similar phenomenon was also found from the previous round robin studies on goethite and SEMS1. It made us believe that the deviation in μ data at high solution pH could be greatly affected by the instrumentation. For further confirmation on this matter, more carefully designed round robins should be carried out.

Sintering aids and dispersant doped silicon nitride slips:

Five ball milled silicon nitride, UBE SN E-10, slips with different sintering aids and dispersant addition conditions were prepared and characterized using microelectrophoresis. The uniformity of the coating was determined by TEM and EDS. Three of them (i.e., Slips I, II, and III) used iso-propanol (IPA) as the suspending medium and the others (i.e., slips IV and V) were in aqueous solutions.

Slip preparation from iso-propanol

The solids loading of the slip was controlled at 15 vol%. To ensure the homogeneity of the Al_2O_3 and Y_2O_3 sintering aids, aluminum tri-sec-butoxide (ASB) and yttrium iso-propoxide (YIP) were used as the Al_2O_3 and Y_2O_3 sources. Two polyelectrolytes, KD-2 and Darvan C, were chosen as the dispersants. Two weight percentages of the sintering aid or the dispersant versus the weight of powder was applied for the addition for each slip. The preparation conditions of the slips were summarized in Table 3.

Slips I, II, and III have similar addition conditions except that Darvan C was used for Slip II instead of KD-2 and a 0.005M organic base, tetramethyl ammonium hydroxide (TMAH), was used for Slip III.

The ball milling process for these slips was separated into two stages. The first stage was done for 20 hours without the addition of ASB. After the addition of ASB, another 20 hours of ball milling was carried out. All the ASB and YIP were added in a nitrogen purged glove box to prevent the fast hydrolysis of the alkoxides during slip preparation.

After ball milling, the slip was poured into a polypropylene beaker and stirred in air. The naturally existing moisture in the air was sufficient to hydrolyze the aluminum and yttrium alkoxide precursors to form aluminum and yttrium hydroxide coatings.

Table 3. Slip preparation conditions and IEP's for iso-propanol systems.

	Slip		
Additives	I	II	III
ASB	2 wt%*	2 wt%*	2 wt%*
YIP	2 wt%**	2 wt%**	2 wt%**
KD-2	2 wt%	-	2 wt%
Darvan C	-	2 wt%	-
TMAH	-	-	0.005M
IEP	8.6	8.2	8.6

* wt% of Al_2O_3; ** wt% of Y_2O_3.

The initial stage of the hydrolysis was allowed to take place under a magnetic stirring until the stirring bar was held by the more and more viscous slip. The slip was then pan-dried on an aluminum plate over night. A 100-mesh sieve was utilized to prepare powder for dry pressing. Some of the sieved powder was used for microelectrophoretic characterization.

Slip preparation from aqueous solution

The sample preparation and ball milling procedures were as same as that in the iso-propanol systems. The differences were the sintering aids, the base used, and the drying process. Besides, a glove box was not used for the doping. Table 4 summarized the preparation conditions for slips obtained from the aqueous solutions.

The aluminum and yttrium nitrates were used as the alumina and yttria sources instead of alkoxides. KD-2 was the only dispersant used for the study. The only difference between Slips IV and V was a 80 μL of 0.1N KOH was applied in Slip V.

An oven with a 60 °C setting was used for drying the aqueous slips. It took more than 6 hours to dry Slip IV and used much longer time (~16 hours) for the Slip V. A 100-mesh sieve was also applied to prepare the powder for dry pressing and for microelectrophoretic characterization.

Table 4. Slip preparation conditions and IEP's for aqueous systems.

	Slip	
Additives	IV	V
Aluminum nitrate	2 wt%*	2 wt%*
Yttrium nitrate	2 wt%**	2 wt%**
KD-2	2 wt%	2 wt%
KOH (0.1N)	-	80 μL
IEP	9.4	9.4

* wt% of Al_2O_3; ** wt% of Y_2O_3.

Microelectrophoretic characterization

Suspensions with 0.005 vol% solids loading in 0.01M KNO_3 solution at different pH values for each slip were prepared for μ measurement. All the suspensions were aged for a day prior to the measurement.

Figure 6 showed that the adsorption of the dispersant and the sintering aids for the IPA-ball-milled UBE SN E-10 powder gave more positive surface potential than the intrinsic one for almost the entire pH spectrum. This was also found for the use of Darvan C, a highly negatively charged dispersant.

In general, there were no significant μ differences between samples with and without base for both aqueous and IPA systems. Slips with different preparation routes showed different electrokinetic properties in terms of μ measurement (Figure 6). The IEP values for Slips I, II, and III were included in Table 3. Table 4 showed the IEP data of Slips IV and V.

TEM and EDS characterization of sintering aids doped silicon nitride powder:

The powder obtained from Slip I was used for the preparation of the TEM sample. An electron micrograph showed a uniform and smooth coated layer on the silicon nitride powder surfaces (Figure 7). The thickness of the coated layer was about 5 to 10 nm, which included the intrinsic oxide layer.

The elemental composition of the coated layer was analyzed by EDS. The spectrum showed the intensities of the elements of the coated materials, such as aluminum and yttrium (Figure 8). A strong silicon signal was obtained from both bulk silicon nitride and from the silica layer of the powder. Intense carbon and copper signals were also picked

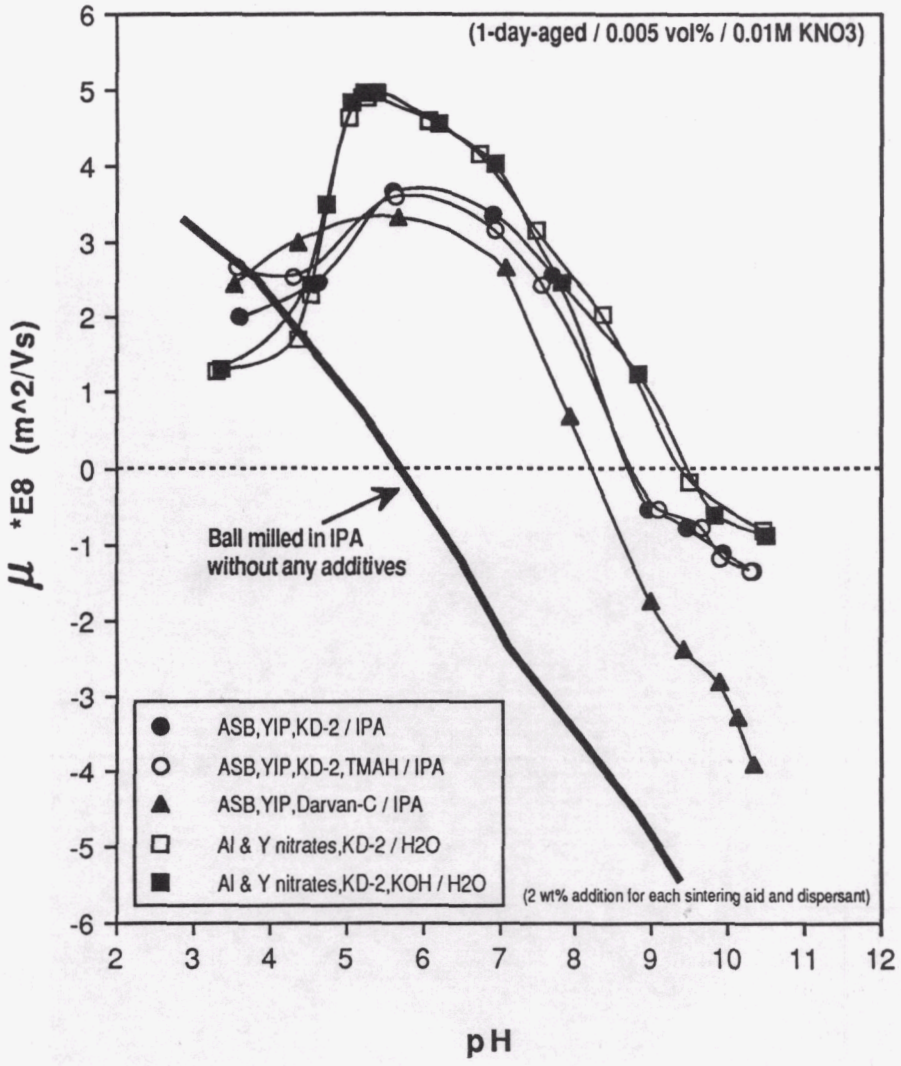

Figure 6. Microelectrophoretic characterization of sintering aids and dispersant doped UBE SN E-10 powder.

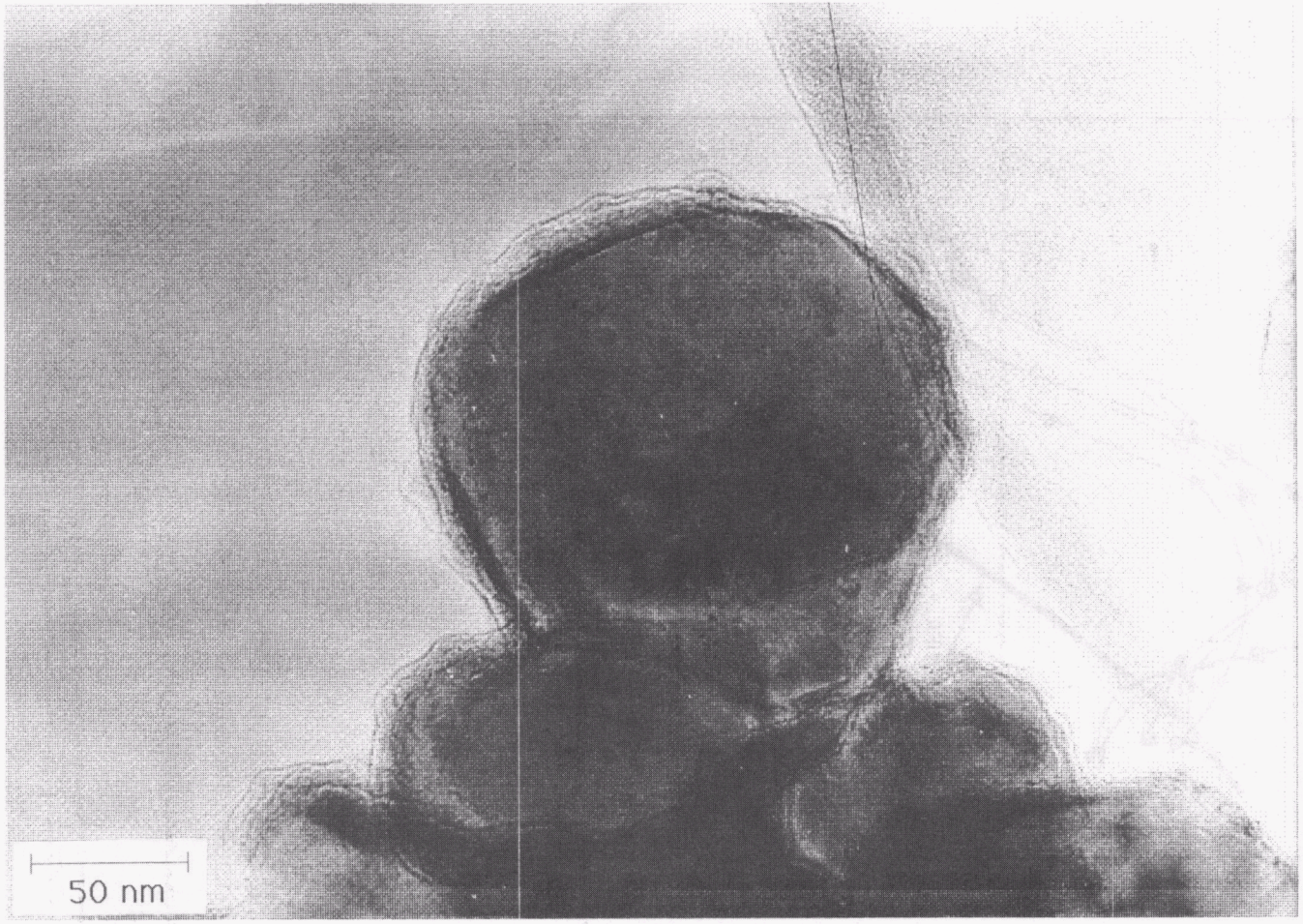

Figure 7. Micrograph of sintering aids doped UBE SN E-10 powder.

SLIP I – ASB, YIP, KD-2 / IPA

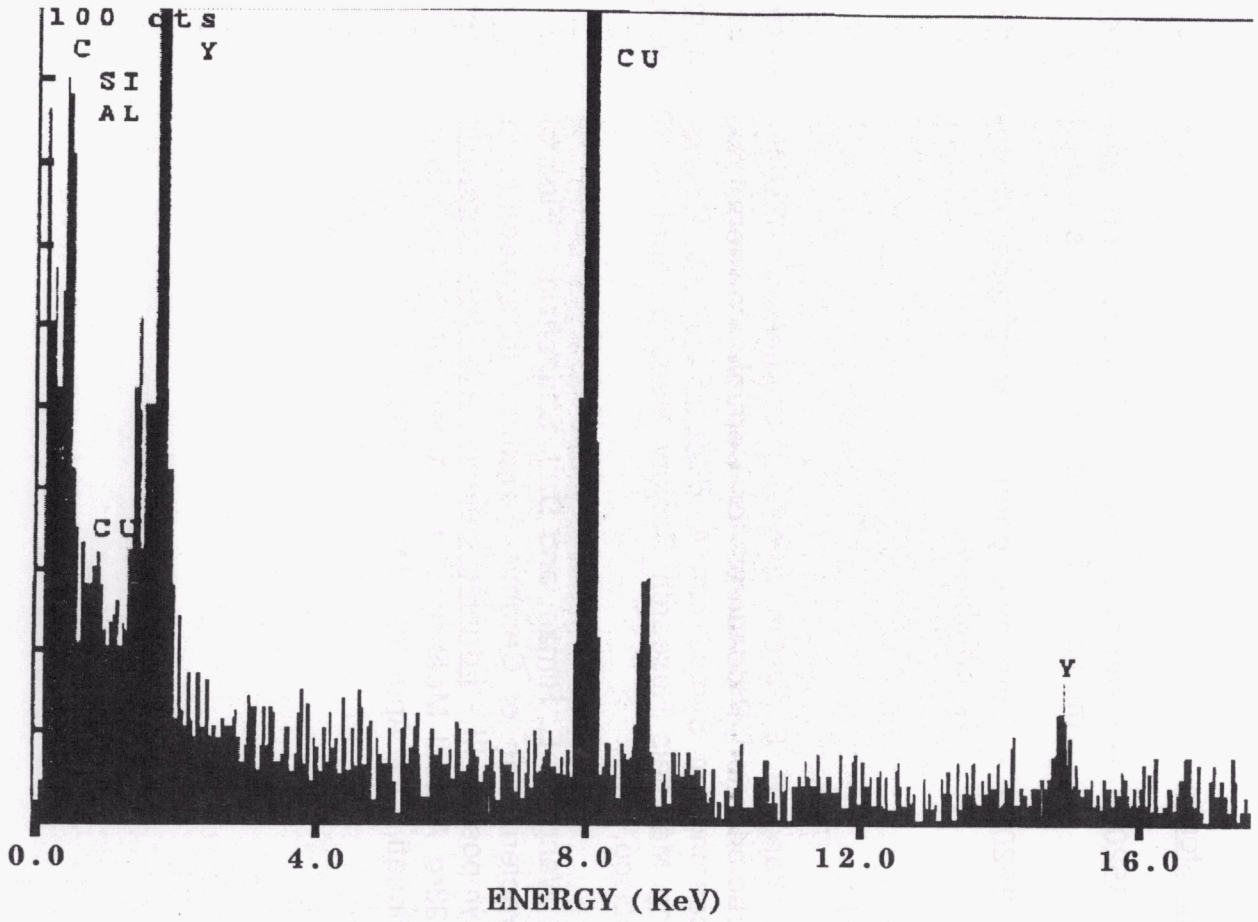

Figure 8. EDS spectrum of sintering aids doped UBE SN E-10 powder.

up by EDS. These signals were mainly generated from the graphite-coated TEM copper grid.

The amount of additives will be minimized to have the full coverage of the coating. Certainly, the powder obtained from different preparation routes will also be characterized in terms of green and fired densities and the microscopy.

Status of milestones

Milestone 352008 -- Determine effects of dispersants on electrophoretic mobility of silicon nitride -- is completed.

Milestone 352009 -- Determine good sintering aids for silicon nitride -- is completed.

Publications

1. J.-F. Wang, R. E. Riman, and D. J. Shanefield, "Reliable Electrokinetic Characterization Procedures for Ceramic Powders," to appear in the Proceedings of Symposium A, Better Ceramics Through Chemistry IV, Spring Materials Research Society Meeting, April 16-20, 1990, San Francisco, CA.

2. J.-F. Wang, R. E. Riman, and D. J. Shanefield, "Electrokinetic Characterization of Ceramic Powders," to appear in the Proceedings of Symposium III - Forming Science and Technology for Ceramics of the 93rd Annual Meeting of the American Ceramic Society, Cincinnati, OH, April 29 - May 2, 1991.

4.0 TECHNOLOGY TRANSFER

4.1 TECHNOLOGY TRANSFER

4.1.1 Technology Transfer

Technology Transfer
D. R. Johnson (Oak Ridge National Laboratory)

Technology transfer in the Ceramic Technology Project is accomplished by a number of mechanisms including the following:

Trade Shows - A portable display describing the program has been built and has been used at numerous national and international trade shows and technical meetings.

Newsletter - A Ceramic Technology Newsletter is published regularly and sent to a large distribution.

Reports - Semiannual technical reports, which include contributions by all participants in the program, are published and sent to a large distribution. Informal bimonthly management and technical reports are distributed to the participants in the program. Open-literature reports are required of all research and development participants.

Direct Assistance - Direct assistance is provided to subcontractors in the program via access to unique characterization and testing facilities at the Oak Ridge National Laboratory.

Workshops - Topical workshops are held on subjects of vital concern to the ceramics community.

International Cooperation - This program is actively involved in and supportive of the cooperative work being done by researchers in West Germany, Sweden, the United States, and, most recently, Japan under an agreement with the International Energy Agency. This effort is ultimately aimed at development of international standards and includes physical, morphological, and micro-structural characterization of ceramic powders and dense ceramic bodies, and mechanical characterization of dense ceramics.

IEA ANNEX II Management
V. J. Tennery (Oak Ridge National Laboratory)

Objective/scope

The purpose of this task is to organize, assist, and facilitate international research cooperation on the characterization of advanced structural ceramic materials. A major objective of this research is the evolution of measurement standards for key material properties. This task, which is managed in the United States by Oak Ridge National Laboratory (ORNL), now includes a formal International Energy Agency (IEA) Annex agreement identified as Annex II between the United States, the Federal Republic of Germany, Sweden, and Japan. The original annex included four subtasks: (1) information exchange, (2) ceramic powder characterization, (3) ceramic chemical and physical characterization, and (4) ceramic mechanical property measurements. The research in Subtasks 2, 3, and 4 is now completed. For the new Subtasks 5 and 6, there are 35 and 45 laboratories participating, respectively. During CY 1990, agreements were reached for Japan to join the Annex and for research in two new subtasks to be initiated. These include Subtask 5, Tensile and Flexural Properties of Ceramics, and Subtask 6, Advanced Ceramic Powder Characterization.

The Executive Committee agreed at the Cocoa Beach conference on January 17, 1991, that the next Executive Committee meeting will be held at the Japan Fine Ceramics Center in Nagoya, Japan, on October 15, 1991. The Executive Committee approved a change in the completion date for Amended Annex II from December 31, 1991, to December 31, 1993. At a future Executive Committee meeting, the Executive Committee may elect to establish further subtasks within Annex II.

A working group meeting for Subtask 5, U.S. participants, has been scheduled during the Department of Energy Contractor's Coordination Meeting in Dearborn, Michigan, on October 28, 1991. During this time, presentations will be given by V. J. Tennery, M. K. Ferber, C. Johnson, J. Cuccio, and T. Whalen on the status of research (Subtask 5) in the United States.

Technical progress

Subtask 5, Flexural and Tensile Properties of Ceramics

United States

Analysis of the flexural strength data is proceeding. To date we have not received the fractography data from Corning and General Electric. Corning has indicated that their data may be available some time in November 1991. General Electric has indicated that their data should be provided to ORNL by the end of October.

All machining on the IEA tensile specimens (125 straight collet and 50 tapered collet) by Chand/Kare was completed on April 22, 1991. In addition, the inspection by our staff was completed on April 22, 1991. As of April 22, 1991, 135 specimens had been sent to HiTec Corp., Westford, Massachusetts, for the application of 9 gages at 7 locations in the gage

section. On April 29, 1991, the last 20 specimens for the application of 9 gages (7 locations) were sent. On April 29, 1991, 20 specimens for the application of 11 gages (9 locations) were sent to HiTec Corporation. To date, the application of 9 gages (7 locations) has been completed on all specimens (155). The final 20 with the 11 gage configurations (9 locations) were completed the first of June 1991 and received on June 15, 1991. Tensile specimen collets were ordered and received from United Machine and Tool, Oak Ridge, Tennessee.

Information for scheduling the tensile testing of GN-10 specimens in the High Temperature Materials Laboratory (HTML) at Oak Ridge or at the participant's site by the participating laboratories during the months of June, July, and August 1991 has been received. The original plan was for each laboratory to measure the strength of five straight-collet and five tapered- collet specimens at the HTML, followed by measurement of five specimens at the participating laboratory. M. Jenkins of the HTML staff has written guidelines for completing the tensile strength measurements, and they have been provided to all U.S. participants. Due to the lack of specialized equipment required for tensile strength measurements at some of the participating laboratories, all measurements for these laboratories were done at ORNL in the HTML. Table 1 lists the schedule for measurements at participating laboratories with tensile measuring facilities and dates (M. K. Ferber and M. G. Jenkins, HTML staff, participated in the measurements). Table 2 lists the participating laboratories and dates when the measurements were completed at ORNL. Each participating laboratory took the fractured specimens back to their laboratories to do 100% fractography. We have requested that they return the fractography results and broken specimens to us by November 15, 1991. Instructions for fractographic examination of GN10 tensile specimens were sent to the U.S. participants on August 21, 1991.

Table 1. Status of Tensile Strength Measurements Completed at Participating Laboratories with Tensile Testing Facilities

Laboratory	Date	No. of straight-collet specimens[a]
GTE Laboratories	August 19, 1991	4 (7 Locations)
		1 (9 Locations)
Norton Company	August 20, 1991	4 (7 Locations)
		1 (9 Locations)
Garrett Auxiliary Power Division	September 23,1991	4 (7 Locations)
		1 (9 Locations)

[a]Seven location specimens include nine gages; nine location specimens include eleven gages.

Table 2. Status of Participation in Tensile Strength Measurements Completed in the High Temperature Materials Laboratory Oak Ridge National Laboratory

Laboratory	Date	No. of straight collet specimens[a]	No. of tapered collet specimens[a]
ORNL	June 7, 1991	9 (7 Locations) 1 (9 Locations)	4 (7 Locations) 1 (9 Locations)
GTE Laboratories	July 19, 1991	5 (7 Locations)	4 (7 Locations) 1 (9 Locations)
Corning	July 23, 1991	9 (7 Locations) 1 (9 Locations)	4 (7 Locations) 1 (9 Locations)
Garrett Auxiliary Power	July 31, 1991	5 (7 Locations)	4 (7 Locations) 1 (9 Locations)
Ford Motor Co./ORNL	August 2, 1991	9 (7 Locations) 1 (9 Locations)	4 (7 Locations) 1 (9 Locations)
Allison Gas Turbine Division	August 13, 1991	9 (7 Locations) 1 (9 Locations)	4 (7 Locations) 1 (9 Locations)
General Electric	August 26, 1991	9 (7 Locations) 1 (9 Locations)	4 (7 Locations) 1 (9 Locations)
NASA Lewis	August 29, 1991	9 (7 Locations) 1 (9 Locations)	4 (7 Locations) 1 (9 Locations)
Carborundum	September 25, 1991	9 (7 Locations) 1 (9 Locations)	4 (7 Locations) 1 (9 Locations)
Norton Company	September 30, 1991	5 (7 Locations)	4 (7 Locations) 1 (9 Locations)

[a]Seven location specimens include nine gages; nine location specimens include eleven gages.

Germany

Subtask 5 is moving slowly in Germany. At the Subtask 5 Germany/Sweden working group meeting (June 13, 1991) held in Göteborg, Sweden, plans were completed for preparing the flexure specimens, and much discussion was held to resolve the question of the number of strain gages to be used on the tensile specimens. The German flexure specimens should be ready for distribution by the middle of September 1991. The previous German plan was to strain gage only about 20% of the tensile specimens, but all of the other national representatives strongly recommended strain gaging 100% of the specimens, as they are doing. The latest communication (July 10, 1991) from Dr. Thomas Hollstein, Fraunhofer-Institute für Werkstoffmechanik, Freiburg, indicates that they are seeking funding to finance the application of strain gages on all tensile specimens. They hope to complete machining of the specimens by the end of August 1991 with the tensile testing to start at the end of September 1991, at which time they would exchange the tensile specimens with the United States.

Dr. Seitz, PLR, Jülich, stated by letter of September 11, 1991, that Wemhöner & Popp will send the 30 flexure specimens to us by the end of September 1991. The flexure specimens were not received by the end of this report period. The Fraunhofer-Institut für Werkstoffmechanik will provide us with the five tensile specimens with gages before the end of October 1991.

Germany will have a short German-Swedish group meeting on October 7, 1991, in Karlsruhe, to discuss the status of their work.

Sweden

Subtask 5 is moving slowly in Sweden due to funding problems. The Swedish flexure specimens should be ready for distribution by the middle of September 1991. Dr. Lars Pejryd, Volvo Flygmotor AB, Trollhättan, Sweden, will inform us soon concerning the time schedule for tensile strength measurements in Sweden and a proposed schedule for exchanging tensile specimens.

Lars Pejryd visited the HTML and presented a seminar entitled, "Ceramics in Aerospace Applications," and discussed the IEA Annex II, Subtask 5 status with V. J. Tennery on September 11, 1991.

Dr. Ericsson, Linköping Institute of Technology, Sweden, stated in his telefax of September 10, 1991, that they were waiting to receive the machined specimens from Wemhöner and Popp. After their meeting on October 7, 1991, will ship the Swedish tensile specimens to the United States as soon as they are available.

Dr. Ericsson sent minutes of the German-Swedish Subtask 5 working group meeting which was held in Sweden on June 13, 1991.

Japan

On June 10, 1991, we received notification from Eiji Yamada, Office of Energy Technology Research and Development, International Energy Agency, Organisation for Economic Co-Operation and Development, Paris, France, that Dr. A. Fukutome of the New Energy and Industrial Technology Development Organization (NEDO) signed the Implementing Agreement for a Programme of

Research and Development on High Temperature Materials for Automotive Engines on May 29, 1991, formally making Japan a member of Annex II. The NEDO has been designated as the Contracting Party by the Government of Japan. Mr. Hiroshi Terasawa, Director General, Energy Conversion and Storage Department, NEDO, replaces Mr. Soichi Nagamatsu, Ministry of International Trade and Industry (MITI), as the Executive Committee Member from Japan. Mr. Hisao Ogiyama, NEDO, is the Alternate Executive Committee Member from Japan (from August 23, 1991, letter from Dr. Atsushi Fukutome, NEDO. This became effective on May 29, 1991, when signed by the Japanese representative in Paris.)

Dr. Awaji indicated on June 24, 1991, that Japan had fractured all of the Japanese Subtask 5 flexure specimens at room and high temperatures as well as the 30 U.S. specimens (at room temperature). Japan has agreed to use the same strain gage configuration on their tensile specimens (nine strain gages in seven locations) as we are using in the United States (June 1991 correspondence). Their intent is to exchange specimens with us in September 1991.

A communication (September 1991) from Dr. Awaji, Japan Fine Ceramics Center (JFCC), indicated that the exchange of tensile specimens would not be ready until the end of October 1991.

Subtask 6, Advanced Ceramic Powder Characterization

Major responsibility for this subtask in the United States is at the National Institute of Standards and Technology (NIST), and a detailed report of progress on this subtask is provided in the section of this report submitted by NIST. Only a brief summary is provided here.

The U.S. Working Group on powder characterization met at NIST on April 22-23, 1991, to review the data. At this meeting, the data received until that time were reviewed, comments were prepared for any data for which more information was required, and preliminary analysis of the data was carried out. The participants found a significant improvement in the inter-laboratory comparison data of those laboratories that had followed the "recommended" procedures. In addition, many data sets required additional experimental descriptions, especially for those data that were produced using modifications of the recommended procedure.

Data input activity is continuing with the primary emphasis on incorporating additional data and improving the data format. Questionnaires have been sent to Dr. Tsubaki, Technical Leader in Japan, requesting additional information on some of the Japanese data.

The proceedings and comments of the U.S. Working Group meeting held on April 22-23, 1991, were sent to all the U.S. participants and technical leaders for review. Some participants have returned their comments. We are working with the rest to respond.

Dr. Tsubaki Junichiro, Technical Leader of Japan, was at NIST to discuss their results and review Japan's standardization programs on ceramic powders. In addition, he discussed preliminary data analysis on the particle size distribution carried out at the JFCC.

The U.S. Working Group is planning to meet at NIST in October 1991 for a data review.

The first version of a report on preliminary analysis of powder characterization data was prepared at NIST. This report contains all the

data that was received at NIST up to August 1991. Some additional data have arrived from Germany and the United States after this date. In this report, the powder characterization data were provided in the form of simple statistics, plots, and tables. These data show significant improvement in repeatability and reproducibility of some of the procedures, especially when the participants have followed the recommended procedures. Data obtained by using non-recommended procedures appear to be easily identified. The results will be discussed at the upcoming working group meeting of the technical leaders in Nagoya, Japan, on October 14, 1991. The discussions are expected to lead to the development of preliminary conclusions on the Subtask 6 data. Most of the data from Germany have arrived. Some of these data were not included in the above mentioned report because it arrived after August 31, 1991. This report, containing preliminary analysis, will be revised by incorporating all data received through November 15, 1991. The revised version will be distributed to the participants in December 1991.

References

None

Status of milestones

Milestone No. 411510: Due to changes in test scheduling by U.S. participants, this milestone date has been changed to December 31, 1991, and is on schedule. This Milestone is an ORNL internal milestone (No. 92CC54).

Milestone No. 411511: Due to delays in receiving data from other participating countries, this milestone date has been changed to September 30, 1992.

Publications

V. J. Tennery attended the German/Swedish Technical Working Group Meeting, Göteborg, Sweden, on June 13, 1991, and presented a status report of the U.S. Subtask 5 research. V. J. Tennery also attended the Subtask 6 Technical Meeting.

Michael Jenkins, Mechanical Properties User Center staff, visited JFCC, Nagoya, Japan, on July 18, 1991. He presented a seminar entitled "Administrative and Limited Technical Aspects of the United States Participation in the International Energy Agency (IEA) Annex II Agreement."

Characterization of Ceramic Powders

S. G. Malghan, L.-S. Lum, J. F. Kelly, E. Begley and S. M. Hsu
(National Institute of Standards and Technology)

Objective/Scope

Ceramics have been successfully employed in engines on a demonstration basis. The successful manufacture and use of ceramics in advanced engines depends on the development of reliable materials that will withstand high, rapidly varying thermal stress loads. Improvement in the characterization of ceramic starting powders is a critical factor in achieving reliable ceramic materials for engine applications. The production and utilization of such powders require characterization methods and property standards for quality assurance.

The objectives of the NIST program are (1) to assist with the division and distribution of five ceramic starting powders for an international round-robin on powder characterization; (2) to provide reliable data on physical (dimensional), chemical and phase characteristics of powders; and (3) to conduct statistical assessment, analysis and modeling of round-robin data. This program is directed toward a critical assessment of powder characterization methodology and toward establishment of a basis for the evaluation of fine powder precursors for ceramic processing. This work will examine and compare by a variety of statistical means the various measurement methodologies employed in the round-robin and the correlations among the various parameters and characteristics evaluated. The results of the round-robin are expected to provide the basis for identifying measurements for which Standard Reference Materials are needed and to provide property and statistical data which will serve the development of internationally accepted standards.

Technical Progress

The technical progress covered in this report is on the data collection, compilation and analysis of data related to IEA Subtask 6 on ceramic powders characterization.

Data Collection. At this time, approximately 90% of the committed data have been received from all four participating countries. Japan's participants responded on-time and with all their data. German participants, in general, were slow in responding; whereas, most of the U.S. participants submitted their data as planned. Delay experienced in obtaining data from participants in the U.S. and Germany is most probably due to adverse economic conditions and change of personnel related to this project. Some participants decided not to submit data from certain techniques because they have discontinued its use and/or personnel trained in such techniques no longer are available in-house. Some participants in Germany and the U.S. have discontinued participation due to corporate restructure. In Germany, Hüls discontinued participation after submitting most of the data. Similarly, in the U.S., Ferro Corporation and GTE Laboratories also discontinued further participation after submitting their data.

Data Compilation. Inspite of delay experienced in obtaining data from a number of participants, NIST has been able to provide additional man-hours in order to maintain the overall schedule. The data compilation activity has produced two different types of reports: 1) Tabulation of data, 2) Technical information related to analysis procedure and samples. The first report has been distributed to participants in Japan, U.S. and Sweden. This report is being revised now to include German data. The revised report will be distributed to all participants in December 1991. The second report on data contains detailed information reported by the participants, and such information is useful in the interpretation of data. This report is available in a hard copy format and on two diskettes.

Data Analysis. The preliminary data analysis report has been prepared and distributed to all participants in Japan, U.S., and Sweden. The updated version of this report will be distributed to German participants in December 1991. The preliminary data analysis consists of graphical presentation of primary data and simple statistical parameters such as mean of each data set, mean of data for all participants, and standard deviation. Some of the data analyzed so far is summarized below.

Particle Size Distribution-- Data obtained by using the recommended procedures of Subtask 6 appear to show excellent repeatability and reproducibility. In the case of data from Sedigraph, the entire particle size distribution show good agreement between the participating laboratories, indicating that deagglomeration related problems are negligibly small. This could be due to a large amount of effort expended to investigate dispersion phenomena during the procedure development stage. Data from both silicon nitride and silicon carbide powders show similar trends. The data on aluminum nitride does not show the same goodness of reproducibility, most probably due to lack of complete dispersion and limited experience with the powder.

The size distribution data from light scattering equipment also shows good repeatability and reproducibility, in spite of the fact that the participants used a number of different equipment that utilize different operating principles. Since the same dispersion procedure was used for both sedimentation (Sedigraph) and light scattering equipment, agglomeration related problems were absent in both cases. There is a slightly larger variation in the d_{10} size range in both sets of data, most probably due to equipment related problems such as limited applicability of the working principle at extremely fine sizes.

Specific Surface Area-- The specific surface area data show a reasonably good level of repeatability and reproducibility. Some of the scatter could be due to judgement exercised by participants in the application of the recommended procedure and inherent problems in the procedure itself. A detailed analysis of the data might reveal the underlying problems with the data. If data obtained by not strictly following the procedure are eliminated, the remaining data appears to show an excellent agreement. Between the single and multi-point BET data, the

former appears to show better agreement than the latter. This difference is an indication of insensitivity of the single point BET method to minor variations in the procedure.

Data from other methods are being analyzed.

Interactions and Reviews. A meeting of the U.S. participants was held at NIST on April 22-23, 1991. Nine participants attended this meeting to review and discuss the data. Each set of data was discussed and questions or comments were developed. These comments will be returned to the participants so that they can respond. These responses will be incorporated into the data report. In addition, preliminary analysis was carried out to get a glimpse of the lab-to-lab data variation. Tentative formats for data presentation were also discussed.

Similar meetings were held in Japan and Sweden. In a meeting of the participants in Japan, the data were discussed, according to Dr. Tsubaki, and comments were collected. These comments were discussed at the meeting in Göteborg, and a set of combined comments were developed. Responses to these comments will be addressed by contacting individual participants.

The Technical Leaders of Subtask 6 met at Göteborg, in conjunction with the 4th International Symposium on Ceramic Materials and Components for Heat Engines on June 10-12, 1991. At this meeting, each leader presented reviews of technical progress and exchanged ideas on data analysis. The technical leaders decided that while each leader will provide input to the data analysis activity, statistical analysis of the data will be carried out at NIST.

A preliminary report on the data analysis was distributed to the leaders in the first week of October 1991. At the October 14, 1991 meeting of the Technical Leaders in Nagoya, Japan, the results of preliminary data analysis were reviewed. This review indicated that data obtained using a number procedures were in good agreement, while some other data showed large scatter. One of the major technical issues remains to be solved is samples preparation.

ASTM Activities. We are continuing to assist ASTM activities on powders standards development. Two major tasks undertaken are: 1) to provide leadership to the standards development on particle size distribution by gravity sedimentation using Sedigraph, 2) provide one set of silicon nitride samples to the ASTM round-robin on particle size distribution. Both activities are proceeding as planned.

A sample of the SNE-3 powder has been prepared exclusively for the ASTM round-robin studies. This sample will be offered to the ASTM subcommittee involved in the development of standards on powders. A meeting of the C-28-05-04 has been scheduled to take place in conjunction with the Composites Conference in Cocoa Beach, FL. At this meeting, discussions will be held on the distribution of this sample and extent of a round-robin activity.

Status of Milestones

On target.

Publication/Presentations

1. A report on compilation of procedures used in Subtask 6 has been prepared.

2. Two reports on data and samples analysis details have been distributed to IEA participants.

3. A report on preliminary analysis of IEA Subtask 6 data was distributed to participants.

4. "Analysis of Physical Properties of Ceramic Powder in an International Interlaboratory Comparison Program" with A. L. Dragoo, S. M. Hsu, H. Hausner and R. Pompe, Proc. 4th International Symp. on Ceramic Materials, Sweden, June 1991.

5. S. M. Hsu, Review of progress of IEA Subtask 6 Program at the IEA Executive Committee Meeting, Nagoya, Japan, October 15, 1991.

6. S. G. Malghan, Technical Analysis of IEA Subtask 6 data at the Japan's participants meeting, JFCC, Nagoya, Japan, October 23, 1991.

7. S. G. Malghan, Standards Development, NEDO, Tokyo, Japan, October 24, 1991.

Ceramic Mechanical Property Test Method Development

George D. Quinn
(National Institute of Standards and Technology)

Objective/Scope

This task is to develop mechanical test method standards in support of the Ceramic Technology for Advanced Heat Engines and Advanced Turbine Technology Applications Programs. The prime DOE contractors and subcontractors will be surveyed to assess their needs and capabilities. Test method development should also consider the general USA structural ceramics community as well as foreign laboratories and companies, but emphasis will be placed on the needs on the DOE community.

Draft recommendations for practices or procedures shall be developed based upon the needs identified above and circulated within the DOE ceramics heat engine community for review and modification. Round robins will be conducted as necessary, but shall be well-focussed, limited in scope and not interfere with ongoing IEA round robins. Procedures developed in this program shall be presented as ATTAP or CTAHE "standard procedures." Alternatively, (and eventually) these will be advanced for final standardization by ASTM or by the U.S. Army as possible MIL STD's.

Technical Highlights

A set of handout fliers have been revised and are available on a simple room temperature flexure test fixture that can be machined by any competent shop at a reasonable cost. A draft of a similar set of design notes is being prepared for a rolling-pin high-temperature flexure fixture. Guidelines such as these will enable DOE contractors to develop competent testing capabilities if they are unable or unwilling to purchase off-the-shelf commercial fixtures.

The issue of what value the flexure test data has for design was reviewed and a definitive paper was published: "Design Data for Engineering Ceramics: A Review of the Flexure Test" by G. Quinn and Dr. R. Morrell in the National Physical Laboratory in England (the U.K. analogue of NIST). A number of assumptions all must be met for flexure data to be useful for design. For example, both the average microstructure and the extreme microstructural features, the defects, must be identical in the test specimens and the components. Consistency is the key issue. In most instances, one or more of the assumptions are not met, and the flexure data has limited applicability. Unfortunately, many of the assumptions apply equally well to direct tension data as well and there is a risk that even tension data will be misleading. The assumptions are listed in a checklist fashion in the manuscript such that they can be addressed for each problem a designer may confront. There is some cause for optimism however, since the literature review showed that there were at least several dozen instances where flexure data scaled quite well to uniaxially stressed components.

One unresolved topic regarding flexure testing was whether it is essential for loading pins to roll at elevated temperature. It is well known that a serious experimental error exists if fixed pins are used. This had been verified at room temperature, but no data existed at elevated temperature. This matter was a key issue with respect to the draft flexure standard for high-temperature flexure testing under development for ASTM C-28. Experimental testing was done, both in fast fracture and in stress rupture modes of loading, with the results shown in Figures 1-3. It is evident that the fast fracture strengths of an alumina and a silicon nitride are systematically in error by 7 and 4%, respectively. The stress rupture curve for NC-132 hot pressed silicon nitride at 1200°C is similarly displaced by 7%. These results were presented at the 2nd European Ceramic Society conference in Augsburg, Germany in Sept. 1991, and will also be presented at the American Ceramic Society conference at Cocoa Beach in January 1992. This testing sequence and results typify one of the objectives of this program, "To Eliminate Loose Ends and Refine Test Procedures".

Four standards are under development as part of this task. Three of the four standards are in close cooperation with other CTAHE subcontractors. The four standards are:

1. ASTM Draft Standard: "Dynamic Young's Modulus, Shear Modulus, and Poisson's Ratio for Advanced Ceramics by Sonic Resonance," by S. Gonczy, G. Quinn and J. Helfinstine.

2. ASTM draft standard: "Standard Test Method for Flexural Strength of Advanced Ceramic at Elevated Temperature," by G. Quinn in cooperation with ASTM task group of same name.

3. U. S. Army draft standard: "Standard Practice for Characterizing Strength Limiting Defects in Advanced Structural Ceramics", with M. Slavin and J. Swab.

4. ASTM draft standard: "Reporting Strength Data and Estimating Weibull Distribution Parameters for Advanced Ceramics," by S. Duffy and G. Quinn.

The following progress occurred for these four projects during the current six month period.

The draft standard for elastic modulus determination has been developed in cooperation with Dr. S. Gonczy of Allied Signal and Mr. John Helfinstine of Corning. This draft standard is a modification to ASTM standards already on the books as ASTM standards (Whitewares and Glass Ceramics) but has been modernized and adapted to make it suitable for advanced ceramics. It is based on the well-known beam resonance methods. A review of the equations had to be made and extended back through 70 years of the literature to Timoshenko. (The Japanese elastic modulus standard for advanced ceramics: JIS R 1604 includes this method). During this six month period the draft passed both ASTM C-28 main and subcommittee ballot. It was balloted at the ASTM Society level in August 1991.

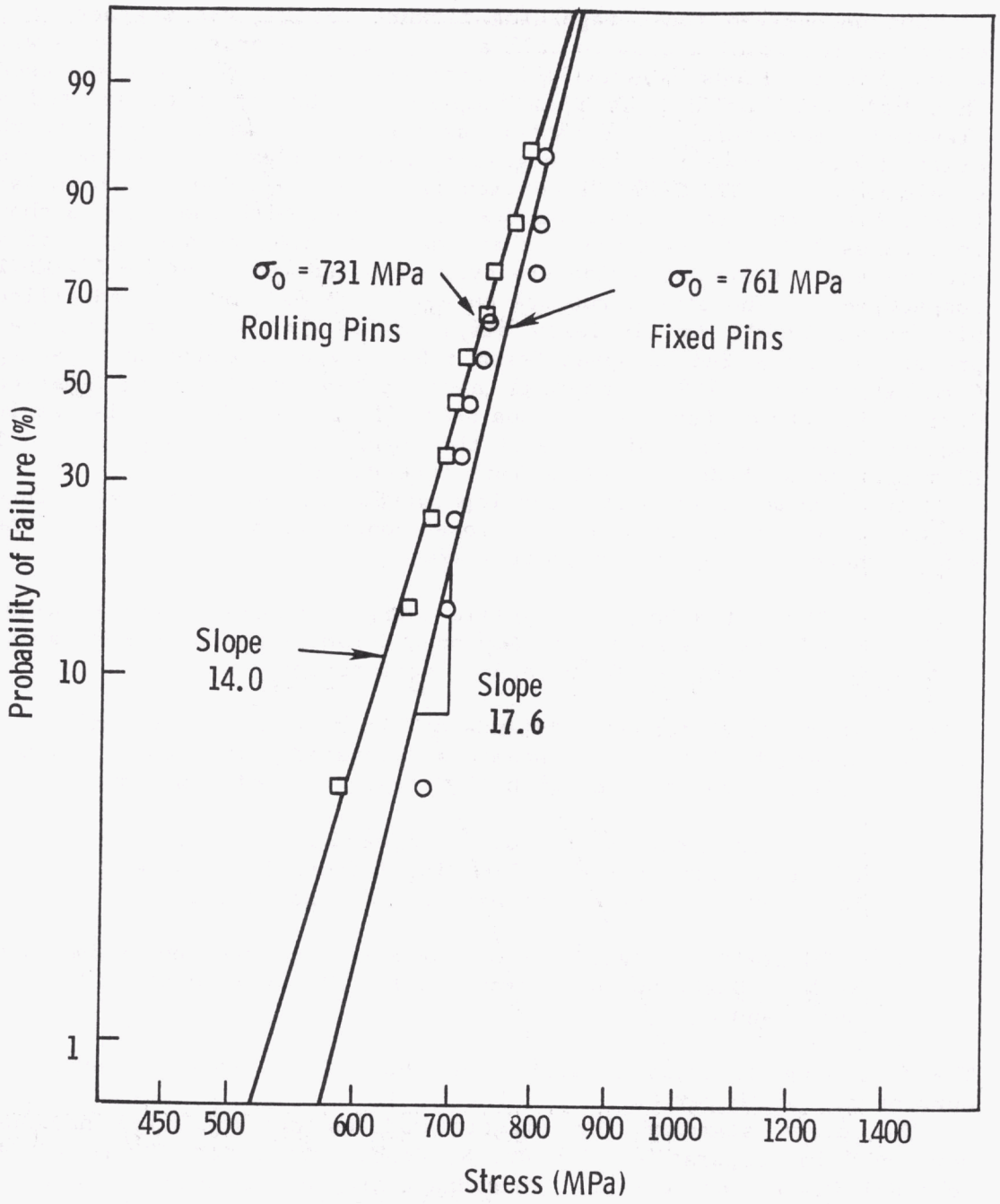

FIGURE 1. Flexure fast-fracture strength at 1000°C for NC 132 hot-pressed silicon nitride. The friction error associated with fixed pins displaced the Weibull curve by 4%.

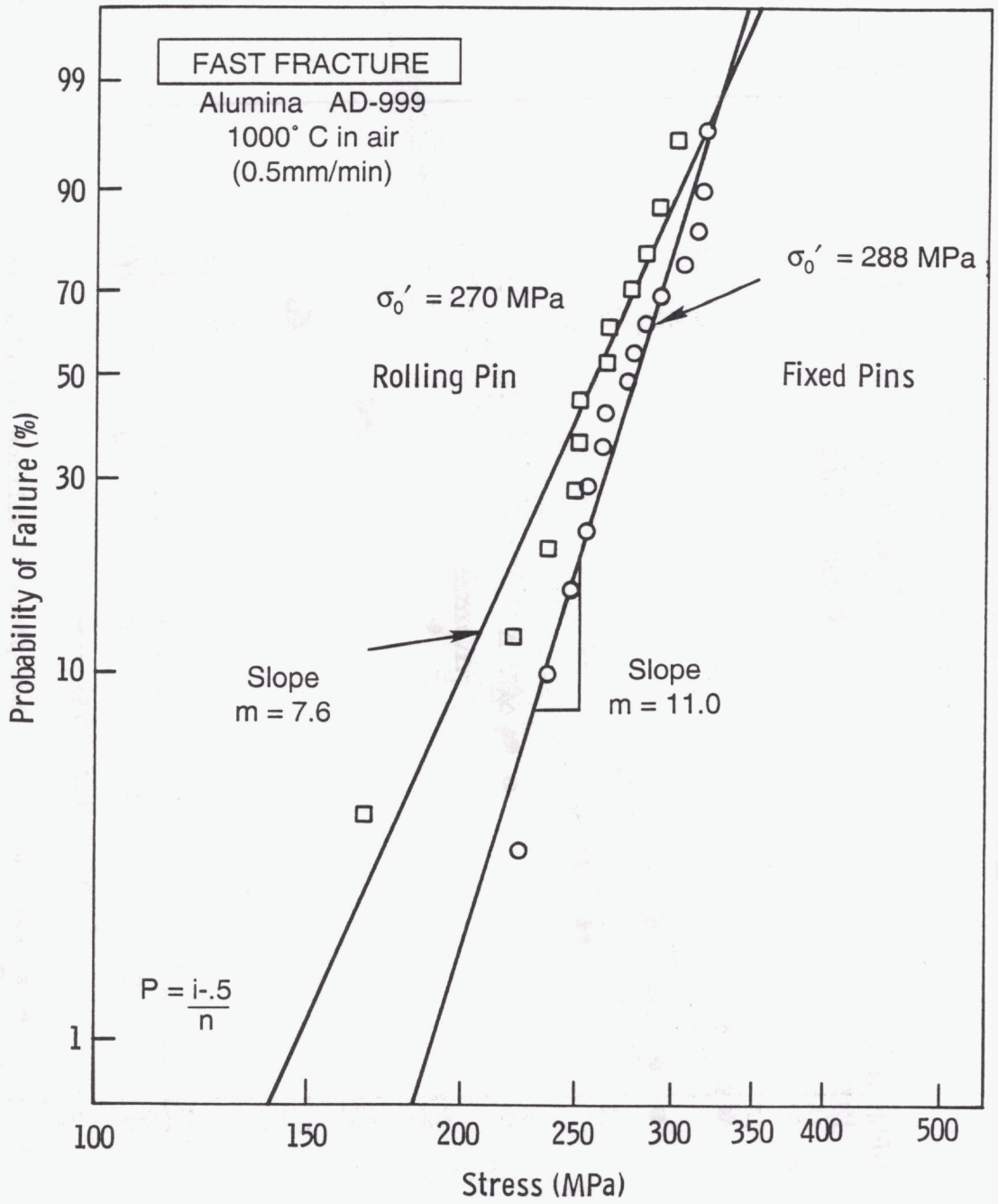

FIGURE 2. Flexure fast-fracture strength at 1000°C for a sintered alumina. The friction error displaces the Weibull curve by 7%.

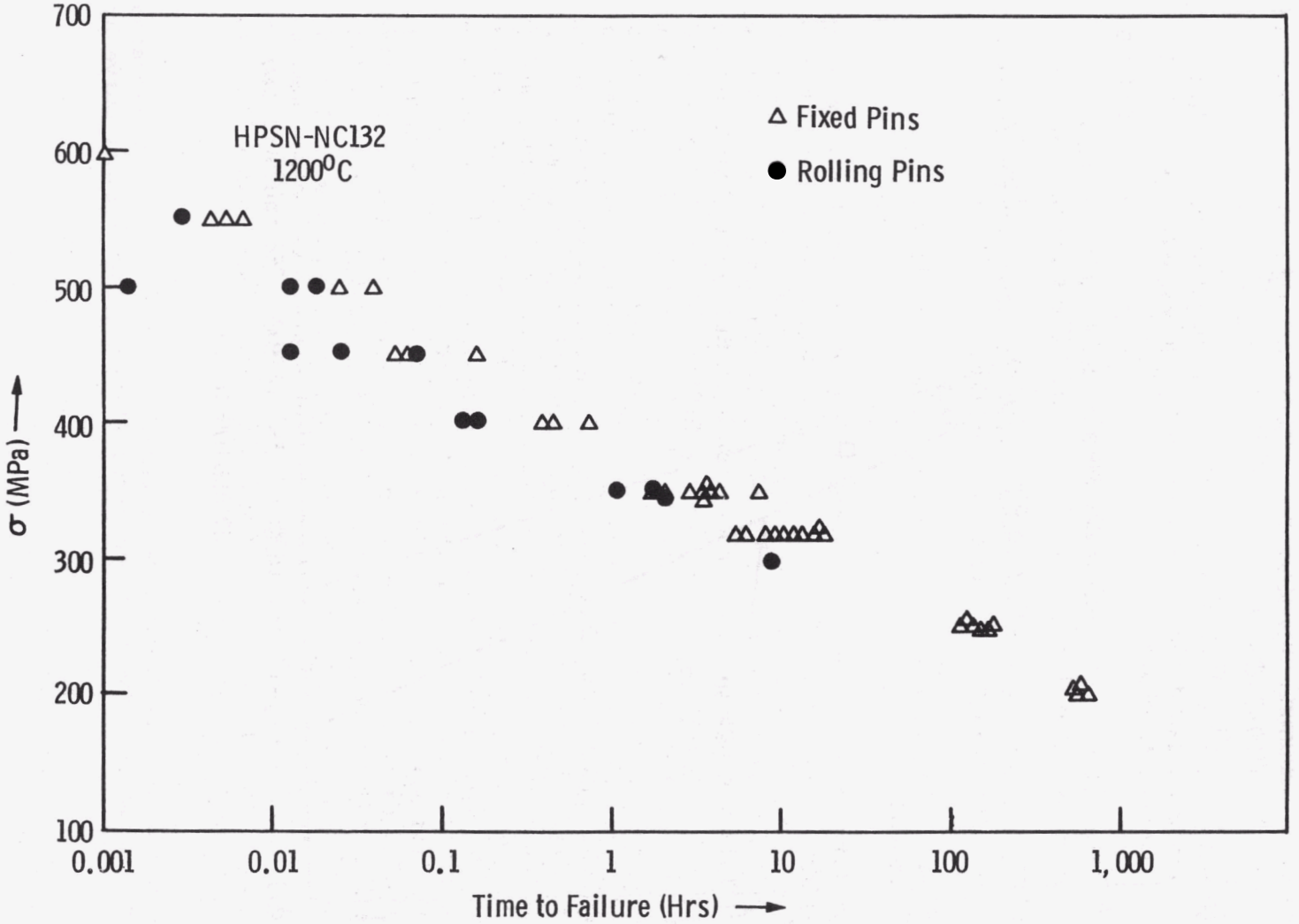

FIGURE 3. Flexure stress-rupture of hot-pressed silicon nitride at 1200°C. The friction error displaces the lifetime curve by 7% in stress.

The draft standard for high temperature flexure standard was submitted for a subcommittee ballot (draft #3) in April 1991. Four negative ballots were received, and three were sustained. In response to the revisions mandated, draft 4 has been prepared and sent to ASTM headquarters for distribution for a concurrent main and subcommittee ballot in Sept 1991. The revisions include:

1. Deletion of the option of using fixed pin fixtures. This revision was directly influenced by the experimental results referred to above.

2. Relaxation of the requirement that the furnace be held constant from 1 degree to 2 degrees Celsius during the test.

3. Inclusion of a new requirement that the time for the furnace and the load train system be measured.

4. Inclusion of a sample reporting format-template as an appendix.

The first review has been accomplished on the draft standard for fractographic analysis of strength limiting defects in advanced ceramics. Several technical presentations have been given to highlight the objectives and approach that this standard will have, and to solicit input. This project is in collaboration with Mr. Jeffrey Swab and Mr. Michael Slavin of the U. S. Army MTL. A preliminary draft standard was sent to approximately 40 experts in the fractography field and some excellent constructive criticism has been obtained. Major revisions to the draft standard are now being written. General guidelines for fractographic analysis will be given including procedures for mechanical testing, specimen preservation, visual examination, optical microscopic and scanning electron microscopic examination. The goal of the standard is to develop common guidelines for the detection and characterization of strength limiting defects in advanced ceramics. The following Table illustrates the required characterization and reporting scheme, for strength limiting defects. It is mandatory to report the first two aspects of a defect; the third is optional. Very careful distinction must be made with respect to whether a flaw is distributed in the volume or the surface, and where the specific flaw was actually located in the particular specimen. For example, volume distributed pores may be located (in any one specimen) in the bulk (volume), at the surface, or at an edge. Thus, in characterizing a flaw, it is important to specify a location parameter twice as is illustrated below:

FLAW CHARACTERIZATION SCHEME

FLAW TYPE (identity, and how distributed)	FLAW LOCATION (specific location in a specimen)	FLAW SIZE (nominal diameter)
Pore, Volume distributed	Surface	120 μm
Inclusion, Volume distributed	Volume	50 μm
Machining Damage, Surface dist.	Surface	30 μm

The original thrust to characterize strength limiting defects has to be modified somewhat. In older structural ceramics, strength was limited by gross microstructural aberrations such as pores or inclusions. The remarkable improvements in structural ceramics over the last decade have led to new materials which no longer fail from such defects, but from "mainstream microstructural features." This latter phrase (coined by Roy Rice) refers to microstructural features such as large grains or zones of slightly irregular structure (i.e. microporosity) which are part of the "normal" range of the microstructure. It is a matter of semantics as to whether these features can be considered "defects." From a fracture mechanics standpoint, they are; but from a materials processing perspective, they are not. Another issue that was uncovered (by Bruce Adams) is the legal ramifications of using the words "defect" or "flaw." Such words are avoided in the glass industry. We must consider the consequences of using these words if we envision using ceramics in general structural applications. In view of these two issues, it has been decided that the fractography standard will focus on characterization of "fracture origins", but will include a discussion of defects.

It is now planned that the document will become a MIL HDBK (Military Handbook). Ultimately, it is the goal to have interrelated standards for mechanical testing, fractography and statistical interpretation as illustrated in Figure 4. The test method standards are either on the books or are in development. The fractography standard is targeted for a 1991 approval as a MIL HDBK and will then be brought into the ASTM C-28 forum for consideration. The Weibull Statistical Analysis standard is being developed in ASTM Committee C-28.

The Weibull statistical analysis draft standard is beginning to take shape in the Design and Evaluation Subcommittee C28-02. G. Quinn prepared a strawman draft standard whose function was to propose one scheme, but more importantly, to provoke action by that subcommittee and to focus its work. The latter objectives were successful and the subcommittee is now industriously working towards a draft standard. Dr. Steven Duffy of NASA-Lewis has the lead in this initiative and a new draft was presented at the Philadelphia meeting in May. G. Quinn translated a German draft standard: "Testing of Advanced Technical Ceramics: 4-Point Bending Test; Statistical Evaluation; Determination of the Weibull parameters." This document has already been approved in

Figure 4

The mechanical testing standards, the fractography standard, and the statistical standards are interrelated as shown.

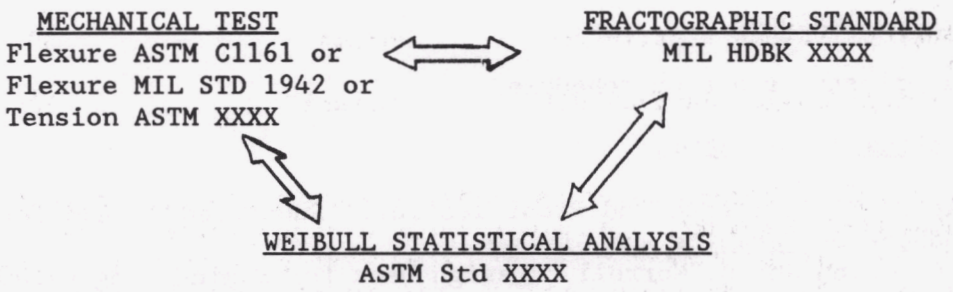

the German Standards Body DIN and assigned a number DIN 51-110 Part 3. It calls for a Maximum Likelihood analysis (and forbids the least squares regression method) but also mandates that the results be plotted on a conventional Weibull graph with the double natural log ordinate axis and the natural log stress abscissa. In light of this, and also considering new statistical analyses conducted by Dr. C. Johnson and Dr, W. Tucker of G.E., (reported in Section 2.3 New Concepts of this report) it now appears that the Maximum Likelihood analysis should become the DOE and ASTM standards.

Standardization of fracture toughness testing remains elusive. Pending successful progress in the above four standards, a major effort will be made in the current program to tackle standardization of fracture toughness. This is a very contentious issue since very strong preferences and opinions have developed over the years. There is at the moment, only a small amount of actual work ongoing on optimizing or refining the measurement of fracture toughness. The likelihood of standardizing a specific method within ASTM is hard to anticipate, but it may be a difficult process. The author is visiting DOE contractors and subcontractors and is assessing their needs and preferences. The indented flexure strength and chevron notch methods are surprisingly popular.

During this interval, Mr. Quinn was appointed international leader of VAMAS (Versailles Advanced Materials and Standards) Technical Working Area #3, Ceramics. This is an international collaboration of prestandardization research which involves cooperative work by the G-7 economic powers (United States, Japan, Germany, Italy, United Kingdom, Canada, France and the European Community.) At the moment, there is intensive work on fracture toughness evaluation and two round robins are underway. This work is relevant to the DOE programs since the new round robin includes include the chevron notch method. The fracture toughness of zirconia and silicon nitride specimens furnished by the Japan Fine

Ceramics Center as part of the 1989 round robin was measured at NIST. The methods include indentation fracture, indentation strength and the single edge precracked beam (bridge indentation) methods. NIST is currently evaluating these internal results as well as the data produced by four other USA participants: NASA-Lewis (J. Salem), Allied Signal-Garrett (Wimmer and Fang), Norton (Foley), and Worcester Polytechnic Institute (Bar-on). A final report on the USA results will be prepared in November or December 1991.

Status of Milestones

All milestones are on schedule.

Publications/Presentations

1. Chapter 8H "Strength and Proof Testing," Submitted to ASM for the Handbook on Ceramics and Glasses.
2. G. D. Quinn and R. Morrell, "Design Data for Engineering Ceramics: A Review of the Flexure Test," J. Am. Ceram. Soc., 74 [9] (1991) 2037-66.
3. G. D. Quinn, "Refinements to Flexure Testing," presented at the second European Ceramic Society Conference, Augsburg, Germany, Sept. 1991.
4. ASTM Draft Standard: "Dynamic Young's Modulus, Shear Modulus, and Poisson's Ratio for Advanced Ceramics by Sonic Resonance," by S. Gonczy, G. Quinn and J. Helfinstine. Submitted for ASTM Society ballot, May 1991.
5. ASTM draft standard: Standard Test Method for Flexural Strength of Advanced Ceramic at Elevated Temperature," by G. Quinn, Draft 3, balloted at ASTM C-28.01 subcommittee level in April 1991, resubmitted as draft 4 for main and subcommittee ballot, June 1991.
6. U. S. Army draft standard: "Standard Practice for Characterizing Strength Limiting Defects in Advanced Structural Ceramics", with M. Slavin and J. Swab, Draft 2 distributed for review, Sept. 1991.
7. ASTM draft standard: "Reporting Strength Data and Estimating Weibull Distribution Parameters for Advanced Ceramics," by S. Duffy and G. Quinn, Draft 2 prepared April 1991, draft 3 prepared Sept. 1991 for review by subcommittee C28.02 Design and Evaluation.
8. G. D. Quinn, "Flexure Testing of Advanced Ceramics: A Round-Robin," Presented at the Annual Meeting of the American Ceramic Society, Cincinnatti, Ohio, April 30, 1991.

ORNL/TM-11984

INTERNAL DISTRIBUTION

1-2. Central Research Library
3. Document Reference Section
4-5. Laboratory Records Department
6. Laboratory Records, ORNL RC
7. ORNL Patent Section
8-10. M&C Records Office
11. L. F. Allard, Jr.
12. L. D. Armstrong
13. P. F. Becher
14. R. F. Bernal
15. T. M. Besmann
16. P. J. Blau
17. A. Bleier
18. E. E. Bloom
19. K. W. Boling
20. R. A. Bradley
21. C. R. Brinkman
22. V. R. Bullington
23. R. S. Carlsmith
24. P. T. Carlson
25. G. M. Caton
26. S. J. Chang
27. R. H. Cooper, Jr.
28. S. A. David
29. J. H. DeVan
30. J. L. Ding
31. M. K. Ferber
32. F. M. Foust
33. W. Fulkerson
34. R. L. Graves
35. D. L. Greene
36. E. E. Hoffman
37. C. R. Hubbard
38. M. A. Janney
39. M. G. Jenkins
40-44. D. R. Johnson
45. W. F. Jones
46. D. Joslin
47. R. R. Judkins
48. M. A. Karnitz
49. M. R. Kass
50. B. L. Keyes
51. H. D. Kimrey, Jr.
52. T. G. Kollie
53. K. C. Liu
54. E. L. Long, Jr.
55. W. D. Manly
56. R. W. McClung
57. D. J. McGuire
58. J. R. Merriman
59. B. J. Moses
60. T. A. Nolan
61. J. L. Rich
62. C. R. Richmond
63. J M Robbins
64. M. L. Santella
65. A. C. Schaffhauser
66. S. Scott
67. G. M. Slaughter
68. E. J. Soderstrom
69. D. P. Stinton
70. R. W. Swindeman
71. V. J. Tennery
72. T. N. Tiegs
73. J. R. Weir, Jr.
74. B. H. West
75. F. W. Wiffen
76. S. G. Winslow
77. J. M. Wyrick
78. C. S. Yust

EXTERNAL DISTRIBUTION

79. James H. Adair
University of Florida
Materials Science &
Engineering
323 MAE Bldg.
Gainesville, FL 32611-2066

80. Donald F. Adams
University of Wyoming
Mechanical Engineering
Department
P. O. Box 3295
Laramie, WY 82071

81. Jalees Ahmad
AdTech Systems Research, Inc.
1342 North Fairfield Road
Dayton, OH 45432-2698

82. Yoshio Akimune
NISSAN Motor Co., Ltd.
Materials Research Laboratory
1 Natsushima-Cho
Yokosuka 237
JAPAN

83. Mufit Akinc
Iowa State University
322 Spedding Hall
Ames, IA 50011

84. Ilhan A. Aksay
University of Washington
Materials Science and Engineering
Department, FB-10
Seattle, WA 98195

85. R. G. Alexander
BASE
26 Malvern Close
Kettering Northants NN16 AJP
UNITED KINGDOM

86. Richard L. Allor
Ford Motor Company
Material Systems
Reliability Department
20000 Rotunda Drive
P.O. Box 2053, Room S-2031
Dearborn, MI 48121-2053

87. Richard T. Alpaugh
U.S. Department of Energy
Advanced Propulsion Division
CE-322, Forrestal Building
Washington, DC 20585

88. Joseph E. Amaral
Instron Corporation
Corporate Engineering Office
100 Royale Street
Canton, MA 02021

89. Edward M. Anderson
Anderson & Associates
4300 Pyles Ford Road
Centreville, DE 19807

90. Norman C. Anderson
Ceradyne, Inc.
Ceramic-to-Metal Division
3169 Redhill Avenue
Costa Mesa, CA 92626

91. Don Anson
Battelle Columbus Laboratories
Thermal Power Systems
505 King Avenue
Columbus, OH 43201-2693

92. Thomas Arbanas
G.B.C. Materials Corporation
580 Monastery Drive
Latrobe, PA 15650-2698

93. Frank Armatis
3M Company
3M Center
Building 60-1N-01
St. Paul, MN 55082

94. Everett B. Arnold
Detroit Diesel Corporation
Mechanical Systems Technology
13400 Outer Drive, West
Detroit, MI 48239-4001

95. Richard M. Arons
PA Consulting Group
279 Princeton Road
Hightstown, NJ 08550

96. Bertil Aronsson
Sandvik AB
S-12680
Stockholm Lerkrogsvagen 19
SWEDEN

97. Dennis Assanis
University of Illinois
Department of Mechanical Engineering
1206 W. Green Street
Urbana, IL 61801

98. William H. Atwell
Dow Corning Corporation
3901 South Saginaw Road
MS:540
Midland, MI 48686-0995

99. V. S. Avva
North Carolina A&T State University
Department of Mechanical Engineering
Greensboro, NC 27411

100. Patrick Badgley
Adiabatics, Inc.
3385 Commerce Drive
Columbus, IN 47201

101. Sunggi Baik
Pohang Institute of Science & Technology
Department of Materials Science and Engineering
P.O. Box 125
Pohang 790-600
KOREA

102. John M. Bailey
Caterpillar Inc.
Technical Center
Building L
P.O. Box 1875
Peoria, IL 61656-1875

103. Bob Baker
Ceradyne, Inc.
3169 Redhill Avenue
Costa Mesa, CA 92626

104. Frank Baker
Aluminum Company of America
Alcoa Technical Center
Alcoa Center, PA 15069

105. J. G. Baldoni
GTE Laboratories Inc.
40 Sylvan Road
Waltham, MA 02254

106. Clifford P. Ballard
Allied-Signal, Inc.
Ceramics Program
P.O. Box 1021
Morristown, NJ 07962-1021

107. M. Balu
Amoco Performance Products Inc.
4500 McGinnis Ferry Road
Alpharetta, GA 30202

108. B. P. Bandyopadhyay
University of North Dakota
University Station
Box 8214
Grand Forks, ND 58202

109. P. M. Barnard
Ruston Gas Turbines Limited
Metallurgical Laboratory
P. O. Box 1
Lincoln LN2 5DJ
ENGLAND

110. Harold N. Barr
Hittman Corporation
9190 Red Branch Road
Columbia, MD 21045

111. Renald D. Bartoe
Vesuvius McDanel
510 Ninth Avenue
Box 560
Beaver Falls, PA 15010-0560

112. Donald M. Bartos
Dow Corning Corporation
Advanced Ceramics Program
Midland, MI 48686-0995

113. David L. Baty
Babcock & Wilcox-LRC
P.O. Box 11165
Lynchburg, VA 24506-1165

114. Donald F. Baxter, Jr.
ASM International
Advanced Materials and Processes
Materials Park, OH 44073-0002

115. Robert Beck
Teledyne CAE
Materials Engineering/Programs
1330 Laskey Road
P.O. Box 6971
Toledo, OH 43612

116. John C. Bell
Shell Research Limited
Thornton Research Centre
P.O. Box 1
Chester, Ch1 3SH
ENGLAND

117. Albert H. Bell, III
General Motors Technical Center
30200 Mound Road
Engineering Building/W3 Turbine
Warren, MI 48090-9010

118. M. Bentele
Xamag, Inc.
259 Melville Avenue
Fairfield, CT 06430

119. Larry D. Bentsen
BF Goodrich Company
R&D Center
9921 Brecksville Road
Brecksville, OH 44141

120. Joseph C. Bentz
ENCERATEC
2525 Sandcrest Drive
Columbus, IN 47203

121. Louis Beregszazi
Defiance Precision Products
P.O. Box Drawer 428
Defiance, OH 43512

122. Tom Bernecki
Northwestern University
BIRL
1801 Maple Avenue
Evanston, IL 60201-3135

123. Charles F. Bersch
Institute for Defense Analyses
1801 North Beauregard Street
Alexandria, VA 22311

124. Ram Bhatt
NASA Lewis Research Center
21000 Brookpark Road
Cleveland, OH 44135

125. Deane I. Biehler
Caterpillar Inc.
Engineering and Research Materials
Technical Center, Building E
P.O. Box 1875
Peoria, IL 61656-1875

126. John. W. Bjerklie
Consolidated Natural Gas Service Co., Inc.
Research Department
CNG Tower
Pittsburgh, PA 15222-3199

127. William D. Bjorndahl
TRW, Inc.
One Space Park
Building 01, Room 2040
Redondo Beach, CA 90278

128. Keith A. Blakely
Advanced Refractory Technologies, Inc.
699 Hertel Avenue
Buffalo, NY 14207

129. Edward G. Blanchard
Netzsch Inc.
119 Pickering Way
Exton, PA 19341

130. Keith Blandford
Boride Products, Inc.
2879 Aero Park Drive
Traverse City, MI 49684

131. Bruce Boardman
Deere and Company Technical Center
3300 River Road
Moline, IL 61265

132. Russell Bockstedt
Hoechst Celanese Corporation
150 JFK Parkway
Short Hills, NJ 07078

133. M. Boehmer
DLR German Aerospace Research Establishment
Postfach 90 60 58
D-5000 Koln 90
GERMANY

134. Lawrence P. Boesch
EER Systems Corp.
1593 Spring Hill Road
Vienna, VA 22182-2239

135. Donald H. Boone
Boone & Associates
2412 Cascade Drive
Walnut Creek, CA 94598-4313

136. Tom Booth
Allied-Signal Aerospace Company
AiResearch Los Angeles Division
2525 West 190th Street
Torrance, CA 90509-2960

137. Tibor Bornemisza
Sundstrand Power Systems
4400 Ruffin Road
San Diego, CA 92186-5757

138. J.A.M. Boulet
University of Tennessee
Department of Engineering Science and Mechanics
310 Perkins Hall
Knoxville, TN 37996-2030

139. H. Kent Bowen
Massachusetts Institute of Technology
77 Massachusetts Avenue
Room E40-434
Cambridge, MA 02139

140. Leslie J. Bowen
Materials Systems
53 Hillcrest Road
Concord, MA 01742

141. Steven C. Boyce
Air Force Office of Scientific Research
AFOSR/NA Bldg. 410
Bolling AFB DC 20332-6448

142. Gary L. Boyd
CEC
400 Howell Avenue, No. 4
Warland, WY 82401

143. Steve Bradley
UOP Research Center
50 East Algonquin Road
Des Plaines, IL 60017-6187

144. Michael C. Brands
Cummins Engine Company, Inc.
P.O. Box 3005
Mail Code 50179
Columbus, IN 47201

145. Raymond J. Bratton
Westinghouse Science and Technology Center
1310 Beulah Road
Pittsburgh, PA 15235

146. John J. Brennan
United Technologies Corporation
Research Center
Silver Lane, MS:24
East Hartford, CT 06108

147. Jeff D. Bright
Ceramatec, Inc.
2425 South 900 West
Salt Lake City, UT 84108

148. Terrence K. Brog
Coors Ceramics Company
Corporate Development and Technology
4545 McIntyre Street
Golden, CO 80403

149. Gunnar Broman
317 Fairlane Drive
Spartanburg, SC 29302

150. Al Brown
High-Tech Materials Alert
P.O. Box 882
Dayton, NJ 08810

151. Jesse Brown
Virginia Polytechnic Institute and State University
Center for Advanced Ceramic Materials
Blacksburg, VA 24061-0256

152. Sherman D. Brown
University of Illinois
Materials Science and Engineering Department
105 South Goodwin Avenue
204 Ceramics Building
Urbana, IL 61801

153. S. L. Bruner
Ceramatec, Inc.
2425 South 900 West
Salt Lake City, UT 84119

154. Adolfo Brusaferro
Keramont Corporation
4231 South Fremont Avenue
Tucson, AZ 85714

155. W. Bryzik
U.S. Army Tank Automotive Command
R&D Center
Propulsion Systems Division
Warren, MI 48397-5000

156. S. T. Buljan
GTE Laboratories Inc.
40 Sylvan Road
Waltham, MA 02254

157. S. J. Burden
GTE Valenite
1711 Thunderbird
Troy, MI 48084

158. Curt V. Burkland
AMERCOM, Inc.
8928 Fullbright Avenue
Chatsworth, CA 91311

159. Bill Bustamante
AMERCOM, Inc.
8928 Fullbright Avenue
Chatsworth, CA 91311

160. Oral Buyukozturk
Massachusetts Institute of Technology
77 Massachusetts Avenue
Room 1-280
Cambridge, MA 02139

161. David A. Caillet
Ethyl Corporation
451 Florida Street
Baton Rouge, LA 70801

162. Frederick J. Calnan
Heany Industries, Inc.
249 Briarwood Lane
P.O. Box 38
Scottsville, NY 14546

163. Roger Cannon
Rutgers University
Department of Ceramics
P.O. Box 909
Piscataway, NJ 08855-0909

164. Scott Cannon
P.O. Box 567254
Atlanta, GA 30356

165. Harry W. Carpenter
19945 Acre Street
Northridge, CA 91324

166. David Carruthers
Kyocera Industrial Ceramics Company
P.O. Box 2279
Vancouver, WA 98668-2279

167. Calvin H. Carter, Jr.
Cree Research, Inc.
2810 Meridian Parkway
Durham, NC 27713

168. J. David Casey
35 Atlantis Street
West Roxbury, MA 02132

169. Jere G. Castor
J. C. Enterprise
5078 North 83rd Street
Scottsdale, AZ 85250

170. James D. Cawley
Case Western Reserve University
Materials Science and
Engineering Department
Cleveland, OH 44106

171. Thomas C. Chadwick
Den-Mat Corporation
P.O. Box 1729
Santa Maria, CA 93456

172. Ronald H. Chand
Chand Kare Technical Ceramics
2 Coppage Drive
Worcester, MA 01603

173. Robert E. Chaney
EG&G Idaho, Inc.
Idaho National Engineering
Laboratory
P.O. Box 1625
Idaho Falls, ID 83415-3525

174. Frank C. Chang
U.S. Army Materials
Technology Laboratory
AMTL-EMM
405 Arsenal Street
Watertown, MA 02172

175. Robert M. Chapman
Allied-Signal Aerospace
Company
1530 Wilson Boulevard,
10th Floor
Arlington, VA 22209

176. William Chapman
Williams International
Corporation
2280 West Maple Road
Walled Lake, MI 48390-0200

177. Charlie Chen
LECO Corporation
P.O. Box 211688
Augusta, GA 30917

178. Albert A. Chesnes
U.S. Department of Energy
Transportation Technologies
CE-30, Forrestal Building,
6B-094
Washington, DC 20585

179. Kaiyin Chia
Carborundum Company
P.O. Box 832
Niagara Falls, NY 14302

180. Frank Childs
EG&G Idaho, Inc.
Idaho National Engineering
Laboratory
P.O. Box 1625
Idaho Falls, ID 83415-3527

181. William J. Chmura
Torrington Company
59 Field Street
Torrington, CT 06790-4942

182. Tsu-Wei Chou
University of Delaware
Center for Composite
Materials
201 Spencer Laboratory
Newark, DE 19716

183. R. J. Christopher
Ricardo Consulting Engineers
Bridge Works
Shoreham-By-Sea West Sussex
Shoreham BN43 5FG
ENGLAND

184. Joel P. Clark
Massachusetts Institute of
Technology
Room 8-409
Cambridge, MA 02139

185. Giorgio Clarotti
Commission of the European
Communities
DGXII-C3, M075, 1-53;
200 Rue de la Loi
B0-1049 Brussels
BELGIUM

186. W. J. Clegg
ICI Advanced Materials
P.O. Box 11
The Heath, Runcorn Cheshire
WA7 4QE
ENGLAND

187. Joseph Cleveland
GTE Products Corporation
Hawes Street
Towanda, PA 18848-0504

188. Gloria M. Collins
ASTM
1916 Race Street
Philadelphia, PA 19103

189. William C. Connors
Sundstrand Aviation Operations
Materials Science and
Engineering Department
4747 Harrison Avenue
P.O. Box 7002
Rockford, IL 61125-7002

190. John A. Coppola
Carborundum Company
P.O. Box 156
Niagara Falls, NY 14302

191. Normand D. Corbin
Norton Company
Advanced Ceramics
Goddard Road
Northboro, MA 01532-1545

192. Douglas Corey
Allied-Signal Aerospace
Company
2525 West 190th Street
MS:T52
Torrance, CA 90504-6099

193. Keith P. Costello
Chand/Kare Technical Ceramics
2 Coppage Drive
Worcester, MA 01603-1252

194. Ed L. Courtright
Pacific Northwest
Laboratory
MS:K3-59
Richland, WA 99352

195. Anna Cox
Mitchell Market Reports
P.O. Box 23
Monmouth Gwent NP5 4YG
UNITED KINGDOM

196. Thomas Coyle
Unocal Corporation
Unocal Science & Technology
Division
376 South Valencia Avenue
Brea, CA 92621

197. Art Cozens
Instron Corporation
3414 Snowden Avenue
Long Beach, CA 90808

198. Robert C. Craft
American Ceramic
Society, Inc.
757 Brooksedge Plaza Drive
Westerville, OH 43081

199. Mark Crawford
New Technology Week
4604 Monterey Drive
Annandale, VA 22003

200. Richard A. Cree
Markets & Products, Inc.
P.O. Box 14328
Columbus, OH 43214-0328

201. Les Crittenden
Vesuvius McDanel
Box 560
Beaver Falls, PA 15010

202. William J. Croft
U.S. Army Materials
Technology Laboratory
405 Arsenal Street
Watertown, MA 02172

203. M. J. Cronin
Mechanical Technology, Inc.
968 Albany-Shaker Road
Latham, NY 12110

204. Gary M. Crosbie
Ford Motor Company
1430 Culver Avenue
S-2079, SRL Building
Dearborn, MI 48121-4036

205. Floyd W. Crouse, Jr.
U.S. Department of Energy
Morgantown Energy
Technology Center
Collins Ferry Road
P.O. Box 880
Morgantown, WV 26505

206. John Cuccio
Allied-Signal Aerospace
Company
Garrett Auxiliary Power
Division
P.O. Box 5227, MS:1302-2Q
Phoenix, AZ 85010

207. Raymond Cutler
Ceramatec, Inc.
2425 South 900 West
Salt Lake City, UT 84119

208. Charles D'Angelo
GTE Laboratories, Inc.
40 Sylvan Road
Waltham, MA 02154

209. Stephen C. Danforth
Rutgers University
Ceramic Engineering Department
P.O. Box 909
Piscataway, NJ 08855-0909

210. Sankar Das Gupta
Electrofuel Manufacturing
Co., Ltd.
9 Hanna Avenue
Toronto Ontario MGK-1W8
CANADA

211. Charles Davis
Sverdrup Technology,
Inc., MSFC
620 Discovery Drive
Huntsville, AL 35806

212. Robert F. Davis
North Carolina State
University
Materials Engineering
Department
229 Riddick Laboratory
P.O. Box 7907
Raleigh, NC 27695

213. Thomas DeAngelis
Carborundum Company
Niagara Falls R&D Center
P.O. Box 832
Niagara Falls, NY 14302

214. George DeBell
Ford Motor Company
Material Systems Reliability
Department
20000 Rotunda Drive
P.O. Box 2053, Room S-2023
Dearborn, MI 48121-2053

215. Michael DeLuca
AMP-AKZO
West Lane
Aquebogue, NY 11931

216. Gerald L. DePoorter
Colorado School of Mines
Metallurgical and Materials
Engineering Department
Golden, CO 80401

217. Nick C. Dellow
Materials Technology
Publications
40 Sotheron Road
Watford Herts WD1 2QA
UNITED KINGDOM

218. L. R. Dharani
University of Missouri-Rolla
224 M.E.
Rolla, MO 65401

219. John Dodsworth
Vesuvius Research &
Development
Technical Ceramics Group
Box 560
Beaver Falls, PA 15010

220. B. Dogan
Institut fur Werkstofforschung
GKSS-Forschungszentrum
Geesthacht GmbH
Max-Planck-Strasse
D-2054 Geesthacht
GERMANY

221. Jean-Marie Drapier
FN Moteurs S.A.
Material and Processing
B-4041 Milmort (Herstal)
BELGIUM

222. Kenneth C. Dreitlein
United Technologies
Research Center
Silver Lane
East Hartford, CT 06108

223. Robin A.L. Drew
McGill University
Department of Mining and
Metallurgical Engineering
3450 University Street
Montreal Quebec H3A 2A7
CANADA

224. Winston H. Duckworth
Battelle Memorial Institute
Columbus Division
505 King Avenue
Columbus, OH 43201-2693

225. Edmund M. Dunn
Texel Company
6 Third Street
Lexington, MA 02173

226. Bill Durako
Sundstrand Aviation Operations
Department 789-6
4747 Harrison Avenue
P.O. Box 7002
Rockford, IL 61125-7002

227. Ernest J. Duwell
212 Elm Street
Hudson, WI 54016

228. Chuck J. Dziedzic
Coors Ceramics Company
Structural Products Group
17750 West 32nd Avenue
Golden, CO 80401

229. Jeffrey Eagleson
Lanxide Corporation
1001 Connecticut Avenue, N.W.
Washington DC 20036

230. Harry E. Eaton
United Technologies Corporation
Research Center
Silver Lane
East Hartford, CT 06108

231. Harvill C. Eaton
Louisiana State
University
Office of Research
and Economic Development
240 Thomas Boyd Hall
Baton Rouge, LA 70803

232. Christopher A. Ebel
Carborundum Company
Technology Division
P.O. Box 337
Niagara Falls, NY 14302

233. J. J. Eberhardt
U.S. Department of Energy
Office of Advanced
Transportation Materials
CE-34, Forrestal Building
Washington, DC 20585

234. Jim Edler
Eaton Corporation
26201 Northwestern
Highway
P.O. Box 766
Southfield, MI 48037

235. William A. Ellingson
Argonne National Laboratory
Materials Science Technology
Division
9700 South Cass Avenue
Argonne, IL 60439

236. William S. Ellis
Machined Ceramics
629 N. Graham St.
N. Industrial Park
Bowling Green, KY 42101

237. Glen B. Engle
Nuclear & Aerospace Materials
Corporation
16716 Martincoit Road
Poway, CA 92064

238. Jeff Epstein
Ceramic Technologies, Inc.
2107 Jamara Lane
Houston, TX 77077

239. Kenneth A. Epstein
Dow Chemical U.S.A.
Ceramics and Advanced Materials
800 Building
Midland, MI 48667

240. Art Erdemir
Argonne National Laboratory
Materials and Components
Technology Division
9700 South Cass Avenue
Argonne, IL 60439

241. E. M. Erwin
Lubrizol Corporation
1819 East 225th Street
Euclid, OH 44117

242. Kenji Esaki
Toyota Technical Center
U.S.A., Inc.
2000 Town Center, Suite 500
Southfield, MI 48075

243. Jose L. Escalante
Anglo-Mex-Tech. Inc.
3923 N.W. 24th Street
Miami, FL 33142

244. John N. Eustis
U.S. Department of Energy
Industrial Energy Efficiency
Division
CE-221, Forrestal Building
Washington, DC 20585

245. Robert C. Evans
NASA Lewis Research Center
Terrestrial Propulsion Office
21000 Brookpark Road, MS:86-6
Cleveland, OH 44135

246. W. L. Everitt
Kyocera International, Inc.
8611 Balboa Avenue
San Diego, CA 92123

247. Gordon Q. Evison
332 South Michigan Avenue
Suite 1730
Chicago, IL 60604

248. John W. Fairbanks
U.S. Department of Energy
Advanced Propulsion Division
CE-322, Forrestal Building
Washington, DC 20585

249. Tim Fawcett
Dow Chemical Company
Central Research, Advanced
Ceramics Laboratory
1776 Building
Midland, MI 48674

250. Robert W. Fawley
Sundstrand Power Systems
Division of Sundstrand
Corporation
4400 Ruffin Road
P.O. Box 85757
San Diego, CA 92186-5757

251. John J. Fedorchak
GTE Products Corporation
Hawes Street
Towanda, PA 18848-0504

252. Jeff T. Fenton
Vista Chemical Company
900 Threadneedle
Houston, TX 77079

253. Larry Ferrell
Babcock & Wilcox
Old Forest Road
Lynchburg, VA 24505

254. Raymond R. Fessler
BIRL
Industrial Research Lab
1801 Maple Avenue
Evanston, IL 60201

255. Michelle Finch
E. I. DuPont de Nemours &
Company, Inc.
Experimental Station
Information Center E302/301
Wilmington, DE 19898

256. Arthur D. Fine
United Technologies Corporation
Pratt & Whitney Aircraft
400 Main Street
MS:163-10
East Hartford, CT 06108

257. Ross F. Firestone
Ross Firestone Company
188 Mary Street
Winnetka, IL 60093-1520

258. Sharon L. Fletcher
Arthur D. Little, Inc.
15 Acorn Park
Cambridge, MA 02140-2390

259. Thomas F. Foltz
Textron Specialty Materials
2 Industrial Avenue
Lowell, MA 01851

260. Renee G. Ford
Materials and Processing Report
P.O. Box 72
Harrison, NY 10528

261. John Formica
Supermaterials
2020 Lakeside Avenue
Cleveland, OH 44114

262. Jennifer M. Fox
Dyson Refractories Limited
R&D Laboratory
Owler Bar
Sheffield S17 3BJ
UNITED KINGDOM

263. Edwin Frame
Southwest Research Institute
Division 2
P.O. Box Drawer 28510
San Antonio, TX 78284

264. Armanet Francois
French Scientific Mission
4101 Reservoir Road, N.W.
Washington DC 20007-2176

265. R. G. Frank
Technology Assessment Group
10793 Bentley Pass Lane
Cincinnati, OH 45140

266. David J. Franus
Forecast International
22 Commerce Road
Newtown, CT 06470

267. Marc R. Freedman
NASA Lewis Research Center
21000 Brookpark Road
MS:49-3
Cleveland, OH 44135

268. Douglas Freitag
LTV Missiles Division
P.O. Box 650003
MS:WT-21
Dallas, TX 75265-0003

269. Brian R.T. Frost
Argonne National Laboratory
9700 South Cass Avenue
Building 900
Argonne, IL 60439

270. Lawrence R. Frost
Instron Corporation
100 Royall Street
Canton, MA 02021

271. George A. Fryburg
Norton/TRW Ceramics
7A-4 Raymond Avenue
Salem, NH 03079

272. Xiren Fu
Shanghai Institute of Ceramics
Chinese Academy of Sciences
1295 Ding-xi Road
Shanghai 200050
CHINA

273. John Gahimer
P.O. Box 1302
Dublin, OH 43017

274. J. P. Gallagher
University of Dayton Research Institute
300 College Park, JPC-250
Dayton, OH 45469-0120

275. Tom Garritano
University of Tennessee
Science Alliance
101 South College
Knoxville, TN 37996-1328

276. Joy A. Garwood
Norton Company
Advanced Ceramics
Goddard Road
Northboro, MA 01532-1545

277. H. Maury Gatewood
Reynolds Metals Company
Corporate R&D
Fourth and Canal Streets
P.O. Box 27003
Richmond, VA 23261

278. L. J. Gauckler
ETH-Zurich
Sonneggstrasse 5
CH-8092 Zurich 8092
SWITZERLAND

279. Peter A. Gaydos
Battelle Columbus Laboratories
505 King Avenue
Columbus, OH 43201

280. George E. Gazza
U.S. Army Materials
Technology Laboratory
Ceramics Research Division
405 Arsenal Street
Watertown, MA 02172-0001

281. D. Gerster
CEA-DCOM
33 Rue De La Federation
Paris 75015
FRANCE

282. John Ghinazzi
Coors Technical Ceramics
Company
1100 Commerce Park Drive
Oak Ridge, TN 37830

283. Robert Giddings
General Electric Company
Research Laboratory
P.O. Box 8
Schenectady, NY 12301

284. A. M. Glaeser
University of California
Materials Science and Mineral
Engineering
Lawrence Berkeley Laboratory
Hearst Mining Building
Berkeley, CA 94720

285. Paul Glance
Concept Analysis
R&D
950 Stephenson Highway
Dupont Automotive Development
Building
Troy, MI 48007-7013

286. Joseph W. Glatz
Naval Air Propulsion Test
Center
Systems Engineering Division
P.O. Box 7176, PE24
Trenton, NJ 08628

287. W. M. Goldberger
Superior Graphite Company
R&D
2175 East Broad Street
Columbus, OH 43209

288. Allan E. Goldman
U.S. Graphite, Inc.
907 West Outer Drive
Oak Ridge, TN 37830

289. Stephen T. Gonczy
Allied Signal Research
P.O. Box 5016
Des Plaines, IL 60017

290. Jeffrey M. Gonzales
GTE Products Corporation
Hawes Street
Towanda, PA 18848-0504

291. Robert J. Gottschall
U.S. Department of Energy
ER-131, MS:G-236
Washington, DC 20545

292. Earl Graham
Cleveland State University
Department of Chemical Engineering
Euclid Avenue at East 24th Street
Cleveland, OH 44115

293. William A. Graham
Lanxide Corporation
P.O. Box 6077
Newark, DE 19714-6077

294. Robert E. Green, Jr.
Johns Hopkins University
Materials Science and Engineering Department
Baltimore, MD 21218

295. Lance Groseclose
General Motors Corporation
Allison Gas Turbine Division
P.O. Box 420, MS:W-5
Indianapolis, IN 46206

296. Mark F. Gruninger
Union Carbide Corporation
Specialty Powder Business
1555 Main Street
Indianapolis, IN 46224

297. Ernst Gugel
Cremer Forschungsinstitut GmbH&Co.KG
Oeslauer Strasse 35
O-8633 Roedental 8633
GERMANY

298. Donald L. Guile
Corning Glass Works
SP-DV-1-9
Corning, NY 14831

299. Bimleshwar P. Gupta
Solar Energy Research Institute
Mechanical and Industrial Technology Division
1617 Cole Boulevard
Golden, CO 80401

300. John P. Gyekenyesi
NASA Lewis Research Center
21000 Brookpark Road, MS:6-1
Cleveland, OH 44135

301. Nabil S. Hakim
Detroit Diesel Corporation
13400 West Outer Drive
Detroit, MI 48239

302. Philip J. Haley
General Motors Corporation
Vehicular Engineering
P.O. Box 420, MS:T12A
Indianapolis, IN 46236

303. Judith Hall
Fiber Materials, Inc.
Biddeford Industrial Park
5 Morin Street
Biddeford, ME 04005

304. Y. Harada
IIT Research Institute
Nometallic Materials and Composites
10 West 35th Street
Chicago, IL 60616

305. R. A. Harmon
25 Schalren Drive
Latham, NY 12110

306. Amy Harmon-Barrett
Martin Marietta Laboratories
1450 South Rolling Road
Baltimore, MD 21227

307. Norman H. Harris
Hughes Aircraft Company
P.O. Box 800520
Saugus, CA 91380-0520

308. Alan Hart
Dow Chemical Company
Advanced Ceramics Laboratory
1776 Building
Midland, MI 48674

309. Pat E. Hart
Battelle Pacific Northwest Laboratories
Ceramics and Polymers Development Section
P.O. Box 999
Richland, WA 99352

310. Stephen D. Hartline
Norton Company
Advanced Ceramics
Goddard Road
Northboro, MA 01532-1545

311. Michael H. Haselkorn
Caterpillar Inc.
Engineering Research Materials
Technical Center, Building E
P.O. Box 1875
Peoria, IL 61656-1875

312. N. B. Havewala
Corning Inc.
SP-PR-11
Corning, NY 14831

313. John Haygarth
Teledyne WAA Chang Albany
P.O. Box 460
Albany, OR 97321

314. Norman L. Hecht
University of Dayton Research Institute
300 College Park
Dayton, OH 45469-0172

315. Peter W. Heitman
General Motors Corporation
Allison Gas Turbine Division
P.O. Box 420, MS:W-5
Indianapolis, IN 46206-0420

316. Robert W. Hendricks
Virginia Polytechnic Institute and State University
Materials Engineering Department
210 Holden Hall
Blacksburg, VA 24061-0237

317. Wayne Henley
Hertel Cutting Technologies Inc.
1000 Clearview Court
Oak Ridge, TN 37830

318. Thomas L. Henson
GTE Products Corporation
Chemical & Metallurgical Division
Hawes Street
Towanda, PA 18848

319. Thomas P. Herbell
NASA Lewis Research Center
21000 Brookpark Road
MS:49-3
Cleveland, OH 44135

320. Marlene Heroux
Rolls-Royce, Inc.
2849 Paces Ferry Road
Suite 450
Atlanta, GA 30339-3769

321. Robert L. Hershey
Science Management Corporation
1255 New Hampshire Ave., NW
Suite 1033
Washington DC 20036

322. Hendrik Heystek
Bureau of Mines
Tuscaloosa Research Center
P.O. Box L
University, AL 35486

323. Wallace C. Higgins
Norwal Unlimited
P.O. Box 1258
Alfred, NY 14802

324. Robert V. Hillery
GE Aircraft Engines
One Neumann Way, M.D. H85
Cincinnati, OH 45215

325. Arthur Hindman
Instron Corporation
100 Royall Street
Canton, MA 02021

326. Jon Hines
American Ceramic Society, Inc.
757 Brooksedge Plaza Drive
Westerville, OH 43081-6136

327. Hans Erich Hintermann
CSEM
Materials and Micromechanics Division
Rue Breguet 2
Neuchatel 2000
SWITZERLAND

328. Shinichi Hirano
Mazda R&D of North America, Inc.
1203 Woodridge Avenue
Ann Arbor, MI 48105

329. Tommy Hiraoka
NGK Locke, Inc.
1000 Town Center
Southfield, MI 48075

330. John M. Hobday
U.S. Department of Energy
Morgantown Energy Technology Center
Collins Ferry Road
P.O. Box 880
Morgantown, WV 26507

331. Greg Hoenes
Vista Chemical Company
900 Threadneedle
P.O. Box 19029
Houston, TX 77079-2990

332. Clarence Hoenig
Lawrence Livermore National Laboratory
P.O. Box 808, Mail Code L-369
Livermore, CA 94550

333. Thomas Hollstein
Fraunhofer-Institut fur Werkstoffmechanik IWM
Wohlerstrabe 11
D-7800 Freiburg
GERMANY

334. Richard Holt
National Research Council of Canada
Structures and Materials Laboratory
Ottawa Ontario K1A 0R6
CANADA

335. Joe Homeny
University of Illinois
Department of Materials Science and Engineering
105 South Goodwin Avenue
Ceramics Building
Urbana, IL 61801

336. A. T. Hopper
Battelle Columbus Laboratories
Metals and Ceramics Department
505 King Avenue
Columbus, OH 43201-2693

337. Woodie Howe
Coors Technical Ceramics Company
1100 Commerce Park Drive
Oak Ridge, TN 37830

338. Stephen M. Hsu
National Institute of Standards and Technology
Gaithersburg, MD 20899

339. Hann S. Huang
Argonne National Laboratory
9700 South Cass Avenue
Argonne, IL 60439-4815

340. Gene Huber
Precision Ferrites & Ceramics
5576 Corporate Drive
Cypress, CA 90630

341. M. L. Huckabee
GTE Laboratories, Inc.
40 Sylvan Road
Waltham, MA 02254

342. Harold A. Huckins
Princeton Advanced Technology, Inc.
56 Finley Road
Princeton, NJ 08540

343. Fred Huettic
Advanced Magnetics Inc.
45 Corey Lane
Mendham, NJ 07945

344. Bill Huffman
Zircar
110 North Main Street
Florida, NY 10921

345. Brian K. Humphrey
Lubrizol Petroleum
Chemicals Co.
3000 Town Center, Suite 1340
Southfield, MI 48075-1201

346. Robert M. Humrick
Dylon Ceramic Technologies
3100 Edgehill Road
Cleveland Heights, OH 44118

347. Lorretta Inglehart
National Science Foundation
Division of Materials Research
1800 "G" Street, N.W., Room 408
Washington, DC 20550

348. Michael S. Inoue
Kyocera International, Inc.
KII Library
8611 Balboa Avenue
San Diego, CA 92123-1580

349. Osama Jadaan
University of Wisconsin-
Platteville
General Engineering Division
1 University Plaza
Platteville, WI 53818

350. Curtis A. Johnson
General Electric Company
Corporate R&D
Room MB-187
P.O. Box 8
Schenectady, NY 12301

351. Sylvia Johnson
SRI International
333 Ravenswood Avenue
Menlo Park, CA 94025

352. Thomas A. Johnson
Lanxide Corporation
1300 Marrows Road
P.O. Box 6077
Newark, DE 19714-6077

353. W. S. Johnson
Indiana University
One City Centre, Suite 200
Bloomington, IN 47405

354. L. A. Joo
Great Lakes Research
Corporation
P.O. Box 1031
Elizabethton, TN 37643

355. A. D. Joseph
SPX Corporation
700 Terrace Point
Muskegon, MI 49443

356. Adam Jostsons
Australian Nuclear Science &
Technology Organization
Lucas Heights Research
Laboratories
New Illawarra Road
Lucas Heights New South Wales
AUSTRALIA

357. Matthew K. Juneau
Ethyl Corporation
451 Florida Street
Baton Rouge, LA 70801

358. Hartmut Kainer
Didier-Werke AG
Anlagentechnik Wiesbaden
Abraham-Lincoln-Str. 16
D-62 Wiesbaden
GERMANY

359. Tom Kalamasz
Norton/TRW Ceramics
7A-4 Raymond Avenue
Salem, NH 03079

360. Lyle R. Kallenbach
Phillips Petroleum Company
R&D
Mail Drop:123AL
Bartlesville, OK 74004

361. Nick Kamiya
Kyocera Industrial Ceramics
Corporation
2700 River Road
Des Plaines, IL 60018

362. Roy Kamo
Adiabatics, Inc.
3385 Commerce Park Drive
Columbus, IN 47201

363. S. Kang
GTE Laboratories, Inc.
40 Sylvan Road
Waltham, MA 02254

364. Chih-Chun Kao
Industrial Technology Research Institute
Materials Research Laboratories
195 Chung-Hsing Road, Sec. 4
Chutung Hsinchu 31015 R.O.C.
TAIWAN

365. Keith R. Karasek
Allied-Signal, Inc.
Engineered Materials Research Center
50 East Algonquin Road
P.O. Box 5016
Des Plaines, IL 60017-5016

366. Robert E. Kassel
Ceradyne, Inc.
3169 Redhill Avenue
Costa Mesa, CA 92626

367. Allan Katz
Wright Laboratory
Metals and Ceramics Division
WL/MLLM
Wright-Patterson AFB, OH 45433

368. R. Nathan Katz
Worcester Polytechnic Institute
Dept. of Mechanical Engineering
100 Institute Road
Worcester, MA 01609

369. Ted Kawaguchi
Tokai Carbon America, Inc.
375 Park Avenue, Suite 3802
New York, NY 10152

370. Noritsugu Kawashima
TOSHIBA Corporation
Mechanical Engineering Laboratory
4-1 Ukishima-Cho
Kawasaki-Ku Kawasaki 210
JAPAN

371. Lisa Kempfer
Penton Publishing
Materials Engineering
1100 Superior Avenue
Cleveland, OH 44114-2543

372. Frederick L. Kennard, III
General Motors Corporation
AC Rochester
Department 32-24, EB
1300 North Dort Highway
Flint, MI 48556

373. David O. Kennedy
Lester B. Knight Cast Metals Inc.
549 West Randolph Street
Chicago, IL 60661

374. George Keros
Photon Physics
3175 Penobscot Building
Detroit, MI 48226

375. Pramod K. Khandelwal
General Motors Corporation
Allison Gas Turbine Division
P.O. Box 420, MS:W-5
Indianapolis, IN 46206

376. Jim R. Kidwell
Allied-Signal Aerospace Company
Garrett Auxiliary Power Division
P.O. Box 5227
Phoenix, AZ 85010

377. Han J. Kim
GTE Laboratories, Inc.
40 Sylvan Road
Waltham, MA 02254

378. Shin Kim
Korea Institute of Machinery & Metals
66 Sangnam-dong, Changwon
Kyungnam 641-010
KOREA

379. W. C. King
Mack Truck, Z-41
1999 Pennsylvania Avenue
Hagerstown, MD 21740

380. Carol Kirkpatrick
MSE, Inc.
CDIF Technical Library
P.O. Box 3767
Butte, MT 59702

381. Tony Kirn
Caterpillar Inc.
Defense Products Department, JB7
Peoria, IL 61629

382. James D. Kiser
NASA Lewis Research Center
21000 Brookpark Road, MS:49-3
Cleveland, OH 44135

383. Max Klein
Gas Research Institute
Thermodynamics
8600 West Bryn Mawr Avenue
Chicago, IL 60631

384. Richard N. Kleiner
Coors Ceramics Company
4545 McIntyre Street
Golden, CO 80403

385. Stanley J. Klima
NASA Lewis Research Center
21000 Brookpark Road
MS:6-1
Cleveland, OH 44135

386. Chris E. Knapp
Norton Advanced Ceramics of Canada Ltd.
8001 Daly Street
Niagara Falls, Ontario L2G 6S2
CANADA

387. Albert S. Kobayashi
University of Washington
Mechanical Engineering Department
MS:FU10
Seattle, WA 98195

388. Shigeki Kobayashi
Toyota Central Research Labs, Inc.
Nagakute Aichi 480-11
JAPAN

389. Richard A. Kole
Z-Tech Corporation
8 Dow Road
Bow, NH 03304

390. E. Kostiner
University of Connecticut
Chemistry Department, U-60
Storrs, CT 06269-3060

391. Kenneth A. Kovaly
Technical Insights Inc.
P.O. Box 1304
Fort Lee, NJ 07024-9967

392. Ralph G. Kraft
Spraying Systems Company
North Avenue at Schmale Road
Wheaton, IL 60189-7900

393. Saunders B. Kramer
U.S. Department of Energy
Advanced Propulsion Division
CE-322, Forrestal Building
Washington, DC 20585

394. Arthur Kranish
Trends Publishing Inc.
1079 National Press Building
Washington DC 20045

395. A. S. Krieger
Radiation Science, Inc.
P.O. Box 293
Belmont, MA 02178

396. Pieter Krijgsman
Ceramic Design International
Holding B.V.
P.O. Box 68
Hattem 8050-AB
THE NETHERLANDS

397. Waltraud M. Kriven
University of Illinois
Materials Science &
Engineering Department
105 South Goodwin Avenue
Urbana, IL 61801

398. Edward J. Kubel, Jr.
ASM International Advanced
Materials & Processes
Materials Park, OH 44073

399. Dave Kupperman
Argonne National Laboratory
9700 South Cass Avenue
Argonne, IL 60439

400. Oh-Hun Kwon
Norton Company
Advanced Ceramics
Goddard Road
Northboro, MA 01532-1545

401. W. J. Lackey
Georgia Institute of Technology
Materials Science and
Technology
Atlanta, GA 30332

402. Jai Lala
Tenmat Ltd.
40 Somers Road
Rugby Warwickshire CV22 7DH
ENGLAND

403. Richard L. Landingham
Lawrence Livermore National
Laboratory
Ceramics, Corrosion, and
Thermochemistry
P.O. Box 808, L-369
Livermore, CA 94550

404. Charles J. Landry
Chand Kare Technical Ceramics
712 Flat Hill Road
Lumenburg, MA 01462

405. Manfred W. Langer
Volkswagen AG
Material Technology
3180 Wolfsburg 1
GERMANY

406. James Lankford
Southwest Research Institute
Department of Materials
Sciences
6220 Culebra Road
San Antonio, TX 78228-0510

407. Stanley B. Lasday
Business News Publishing Co.
Manor Oak One
1910 Cochran Road, Suite 630
Pittsburgh, PA 15220

408. Mark S. Laser
Solar Turbines, Inc.
2211 Erie Street
San Diego, CA 92110

409. S. K. Lau
Carborundum Company
Technology Division
P.O. Box 832, B-100
Niagara Falls, NY 14302

410. Edward A. Lauder
Advanced Composite Materials
Corporation
1525 South Buncombe Road
Greer, SC 29651-9208

411. J. Lawrence Lauderdale
Babcock & Wilcox
Contract Research Division
1850 "K" Street, Suite 950
Washington DC 20006

412. Harry A. Lawler
Carborundum Company
Technology Division
P.O. Box 832
Niagara Falls, NY 14302

413. Jean F. LeCostaouec
Textron Speciality Materials
2 Industrial Avenue
Lowell, MA 01851

414. Benson P. Lee
Interscience, Inc.
9718 Lake Shore Boulevard
Cleveland, OH 44108

415. Burtrand I. Lee
Clemson University
Department of Ceramic Engineering
Olin Hall
Clemson, SC 29634-0907

416. June-Gunn Lee
KIST
Structural Ceramic Lab
P.O. Box 131, Cheong-Ryang
Seoul 130-650
KOREA

417. Ran-Rong Lee
Ceramics Process Systems Corporation
155 Fortune Boulevard
Milford, MA 01757

418. Stan Levine
NASA Lewis Research Center
21000 Brookpark Road
MS:49-3
Cleveland, OH 44135

419. Alan V. Levy
Lawrence Berkeley Laboratory
One Cyclotron Road, MS:62-203
Berkeley, CA 94720

420. Ai-Kang Li
Materials Research Laboratories, ITRI
195-5 Chung-Hsing Road, Sec. 4
Chutung Hsinchu 31015 R.O.C.
TAIWAN

421. Winston W. Liang
Hong Kong Industrial Technology Centre Co. Ltd.
78 Tat Chee Avenue
4/F, HKPC Building
Howloon
HONG KONG

422. Robert Licht
Norton Company
Advanced Ceramics
Goddard Road
Northboro, MA 01532-1545

423. E. Lilley
Norton Company
Advanced Ceramics
Goddard Road
Northboro, MA 01532-1545

424. Laura J. Lindberg
Allied-Signal Aerospace Company
Garrett Fluid Systems Division
1300 West Warner
MS: 93-901-1207-4TT
P.O. Box 22200
Tempe, AZ 85285-2200

425. Leonard C. Lindgren
General Motors Corporation
Allison Gas Turbine Division
P.O. Box 420, Speed Code:T-20A
Indianapolis, IN 46206-0420

426. Hans A. Lindner
Cremer Forschungsinstitut GmbH&Co.KG
Oeslauer Strasse 35
D-8633 Rodental 8866
GERMANY

427. Ronald E. Loehman
Sandia National Laboratories
Chemistry & Ceramics Department 1840
P.O. Box 5800
Albuquerque, NM 87185

428. Jeffrey C. Logas
Winona State University
Composite Materials Engineering
115 Pasteur Hall
Winona, MN 55987

429. Bill Long
Babcock and Wilcox
P.O. Box 11165
Lynchburg, VA 24506

430. William D. Long
Wacker Chemicals (USA), Inc.
ESK Engineered Ceramics
50 Locust Avenue
New Canaan, CT 06840

431. L. A. Lott
EG&G Idaho, Inc.
Idaho National Engineering Laboratory
P.O. Box 1625
Idaho Falls, ID 83415-2209

432. Raouf O. Loutfy
MER Corporation
7960 South Kolb Road
Tucson, AZ 85706

433. Gordon R. Love
Aluminum Company of America
Alcoa Technical Center
Alcoa Center, PA 15069

434. Lydia Luckevich
Ortech International
2395 Speakman Drive
Mississauga Ontario L5K 183
CANADA

435. James W. MacBeth
Carborundum Company
Structural Ceramics Division
P.O. Box 1054
Niagara Falls, NY 14302

436. H. MacLaren
General Electric Company
Thomson Laboratory, Materials Engineering 36807
1000 Western Avenue
Lynn, MA 01910

437. George Maczura
Aluminum Company of America
Industrial Chemicals Division
670 One Allegheny Square
Pittsburgh, PA 15212

438. David Maginnis
Tinker AFB
OC-ALC/LIIRE
Tinker AFB OK 73145-5989

439. Frank Maginnis
Aspen Research, Inc.
220 Industrial Boulevard
Moore, OK 73160

440. Tai-il Mah
Universal Energy Systems, Inc.
Ceramics and Composites Research
4401 Dayton-Xenia Road
Dayton, OH 45432

441. Kenneth M. Maillar
Barbour Stockwell Company
83 Linskey Way
Cambridge, MA 02142

442. Lorenzo Majno
Instron Corporation
100 Royall Street
Canton, MA 02021

443. S. G. Malghan
National Institute of Standards and Technology
I-270 & Clopper Road
Gaithersburg, MD 20899

444. Lars Malmrup
United Turbine AB
Box 13027
Malmo S-200 44
SWEDEN

445. John Mangels
Ceradyne, Inc.
3169 Redhill Avenue
Costa Mesa, CA 92626

446. Russell V. Mann
Matec Applied Sciences, Inc.
75 South Street
Hopkinton, MA 01748

447. William R. Manning
Champion Aviation Products Division
Old Norris Road
P.O. Box 686
Liberty, SC 29657

448. Ken Marnoch
Amercom, Inc.
8928 Fullbright Avenue
Chatsworth, CA 91311

449. Robert A. Marra
Aluminum Company of America
Alcoa Technical Center
Advanced Ceramics Center - E
Alcoa Center, PA 15069

450. Chauncey L. Martin
3M Company
3M Center, Building 60-1N-01
St. Paul, MN 55144

451. Steven C. Martin
Advanced Refractory
Technologies, Inc.
699 Hertel Avenue
Buffalo, NY 14207

452. Kelly J. Mather
Williams International
Corporation
2280 West Maple Road
P.O. Box 200
Walled Lake, MI 48088

453. James P. Mathers
3M Company
3M Center
Building 201-3N-06
St. Paul, MN 55144

454. Marshall Mayer
Instron Corporation
3815 Presidential Parkway,
Suite 100
Atlanta, GA 30340

455. Ron Mayville
Arthur D. Little, Inc.
15-163 Acorn Park
Cambridge, MA 02140

456. F. N. Mazadarany
General Electric Company
Research Laboratory
Building K-1, Room MB-159
P.O. Box 8
Schenectady, NY 12301

457. James W. McCauley
Alfred University
NYS College of Ceramics
Binns-Merrill Hall
Alfred, NY 14802

458. Louis R. McCreight
2763 San Ramon Drive
Rancho Palos Verdes, CA 90274

459. Colin F. McDonald
McDonald Thermal Engineering
1730 Castellana Road
La Jolla, CA 92037

460. B. J. McEntire
Norton Company, TRW Ceramics
Goddard Road
Northboro, MA 01532-1545

461. Chuck McFadden
Coors Ceramics Company
600 9th Street
Golden, CO 80401

462. Henry McFadden
Magnetic Bearings, Inc.
Engineering Library
609 Rock Road
Radford, VA 24141

463. Thomas D. McGee
Iowa State University
Materials Science and
Engineering Department
110 Engineering Annex
Ames, IA 50011

464. Carol McGill
Corning Inc.
Sullivan Park, FR-02-08
Corning, NY 14831

465. T. C. McLaren
Cameron Forged Products
Company
P.O. Box 1212
Houston, TX 77251-1212

466. James McLaughlin
Sundstrand Power Systems
4400 Ruffin Road
P.O. Box 85757
San Diego, CA 92186-5757

467. Arthur F. McLean
6225 North Camino Almonte
Tucson, AZ 85718

468. Matt McMonigle
U.S. Department
of Energy
Improved Energy Productivity
Division
Forrestal Building,
CE-231
Washington, DC 20585

469. Dennis McMurtry
EG&G Idaho, Inc.
Idaho National Engineering
Laboratory
P.O. Box 1625
Idaho Falls, ID 83415

470. D. B. Meadowcroft
National Power Technology
and Environmental Centre
Kelvin Avenue
Leatherhead Surrey
KT22 7SE
ENGLAND

471. Jo Meglen
11004 Birdfoot Court
Reston, VA 22091

472. Pankaj K. Mehrotra
Kennametal, Inc.
P.O. Box 639
Greensburg, PA 15601

473. Joseph J. Meindl
Reynolds International, Inc.
6603 West Broad Street
P.O. Box 27002
Richmond, VA 23261-7003

474. Michael D. Meiser
Allied-Signal Aerospace Company
Garrett Ceramic Components
Division
19800 South Van Ness Avenue
Torrance, CA 90509

475. George Messenger
National Research Council of
Canada
Engine laboratory
Building M-7
Ottawa Ontario K1A OR6
CANADA

476. D. Messier
U.S. Army Materials Technology
Laboratory
SLCMT-EMC
405 Arsenal Street
Watertown, MA 02172-0001

477. Gary L. Messing
Pennsylvania State University
Ceramic Science and Engineering
Department
119 Steidle Building
University Park, PA 16802

478. Arthur G. Metcalfe
Arthur G. Metcalfe and
Associates, Inc.
2108 East 24th Street
National City, CA 91950

479. R. Metselaar
Eindhoven University
Centre for Technical Ceramics
P.O. Box 513
Eindhoven 5600 MB
THE NETHERLANDS

480. David J. Michael
Harbison-Walker Refractories
Company
P.O. Box 98037
Pittsburgh, PA 15227

481. Ken Michaels
Chrysler Motors Corporation
Ceramics Development
Metallurgical Processes
P.O. Box 1118, CIMS:418-17-09
Detroit, MI 48288

482. Bernd Michel
Institute of Mechanics
Fracture and Micromechanics Department
P.O. Box 408
D-9010 Chemnitz
GERMANY

483. John V. Milewski
Superkinetics, Inc.
P.O. Box 8029
Santa Fe, NM 87504

484. Carl E. Miller
AC Rochester
1300 North Dort Highway, MS:32-31
Engineering Building B
Flint, MI 48556

485. Mike Miller
McGraw Hill Aviation Week
Performance Materials
1156 15th Street, N.W.
Washington DC 20005

486. Charles W. Miller, Jr.
Centorr Furnaces/Vacuum Industries
542 Amherst Street
Nashua, NH 03063

487. R. Mininni
Enichem America
2000 Cornwall Road
Monmouth Junction, NJ 08852

488. Michele V. Mitchell
Allied-Signal Aerospace Company
Garrett Ceramic Components Division
19800 South Van Ness Avenue
Torrance, CA 90501-1149

489. Howard Mizuhara
GTE - WESGO
477 Harbor Boulevard
Belmont, CA 94002

490. Francois R. Mollard
Metalworking Technology, Inc.
1450 Scalp Avenue
Johnstown, PA 15904

491. Phil Mooney
Panametrics
NDE Division
221 Crescent Street
Waltham, MA 02254

492. Thomas Morel
Ricardo North America
645 Blackhawk Drive
Westmont, IL 60559

493. Geoffrey P. Morris
3M Company
3M Traffic Control Materials Division
Bldg. 209-BW-10, 3M Center
St. Paul, MN 55144-1000

494. Jay A. Morrison
Rolls-Royce, Inc.
Engineering and Information Center, Overlook 1
2849 Paces Ferry Road, Suite 450
Atlanta, GA 30339-3769

495. Joel P. Moskowitz
Ceradyne, Inc.
3169 Redhill Avenue
Costa Mesa, CA 92626

496. Brij Moudgil
University of Florida
Material Science & Engineering
Gainesville, FL 32611

497. Christoph J. Mueller
Sprechsaal Publishing Group
P.O. Box 2962, Mauer 2
D-8630 Coburg
GERMANY

498. Thomas W. Mullan
Vapor Technologies Inc.
345 Route 17 South
Upper Saddle River, NJ 07458

499. M. K. Murthy
MKM Consultants International
10 Avoca Avenue, Unit 1906
Toronto Ontario M4T 2B7
CANADA

500. Solomon Musikant
TransCon Technologies, Inc.
Materials Science & Engineering
1508 Waynesboro Road
Paoli, PA 19301

501. David L. Mustoe
Custom Technical Ceramics
8041 West I-70 Service Road,
Unit 6
Arvada, CO 80002

502. Curtis V. Nakaishi
U.S. Department of Energy
Morgantown Energy Technology
Center
Collins Ferry Road
P.O. Box 880
Morgantown, WV 26507-0880

503. Yoshio Nakamura
Faicera Research Institute
2-5-8 Hiyakunin-cho Shinjuku-Ko
Tokyo
JAPAN

504. K. S. Narasimhan
Hoeganaes Corporation
River Road
Riverton, NJ 08077

505. Samuel Natansohn
GTE Laboratories, Inc.
40 Sylvan Road
Waltham, MA 02254

506. Robert Naum
Applied Resources, Inc.
P.O. Box 241
Pittsford, NY 14534

507. Malcolm Naylor
Cummins Engine Company, Inc.
P.O. Box 3005, Mail Code 50183
Columbus, IN 47202-3005

508. Jeffrey Neil
GTE Laboratories, Inc.
40 Sylvan Road
Waltham, MA 02254

509. Fred A. Nichols
Argonne National Laboratory
9700 South Cass Avenue
MCT - Building 212
Argonne, IL 60439

510. H. Nickel
Furschungszentrum Jüelich GmbH
P.O. Box 1913
Jüelich 1-5170 BRD NRW
GERMANY

511. Dale E. Niesz
Rutgers University
Center for Ceramic Research
P.O. Box 909
Piscataway, NJ 08855-0909

512. David M. Nissley
United Technologies Corporation
Pratt & Whitney Aircraft
400 Main Street, MS:163-10
East Hartford, CT 06108

513. Richard D. Nixdorf
ReMaxCo Technologies, Inc.
11317 Snyder Road
Knoxville, TN 37932

514. Bernard North
Kennametal, Inc.
P.O. Box 639
Greensburg, PA 15601

515. Bruce E. Novich
Ceramics Process Systems
Corporation
155 Fortune Boulevard
Milford, MA 01757

516. Daniel Oblas
GTE Laboratories, Inc.
40 Sylvan Road
Waltham, MA 02254

517. Don Ohanehi
Magnetic Bearings, Inc.
1908 Sussex Road
Blacksburg, VA 24060

518. Robert Orenstein
General Electric Company
55-112, River Road
Schenectady, NY 12345

519. Norb Osborn
Aerodyne Dallas
151 Regal Row,
Suite 120
Dallas, TX 75247

520. A. M. Paddick
BP International Limited
BP Research Centre, Main
Library
Chertsey Road
Subury-on-Thames
Middlesex TW16 7LN
UNITED KINGDOM

521. Russell J. Page
Kanthal-Artcor
3001 Redhill Avenue, II-109
Costa Mesa, CA 92705

522. Richard Palicka
Cercom, Inc.
1960 Watson Way
Vista, CA 92083

523. Muktesh Paliwal
GTE Products Corporation
Hawes Street
Towanda, PA 18848

524. Joseph E. Palko
General Electric Company
55-113, River Road
Schenectady, NY 12345

525. Hayne Palmour, III
North Carolina State
University
Materials Science and
Engineering Dept.
Raleigh, NC 27605-7905

526. Joseph N. Panzarino
Norton Company
Advanced Ceramics
Goddard Road
Northboro, MA 01532-1545

527. Pellegrino Papa
Corning Inc.
MP-WX-02-1
Corning, NY 14831

528. E. Beth Pardue
Technology for Energy
Corporation
One Energy Center
P.O. Box 22996
Knoxville, TN 37933-0996

529. Soon C. Park
3M Company
3M Center
Building 142-4N-02
P.O. Box 2963
St. Paul, MN 55144

530. Hartmut Paschke
Schott Glaswerke
Christoph-Dorner-Strasse 29
D-8300 Landshut
GERMANY

531. Marina R. Pascucci
GTE Laboratories, Inc.
40 Sylvan Road
Waltham, MA 02254

532. Arvid E. Pasto
GTE Laboratories Inc.
40 Sylvan Road
Waltham, MA 02254

533. James W. Patten
Cummins Engine
Company, Inc.
Materials Engineering
P.O. Box 3005, Mail
Code 50183
Columbus, IN 47202-3005

534. Robert A. Penty
Eastman Kodak Company
KAD/D73 - 35612
901 Elmgrove Road
Rochester, NY 14653

535. Robert W. Pepper
Textron Specialty Materials
2 Industrial Avenue
Lowell, MA 01851

536. Peter Perdue
Detroit Diesel Corporation
Research Advanced Development Group
13400 West Outer Drive, Speed Code A-07
Detroit, MI 48239-4001

537. Bruce Peters
Dow Chemical Company
Building 52
Midland, MI 48667

538. John J. Petrovic
Los Alamos National Laboratory
Group MST-4, MS:6771
Los Alamos, NM 87545

539. Frederick S. Pettit
University of Pittsburgh
Pittsburgh, PA 15261

540. Ben A. Phillips
Phillips Engineering Company
721 Pleasant Street
St. Joseph, MI 49085

541. Richard C. Phoenix
Ohmtek, Inc.
2160 Liberty Drive
Niagara Falls, NY 14302

542. Bruce J. Pletka
Michigan Technological University
Metallurgical & Materials Engineering Department
Houghton, MI 49931

543. John P. Pollinger
Garrett Ceramic Components
19800 South Van Ness Avenue
Torrance, CA 90509

544. P. Popper
High Technology Ceramics International Journal
22 Pembroke Drive
Westlands Newcastle-under-Lyme Staffs ST5 2JN
ENGLAND

545. F. Porz
Universitat Karlsruhe
Institut fur Keramik Im Maschinendau
Postfach 6980
D-7500 Karlsruhe
GERMANY

546. Harry L. Potma
Royal Netherlands Embassy
Science and Technology
4200 Linnean Avenue, N.W.
Washington DC 20008

547. Bob R. Powell
General Motors Research Laboratories
Metallurgy Department
30500 Mound Road
Box 9055
Warren, MI 48090-9055

548. David B. Powell
Southern Research Institute
Experimental Mechanics Section
2000 Ninth Avenue South
P.O. Box 55305
Birmingham, AL 35255-5305

549. Stephen C. Pred
ICD Group, Inc.
1100 Valley Brook Avenue
Lyndhurst, NJ 07071

550. Karl M. Prewo
United Technologies Research Center
411 Silver Lane
MS:24
East Hartford, CT 06108

551. Peter E. Price
Industrial Materials Technology, Inc.
P.O. Box 9565
Andover, MA 01810

552. Joseph M. Proud
GTE Laboratories Inc.
Materials Science Laboratory
40 Sylvan Road
Waltham, MA 02254

553. Vimal K. Pujari
Norton Company
Advanced Ceramics
Goddard Road
Northboro, MA 01532-1545

554. George Quinn
National Institute of Standards and Technology
Ceramics Division, Bldg. 223
Gaithersburg, MD 20899

555. Ramas V. Raman
Ceracon, Inc.
1101 North Market Boulevard, Suite 9
Sacramento, CA 95834

556. K. S. Ramesh
Battelle Columbus Laboratories
Metals and Ceramics Department
505 King Avenue
Columbus, OH 43201-2693

557. Charles F. Rapp
Owens Corning Fiberglass
2790 Columbus Road
Granville, OH 43023-1200

558. Dennis W. Readey
Colorado School of Mines
Department of Metallurgy and Materials Engineering
Golden, CO 80401

559. Wilfred J. Rebello
PAR Enterprises, Inc.
12601 Clifton Hunt Lane
Clifton, VA 22024

560. H. E. Rebenne
GTE Laboratories, Inc.
40 Sylvan Road
Waltham, MA 02254

561. Harold Rechter
Chicago Fire Brick Company
R&D
7531 South Ashland Avenue
Chicago, IL 60620

562. Robert R. Reeber
U.S. Army Research Office
P.O. Box 12211
Research Triangle Park, NC 27709

563. K. L. Reifsnider
Virginia Polytechnic Institute and State University
Department of Engineering Science and Mechanics
Blacksburg, VA 24061

564. Paul E. Rempes
McDonnell Douglass Missle Systems Company
P.O. Box 516,
Mail Code:1066086
St. Louis, MO 63166-0516

565. Gopal S. Revankar
John Deere Company
Metals Research
3300 River Drive
Moline, IL 61265

566. K. T. Rhee
Rutgers University
Mechanical Engineering
P.O. Box 909
Piscataway, NJ 08854

567. James Rhodes
Advanced Composite Materials Corporation
1525 South Buncombe Road
Greer, SC 29651

568. Roy W. Rice
W. R. Grace and Company
7379 Route 32
Columbus, MD 21044

569. David W. Richerson
Ceramatec, Inc.
2425 South 900 West
Salt Lake City, UT 84119

570. Tomas Richter
J. H. France Refractories
1944 Clarence Road
Snow Shoe, PA 16874

571. Michel Rigaud
Ecole Polytechnique
Campus Universite De Montreal
P.O. Box 6079, Station A
Montreal, P.Q Quebec H3C 3A7
CANADA

572. R. E. Riman
Rutgers University
Ceramics Engineering Department
P.O. Box 909
Piscataway, NJ 08855-0909

573. Barry Ringstrom
Superior Graphite Company
P.O. Box 2373
Smyrna, GA 30081

574. John E. Ritter
University of Massachusetts
Mechanical Engineering
Department
Amherst, MA 01003

575. Frank L. Roberge
Allied-Signal Aerospace Company
Garrett Auxiliary Powder
Division
P.O. Box 5227
Phoenix, AZ 85010

576. W. Eric Roberts
Advanced Ceramic Technology, Inc.
990 "F" Enterprise Street
Orange, CA 92667

577. Martha Rohr
U.S. Department of Energy
Oak Ridge Operations
Building 4500N
P.O. Box 2008, MS:6269
Oak Ridge, TN 37831-6269

578. Y. G. Roman
TNO TPD Keramick
P.O. Box 595
Einhoven 5600 AN
HOLLAND

579. Mark D. Roos
Carborundum Company
P.O. Box 156
Niagara Falls, NY 14302

580. Michael Rossetti
Arthur D. Little, Inc.
15 Acorn Park
Cambridge, MA 01240

581. Barry R. Rossing
Lanxide Corporation
1300 Marrows Road
Newark, DE 19714-6077

582. Steven L. Rotz
Lubrizol Corporation
29400 Lakeland Boulevard
Wickliffe, OH 44092

583. Bruce Rubinger
Global Competitiveness, Inc.
One Devonshire Place,
Suite 1011
Boston, MA 02109

584. Robert Ruh
Wright Laboratory
WL/MLLM
Wright-Patterson AFB, OH 45433

585. Robert J. Russell
17 Highgate Road
Framingham, MA 01701

586. L. William Sahley
Supermaterials Company
24400 Highland Road
Richmond Heights, OK 44143

587. Jon Salem
NASA Lewis Research Center
21000 Brookpark Center
Cleveland, OH 44135

588. W. A. Sanders
NASA Lewis Research Center
21000 Brookpark Road,
MS:49-3
Cleveland, OH 44135

589. J. Sankar
North Carolina A&T State
University
Department of Mechanical
Engineering
Greensboro, NC 27411

590. Yasushi Sato
NGK Spark Plugs (U.S.A.), Inc.
1200 Business Center Drive,
Suite 300
Mt. Prospect, IL 60056

591. Maxine L. Savitz
Allied-Signal Aerospace
Company
Garrett Ceramic Components
Division
19800 South Van Ness Avenue
Torrance, CA 90501

592. Ashok Saxena
Georgia Institute of
Technology
Materials Engineering
Atlanta, GA 30332-0245

593. David W. Scanlon
Instron Corporation
100 Royall Street
Canton, MA 02021

594. Charles A. Schacht
Schacht Consulting Services
12 Holland Road
Pittsburgh, PA 15235

595. James Schienle
Allied-Signal Aerospace
Company
Garrett Auxiliary Power
Division
P.O. Box 5227, MS:1302-2P
Phoenix, AZ 85010

596. John C. Schneider
San Juan Technologies
P.O. Box 49326
Colorado Springs, CO 80949-9326

597. Gary Schnittgrund
Rocketdyne, BA05
6633 Canoga Avenue
Canoga Park, CA 91303

598. Mark Schomp
Lonza, Inc.
Corporate Headquarters
17-17 Route 208
Fair Lann, NJ 07410

599. Joop Schoonman
Delft University of Technology
Laboratory for Inorganic
Chemistry
P.O. Box 5045
2600 GA Delft
THE NETHERLANDS

600. John Schuldies
Industrial Ceramic
Technology, Inc.
37 Enterprise Drive
Ann Arbor, MI 48103

601. Robert B. Schulz
U.S. Department of Energy
Office of Transportation
Materials
CE-34, Forrestal Building
Washington, DC 20585

602. Murray A. Schwartz
Materials Technology
Consulting, Inc.
30 Orchard Way, North
Potomac, MD 20854

603. Peter Schwarzkopf
SRI International
333 Ravenswood Avenue
Menlo Park, CA 94025

604. Thomas C. Schweizer
Princeton Economic Research, Inc.
12300 Twinbrook Pkwy., Suite 650
Rockville, MD 20852

605. William T. Schwessinger
Multi-Arc Scientific
Coatings
1064 Chicago Road
Troy, MI 48083-4297

606. W. D. Scott
University of Washington
Materials Science Department
Mail Stop:FB10
Seattle, WA 98195

607. Nancy Scoville
Thermo Electron Technologies
74 West Street
P.O. Box 9046
Waltham, MA 02254-9046

608. Brian Seegmiller
Coors Ceramics Company
600 9th Street
Golden, CO 80401

609. T. B. Selover
AICRE/DIPPR
3575 Traver Road
Shaker Heights, OH 44122

610. Charles E. Semler
Semler Materials Services
4160 Mumford Court
Columbus, OH 43220

611. Thomas Service
Service Engineering Laboratory
324 Wells Street
Greenfield, MA 01301

612. Kish Seth
Ethyl Corporation
R&D Laboratories
P.O. Box 341
Baton Rouge, LA 70821

613. William J. Shack
Argonne National Laboratory
9700 South Cass Avenue
Building 212
Argonne, IL 60439

614. Peter T. B. Shaffer
Technical Ceramics
Laboratories, Inc.
4045 Nine/McFarland Drive
Alpharetta, GA 30201

615. Richard K. Shaltens
NASA Lewis Research Center
21000 Brookpark Road,
MS:301-2
Cleveland, OH 44135

616. Robert S. Shane
238 Hemlock Road
Wynnewood, PA 19096

617. Daniel Shanefield
Rutgers University
Ceramics Engineering
Department
P.O. Box 909
Piscataway, NJ 08855-0909

618. Ravi Shankar
Chromalloy
Research and Technology
Division
Blaisdell Road
Orangeburg, NY 10962

619. Terence Sheehan
Alpex Wheel Company
727 Berkley Street
New Milford, NJ 07646

620. Dinesh K. Shetty
University of Utah
304 EMRO, Dept. of Materials
Science and Engineering
Salt Lake City, UT 84112

621. Masahide Shimizu
Ceramic Society of Japan
2-2-503 Takiyama 6-chome
Higashikurume-Shi Tokyo 203
JAPAN

622. John Shipinski
Toyota Technical Center
U.S.A., Inc.
Technical Research Department
2000 Town Center, Suite 500
Southfield, MI 48075

623. Thomas Shreves
American Ceramic Society, Inc.
Library
757 Brooksedge Plaza Drive
Westerville, OH 43081-2821

624. Jack D. Sibold
Coors Ceramics Company
600 Ninth Street
Golden, CO 80401

625. George H. Siegel
Point North Associates, Inc.
P.O. Box 907
Madison, NJ 07940

626. Richard Silberglitt
Technology Assessment and
Transfer, Inc.
133 Defense Highway, #212
Annapolis, MD 21401

627. Mary Silverberg
Norton Company
Advanced Ceramics Library
Goddard Road
Northboro, MA 01532-1545

628. Gurpreet Singh
Department of the Navy
Internal Combustion & Gas Turbine Engine Division
Code 56X31
Washington DC 20362-5101

629. Maurice J. Sinnott
University of Michigan
Chemical and Metallurgical Engineering
5106 IST Building
Ann Arbor, MI 48109-2099

630. John Skildum
3M Company
3M Center
Building 224-2S-25
St. Paul, MN 55144

631. David P. Smith
Hoskins, Rees & Smith
1910 Cochran Road
Manor Oak II, Suite 658
Pittsburgh, PA 15220

632. Richard H. Smoak
Smoak & Associates
3554 Hollyslope Road
Altadena, CA 91001-3923

633. Jay R. Smyth
Allied-Signal Aerospace Company
Garrett Auxiliary Power Division
P.O. Box 5227
MS:93-173/1303-207
Phoenix, AZ 85010

634. Edward A. Snajdr
Premier Refractories and Chemicals, Inc.
P.O. Box 392
Findlay, OH 44815

635. Rafal A. Sobotowski
British Petroleum Company
Technical Center, Broadway
3092 Broadway Avenue
Cleveland, OH 44115

636. S. Somiya
Nishi Tokyo University
3-7-19 Seijo, Setagaya
Tokyo 157
JAPAN

637. Boyd W. Sorenson
DuPont Lanxide Composites
1300 Marrows Road
P.O. Box 6077
Neward, DE 19707

638. Charles A. Sorrell
U.S. Department of Energy
Advanced Industrial Concepts Division
CE-232, Forrestal Building
Washington, DC 20585

639. C. Spencer
EA Technology
Capenhurst Chester
CH1 6ES
UNITED KINGDOM

640. Allen Spizzo
Hercules Inc.
Hercules Plaza
Wilmington, DE 19894

641. Richard M. Spriggs
Alfred University
Center for Advanced Ceramic Technology
Alfred, NY 14802

642. Charles Spuckler
NASA Lewis Research Center
21000 Brookpark Road
MS: 5-11
Cleveland, OH 44135-3191

643. M. Srinivasan
Material Solutions
P.O. Box 663
Grand Island, NY 14702-0663

644. Gordon L. Starr
Cummins Engine Company, Inc.
Design & Technology
P.O. Box 3005
Mail Code 50182
Columbus, IN 47202-3005

645. Jim Stevenson
Windrock, Incorporated
154 Fairbanks Plaza
Oak Ridge, TN 37830

646. Tom Stillwagon
Allied-Signal Aerospace Company
AiResearch Los Angeles Division, Dept. 93274
2525 West 190th Street, MS:T-42
Torrance, CA 90509

647. Harold L. Stocker
General Motors Corporation
Allison Gas Turbine Division
P.O. Box 420
Indianapolis, IN 46206

648. Paul D. Stone
Dow Chemical USA
1776 "Eye" Street, N.W., Suite 575
Washington DC 20006

649. Roger S. Storm
Carborundum Company
Technology Division
P.O. Box 337
Niagara Falls, NY 14302-0337

650. Peter A. Stranges
4 Chittenden Lane
Owings Mills, MD 21117

651. F. W. Stringer
Aero & Industrial Technology Ltd.
P.O. Box 46, Wood Top
Burnley Lancashire BB11 4BX
UNITED KINGDOM

652. Thomas N. Strom
NASA Lewis Research Center
21000 Brookpark Road
MS:86-6
Cleveland, OH 44135

653. M. F. Stroosnijder
Institute for Advanced Materials
Joint Research Centre
21020 Ispra (VA)
ITALY

654. Karsten Styhr
30604 Ganado Drive
Rancho Palos Verdes, CA 90274

655. T. S. Sudarshan
Materials Modification, Inc.
2946-2H Sleepy Hollow Road
P.O. Box 4817
Falls Church, VA 22044

656. M. J. Sundaresan
University of Miami
Mechanical Engineering Department
P.O. Box 248294
Coral Gables, FL 33124

657. Willard H. Sutton
United Technologies Corporation
Research Center, MS:24
Silver Lane
East Hartford, CT 06108

658. Ron Sviben
100 Indel Avenue
Rancocas, NJ 08073

659. J. J. Swab
U.S. Army Materials Technology Laboratory
Ceramics Research Division
SLCMT-EMC
405 Arsenal Street
Watertown, MA 02172

660. Robert E. Swanson
Metalworking Technology, Inc.
1450 Scalp Avenue
Johnstown, PA 15904

661. Scott L. Swartz
Battelle Columbus Laboratories
Metals and Ceramics
505 King Avenue
Columbus, OH 43201

662. Steve Szaruga
Air Force Wright Aeronautical Laboratory
Materials Directorate
WL/MLBC
Wright-Patterson AFB, OH 45433-6533

663. Yo Tajima
NGK Spark Plug Company, Ltd.
NTK Technical Ceramic Division
2808 Iwasaki
Komaki-shi Aichi-ken 485
JAPAN

664. Fred Teeter
5 Tralee Terrace
East Amherst, NY 14051

665. Monika O. Ten Eyck
Carborundum Company
Technology Division
P.O. Box 832
Niagara Falls, NY 14302

666. D. Scot Thompson
Allied-Signal Aerospace Company
7550 Lucerne Drive, #203
Middleburg Heights, OH 44130

667. David F. Thompson
Corning Glass Works
SP-DV-02-1
Corning, NY 14831

668. Merle L. Thorpe
Hobart Tafa Technologies, Inc.
146 Pembroke Road
Concord, NH 03301

669. Eberhard Tiefenbacher
Daimler-Benz AG Abt. F1S
Mercedes-Strabe 136
Stuttgart 60
GERMANY

670. T. Y. Tien
University of Michigan
Materials Science and Engineering Department
Dow Building
Ann Arbor, MI 48103

671. Julian M. Tishkoff
Air Force Office of Scientific Research
AFOSR/NA
Bolling AFB, DC 20332-6448

672. D. M. Tracey
Norton Company
Advanced Ceramics
Goddard Road
Northboro, MA 01532-1545

673. Dick Trippett
General Motors Corporation
Allison Gas Turbine Division
P.O. Box 420, MS:W-16
Indianapolis, IN 46206-0420

674. L. J. Trostel, Jr.
Box 199
Princeton, MA 01541

675. W. T. Tucker
General Electric Company
Corporate R&D
Building K1-4C35
P. O. Box 8
Schenectady, NY 12301

676. Masanori Ueki
Nippon Steel Corporation
Central R&D Bureau
1618 Ida
Nakahara-Ku Kawasaki 211
JAPAN

677. Filippo M. Ugolini
ATA Studio
Via Degli Scipioni, 268A
ROMA 00192
ITALY

678. Donald L. Vaccari
Allison Gas Turbines
P.O. Box 420
Speed Code S49
Indianapolis, IN 46206-0420

679. Carl F. Van Conant
Boride Products, Inc.
2879 Aero Park Drive
Traverse City, MI 49684

680. Marcel H. Van De Voorde
Commission of the European Communities
Institute for Advanced Materials
Joint Research Centre
P.O. Box 2
1755 ZG Petten
THE NETHERLANDS

681. O. Van Der Biest
Katholieke Universiteit Leuven
Departement Metaalkunde en Toegepaste
de Croylaan 2
B-3030 Leuven
BELGIUM

682. Michael Vannier
Washington University, St. Louis
Mallinckrodt Institute of Radiology
510 South Kings Highway
St. Louis, MO 63110

683. Stan Venkatesan
Southern Coke & Coal Corporation
P.O. Box 52383
Knoxville, TN 37950

684. V. Venkateswaran
Carborundum Company
Niagara Falls R&D Center
P.O. Box 832
Niagara Falls, NY 14302

685. Dennis Viechnicki
U.S. Army Materials Technology Laboratory
405 Arsenal Street
Watertown, MA 02172-0001

686. Ted Vojnovich
U.S. Department of Energy
Office of Transportation Technologies
CE-34, Forrestal Building
Washington, DC 20585

687. John D. Volt
E. I. Dupont de Nemours & Company, Inc.
P.O. Box 80262
Wilmington, DE 19880

688. John B. Wachtman
Rutgers University
Ceramics Department
P.O. Box 909
Piscataway, NJ 08855

689. Shigetaka Wada
Toyota Central Research Labs, Inc.
Nagakute Aichi 480-11
JAPAN

690. Janet Wade
Allied-Signal Aerospace Company
Garrett Auxiliary Power Division, Department 93-772
P.O. Box 5227, MS:1303-2
Phoenix, AZ 85010

691. Richard L. Wagner
Ceramic Technologies, Inc.
537 Turtle Creek South Drive, Suite 24D
Indianapolis, IN 46227

692. J. Bruce Wagner, Jr.
Arizona State University
Center for Solid State Science
Tempe, AZ 85287-1704

693. Daniel J. Wahlen
Kohler, Co.
444 Highland Drive
Kohler, WI 53044

694. Ingrid Wahlgren
Royal Institute of Technology
Studsvik Library
S-611 82 Nykoping
SWEDEN

695. Ron H. Walecki
Allied-Signal Aerospace Company
Garrett Ceramic Components Division
19800 South Van Ness Avenue
Torrance, CA 90501

696. Michael S. Walsh
Vapor Technologies Inc.
2100 Central Avenue
Boulder, CO 80301

697. Chien-Min Wang
Industrial Technology Research Institute
Materials Research Laboratories
195 Chung-Hsing Road, Sec. 4
Chutung Hsinchu 31015 R.O.C.
TAIWAN

698. Robert M. Washburn
ASMT
11203 Colima Road
Whittier, CA 90604

699. Gerald Q. Weaver
Carborundum Specialty Products
42 Linus Allain Avenue
Gardner, MA 01440-2478

700. R. W. Weeks
Argonne National Laboratory
MCT-212
9700 South Cass Avenue
Argonne, IL 60439

701. Ludwig Weiler
ASEA Brown Boveri AG
Corporate Research
Eppelheimer Str. 82
D-6900 Heidelberg
GERMANY

702. James Wessel
Dow Corning Corporation
1800 "M" Street, N.W., Suite 325 South
Washington DC 20036

703. Robert D. West
Therm Advanced Ceramics
P.O. Box 220
Ithaca, NY 14851

704. Thomas J. Whalen
Ford Motor Company
26362 Harriet
Dearborn Heights, MI 48127

705. Ian A. White
Hoeganaes Corporation
River Road
Riverton, NJ 08077

706. Alan Whitehead
General Electric Company
1 River Road, 55-111
Schenectady, NY 12345

707. Sheldon M. Wiederhorn
National Institute of Standards and Technology
Building 223, Room A329
Gaithersburg, MD 20899

708. John F. Wight
Alfred University
McMahon Building
Alfred, NY 14802

709. D. S. Wilkinson
McMaster University
Materials Science and Engineering Department
1280 Main Street, West
Hamilton Ontario L8S 4L7
CANADA

710. James C. Williams
General Electric Company
Engineering Materials Technology Labs
One Neumann Way
Mail Drop: H85
Cincinnati, OH 45215-6301

711. Steve Williams
RCG Hagler Bailly, Inc.
370 L'Enfant Promonade, S.W., Suite 700
Washington DC 20024

712. Craig A. Willkens
Norton Company
Advanced Ceramics
Goddard Road
Northboro, MA 01532-1545

713. Roger R. Wills
TRW, Inc.
Valve Division
1455 East 185th Street
Cleveland, OH 44110

714. David Gordon Wilson
Massachusetts Institute of Technology
Mechanical Engineering Department
77 Massachusetts Avenue, Room 3-455
Cambridge, MA 02139

715. Matthew F. Winkler
Seaworthy Systems, Inc.
P.O. Box 965
Essex, CT 06426

716. Gerhard Winter
Hermann C. Starck Berlin GmbH, Werk Goslar
P.O. Box 25 40
D-3380 Goslar 3380
GERMANY

717. W. L. Winterbottom
Ford Motor Company
Material Systems Reliability Department
20000 Rotunda Drive
SRL, Room E-3182
P.O. Box 2053
Dearborn, MI 48121

718. David G. Wirth
Coors Ceramics Company
600 9th Street
Golden, CO 80401

719. Thomas J. Wissing
Eaton Corporation
Engineering & Research Center
P.O. Box 766
Southfield, MI 48037

720. James C. Withers
MER Corporation
7960 South Kolb Road
Building F
Tucson, AZ 85706

721. Dale E. Wittmer
Southern Illinois University
Mechanical Engineering Department
Carbondale, IL 62901

722. Warren W. Wolf
Owens Corning Fiberglass
2790 Columbus Road, Route 16
Granville, OH 43023

723. George W. Wolter
Howmet Turbine Components Corporation
Technical Center
699 Benston Road
Whitehall, MI 49461

724. James C. Wood
NASA Lewis Research Center
21000 Brookpark Road
MS:86-6
Cleveland, OH 44135

725. Marrill Wood
LECO Corporation
Augusta Division
P.O. Box 211688
Augusta, GA 30917-1688

726. Wayne L. Worrell
University of Pennsylvania
Department of Materials Science and Engineering
3231 Walnut Street
Philadelphia, PA 19104

727. John F. Wosinski
Corning Inc.
ME-2 E-5 H8
Corning, NY 14830

728. Ian G. Wright
Battelle Columbus Laboratories
505 King Avenue
Columbus, OH 43201

729. Ruth Wroe
ERDC
Metals & Materials Industries Division
Capenhurst Chester CH1 6ES
ENGLAND

730. Bernard J. Wrona
Advanced Composite Materials Corporation
1525 South Buncombe Road
Greer, SC 29651

731. Carl C. M. Wu
Naval Research Laboratory
Ceramic Branch, Code 6373
Washington DC 20375

732. J. G. Wurm
Commission of the European Communities
Advanced Materials Research Programme
Rue de la Loi 200
B-1049 Brussels
BELGIUM

733. John C. Wurst
University of Dayton Research Institute
300 College Park
Dayton, OH 45469-0101

734. Neil Wyant
ARCH Development Corp.
9700 South Cass Avenue
Building 202
Argonne, IL 60439

735. Roy Yamamoto
Texaco Inc.
P.O. Box 509
Beacon, NY 12508-0509

736. John Yamanis
Allied-Signal, Inc.
Ceramics Program
P.O. Box 1021
Morristown, NJ 07962-1021

737. Harry C. Yeh
Allied-Signal Aerospace Company
Garrett Ceramic Components Division
19800 South Van Ness Avenue
Torrance, CA 90509

738. Hiroshi Yokoyama
Hitachi Research Lab
4026 Kuji-Cho
Hitachi-shi Ibaraki 319-12
JAPAN

739. Thomas M. Yonushonis
Cummins Engine Company, Inc.
P.O. Box 3005
Mail Code 50183
Columbus, IN 47202-3005

740. Thomas J. Yost
Corning Inc.
Technical Products Division, Main Plant 21-1-2
Corning, NY 14831

741. Jong Yung
Sundstrand Aviation Operations
Department 789-6
4747 Harrison Avenue
Rockford, IL 61125

742. A. L. Zadoks
Caterpillar Inc.
Technical Center, Building L
P.O. Box 1875
Peoria, IL 61656-1875

743. Avi Zangvil
University of Illinois
Materials Research Laboratory
104 South Goodwin Avenue
Urbana, IL 61801

744. Anne Marie Zerega
U.S. Department of Energy
Office of Energy Research, ER-42
Washington, DC 20585

745. Ken Zillmer
Applied Test Systems, Inc.
2571 Mt. Gallant Road
Rock Hill, SC 29730

746. Carl Zweben
General Electric Company
P.O. Box 8555, VFSC/V4019
Philadelphia, PA 19101

747. Klaus M. Zwilsky
National Research Council
National Materials
Advisory Board
2101 Constitution Avenue
Washington, DC 20418

748. Department of Energy
DOE Field Office, Oak Ridge
Assistant Manager for Energy
Research and Development
P.O. Box 2001
Oak Ridge, TN 37831-8600

749–758. Department of Energy
Office of Scientific and
Technical Information
Office of Information
Services
P.O. Box 62
Oak Ridge, TN 37831

For distribution by microfiche
as shown in DOE/OSTI-4500,
Distribution Category UC-332
(Ceramics/Advanced Materials).

☆U.S. GOVERNMENT PRINTING OFFICE: 1992-648-072/60001